NATIONAL TECHNICAL UNIVERSITY OF ATHENS
SCHOOL OF MECHANICAL ENGINEERING
FLUIDS SECTION
LABORATORY OF HYDRAULIC TURBOMACHINES

DEVELOPMENT OF CAVITATION DETECTION METHODOLOGY FOR HYDRAULIC TURBOMACHINES USING EXPERIMENTAL AND NUMERICAL TOOLS

Georgios Mousmoulis

Dissertation submitted to the National Technical University of Athens
for the degree of Doctor of Philosophy

June 2020
Athens

NATIONAL TECHNICAL UNIVERSITY OF ATHENS
SCHOOL OF MECHANICAL ENGINEERING
FLUIDS SECTION
LABORATORY OF HYDRAULIC TURBOMACHINES

DEVELOPMENT OF CAVITATION DETECTION METHODOLOGY FOR HYDRAULIC TURBOMACHINES USING EXPERIMENTAL AND NUMERICAL TOOLS

PhD Thesis

Georgios Mousmoulis

Advisory Committee
I. Anagnostopoulos, Professor, NTUA, (Supervisor)
D. Papantonis, Emeritus Professor, NTUA
N. Aretakis, Associate Professor, NTUA

Examination Committee
I. Anagnostopoulos, Professor, NTUA, (Supervisor)
G. Aggidis, Professor, Lancaster University
N. Aretakis, Associate Professor, NTUA
I. Antoniadis, Professor, NTUA
D. Bouris, Associate Professor, NTUA
D. Mathioulakis, Professor, NTUA
S. Voutsinas, Professor, NTUA

June 2020
Athens

Contents

Abstract

Centrifugal pumps constitute one of the most common and essential component in most industrial procedures and other technical works and applications, while hydraulic turbines operate in numerous hydroelectric power plants worldwide, producing a substantial percentage of the consumed electricity. Consequently, the reliable and efficient operation of these machines is highly required. An important hydraulic excitation mechanism that may affect the steady and dynamic operation of a hydraulic turbomachinery is cavitation, which may be created in the low static pressure zone of the rotor. The re-liquification of the vapour bubbles at downstream positions is a very violent implosion procedure that generates shock pressure waves of extreme local intensity, which can cause extended wear of the solid surfaces of the machine. Long-term operation of a machine under cavitating conditions results in significant material removal, accompanied by strong vibrations and drop of performance. The present Thesis deals with the analysis of the flow conditions in centrifugal pumps that suffer from cavitation, and aims at the development of detection tools capable of identifying the presence of vapour formations promptly.

The present work attempts to approach the problem both experimentally and computationally. Two testing configurations that allow the flow visualisation of the phenomenon are developed; one at the Engineering Department of Lancaster University (LU) and one at the Laboratory of Hydraulic Turbomachines of the NTUA. In both test rigs, the regulation of the pump suction conditions (static pressure) is achieved by throttling the suction valve. The pump installed at the LU has its volute made from transparent material and uses three semi-open, radial impellers; i) one with six backward-curved blades and six splitter blades, ii) one with twelve radial blades, and iii) one with twelve forward-curved blades. On the other hand, the test configuration of the NTUA incorporates an industrial centrifugal pump with a closed impeller that has five backward-curved blades. Significant modifications are made to this pump in order to allow the visualizaton of the flow in its impeller. More specifically, the impeller is re-manufactured from scratch, with the shroud made of transparent material, while a transparent window is opened in the front casing of the pump.

Performance experiments are conducted for all four impellers and they are accompanied by noise and vibration measurements, as well as flow visualizaition observations. Two accelerometers and one acoustic emission sensor are used in each test rig, and their time-series measurements are processed so as to extract cavitation characteristics and develop a detection tool of general application. The signals obtained are processed in the time and frequency domain, with the application of statistical, Root Mean Square and Power Spectral Density tools. Moreover, the Spectral Kurtosis methodology for the construction of band pass filters that unmask cavitation characteristics in the measured data is implemented and tested in the framework of the Thesis.

In parallel, the fluid flow in two of the impellers is simulated under normal and two-phase flow conditions with the use of a commercial CFD algorithm. The modelling approach solves the Reynolds Averaged Navier Stokes Equations (RANS), along with a transport equation that regulates the mass transfer between the vapour and the liquid phase. The turbulence is modelled with the k-ω SST model, while the equations of the flow that correspond to the computational domain of the impeller are solved in the rotating reference frame (‘frozen’ rotor approach).

The characteristic operation curves derived for each impeller of the two test configurations, exhibit the expected trend of low specific speed centrifugal pumps. During cavitating conditions, the total head value remains unchanged until the point where the vapour cavity starts

to block the flowpath and finally, makes the impeller unable to provide power to the working medium (head break down). The flow visualisation data in the LU impellers depict the inception of the cavitation phenomenon and the progressive increase of its extent, as the available suction head level of the test rig decreases. Moreover, the photos obtained from the impellers' flow field, feature the existence of different large-scale cavitating formations, such as travelling bubble, cloud, tip clearance, and attached cavitation.

The flow visualization data and the laboratory measurements confirm the ability of the numerical model to reproduce the total head drop curve due to vapour phase development. The model faces difficulties to identify the vapour travelling bubbles close to their visual onset, due to their strong dynamic nature. However, its ability to predict the actual size and shape of the cavities improves significantly when the attached cavitation mechanism becomes stronger, at the intermediate stages of cavitation development, and well before the total head drop. In the NTUA pump, the computational results are also used to provide an improved prediction for the visual inception point of cavitation. Consequently, the proposed modelling approach can be used for detection of cavitation, provided that both the geometrical and operational data of a pump are given. Moreover, in case of the unshrouded impeller, the numerical results reveal the complex flow pattern at the blades tip clearance region, which includes secondary flows that recirculate part of the tip flow, back to the suction side of the blade, forming the backflow phenomenon. The latter may turn to backflow tip cavitation, when the pump operates under low static pressure conditions.

The noise and vibration measurements are obtained using the AE and accelerometer sensors, which are located on the body of the centrifugal pumps in both configurations. The raw noise and vibration data measured under severe cavitating conditions include peaks that are related to bubble implosion and affect their Gaussian distribution. The statistical analysis of the data associates these differentiations with the fourth statistical moment, the kurtosis parameter, which value deviates significantly from that of the normal distribution. The examination of the frequency spectrum of the noise and vibration signals illustrates the excitation of the wide ranges of the frequency spectrum. The use of RMS and powerband tools is qualified so as to integrate the power of the excited areas and plot it as function of suction conditions. The results demonstrate the successful use of these tools for the prompt detection of cavitation in the vast majority of the examined conditions. However, their difficulty to unmask the phenomenon in low loading conditions of the closed impeller, along with the risk to detect a different kind of impulsive fault (like faults related with rolling-element bearings) instead of cavitation, makes necessary the further analysis of the obtained signals.

For that reason, the Spectral Kurtosis signal processing method is tested to efficiently provide the band pass filter's characteristics that aim to unmask cavitation behaviour. In addition, the filtered signals are demodulated with the use of Hilbert Transformation, so as to confirm the possible periodicity of the characteristics depicted in the filtered signals. The results prove the successful implementation of this methodology that manages to distinguish the appearance of impulses in the filtered signals, which are modulated by the blade passing frequency (BPF) component. The proposed approach specifies the analogy between the impulsive behaviour of the filtered signal and the shock pressure mechanism, and between the BPF modulation of the impulses with the shock pressure waves that occur in the rotating impeller. The latter relate the detection characteristics with the physical mechanism of cavitation wear, and can constitute a robust and reliable detection tool of general application in hydraulic turbomachinery.

Keywords: Acoustic emission measurements; Backflow cavitation; Cavitation; Computational fluid dynamics; Condition monitoring; Experimental measurements; Fast kurtogram; Flow visualization and imaging; Machine diagnostics; Spectral kurtosis; Tip clearance flow; Vibration measurements.

Acknowledgements

I would like to express the deepest appreciation to my supervisor, Professor Ioannis Anagnostopoulos, for his guidance during the running of this project. His great knowledge and open-mindedness were very important for the successful completion of this project. I thank him for his kindness and willingness to assist in any way the present work. I would also like to express my sincere gratitude to Professor Dimitrios Papantonis, for all the support and encouragement he gave me, from my very first week as a member of the laboratory.

I would like to offer my special thanks to Professor George Aggidis, who was my supervisor during my six-month staying in Lancaster University. The experiments conducted in the pump configuration of the Engineering Department of Lancaster University were the basis of this dissertation. I would also like to express my appreciation to Associate Professor Nikolaos Aretakis and Professor Ioannis Antoniadis, who shared their experience in rotating machinery diagnostics, as well as for providing me access to the technical infrastructure of their laboratories.

This work would not have been possible without the significant contribution of three collaborators; Ioannis Kassanos, Sotiris Mavrakis and Dr. Christos Yiakopoulos. Extremely knowledgeable and hardworking, Ioannis helped me the most so as to familiarize with all aspects of centrifugal pumps and hydroturbines. Sotiris assemblied with his own hands all the parts of the new test rig in NTUA, he established the vast majority of the sensors and he solved numerous technical challenges arose during the conduction of the experiments. Christos, a real expert on condition monitoring, helped the outmost by posing all those insightful questions regarding the development of a robust and general cavitation detection tool. I am indebted to all of them.

I would also like to extend my thanks to all those great colleagues that I had the chance to meet all those years in ANYM building. Babis and Thanasis with whom I shared the office during my first year as a PhD student, as well as Alexandros, Marios, Erica, Dimitris and Vassos for their scientific advices and the excellent atmosphere in the laboratory. Many thanks to Marinos, for all his support and the fruitful discussions in all kind of topics. I'm much obliged to Dr. Georgios Kosmadakis for his continuous interest on my work and the excellent collaboration in the projects we worked together. My thanks also go to the new generation, Kostas, Vaso, Dimitris, Charis, Christina and Nikos, the “ANiMated” group, who helped me in numerous ways but mainly because they made the life in laboratory a real joy. I would especially like to thank Eri Marioli, who was always helpful and provided me with her administrative assistance throughout my dissertation. My appreciation goes also to my fellow labmates in Lancaster University, Sean, Ilias and Dimitris.

My gratitude goes to Papadakis Bros S.A, and especially to Michalis and Christos, for all the parts they manufactured, for all their useful advices, but most for their warm attitude and their generosity.

I am also grateful to the Research Committee of NTUA for their financial support to this PhD project the last three years.

I can’t forget all the support of my friends and relatives through those years. I thank them from the bottom of my heart. Special thanks to Dafni, for finding the way to make me happy, even in difficult times. Finally, I would like to express my love and thanks to my parents and my brother. Though small may be the honour, this work is dedicated to them with much gratitude and affection.

List of Symbols

Lower case Greek symbols

a_c	Linear calibration coefficient a
α_l	Liquid volume fraction [-]
α_{nb}	Linearised coefficient for neighboring cell [-]
α_{nuc}	Nucleation site volume fraction [-]
α_p	Linearised coefficient [-]
α_v	Vapour volume fraction [-]
β	Blade angle [°]
β_w	Flow angle [°]
δ	Absolute uncertainty [dimensions of the variable calculated]
δx	Time lag [s]
δf	Frequency domain discretization [-]
δt	Time span [s]
δ_{ij}	Kronecker delta [-]
ε	Number of segments of PSD estimator
ε_{jmn}	Tensor of Levi–Civit [-]
ζ	Hydraulic losses coefficient [-]
ζ_e	Bearing losses coefficient [-]
η	Total efficiency of the pump [-]
η_{mot}	Electric motor's efficiency [-]
θ	Angle of impeller rotation [deg]
κ	Constant of von Karman [-]
μ	Dynamic viscosity [Pa·s]
μ_t	Turbulent viscosity [Pa·s]
ρ	Density [kg·m^3]
ρ_l	Liquid density [kg·m^3]
ρ_m	Mixture density [kg·m^3]
ρ_v	Vapour density [kg·m^3]
σ	Thoma cavitation number [-]
τ	Stress tensor [Pa]
τ_{ij}	Reynolds-stress tensor [Pa]
τ_w	Wall shear stress [Pa]
φ_i	Incidence angle [°]
ω	Specific dissipation rate [s^{-1}]

Upper case Greek symbols

B	Log-law equation constant [-]
Γ_ω	Effective diffusivity of ω [kg·m^{-1}·s^{-1}]
Γ_k	Effective diffusivity of k [kg·m^{-1}·s^{-1}]
Δ	Bin's width
ΔH_{dyn}	Dynamic pressure differential [m]
$\Delta H_{z,e}$	Height difference between the suction of the pump and the suction tank [m]

ΔH_{st}	Static pressure differential [m]
ΔH_z	Geodetic pressure differential [m]
Φ	Non-dimensional total flowrate [-]
Ψ	Non-dimensional total head [-]
Ψ_{ST}	Non-dimensional static pressure number [-]
Ω	Rotation speed [rad·s^{-1}]
Ω_{ij}	Vorticity tensor [s^{-1}]
Ω_m^{Rot}	Components of the system rotation vector [s^{-1}]

Lower case Latin symbols

b	Linear form of source term of φ variable
b_c	Linear calibration coefficient b
b_I	Blade width [m]
b_V	Volute width [m]
br	DAQ resolution
c	Mean pipe velocity [m·s^{-1}]
c_M	Rotating disc losses coefficient [-]
d	Impeller diameter [m]
d_p	Pipe diameter [m]
ds	Distance [m]
dt	Time span between the sampling increments [s]
e	Blade thickness [mm]
e_d	Envelope of a signal
$e_{1,2}$	Number of cells at two areas of impeller mesh [-]
f	Frequency [Hz]
f_c	Band pass filter's central frequency [Hz]
f_{cutoff}	Cutoff frequency of the analog, low pass filter [kHz]
f_{ncg}	Non-condensable gasses mass fraction [-]
f_r	Range of the analog and digital band pass filters [kHz]
f_s	Sampling frequency [kHz]
f_v	Vapour mass fraction [-]
f_N	Nyquist frequency [Hz]
g	Gravitational acceleration vector [m·s^{-2}]
h	Digitised time vector [s]
j	Cell face
k	Turbulent kinetic energy [m^2·s^{-2}]
$\dot{m}^-$	Mass transfer evaporation [kg·m^{-3}·s^{-1}]
$\dot{m}^+$	Mass transfer condensation [kg·m^{-3}·s^{-1}]
n	Rotational speed [rpm]
n_q	Specific speed
p	Static pressure [Pa]
p_c	Pressure calibration correction [Pa]
p_{sat}	Saturation pressure [Pa]
p_B	Atmospheric pressure [Pa]
p_M	Minimum static pressure [Pa]
q	Acceleration of vibration
r	Data acquisition system's resolution
s	Standard Deviation
t	Time [s]
t_s	Sampling duration [s]
t_{tc}	Tip clearance thickness [mm]
u	Tangential velocity [m·s^{-1}]
u^+	Non-dimensional velocity [-]

u_*	Friction velocity [$m \cdot s^{-1}$]
u_c	Characteristic velocity [$m \cdot s^{-1}$]
v	Three dimensional absolute velocity vector [$m \cdot s^{-1}$]
v_n	Normal component of the absolute velocity [$m \cdot s^{-1}$]
v_u	Tangential component of the absolute velocity [$m \cdot s^{-1}$]
v_v	Kinematic viscosity [$m^2 \cdot s^{-1}$]
$v_{v,t}$	Turbulent kinematic viscosity [$m^2 \cdot s^{-1}$]
v_N	Number of independent measurements [-]
v_{RMS}	Velocity vibration RMS [$mm \cdot s^{-1}$]
w	Relative velocity vector [$m \cdot s^{-1}$]
w_u	Tangential component of the relative velocity [$m \cdot s^{-1}$]
xf	Filtered signal
x_o	Original signal
x_{Hf}	Hilbert transform of filtered signal
y	Distance from the next wall [m]
y^+	Non-dimensional wall distance for a wall-bounded flow [-]
z	Vertical distance from the reference level [m]
z_s	Number of impeller blades [-]
$z_{s,s}$	Number of impeller splitter blades [-]

Upper case Latin symbols

A	Surface [m^2]
A_s	Analytic signal
A_v	Amplitude of acceleration vibration [$m \cdot s^{-2}$]
A_w	Volute wetted surface [m^2]
A_{AE}	Amplitude of AE [V]
C_{cond}	Condensation factor [-]
C_f	Skin friction coefficient [-]
C_{vap}	Vaporization factor [-]
D	Cross-diffusion term [$kg \cdot m^{-3} \cdot s^{-2}$]
D_B	Ball diameter of the bearing [m]
D_P	Pitch diameter of the bearing [m]
F	Relative uncertainty [-]
$F_{1,2}$	Blending functions [-]
F_E	External body forces vector [N]
G_ω	Generation of ω [$kg \cdot m^{-3} \cdot s^{-2}$]
G_k	Generation of k [$kg \cdot m^{-1} \cdot s^{-3}$]
H_e	Head of the establishment [m]
H_B	Atmospheric pressure [m]
H_E	Pressure in the suction tank [m]
H_{oa}	Total head at the discharge [m]
H_{oe}	Total head at the suction [m]
H_{tot}	Total head of the pump [m]
I	Unit tensor [-]
L	Characteristic linear dimension [m]
M	The length of PSD estimator
M_e	Torque of bearing mechanical losses [N·m]
M_m	Mechanical torque [N·m]
M_s	Torque of rotating disc mechanical losses [N·m]
N_{faces}	Number of faces that enclose the cell [-]
N	Non-dimensional total mechanical power [-]
$N_{\delta f}$	The number of sectors that the frequency domain is split [-]
N_s	Number of samples [-]

N_B	Number of balls or rollers in the bearing [-]
N_{SB}	Number of splitter blades [-]
P_{el}	Electric power of the motor [W]
P_{mech}	Mechanical power of the pump [W]
P_x	Power spectral density
Q	Flowrate [m^3hr^{-1}]
R	Impeller radius [m]
R_h	Hub radius [m]
R_B	Bubble radius [m]
R_m	Radius at the midspan of the blade [m]
Re	Reynolds number [-]
Re_p	Peripheral Reynolds number [-]
R_x	Autocorrelation function
S	Strain rate magnitude [s^{-1}]
S_φ	Source of φ variable
S_{ij}	Strain tensor [s^{-1}]
S_t	Surface tension [$N{\cdot}m^{-1}$]
T	Temperature [°C]
V	Cell volume [m^3]
V_c	Volt after the application of calibration expressions [V]
V_m	Volt data of calibration measurements [V]
U	Window normalization constant of PSD estimator
W	Window function of PSD estimator
Y_ω	Dissipation of ω [$kg{\cdot}m^{-3}{\cdot}s^{-2}$]
Y_k	Dissipation of k [$kg{\cdot}m^{-1}{\cdot}s^{-3}$]

List of Abbreviations

AE	Acoustic emission
BC	Boundary conditions
BEP	Best efficiency point
BPF	Blade passing frequency
CC	Cavitating conditions
CFD	Computational fluid dynamics
DL	Decomposition value
DNS	Direct numerical simulation
FCM	Full cavitation model
FK	Fast Kurtogram
FFT	Fast Fourier Transformation
FS	Frequency spectrum
ICM	Interface capturing methods
ITM	Interface tracking methods
LE	Leading edge
LES	Large eddy simulation
LHT	Laboratory of Hydraulic Turbomachines
LU	Lancaster University
MCS	Mesh convergence study
MFI	Mass flow inlet
MRF	Multiple reference plane
MS	Midspan
NCC	Non-cavitating conditions
NPSH	Net positive suction head
NS	Navier-Stokes
NTUA	National Technical University of Athens
OP	Operating point
PSD	Power spectral density
RANS	Reynolds-averaged Navier-Stokes
RMS	Root mean square
SK	Spectral Kurtosis
SPO	Static pressure outlet
SST	Shear-stress transport
STFT	Short-time Fourier transformation
TEM	Transport equation-based models
TS	Time series

List of Tables

List of Figures

Introduction

From its first appearance in the reports of naval engineers (Thornycroft, 1895) due to a damaged screw propeller, cavitation phenomenon is synonymous with the problematic behaviour of hydraulic turbomachines. Daugherty's (1915) study that summarises the measurements in several centrifugal pumps and reaction hydroturbines, imputes the power collapse observed in the large flowrates of various machines to cavitation development. In his review for the twenty-year technological progress in centrifugal pumps, Peterson (1933) states that "almost the only complaints that a manufacturer receives concerning the operation of a water works pump relate to noise and cavitation, which often result in corrosion of the impeller". The above depict clearly that cavitation became rapidly popular among the engineers as a fault of critical importance, even though it was a relatively new term.

More than a century after its first appearance, the development of a detection tool that could identify cavitation promplty in a wide range of hydraulic turbomachines, remains an open problem for the research community and the maintenance engineers. Several approaches have been proposed, in order to efficiently identify the phenomenon. The present study reviews the most seminal of these works and examines the two-phase flow development in hydraulic turbomachinery, in order to propose a well-rounded approach towards its prompt and effective detection.

The Introduction of the Thesis:

i. Provides the definition of cavitation phenomenon and describes its physical mechanism (section I.1).
ii. Presents the reasons that make necessary the development of modern detection tools (section I.1).
iii. Presents the possible cavitation formations in hydraulic turbomachinery (section I.2).
iv. Describes the aims and the objectives of this research (section I.3).
v. Summarises the structure and contents of the Thesis (section I.4).

I.1 Cavitation in hydraulic turbomachines: Posing the problem

Cavitation is defined as the process, where vapour formations appear inside a liquid due to its subjection to a decreasing pressure field (Brennen, 2014). The ideal cavitation definition assumes that:

i. The liquid medium is pure, which means that it is not mixed with additional air and gas micro bubbles.
ii. The process is carried out under constant temperature conditions.
iii. The appearance of vapour cavities initiates when the reducing pressure reaches the saturation pressure of the working medium.

The theoretical cavitation process is illustrated in the phase diagram of Fig. I.1a, as the passing from state No. 1 to state No. 2. The ideal onset of cavitation coincides with the crossing of the solid curve that connects the triple (TP) with the critical (CP) point and illustrates the change of saturation pressure, p_{sat}, with the temperature, T. During such conditions, the liquid

phase breaks down and void formations are created, which progressively fill with vapour. According to the Rayleigh-Plesset equation (Eq. I.1), the magnitude, R_B, of an ideal spherical vapour bubble (Fig. I.1b) is a function of the liquid's properties (ν_v, ρ_l, S_t) and it is driven by the pressure differential between the inner part of the bubble, p_B, and the uniform decreased pressure field of the liquid, p_∞.

$$\frac{p_B(t)-p_\infty(t)}{\rho_l}=R_B\frac{d^2R_B}{dt^2}+\frac{3}{2}\left(\frac{dR_B}{dt}\right)^2+\frac{4\nu_v}{R_B}\frac{dR_B}{dt}+\frac{2S_t}{\rho_l R_B} \tag{I.1}$$

where the ν_v is the uniform kinematic viscosity of the liquid, ρ_l its density and S_t its surface tension. The theoretical approach of Eq. I.1 for the determination of bubble magnitude is based on the following assumptions:

i. The temperature of the liquid, T_∞ and its dynamic viscosity, μ is constant and uniform.
ii. The liquid is Newtonian, incompressible and its density, ρ_l is constant.
iii. The contents of the bubble are homogeneous.
iv. The pressure, p_B and temperature, T_B inside the bubble are uniform.
v. The vapour density, ρ_v in the bubble is $\rho_v << \rho_l$.

The Navier-Stokes equations are used under the assumption of spherical symmetry, so as to derive Eq. I.1. The Rayleigh-Plesset equation is a fundamental equation that is used as the basis of several models that describe either the development of a single bubble or cavitating flows as a whole (Niedźwiedzka, 2016). Some of these models are used in parallel with computational fluid dynamic (CFD) codes, in order to simulate two-phase flow conditions in several engineering applications. The models used most frequently in hydraulic turbomachinery applications are reviewed in section 1.3.2.

Heretofore, the analysis of cavitation phenomenon is based on simplifications, which mainly deal with the purity and the uniformity of the liquid and the bubble's content. However, in engineering applications the working medium is usually impure and contaminated with a large number of microscopic air or gas particles that favour the formation of vapour cavities, since they reduce significantly the tension that the liquid is able to sustain (Arndt, 1981; Best, 1993). In addition, the solid boundaries of the flow usually have discontinuities, slots and protrusions that make easier the onset of the phenomenon (Papantonis, 2016).

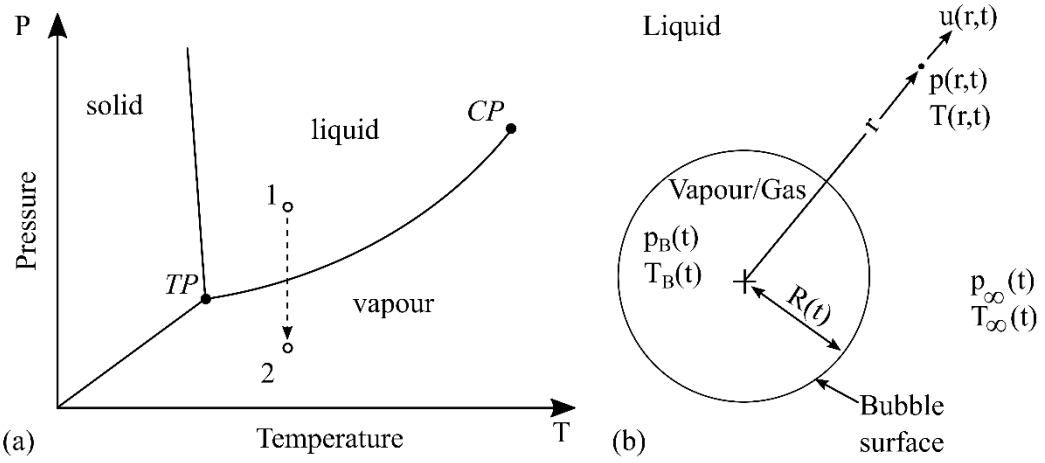

Figure I.1 a) Cavitation process (1→2) in a phase diagram, **b)** assumption of spherical bubble in an infinite liquid (Brennen, 2014).

Hence, for the engineering applications an alternative definition for cavitation is usually used that relates the phenomenon with its collapse rather than its inception. More specifically, in hydraulic turbomachinery, cavitation phenomenon is created locally at low static pressure zones of the machine due to its improper installation or due to operation under high rotation speeds,

flow rates and medium temperatures. Even without the above conditions, high flow velocities could be developed in the complex three dimensional flow of a hydrodynamic machine that could locally favour the formation of vapour cavities. However, the dynamic flow conditions in the machine drive the vapour bubbles away, along with the main liquid flow. Consequently, when the liquid's conditions change and the p_∞ value increases, the vapour bubbles are forced to return to their initial state in the opposite direction of that presented in Fig. I.1a. The reliquification procedure of the bubbles is adequately described from the series of photographs presented in Fig. I.2 (Mancuso, 2020):

i. The reduction of the bubble's magnitude is presented in photographs No. 6 – No. 8 of Fig. I.2.
ii. The formation of the internal micro-jet and the final implosion of the bubble is illustrated in the photographs No. 9 – No. 15 of Fig. I.2.

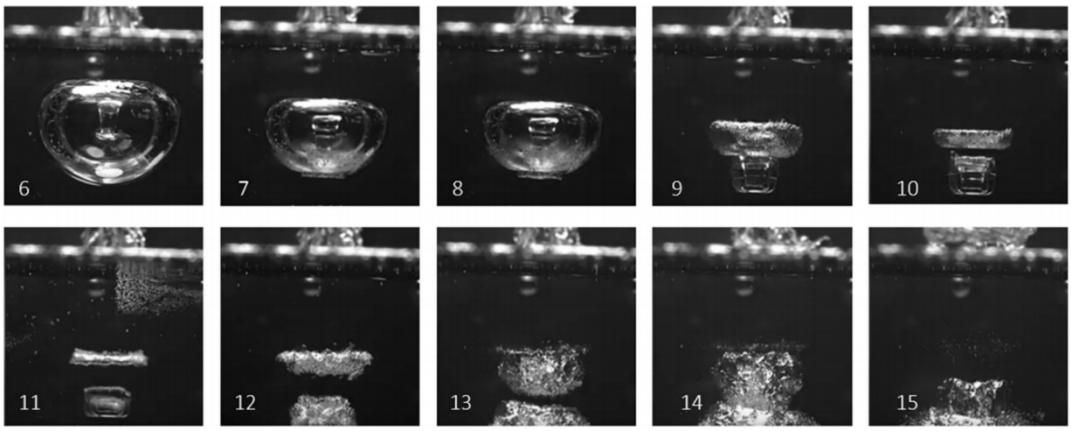

Figure I.2 The bubble collapse procedure in sequential photographs (Mancuso, 2020).

The reliquification of the bubble is a very violent procedure, where the jet formation and the implosion generate shock pressure waves of extreme intensity. The description of the latter mechanism justifies the selection of engineers to define cavitation with respect to its collapse rather than its onset. As a result, in engineering applications cavitation phenomenon is defined as the abrupt reliquification of the vapour bubble in the liquid medium as the result of its recovery in pressure values over the saturation pressure (Kim, 2014). A practical way to estimate the maximum possible value of the energy of the pressure waves during the implosion is with the use of Eq. I.2 (Gülich, 2008), where p_{sat} the saturation pressure, $R_{B,o}$ is the radius of the bubble at the start and $R_{B,e}$ the radius at the end of implosion:

$$E_{i,max} = \frac{4}{3}\pi\left(R_{B,o}{}^3 - R_{B,e}{}^3\right)\left(p_\infty - p_{sat}\right) \tag{I.2}$$

When the vapour bubbles implode close to solid boundaries of the hydraulic turbomachinery, these impulsive waves impinge the internal walls (Fig. I.2b) and significantly stress the material structure (Shengcai, 2000). The collapse of the cavities is followed from noise due to the aforementioned production of shock pressure waves. Nevertheless, the mechanical and hydraulic noise excited from hydraulic turbomachines usually masks the noise excited from cavitation implosion, and the phenomenon is not detected during its initial stage of development. After certain operation time under such conditions, the stressing can cause significant wear and material removal (Fig. I.3) at the internal rotating surfaces (i.e. the blades, the hub and the shroud of the rotor) of the hydraulic turbomachine (Brennen, 2005, 2014). In the case of turbomachines, the material removal from the rotor reduces their performance but also increases the unbalance of the system and creates additional oscillations that stress the bearings.

The inability to identify the phenomenon promptly, results operation of the machine under low efficiency, as well as it causes severe damage, not only to the hydraulic components (Fig. I.3) of the machine but also to its mechanical parts, such as the shaft and the bearings. As a consequence, the significant effect of cavitation in the performance and material wear of the hydraulic turbomachine justifies the interest of researchers and engineers regarding the adequate and prompt detection of the phenomenon and also explaines its alternative definition.

Figure I.3 Typical cavitation damage on the blades of centrifugal pumps (Brennen, 2014; Kamiel, 2015).

I.2 Large-scale cavitation formations in hydraulic turbomachinery

The studies of cavitation inside hydraulic turbomachines approach the phenomenon from a large-scale perspective rather than that of single bubble, since the two-phase flow area usually consists of a large number of bubbles that act collectively towards the deterioration of machine's performance. Six main types of large-scale cavitation have been observed experimentally inside the various parts of hydraulic turbomachinery; i) bubble or travelling bubble cavitation (Fig. I.4a), ii) vortex cavitation (Figs. I.4b,c & I.5), iii) attached or sheet cavitation (Fig. I.4d), iv) cloud cavitation (Fig. I.4e), v) backflow cavitation (Figs. I.6, I.7) and vi) rotating types of cavitation (Figs. I.8, I.9). It is underlined that more than one type of cavitation could co-exist inside a hydraulic turbomachinery.

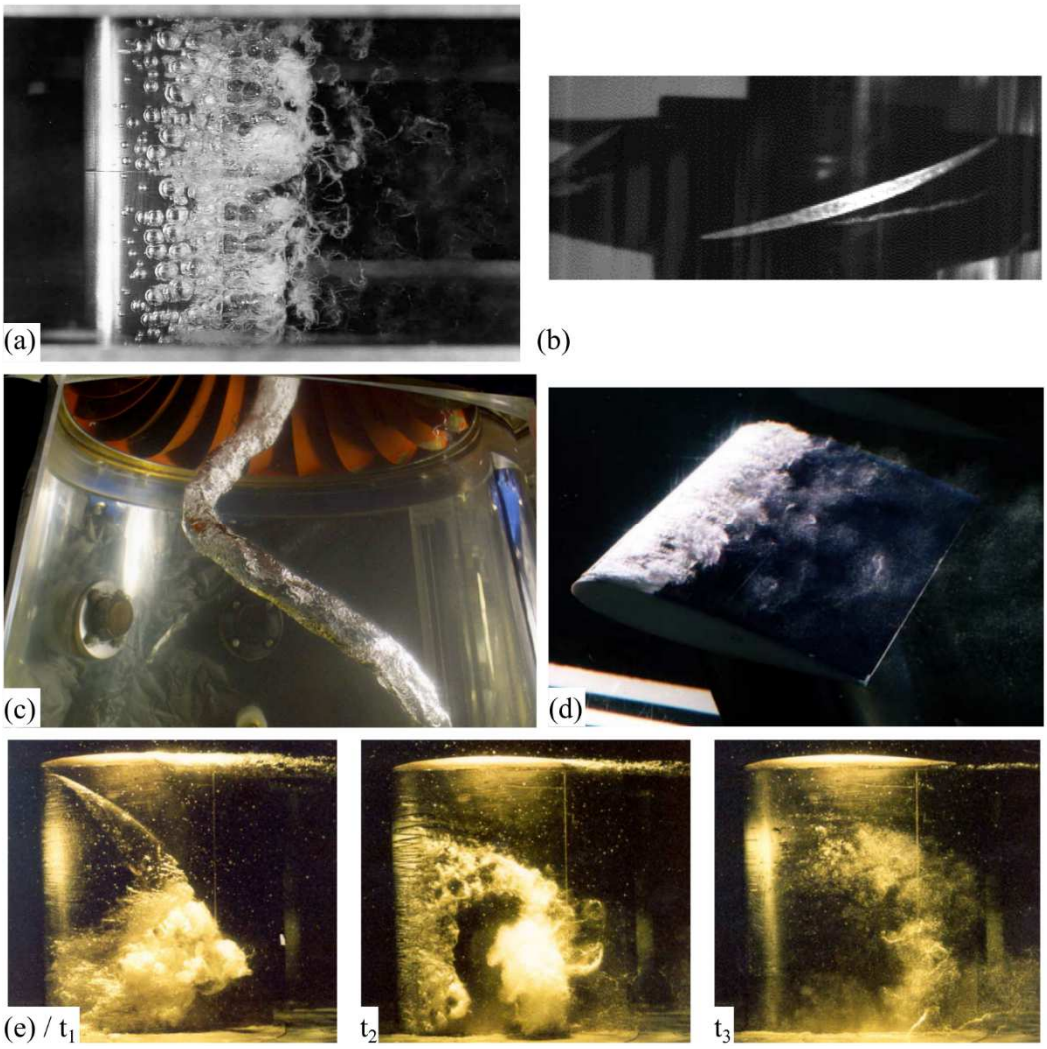

Figure I.4 a) Dense travelling bubble cavitation on the surface of a hydrofoil (Kermeen, 1956), **b)** Tip leakage vortex cavitation in an axial pump (Zhang D., 2015b), **c)** Vortex rope in the draft tube of Francis turbine model (Iliescu, 2008), **d)** attached cavitation on a hydrofoil (University of Tokyo, Applied Fluid Engineering Laboratory), **e)** Cloud cavitation in three frames ($t_1<t_2<t_3$) that highlight the formation (t_1), separation (t_2), and collapse (t_3) of vapour formations on a hydrofoil (Brennen, 2014).

The bubble travelling cavitation is depicted in Fig. I.4a at the suction side of the hydrofoil. Here, the two-phase flow area consists of individual bubbles, which are formed at the suction of a hydrofoil and they collapse in the higher pressure areas (Brennen, 2011). Such formations of large vapour bubbles have been observed in the internal surface at the leading edge area of

the runner's blade, when the reaction hydroturbines operate under low head conditions. Although, the implosion of the bubbles create intensive noise, they are considered harmless for the material wear of the runner, since they are imploded far from its solid surfaces (Papantonis, 2016). Similarly harmless, in terms of the material wear, are also the bubble formations that appear at the spherical part of the runner's hub in the case of Kaplan hydroturbines, that however, can reduce significanly the hydraulic efficiency of the machine (Papantonis, 2016).

The vortex cavitation type appears in areas with extensive vorticity, where the pressure usually takes its minimum value at the vortex core. This type of large-scale cavitation consists of four main sub-categories; i) the tip leakage vortex (Fig. I.4b), ii) the vortex rope (Fig. I.4c), iii) the inter blade vortices (Fig. I.5), and iv) the Karman vortex street. The first appears at the tip clearance of the blades of open or semi-open rotors (Fig. I.4b) and its vortices appear due to the interaction of the end-wall boundary with the main flow and the rotor's rotation. This type of cavitation formation appears in pumps and hydroturbines, and is possible to cause significant wear in the rotor, nevertheless, it does not reduce the hydraulic efficiency of the machine (Zhang D., 2015b; Papantonis, 2016).

The vortex rope mechanism (Fig. I.4c) is related with the existence of the tangential component of the absolute velocity at the exit of the runner, in the draft tube of reaction hydroturbines, when the machine operates either in part or over load conditions. Kaplan-type reaction turbines are less possible to retain tangential velocity component at the exit of their runner, since their rotating blades are not fixed on the rotor (as in Francis turbines) and can be adjusted so as to perform with maximum efficiency for a large range of flowrates. The study of vortex rope cavitation are of significant importance for the hydropower industry, since it could cause flow induced power swings and its low frequency could excite the natural frequency of either the turbine or the powerhouse. Vortex rope cavitation is rarely related with material wear, since it is developed in the core of the flow, which is usually away from the solid boundaries of draft tube.

The inter blade cavitation vortices (Fig. I.5) appear during deep part load conditions in the blade to blade channels of hydroturbine's runners. Although the identification of the cause of the inter blade vortices is still under investigation, it is possibly related with the flow separation on the runner's hub wall (Yamamoto, 2016). Finally, depending on the trailing edge shape of the stay, guide and rotating blades, Karman vortices can be formed that during the operation of the machine under low pressures levels are possible to cavitate. The Karman vortex street is usually formed inside hydroturbines, it is followed from vibrations and pressure oscillations, but it does not causes damage on the surfaces of the machine (Papantonis, 2016).

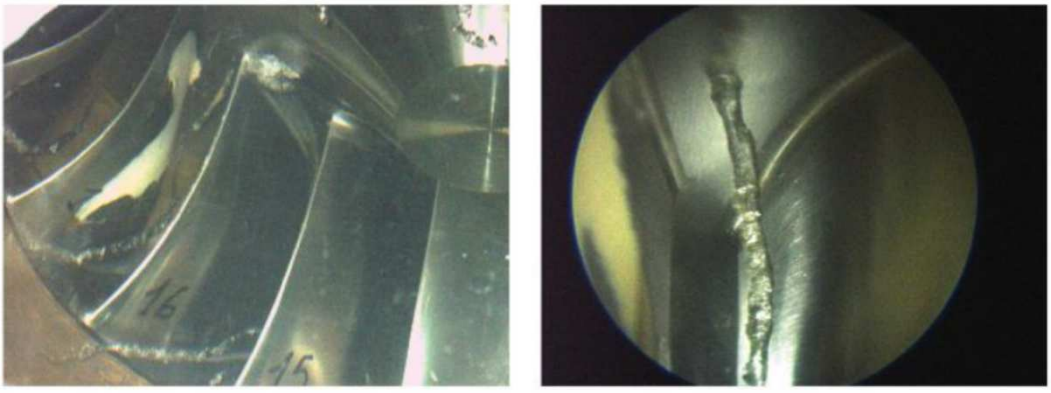

Figure I.5 Inter-blade cavitation vortex in the runner of a Francis turbine (Yamamoto, 2016).

The attached cavitation is depicted in Fig. I.4d and appears at the suction side of the hydrofoil, similarly to bubble cavitation. Nevertheless, in the case of attached cavitation, the two-phase flow area is represented by a denser, more uniform formation. This single vapor-filled separation zone at the suction side of the blade appears usually at large angles of attack. Another interesting observation regarding this type of cavitation is that it exhibits quasi steady state characteristics (Shen, 1989; Batchelor, 2000; Kunz, 2000; Barre, 2009) in terms of its macroscopic shape.

Especially in centrifugal pumps, the formation of steady attached cavities can change the hydrodynamic shape of the blade (Fig. I.6), even for blades with relatively low incidence angle, φ_i, and create flow recirculation and separation regions that decrease the overall efficiency of the pump (Papantonis, 2016). Under very low suction conditions the extend of the cavity could reach the TE of the blade of the pump. In this case, the attached cavitation is named supercavitation and its particular shape is illustrated in Fig. I.6.

A typical cloud cavitation formation is illustrated in Fig. I.4e in a flow around a hydrofoil in three different snapshots. This kind of large-scale cavitation formation develops in hydraulic turbomachines and exhibits a characteristic periodic formation and collapse of vapour bubbles that form a cloud unsteady structure (Brennen, 2014). The complex mechanism that drives the periodicity of the formation and collapse procedure is affected from both the shedding of cavitating vortices, as well as from the periodicities imposed by the individual flow characteristics of each application (rotor-stator interaction etc.). The unsteady nature of the phenomenon may cause more noise, vibration and damage to the neighbouring solid surfaces than large-scale cavitation types that do not exhibit strong fluctuations in their shape (i.e. attached cavitation formations).

Backflow cavitation is strongly related with the backflow recirculation area, sketched in Figs. I.6, I.7 and may appear in centrifugal pumps with open or semi-open impellers. In such pumps, the tip clearance favours the creation of a pressure differential between the pressure and suction side of the blade, and the inlet of the pump (Figs. I.6, I.7). Figure I.6 represents the case of axial pumps, while Fig. I.7 the case of radial semi-open impeller pump.

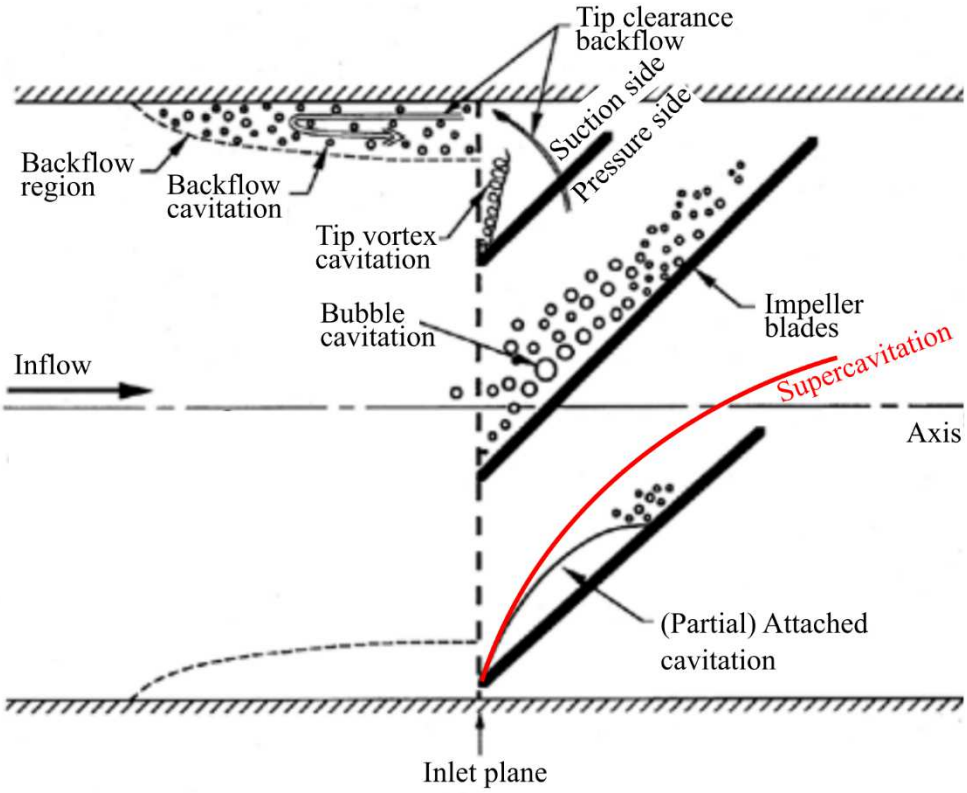

Figure I.6 Types of cavitation inside an impeller of a pump (Brennen, 2011).

The existence of the tip clearance acts as a path for this recirculation, which typically accelerates the leakage flow, when the latter passes through the narrow area of the tip. Under low pressure suction conditions, such flow acceleration favours the formation of cavities, which are recirculated in the low pressure suction area of the blade and the inlet of the pump. During developed cavitating conditions the recirculated two-phase flow formations re-enter the impeller and deteriorate the suction performance of the machine. According to Brennen (2011), the effect of backflow cavitation becomes more apparent when the pump operates under partial flowrates, since this backflow becomes comparable to the main inflow.

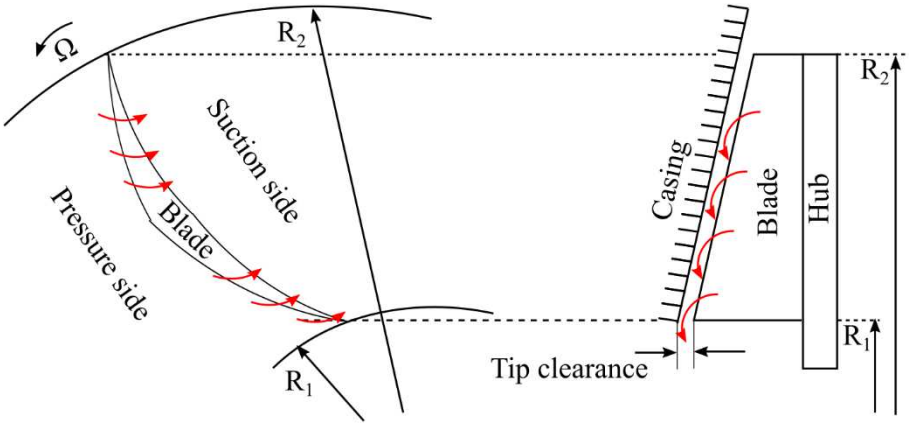

Figure I.7 Area of backflow recirculation in a radial semi-open impeller.

Finally, the rotating types of cavitation are introduced in this section, which include the development of vapour formations that rotate relatively to the shaft of the machine. There are two rotating types of cavitation, i) the rotating stall with cavitation, and ii) the rotating cavitation (Brennen, 2011). The rotating stall instability occurs in axial flow machines under operating conditions where the inlet flow angle, β_{1w} deviates significantly from that of blade's LE, β_1 (Fig. I.8), and hence creates a large relative incidence angle ($\varphi_i=\beta_1-\beta_{1w}$), close to values where the blades could stall. At such conditions, if flow separation is combined with local flow irregularities, it is possible to block the inflow of one blade, say blade B in Fig. I.8 at $t=t_1$. As a result, the flow is displaced in the neighbouring blades (A & C) and influences in a different way their inflow conditions at $t=t_2$. On the one hand, the flow displacement further decreases β_{1w} of blade A ($\beta_{1w,A}$) and strengthens the separation, while simultaneously increases β_{1w} of blade C ($\beta_{1w,C}$), where φ_i decreases and improves its flow conditions. This asymmetric change of the inflow conditions displaces the stall cell and makes it to rotate around the axis of the machine with a frequency (RSF) that has been found to be sub-synchronous [χ = 0.5 – 0.9] to the rotational frequency (RF) of the shaft (Eq. I.3).

$$RSF = \chi \cdot RF \tag{I.3}$$

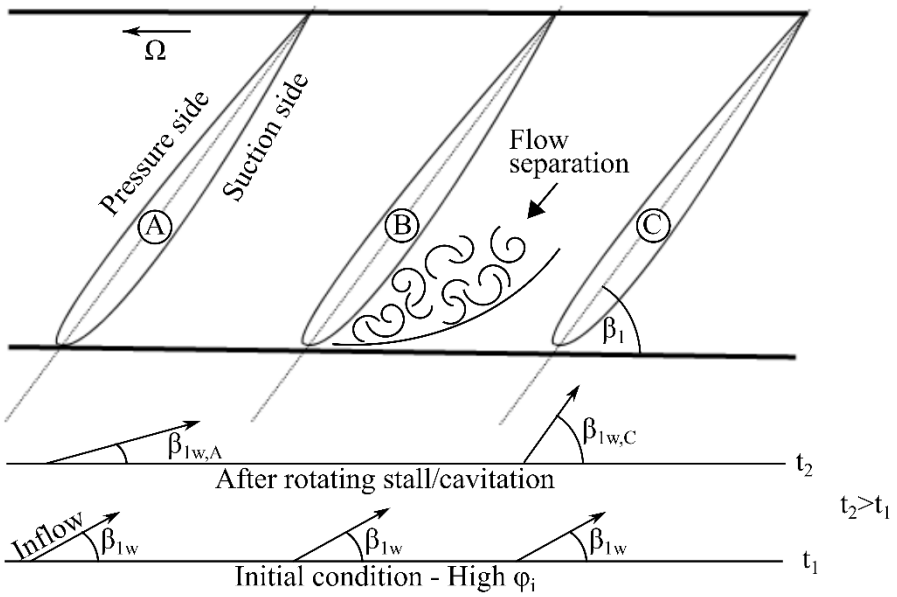

Figure I.8 Schematic of rotating stall in a rotor along with the theoretical inlet flow angle deviation before and after its formation.

In general, the rotating stall instability usually occurs in compressors with large number of blades. However, there have been few studies (Lenneman, 1970; Yoshida, 1991) that centrifugal pumps are found to suffer from rotating rotating flow separation, usually during conditions of high incidence angles and low flowrates, where the slope of the head characteristic curve (dH_{tot}/dQ) becomes positive. Consequently, when this phenomenon occurs under low static pressure conditions, it could be accompanied by vapour bubble formations, a phenomenon that is described as rotating stall with cavitation (Brennen, 2011). It should be underlined that in the case of rotating cavitation, the dynamics of this mechanism dominate the flow conditions. Also, this rotating instability is more possible to occur in centrifugal pumps rather than in reaction hydroturbines, where the inlet flow angle is adjusted from the guide vanes, so as to reduce the incidence angle.

On the other hand, rotating cavitation (Fig. I.9) occurs in impellers when one or two blades exhibit stronger vapour formations due to flow assymetries and assymetric increase of the cavity volume. The phenomenon occurs at low static pressure areas, close to the total head drop of the pump. In this case, the cavitation zone rotates relative to the rotor in a similar way with rotating stall that have just discussed (Brennen, 2011). However, in this case the phenomenon occurs at higher flow conditions, where the slope of the total head curve is negative and the machine's operation is in general stable. The rotation frequency of rotating cavitation (RCF) is found to be sligtly higher than that of the rotor (RF), and it can be calculated from Eq. I.4 (Kamijo, 1977, 1992; Brennen, 2011), where χ = [1.1 – 1.2]

$$RCF = \chi \cdot RF \tag{I.4}$$

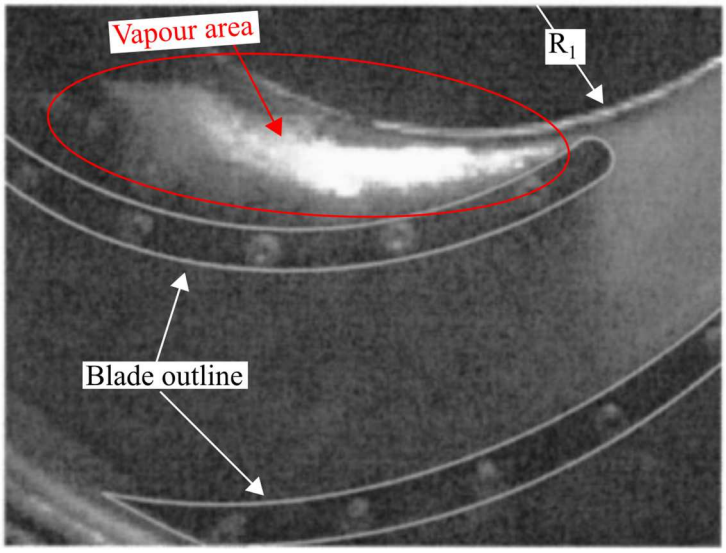

Figure I.9 Photograph of rotating cavitation in the blade paths of a radial impeller (Friedrichs, 2002).

I.3 Aims and objectives of the Thesis

Section I.1 highlights the need towards the prompt and efficient detection of cavitation in centrifugal pumps and hydroturbines. The aim of the present Thesis is to investigate the methodologies proposed in the literature for the detection of cavitation and to enrich them with the formulation of a general cavitation detection criterion that could be applied in hydraulic turbomachines. In addition, the present Thesis proposes a modelling approach that will be used, in order to analyse the complex internal characterstics of the flow field in the machine and to identify cavitation formations in different stages of its development, under various operating conditions. It should be noted that the study focuses on the detection of two-phase flow development in closed hydraulic turbomachines, i.e. in centrifugal pumps or reaction hydroturbines, and not in freely rotating impellers, mixers, propellers, etc.. Henceforward, in the present study, the use of the term "hydraulic turbomachinery" refers only to the closed hydraulic turbomachines.

To achieve these aims, several experiments are conducted in two configurations; i) one established at the Engineering Department of the Lancaster University, UK, and ii) one established at the Laboratory of Hydraulic Turbomachines (LHT) of the National Technical University of Athens (NTUA). In parallel, a numerical model is developed that is validated with the use of the aforementioned experimental data. The main objectives and the steps that are followed for the completion of this Thesis are presented below:

i. To conduct experiments under normal and cavitating conditions in the pump laboratory established at the Engineering Department of Lancaster University.
   - The tests include the examination of three semi-open impellers with different blade designs, while the casing is made from transparent material, so as to visualise the cavitating formations in the pump.
   - The tests for each impeller under normal conditions include the examination of 10 flowrates for 4 different rotational speeds.
   - The tests for each impeller under cavitating conditions include the examination of 10 σ operating point for 4 different flowrates. For each operating point, noise and vibration measurements are obtained, along with photographs that depict the location and the extent of the two-phase flow formations in the pump.

ii. To process the measurements obtained in the Lancaster University. The analysis includes:
   - The derivation of the characteristic curves for the three pumps.
   - The application of the traditional signal processing tools in the noise and vibration measurements, and the investigation for their detection capability.
   - The association of the flow visualisation results with the cavitation characteristic curves and with the noise and vibration results.

iii. To develop a numerical model for the semi-open impeller of Lancaster University with the radial blades so as to study and detect two-phase flow formations in the pump. The model includes the solution of Reynolds-averaged Navier–Stokes (RANS) equations in combination with an additional transfer equation that regulates the mass exchange between the two phases (liquid & vapour). In all the cases examined in the present study, the modelling of turbulence is done with the use of k-ω SST model. More specifically, the modelling procedure includes:
   - Derivation of the three dimensional computational domain that includes the impeller, the tip clearance, the volute, and the suction and discharge pipes.
   - Construction of various meshes for the conduction of grid dependence study under cavitating conditions, and the selection of the final computational mesh to be used in the simulations.
   - Flow simulations for the calculation of the characteristic curves under normal and cavitating conditions. The mass flow rate and pressure boundary conditions are obtained directly from the experimental measurements.

- Extended evaluation of the numerical results, against the corresponding experimental characteristic curves and the flow visualisation of cavitation formations.
- Use of the model, in order to study the two-phase flow development in the impeller and its tip clearance for various flow conditions.
- Parametric analysis, in order to examine the effect of the tip clearance thickness to the performance of the pump, under normal and cavitating conditions.

iv. To design and built an experimental configuration for testing of centrifugal pumps under single and two-phase flow conditions in the Laboratory of Hydraulic Turbomachines (LHT) of National Technical University of Athens (NTUA). In this test rig the two-phase flow development in a closed impeller is investigated. For this reason, additional modifications are made on the casing of the pump, where a transparent window is opened, and the shroud of the closed impeller that is re-constructed from transparent material, so as to be possible to visualise the internal flow conditions.

v. To apply steps i to iii for the closed impeller of the NTUA test rig.

vi. To apply the Spectral Kurtosis methodology in the measurements of all pumps, in order to investigate the application of band pass filters, on the measured signals, that are based on the maximum value of the kurtosis in the frequency spectrum. In this way, the ability of such filters towards the unmasking of the machine's mechanical and hydraulic noise, is examined. Moreover, this procedure may also improve the signal demodulation proposed from a small number of researchers.

I.4 Thesis outline

The research work carried out in the framework of the present Thesis is presented in seven Chapters.

Chapter 1 describes the different maintance approaches towards fault detection in rotating machines and underlines the reasons for the selection of the noise and vibration monitoring for the efficient maintenance of centrifugal pumps and hydroturbines. Furthermore, it attempts to summarise all the possible hydraulic and mechanical faults related with hydraulic turbomachines by featuring their physical mechanism and providing the fault signature in the noise and vibration pattern. Chapter 1 categorises and reviews the published experimental methodologies that attempt to detect cavitation in hydraulic turbomachines, while in paraller it investigates their strengths and weaknesses. Finally, the chapter ends with the presentation of the most frequently used numerical approaches that are used towards the study of two-phase flow formations in centrifugal pumps and hydroturbines.

Chapter 2 provides all the theoretical background regarding the performance and the testing of centrifugal pumps, as well as the mathematical formulations of the processing techniques applied in the noise and vibration signals, so as to detect cavitation. Chapter 2 ends with the presentation of the two experimental configurations along with the details of the impellers and the sensors used during the experiments.

Chapter 3 presents the results of the experimental measurements regarding the derivation of the characteristic curves of the four pumps studied in this Thesis, under single and two-phase flow conditions. The presentation of the cavitation characteristic curves is accompanied by the flow visualisation results, where the various forms of large scale vapour formations are illustrated.

Chapter 4 includes the presentation of the theoretical background of the numerical model, the computational domains used, the meshing approach and the application of boundary conditions. In the same chapter an extended validation of the model is shown that aims to investigate its ability to identify two-phase flow formations in the pump under various operating conditions. The validation part includes the comparison of; i) the numerically obtained characteristic curves under single and two-phase flow conditions, with the corresponding experimental (presented in Chapter 3), and ii) the extent and location of the numerically obtained two-phase flow area with the flow visualisation results of Chapter 3.

Chapter 5 incorporates the numerical results regarding the flow characteristics of impeller No. 2, under single and two-phase flow conditions. More specifically, the complex flow field is analysed and the effect of the tip clearance on the overall performance of the pump is investigated. In addition, the modelling approach developed in impeller No. 2 is applied to impeller No. 4, so as to examine its applicability towards the identification of cavitation development in the closed impeller geometry.

Chapter 6 presents the analysis of noise and vibration data from the traditional signal processing perspective, as function of the suction conditions of each impeller. More specifically, the analysis initiates with the demonstration of the raw signals in time and the discussion of their statistical characteristics. Afterwards, the effect of cavitation on the frequency domain of the signals is highlighted, while the applicability of powerband results towards the detection of cavitation in centrifugal pumps is evaluated. Finally, Chapter 7 describes the implementation of Spectral Kurtosis approach so as to improve the detection of the resonances excited by the two-phase flow development, to unmask the impulsive characteristics of the filtered signals and to demodulate them in a more efficient way. The results presented in Chapter 7 aim not only to detect cavitation but also to associate in a general way the specific characteristics of the filtered signal in time, as well as of the signal's envelope with the fault mechanism, no matter the pump or test configuration examined.

Finally, Chapter 8 contains a summary of all the outcomes of this study, its contribution to the research in the field and the innovative aspects, and closes with some proposals and suggestions for future research.

1. Literature Review

1.1 Introduction

The first Chapter of the Thesis is divided in two sections; i) one that justifies and reviews the use of noise and vibration measurements for the monitoring of hydraulic and mechanical faults in hydrodynamic machines (section 1.2), and ii) one that reviews the research works that aim to detect cavitation with the use of noise and vibration measurements and with the modelling of internal flow conditions (section 1.3). Section 1.2 introduces the various maintenance approaches and reveals the benefits of condition-based techniques with the use of noise and vibration measurements for the detection of faults related with hydraulic turbomachinery. In addition, section 1.2 attempts to summarise the noise and vibration signatures of the hydraulic and mechanical faults that are possible to appear in such rotating machines. The knowledge of the faults pattern is of high significance so as to differentiate them from the cavitation noise and vibration signature. Section 1.3 reviews the experimental methods proposed in literature for the detection of cavitation and presents the most frequently used numerical models for the study of two-phase flow development in hydraulic turbomachines.

1.2 Faults related with hydraulic turbomachinery

Maintenance strategies attempt to answer when is the time to maintain the various machine's components so as to reduce the cost of repair or replacement. Three types of maintenance methodologies have been applied; i) the run-to-break strategy, ii) the time-based preventive maintenance, and iii) the condition-based or predictive maintenance. The first strategy allows the operation of the machine until the moment of the breakdown and is used mainly for the maintenance of low priced machines (or machine components) of minor importance. The second requires the maintenance to be carried out at shorter intervals from the expected time between failures and is applied decently for components, whose expected failure time is accurately known. The latter methodology deals with the regular monitoring of various parameters, in order to predict the potential failure and to optimise the answer regarding the appropriate time to maintain the machine component (Randall, 2011).

Hydraulic turbomachinery cover a wide range of applications and are manufactured in several magnitude scales. Consequently, all the approaches could be used for their maintenance. However, when dealing with the maintance of critical hydraulic turbomachines, such as the majority of hydroturbines and large pumps installed in the the oil, gas, power, chemical and other idustrial sectors, the run-to-brake strategy is impracticable. In addition, centrifugal pumps and hydroturbines are rotating machinery, whose normal operation depends heavily on the condition of their bearings. The bearing's expected failure time cannot be predicted accurately and this makes the application of time-based preventive maintenance technique to result either in the replacement of several healthy components or the failure of the machine due to an early bearing fault (Neale, 1978). The latter conclusion reveals the utility of condition-based methods in hydraulic turbomachinery applications of critical importance relative to the run-to-break and time-based preventive maintenance strategies.

The main prerequisite for the successful implementation of a condition-based maintenance technique is the access to condition monitoring tools that reliably evaluate machine's operation and provide accurate predictions regarding the useful life of its mechanical components (Randall, 2011). Literature proposes the measuring of several parameters, in order to provide the data, at which the condition monitoring tools will be applied. The data most frequently analysed during condition-based maintenance of rotating machinery could be obtained either from; i) lubricant samples, ii) noise and vibration, iii) performance, or iv) temperature measurements.

Noise and vibration measurements present a significant advantage over the other parameters, because they are not only able to highlight the actual damaged component of the machine, but also to depict the early-stage fault signature characteristics. On the other hand, the analysis of lubricant samples could last several days and sometimes is difficult to identify the exact faulty component, since the debris characteristics do not variate significantly in similar components. Often, the temperature of the mechanical components rises at the latest stages of fault development and makes thermography improper for the prompt detection of the corresponding faults (Randall, 2011). Similarly to the temperature measurements, the performance monitoring that is widely used in hydraulic turbomachines of critical importance, cannot highlight the development of a fault during its initial stages, since performance usually deteriorates belatedly.

In practice, industry uses all of the aforementioned parameters, in order to monitor the faults of hydraulic turbomachinery. Nevertheles, centrifugal pumps and hydroturbines involve individual hydraulic mechanisms that excite noise and vibration and affect their operation. These hydraulic excitations are usually treated similarly with the mechanical faults, since they are able to deteriorate machine's performance (Dörfler, 2012). The hydraulic excitation mechanisms include the various vortex flows, forces due to rotor-stator interaction, rotating stall and cavitation (Lobanoff, 2013; Wu, 2013). The common characteristic of the above mechanisms is that all cause unsteady fluctuations in the velocity and pressure field of the machine. For this reason, a common practice in hydraulic turbomachinery industry is to use static pressure sensors for the study and detection of such phenomena, along with the traditional measurements (noise, vibration, temperature, oil measurements). However, it should be emphasised that pressure measurements can not replace the traditional techniques, since they could not be applied for the detection of mechanical faults. In addition, it is evident that the temperature, oil and performance measurements analysis can not provide answers regarding hydraulic mechanisms that develop inside the flow field under constant temperature conditions and are of dynamic nature.

From the above discussion it can be concluded that noise and vibration measurements are the most appropriate types of measurements for the parallel monitoring of hydrodynamic and mechanical faults in hydraulic turbomachines. Their ability to provide prompt answers regarding the development of the faults, as well as to locate the actual faulty component in a complex machine, gives them a significant advantage over the rest traditional (temperature, oil and performance) techniques. Furthermore, their adequate response on the dynamic excitations make them appropriate for the monitoring of hydraulic excitations. Nevertheless, the proper use of noise and vibration measurements for the condition monitoring in hydraulic turbomachinery, requires the development of robust signal processing tools that are able to extract the diagnostic information from the measured signal.

The latter conclusion justifies the direction of the recent research towards the analysis of noise and vibration signals for the detection of faults in centrifugal pumps and hydroturbines (Gülich, 2008; Dörfler, 2012; Lobanoff, 2013; Wu, 2013). The aim of this section is to briefly introduce the most typical faults that are possible to occur in hydraulic turbomachines along with their signature on the noise or vibration signal. In addition, for each case, the signal processing techniques applied for the extraction of their noise and vibration characteristics in time and frequency domain are given. For some of the cases, such as this of bearing's failures, the literature provides a large number of methodologies for their detection. The review of all those tools is out of the scope of this Thesis and consequently, the most influential studies are described and referenced. The tools used for the detection of cavitation in hydraulic

turbomachinery are presented seperately in section 1.3 and include some additional techniques, such as the performance monitoring methods or CFD tools, besides the noise and vibration measurements.

Sections 1.2 and 1.3 include the presentation of several studies in hydroturbines and centrifugal pumps, where sensors or numerical monitoring points are located in different parts of the machine. In order to improve reader's comprehension, two sketches that illustrate the possible positions of the monitoring points are drawn. The first is presented in Fig. 1.1a and depicts a typical reaction hydroturbine, while the second shows a typical centrifugal pump configuration (Fig. 1.1b). In the case of reaction hydroturbines the possible positions for the mounting of noise and vibration sensors are; i) the upper guide, the lower guide and the turbine guide bearings, ii) the stay and the guide vanes, iii) the spiral casing, and iv) the draft tube. In centrifugal pumps, the possible mounting positions are, i) the bearings A, B, ii) the front and the back volute walls, iii) the pump foundation and the inlet and outlet flanges. The sketches of Fig. 1.1 are accompanied from coordinates systems that are used as a reference, in order to provide the exact position of the sensors.

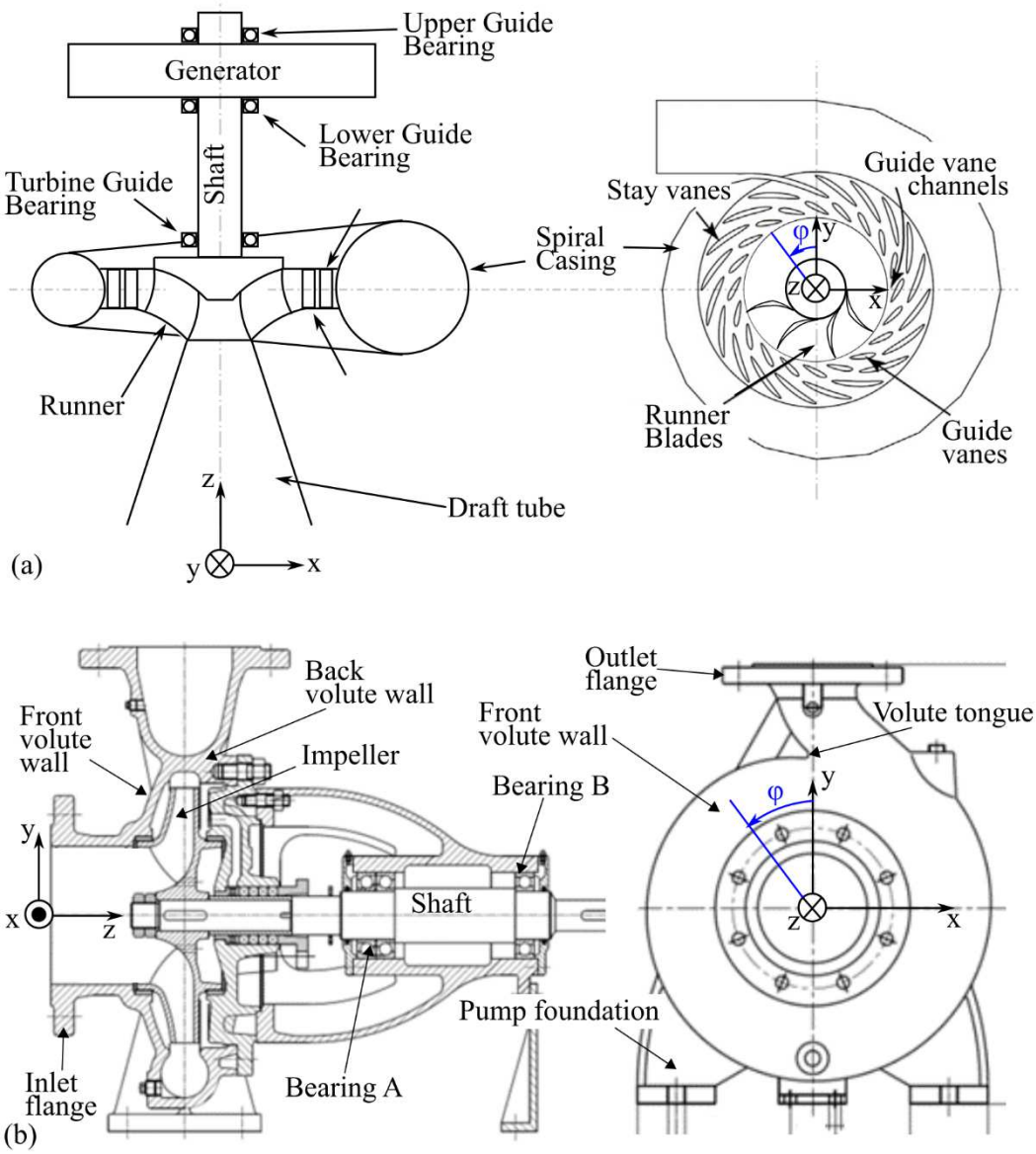

Figure 1.1 Sketch of a typical **a)** reaction hydroturbine, and **b)** centrifugal pump.

1.2.1 Hydrodynamic excitations

The study of hydrodynamic excitations has only recently become part of the ongoing research on hydraulic turbomachines. The first step of the researchers and engineers is to examine the phenomena in a way to improve the understanding of their complex, unsteady, physical mechanism. Consequently, the majority of the published studies, which examine hydrodynamic mechanisms, use as a primary tool the static pressure measurements, and only few of them investigate their monitoring perspective through noise and vibration measurements. For this reason, there is a small number of published noise and vibration results in the literature regarding the monitoring of unsteady hydraulic mechanisms. As a result, for cases, where additional clarification of the mechanism is needed, static pressure measurements are presented along with the noise and vibration signals.

Another significant observation regarding the excessive complexity of the examinations of hydrodynamic excitations deals with their interaction with other (hydraulic or mechanical) instabilities in the hydrodynamic machine. A typical example deals with the appearance of two-phase flow formations when the appearance of a hydraulic instability coincides with a low static pressure field. This more frequently applies for hydrodynamic excitations, whose unsteady structure is characterised from strong vortex formations or intensive separation. As a result, some of the studies presented in this section are experiments, where the hydraulic mechanisms under investigation interact with one or more instabilities.

1.2.1.1 Unstable flows at the rotor, volute casing, guide and stay vanes

The most significant representative of hydrodynamic excitations in closed hydraulic turbomachinery is the blade passing frequency (BPF) that results from the rotor interaction with the non-axisymmetric flow and geometry of the casing (rotor-stator interaction). The latter is created from the unevenly distributed flow at the spiral casing and the effect of volute tongue (Wu, 2013). In pumps, the BPF excitation is generated by the pitch-wise non-uniform velocity profile at the outlet of the impeller, while in reaction hydroturbines at the inlet of the runner (Gülich, 2008).

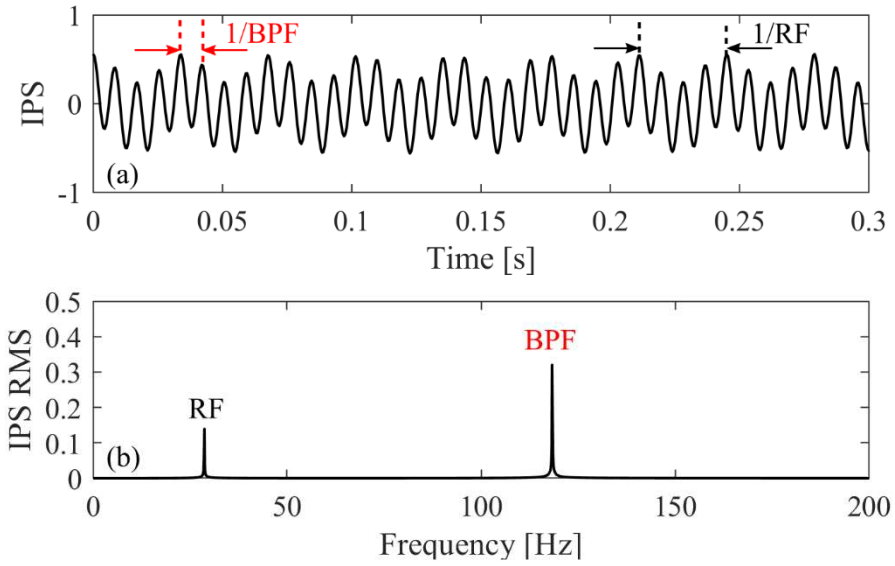

Figure 1.2 Theoretical shape of a vibration signal for a centrifugal pump (Taylor, 2005), **a)** in time, and **b)** frequency spectrum.

Moreover, in reaction hydroturbines, an additional source of flow asymmetries is created from the guide and the stay vanes and generates similar instabilities with that of BPF. The frequencies excited from BPF of rotor, guide and stay vanes are calculated from Eq. 1.1, where

z_s can be the number of rotor, guide or stay vanes, and n is the rotational frequency (RF) of the rotor:

$$BPF = \frac{n \cdot z_s}{60} = z_s \cdot RF \tag{1.1}$$

The theoretical pattern of a vibration signal that illustrates the pattern of BPF excitations in a centrifugal pump is given by Taylor (2005) in the time and the frequency domain of Fig. 1.2. A typical vibration signal includes the high frequency, BPF component that rides the lower RF component, which usually appears due to imperfect balancing of the rotor (see section 1.2.2.1), while both frequencies are in phase.

Unfortunately, the actual vibration signals usually obtained from hydraulic turbomachines include various noise and vibration sources (bearings, motor, generator, turbulence etc.) that spoil the uniformity of the theoretical signal of Fig. 1.2 (McNulty 1982; Cernetič, 2008; Gülich, 2008; Yao, 2011; Lobanoff, 2013; Farokhzad, 2013). In order to provide a view of a real vibration signal that corresponds to a machine that suffers from BPF excitation, the work of Yao et al. (2011) is presented.

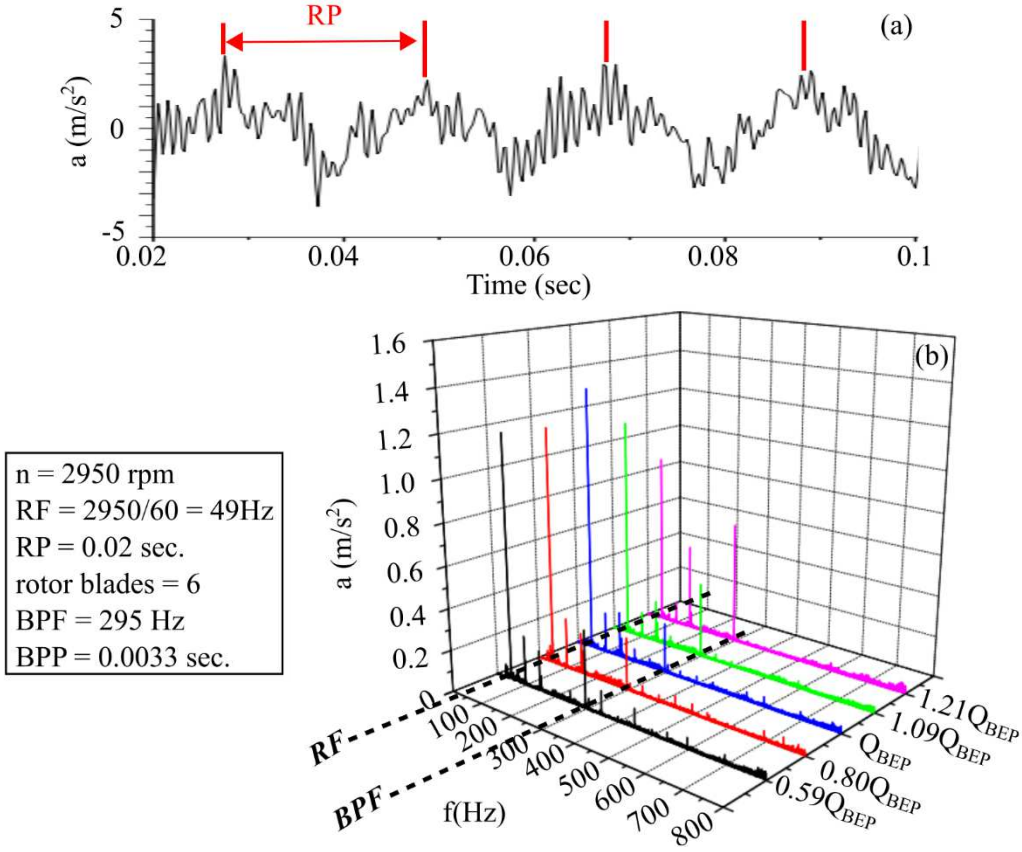

Figure 1.3 Real vibration signals in **a)** time and **b)** frequency domain obtained from the casing of a centrifugal pump (Yao, 2011).

Yao et al. (2001) present vibration results in time (Fig. 1.3a) and frequency domain (Fig. 1.3b), obtained from a sensor mounted at the spiral casing of a double suction centrifugal pump. The vibration sensor is located at the front side of the volute at an angular position with φ=180° (Fig. 1.1b). The legend in Fig. 1.3 shows the rotational frequency (RF), the BPF and the corresponding periods of RP and BPP. It should be noted that when in the present study refer to periodicity in time of RF and BPF, the last F is replaced with P, and they become RP, TBPP and BPP, respectively. As it is expected, the vibration in time (Fig. 1.3a) is a noisy signal that reveals the contribution of rotational period, RP and differs significant from the theoretical

presented in Fig. 1.2a. In addition, the higher frequency oscillations presented in Fig. 1.3a are faster than the BPP and do not form a robust pattern, which reveals the dominant effect of the rest noise sources on the vibration signal.

For this reason, the signal's power distribution in the frequency domain (Fig. 1.3b) is examined after the application of the Fast Fourier Transformation. In Fig. 1.3b, the frequency spectrum of the same sensor is shown, at various flowrate conditions. Here, the RF component is the strongest of the spectrum and this of BPF follows, no matter the flowrate tested. In addition, the amplitude of the BPF component exhibits a minimum amplitude value when pump operates at its best efficiency point (BEP), Q_{BEP}, which reveals the optimum flow conditions in terms of rotor-volute interaction at this point.

In the same study (Yao, 2011), static pressure is measured in parallel with vibration measurements, in the casing of the machine for angular positions with φ=80º, 135º and 220º, (Fig. 1.1b) that correspond to sensors p_2 – p_4. In this way the effect of BPF can be effectively examined, since pressure measurements are not contaminated with the mechanical noise. Interestingly, the frequency spectrum for p_3 (Fig. 1.4a), confirms the amplitude BPF pattern of vibration measurements, as well as the vanishing of RF that is related with low frequency mechanical mechanisms. The corresponding pressure data in time are plotted in Fig. 1.4b, where the sinusoidal form of the BPF is determined along with the effect of sensor positioning. More specifically, the sinusoidal shape becomes clearer for sensors mounted closer to the volute tongue (p_2, p_3) and deteriorates for p_4 that is placed in a 220º rotating distance. The results regarding the BPF amplitude pattern and the sinusoidal shape of BPF can be also observed in similar studies in closed hydraulic turbomachinery (Hasegawa, 1990; Chu, 1995; Barrio, 2008; Gülich, 2008).

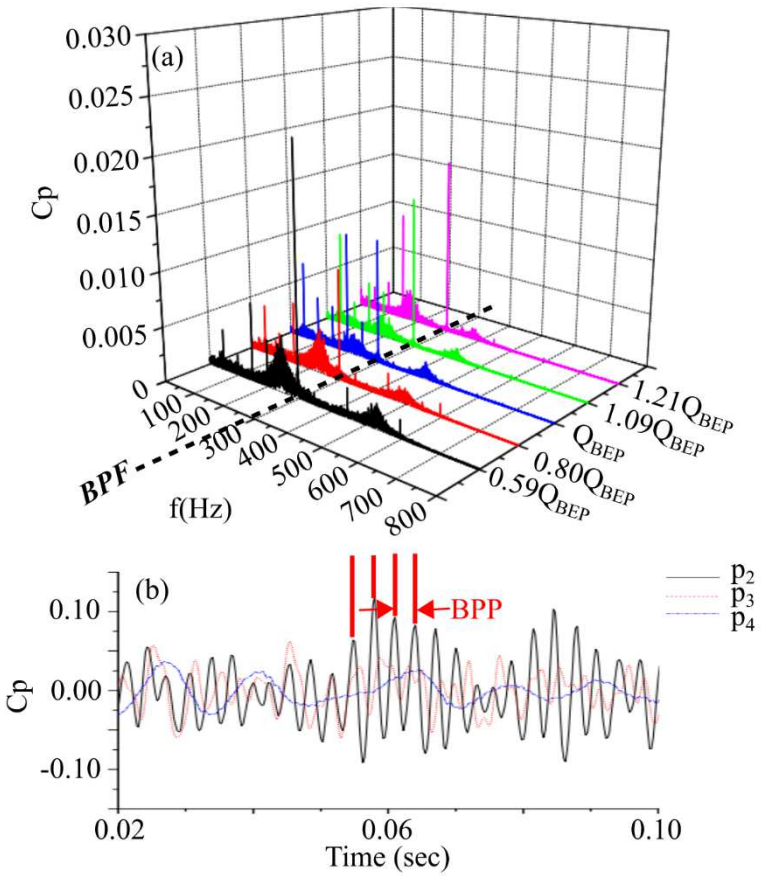

Figure 1.4 a) The frequency spectrum of static pressure measurements at position p_3 **b)** static pressure measurements in time at p_2, p_3, p_4 (Yao, 2011).

1.2.1.2 Vortex rope instability

In section I.2, the vortex rope mechanism (Fig. I.4c) is introduced as one of the main large-scale types of cavitation in reaction hydroturbines. Vortex rope instability is also accompanied by large-scale vapour cavities due to the low static pressure at the centre of the vortex core and due to the local pressure conditions. The mechanism of vortex rope is presented in Fig. 1.5, where the velocity triangle at the exit of a typical runner of a hydroturbine is presented.

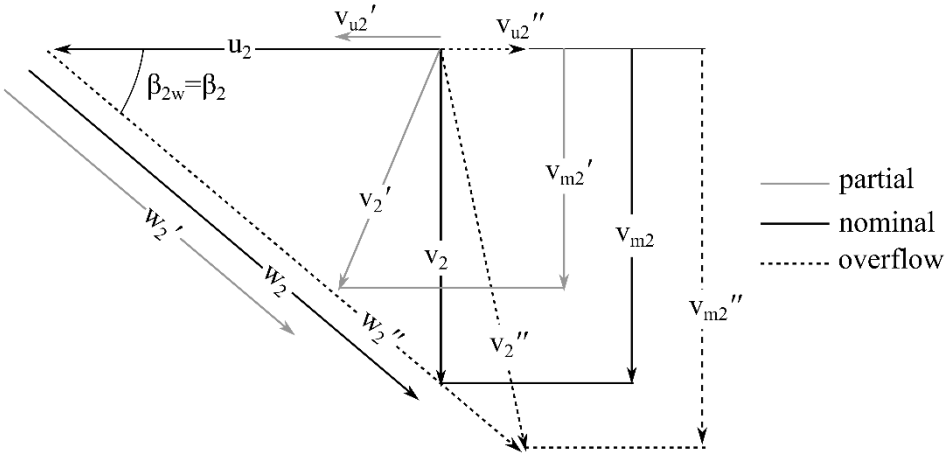

Figure 1.5 Velocity triangle at the exit of runner at nominal, partial (`) and overload (``) flowrates (Papantonis, 2016).

The velocity triangle at the BEP flowrate is illustrated with the solid black line in Fig. 1.5 and exits the runner with zero tangential component (v_{u2}=0 m·s^{-1}). When the machine operates under partial flowrate conditions (grey colour solid line in Fig. 1.5) the flow exits the runner with a remaining tangential component, v_{u2}', that forms the helical vortex rope in the draft tube of Fig. 1.6a. The direction of v_{u2}' is the same with this of u_2 (Fig. 1.5) and as a result, the helical vortex rope rotates in the same direction with the runner. Under overflow conditions (dashed line in Fig. 1.5), the remaining tangential component v_{u2}'', has the opposite direction than this of v_{u2}' and the onion-shape vortex rope that is formed at the draft tube (Fig. 1.6b) is counter-rotating relative to the runner's rotation. In practice, the appearance of the vortex rope under partial and overflow conditions reveals the inability of the runner to utilise the total tangential moment (and hence the hydraulic energy) of the water.

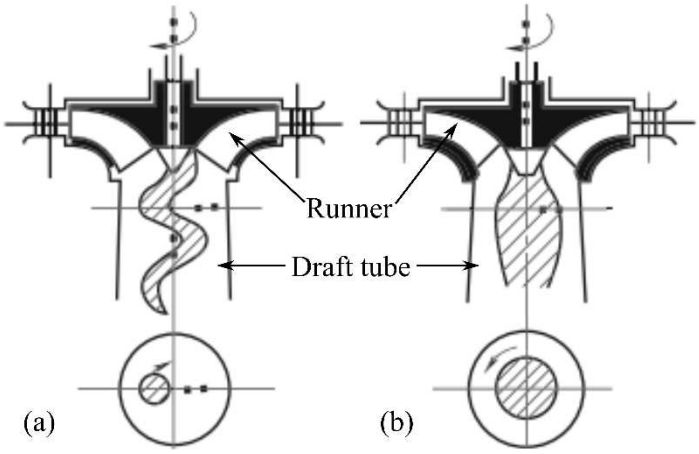

Figure 1.6 a) Helical vortex rope under partial flowrate conditions, **b)** onion shape vortex rope under overflow conditions (Wu, 2013).

The frequency of the onion shape vortex rope coincides with this of runner's speed, n, while this of helical at partial flowrates rotates slower than n (subharmonic) and is calculated from

Eq. 1.2, where χ is a parameter that changes with the geometrical design and according to literature results (Jacob, 1996; Pennacchi, 2012a,b; Wu, 2013; Escaler, 2015; Valero, 2019) is lower than 0.5. The interaction of low rotational frequency of the vortex rope with the turbine's nature frequency can excite significant vibration that deteriorates the power plant's perfomance (Zielke, 1974; Dörfler, 1982).

$$f_{hvr} = \frac{n \cdot \chi}{60} \tag{1.2}$$

The frequency excitation at the vibration measurements of Kaplan hydroturbine is presented in Fig. 1.7. The vibration sensor is located to the x-direction of turbine guide bearing (Fig. 1.1a). The change at the machine's load in time is highlighted in the power curve (Fig. 1.7a) and the analysis covers a wide range of operating conditions, from the startup (0 shaft revolutions, 0 kW) through partial load conditions (350 shaft revolutions, 3.2 MW), towards the BEP of the turbine (1500 shaft revolutions, ~20 MW). The time in the plots of Figs. 1.7a,b is expressed as shaft's revolution. The spectrogram presented in Fig. 1.7b, is constructed from the consecutive frequency spectra, as machine operation varies with time. Here, the low frequency sub-harmonic area with the increased vibration amplitude can be observed clearly. The vibration maximum amplitude is obtained at $0.11 \cdot n$, where the helical vortex rope frequency can be observed along with a $2.2 \cdot n$ excitation that corresponds to the first lateral eigenmode of the shaft-line. Consequently, the signal processing method used by Penacchi et al. (2012a) identifies not only the hydraulic instability of the vortex but also the parallel excitation of the structure. Typical results that depict the occurrence of vortex rope instabilities in the signal of noise and vibration measurements could be found in the studies of (Escaler, 2002, 2006; Wang, 2007).

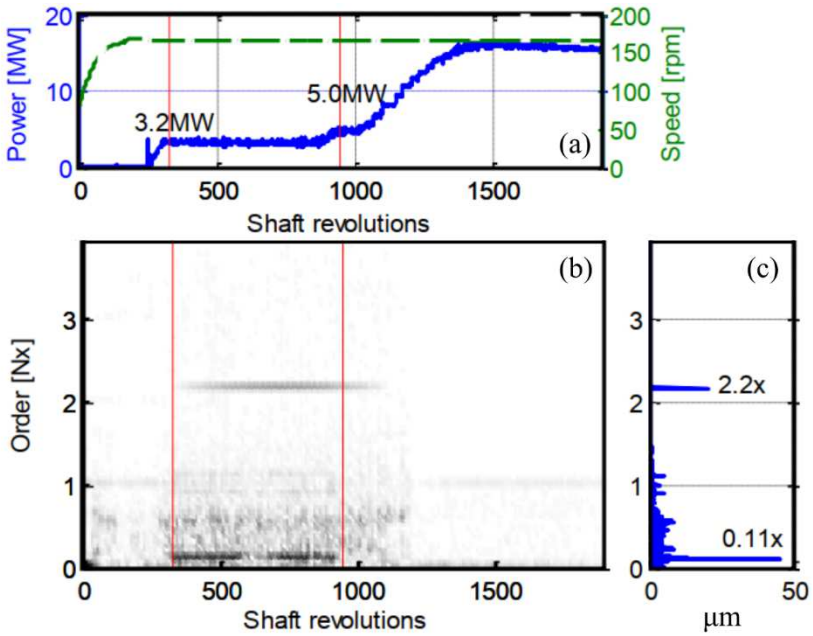

Figure 1.7 a) Kaplan turbine test under various load conditions, **b)** vibration order spectrogram during the test, **c)** order spectrum during partial load operation (Pennacchi, 2012a).

1.2.1.3 The Karman vortex street

A second hydrodynamic mechanism that could affect the operation of hydraulic turbomachines, and especially reaction hydroturbines, is the Karman vortex street (Fig. 1.8a). The Karman vortex street is created under specific flow conditions from the transient separation of the flow downstream from the TE of the blades (Dörfler, 2012; Wu, 2013). In pump

literature, it has not been reported an increase of vibration due to the Karman vortices created at the TE of the blades. This could be justified from the fact the flow at the outlet of the impeller presents strong irregularities that make impossible the formation of characteristic Karman vortices (Gülich, 2008). In reaction hydroturbines, the vortex street is possible to appear at the TE of the stay, guide or runner blades (Figs. 1.8b,c) and the frequency excited from the phenomenon can be calculated from the Strouhal Eq. 1.3:

$$f_{Kv} = Sh\frac{w_2}{e_2} \tag{1.3}$$

where, Sh is the Strouhal number that take values (0.18 – 0.25), w_2 the velocity at the TE of the blade that in the case of runner blades equals to the relative velocity (Figs. 1.8b,c), and e_2 is the thickness at the TE of the blade (Gummer, 1992; Dörfler, 2012).

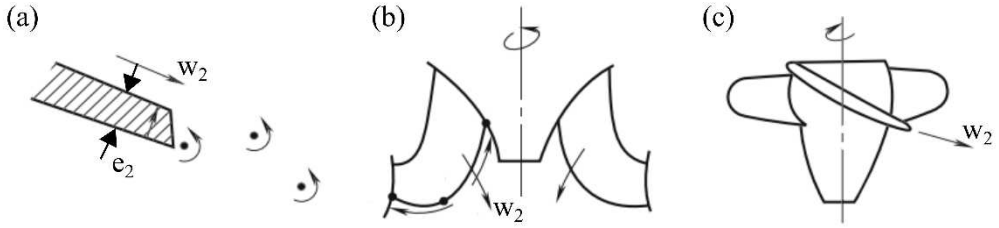

Figure 1.8 a) The Karman vortex street at the trailing edge of the blade, the relative velocity vector at the trailing edge **b)** of a Francis turbine, and **c)** of a Kaplan turbine (Wu, 2013).

Equation 1.3 relates the frequency of the Karman vortex street with the design of the outer part of the runner's blade. For this reason, additional emprirical formulas for the estimation of f_{Kv} at the stay, guide and runner blades of hydroturbines could be found in the studies of Heskestad and Olberts (1960) and Torbjørn et al. (2001). In addition, the effect of the TE geometry on the intensity of the phenomenon can be found in the studies of Toebes and Eagleson (1961) and Dörfler et al. (2012).

Karman vortex street is also related with the appearance of cavities, at the core of the vortex, especially when local pressure conditions allow it. Although, literature is rich in numerical and experimental investigations regarding the analysis of Karman vortex street in hydrofoils, there are only few studies (Escaler, 2006; Jain, 2017) that monitor the phenomenon with the use of vibration measurements obtained from a hydroturbine model or prototype. In addition, both of these studies cannot isolate the phenomenon and they examine it along with the presence of overload cavitation.

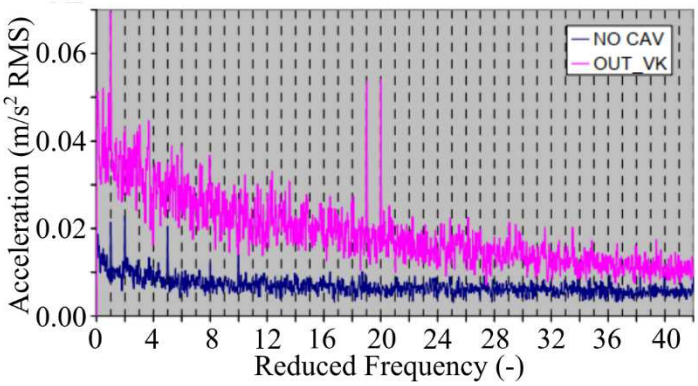

Figure 1.9 Frequency spectrum of the vibration's envelope of the demodulated signal under normal and Karman vortex street formation (Escaler, 2006).

Escaler et al. (2006) analyses the vibrations measured in the x-direction of the turbine guide bearing of a Francis turbine and the static pressure measurements at the draft tube at the outlet of the runner (Fig. 1.1a). The turbine has 19 rotating blades in the runner and 20 guide vanes. In this study both signals are processed so as to demodulate them and extract the frequency spectrum of their envelope with the use of Hilbert Transformation. Signal demodulation is a common practice for the detection of bearing faults (Nikolaou, 2002; Sheen, 2009) that is also used for the detection of hydrodynamic excitations (Bourdon, 1994; Escaler, 2002, 2004; Nikolaou, 2002). In this study, the band pass filter's central frequency, f_c=12.5 kHz and bandwidth, f_r=[10 – 15] kHz, are selected after examining several pairs of f_c and f_r. The results of envelope's reduced frequency spectrum, which is normalised with respect to the rotational frequency, are presented in Fig. 1.9 in two conditions, one with (purple colour), and one without (blue colour) the presence of Karman vortices and outlet cavitation. According to their results, the high carrier frequency is modulated from the RF and the BPF of the runner (19·RF) and the guide vanes (20·RF). The results are identical for both vibration and pressure measurements (Fig. 1.10), which highlights the negligible effect of low frequency mechanical phenomena in this experiment.

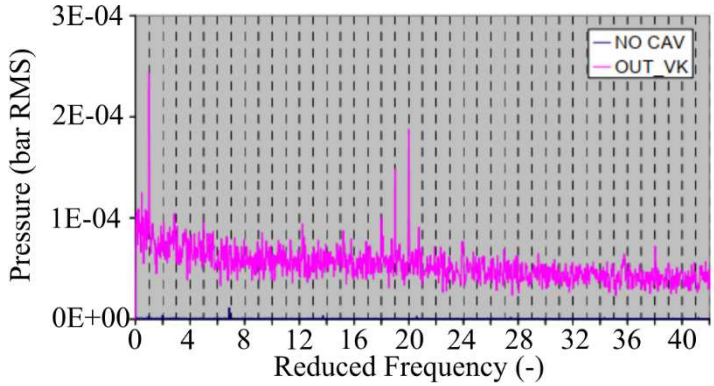

Figure 1.10 Frequency spectrum of the pressure's envelope of the demodulated signal under normal and Karman vortex street formation (Escaler, 2006).

1.2.1.4 Rotating stall

The rotating stall phenomenon is introduced in section I.2 (Fig. I.8) and occurs during operating points where the total head curve of the pump shows a positive slope. In practice, for high efficiency impellers, this is more likely to happen under extremely partial flowrates, close to the maximisation of total head, as in the example of Fig. 1.11.

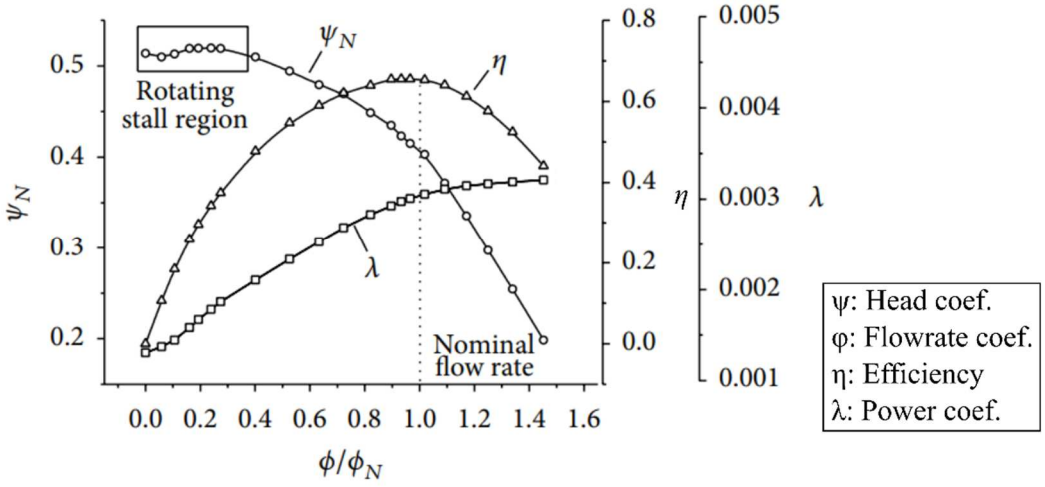

Figure 1.11 Rotating stall region area at the characteristic curves plots of a centrifugal pump (Zhang N., 2015a).

The imprint of rotating stall in the vibration signal of six vibration sensors, located at the volute (blue, pink & yellow colour line, in Fig. 1.12, at the tongue of the volute (black), at the discharge (red) and the suction (green) flanges of a centrifugal pump, is depicted in Fig. 1.12. These results correspond to measurements made in parallel with the derivation of the characteristic curves of Fig. 1.11. According to the plot of Fig. 1.12, the passing to rotating stall region, for φ/φ_N<0.4, cause an incease of the RMS applitude of all sensors, no matter their mounting position. In addtion, when the pump operates at minimum flowrates (φ/φ_N<0.1), during extreme rotating stall conditions, the RMS value increases by 3 dBs and maximises. The vibration energy trends of the various sensors exhibit identical patterns, however a significant offset exists between them.

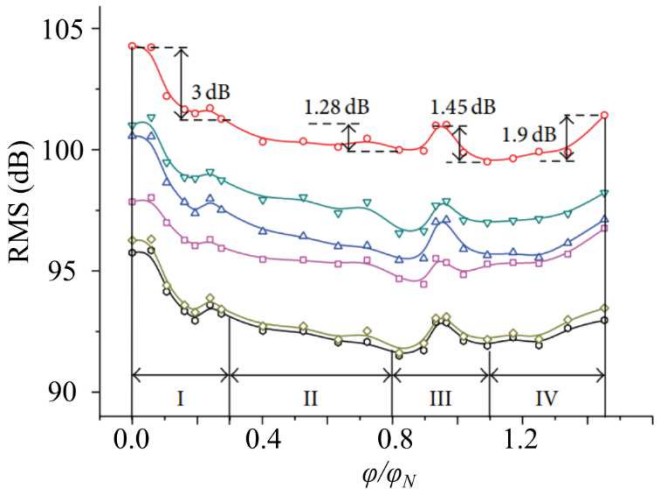

Figure 1. 12 Vibration level in 6 positions, during the derivation of characteristic curve of Fig. 1.17 (Zhang N., 2015a).

Botero et al. (2014) examines the rotating stall in a centrifugal pump that operates as a hydroturbine. In that study, mechanical vibration measurements are obtained at the guide vanes on z-direction with an angular position, φ~270º (Fig. 1.1a) in parallel with flow visualisation, while the turbine is operated under different operating conditions. The runner consists of 9 blades, while the spiral casing has positioned one raw of 20 guide and one raw of 20 stay vanes. The results of Fig. 1.13 present the time series of vibration (Fig. 1.13a), their normalised frequency spectrum calculated with the use of Welch estimator (Welch, 1967) of PSD (Fig. 1.13b), while Fig. 1.14 presents their corresponding integrated cyclic coherence in the cyclic domain. The latter has been proved to be an effective tool when it is used for the demodulation of fault information that is hidden in an noisy vibration signal from a rotating machine (Antoni, 2004, 2007a; Dong, 2012; Teng, 2017).

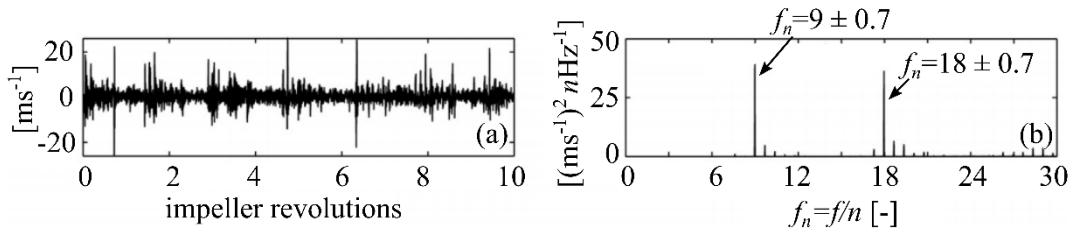

Figure 1.13 a) Vibration signal in time during rotating stall conditions, **b)** frequency spectrum of Fig. 1.13a (Botero, 2014).

The measured signal in time, which is expressed as impeller revolutions, seems to be modulated from a relatively slow frequency, lower than this of impeller rotation. Its corresponding frequency spectrum, which depicts the stationary perspective of the power

distribution, shows that the latter is mainly concetrated close to the BPF and its second harmonic. As it is explained in section 1.2.1.1, this is very typical behaviour of the frequency spectrum when it comes to applications of rotating machinery. However, carefull observation of Fig. 1.13b reveals the appearance of three pairs of sidebands with frequency close to 0.7·RF at both BPF components. This frequency of the sidebands can be related with rotating stall oscillations, according to Eq. I.3, and fits to the low frequency modulation of the time signal of Fig. 1.13a. This observation is finally clarified with the presentation of the cyclic spectrum of the integrated cyclic coherence (ICC) in Fig. 1.14.

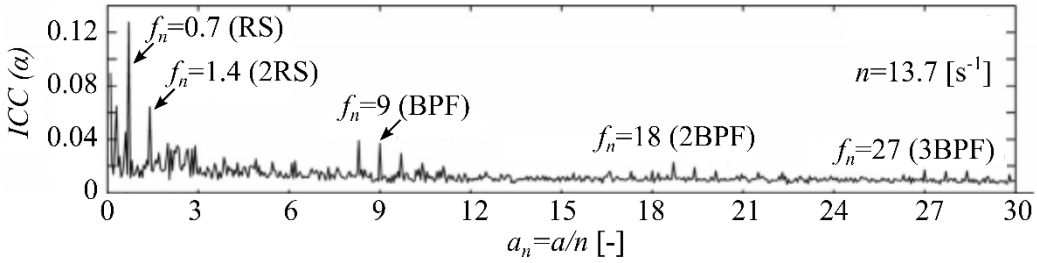

Figure 1. 14 Integrated cyclic coherence in cyclic spectrum of Fig. 1.13a (Botero, 2014).

1.2.2 Mechanical faults

The use of vibration signature analysis for the study of mechanical faults in rotating machinery has been investigated for several years (Braun, 1986), and the vibration patterns of the majority of the mechanical faults have been identified. As a consequence, the results of the mechanical signature analysis have been already implemented in the maintenance plans of rotating machinery industry. The faulty signals presented in this section are split in three categories that refer to i) the subharmonics and low harmonics of the shaft's rotational frequency (RF), ii) the electric machines, and iii) the rolling element bearings. The study of the first two types of faults produces signals more direct patterns than that of bearings, and their analysis is usually done in the time and frequency domain without the implementation of sophisticated signal processing tools. On the other hand, faults detection at the bearings is proved to be a more complicated procedure that requires the application of more sophisticated tools. In addition, bearing faults mechanism exhibits impulsive behaviour (see section 1.2.2.3), which is expected to be similar with that of vapour bubbles' implosion. As a result, the bearing's section, not only focuses on their faults signature but also reviews the tools applied for bearings detection, after considering their association with the detection of the two-phase flow development.

1.2.2.1 Subharmonics and harmonics of RF

Four main types of mechanical faults related with the fundamental rotational frequency (RF) of the rotor are given in time (Figs. 1.15a,b,c,d) and frequency (Fig. 1.15e) domain (Taylor, 2005). The signals for each type of malfunction are on purpose plot with a different fundamental RF value so as to make impossible the coincidence of their harmonics on their frequency spectrum, in Fig. 1.15c.

The first source of RF vibration reviewed is unbalance, which is caused when the center of rotating mass is different from the centre of rotation. In practice, unbalance appears for every rotating machine due to the manufacturing procedure imperfections or due to unwanted events during the operation or maintenance of the machine. The centrifugal forces developed in the unbalanced points of the rotor are proportional to the square of the rotation speed and, consequently, they rise significantly with the increase of Ω.

Intense unbalance problems could cause severe damage to all components of the machine and is probably the most frequent reason for the downtime of hydraulic turbomachinery (Lobanoff, 2013). For a well conditioned machine that suffers only from unbalance and

operates in constant rotation speed, Ω the vibration signal in time would be sinusoidal, with a frequency that coincides this of RF and an amplitude that remains relatively unchanged, as it is shown in Fig. 1.15a. The y-axis value of Fig. 1.15 depicts the velocity vibration expressed in inch per second. The frequency spectrum for unbalance, presented in Fig. 1.15e with the black colour line, reveals the concentration of the total energy in the RF component of the spectrum. A practical way to detect unbalance in a rotating machine driven from a motor of variable speed is to change RF and monitor the amplitude of vibration in the time and the frequency domain.

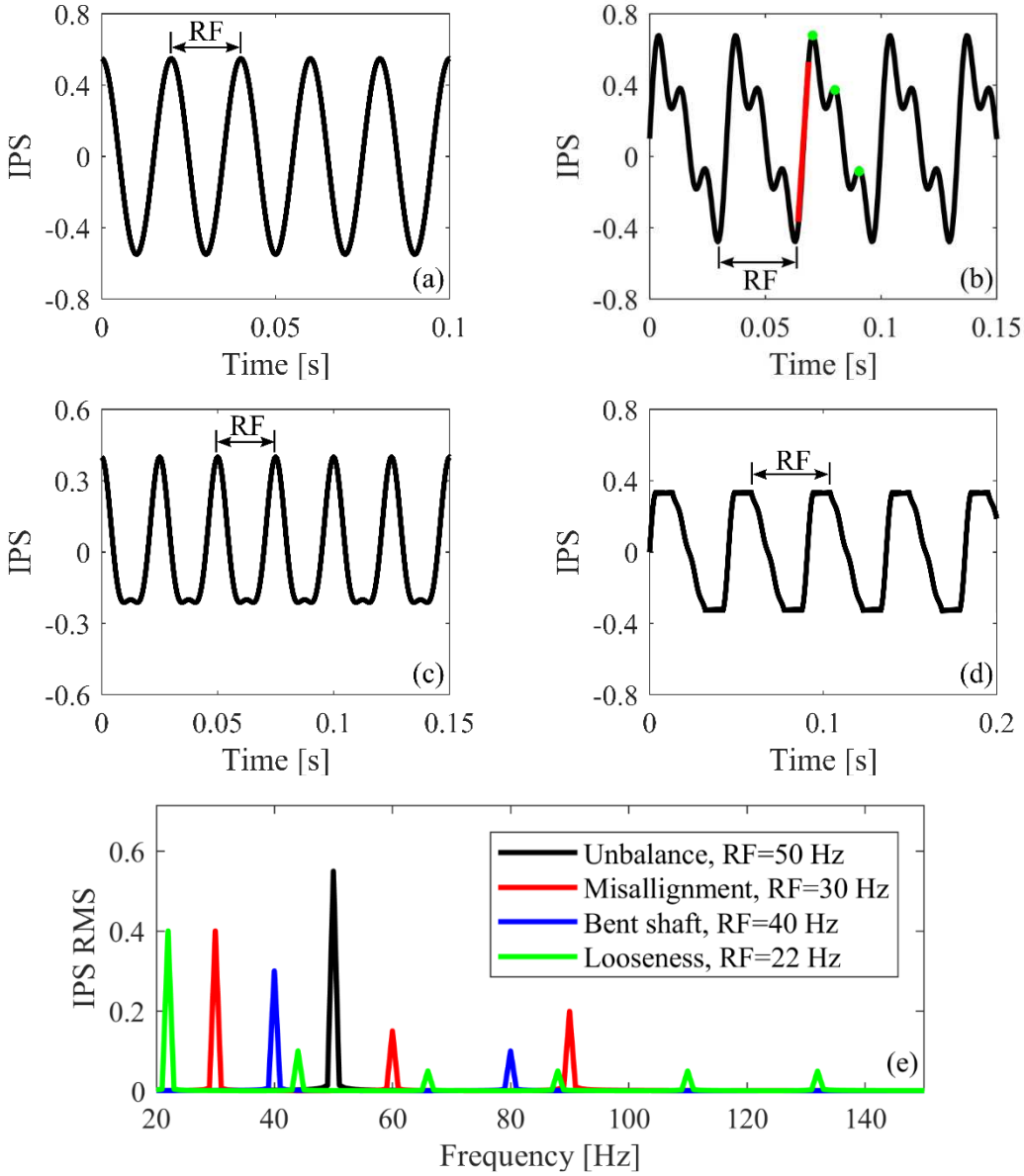

Figure 1.15 Vibration signal in time for **a)** unbalance, **b)** misalignment, **c)** bent shaft, **d)** looseness and **e)** their representation in frequency domain (Taylor, 2005).

In hydraulic turbomachinery, significant imperfections during the manufacturing procedure could result in deviations between the geometry of the various flowpaths of the rotor. Under such conditions, the pressure field in the rotor is not uniformly distributed, and this results in a hydraulic force that acts similarly with unbalance. In this case, the mass of fluid that corresponds to the non-uniform pressure field rotates with the shaft's rotation speed and creates vibrations similar to those presented in Fig. 1.15a. This phenomenon is possbile to exceed the mechanical unbalance in the cases of multistage centrifugal pumps, where the total head per stage is larger than 400 m (Gülich, 2008). Similarly to mechanical unbalance, the phenomenon

is affected by the rotating mass and thus exhibits stronger characteristics when the machine operates at higher flowrates.

Another typical fault mechanism is misalignment, which in hydraulic turbomachines is mainly caused due to the wrong coupling between the shafts of the rotor and this of the electric machine. When a machine operates under such conditions, shaft deformation creates strong bending moments that, consequently, increase the level of machine's vibration. These vibrations are usually composed form the first three harmonics of the RF, as it can be observed in Fig. 1.15e with the red colour line. For every rotation, the coupling used between the two shafts bends and then frees up (Taylor, 2005), which produces a move that affects the vibration's signature in time. The latter is given in Fig. 1.15b and consists of two areas; i) one fast increase (red colour line) that corresponds to the bending of the coupling, and ii) one slower that includes three peaks (green bullets) and depicts the disengagement of the coupling.

Another characteristic of the signal in time emerges from the fact that the harmonics of Fig. 1.15e are in phase and consequently, the signal amplitude is truncated on the negative side. Three main types of misalignment occur in rotating machinery; i) parallel (vertical or horizontal), ii) angular, and iii) mixed. A practical way to determine the exact type is the measurement of vibration in axial and radial direction. Angular and parallel misalignment appear when the three harmonics of RF are distinctive in the frequency spectrum of the axial and radial direction, respectively. The fact that the increase of RF does not affect the amplitude of misalignment vibration, signifies a way to differentiate the latter from a possible unbalance fault case.

The bent shaft can be considered as a form of unbalance, however it is also related with misalignment since a bent shaft usually deteriorates the alignment of the shafts. The frequency spectrum of a rotor with a shaft that suffers from bend is depicted in Fig. 1.15e, with the blue curve. In this case, the fundamental and its second harmonic frequency appear and, according to the time series presented in Fig. 1.15c, the second harmonic must be in phase. For the specific case, where the bend shaft creates simultaneously misalignment problem, the spectrum will probably has a third harmonic, but in this case the second harmonic is expected to dominate the spectrum.

Mechanical looseness is the fault condition where the machine's vibration increases because of the existence of loose headbolts and bearings. A typical representation of looseness in the time domain is presented in Fig. 1.15d. During the presence of mechanical looseness, the vibration signal is composed from a large number of RF harmonics and the peaks of the amplitudes are of rectangular shape. This behaviour is also depicted in the frequency spectrum of Fig. 1.15e, with the green colour line. Further deterioration of the current fault is possible to excite $0.5 \cdot$RF sub-synchronous vibrations, as well as the increase of the number of $0.5 \cdot$RF and RF harmonics. In hydraulic turbomachinery, the operation of the machine in higher flowrates increases the load and acts beneficially towards looseness vibration, since it decreases the amplitude. On the other hand, the decrease of the machine's load deteriorates the behaviour of loose bolts and bearing and increases vibration.

1.2.2.2 Electro-magnetic faults

Additional faults of electromagnetic nature can occur in the electric machine that is coupled to the hydraulic turbomachine. As it is presented in Chapter 2, the present study includes the use of two alternating current (AC) induction motors and consequently, the vibration review focuses on this kind of machines. The fundamental differentiation between synchronous and induction motors lies in the fact that the former rotate at the synchronous rotational frequency, SRF and the latter at a slightly slower value than SRF. The synchronous frequency can be calculated from Eq. 1.4:

$$SRF = \frac{2 \cdot GF}{n_p} \tag{1.4}$$

where n_p is the number of poles and GF the electric grid's frequency (50 Hz in Europe). The difference of induction motor's RF with the SRF is the slip frequency, SF, given from Eq. 1.5:

$$SF = SRF - RF \tag{1.5}$$

In case of a fault in the stator of the electric motor, the possible discrepancy at the stator acts in a similar way with the tongue of the spiral casing in a hydraulic turbomachine, but in the case of electric motors excites the pole passing frequency, PPF which is calculated from Eq. 1.6:

$$PPF = n_p \cdot SRF = 2 \cdot GF \tag{1.6}$$

The use of the Eq. 1.6 facilitates the detection of electromagnetic faults in the stator of induction motors, since the frequencies related with the stator appear at the second harmonic of GF. A higher induction motor efficiency results in lower slip values and consequently, in increased demand for adequate discretisation of the frequency domain, so as to be able to differentiate the mechanical from electro-magnetic faults. Figure 1.16 highlights a typical stator fault in an induction motor with one pair of poles and GF=50 Hz. Here, the stator fault excites the second harmonic of the GF (100 Hz) and lies next to the weaker 2RF.

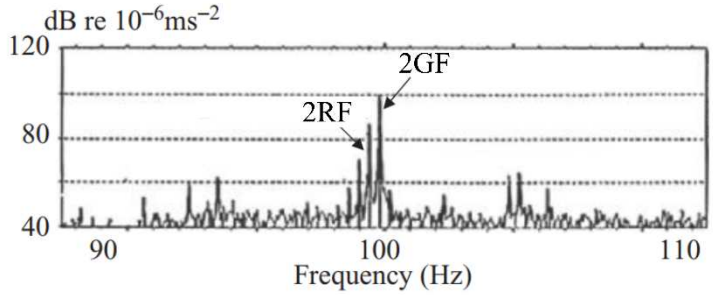

Figure 1.16 Focusing on the narrow frequency range of the vibration spectrum of an induction electric motor with a stator fault (Randall, 2007).

On the other hand, the rotor of the electric motor rotates with RF, which makes necessary to find additional characteristics in the frequency and time domain, in order to differentiate the rotor related faults from the mechanical faults of section 1.2.2.1. One strong indication that the electric motor suffers from a faulty rotor or from a broken rotor bar is that the signal is modulated by sidebands with a range frequency SBF_R that is calculated from Eq. 1.7 (Maxwell, 1983).

$$SBF_R = \pm SF \cdot n_p \rightarrow \text{Broken rotor bar or rotor} \tag{1.7}$$

Figure 1.17 presents the frequency spectrum for a specific case of a rotor's fault, this of broken rotor bar (Taylor, 2005). The induction motor of this figure has RF=59.5 Hz, SF=0.45 Hz, and it has two poles. In the spectrum of Fig. 1.17, the RF of the rotor appears at the spectrum, however the appropriate digitisation of the vibration signal and the focusing close to the RF area reveals the existence of sideband that appear at $\pm SBF_R$. In addition, the peak at 58.6 Hz ($-1 \cdot SBF$) exhibits the strongest amplitude of this part of the domain, which also highlights the appearance of an electro-magnetic fault coming from the motor.

In case of a loose rotor bar in the electric motor, the modulating mechanism remains but the frequency of the sidebands changes and equals the frequency of the passing of loose bar in front of each pole (LBPP). When a bar of the rotor becomes loose it results in an asymmetry in the electric circuit that increases the electromagnetic force in the bar at the opposite side of the electric armature. As a result a high frequency vibration is excited that follows the armature's

bar passing frequency (ABPF) and its amplitude is maximised when the loose bar passes from the poles (LBPP). The latter phenomenon is periodic and modulates the ABPF frequency, which acts as a carrier frequency in the vibration signal.

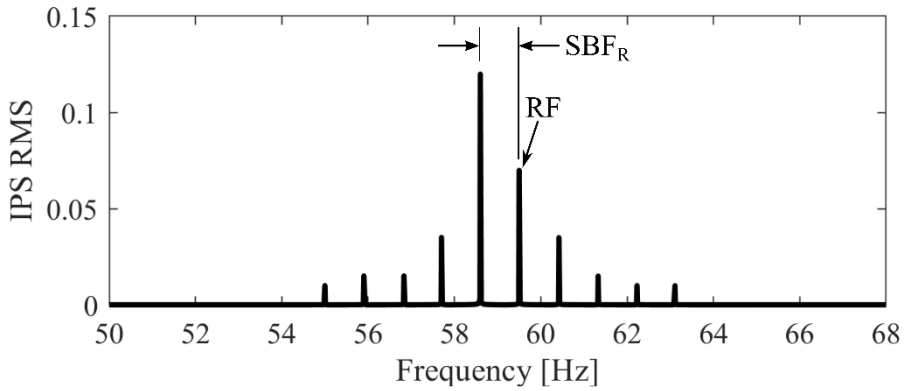

Figure 1.17 Focusing on the narrow frequency range of the vibration spectrum of an induction electric motor with a rotor fault (Taylor, 2005).

An interesting observation is that LBPP is independent of the number of poles, since it is the product of SRF with n_p, which practically means that for every kind of induction motor it coincides with the second harmonic of the grid's frequency. As a result, in case of a loose rotor bar, the frequency spectrum will be similar to that of Fig. 1.17, with maximum frequency the ABPF and sideband's frequency calculated from Eq. 1.8.

$$SBF_L = LBPP = SRF \cdot n_p = \pm 2 \cdot GF \rightarrow \text{Loose rotor bar} \tag{1.8}$$

1.2.2.3 Rolling element bearing faults

The most widely used mechanical component in rotating machinery industry is rolling element bearings. The bearings carry the loads of the machine, and condition maintenance strategies focus on their adequate monitoring, so as to ensure their optimum operation and the prompt detection of possible faults. In general, bearing faults exhibit impulsive behaviour that becomes more observable as the fault develops. Four frequencies can be excited by a defected rolling element bearing, which are related with the following mechanical parts; i) the outer race, ii) the inner race, iii) the cage, and iv) the rolling element. Their calculation is done with the use of kinematic Eqs. 1.9-1.12:

$$BPFO = RF \cdot 0.5 \cdot N_B \cdot \left(1 - \frac{D_B}{D_P}\cos\varphi_a\right) \tag{1.9}$$

$$BPFI = RF \cdot 0.5 \cdot N_B \cdot \left(1 + \frac{D_B}{D_P}\cos\varphi_a\right) \tag{1.10}$$

$$FTF = RF \cdot 0.5 \cdot \left(1 - \frac{D_B}{D_P}\cos\varphi_a\right) \tag{1.11}$$

$$BSF = RF \cdot \left(\frac{D_P}{2 \cdot D_B}\right) \cdot \left[1 - \left(\frac{D_B}{D_P}\cos\varphi_a\right)^2\right] \tag{1.12}$$

where BPFO is the ball pass frequency of the outer race, BPFI the ball pass frequency of the inner race, FTF the fundamental train frequency, and BSF the rolling element spin frequency. The calculation of the kinematic frequencies is based on the rolling element diameter, D_B, the pitch diameter, D_P, the number of rolling elements N_B and the angle, φ_a, between the total force applied to the bearing relative to the radial plane, as they are presented in Fig. 1.18.

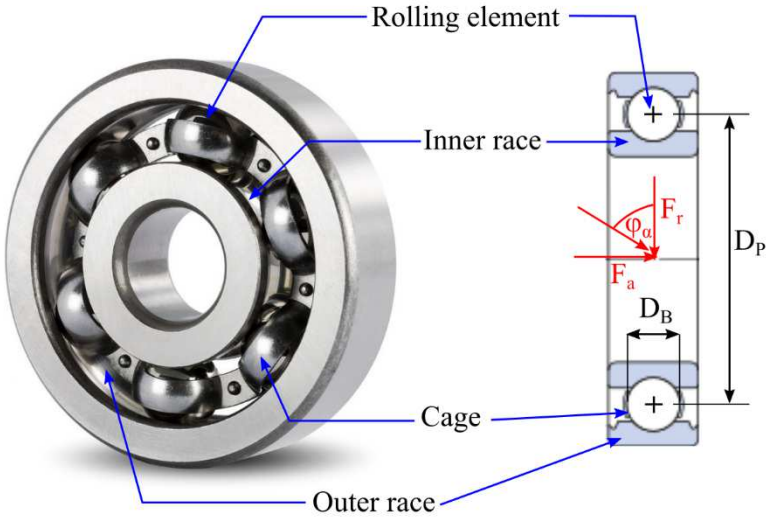

Figure 1.18 Ball bearing element along with the dimensions used for the kinematic frequencies calculation.

The kinematic Eqs. 1.9-1.12 assume that the contacts between the rollers and the races are ideal and there is pure rolling with no slip. In fact, there is always some slip due to the change of φ_α value at each rolling element as the radial and axial loads vary, which make each rolling element to roll at a different speed. At the same time, the cage of the bearing forces all elements to have the same mean speed, and consequently, introduces some random slip. In practice, the slip does not change much the calculated value of Eqs. 1.9-1.12 ($\leq 2\%$), however, it influences significantly the type of the measured signal in a way that makes impossible the detection of the fault frequency.

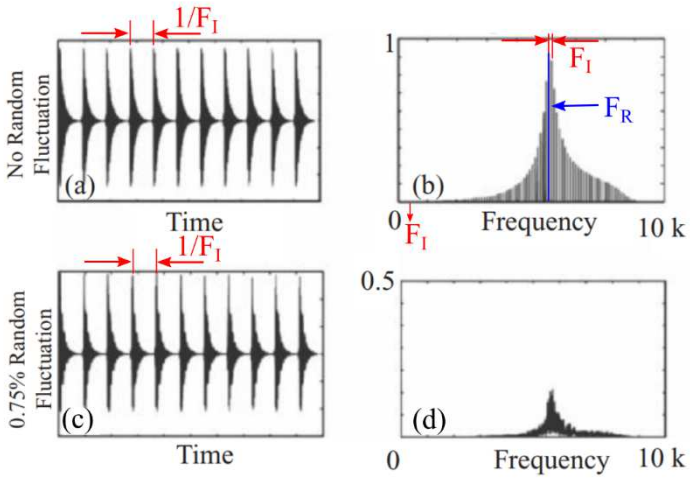

Figure 1.19 Impulse created by a bearing fault without slip (a-b) and with 0.75% slip (c-d) at a,c) time and b,d) frequency domain (Randall, 2007).

The effect of slip randomness is illustrated in Fig. 1.19 (Randall, 2007), by the comparison of the raw time domain (Figs. 1.19a,c) and its frequency spectrum (Figs. 1.19b,d) between an impulse with zero slip (Figs. 1.19a,b) and an impulse with 0.75% slip (Figs. 1.19c,d). As it is

expected, the introduction of such a small amount of randomness in the impulsive signal of Fig. 1.19a does not change its characteristics in the time domain of Fig. 1.19c. On the other hand, the corresponding frequency spectrum of the ideal case (Fig. 1.19b) depicts the high frequency resonance, F_R, created from the impulses of Fig. 1.19a. Here, F_R appears with a value almost two orders of magnitude higher than that of the impulse frequency, F_I. In addition, at the zero slip case of Fig. 1.19b, F_I can be observed clearly in the area close to resonance.

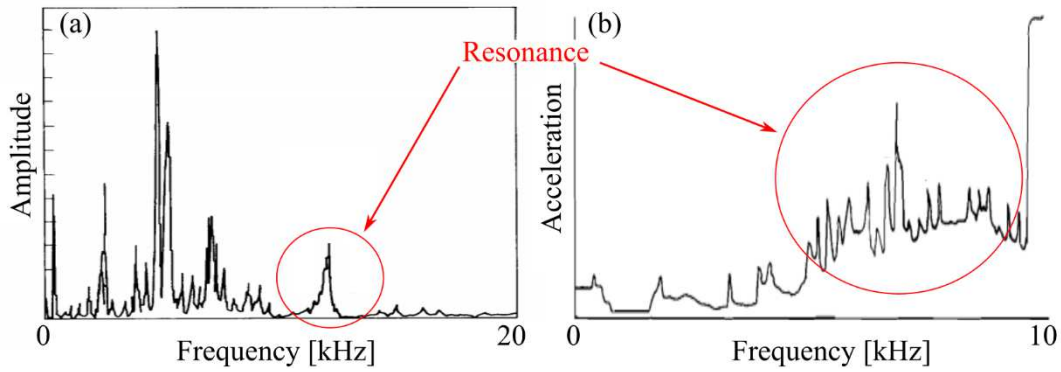

Figure 1.20 Resonances excited from bearings in the frequency spectrum of vibration measurements, **a)** McFadden, 1984b, **b)** Prashad, 1985.

In contrast to the time series plots, the addition of 0.75% slip deteriorates the characteristics of frequency spectrum (Fig. 1.19d), since it reduces the amplitude and complicates the identification of F_I close to F_R. The plot of Fig. 1.19d is of high significance, because it highlights the difficulty to detect faults that exhibit impulsive behaviour combined with randomness in the frequency spectrum of the raw signal. Typical frequency plots that present the excitation of high frequency resonance area due to bearing impulses are also provided in the plots of Figs. 1.20 and 1.21.

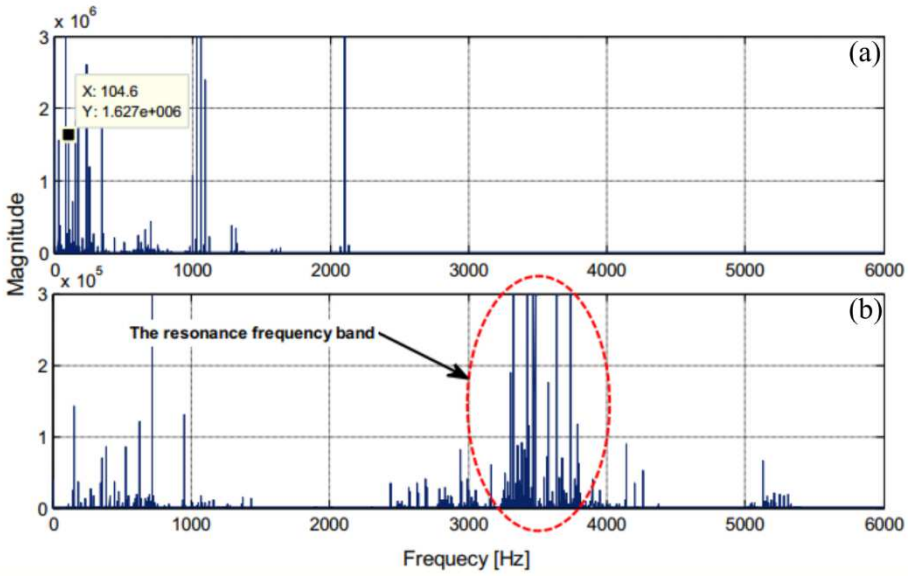

Figure 1.21 Frequency spectrum of the raw vibration signal **a)** under healthy bearing conditions, **b)** with a bearing that suffers from an outer race fault (Saidi, 2014).

The increased complexity of the frequency spectrum complicates the detection of the impulsive behaviour of bearing faults. In order to overcome those difficulties, the calculation of the envelope's frequency spectrum has been proposed (Fig. 1.22). The two plots of Figs. 1.22 correspond to the theoretical time signals of Fig. 1.19a,c and depict the minimum effect of the slip in the envelope's frequency spectrum. The calculation of the envelope requires the

construction of the analytic signal that is formed from two parts; i) one real part made from the filtered time series of the original signal and ii) one imaginary that is the Hilbert transformation of the filtered signal. The mathematical interpretation of this procedure is given analytically in the theoretical part of the signal processing techniques in Chapter 2.

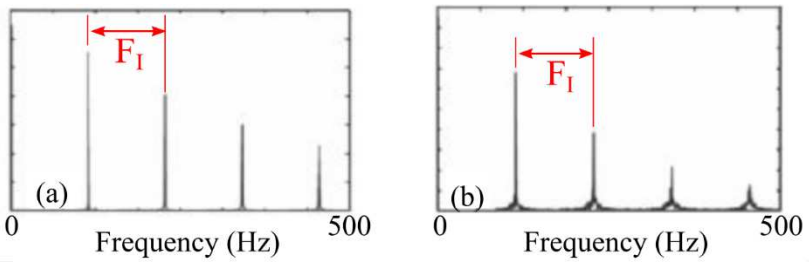

Figure 1.22 Envelope's frequency spectrum of the impulsive time series **a)** with zero slip, and **b)** with 0.75% slip (Randall, 2007).

As it can be concluded from the above, the adequate filtering of the measured signal is of high significance during the calculation of the envelope. Through the years, different approaches have been proposed for the adequate selection of the filter's characteristics. Some of them propose the demodulation of the high frequency resonance area (Figs. 1.20, 1.21b), while others propose the filtering of the frequency range that exhibits the largest difference in amplitude after the development of the fault (Darlow, 1974; McFadden, 1984a; Randal & Antoni, 2011). This discussion was relatively open until 2006, when Antoni presented the complete mathematical formulation of Spectral Kurtosis (SK), a tool that was found to be extremely efficient in the identification of frequency bands that show non-stationary, impulsive behaviour (Antoni, 2006; Antoni & Randal, 2006).

The term of spectral kurtosis was not new; Dwyer (1983a) has first introduced it as a tool to identify transients masked in seemingly stationary signals. Dwyer came to this important conclusion after observing the statistical moments of under-ice ambient noise signals. The focusing in specific frequency bands, such as this of [300 – 400] Hz that is presented in Fig. 1.23, shows that the three first statistical moments (Figs. 1.23a-c) exhibit relatively stationary and Gaussian characteristics, since their values remained constant over time and their absolute values were equal to that of Gaussian distribution. On the other hand, kurtosis moment (Fig. 1.23d) deviated significantly in time and took values that are very different from a Gaussian distribution.

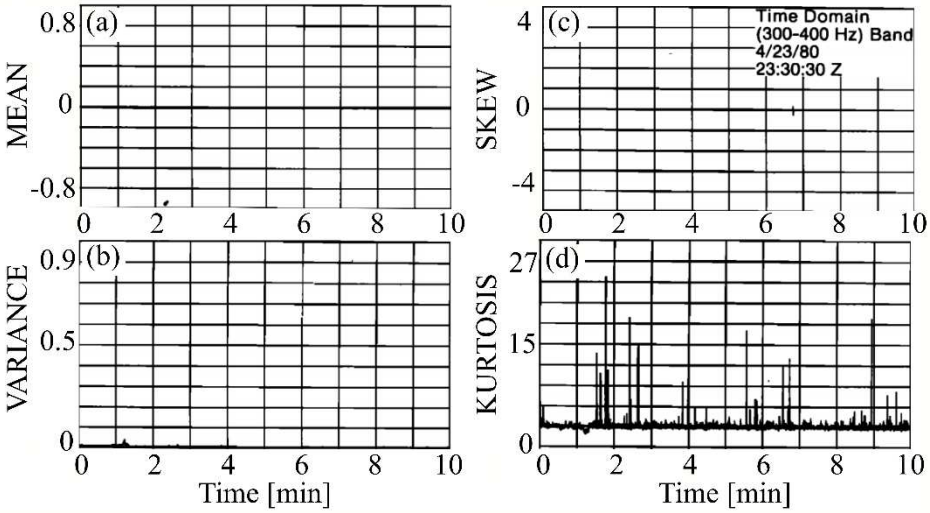

Figure 1.23 The deviation in time of **a)** mean, **b)** variance, **c)** skewness, and **d)** kurtosis values for the [300 – 400] Hz band (Dwyer, 1981 & 1983b).

As it can be observed in the plot of Fig. 1.23d, the kurtosis value of the noise signal reaches peaks with amplitude nine times larger than that of Gaussian kurtosis value, which equals 3. Furthermore, Dwyer investigated the effect of the frequency bands and realised that there is a particular frequency range, where the value of kurtosis is maximised. The latter conclusion was of extreme importance, because it constituted the basis of the SK theory that was established afterwards by Antoni (2006), and was implemented with the use of the Fast Kurtogram (Antoni, 2007b). More specifically, the identification of the range in which the kurtosis is maximised provides the optimum range of the filter to be used for the formation of the analytic signal. The amplitude of that analytic signal is the envelope of the non-stationary process that, in case of the bearings, is the impulsive behaviour of their faulty condition. The mathematical interpretation of SK is given in the theoretical part of the signal processing techniques in Chapter 2.

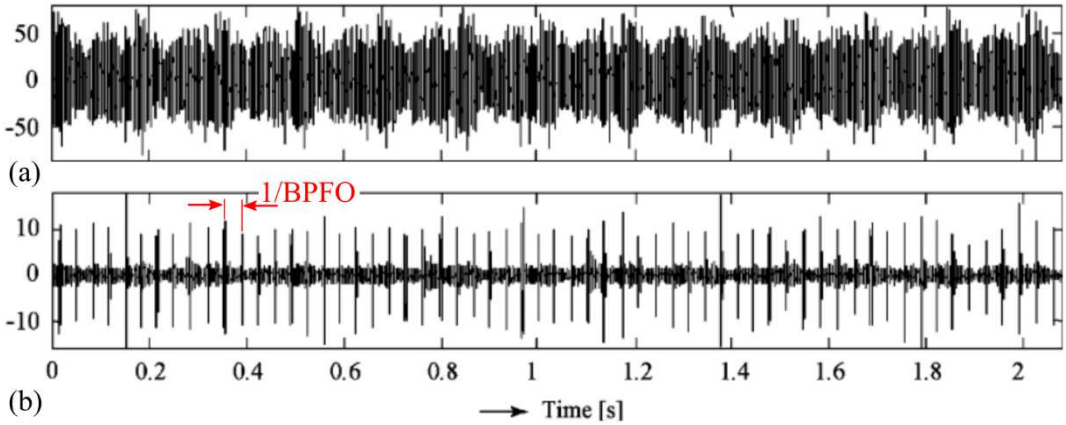

Figure 1.24 a) The raw measured vibration time series from a machine with an outer race bearing fault, and **b)** its corresponding filtered time series after the application of SK (Antoni & Randall, 2006).

The extraction of the faulty bearing patterns in the filtered time domain and the frequency spectrum of the envelope after the adequate use of SK tools has been confirmed from several authors (Sawalhi, 2004; Antoni & Randall, 2006; Bechhoefer, 2011; Ruiz-Cárcel, 2014; Saidi, 2014; Xiang, 2015; Ren, 2019). The ability of the method to extract the bearing faults information even during its initial stages of development in Fig. 1.24, is confirmed for the case of an outer race bearing fault (Antoni & Randall, 2006). In this plot it can be observed that the impulses in the raw measured signal are masked from the overall noise of the machine.

Figure 1.25, depicts the expected form of the impulsive bearing faults in the filtered signal time domain, along with their envelopes. The outer race fault refers to wear that appears at the stationary outer race (or ring) of the bearing (Fig. 1.18) and is usually caused due to the inadequate lubrication or by the faults discussed in section 1.2.2.1. During the operation of the machine, every passing of the rolling element from the faulty area creates an impulse that excites some of the bearing's or the machine's resonances (Figs. 1.20, 1.21). The impulses of the outer race fault are depicted in the time series of Fig. 1.25a, and their amplitude remains relatively constant, since the location of the fault remains stationary against the outer race. The impulse signal in time is composed by the resonance component, which behaves as the carrier frequency that its amplitude is modulated by the BPFO period (1/BPFO, Fig. 1.25a). In the corresponding frequency spectrum of the envelope (Fig. 1.25a) the BPFO and its first harmonics usually appear.

The inner race fault refers to wear that appears at the inner race of the bearing, which rotates along with the shaft (Fig. 1.18), and is caused by the same reasons previously discussed for the outer race fault. Similarly to the outer race fault, during the machine's operation, every passing of the rolling element from the faulty area creates an impulse that excites some of the the machine's resonances. The impulses of the inner race fault are depicted in the time series of Fig. 1.25b, where their amplitude behaves differently to the outer race fault, although the

resonance excited plays the role of the carrier frequency. In this case, the amplitude of the impulses is modulated from both the BPFI and RF, as it is presented in Fig. 1.25b. In the corresponding frequency spectrum of the envelope (Fig. 1.25b) the RF, the BPFO with sidebands at RF and its first harmonics are expected to appear. In general, the vibrations related with the inner race fault are usually weaker than those of the outer race fault, since signal's intensity reduces as the latter travels towards the accelerometer.

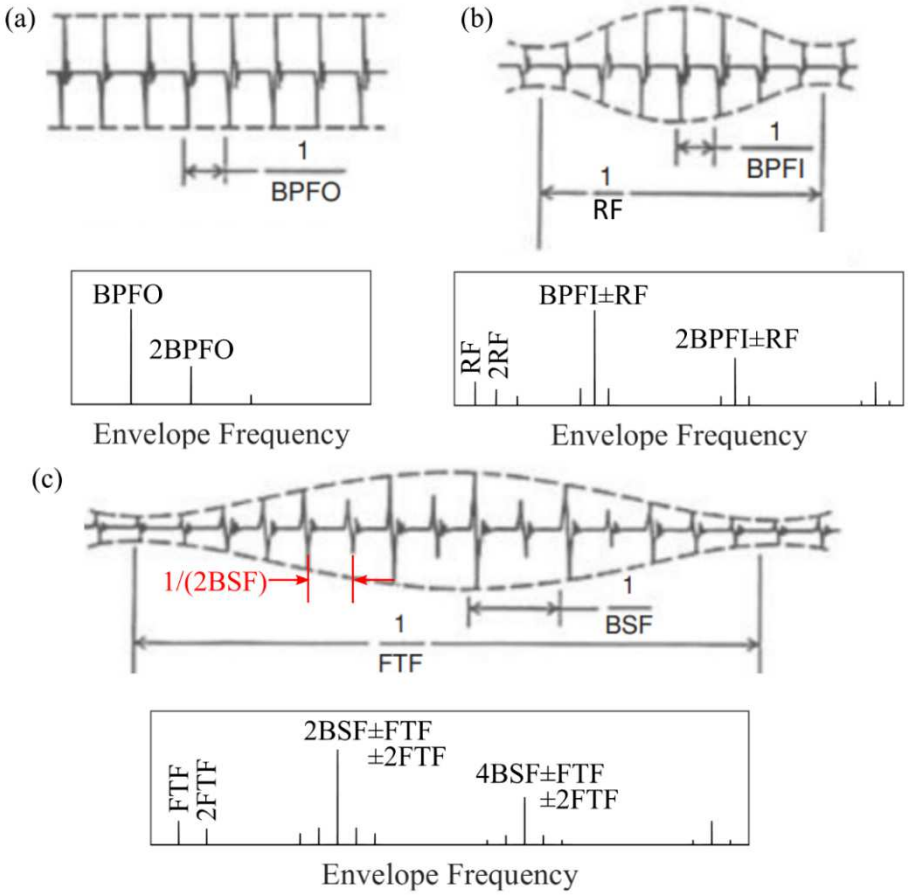

Figure 1.25 Typical shape of impulse in time (Randall, 2007) and frequency of the envelopes during the formation of **a)** outer race, **b)** inner race, and **c)** rolling element faults.

Another mechanism discussed in this section is that of a faulty rolling element, usually caused due to inadequate lubrication. The rolling elements (Fig. 1.18) are kept together with the use of the cage and rotate with the same speed, while each of them rotates additionally around its axis at BSF frequency. Similarly to the previous bearing faults discussed, during a rolling element fault impulses are created that excite some resonances. In this case, two impulses are created in one ball spin period (1/BSF), one when the roller passes from the inner race and one when it passes from the outer race. Consequently, the time span between the two impulses is 1/2BSF, while the time span between two impulses created in the same race is 1/BSF. Similarly to the other bearing faults, the resonance excited is the carrier frequency but now it is modulated from the 2BSF and the FTF (Fig. 1.25c). The expected envelope's frequency is also given in Fig. 1.25c, where the FTF, the BSF with sidebands at FTF and its first harmonics are expected to appear.

Finally, the fault mechanism related with the cage (Fig. 1.18) of the bearing is discussed. This type of fault does not produce impulsive behaviour and mainly behaves similarly to unbalance, since its mechanism deals with the wear and the material removal of the cage. The vibration signature of this fault in time is sinusoidal, following an FTF frequency and, consequently, it is possible to identify its presence at the frequency spectrum, similarly to the faults discussed in section 1.2.2.1.

1.3 Detection and study of cavitation in hydraulic turbomachines

In section I.2 the different types of large-scale cavitation developed in hydraulic turbomachines is introduced. When the operation of the machine is accompanied by cavitation, bubble implosion stresses significantly the material of the nearby solid surfaces and creates wear and material removal. In case of hydraulic turbomachines, the area most prone to cavitate is that of the impeller/runner, where the flow is accelerated relative to the stationary parts. As a result, the rotating solid surfaces of the machine (blades, hub & shroud) are those that usually suffer from wear and material removal. In a rotating machine, material removal at the rotor is expected to increase the unbalance and creates additional mechanical vibrations that further stress the bearings. The failure of prompt detection of cavitation at this stage can cause permanent failure on rotor's blades and make the hydraulic turbomachine unable either to provide power to the fluid in case of pumps or to produce electric power in the case of hydroturbines, as efficiently as it is designed to.

It should be noted that in some centrifugal pumps, manufacturers have proposed the use of an axial inducer upstream of the impeller, in order to improve their suction performance and avoid the implications of cavitation. By this way, the static pressure of the flow is increased before entering the pump, and as a consequence, cavities formation is reduced. Even with the use of an inducer or other specific design of the pump to improve its suction behaviour, sometimes vapour bubbles are developed close to its inlet, as a result of improper installation or operating conditions of the pump.

The aforementioned effects on machine's normal operation forced scientists and engineers to develop various methodologies in order to study and detect the onset and development of cavitation. For many years, these methods were mainly experimental, however the increase of available computational power allowed the implementation of CFD algorithms towards the study of the phenomenon. This section reviews the most significant experimental methods that have been proposed for the detection of cavitation, as well as the numerical tools used for the study of two-phase flow development in hydraulic turbomachines. The various methods and their application in several experimental and numerical works are discussed in the next sections, and their advantages and disadvantages are identified.

1.3.1 Experimental approach

The development of experimental tools for the detection of cavitation in reaction hydroturbines and centrifugal pumps requires the performance of cavitation tests, the selection of proper sensors and their mounting positions, as well as the analysis tools used for the processing of the signals measured. This part of the Thesis reviews the various types of tests, sensors and signal processing techniques proposed in the literature and highlights their effectiveness and applicability, along with their weaknesses. At first, the various techniques used for the execution of cavitation tests in closed hydraulic turbomachines are presented, while the main body of this section classifies the methods with respect to the cavitation detection criterion and the signal processing techniques used. All the experiments presented in this study have been conducted with the use of water as fluid medium.

1.3.1.1 Cavitation test configurations

Three types of cavitation tests for centrifugal pumps are proposed in ISO 9906:2012; i) the closed loop arrangement, ii) the open sump with level control, and iii) the open sump with throttle valve. All of the tests aim to derive the cavitation characteristic curve of the pump (σ-Ψ), which describes the variation of its total head, Ψ, under constant flowrate conditions, Φ, as a fuction of Thoma cavitation number, σ. The mathematical definition of these parameters is given in Chapter 2. The Thoma cavitation number illustrates the difference of suction pressure from this of vapour pressure value. A typical map of σ-Ψ characteristic curve at constant flowrate conditions is presented in Fig 1.26. Here, it can be observed that when the σ value

reduces, there is a point, σ_o, where the total head starts to drastically drop. In practice, the σ-Ψ curve illustrates the effect of cavitation on the ability of the pump to provide power to the working medium. The curve of Fig. 1.26 applies also for reaction hydroturbines, and is the basis of the majority of cavitation related studies that are discussed in the present Thesis.

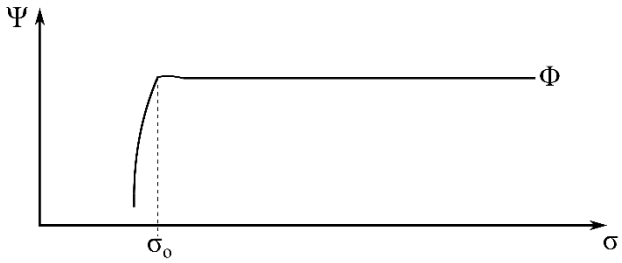

Figure 1.26 Typical σ-Ψ characteristic curve for hydraulic turbomachines under constant flowrate.

The closed loop arrangement, shown in the sketch of Fig. 1.27a, consists of one closed tank (1) that supplies the centrifugal pump under examination (2). The water after the pump returns to the closed tank. In this case, the static pressure level is regulated from a vacuum pump (3) the suction of which is positioned at the upper part of the closed tank. The main advantage of this method is that the static pressure is controlled accurately and the fact that its regulation does not affect the flowrate. However, the forced circulation of fluid medium in a closed loop configuration increases its temperature, and for this reason a heat exchanger (4) is established, so as to keep the medium's temperature constant. The use of additional mechanical equipment, such as the vacuum pump and the heat exchanger, makes this type of configuration the most expensive. During the review of the published studies, the closed loop arrangement will be noted as CTA.

The open sump with the level control is shown in Fig. 1.27b, and regulates the pressure level in the configuration from the unloading ($z_1 \rightarrow z_2 \rightarrow z_3$) of the tank (1) at the suction of the tested pump (2), with the aid of a second tank (3) and pump (6), after properly regulating valves (4) and (5). The disadvantage of the aforementioned procedure is that increases significantly the time duration of the experiment but also the number of the establishments (two tanks) and the hydraulic equipments (centrifugal pumps, valves etc.) that are used. During the review of the published studies, the open sump with the level control arrangement will be noted as CTB.

The open sump with throttle valve configuration is presented in Fig. 1.27c and consists only from the pump (1) and one open tank (2). In this case, the lowering of the static pressure level is achieved by throttling the suction valve (3) that consequently changes the system's characteristic curve and the flowrate. In order to restore the flowrate for the conduction of the test under constant Φ conditions, the discharge valve (4) has to be further regulated. This configuration is simpler than the two preceded, however the throttling of the suction valve is possible to disturb the axisymmetric flow at the inlet of the impeller. During the review of the published studies, the open sump with throttle valve arrangement will be noted as CTC.

There are several cavitation studies on centrifugal pumps (Al Hashmi, 2009; Al Thobiani, 2010; Stopa, 2013; Al Obaidi, 2019; Lu, 2019), where the detection of two-phase flow development does not follow any of the three proposed from the ISO 9906:2012 techniques. On the contrary, they operate the machine at higher flowrates, where the flow field is accelerated and the pump is more prone to cavitate, and compare those measurements with those obtained in lower flowrates. The conclusions drawn from these works can be used only for the detection of the phenomenon but not for the study of its development, which should be a function only of σ. During the review of the published studies, that arrangement will be noted as CTD.

The first two configurations presented (Figs. 1.27a,b) can be used for the derivation of σ-Ψ curves of reaction hydroturbines. The closed loop arrangement for hydroturbines is given in Fig. 1.27d. In these tests, the hydroturbine (1) is established at the discharge of a pump (2), which provides the turbine with medium of increased hydraulic power. At this point, it is

significant to mention the differentiation that takes place in case of testing hydroturbine prototypes, where it is evident that the derivation of σ-Ψ curves is impossible. In such tests, the examination of two-phase flow conditions is achieved with the operation of the machine in extreme conditions (part or full loads) by simply regulating the guide vanes of the turbine (Bourdon, 1994; Escaler, 2002, 2003, 2004, 2006, 2015; Schmidt, 2014). During the review of the published studies, that method will be noted as CTE.

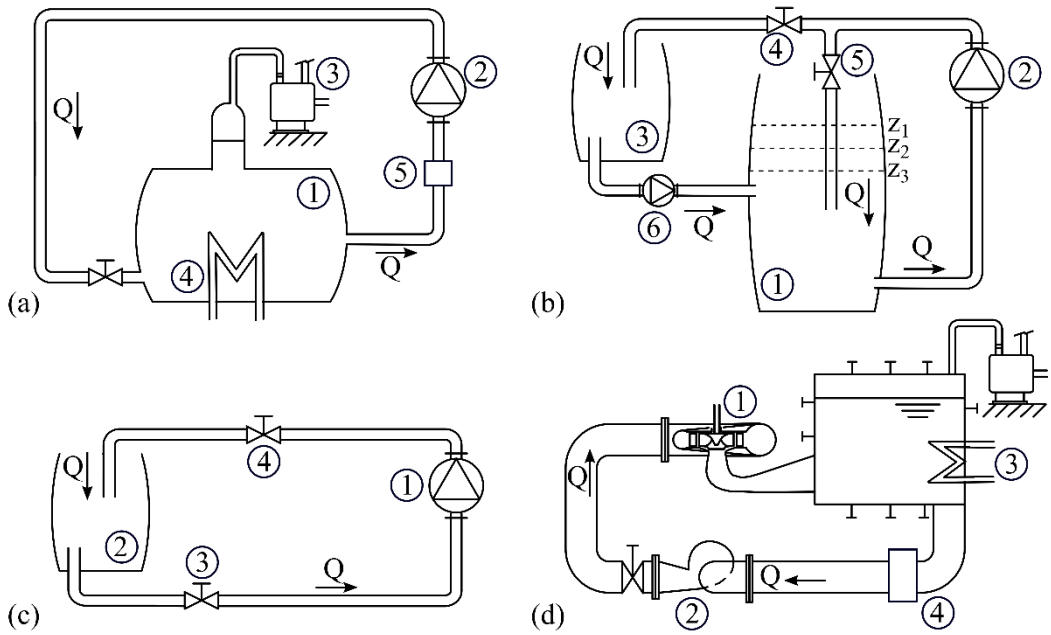

Figure 1.27 Cavitation test configurations for **a,b,c)** centrifugal pumps and **d)** hydroturbines, **a,d)** closed loop arrangement (Papantonis, 2016), **b)** open sump with the level control and **c)** open sump with throttle valve.

For a minority of published studies on hydraulic turbomachines, the derivation of cavitation characteristic curves is accompanied with flow visualisation measurements. Especially in studies that focus on the detection of cavitation, the latter is used as a tool that validates the existence of vapour formations and examines the possible changes of their shape and extent as function of σ. In order to conduct flow visualisation tests, parts of the machine are manufactured by transparent materials, usually Plexiglas. For cavitation tests in centrifugal pumps, these parts include the front casing, and the shroud in the case of closed impellers (Duplaa, 2010; Dong, 2019). In hydroturbine models, the draft tube is most frequently made of Plexiglass for the investigation of the vortex ropes (Fig. I.4c) and the cavitation at the TE of the blades (Iliescu, 2008; Zuo, 2014).

It should be noted that the increased complexity introduced from the manufacturing of the transparent parts and their assembling with the metallic parts of the machine, justifies the few published works that use the flow visualisation method along with detection measurements. However, the derivation of σ-Ψ curves with the methods CTA, CTB and CTC ensures the existence of cavities, especially after the drop of the total head. For this reason, flow visualisation methods are considered as a useful but not necessary tool for the conduction of detection measurements in hydraulic turbomachines. According to the author's opinion, only the results drawn after the conduction of cavitation experiments with the use of CTD method could be questioned in terms of cavities appearance, if they are not accompanied by flow visualisation observations. Nonetheless, results from such works that agree with the general trend of literature conclusions are also presented in this section.

For some specific tests, it is significant to control the amount of air and gas particles in the fluid that circulates in the test configuration. In Introduction it is concluded that the increased amount of such particles in the fluid makes it more prone to cavitate. Typical examples of such tests are those that deal with the improvement of the rotor design of a hydraulic turbomachine

in terms of cavitation behaviour or the extraction of suction behaviour of a prototype from a model tested in a laboratory. In these cases, the comparison of the results between two rotors (initial and optimised, model and prototype) can be made when the air and gas content of the fluid is similar. In fact, the use of model tests require additionally the satisfaction of the geometric, dynamic (Φ,Ψ), pressure (σ) and Froude similitude (Papantonis, 2016).

The control of the air and the dissolved gasses is made of the use of the heat exchanger presented in Figs. 1.27a (4) and 1.27d (3). This procedure dissolves the particles and the heating continues until to obtain water with 0.3-0.5% gas content (Papantonis, 2016). The measurements of the gas content in the fluid is done with the use of special arrays ((5) in Fig. 1.27a, (4) in Fig. 1.27d), which are established in the configuration. The description of cavitation test methods reveals that the uniform heating of the fluid can be achieved only in the case of closed loop arrangements. Nevertheless, in cases where the detection of cavitation is attempted or in cases where different designs are tested with the use of the same medium under identical thermodynamic conditions, there is no such requirement. This justifies the fact that the vast majority of the research studies reviewed and presented in this section, have not presented any data regarding the air and gas content.

1.3.1.2 Performance monitoring of hydraulic turbomachines

The first approaches towards the study and the detection of cavitation in hydraulic turbomachines is done with the development of the Net Positive Suction Head available (NPSH) equation for the pump's establishment. The corresponding value for hydroturbines is defined as Net Positive Discharge Head (NPDH), since hydroturbines exhibit minimum pressure condition at their discharge (Schiavello, 2009). Henceforward, until otherwise mentioned, the references to NPDH are skipped, since they are the same with those for the NPSH. In addition, Thoma (1935) non-dimensionalised the NPSH available number with the use of the total head of the hydraulic turbomachine and created Thoma cavitation number, σ. The mathematical definitions for NPSH and σ parameters are given analytically in the theoretical part of Chapter 2.

The use of NPSH and σ numbers allows the study of centrifugal pump operation as a function only of the suction conditions under constant flowrate (Φ). This is accomplished with the derivation of NPSH-H_{tot} curves or their non-dimensionalised form, σ-Ψ (Fig. 1.26) for several flowrates, as it is depicted in Fig. 1.28. The study of machine's operation is examined by progressively reducing the static pressure level of the configuration with the ways already discussed in section 1.3.1.1. As NPSH takes lower values, the working liquid fluid in the test configuration reaches closer to its vapour state and for NPSH=$NPSH_{VI}$ the first bubbles can be visually observed (blue colour markers in Fig. 1.28).

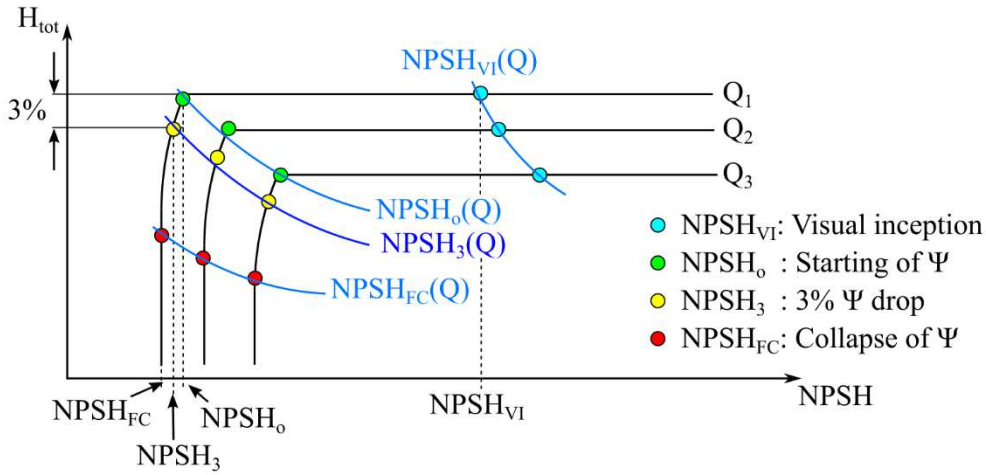

Figure 1.28 Typical cavitation characteristic curves along with various cavitation detection criteria.

As it is expected, the visual inception of the phenomenon does not influence the total head which remains relatively constant until NPSH= $NPSH_o$, where its value starts to decrease (green colour markers in Fig. 1.28). Between these two OPs ($NPSH_{VI}$, $NPSH_o$) the cavitation area increases without an actual impact on the machine's performance. However, the further reduction of NPSH at lower values from $NPSH_o$, drives H_{tot} value in a rapid collapse (Fig. 1.28). This drop is characterised from three operating points (Schiavello, 2009), $NPSH_1$, $NPSH_3$ and $NPSH_{FC}$ that correspond to the NPSH value when H_{tot} drops by 1%, 3% (yellow colour markers in Fig. 1.28) and 10% (red colour markers in Fig. 1.28), respectively.

The separation of NPSH-H_{tot} curve in different stages of cavitation development ($NPSH_{VI}$, $NPSH_o$, $NPSH_1$, $NPSH_3$ & $NPSH_{FC}$) was of fundamental importance, because provided engineers with the first practical tool for the characterisation and the detection of cavitation in hydraulic turbomachines. The cavitation was characterised as harmless for the machine's performance for NPSH>$NPSH_o$ and damaging for NPSH<$NPSH_o$. In order to generalise this conclusion, the testing of several flowrates (Fig. 1.28) allows the development of $NPSH_{VI}$(Q), $NPSH_o$(Q), $NPSH_1$(Q), $NPSH_3$(Q) and $NPSH_{FC}$(Q) curves. In this way, every manufactured machine has limits for the total range of its operating conditions (Q) that correspond to the passage from one cavitation state to another.

Among these curves, the $NPSH_3(Q)$ prevailed and is used from manufactures until nowadays. The reason for the broad use of $NPSH_3(Q)$ curve deals with; i) its direct calculation, ii) the 3% drop of the head is easily observable even with the use of low precision measuring devices, and iii) the fact that it sets an alarm during the initial stages of total head drop. In the case of large machines that are of critical importance, the $NPSH_1$ criterion is used, in order to detect cavitation at an earlier stage. It is underlined that 1% criterion requires the use of high precision sensors. Consequently, the $NPSH_3(Q)$ or its non-dimensional form σ_3 describes the machine's behaviour and is provided from the manufacturer to the users along with the rest characteristic curves of the machine under non-cavitating conditions. In this way, the detection of cavitation could be achieved by the monitoring of performance quantities of the hydraulic turbomachinery.

1.3.1.3 Application of traditional tools in noise and vibration measurements

The use of the 3% of total head drop represents the first attempt of the engineers towards the detection of cavitation in hydraulic turbomachines. According to the section 1.2, the $NPSH_3$ method can be classified as a performance-based condition monitoring technique. However, the application of such a strategy implies some risk for the efficient operation of the machine. As it is shown in the Introduction of this Thesis, cavitation even at earlier stages can cause significant wear, noise and vibration. The early stages of two-phase flow development are defined as those OPs that lie in the area between the visual inception point and the 3% of total head drop. Under such conditions, cavitation may cause significant damage in the machine in long term operation, though it is not detected by its performance monitoring.

As a consequence, additional tools have been developed for the monitoring of hydraulic turbomachines that identify cavitation presence, based on noise and vibration measurements. The latter attempt to detect the sound and the mechanical oscillations generated during the implosion of vapour cavities. The advantages of noise and vibration measurements with respect to their application in condition-based maintenance strategies in hydraulic turbomachinery are summarised in section 1.2. The experiments are conducted in the configurations described in section 1.3.1.1, and in parallel, the noise and vibration measurements are obtained.

In the case of vibration measurements, usually accelerometer sensors are used, which measure the acceleration of vibrations and are located at the external casing of the machines or at their bearings. On the other hand, there are three types of sensors able to measure sound pressure depending on the propagation medium; microphones, hydrophones and acoustic emission (AE) sensors. The first are usually located in a small distance from the machine, the second are positioned in the flow and the third at the external solid parts of the casing, similarly to vibration sensors. The exact mounting positions of the sensors, whose results are discussed here, are illustrated with the use of Fig. 1.1, similarly to the results of section 1.2.1.

In this section, the studies that use–noise and vibration measurements and process their signals with a traditional approach are reviewed. The traditional approach includes the analysis of i) the raw measured signal in time, ii) the Root Mean Square factor, iii) the frequency spectrum with the use of Fourier Tranformations or Power Spectral Density algorithms, and iv) the use of powerband tools that quantify the energy included in discrete bands or a range of frequencies.

The signal in time domain

Al Hashmi (2009) tests one radial centrifugal pump and measures its vibrations at the front volute casing (Fig. 1.1b), in z-direction, close to the outlet pipe (φ=0º) with a high frequency accelerometer that has resonance at 20 kHz. The tests are conducted with the application of the CTD method and include the examinations of seven flowrates, the higher of which could be accompanied with cavitation. The formation of cavities in the suction of the pump is not studied visually, which slightly complicates the drawing of robust conclusions. Nevertheless, the results of this study are discussed because are the only found in the literature, where the time series of the raw vibration signals (Fig. 1.29b) are given in time along with their corresponding histograms (Fig. 1.29a).

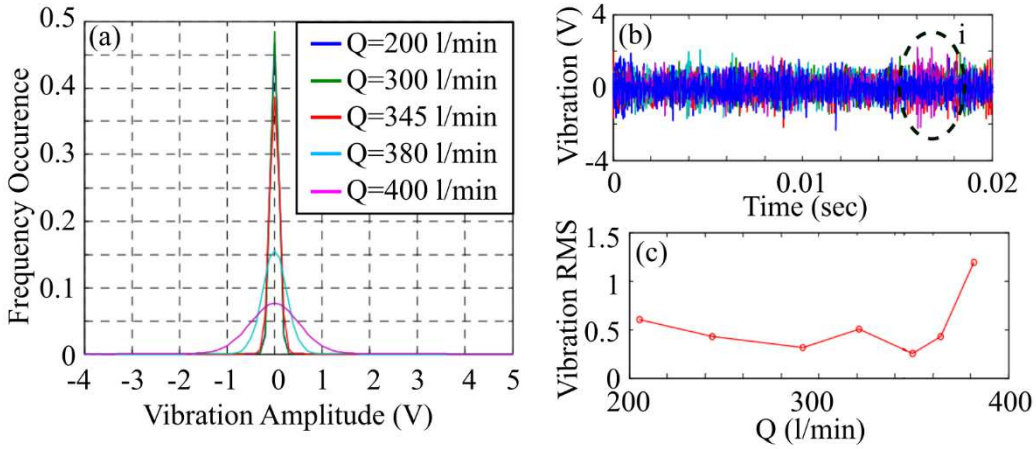

Figure 1.29 a) The normalised histogram, **b)** the measured time series, **c)** the RMS values of vibration measurements in different flowrates (Al Hashmi, 2009)

The overlaid raw measured time series, which were plotted for five representative flowrates, do not exhibit significant differences for the short time span (0<t<0.02 sec) that are presented. In general, this is an expected behaviour, since the un-processed vibration signal obtained from a hydraulic turbomachine contains a large number of mechanical and hydraulic noise sources (Cernetič, 2008; Farokhzad, 2013). After a closer observation, few peaks that correspond to the highest flowrate under examination (Q=400 l/min) occur for 0.016<t<0.018 sec (area i), which increase locally the vibration amplitude of the time series. The presence of such peaks is highlighted in the histogram results presented in Fig. 1.29a, where the passing to higher flowrates results in a probability distribution of larger deviation. The larger deviation is created from measured values that lay at the limits of the sample and are associated with the area (i) of increased amplitude shown in Fig. 1.29b. Those changes at the histogram characteristics appear also for Q=380 l/min, which manifest the impact of higher flowrates in the obtaining of extreme vibration values. Similarly to these results, the RMS values presented in Fig. 1.29c as a function of flowrate, depict also a significant increase at the highest flowrate.

A clearer depiction of the effect of cavitation in vibration signal is given in the study of Duplaa et al. (2010), where the behaviour of a radial centrifugal pump under fast startups conditions is examined. In order to ensure the fast start up, the pump is coupled with the motor with the use of an electromagnetic clutch, after the latter reaches its nominal rotational speed (n=3000 rpm). The duration of the fast start up is achieved in 0.6 sec, as it can be seen in the plot of rotation speed that is given in Fig. 1.30a as function of time. The tests are performed in

different suction conditions, after the application of CTA so as to study the effect of cavitation during fast start ups. The comparison of the vibration results under normal (Fig. 1.30b) and cavitating conditions (Fig. 1.30c) highlights the effect of two-phase flow formation during the fast start up, for 0.3<t<0.6 sec. In this time span, the onset of strikes is depicted, which abruptly rises the amplitude of vibrations and weakens only after the stabilization of the rotation speed of the pump. The plot of Fig. 1.30c is important because it clearly illustrates the cavitation impulses, although it is obtained under heavily transient conditions, which complicates the further study of possible periodical modulations on it.

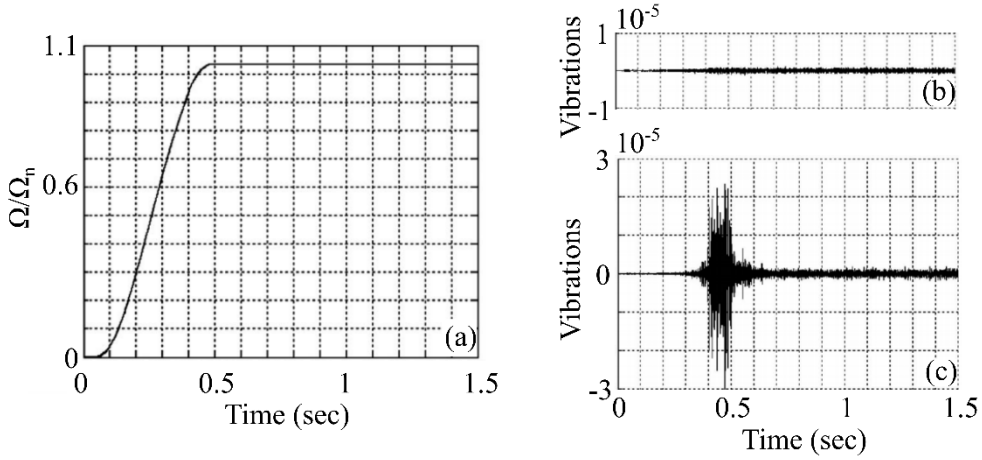

Figure 1.30 a) The change in rotational speed with time, and the simultaneous time series of non-dimensional vibration measurements under **b)** non-cavitating, and **c)** cavitating conditions (Duplaa, 2010).

The pattern of cavitation in the measured acoustic time series (Fig. 1.31) is observed in the results of Schmidt et al. (2014) for a Kaplan turbine prototype. That signal corresponds to operation under high flowrates, which lay above the cavitation limit that is provided from the manufacturer. The AE sensor is located in the inner cover above the runner at x-direction, for x=0 m (Fig. 1.1a). According to their results, the operation of Kaplan at overload conditions, creates impulses, signal areas of small duration of increased amplitude (Fig. 1.31). The impulses of Fig. 1.31 exhibit a periodic behaviour that follows the BPF and the guide vanes frequency. In contrast to the transient results of Fig. 1.30, the conditions of Fig. 1.31 can be considered as steady state, since the rotation speed and the flowrate of Kaplan remain constant during the AE measurements. This difference in operating conditions justifies the differences between the pattern of the impulses of Fig. 1.30 with those of Fig. 1.31 that exhibit the periodicity produced from the constant rotation speed of the machine.

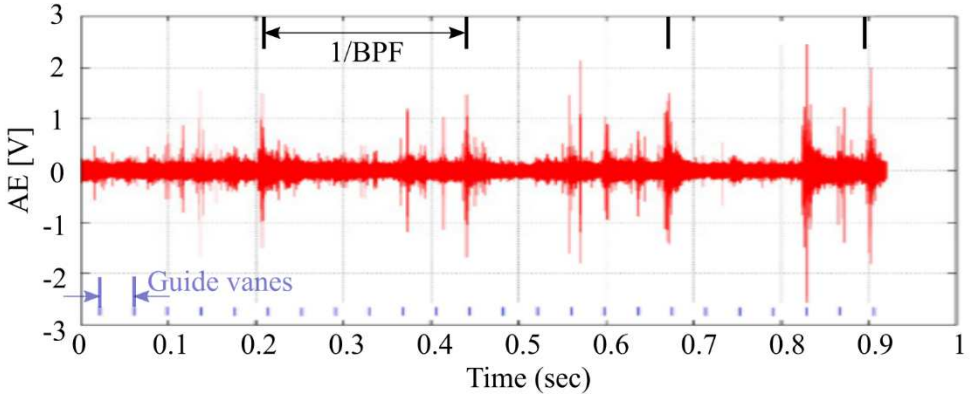

Figure 1.31 Measured AE time series during overload conditions in a Kaplan hydroturbine (Schmidt, 2014).

The signal in frequency domain

Interesting results have been published with respect to the effect of cavitation on the frequency spectrum of vibration (Fig. 1.32a,b) and noise (Fig. 1.32c,d) measurements (Cernetič, 2008; Chudina, 2009a). In general, cavitation impulses increase the amplitude of the measurements in a wide range of frequencies. In the results of Fig. 1.32, this range appears to be strongly affected from the type of impeller (closed or semi-open) and its material (metallic or plastic). On the one hand, the closed impeller results (Figs. 1.32a,c) show a clearer increase for frequencies, f>2 kHz, while those of semi-open impeller (Figs. 1.32b,d) excite the total frequency band.

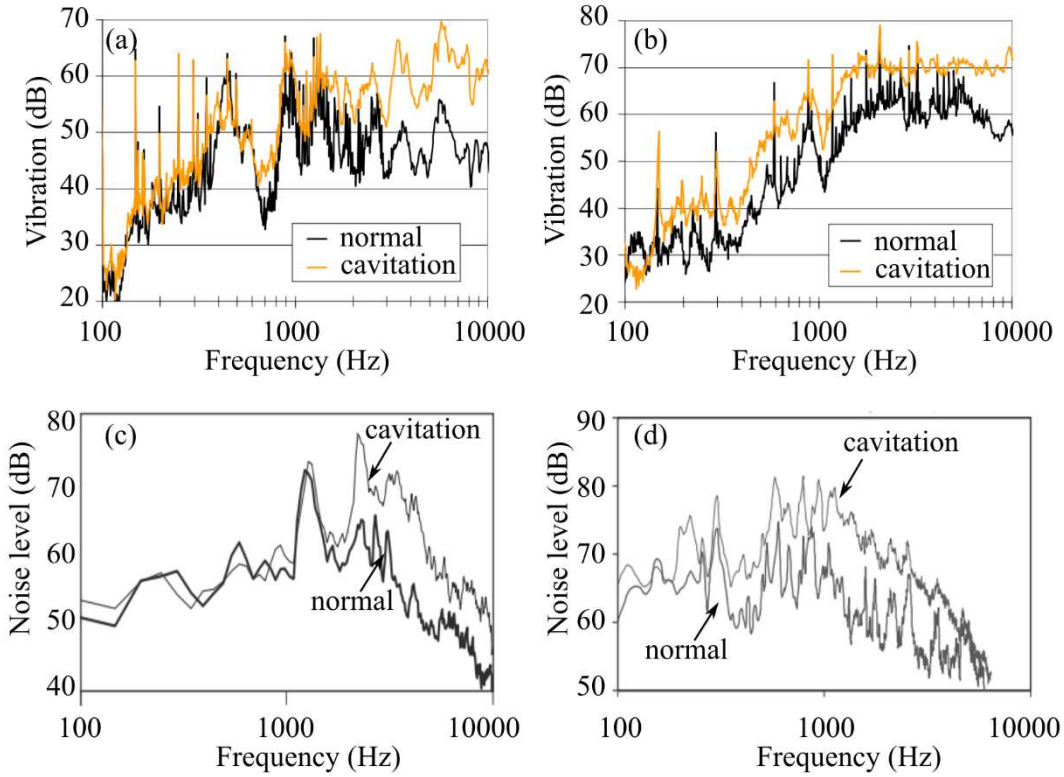

Figure 1.32 Frequency spectrum of **a,b)** vibration (Cernetič, 2008) and **c,d)** noise (Chudina, 2009a) signals, measured from pumps with **a,c)** metallic closed and **b,d)** plastic semi-open impellers that operate under normal and cavitating conditions.

This trend is the same, no matter the type of noise and oscillations measured, solid-borne (Figs. 1.32a,b) or air-borne (Figs. 1.32c,d). These conclusions made for closed impellers have also been confirmed by several studies (Ganeriwala, 2011; Zhang N., 2015a; Abdulaziz, 2017). In addition, the overall amplitude of noise and vibration measurements is higher for the semi-open impeller, even though the microphone in the case of Fig. 1.32c, is located closer to the pump (distance=0.1m) compared to this of Fig. 1.32d (distance=0.5m). This behaviour is justified from the fact that in the case of closed impellers (Fig. 1.32c), the pressure shock waves have to surpass the additional shroud surface so as to reach the sensor, which reduces further their intensity.

The effect of sensor positioning in terms of the frequency spectrum excitation due to cavitation has been studied from Lu et al. (2019). The experiment includes a centrifugal pump with a closed impeller that has four vibration sensors mounted in its casing and tested with the use of CTD method. When the machine operates under high flowrate conditions, cavitation appears and the high frequency spectrum of all vibration sensors is excited. The results from two of the sensors are presented in the plots of Fig. 1.33; i) one accelerometer mounted at the front casing close to the midspan (MS) of the blade an angular position φ~300º (Fig. 1.1b) and ii) one sensor on the top of the casing that measures vibration on y-direction. According to the

results of Fig. 1.33, the sensor located closer to the suction (Fig. 1.33a) shows a much clearer increase in its amplitude, for frequencies, f>2 kHz, similary to the results of the closed impellers in Figs. 1.32a,c. The higher values obtained at the high frequency vibration spectrum from the sensor located closer to the suction of centrifugal pumps have been confirmed also in the studies of Gülich (1989) and Zhang N. et al. (2015a).

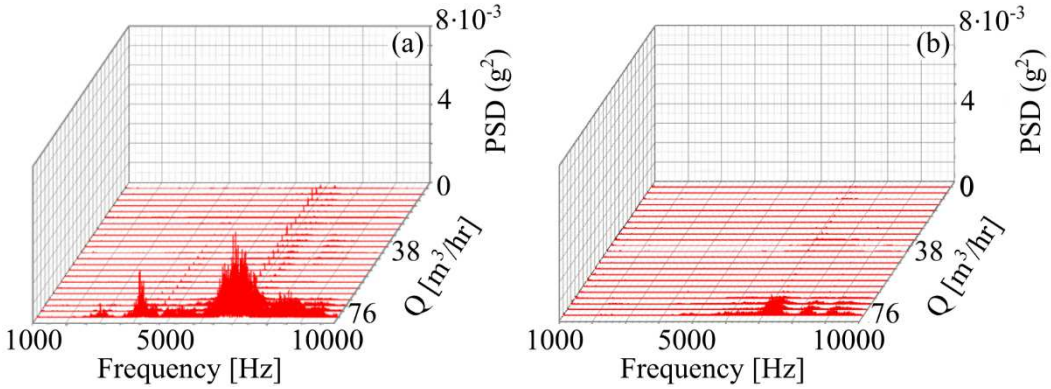

Figure 1.33 Vibration frequency spectrum for various flowrates for two sensors located at the casing of the centrifugal pump (Lu, 2019).

Furthermore, the high frequency excitation of plot of Fig. 1.33a is less distributed in the spectrum compared to Fig. 1.32, and presents some areas where the increase is clearly maximised. In order to describe the areas that are excited from impulsive phenomena and present the patterns of Fig. 1.33a, traditional detection literature (Randall, 2011) uses the term high frequency resonances, while Gülich (1989) uses the term dominant band. Results that depict the appearance of such resonances have been published by Al Obaidi (2019) and Abdulaziz et al. (2017) for vibration measurements. It is very interesting to notice the similarities between the form of the resonances created form cavitation (Fig. 1.33a) with those presented for bearing excitation in Figs. 1.20 and 1.21. According to the author's opinion, the impulsive behavior produced from the bubble implosion is possible to excite resonances that are modulated from low frequency phenomena in a similar way with the bearing faults. This is the reason that justifies part of the detection approach of this Thesis.

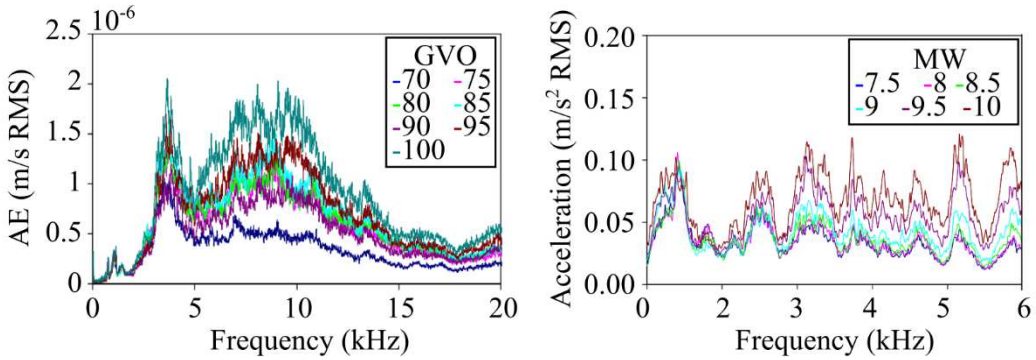

Figure 1.34 Frequency spectrum of **a)** AE and **b)** vibration measurements in two Francis turbine prototypes for several operating points (Escaler, 2003, 2004).

The general pattern of excitations presented in Figs. 1.32 and 1.33 for a centrifugal pump is also found in the AE (Fig. 1.34a) and vibration (Fig. 1.34b) frequency spectra presented by Escaler et al. (2003, 2004) for two Francis hydroturbines prototypes with similar nominal power (11 & 10 MW). Both machines suffer from leading edge cavitation that appears at the suction side of the blades of runner, when the turbines operate at high flowrates, close to the total opening (100%) of the guide vanes. The AE sensor is mounted on the upper part of the turbine guide bearing wall for an angular position with φ=230º, while the accelerometer is mounted on

the shaft of the runner (Fig. 1.1a). The plots of Fig. 1.34 depict the increase of high frequency (>3 kHz) noise and vibration spectrum, when the flowrate and the load increase. Moreover, in the study of Escaler (2004) a third Francis prototype is examined that do not show cavitation during the full openings of the guide vanes. In this case, the vibration frequency spectrum results at the same location with that of Fig. 1.34b, and remains identical for all the OPs examined. The results of Fig. 1.34 are significant because they extend the conclusions made for pumps of small horsepower power (<10 kW), shown in Figs. 1.32 and 1.33, to large-scale turbines of ~10 MW.

The pattern of powerbands

The literature quantifies the results presented in Figs. 1.32, 1.33 and 1.34 either by calculating the noise or vibration power content of a discrete frequency or by integrating the power content in a specific frequency range. In this study, both kind of plots are referred as powerbands and the already published results are presented as function of σ. Unfortunately, the quantified results presented in the literature do not exhibit a robust behaviour as they deviate with σ. The main reason for such deviations is the selection of different discrete frequencies or bands for the detection of two-phase flow development. Literature provides several different approaches for the adequate selection of different discrete frequencies and bands, which are listed bellow:

i. Gülich (1989) proposes a general guideline that deals with the measurement of the high frequency air, fluid or solid-borne noise, with f>10 kHz. In this way, it is possible to ignore the interference of cavitation noise with the low frequency mechanical and hydraulic noise components (Varga, 1969; Chudina, 2003b).
ii. Escaller et al. (2003) highlight the study of frequency spectrum (Fig. 1.34a), and implicitly proposes to intergrate the range above the frequency, where the increase of amplitude spectrum becomes clearer. In the case of Fig. 1.34A, this frequency is 3 kHz.
iii. Chudina and Prezelj (2009) and Zhang N. et al. (2015a) propose the monitoring of those frequency components that show the highest change in noise level due to the operation under cavitating conditions. This approach is very similar with that suggested by Darlow et al. (1974), McFadden and Smith (1984a), and Randal and Antoni (2011), for the selection of the band pass filter to be used during the demodulation procedure of noise signals that include bearing faults.
iv. Few authors present the total frequency band measured from the sensors used (Alfayez, 2004; Schmidt, 2014; Dong, 2019). This approach is usually implemented when AE sensors are used and the acquisition process includes band pass filters that remove large parts of the low frequency domain.
v. Few authors present their results as a function of different discrete frequencies or different range of frequencies (Pearsall, 1966; Gopalakrishnan, 1985; Chudina, 2003b; Zhang N., 2015a).
vi. Few authors do not justify their selection (McNulty, 1982; Bourdon, 1994; Neill, 1997).

The reason behind the existence of so many approaches deals with the deviation of the resonance in the various configurations, due to the geometrical characteristics of the machine, its material and its operating conditions. The above discussion justifies the various patterns presented from powerbands in the literature, especially in the case of centrifugal pumps. These deviations usually refer to two areas of the powerband; i) the point of powerband maximisation, $\sigma_{PB,M}$ and ii) the behaviour of the pattern after the maximisation. In order to effectively summarise and simplify the discussion of this section, the published results are grouped with respect to the aforementioned deviations. More specifically, the powerbands as a function of σ could take the three forms presented in Fig. 1.35a, while the $\sigma_{PB,M}$ value could lie in the areas between σ_{VI} value and 0, as it is shown in Fig. 1.35b.

From the trend of the graphs of Fig. 1.35a, it is concluded that in the case of Pattern 3, the air, fluid and solid-borne noise maximises always for $\sigma_{PB,M}<\sigma_3$ (area A). A common conclusion extracted from the majority of the published results is that the powerband increases due to the drop of σ and the appearance of two-phase flow development (blue colour area in Fig. 1.35).

For studies, where the powerbands are accompanied by flow visualisation results (Liang, 2018; Dong, 2019) this increase almost coincides with the visual onset of the phenomenon. Another common characteristic is that the value of all powerbands maximises at $\sigma<\sigma_{VI}$. The simultaneous satisfaction of those criteria forms a robust detection tool that could accompany the studies related to powerbands. For the majority of the cases examined, the sensors mounted close to the suction of the pump are able to detect the aforementioned pattern due to bubble implosion.

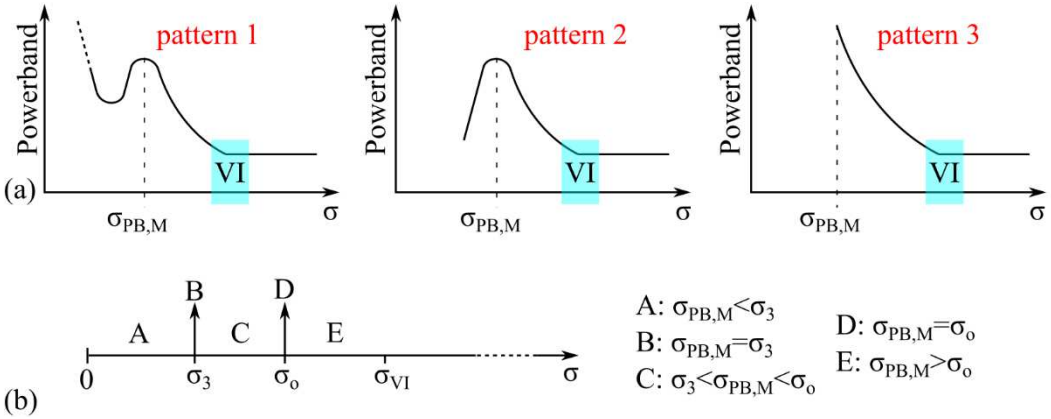

Figure 1.35 a) Typical air, fluid and solid-borne noise powerband patterns in centrifugal pumps, **b)** the area, where $\sigma_{PB,M}$ could lie.

The results that did not follow a common behaviour are discussed with respect to the Table 1.1 and their corresponding occurring frequencies in Fig. 1.36. In Table 1.1, the results of all published works are grouped according to the specifications of Fig. 1.35 (second column of Table 1.1), and they are presented as a function of the flowrate (Φ/Φ_{BEP}), the frequency bands selected, the type of sensor used and the rotation speed of the rotor. When no data are available, the question mark (?) is completed. In Table 1.1, there are 74 powerbands presented for pumps that operate between 900 and 3600 rpm.

The majority of the published powerbands (53%, Fig. 1.36a) agree with the trend of Pattern 2 (Fig. 1.35a), where the noise maximisation is followed by a continuous decrease. This decrease is, according to Gülich (2008), the result of two mechanisms. The lowering of σ value reduces the pressure of the surrounding liquid (p_∞), which consequently, reduces the pressure differential that drives the implosion energy, according to Eq. I.2. In addition, the formation of large cavities at the suction of the impeller acts as an additional surface between the sensor and the implosion, which absorbs part of the noise emitted (Gülich, 2008).

Table 1.1 Summary of the published powerbands during the derivation of cavitation characteristic curves.

	Pattern/$\sigma_{PB,M}$	**Author**	**Φ/Φ_{BEP}**	**Frequency**	**Sensor**	**rpm**
1	1/A	(Chudina, 2003b)	0.8	[0 – 20] kHz	Micr/ne	2910
2	1/B	(Chudina, 2003b)	0.55	[0 – 20] kHz	Micr/ne	2910
3			0.7			
4			0.9			
5		(Cernetič, 2008)	1	148 Hz	Acc/ter	2910
6		(Zhang N., 2015a)	1	[10 – 500] Hz	Acc/ter	1450
7				[10 – 25] kHz		
8			1.1	[10 – 500] Hz		
9				[5 – 10] kHz		
10				[10 – 25] kHz		
11			1.2	[10 – 500] Hz		
12				[5 – 10] kHz		
13				[10 – 25] kHz		

14			1.3	[10 – 500] Hz		
15				[0.5 – 5] kHz		
16				[5 – 10] kHz		
17				[10 – 25] kHz		
18			1.4	[10 – 500] Hz		
19				[5 – 10] kHz		
	1/C	x	x	x	x	x
20	1/D	(Sloteman, 2007)	1	>10 kHz	Micr/ne	1500
21		(Gopalakrishnan, 1985)	?	[20 – 40] kHz	AE	3600
22				[40 – 60] kHz		
23				[60 – 80] kHz		
24				[80 – 120] kHz		
25	1/E	(McNulty, 1982)	?	40 kHz	Micr/ne	?
26		(Alfayez, 2004)	0.9	[0.1 – 1] MHz	AE	?
27	2/A	(Chudina, 2009b)	1	125 Hz	Micr/ne	2910
28				147 Hz		
29				1450 Hz		
30				4 kHz		
31				8 kHz		
32				14.5 kHz		
33				16 kHz		
34				18.5 kHz		
35		(Cernetič, 2012)	1.6	147 Hz	Micr/ne	2910
36		(Zhang N., 2015a)	1.4	[0.5 – 5] kHz	Acc/ter	1450
37		(Dong, 2019)	0.5	[0.5 – 8] kHz	Acc/ter	1450
38				[20 – 100] kHz	Micr/ne	
39				[20 – 200] kHz	Hyd/ne	
40			1	[0.5 – 8] kHz	Acc/ter	
41				[20 – 100] kHz	Micr/ne	
42				[20 – 200] kHz	Hyd/ne	
43			1.5	[0.5 – 8] kHz	Acc/ter	
44				[20 – 100] kHz	Micr/ne	
45				[20 – 200] kHz	Hyd/ne	
46	2/B	(Chudina, 2009a)	0.7	2176 Hz	Hyd/ne	2900
47			?	760 Hz	Hyd/ne	910
48		(Chudina, 2009b)	0.7	2176 Hz	Acc/ter	2900
49				2176 Hz	Micr/ne	
50			1	2176 Hz	Acc/ter	
51				2176 Hz	Micr/ne	
52			1.3	2176 Hz	Acc/ter	
53				2176 Hz	Micr/ne	
54			1.6	2176 Hz	Acc/ter	
55				2176 Hz	Micr/ne	
56		(Cernetič, 2012)	0.7	147 Hz	Micr/ne	2910
57	2/C	(Chudina, 2003b)	0.9	147 Hz	Micr/ne	2910
58		(Cernetič, 2012)	0.4	147 Hz	Micr/ne	2910
59			1			
60			1.3			
61		(Zhang N., 2015a)	1.4	[10 – 25] kHz	Acc/ter	1450
62	2/D	(Gülich, 2008)	?	[10 – 180] kHz	Micr/ne	?
63		(Sloteman, 2007)	0.5	>10 kHz	Micr/ne	1500
64	2/E	(Gülich, 1989)	1	>10 kHz	Micr/ne	?
65		(Neil, 1997)	?	[0.5 – 1] MHz	AE	2980

66	3/A	(Pearsall, 1966)	?	20 kHz	Micr/ne	?
67				12.5 kHz		
68		(Chudina, 2003b)	1	[0 – 20] kHz	Micr/ne	2910
69			1.1			
70		(Cernetič, 2008)	1	1600 Hz	Acc/ter	2910
71		(Zhang N., 2015a)	1	[0.5 – 5] kHz	Acc/ter	1450
72			1.1			
73			1.2			
74			1	[5 – 10] kHz		

The same mechanism is activated during the reduction of the noise in the case of Pattern 1 (Fig. 1.35a), which appears at the 35% of the presented results (Fig. 1.36a). In this case the second increase appears under extreme conditions of cavitation development, for the minimum σ values. Several mechanisms could cause the noise to exhibit the behaviour of Pattern 1. One is related with the excitation of machine's resonances from intense cavitation that could contribute to the noise level. In addition, at minimum σ value the blocking of the inflow of the pump from vapour cavities is possible. In this case, strong flow recirculations occur, which also increase the oscillations' intensity.

One last reason is that the second increase could be geometry dependent, with respect to the suction geometrical characteristics of the impeller, such as the inlet blade angle. In case of high incidence angles, recirculation can occur due to flow separation from the blade, and this can significantly increase the overall vibrations emitted (Hergt, 1985; Gülich, 2008; Lobanoff, 2013).

According to the Table 1.1, Pattern 3 (Fig. 1.35a) that has the lowest occurring frequency in the literature (12%, Fig. 1.36a), is strongly related with the flowrate. For the majority of studies (7/9), Pattern 3 appears at the design (Φ_{BEP}) or larger flowrates. In larger flowrates the two-phase flow area increases more rapidly due to the accelerated flow field, and reaches faster the minimum σ value and the maximum emission.

The occurring frequency of $\sigma_{PB,M}$ value, presented in Fig. 1.36b, is significantly higher for the cases A and B. The reason is that noise and vibration intensity increase by lowering the σ value (Fig. 1.26), and maximise under heavy cavitating conditions, for $\sigma \leq \sigma_3$. According to Gülich (2008), the filtering of low frequency mechanical noise (<10 kHz) would result in a noise maximum close to σ_o. However, the majority of the presented studies (46%, Fig. 1.36c) include the low frequency content (<5 kHz) in the calculation of their powerbands, which probably creates this shifting of noise maximisation at lower σ values.

Moreover, the examination of Table 1.1 show a similar tendency for Pattern 1, with those have just discussed. More specifically, the higher the frequency bands selected for the calculation of the powerband, the sooner the maximum powerband has been calculated. For the cases of $\sigma_{PB,M} \leq \sigma_o$ (A, B & C), the frequency ranged between [0 – 25] kHz, while for those with $\sigma_{PB,M} > \sigma_o$ ranged between [10 – 1000] kHz. In practice, the above discussion concludes that the integration of the content of higher frequencies results in the shifting of powerband maximisation in higher σ conditions. The use of higher frequencies and the rejection of those lower than 10 kHz, ensures the filtering of the low frequency components and make those powerbands more sensitive to the appearance of noise due to cavitation. The tendency is also apparent in the results of Pattern 2, where the lower frequency used in the integration of powerbands for cases D and E is 10 kHz.

In terms of sensor selection (Fig. 1.36d), the authors prefer the use of accelerometers (39%) and microphones (46%) in the majority of the cases reviewed. The main reason for this selection is that these sensors are usually cheaper than the AE sensors and their mounting on the machine (or the machine's environment in the case of microphones) is more practical than of hydrophones that require the drilling of solid boundaries and the positioning of the sensor in the flow.

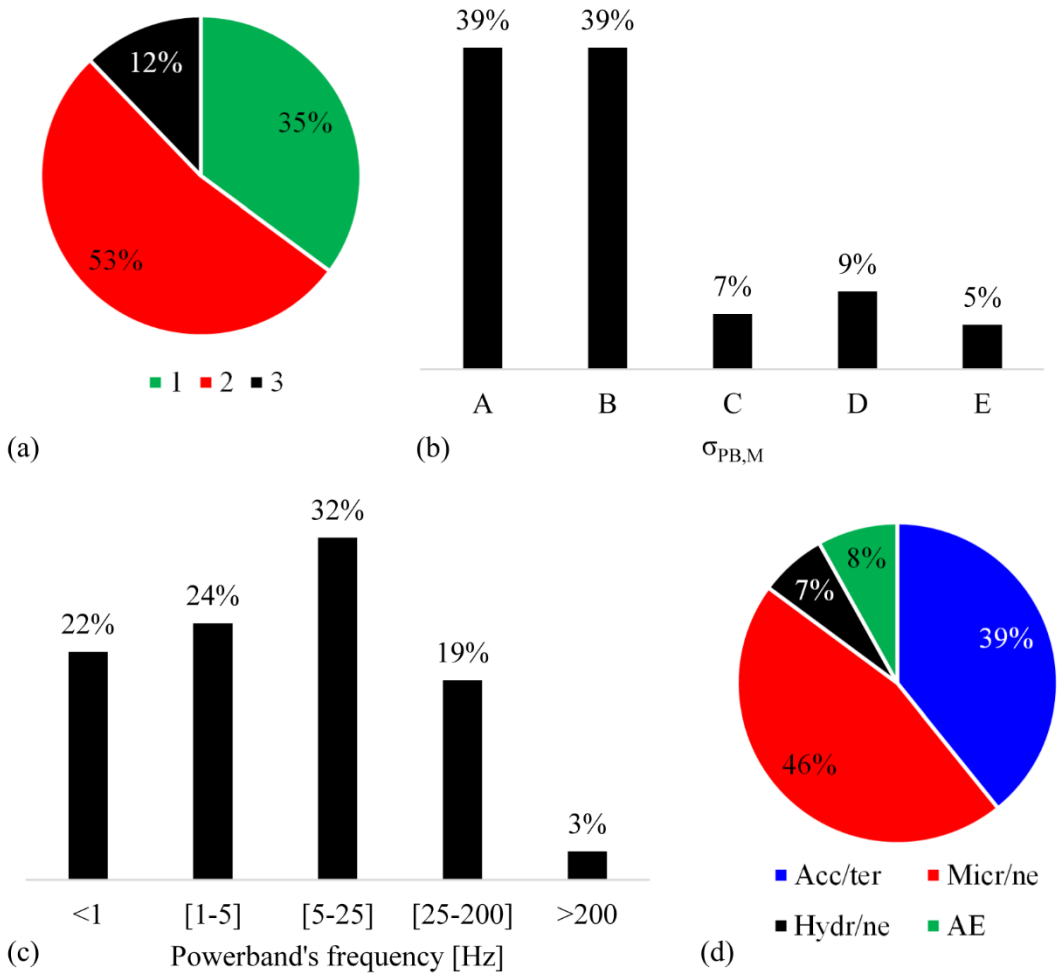

Figure 1.36 Charts that depict the frequency of the **a)** pattern appearance, **b)** $\sigma_{PB,M}$ appearance, **c)** use of powerbands at different frequency ranges, and **d)** use of each dynamic sensor.

In the case of hydroturbine's prototypes testing (CTE method), the few powerband results presented (Bourdon, 1994; Escaler, 2003; Schmidt, 2014; Escaler, 2015) show a more robust trend compared to this of centrifugal pumps. A typical example is presented in Fig. 1.37, where the powerbands of a Francis prototype with a maximum power of 26 MW is presented for various load conditions. One AE sensor and two accelerometers (AC TGB1 & AC TGB2) are located at the turbine guide bearing pedestal, at z, y and x direction, respectively (Fig. 1.1a). In addition, one accelerometer is mounted on the guide vane at z-direction and one at the draft tube at x-direction (Fig. 1.1a). Concerning the accelerometers, the [15 – 20] kHz frequency range is selected for the calculation of powerbands, while this of [40 – 45] kHz is selected in the case of AE sensors. The results of Fig. 1.37, present a uniform trend, no matter the position or the frequency range are selected. Two peaks appear for all sensors, one close to 16 MW and one at the full load, for 26 MW. The sensor mounted on the draft tube is the only exception, since it exhibits only the first peak. The trend presented here is similar with that shown by Escaler et al. (2003) for a Francis of 11 MW, especially for the case of measurements at the guide turbine bearing. Increasing trends with the load, the opening of the guide vanes, and the flowrate have been presented also in the noise and vibration powerbands of Schmidt et al. (2014) and Bourdon et al. (1994), and manifest the operation of the turbines under transient conditions and cavitation. In these studies, the results of the powerbands are not further analysed because, in the form of Fig. 1.37, they could not provide more information regarding the exact type or the location of cavitation in the prototype's runner.

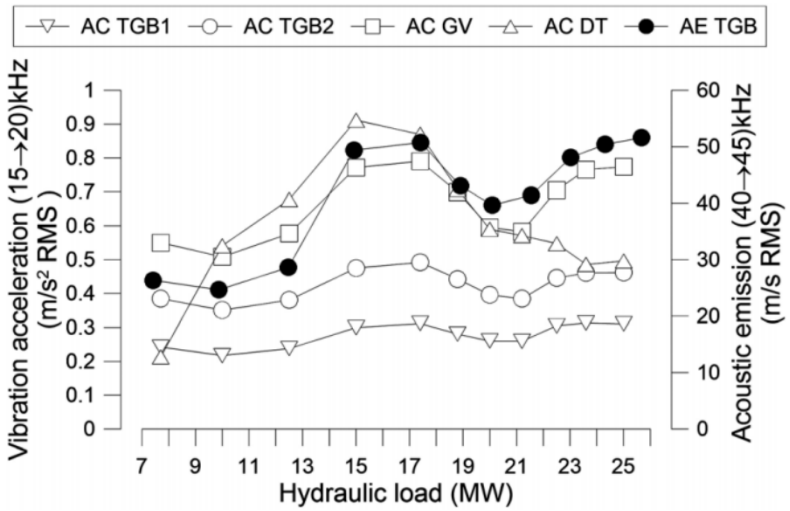

Figure 1.37 Powerbands from sensors located on a Francis turbine prototype (Escaler, 2015).

1.3.1.4 Application of amplitude modulation tool

The discussion of the results of the previous section highlights the increase of noise and vibration powerbands with the appearance of cavitation in both centrifugal pumps and turbines. The fact that sensors, which are located in the noisy environment of the hydraulic turbomachines, are able to identify the noise coming from hydrodynamic sources, such as cavitation, is of paramount importance and justify their use in a large number of studies. However, the discussion in section 1.3.1.3 reveals the significant effect that a large number of parameters have on the shape of the powerband, which complicates the extraction of a common cavitation detection criterion. In the previous section, it is concluded that the powerband results are dependent from; i) the frequency band used during powerband calculation, ii) the geometrical characteristics, iii) the flowrate and iv) the material of the machine. In addition, the effective use of powerbands requires the information regarding the noise and vibration levels when the machine operates under non-fault conditions, so as to identify the possible increase, especially during the initial stages of the phenomenon. However, the fact that this information is not always available from the machine's user, complicates further the detection procedure.

The difficulties associated with the powerbands could be overcome with the application of demodulation techniques on the noise and vibration signals, as they were proposed in few cavitation studies on hydroturbines (Bourdon, 1994; Escaler, 2002, 2004). As a consequence, the signal's envelope could be studied in the time and frequency domain after the formation of the analytic signal. The aforementioned studies followed a common approach towards the detection of cavitation related faults, which is summarised in the following steps:

i. Calculation of the frequency spectrum of the measured signals of each sensor, with the use of FFT or PSD tools, and identification of possible resonance areas.
ii. The range and the central frequency of the resonance selected is used as the bandwidth and the central frequency of the band pass filter that is applied on the raw measured signal.
iii. Application of the Hilbert Transform on the filtered signal.
iv. Use of the filtered signal and its Hilbert Transform towards the formation of the analytic signal.
v. Study of the signals envelope in the frequency domain.

The mathematical interpretation of the demodulation procedure is given analytically in the theoretical part of the signal processing techniques in Chapter 2.

Bourdon et al. (1994), test two Francis prototypes, Francis A (240 MW) and Francis B (200 MW), and examines the positions of material wear after the testing. The instrumentation used includes the mounting of three accelerometers at the lower guide bearing of the turbines and

one accelerometer at the draft tube (Fig. 1.1a). In the case of Francis B, the signal is demodulated at the [28 – 44] kHz frequency range and the envelope's frequency spectrum highlights the appearance of the guide vane passing frequency and its first three harmonics, while the study of the runner indicates wear at the leading edge of the runner. On the other hand the envelope spectrum for Francis A relates the appearance of leading edge cavitation with a 60 Hz discrete frequency component at the envelope's spectrum, when the machine operates between [60% – 90%] guide vane opening.

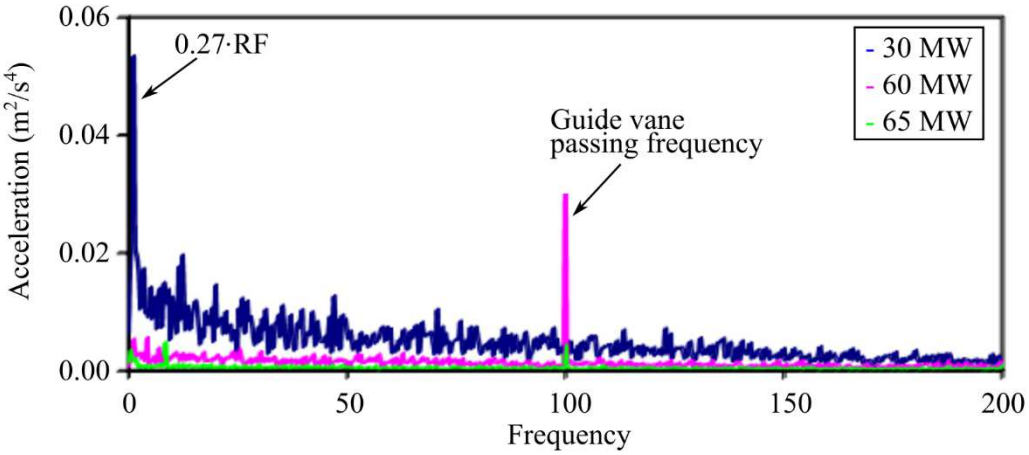

Figure 1.38 Envelope's frequency spectrum at three loads (Escaler, 2002).

The results that associate the leading edge cavitation with the guide vane passing frequency of the machine are also confirmed in the study of Escaler et al. (2002), in a Francis turbine prototype (65 MW). In this study vibrations are measured closer to the machine, at the pedestal of the turbine guide bearing (Fig. 1.1a). The envelope frequency spectrum for the [30 – 40] kHz frequency range at three different loads is presented in Fig. 1.38. According to this plot, the operation of the Francis under part load condition results in a signal that is modulated from the rope's frequency of 0.27·RF. In addition, when the machine operates close to its full load, LE cavitation appears and its signal is modulated from the guide vanes passing frequency, similarly to Bourdon et al. (1994).

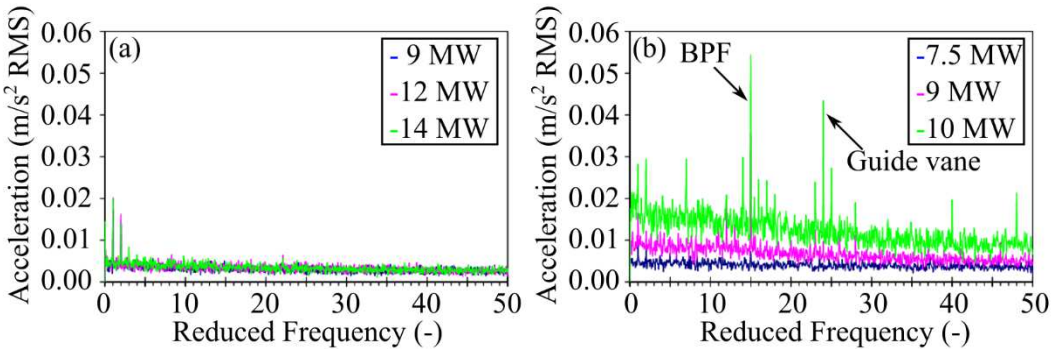

Figure 1.39 Vibration envelope spectrum at the shaft of **a)** Francis A, and **b)** Francis B (Escaler, 2004).

Finally, Escaler et al. (2004) examine the vibration performance of two Francis prototypes, Francis A (14 MW) that operates without cavitation problems and Francis B that suffers from leading edge cavitation. Both machines are operated under three loads, where the maximum coincides with the full load conditions of the hydroturbine. The vibration measurements are obtained from the shaft, the turbine guide bearing and the draft tube, and the signal is demodulated with the use of [3 – 6] kHz frequency range. The envelope's frequency spectra at the sensor located at the shaft of Francis A and B, are presented for the three different loads in Fig. 1.39a,b, respectively. The x-axis is normalised with respect the RF frequency. The

presence of two-phase flow formations at the full load condition of Francis B is apparent, since the envelope's spectrum is excited by the blade passing frequency and the guide vane frequency.

The last three studies complete the review of the experimental methodologies developed so as to detect cavitation in hydraulic turbomachines, with the use of noise and vibration measurements. In the last section of this literature review (section 1.3.2), the numerical tools that are used towards the study of cavitation development in hydraulic turbomachines are examined.

1.3.2 Numerical approach

In the literature, there are different numerical models that aim to study the behaviour of vapour formations in the flow around hydrofoils and in hydraulic turbomachines. The development of such models is a process of increased complexity, since the accurate simulation of cavitation requires the consideration of several parameters, such as:

i. The variation of density between the liquid and vapour phase.
ii. The mass exchange and the thermal transfer between the liquid and vapour phase.
iii. The relative motion (slip) between the liquid and vapour phase.
iv. The irregular shape of the interface between the liquid and vapour phase.
v. The effect of the non-condensable

Moreover, the model must overcome the problems related to stability and robustness of the numerical procedure so as to be applicable in the various applications. The inability to satisfy all the above requirements with the development of one common numerical approach justifies the existence of a variety of numerical models, which make different assumptions and simplifications. The appropriate selection of the modelling approach depends on the individual characteristics of the problem investigated and the availability of the computational resources. This section attempts to review the proposed numerical modelling techniques and to present their applicability towards hydraulic turbomachinery applications, along with their simplifications and limitations.

The computational methodologies that aim to simulate cavitation can be split in two main categories (Chen, 1994; Liu, 2006); i) the Interface Tracking Methods (ITM), and ii) the Inteface Capturing Methods (ICM). The ITM provide the solution of the incompressible liquid flow along with the boundary of the attached vapour area. The interface of the latter is treated as a boundary of the liquid's computational domain, at which the pressure value is constant and equals the vapour pressure value. Due to the non-linear relation between the cavity shape and the external liquid flow field, the interface of the vapour area is obtained after the implementation of an iterative procedure.

The latter initiates after a first assumption of the attached vapour interface extent and is updated iteratively until a converged shape is achieved. In order to ensure that the vapour interface matches the constant vapour pressure value, a wake closure model is employed for the wake region (Hejranfar, 2015). This approach has been found capable to predict successfully the extent of the cavity (Chen, 1994; Deshpande, 1994; Liu, 2006) and the machine's performance deterioration under heavy cavitating conditions (Hirschi, 1998). Nevertheless, ITM face difficulties when they are used so as to model three-dimensional flows, since they are not able to accurately track the three-dimensional wake (Chen, 1996; Gopalan, 2000). In addition, ITM are not able to model cavitation types other than attached vapour formations.

In the case of ICM, the total domain is solved, where both phases are treated as a homogeneous mixture fluid. The density of this single medium varies between the minimum vapour density and the maximum liquid density. The fluid is defined as homogeneous, since it is assumed that there is no slip between the two phases. Unlike the ITM, the ICM allow the modelling of all types of dynamic vapour formation, included the bubble, vortex and tip cavitation. Two different approaches are used towards the calculation of the mixture's density:

- The barotropic approach, where the density is associated with the local static pressure, $\rho(p)$, with the use of a barotropic state law (Dellanoy, 1990), as well as with the vapour volume fraction, α_v with Eq. 1.13. Here, ρ_m, ρ_v and ρ_l are the mixture's, vapour and liquid's density. This approach assumes that there is not mass exchange between the vapour and liquid phase. Barotropic models have been used successfully from several authors for the simulation of the two-phase flow development, mainly around hydrofoils (Pascarella, 2001; Qin, 2003; Rapposelli, 2003; Frikha, 2008; Barre, 2009; Blume, 2015; Hejranfar, 2015). There are only a few works that the barotropic model is implemented for the study of the three-dimensional flow of a hydraulic turbomachinery (Jese, 2014; Limbach, 2015). For all these cases the heat transfer between the two phases is ignored and the two phases are assumed to be in a complete thermodynamic equilibrium.

$$\alpha_v = \frac{\rho_m - \rho_l}{\rho_v - \rho_l} \tag{1.13}$$

- The Transport Equation-based Models (TEM), where a transport equation is used for the mass and volume fraction that regulates the mass transfer between the two phases. The transport equation is expressed in terms of changes in the liquid mass, as it is shown in Eq. 1.14, where, α_l is the liquid volume fraction and $\dot{m}^+$, $\dot{m}^-$, are the source terms that express the condensation (increase of liquid mass) and the evaporation (decrease of liquid mass) rates, respectively (Eq. 1.15). A great number of models have been proposed, in order to describe the net mass transfer between the liquid and vapour phase at the bubble interface (Kunz, 2000; Schnerr, 2001; Singhal, 2002; Saito, 2003; Zwart, 2004; Dauby, 2006). The expressions used for the source terms are usually based in empirical condensation and evaporation terms, as well as in terms that originate from simplified forms of the Rayleigh equation (Eq. I.1).

$$\frac{\partial}{\partial t}\left(\rho_l \alpha_l\right) + \nabla\left(\rho_l \alpha_l \vec{v}\right) = \dot{m}^+ + \dot{m}^- \tag{1.14}$$

$$\dot{m} = \begin{cases} \dot{m}^+, \text{ for } p > p_{sat} \\ \dot{m}^-, \text{ else} \end{cases} \tag{1.15}$$

Typical results that refer on the application of the TEM on three-dimensional hydraulic turbomachinery applications are given in sections 1.3.2.1 to 1.3.2.3. At these sections, the review focuses in the implementaion of; i) Kunz et al. (2000) model, ii) full cavitation model (FCM) proposed by Singhal et al. (2002), and iii) Zwart et al. (2004) model. These TEM are the most frequently used among the various researchers, due to their robustness when they are implemented along with computational fluid dynamic (CFD) algorithms. The review discusses the ability of each model to simulate the machine's operation under cavitating conditions and identify the two-phase flow development.

A great variety of large-scale cavitation types (section I.2) can be found in the results presented in sections 1.3.2.1 to 1.3.2.3. The validity of the discussed results is ensured, since the majority of the studies are accompanied by experimental flow visualisation techniques that confirm the appearance, the extent and the location of two-phase flow area, as well as its effect on the machine's performance. The review of this section is done from the two-phase flow modelling perspective. Obviously, the numerically obtained results are significantly affected by other parameters, such as the computational domain inlcuded to the simulation, the turbulence modelling and the mesh density and quality. As a consequence, Table 1.2 at the end of this review provides, for each study, additional information regarding the characteristics of the machine, the grid and the turbulence modelling.

1.3.2.1 Kunz et al. model

The modelling approach (Eq. 1.16) proposed by Kunz et al. (2000) relates evaporation ($\dot{m}^-$) with the liquid volume fraction, α_l, and the difference between static pressure, p, and vapour saturation pressure, p_{sat} (Eq. 1.16a). On the other hand, the condensation ($\dot{m}^+$) procedure is related with the liquid (α_l) and non-condensable gases (α_{ncg}) volume fractions (Eq. 1.16b). The expressions are non-dimensionalised with respect to a mean flow time scale and include the effect of the empirical constants C_{vap} and C_{cond}, which values are proposed from Kunz et al. (2000) to be equal to 100.

$$\dot{m}^- = \frac{C_{vap}\ \alpha_l\ \rho_v}{0.5\rho_l\ u_\infty^2\ t_\infty}\left(p - p_{sat}\right) \tag{1.16a}$$

$$\dot{m}^+ = \frac{C_{cond}\,\rho_v\left(\alpha_l - \alpha_{ncg}\right)^2}{t_\infty}\left(1 - \alpha_l - \alpha_{ncg}\right) \tag{1.16b}$$

Medvitz et al. (2002) apply this model for the analysis of the performance of a centrifugal pump that is also experimentally examined by the derivation of its characteristic curves and by flow visualisation photos. According to their results, the numerical model predicts sufficiently both the pattern of σ-Ψ curve and the point of σ_o, where the head started to drop. However, differences occur on the location where cavitation initiates; in the case of the visual observation, vapour bubbles occupy the TE of the blade's suction side, while the numerical model predicts cavitation at the LE of the blade. Zhang H. et al. (2012) propose the use of a modelling approach based on Kunz et al. model for the cavitation studies on a Francis turbine. The model includes the spiral casing, the runner and the draft tube of the hydroturbine (Fig. 1.1a). The transient simulations conducted are able to predict the vortex rope formation at the draft tube, as well as the cavitation that is developed at the TE of the runner. Experimental flow visualisations validate the vortex rope formations, while the TE cavitation results are considered reliable, since typical runners suffer at the same area from significant material wear. Similar results, with respect to the TE cavitation at the runner, are also presented in Panov et al. (2012) study for two Francis hydroturbines prototypes.

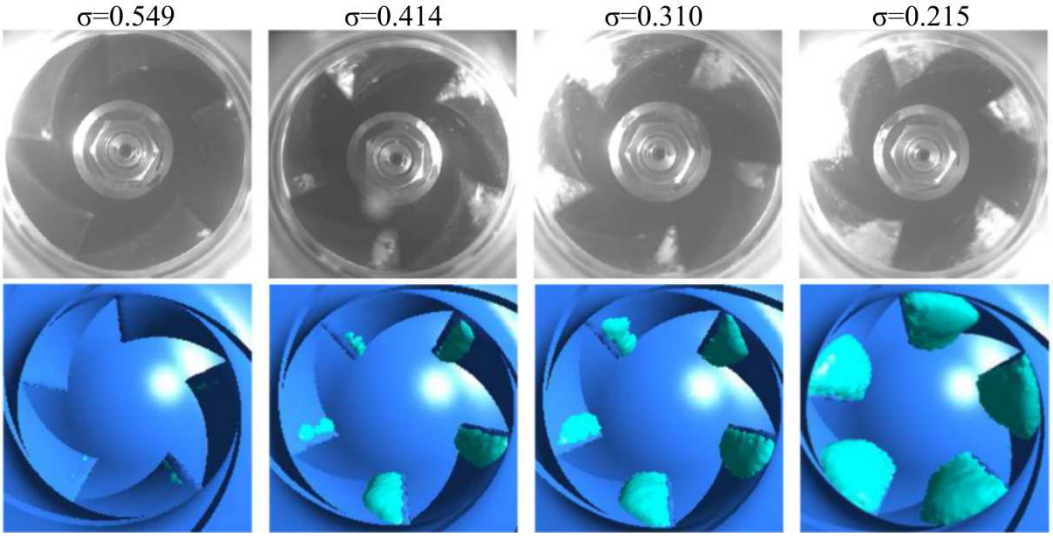

Figure 1.40 Comparison of the numerically obtained two-phase flow area with experimental flow visualization photos at various suction conditions (Liang, 2018).

Liang et al. (2018) conduct a numerical study with the use of Kunz et al. model for the study of cavitation in centrifugal pumps. The simulations are accompanied by the flow visualisation results in the same machine and the results are presented in Fig. 1.40, where the light blue

colour depicts the vapour phase isosurface area calculated from the numerical model. According to these results, lowering of static pressure conditions (σ) results in the development of the first vapour formations at the suction side of the blade, which increases significantly with the further lowering of σ. These formations are attached to the suction side of the blade and show the macroscopic characteristics of the sheet cavitation. The results of Fig. 1.40 show sufficient agreement with the experimental visual observations, with respect to the location and the extent of the two-phase flow area. Moreover, Wang et al. (2016) use the same configuration with that of Liang et al. (2018) and presents the results of the σ-Ψ numerically derived curves. The results are obtained with the use of Kunz et al. (2000) model and show some differences compared to those previously discussed by Medvitz et al. (2002). More specifically, although both studies overpredict the Ψ calculation of the pump, the Wang et al. (2016) results calculate the point of total head drop at lower σ values, for all the flowrates examined.

1.3.2.2 Full cavitation model

The full cavitation model (FCM) is proposed by Singhal et al. (2002) and as its name implies, it takes into consideration many factors in the formation of the model's expressions. The latter are given in Eq. 1.17 for evaporation (Eq. 1.17a) and condensation (Eq. 1.17b), where f denotes the mass fraction. The source terms of include the effects of the turbulent kinetic energy, k, the surface tension, S_t, and the non-condensable gases mass fraction in the liquid medium, f_{ncg}. According to Singhal et al. (2002) study, the empirical constants should take values equal to C_{vap}=0.02 and C_{cond}=0.01, when the model is used for two-phase flow simulations in hydraulic turbomachinery.

$$\dot{m}^{-} = -C_{vap}\frac{\sqrt{k}}{S_t}\rho_v\rho_l\sqrt{2\frac{(p_{sat}-p)}{3\rho_l}}\left(1-f_v-f_{ncg}\right) \tag{1.17a}$$

$$\dot{m}^{+} = C_{cond}\frac{\sqrt{k}}{S_t}\rho_l\rho_l\sqrt{2\frac{(p-p_{sat})}{3\rho_l}}f_v \tag{1.17b}$$

The two-phase flow examinations of Athavale et al. (2002) and Liu et al. (2005) in pumps and Francis turbines, respectively, are the first studies that applied the FCM. Those examinations do not include experimental test, however their results are considered satisfactory after their evaluation in terms of their physical plausibility and the robustness of the solution convergence. The results of the pump identify the vapour formation at the suction side of the blade close to its LE, while those on Francis turbines at the exit of the runner and the draft tube. In both studies, it is possible to obtain the σ value where the machine's efficiency starts to deteriorate. Three studies (Mostafa, 2006; Zhou, 2008; Li, 2014) that are accompanied by experimental tests, validate the ability of the model to predict the cavitation characteristic curves, as well as the extent and the location of the two-phase flow area. Mostafa et al. (2006) validate the numerical results derived with FCM for the tip cavitation in an axial flow pump, with a blade angle of 30°. Their numerically obtained results show decent agreement with the flow visualisations, since in both cases two-phase flow formations occur at the suction tip edge of the blade.

Zhou et al. (2008) study the development of two-phase flow area in the runner of a Francis turbine and compares the numerically σ-Ψ curve with that of the tested model. The lowering of the σ value initiates cavitation at the centre of the hub's runner, while its further reduction increases the extent of the cavity towards the suction of the blade. At such conditions a slight increase appears at the efficiency value calculated and presented in Fig. 1.41a (red colour marker), along with the corresponding experimental. This local increase is the result of the significant reduction of the friction losses due to the development of the vapour phase close to the solid boundaries of the machine (Papantonis, 2016). The results for the simulations conducted at the lowest σ values (σ<0.1) show that vapour area covers the total flow path, which

justifies the deterioration of the numerical and experimental efficiency (Fig. 1.41a). This drop occurs relatively sooner in the simulations than in the test, an observation confirmed also by authors who used FCM for two-phase flow examinations in pumps (Ding, 2011; Li, 2014).

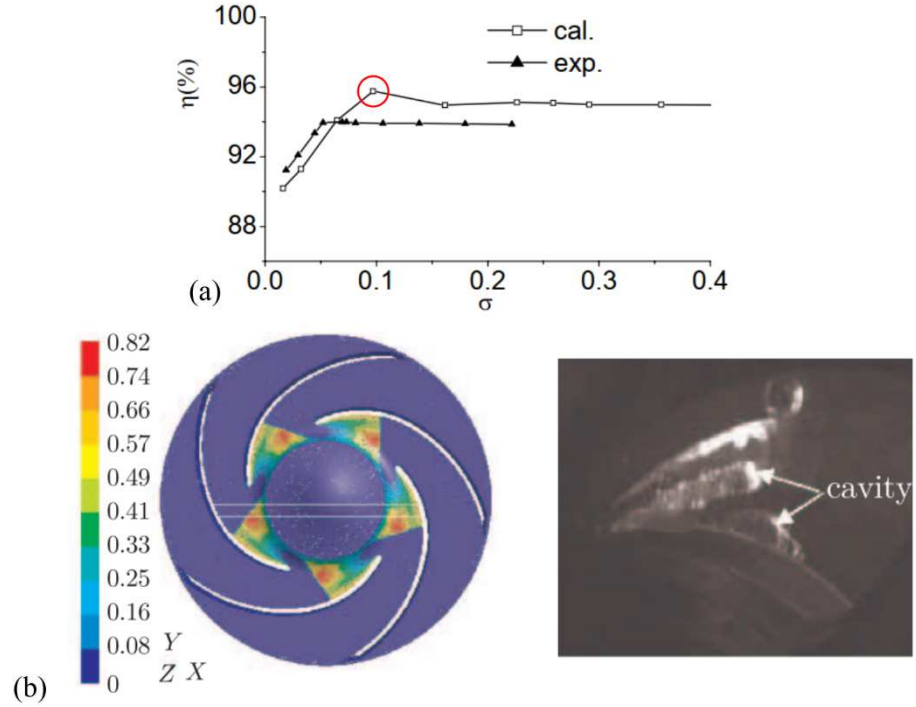

Figure 1.41 Numerical and experimental **a)** σ-η curves for a Francis turbine (Zhou, 2008), and **b)** cavitation location and extent in a centrifugal pump (Li, 2014).

The effect of the non-condensable gas content on the pattern of σ-Ψ curve is examined in the results of Li (2014) for a centrifugal pump. As it is concluded, a mixture with non-condensable gas content higher than 15 ppm alters the σ-Ψ curve of the pump and can even change significantly the σ value that corresponds to the total head collapse. In the same study a comparison between the standard k-ε and RNG k-ε turbulence models is conducted. According to the results, the RNG k-ε model has the poorest prediction of the Φ-Ψ curve under non-cavitating conditions and also is not able to reach the breakdown conditions for minimum σ values, due to convergence issues. On the other hand, the numerically obtained results regarding the location and extent of two-phase flow development, with the use of standard k-ε, exhibit acceptable agreement with the experimental flow visualisations (Fig. 1.41b).

1.3.2.3 Zwart et al. model

Zwart et al. (2004) propose expressions, which are based on the Rayleigh-Plesset equation and relate evaporation and condensation source terms with the bubble radius and its dynamics. The derivation of the Zwart et al. model expressions are given and discussed in section 4.2.4, where the numerical model of the present study is shown. The implementation of this model in robust CFD commercial solvers make it very popular among the researchers and engineers that examine cavitation problems in hydraulic turbomachinery. This justifies the large number of works found in the literature that confirm the applicability of the model in all types of machines.

Kang et al. (2009, 2010) apply this model, in order to study the effect of design of the axial inducer and its circumferential grooves on cavitation instabilities. The model is validated after the comparison of the calculated two-phase flow area with the experimental flow visualisations. In these studies, cavitation is developed at the tip of the blade and strongly interacts with the LE of the next blade, as it is presented in both the numerical and experimental results of Fig. 1.42a. Studies that focus in axial machines have been also been conducted from Zhang R. et al. (2013) and Zhang D. et al. (2015b) in axial pumps and from Jost et al. (2015) in a Kaplan

turbine. The work of Zhang D. et al. (2015b) focuse on the examination of the unsteady tip leakage vortex flow that is followed by different kinds of two-phase flow formations, which are presented in Fig. 1.42b in both the numerical and experimental results.

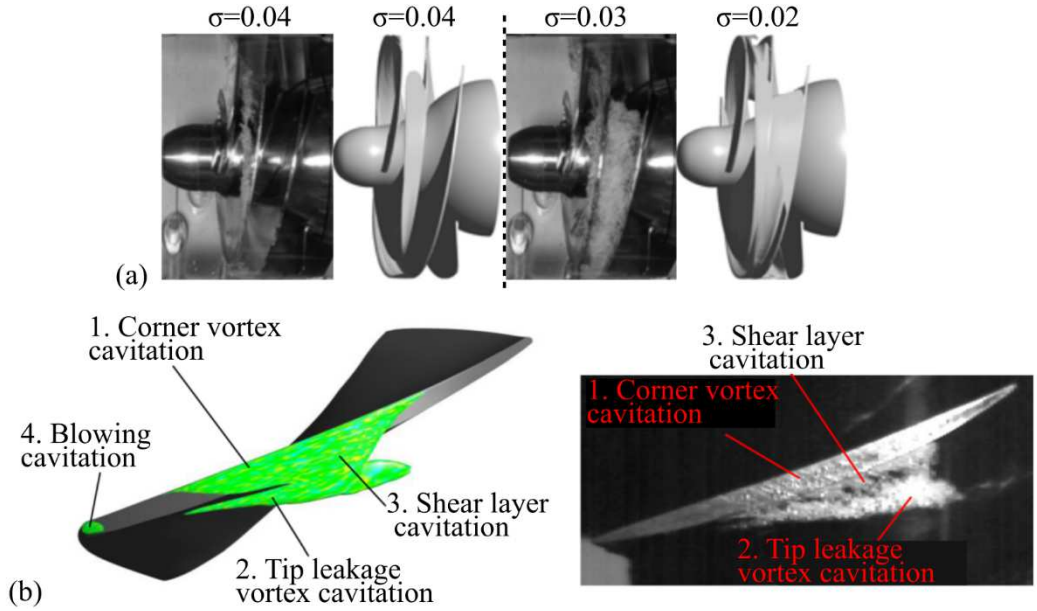

Figure 1.42 Comparison of numerical results with visual observations **a)** Kang et al. (2009), **b)** Zhang D. et al. (2015b).

Kobayashi and Chiba (2010) and Hatano et al. (2014) examine two-phase flow formations with the use of Zwart et al. model in radial and mixed flow impellers. Both of these works validate their numerical results with the use of static pressure measurements. Moreover, Kobayashi and Chiba (2010) find that during the development of unsteady vapour formations, symmetrical peaks and minimums in the loading of the blades and the overall torque can occur. On the other hand, Hatano et al. (2014) study experimentally with the use of static pressure transducers different instabilities that occur during low σ numbers and associated their effect on the performance with their numerically derived cavitation extent in the impeller. Furthermore, Cunha and Nova (2013) investigate the development of the cavitation at low specific speed impellers. Their modelling approach has been first validated in an injection nozzle case, where experimental results were available. The implementation of the model in the centrifugal pump allowed them to illustrate the extent of the cavitation area as function of NPSH and to obtain the $NPSH_3$ value under nominal conditions.

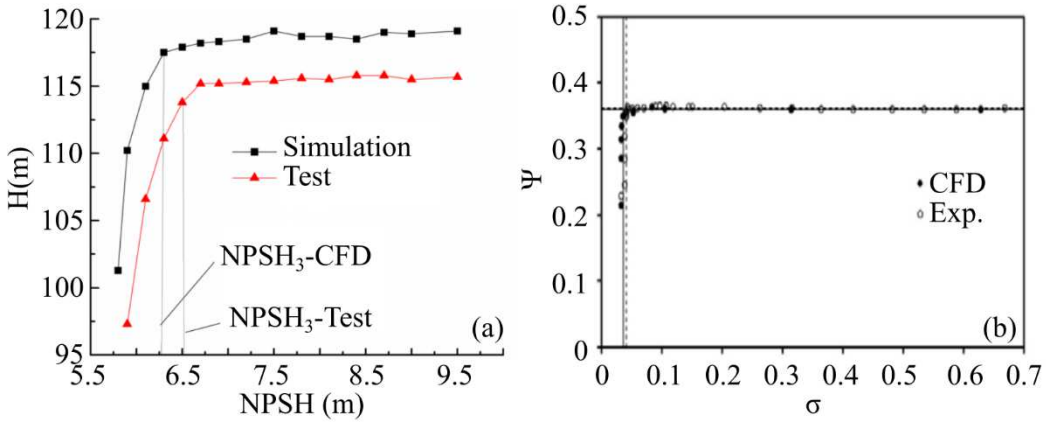

Figure 1.43 Comparison of numerically obtained and experimental σ-Ψ curves **a)** Zhang F. et al. (2017), **b)** Kim et al. (2012).

In a similar manner, Lorusso et al. (2017) examine the effect of the mesh density in the identification of the $NPSH_3$ point and conclude that relatively coarse meshes are able to sufficiently predict its value, even though there is significant disagreement in the total head value calculation. The ability of the Zwart et al. model on the simulation of the σ-Ψ curves for various flow conditions has been investigated in the works of Kim et al. (2012) and Zhang F. et al. (2017). According to their results, no matter the conditions examined, small differences occurred between the experimental and the computational curves, which remained <10% for both the Ψ and $NPSH_3$ values (Fig. 1.43).

Several studies examine the application of Zwart et al. model with respect to the cavitation formations in the runner and the draft tube of Francis turbines. Zuo et al. (2013, 2014) investigate the unsteady vortex two-phase flow patterns developed at the inter blade and the draft tube and evaluate the simulation results with those obtained from flow visualisations tests. In the case of inter-blade vortex lines, the application of the two-phase flow model improves the predicted vorticity compared to single flow simulations. The numerically obtained cavity showed lower extent compared to the flow visualisation photos during the initial stages of two-phase flow development. Nevertheless, these differences minimise at lower σ values. Furthermore, the helical vortex rope (Fig. 1.6a) is formed at the partial flowrate and the vapour formation is stronger closer to the runner and tends to break up into smaller scale vortices at the end of the draft tube. On the other hand, the onion shape vortex rope shows stronger characteristics than the visual observation, as shown in Fig. 1.44a. Similar results with respect to the vortex rope formations are obtained in other studies that also applied the Zwart et al. model (Yang, 2016; Gohil, 2016).

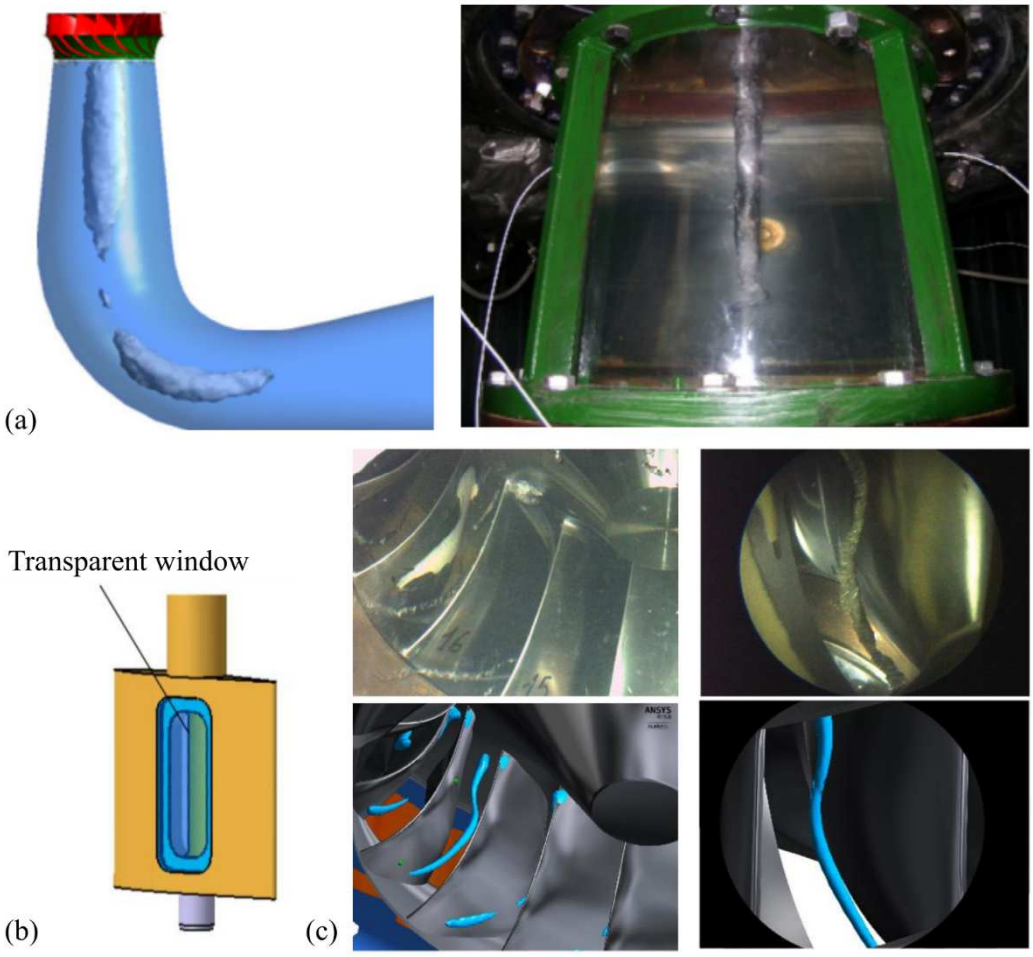

Figure 1.44 a) Onion-shape vortex rope simulation and experimental result (Zuo, 2014), **b)** Transparent window on the guide vane (Yamamoto, 2016), **c)** numerical and experimental investigation of inter blade cavitation (Yamamoto, 2016).

Wack et al. (2015) and Yamamoto et al. (2016) investigate with the same modelling approach the two-phase flow vortex formations that occur at the inter blade area. The first conducted a grid convergence study that is focused on the quantification of unsteady total vapour volume and shows that only fine meshes are able to resolve the inter blade vortices. However, even in this case the simulation results underestimate the extent of the vortices at the exit of the runner compared to the visual observations. In order to overcome the geometrical limitations of the Francis turbine and make possible the visual observation of the phenomenon inside the runner, Yamamoto et al. (2016) manufacture guide vane blades with parts made of transparent material (Fig. 1.44b). In this way the manage to take photos from the inner side of the machine and observe experimentally the vortex formations that are stronger close to the hub area (Fig. 1.44c). Finally, the results of their numerical model are able to efficiently locate the formation of the vortex, as well as to predict its actual shape.

Table 1.2 summarises all the above studies included in this review of the numerical tools, and provides additional information for the type (3rd & 4th column) and the magnitude of the machine (5th column), the type of the numerical grid (6th collumn) and the modelling of turbulence (7th column). The specific speed, n_q value is calculated for both pumps and turbines from Eq. 1.18, by using the same units; rotation speed in rpm, flowrate in m^3/hr and head in meters of water column. Similarly to Table 1.1, when no data are available, the question mark (?) is completed. In case of pumps studies where n_q cannot be calculated due to the lack of operating information, the type of machine (radial, mixed, axial) is extracted from its meridional view.

$$n_q = n\frac{\sqrt{Q_{BEP}}}{H_{tot,BEP}^{0.75}} \tag{1.18}$$

Table 1.2 List and additional details of the numerical studies reviewed.

	Author	**Machine**	**Type, n_q**	**D [mm]**	**Mesh**	**Turb.**	**Model**
1	(Medvitz, 2002)	Pump	Mixed	?	Struct.	k-ε	Kunz
2	(Zhang H., 2012)	Francis	2200	1750	Unstr.	k-ω SST	Kunz
3	(Panov, 2012)	Francis	6100	?	?	k-ε	Kunz
4	(Panov, 2012)	Francis	4400	?	?	k-ε	Kunz
5	(Wang, 2016)	Pump	1700	169	Struct.	k-ε	Kunz
6	(Liang, 2018)	Pump	1700	169	Struct.	k-ε	Kunz
7	(Athavale, 2002)	Inducer	?	?	?	k-ε	FCM
8	(Liu, 2005)	Francis	4800	9800	?	RNG k-ε	FCM
9	(Mostafa, 2006)	Pump	Axial	50	?	k-ε	FCM
10	(Zhou, 2008)	Francis	?	350	Unstr.	RNG k-ε	FCM
11	(Ding, 2011)	Pump	Axial	?	Unstr.	k-ε	FCM
12	(Li, 2014)	Pump	2000	278	Hybrid	k-ε	FCM
13	(Kang, 2009, 2010)	Inducer	?	150	Struct.	k-ω	Zwart
14	(Kobayashi, 2010)	Pump	1200	1270	Struct.	LES	Zwart
15	(Kim, 2012)	Pump	Radial	128	Struct.	k-ω SST	Zwart
16	(Zuo, 2013, 2014)	Francis	?	420	Hybrid	RNG k-ε	Zwart
17	(Cunha, 2013)	Pump	675	?	Struct.	k-ε	Zwart
18	(Lorusso, 2017)	Pump	?	?	Unstr.	k-ω SST	Zwart
19	(Zhang R., 2013)	Pump	Axial	300	Struct.	k-ε	Zwart
20	(Yang, 2016)	Francis	Mixed	?	Hybrid	LES	Zwart
21	(Hatano, 2014)	Pump	Radial	?	Struct.	k-ε	Zwart
22	(Jost, 2015)	Kaplan	?	?	Hybrid	k-ω SST	Zwart
23	(Wack, 2015)	Francis	?	?	Struct.	k-ω SST	Zwart
24	(Zhang D., 2015b)	Pump	12000	198	Struct.	k-ω SST	Zwart
25	(Gohil, 2016)	Francis	3800	465	Unstr.	k-ω SST	Zwart

26	(Yamamoto, 2016)	Francis	?	?	Struct.	SST-SAS	Zwart
27	(Zhang F., 2017)	Pump	630	236	Struct.	k-ω SST	Zwart

1.4 Synopsis

The development and application of experimental tools for the detection of cavitation in hydraulic turbomachines lasts for almost a century. The first approaches, which are used in industry until nowadays, managed to define an operational limit ($NPSH_3$ or $NPSH_1$) related with the suction and discharge conditions of pumps and hydroturbines, respectively. Under this limit the machine suffers extensive cavitation and the total head and efficiency deteriorate. Nevertheless, flow visualisation studies have proved that cavities initiate far before this operating limit, and they are able to create significant wear on the solid surfaces of the machine, which eventually results in causes drop of performance, if they are not detected promptly.

In order to overcome the aforementioned weaknesses, the use of noise and vibration measurements has been proposed so as to identify the shock pressure waves generated from the vapour bubble implosion. In this case, the challenge deals with the adequate acquisition and processing of the signals, so as to extract the two-phase flow information from the noisy environment of the hydraulic turbomachine. In general, the time series obtained from pumps and hydroturbines include a large number of mechanical and hydraulic noise sources that are not related with cavitation. The traditional signal processing tools include the study of the signal in time and frequency domain, and its power content at different discrete or range of frequencies, with the use of the powerband tools. In the case of raw time domain analysis, only two studies (Duplaa, 2010; Schmidt, 2014) manage to depict the impulsive behaviour of cavities formation. In the majority of the studies there has not been reported any impulsive signals, even in the cases where the authors use high frequency measurements and filter out low frequency noise (Gopalakrishnan, 1985; Neil, 1997; Alfayez, 2004; Dong, 2019).

On the other hand, the impact of cavitation becomes much clearer when the frequency spectrum of the measurements is investigated. In the majority of the reviewed cases, the onset and development of cavitation seem to excite wide band ranges. The power of those frequency bands is integrated with the use of powerbands and is able to detect cavitation promptly. The difficulty introduced at this point, deals with the fact that the frequencies excited by cavitation change between different testing configurations, machines, sensors and operating conditions. The different behaviour has been clearly depicted in the various patterns of powerbands, presented in section 1.3.1.3. Consequently, it is not possible to formulate a common reliable detection methodology that could be applied in different configurations.

Towards this direction, the study of the signal's envelope in frequency domain has been proposed from few authors (Bourdon, 1994; Escaler, 2002, 2004), in order to examine the possible modulation of the high frequencies excited by cavitation noise. These studies focuse on cavitation formations in the runner and the draft tube of Francis turbines, and managed to associate cavitation with discrete low frequency components of the spectrum. With this approach it is possible to extract the detection information needed to form a common criterion. However, the proper identification of the frequency band, used for the signal's demodulation, remains an open problem, since it deviates significantly among the different testing configurations. In order to overcome this difficulty, the present Thesis proposes the use of the Spectral Kurtosis methodology, which is introduced in section 2.4.5 and is applied in Chapter 7.

According to the discussion in section 1.3.2, the two-phase flow models are found capable to predict the location and the extent of the two-phase flow development in hydrofoils and hydraulic turbomachines. However, the interface tracking methods (ITM) face difficulties to model the three-dimensional wake and are only capable to track the interface of the attached cavitation. On the other hand, the interface capturing methods (ICM) overcome the aforementioned difficulties and allow the modelling of cavitation types that are not attached on the rotor's surfaces. Among the barotropic and transport equation-based models (TEM), the latter are found to be used more frequently in the several works related with three dimensional flow simulations of hydraulic turbomachines, since they include the effect of mass exchange between the vapour and liquid phases. The review of the literature reveals that the TEM are

provide good predictions regarding the behaviour of cavitation curves and the point of the 3% of total head drop.

2. Experimental Tools & Configurations

2.1 Introduction

In this chapter the configuration and the theoretical background of the experimental tools used in the present dissertation, are presented. The cavitation phenomenon is experimentally investigated in two laboratory test rigs; i) at the pump laboratory established in the Engineering Department of Lancaster University and ii) at the Laboratory of Hydraulic Turbomachines, National Technical University of Athens. The first part of this chapter (section 2.2) includes the mathematical formulations regarding the analysis of centrifugal pump operation under normal and cavitating conditions. The second part (section 2.3) presents the testing procedures followed, in order to conduct the non-cavitating and cavitating pump performance tests. The expressions used to estimate the uncertainty of the present study measurements are also provided in section 2.3. In addition, all the formulas used for the acquisition and the signal processing of noise and vibration measurements are given in section 2.4. In the last section 2.5, a detailed description of the components (pumps and sensors) and the set-up of the two test rigs used in this present dissertation is given.

2.2 Centrifugal pumps

2.2.1 Fundamental performance equations

Centrifugal pumps aim to transport liquids or two-phase fluids by increasing their energy level at a specified flowrate, Q. The energy increase is achieved by transfering the mechanical power, which is provided to the pump's shaft by an electric motor, to the fluid through a rotating impeller with hydrodynamic blades. This operation is done under constant rotation speed, Ω (Fig. 2.1). The quantification of the energy per unit flow weight transmitted to the working fluid is expressed in meters of liquid column (MLC), and it is defined as the centrifugal pump (total) head, H_{tot}. Its calculation is done through Eq. 2.1 (Papantonis, 2016) by subtracting the total amount of energy that the fluid has at the pump inlet (suction), from its total energy at the pump exit (discharge).

$$H_{tot} = H_{oa} - H_{oe} = \Delta H_{st} + \Delta H_{dyn} + \Delta H_z \tag{2.1}$$

$$H_{oa} = \frac{p_a}{\rho g} + \frac{c_a^{\,2}}{2g} + z_a \tag{2.2}$$

$$H_{oe} = \frac{p_e}{\rho g} + \frac{c_e^{\,2}}{2g} + z_e \tag{2.3}$$

$$\Delta H_{st} = \frac{1}{\rho g}\left(p_a - p_e\right) \tag{2.4}$$

$$\Delta H_{dyn} = \frac{1}{2g}\left(c_a{}^2 - c_e{}^2\right) \tag{2.5}$$

$$\Delta H_z = z_a - z_e \tag{2.6}$$

where H_{oa} (Eq. 2.2) and H_{oe} (Eq. 2.3) are the total energy per unit weight at the discharge (α) and the suction side (e) of the pump (Fig. 2.1). The energy difference described by Eq. 2.1, consists of three contributions, ΔH_{st} (Eq. 2.4), ΔH_{dyn} (Eq. 2.5) and ΔH_z (Eq. 2.6) that reflect the static, dynamic (or kinetic) and potential (gravitational) energy of the fluid, respectively. Here, ρ is the fluid density, g is the gravitational acceleration, p is the static pressure, c the mean pipe velocity, and z indicates the vertical distance between a reference elevation level and the level of suction (e) and discharge (α) points where the static pressure is measured. In the case of Fig. 2.1, the reference level coincides with that of z_e.

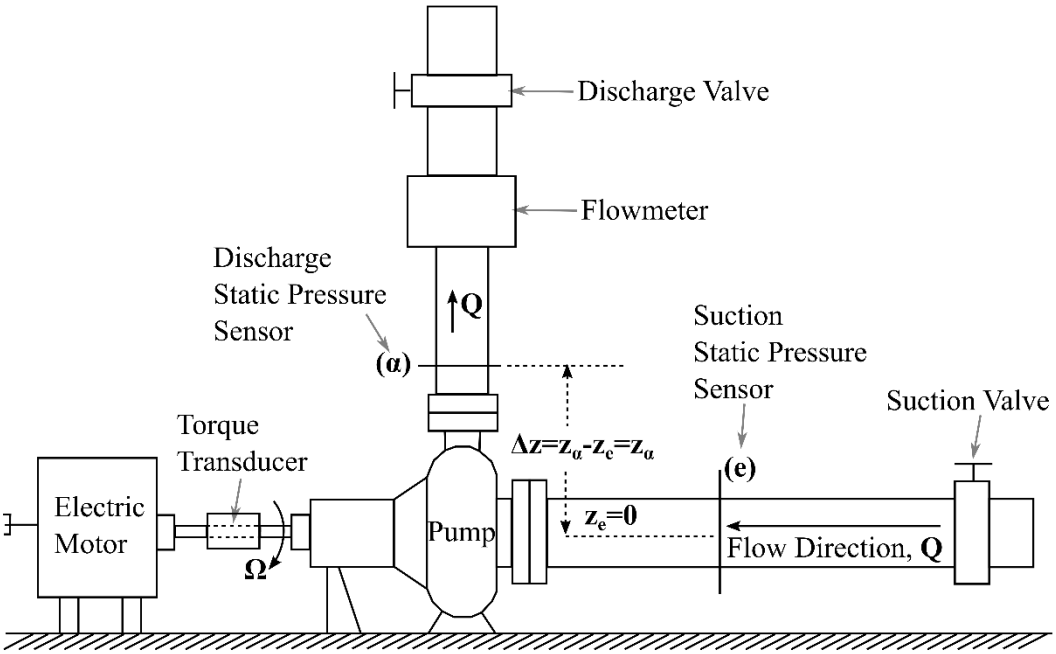

Figure 2.1 Sketch of a typical centrifugal pump configuration.

The ability of the pump to provide the mechanical power to the working fluid defines the (total) efficiency, η of the pump. The efficiency and the mechanical power, P_{mech}, are calculated by Eqs. 2.7 and 2.8, respectively:

$$\eta = \frac{\text{hydraulic power}}{\text{mechanical power}} = \frac{\rho g H_{tot} Q}{P_{mech}} \tag{2.7}$$

$$P_{mech} = M_m \Omega \tag{2.8}$$

where Ω is the rotation speed and M_m the torque measured at the shaft of the pump (Fig. 2.1). In cases, where the electric power, P_{el} of the motor is measured and the motor's efficiency (η_{mot}) is provided, P_{mech} is calculated alternatively from Eq. 2.9:

$$P_{mech} = P_{el}\eta_{mot} \tag{2.9}$$

Finally, the characteristic curves of geometrically similar impellers (or of the same impeller at different rotation speed) can be derived by the affinity laws (Eq. 2.10 – 2.12).

$$\frac{Q'}{Q''}=\left(\frac{d_2{}'}{d_2{}''}\right)^3\left(\frac{n'}{n''}\right) \tag{2.10}$$

$$\frac{H_{tot}{}'}{H_{tot}{}''}=\left(\frac{d_2{}'}{d_2{}''}\right)^2\left(\frac{n'}{n''}\right)^2 \tag{2.11}$$

$$\frac{P_{mech}{}'}{P_{mech}{}''}=\left(\frac{d_2{}'}{d_2{}''}\right)^5\left(\frac{n'}{n''}\right)^3 \tag{2.12}$$

The main pump quantities (and their characteristic operation curves) can be expressed in normalised form with the use of non-dimensional quantities, flowrate, Φ (Eq. 2.13), total head, Ψ (Eq. 2.16) and power, N (Eq. 2.17), so as to be indicative of the hydrodynamic design of the pump, regardless its specific size. (Papantonis, 2016).

$$\Phi=\frac{v_{n2}}{u_2} \tag{2.13}$$

$$v_{n2}=\frac{Q}{\left(\pi d_2-z_s e_2\right)b_{I,2}} \tag{2.14}$$

$$u_2=\Omega R_2 \tag{2.15}$$

$$\Psi=\frac{2gH_{tot}}{u_2{}^2} \tag{2.16}$$

$$N=\frac{P_{mech}}{\rho\Omega^3 d_2{}^5} \tag{2.17}$$

where v_n is the normal component of the absolute velocity (Figs. 2.2b,c), v, u is the tangential velocity (Figs. 2.2b,c), z_s the number of impeller blades, e the blade thickness, b_I the blade width (Fig. 2.2a) and R the radius of the impeller (Fig. 2.2a).

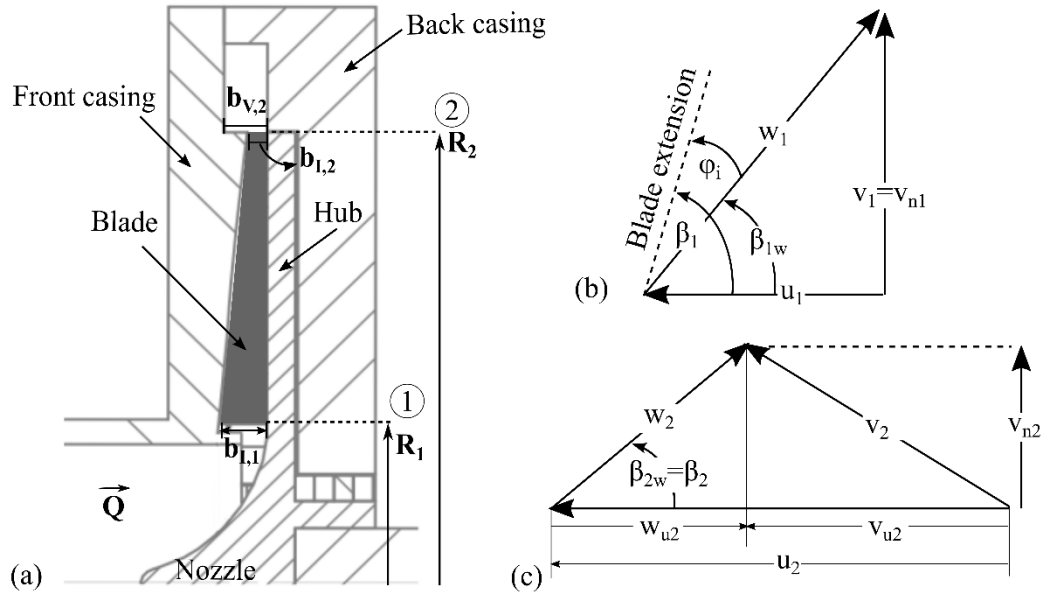

Figure 2.2 a) Meridional view of a centrifugal pump with a semi-open radial impeller and typical velocity triangles at **b)** R_1**, c)** R_2.

In the present Thesis, subscripts 1 and 2 symbolise the area at the inlet and the outlet of the blade, which is illustrated in the Fig. 2.2a, along with their corresponding velocity triangles (Figs. 2.2b,c). In Fig. 2.2, *w* denotes the relative velocity, the *u* subscript represents tangential velocity component and the *n* the normal components , while $b_{V,2}$ is the volute width at the inlet of the volute.

An important note regarding the velocity triangles of Fig. 2.2 refers to the use of the Euler's assumptions that; i) the working fluid enters the bladed area of the impeller with zero pre-rotation (Fig. 2.2b), v_{u1}=0 m·s^{-1} (v_1=v_{n1}), and ii) the impeller is ideal with infinite number of zero width blades. The latter practically means that the slope, β_{2w} of the flow relative velocity vector (w_2) at the exit of the impeller, R_2, equals the blade angle, β_2 (Fig. 2.2c). In the velocity triangle of Fig. 2.2b, the inlet blade angle, β_1 is presented along with the flow inlet angle, β_{1w} and their difference, the incidence angle φ_i.

The fundamental Eqs. 2.13, 2.16 and 2.17 are used for the derivation of the total head, power and efficiency characteristic curves of the pump, using the the measurements or the simulation results of the physical variables that are involved in Eqs. 2.2 to 2.6.

2.2.2 Cavitation

As it is mentioned in the Introduction, cavitation is a hydrodynamic phenomenon of liquid vaporization due to local drop of static pressure, which is frequently created at the suction side of centrifugal pumps and mainly just after the flow entrance into the impeller region, where the static pressure takes its lowest value, that may become lower than the liquids vapour pressure, p_{sat}. A typical distribution of the static pressure in a centrifugal pump, from the suction (e) to the discharge (a), is given in Fig. 2.3, where p_B is the atmospheric pressure. The point M (Fig. 2.3), denotes the minimum static pressure point that lies at the suction side of the blade, where cavitation appears, when:

$$p_M < p_{sat} \tag{2.18}$$

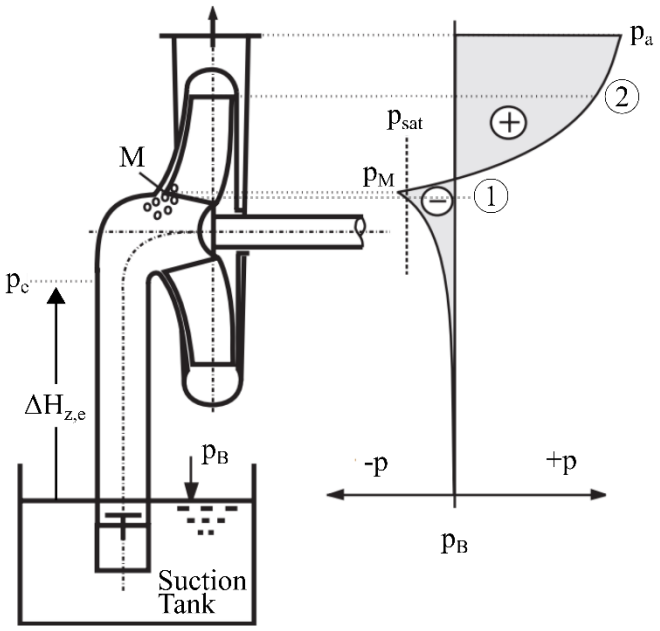

Figure 2.3 Static pressure distribution in a centrifugal pump (Chudina, 2007).

The difficulty to measure or analytically calculate the p_M value makes the criterion of Eq. 2.18 impractical. In order to overcome it, the use of the NPSH expression has been proposed for the centrifugal pumps:

$$NPSH = H_{oe} - H_{sat} = \left(H_M - H_{sat}\right) + \lambda_w \frac{w_1^2}{2g} + \lambda_v \frac{v_1^2}{2g} \tag{2.19}$$

$$H_{sat} = \frac{p_{sat}}{\rho g} \tag{2.20}$$

$$\lambda_w = \left(\frac{w_M}{w_1}\right)^2 - 1 \tag{2.21}$$

$$\lambda_v = 1 + \zeta_E \tag{2.22}$$

where ζ_E is the loss coefficient at the inlet, H_{sat} the saturation pressure expressed in meters, λ_v coefficient that represents the friction losses and varies between 1.1 and 1.35, and λ_w a coefficient that depends mainly on the incidence angle (Lobanoff, 2013), and ranges from 0.1 to 2.5 (Gülich, 2008).

When the first bubbles are formed at the minimum static pressure location (M), the NPSH value of the pump becomes critical, $NPSH_r$ and $H_M \sim H_{sat}$, which modifies Eq. 2.19 as follows (Gülich, 2008; Lobanoff, 2013; Papantonis, 2016):

$$NPSH_r = \lambda_w \frac{w_1^2}{2g} + \lambda_v \frac{v_1^2}{2g} \tag{2.23}$$

The $NPSH_r$ expression characterises the pump, and its value depends on the operating characteristics of the machine (v_1, w_1, λ_w), as well as on the desing and the quality of manufacturing procedure at the inlet of the blade (1) (Papantonis, 2016). Consequently, pump manufacturers provide $NPSH_r$-Q curve along with the rest charactiristic curves of the pump. The study of Eq. 2.23 reveals the increase of $NPSH_r$ value as the pump operates in higher flowrates, which in practice means that the pump is more prone to cavitate when it operates at such conditions (Fig. 2.4). The expression used, in order to non-dimensionalise the NPSH values discussed so far, is the Thoma cavitation number, σ given in Eq. 2.24 (Karassik, 2007; Brennen, 2011):

$$\sigma = \frac{NPSH}{H_{tot}} \tag{2.24}$$

The negative effects of cavitation on the performance and the solid surfaces of hydraulic turbomachinery has been discussed in the Introduction and in Chapter 1 of this Thesis. In order to operate the machine without cavitation, the installation of the pump is properly adjusted. The combination of Eqs. 2.19 and 2.23, gives Eq. 2.25, where H_{oe}-H_{sat} difference forms the NPSH available equation (Eq. 2.26) that describes the installation of the pump and expresses the difference of total hydraulic energy at the suction from the saturation pressure in meters of working fluid column (Papantonis, 2016).

$$NPSH = H_{oe} - H_{sat} = \left(H_M - H_{sat}\right) + NPSH_r \tag{2.25}$$

$$NPSH = H_{oe} - H_{sat} = H_E - \Delta H_{z,e} - \zeta_e Q^2 - H_{sat} \tag{2.26}$$

where H_E is the pressure at the surface of the suction tank in meters, $\Delta H_{z,e}$ is the height difference between pump suction (e) and the tank (Fig. 2.3), and the term $\zeta_e Q^2$ represents the hydraulic losses from the suction tank (Fig. 2.3) until (e). In the case of open tanks, as in the example of Fig. 2.3, $H_E = H_B = (p_B/\rho \cdot g)$. As a consequence, the criterion regarding the operation

of the pump under non-cavitating conditions, described from Eq. 2.18, can now be expressed from Eq. 2.27, after the combination of Eqs. 2.25 and 2.26 (Papantonis, 2016).

$$\begin{aligned} &NPSH > NPSH_r, \text{ for safe operation} \\ &NPSH \approx NPSH_r, \text{ for risky operation} \\ &NPSH < NPSH_r, \text{ for unsafe operation} \end{aligned} \tag{2.27}$$

Equation 2.26 is the key for the conduction of cavitation experiments with the use of the CTA, CTB and CTC methods introduced in section 1.3.1.1. Each of these methods attempt to regulate one of the terms of Eq. 2.26 so as to decrease the NPSH available by the installation, and force the machine to operate under controlled cavitating conditions. More specifically:

i. CTA method reduces the pressure of the closed suction tank expressed by the H_E term.
ii. CTB method increases the $\Delta H_{z,e}$ term by the reduction of the suction tank's level.
iii. CTC method increases the losses term ($\zeta_e Q^2$) by throttling the suction valve.

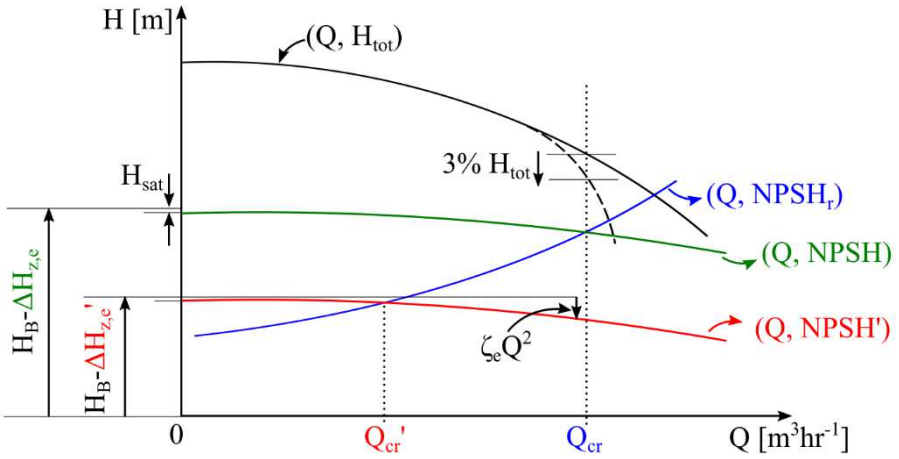

Figure 2.4 Net positive suction head available (NPSH) curve as a function of flowrate and suction conditions for a centrifugal pump establishment (Papantonis, 2016).

Finally, the effect of the installation changes on the NPSH available value and on the pump's performace are discussed with the use of Fig. 2.4 (Papantonis, 2016). For the configuration of Fig. 2.3, the NPSH available decreases as the flowrate (Q) increases under constant H_B, ζ_e, $\Delta H_{z,e}$ and H_{sat}, as it is illustrated by the green colour curve of Fig. 2.4. On the other hand, as it has been already discussed. the $NPSH_r(Q)$ curve has the oposite trend, since it increases at higher flowrates. Therefore, the pump can operate under non-cavitating conditions from until a critical flowrate Q_{cr} (Fig. 2.4). If the characteristics of the installation change ($\Delta H_{z,e} \rightarrow \Delta H_{z,e}$') and the height difference between the inlet of the pump (e) and the suction tank (Fig. 2.3) increases ($\Delta H_{z,e}$' > $\Delta H_{z,e}$) the new NPSH available characteristic curve (red colour curve of Fig. 2.4) exhibits lower values, and the new maximum Q_{cr}' value reduces.

2.3 Testing procedures

2.3.1 Tests under no-cavitating conditions

The aim of the tests under normal operating conditions, is the derivation of the characteristic curves of the pumps, so as to map their performance at various operating points and then be able to compare with the coresponding behaviour under cavitating flow. Three characteristic curves are obtained, as a function of the pump flowrate; i) the total head curve (Q-H_{tot}), the mechanical power curve (Q-P_{mech}), and the efficiency curve (Q-η).

$$H_{tot} = \frac{1}{\rho g}\left(p_a - p_e\right) + \frac{8Q^2}{\pi^2 g}\left(\frac{1}{d_{p,a}{}^4} - \frac{1}{d_{p,e}{}^4}\right) + z_a \tag{2.28}$$

The flow and operating variables, as well as the geometrical dimensions required for the use of Eqs. 2.28, 2.8, 2.9 and 2.7 are given in Table 2.1. More specifically, the derivation of the centrifugal pump's characteristic curves must include the measurements of:

i. the static pressures at the suction, p_e and discharge p_α of the machine (Fig. 2.1),
ii. the flowrate, Q,
iii. the mechanical torque at the rotating shaft, M_m or alternatively, the electric power of the motor, P_{el} and
iv. the rotation speed, Ω of the rotating shaft.

The sensors used for the measurement of each of the above quantities are given for each test rig in sections 2.5 and 2.6. In addition, the geometric dimensions of suction ($d_{p,e}$) and discharge ($d_{p,\alpha}$) pipe diameters are provided along with the elevation head z_α. The geometric dimensions of each pump test rig are summarised in section 2.5. In cases where Eq. 2.9 is used instead of Eq. 2.8, the motor characteristic curves are also used. After their calculation, the total head and power curves become dimensionless with the use of Eqs. 2.13, 2.16 and 2.17.

Table 2.1 Flow and operating variables and geometrical dimensions required for the derivation characteristic curves under normal conditions.

	H_{tot} (Eq. 2.28)	**P_{mech} (Eqs. 2.8, 2.9)**	**η (Eq. 2.7)**
Flow and operating variables	p_α, p_e, Q	M_m, Ω, P_{el}, η_{mot}	Q, M_m, Ω
Geometric dimensions	$d_{p,\alpha}$, $d_{p,e}$, z_α	-	-

The three characteristic curves of each pump are derived in six repeated experiments; three set of measurements are performed for continuously increasing flowrates and other three for reducing flow rates. This procedure is followed, in order to check and verify the repeatability of the measurements, and the possible effect of the discharge valve operation on the accuracy of the derived characteristic curves. A graphical representation of a typical such experiment of all the flow and operating variables as function of time is given in Fig. 2.5. This plot illustrates the measurements at seven operating points (OPs) for the derivation of the characteristic curves reducing flowrate order. The x-axis represents the data acquisition time and not the total duration of the experiments.

In order to provide an adequate presentation of the testing procedure for continuously reducing flowrates, each of its steps is described below, as follows:

i. Before starting the electric motor:
   a. the level of the working fluid in the machine is examined, in order to ensure that exceeds that of the pump. For the pumps with volute and pipes made of a non-transparent material, this is achieved with the inspection of the drilling holes made for the establishment of discharge static pressure transducers.

b. the suction valve should be entirely open and the discharge valve should remain closed (see final step vii)

ii. The variable speed motor starts and its rotationl speed is progressively increased up to the desired value. Then, it is kept constant during the test, as it is shown in Fig. 2.5.

iii. The discharge valve opens entirely, and 30 seconds of waiting time is applied, in order to ensure the minimisation of any flow fluctuations due to valve opening. At this point the pump is considered to operate under steady conditions.

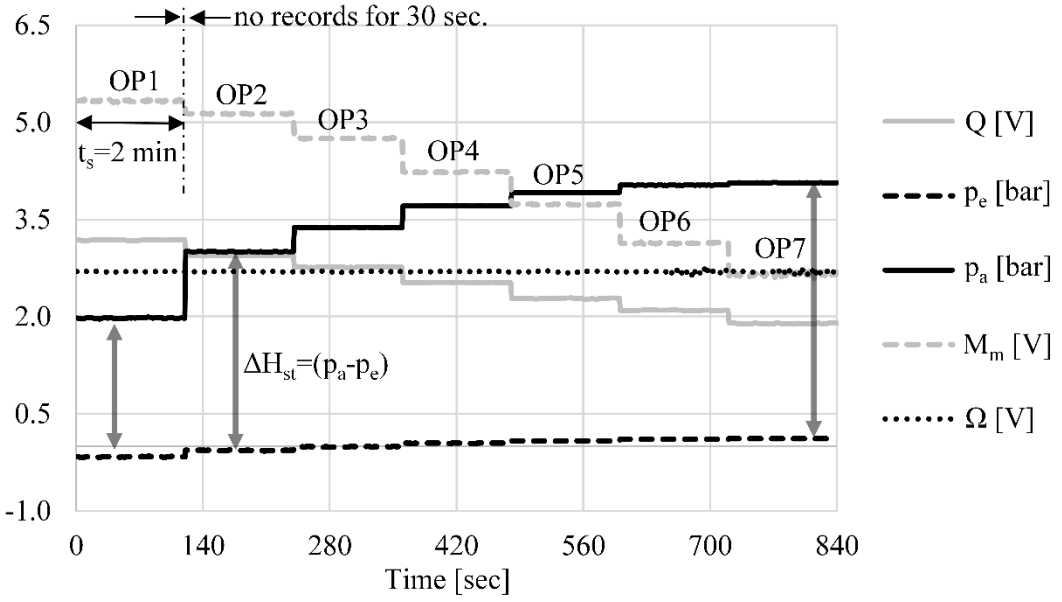

Figure 2.5 Graphical representation of typical raw measurements of the flow and operating variables during a complete cycle of experiments at non-cavitating conditions.

iv. The measurement of the flow and operating quantities begins for the first operating point (OP1, Fig. 2.5). The duration of the recordings for each OP is t_s=120 sec and the sampling rate used for their digitization is f_s =1 kHz (Fig. 2.6). The accuracy of the mean value, which is further discussed in detail in section 2.3.3, depends on the number of measurements and their individual deviations from the mean (IEC 60193, 2019). The mean value ($\overline{\varphi}$) of the raw data of the flow and operating quanitities (name it φ) is calculated from Eq. 2.29 for every second within the two minutes of data acquisition. The results of that calculation are illustrated in Fig. 2.5. As a result, the final seven values that made the operating points that constitute the characteristic curve of Fig. 2.5, are the mean, $\overline{\varphi}_{\overline{\varphi}}$ of the 120 samples' mean value (Eq. 2.30).

v. The signals digitisation pauses after 120 seconds and the discharge valve is throttled until to reach the desired lower flowrate (OP2).

vi. After waiting for 30 seconds (Fig. 2.5), the digitisation begins again and the signals for the new operating point are recorded. As it is expected, the mechanical torque, M_m decreases, while the discharge static pressure, p_α increases significantly. The suction pressure, p_e also shows a slight increase due to a corresponding reduction of the suction losses at a lower flowrate. Consequently, the total static pressure term of Eq. 2.28 that constitutes the major part of the H_{tot}, indubitably rises. The trend of the flow and operating variables as a function of flowrate is discussed in Chapters 4 and 5.

vii. The steps iv to vi are repeated until the completion of testing of all desired flowrates.

viii. The test cycle finishes after closing the discharge valve that must precede the switch-off of the electric motor.

As mentioned above, this procedure is repeated 3 times for increasing and 3 times for decreasing flowrates.

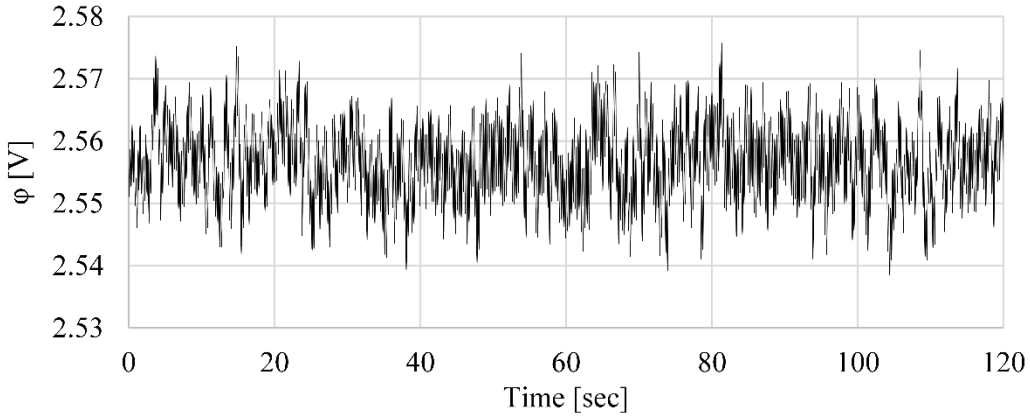

Figure 2.6 Typical flow variable's raw time series measured for a pump operating under steady state conditions.

$$\bar{\varphi} = \frac{1}{1000}\left(\sum_{i=1}^{1000} x_i\right) \tag{2.29}$$

$$\bar{\varphi}_{\bar{\varphi}} = \frac{1}{120}\left(\sum_{i=1}^{120} \bar{\varphi}_i\right) \tag{2.30}$$

2.3.2 Cavitation tests

The tests under cavitating conditions aim to derive the NPSH-H_{tot} and NPSH-η curves or their non-dimensional form, σ-Ψ and σ-η under various flowrates. These tests are performed under constant flowrate, by progressively throttling the suction valve, in order to reduce the static pressure at the inlet of the pump and cause the development of vapour bubbles. In this way the suction losses are increased and the NPSH decreases, however the flowrate is also diminished. As a result, the discharge valve is also properly regulated, in order to restore the flowrate to its initial value.

This procedure introduces a limitation to the minimum attainable value of σ, when the discharge valve reaches its fully open position, because after that OP any further throttling of the suction valve reduces the flowrate. Thus the σ variation range becomes smaller at higher flowrates, where the testing starts with the discharge valve at more open position. The open sump with throttle valve procedure (CTC, see Fig. 1.27, section 1.3.1.1) that is described in this section, is provided from ISO 9906:2012.

In parallel with the calculation of cavitation characteristics curves, the acoustic emission (AE) and vibration measurements are also obtained, along with the flow visualisation photos. By this way, the various positions and extents of vapour phase, along with their noise and vibration signal characteristics are matched to the corresponding suction conditions (NPSH, σ).

Three equations are used for the derivation of cavitation characteristic curves; i) Eq. 2.28 for the total head and Eq. 2.7 for the efficiency, similarly to the non-cavitation tests and ii) the Eq. 2.31 for the NPSH, by the assumption that the level or reference z lies at the suction level (z_e=0 m):

$$NPSH = H_{oe} - H_{sat} = \frac{p_e}{\rho g} + \frac{8Q^2}{g\pi^2 d_{p,e}^{\ 4}} - H_{sat} \tag{2.31}$$

Finally, the cavitation curves are non-dimensionalised with the use of Eqs. 2.16 and 2.24. Along with the physical variables of the total head and efficiency that are presented in Table 2.1, the saturation vapour pressure, H_{sat}, has to be provided. The value of H_{sat} is a function of

temperature of the working fluid, and for water it is approximated by Eq. 2.32, where T it the temperature in Celcius degrees, as shown in Fig. 2.7a. The fluid temperature remains relatively constant during each experiment, in order to avoid any influence on the results.

$$H_{sat} = \frac{p_{sat}}{\rho g} = \frac{(0.1907T - 1.5157)\cdot 1000}{\rho g} \tag{2.32}$$

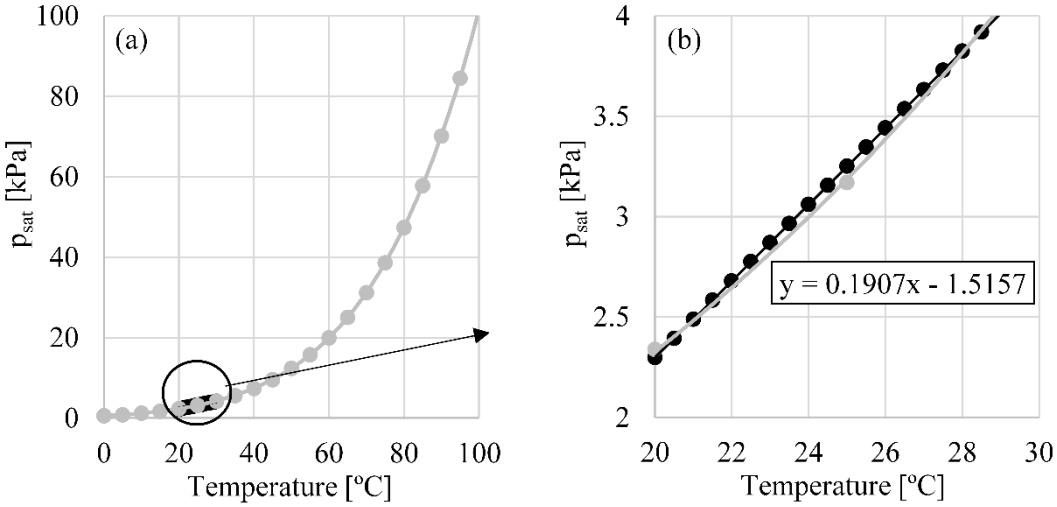

Figure 2.7 Saturation vapour pressure as function of temperature, for water.

The cavitation characteristic curve is derived in three repeated experiments, which are performed for continuously reducing the suction static pressure, p_e. A graphical representation of typical measurements of all the flow and operating variables as function of data acquisition time under cavitating conditions tests is given in Fig. 2.8 (similarly to Fig. 2.5 for non-cavitating conditions). This plot illustrates the measurements at ten successive OPs for the derivation of the cavitation characteristic curve.

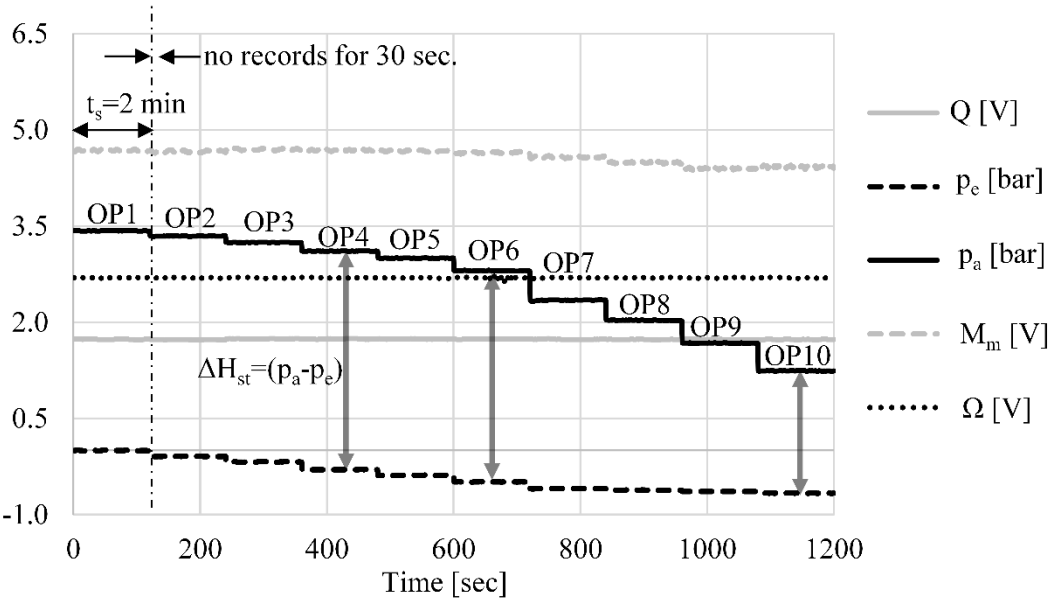

Figure 2.8 Graphical representation of typical raw measurements of the flow and operating variables during a complete cycle of a cavitating condition test.

The testing procedure is described step by step, as follows:

i. This step remains identical with step (i) described under normal conditions (section 2.3.1).
ii. This step remains identical with step (ii) described under normal conditions (section 2.3.1). The constant rotational speed is confirmed by the graph of Fig. 2.8.
iii. The discharge valve opens until the desired flowrate, Q, is achieved. This flowrate should remain constant during this experimental cycle (Fig. 2.8) and characterises the NPSH-H_{tot} curve. The suction valve state remains unchanged and fully open only for the first OP. After awaiting period of 30 seconds, the pump is considered to operate under steady conditions.
iv. The recording of the pump flow and operating variables begins and it is identical with the corresponding procedure under normal conditions. But now the noise and vibration measurements are also performed, along with the photos that illustrate the flow passage between the impeller's blades. The time acquisition, t_s and sampling frequency, f_s of the dynamic measurements (noise and vibration) are selected based on the the dynamic phenomena related with the pump's operation, as well as with the signal processing techniques applied to the time series obtained. More details are given in sections 2.4.1 and 2.5.
v. The signals digitisation pauses after 120 seconds and the suction valve is throttled so as to reduce the suction static pressure, p_e. However, this results in an unwanted drop of flowrate. As a consequence, the discharge valve is properly regulated, in order to restore the flowrate to the initial one in step (iii).
vi. After waiting for 30 seconds (Fig. 2.8), the digitisation begins again and the signals for the new operating point are recorded.
vii. The steps iv to vi are repeated until the the point where the discharge valve is entirely open, and any further throttling of the suction valve causes an uncontrolled flowrate drop.
viii. The test cycle finishes after entirely opening and closing of the suction and of the discharge valve, respectively, and then shut down the electric motor.

The graph of Fig. 2.8 shows that the flowrate, Q, remains constant durinf the measurements until the end of the test cycle (t=1200 sec). On the other hand, the mechanical torque, M_m remains also stable until the OP6 (t=720 sec), but it slightly decreases for t>720 sec. This behaviour is not related with the experiment procedure but with the cavitation development, and it will be discussed in Chapters 4 and 5. The decrease of the suction static pressure, p_e as a result of suction valve throttling can be also observed in Fig. 2.8. Similarly to M_m, the pump operation seems unaffected until OP6, since the discharge pressure, p_α decreases until this OP with the same rate as p_e, and hence the total head remains about the same. But for t>720, the decreasing rate of p_α becomes higher than that of p_e. This behavior is discussed and analysed in detail in the next section 3.3 (Chapter 3) of this dissertation.

2.3.3 Measurements' uncertainty of mean flow and operating variables.

In this section the procedure for the estimation of the total relative uncertainty for each measured mean flow and operating quantity is analysed. In this way, it is possible to quantify the variation range of the actual mean value of each variable.

2.3.3.1 Random relative uncertainty

The use of the mean of multiple samples (Eq. 2.30) as the estimator of the actual mean value of the population is applied for the uncertainty analysis. For an ideal experiment, where every variable is completely controlled the mean values of the each sample, such as those presented in Figs. 2.5 and 2.8, should be identical. However, in practice, the mean values of the 120 samples that constitute each OP, for instance those of $\overline{p}_a$ in Fig. 2.9, they deviate around a mean value, the mean of the multiple samples. The standard deviation, s of the mean of the multiple samples, $\overline{\varphi}_{\overline{\varphi}}$ is then calculated from Eq. 2.33 (Taylor, 1997; Psoinos, 1999; IEC 60193, 2019).

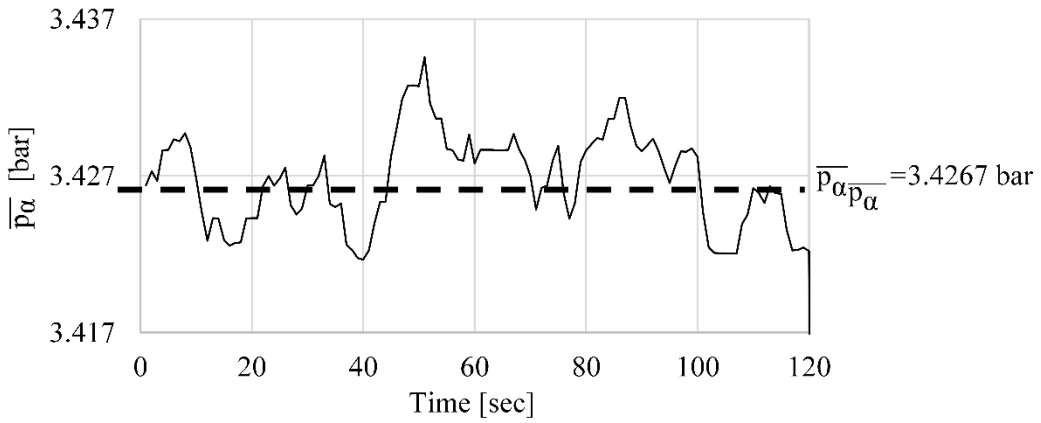

Figure 2.9 Zoom in the discharge mean static pressure value for the OP1 of Fig. 2.8.

Henceforward in this chapter, the mean value of one sample is given as φ, while the mean of the multiple samples as $\bar{\varphi}$, in order to simplify the symbolisations. However, the passing to the Chapters 3,4,5,6 and 7, where the results are shown, only the value of the mean of the multiple samples is discussed and for the same reasons it will be written as φ.

$$s_{\bar{\varphi}} = \frac{s_\varphi}{\sqrt{\nu_N}} \tag{2.33}$$

$$s_\varphi = \sqrt{\frac{1}{\nu_N - 1}\sum_{i=1}^{\nu_N}\left(\varphi_i - \bar{\varphi}\right)^2} \tag{2.34}$$

where ν_N is the number of independent measurements [-].

The total relative uncertainty, $F(\bar{\varphi},t)$, of each measured mean flow and operating variable φ is calculated according to Farrance (2012) and IEC 60193 (2019). The total relative uncertainty of the flowrate ($\overline{Q}$), suction ($\overline{p_e}$) and discharge ($\overline{p_a}$) static pressure, mechanical torque ($\overline{M_m}$), electric power ($\overline{P_{el}}$), rotation speed ($\overline{\Omega}$) and temperature ($\overline{T}$) are calculated through Eq. 2.35:

$$F\left(\bar{\varphi},t\right) = \pm\sqrt{F\left(\bar{\varphi},s\right)^2 + F\left(\bar{\varphi},r\right)^2} \tag{2.35}$$

$$F\left(\bar{\varphi},r\right) = \frac{\delta\left(\bar{\varphi},r\right)}{\bar{\varphi}} \tag{2.36}$$

$$\delta\left(\bar{\varphi},r\right) = t \cdot s_{\bar{\varphi}} \tag{2.37}$$

$$t = 1.96 + \frac{2.36}{\nu_N} + \frac{3.2}{\nu_N^{\,2}} + \frac{5.2}{\nu_N^{\,3.84}} \tag{2.38}$$

where $F(\bar{\varphi},s)$ is the systematic relative uncertainty, $F(\bar{\varphi},r)$ the random relative uncertainty, $\delta(\bar{\varphi},r)$ the absolute random uncertainty, and t the Student parameter (IEC 60193, 2019). The $F(\bar{\varphi},r)$ and $\delta(\bar{\varphi},r)$ are associated with the Student's t distribution and with the uncertainty at the 95% confidence level and they express the errors of repeated measurements obtained under unchanged machine's operating conditions. Equation 2.38 used for the calculation of t parameter is taken from IEC 60193:2019.

The systematic uncertainty of each measured mean flow and operating variable can be expressed after the use of different methodologies such as calibration, interlaboratory comparisons, or judgment/experience (Figliola, 2001). The first, which is considered the

optimum tool for the systematic uncertainty estimation (Figliola, 2001), is adopted in the present study for each of the sensors used for the measurements. For the transducers, where the calibration procedure could not be applied, such as the sensors of Lancaster University test rig and both the temperature sensors, their systematic uncertainty is taken directly from the calibration certificate of the laboratory manufacturer. This uncertainty refers to the percentage of reading accuracy and includes the errors, which are discussed also in the calibration Appendix A, for the NTUA sensors. The systematic uncertainty of each sensor of both test configurations is provided in sections 2.5 and 2.6.

2.3.3.2 Uncertainty propagation

Finally, the systematic and random errors of the measured mean flow and operating variables are propagated in the calculations of the engineering quantities that describe the centrifugal pump operation; $\overline{H_{tot}}$, $\overline{P_{mech}}$, $\bar{\eta}$, $\bar{\Phi}$, $\bar{\Psi}$, $\bar{N}$, $\overline{NPSH}$ and $\bar{\sigma}$. Their levels of total relative uncertainty, $F(\bar{\varphi},t)$ are composed by a systematic and a random part, and they are calculated based on the general formula (Eq. 2.39) for error propagation (Taylor, 1997). Accoding to this formula, the absolute error of a quantity $\bar{\varphi}$ derived from equation $\bar{\varphi}=f(\bar{x}, \bar{y},.., \bar{z})$, where $\bar{x}$, $\bar{y}$, $\bar{z}$ are variables with individual uncertainties, is given by Eq. 2.39:

$$\delta\left(\bar{\varphi},s/r\right)=\sqrt{\left[\frac{\partial\varphi}{\partial x}\delta\left(\bar{x},s/r\right)\right]^2+\left[\frac{\partial\varphi}{\partial y}\delta\left(\bar{y},s/r\right)\right]^2+\ldots+\left[\frac{\partial\varphi}{\partial z}\delta\left(\bar{z},s/r\right)\right]^2} \tag{2.39}$$

The *s/r* symbolises the use of Eq. 2.39 for the estimation of both type of uncertainties, random and systematic. The final form of the expressions used for the calculation of the uncertainty of every calculated quantity is given in Eqs. 2.40-2.49, while the s/r symbolisation is not used for brevity reasons. The procedure made for their derivation is given in the Appendix B. The transformation from the absolute to the relative form of uncertainty (and vice versa) is done through Eq. 2.36. It is underlined that the uncertainties related with the geometrical dimensions, the water density ρ and the gravity acceleration g are considered insignificant and are ignored.

The expression for the total head (Eq. 2.28):

$$\delta\left(\overline{H_{tot}}\right)=\sqrt{\left[\frac{\overline{p_a}}{\rho g}\cdot F\left(\overline{p_a}\right)\right]^2+\left[\frac{\overline{p_e}}{\rho g}\cdot F\left(\overline{p_e}\right)\right]^2+\left[\frac{16\bar{Q}^2}{\pi^2 g}\left(\frac{1}{d_{p,a}{}^4}-\frac{1}{d_{p,e}{}^4}\right)\cdot F\left(\bar{Q}\right)\right]^2} \tag{2.40}$$

The expression for the mechanical power when the mechanical torque and the rotational speed are measured (Eq. 2.8):

$$\delta\left(\overline{P_{mech}}\right)=\overline{P_{mech}}\cdot\left[\sqrt{F\left(\overline{M_m}\right)^2+F\left(\overline{\Omega}\right)^2}\right] \tag{2.41}$$

The expression for the mechanical power when the electric power, P_{el} is measured (Eq. 2.9):

$$\delta\left(\overline{P_{mech}}\right)=\overline{P_{mech}}\cdot F\left(\overline{P_{el}}\right) \tag{2.42}$$

The expression for the total efficiency (Eq. 2.7):

$$\delta\left(\overline{\eta}\right)=\overline{\eta}\cdot\left[\sqrt{F\left(\overline{H_{tot}}\right)^2+F\left(\overline{Q}\right)^2+F\left(\overline{P_{el}}\right)^2}\right] \tag{2.43}$$

$$\delta\left(\overline{\eta}\right)=\overline{\eta}\cdot\left[\sqrt{F\left(\overline{H_{tot}}\right)^2+F\left(\overline{Q}\right)^2+F\left(\overline{M_m}\right)^2+F\left(\overline{\Omega}\right)^2}\right] \tag{2.44}$$

The expression for the non-dimensional flowrate (Eq. 2.13):

$$\delta\left(\overline{\Phi}\right)=\overline{\Phi}\cdot\left[\sqrt{F\left(\overline{Q}\right)^2+F\left(\overline{\Omega}\right)^2}\right] \tag{2.45}$$

The expression for the non-dimensional total head (Eq. 2.16):

$$\delta\left(\overline{\Psi}\right)=\overline{\Psi}\cdot\left[\sqrt{F\left(\overline{H_{tot}}\right)^2+\left[2\cdot F\left(\overline{\Omega}\right)\right]^2}\right] \tag{2.46}$$

The expression for the non-dimensional mechanical power (Eq. 2.17):

$$\delta\left(\overline{N}\right)=\overline{N}\cdot\left[\sqrt{F\left(\overline{P_{mech}}\right)^2+\left[3\cdot F\left(\overline{\Omega}\right)\right]^2}\right] \tag{2.47}$$

The expression for the NPSH (Eq. 2.31):

$$\delta\left(\overline{NPSH}\right)=\sqrt{\left[\frac{\overline{p_e}}{\rho g}\cdot F\left(\overline{p_e}\right)\right]^2+\left[\frac{16\overline{Q}^2}{\pi^2 g d_{p,a}{}^4}\cdot F\left(\overline{Q}\right)\right]^2+\left[\frac{190.7\cdot T}{\rho g}\cdot F\left(\overline{T}\right)\right]^2} \tag{2.48}$$

The expression for the Thoma cavitation number (Eq. 2.24):

$$\delta\left(\overline{\sigma}\right)=\overline{\sigma}\cdot\left[\sqrt{F\left(\overline{H_{tot}}\right)^2+F\left(\overline{NPSH}\right)^2}\right] \tag{2.49}$$

2.4 AE and vibration signals

As it stated in section 2.3.2, dynamic acoustic emission and vibration signals are obtained during the cavitation experiments. In this section, the theoretical background of the signal acquisition (section 2.4.1) and the processing tools (sections 2.4.2 - 2.4.5) used in the dynamic measurements of the present study, are provided. The values selected for the data acquisition are given for each dynamic sensor of each configuration in section 2.5. The implementation of the signal processing tools is done with the use of MATLAB proprietary programming language.

2.4.1 Data acquisition

Before obtaining the noise and vibration signals, the value of two acquisition parameters have to be selected; the duration of a measurement, t_s, and the sampling frequency, f_s. The selection of t_s value is based on the consideration of its correlation with two factors; i) the period of the lowest frequency studied, and ii) the frequency discretisation, δf. On the one hand, the time duration should include the period of the lowest frequency phenomenon expected to be measured, at approximately ten times. In this way, signal processing techinques, such as the Fast Fourier Transformation (FFT) and Power Spectral Density (PSD) can be implemented to detect and study the low frequency sources. In addition, t_s value controls the discretisation of the frequency domain, δf (Figliola, 2001) as follows:

$$\delta f = \frac{1}{N_s dt} = \frac{1}{t_s} \tag{2.50}$$

where N_s is the number of samples obtained and dt the time span between the sampling increments. As a consequence, the higher the t_s value the denser δf is achieved.

The sampling rate, f_s, value is obtained from Eq. 2.51, after consideration of the highest frequency, f_{max}, phenomenon that is expected to be measured and the satisfaction of Nyquist Theorem. The Nyquist Theorem states that, in order to adequately reproduce the analog form of a digitised signal, the latter should be periodically sampled at a rate that is at least two times faster than the highest frequency wished to be recorded. As a result, the highest frequency that can be recorded is named Nyquist frequency, f_N and equals the half value of the f_s. In the present study, the f_N value equals the larger cut-off frequency limit of the anti-aliasing filter (f_{cutoff}, in the case of low pass filters, f_r in the case of bandpass filters). The f_{cutoff} and the f_r values are given in Tables 2.4 and 2.9, for the LU and NTUA configuration, respectively.

$$f_s = 2 f_{max} = 2 f_N = 2 f_{cutoff\,/\,r(max)} \tag{2.51}$$

Moreover, the expression that relates the f_s with the number of samples, N_s, is calculated with the use of Eq. 2.50 and is given by Eq. 2.52.

$$f_s = \frac{N_s}{t_s} \tag{2.52}$$

2.4.2 Statistical properties

After the signal's acquisition, the digitised time series is processed, in order to extract information regarding the cavitation development in the centrifugal pumps. The first step of analysis deals with the study of the statistical properties of the time series, and initiates with the construction of their histograms. The main parameter that influences the plotting of frequency

distribution is the number of bins used for the discretisation of the measured variable (Volts for AE and m/s^2 for acceleration of vibration). This study implements Shimazaki and Shinomoto's methodology (Shimazaki, 2007). In their study, they proposed the selection of bin width, Δ that minimises the function in Eq. 2.53, as the optimum Δ for the histogram representation. The selection is implemented with the repetitive calculations of Eq. 2.53 for different bin widths values, Δ and the examination of CF(Δ) function at the end of the procedure.

$$CF\left(\Delta\right)=\frac{2\bar{\varphi}-s_{\varphi}^{\ 2}}{\Delta^2} \tag{2.53}$$

where φ denotes the measured variable under examination.

The presentation of the histograms is accompanied by the requirement to illustrate how close they are in the normal distribution. This is achieved with the use of normal probability plots (Andersson, 2012; MATLAB, 2015a), a graphical tool that evaluates whether a time series of data comes from a population that is normally distributed. In normal probablity plots, the cumulative probability of the experimentally obtained data (cross marker in Fig. 2.10a) is plotted against the cumulative probability of a theoretical normal distribution (center-line in Fig. 2.10a). The x-axis of the two-dimensional plot represents the range of the measured data and the y-axis represents the cumulative probabilities.

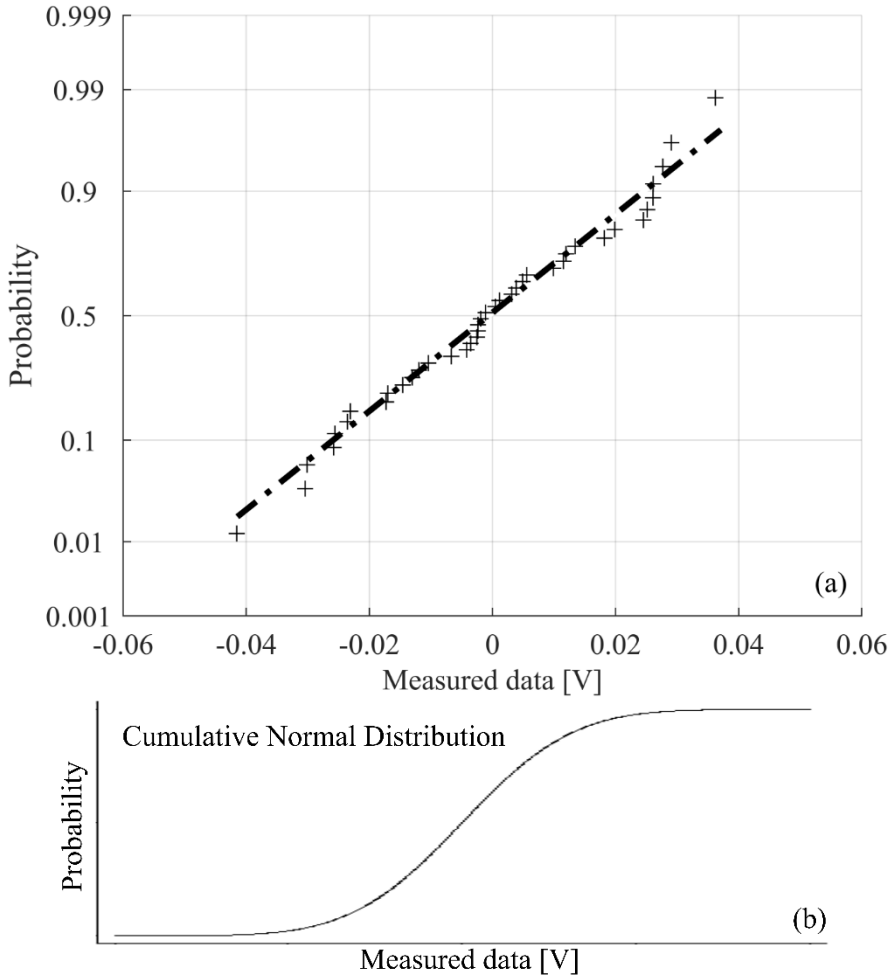

Figure 2.10 a) Typical normal probability plot, and **b)** typical form of the cumulative normal distribution, with the y-axis in linear scale.

In case of normally distributed data, the markers of the plot form an approximately straight line and fit to the theoretical one of the normally distributed data, shown in Fig. 2.10a. In the

opposite case, the assumption of the normal distribution is not justified. The y axis of plot follows a normal probability scale and is not linear, so as to force the normally distributed data to appear as the straight line of Fig. 2.10a. In case of linear y-axis, the normally distributed data would have the form of a typical S-curve plot of cumulative normal distribution (Fig. 2.10b).

Finally the statistical part of the noise and vibration analysis includes the calculation of the four fundamental statistical moments; i) the mean , ii) the standard deviation, iii) the skewness, and iv) the kurtosis. The first two have already been discussed in section 2.3 and their expressions are provided from Eqs. 2.29 and 2.34, respectively, by substituting the number of independent measurements v_N, with the number of samples N_s. The unbiased expressions used for the calculation of skewness and kurtosis are given in Eqs. 2.54 and 2.55, respectively (MATLAB, 2015a). In case of data coming from a normally distributed population, their skewness value is expected to be ~0 and this of kurtosis ~3 (Kim H., 2013; MATLAB, 2015a).

$$\text{skewness} = \frac{\sqrt{N_s\left(N_s-1\right)}}{N_s-2}\frac{\frac{1}{N_s}\sum_{i=1}^{N_s}\left(\varphi_i-\bar{\varphi}\right)^3}{\left[\sqrt{\frac{1}{N_s}\sum_{i=1}^{N_s}\left(\varphi_i-\bar{\varphi}\right)^2}\right]^3} \tag{2.54}$$

$$\text{kurtosis} = \frac{N_s-1}{\left(N_s-2\right)\left(N_s-3\right)}\left\{\left(N_s+1\right)\frac{\frac{1}{N_s}\sum_{i=1}^{N_s}\left(\varphi_i-\bar{\varphi}\right)^4}{\left[\frac{1}{N_s}\sum_{i=1}^{N_s}\left(\varphi_i-\bar{\varphi}\right)^2\right]^2}-3\left(N_s-1\right)\right\}+3 \tag{2.55}$$

2.4.3 Frequency spectrum analysis

In the present study, the frequency spectrum analysis includes methodologies that are based on the estimates of Power Spectral Density and in the powerbands that are used so as to quantify the power included in a specific part of the spectrum. The use of the frequency spectrum analysis has been discussed in detail in section 1.3.1.3 and is categorised from the author as a traditional approach towards the identification of cavitation in hydraulic turbomachinery, which has been applied from various authors (Cernetič, 2008; Chudina, 2009a; Abdulaziz, 2017; Al Obaidi 2019; Lu, 2019). The illustration of the power distribution in the frequency domain of the dynamic measurements in this study is done with the use of the Power Spectral Density (PSD), P_x, calculated from Eq. 2.56:

$$P_x\left(\Omega\right) = \int_{-\infty}^{+\infty} R_x\left(\delta\right)e^{-j\Omega\delta}d\delta \tag{2.56}$$

$$R_x \triangleq \mathrm{E}\left[x\left(t+\delta x\right)x\left(t\right)\right] \tag{2.57}$$

where R_x is the autocorrelation function of the process $x(t)$, δx the time lag and E the expected value (Li, 1999). In the present study the estimation of PSD is done through the non-parametric Welch estimator (Welch, 1967; Allen, 2004) given in Eq. 2.58, after the completion of the following steps; i) division of the discrete measured signal into ε segments, ii) calculation of the modified periodogram non-parametric estimator (Eq. 2.59) at each segment, iii) averaging of the periodogram estimates.

$$P_{\text{Welch}}(\Omega) = \frac{1}{\varepsilon}\sum_{i=1}^{k} P_{\text{Periodogram}}(\Omega) \tag{2.58}$$

$$P_{\text{Periodogram}}(\Omega) = \frac{1}{MU}\left|\sum_{h=0}^{M-1} x[h]W[h]e^{-j\Omega h}\right|^2 \tag{2.59}$$

$$U = \frac{1}{M}\sum_{h=0}^{M-1} W^2[h] \tag{2.60}$$

where M is the length of each segment, $x[h]$ is the digitised signal in time, $W[h]$ is the window function and U is the window normalization constant (Eq. 2.60). The averaging of modified periodograms improves the estimation relative to a single periodogram estimate for the total length of the discrete time series, however the division of original signal in segments reduces the frequency domain discretisation, δf. A representative illustration of the periodogram and Welch estimators of PSD for a vibration signal, is provided in Fig. 2.11.

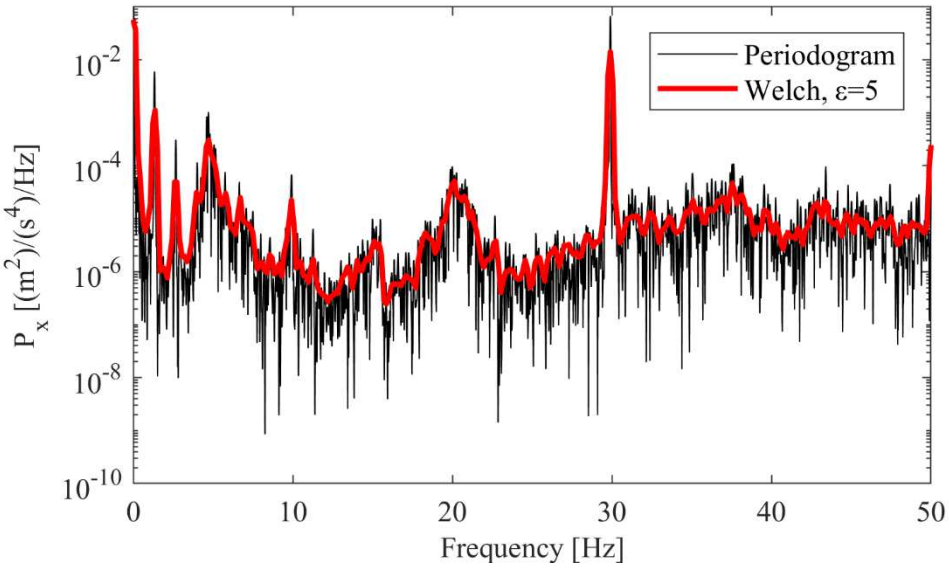

Figure 2.11 Typical shape of the PSD estimators; periodogram and its averaged form, Welch, for a vibration signal.

In parallel, after the definition of the PSD estimator, it is possible to quantify the average power of the signal in a defined frequency range by integrating the estimator, as it is presented in Eq. 2.61:

$$\overline{P}_{\text{Band power}}\left[\Omega_1\text{-}\Omega_2\right] = \int_{\Omega_1}^{\Omega_2} 2P_{\text{Welch}}(\Omega)\, d\Omega \tag{2.61}$$

where the multiplication factor of 2 denotes the splitting of equal amount of power in negative and positive frequencies.

Finally, the Root Mean Square (RMS) that is a fundamental measure of the signals size intensity (Peyton, 1993), is provided in two forms; i) the velocity of vibration RMS value (Eq. 2.62), v_{RMS}, defined from ISO 10816-1, ISO 4413 for the evaluation of machine vibration measurements on non-rotating parts, and ii) the averaged AE_{RMS} value (Eq. 2.65) used for the calculation of noise RMS.

The velocity vibration RMS procedure is probably the most common approach for quantifying the level of vibration in rotating machinery. Its calculation procedure includes the calculation of the frequency spectrum of the measured signal, which is usually an acceleration of vibration signal and the summation of the amplitude content in the range between [10 – 1000] Hz. In this way, only the content of low frequency vibration sources is included in the calculation of v_{RMS}. The low frequency sources present the strongest vibration amplitudes since they are related with the mechanical components of the turbomachinery, such as the bearings, the impeller, the electric motor and the gears. The mathematical procedure for the calculation of v_{RMS} is described by Eq. 2.62:

$$v_{RMS} = \frac{10^3}{2\pi}\sqrt{\left(\frac{q_1}{f_1}\right)^2+\left(\frac{q_2}{f_2}\right)^2+...+\left(\frac{q_q}{f_q}\right)^2}\,,\ f_1 = 10Hz,...,\ f_q = 1000Hz \tag{2.62}$$

where q is the acceleration of vibration amplitude that correspond to each discrete frequency, $k\cdot\delta f$ in the range from 10 to 1000 Hz and it is calculated with the use of Discrete Fourier Transformation (DFT) by Eq. 2.63 (Figliola, 2011):

$$q\left[k\cdot\delta f\right] = \frac{2}{N_s}\left|\sum_{r=0}^{N_S-1} q\left[r\cdot\delta t\right]e^{-j2\pi\left(k\cdot\delta f\right)\left(r\cdot\delta t\right)}\right|,\quad k = 0,1,2,...,\frac{N_s}{2}-1 \tag{2.63}$$

$$\left\{q\left[r\cdot\delta t\right]\right\} = q\left(t\right)\delta\left(t-r\cdot\delta t\right),\quad r = 0,1,2,...,N_s-1 \tag{2.64}$$

where $q[r\cdot\delta t]$ is the sampling function for the acceleration of vibration signal, equivalent with this of $x[h]$ in Eq. 2.59. The v_{RMS} vibration limit for the unrestricted long-term operation, of rotordynamic pumps, in allowable operating range, is 5.1 mm·s^{-1} (ISO 10816-7, 2009).

The AE_{RMS} calculation procedure takes into account all the noise sources included in the digitised signal. In the present study, the AE signal is filtered with the use of band pass filters, the technical characteristics of which are given in section 2.5. In practice, the AE_{RMS} value procedure divides the Volt data in ε segments, with p values at each segment, and calculates the average value of one second with the use of the fundamental RMS equation in Volt, as follows:

$$AE_{RMS} = \left\{\sum_{i=1}^{\varepsilon}\left(\sqrt{\frac{(V_1{}^2+...+V_p{}^2)}{p}}\right)_i\right\}/\varepsilon \tag{2.65}$$

2.4.4 Envelope analysis

The present study investigates the envelope characteristics in the frequency domain towards the detection of cavitation in hydraulic turbomachines. The signal processing approach adopted here is a typical demodulation or enveloping procedure, which is also used for the detection of rolling bearing faults that present impulsive mechanism, similarly to cavitation (McFadden, 1984a; Gryllias, 2008; Yiakopoulos, 2011; Gryllias, 2012). The demodulation procedure is carried out in the following successive steps:

i. The original measured time series is filtered with the use of a band pass filter, $x_o(t)$ and forms the filtered signal, $x_f(t)$. The original signals contain all the noise and vibration sources measured from the sensor and are usually in the form of Fig. 1.24a (section 1.2.2.3). The aim of the filtering procedure is to isolate the fault mechanism and unmask it from the noisy original signal. An example of a successful filtering procedure is given

in Fig. 1.24b (section 1.2.2.3) for the aforementioned vibration signal of Fig. 1.30a. Different filtering approaches are proposed and presented in the literature review section 1.2.2.3. This study proposes the use of Spectral Kurtosis (SK) method for the calculation of the band pass filter's characteristics. The SK method is presented after the description of the demodulation procedure, in section 2.4.5.

ii. The Hilbert Transfomation is applied at the filtered signal, as given by Eq. 2.66. In practice, the Hilbert Transformation forces every Fourier component with a phase shift of -90º, as it is presented in Fig. 2.12.

$$x_{Hf}(t) = \frac{1}{\pi}\int_{-\infty}^{+\infty} \frac{x_f(t)}{t-\tau} d\tau \tag{2.66}$$

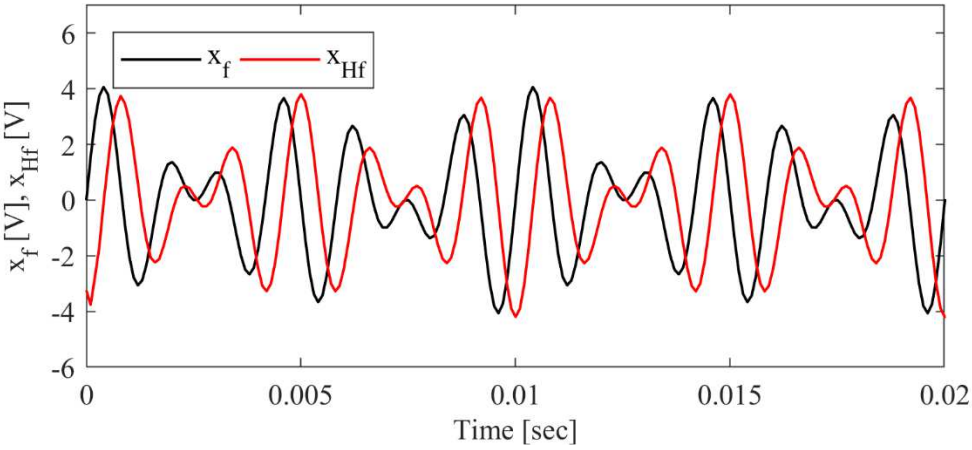

Figure 2.12 Representation of the filtered signal and its Hilbert Transformation.

iii. The analytic signal, $A_s(t)$ is formed with the use of Eq. 2.67, which consists of two parts; one real part that is the filtered signal, calculated from step (i), and one imaginary part that is its Hilbert Transformation, calculated from step (ii). A three dimensional representation of the analytical signal of fundamental complex exponential is given in Fig. 2.13.

iv.

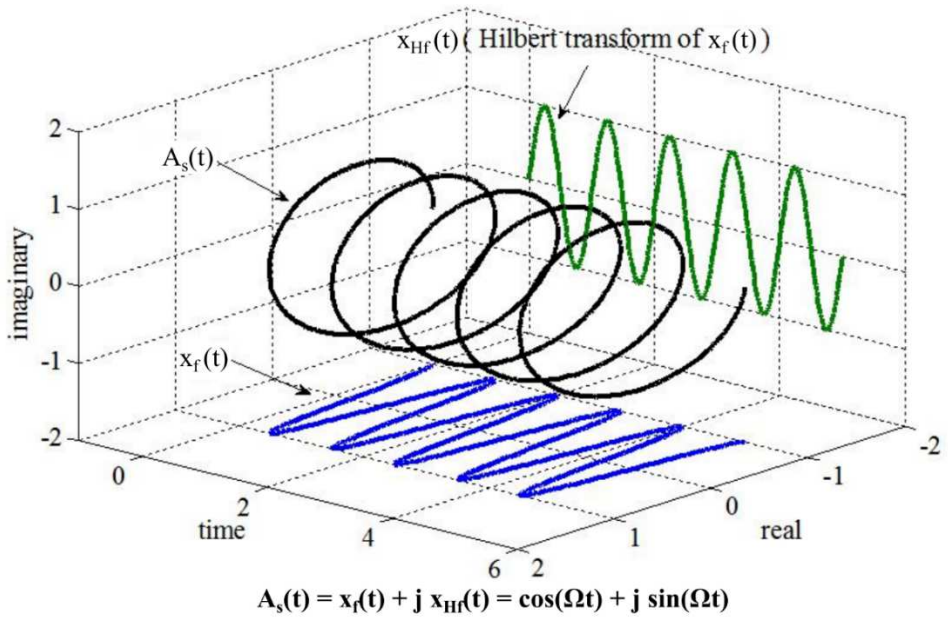

Figure 2.13 3D representation of the analytical signal's formation (Romero, 2012).

$$A_s(t) = x_f(t) + jx_{Hf}(t) \tag{2.67}$$

v. The demodulated time signal is the amplitude of the analytic signal, i.e. the envelope of the filtered time series (Fig. 2.14), calculated from Eq. 2.68:

$$e_d(t) = |A_s(t)| = \sqrt{x_f(t)^2 + x_{Hf}(t)^2} \tag{2.68}$$

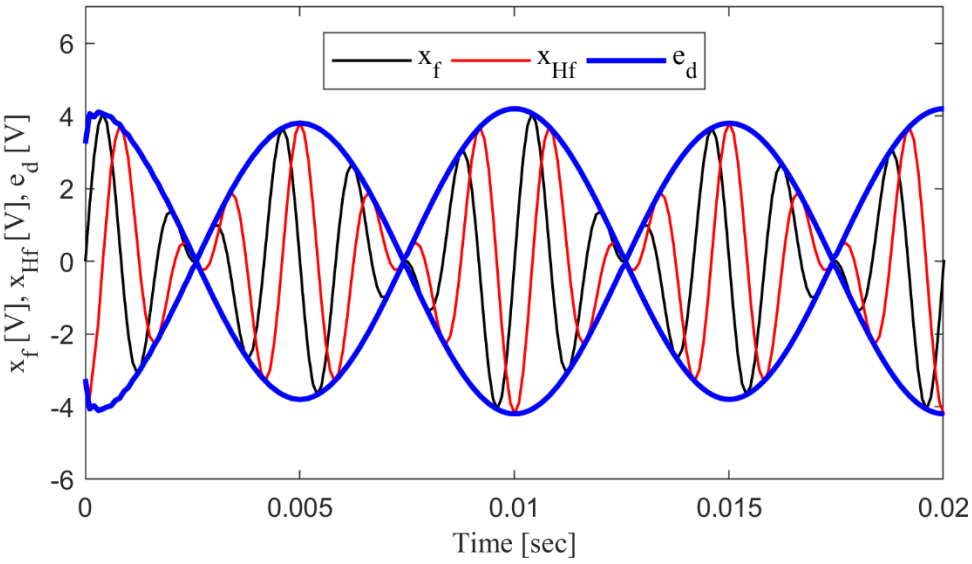

Figure 2.14 A two dimensional representation of the envelope of the analytic signal, formed for the signals of Fig. 2.12.

vi. Finally, the frequency spectrum of the envelope can be calculated from Eq. 2.69:

$$e_d(f) = \int_{-\infty}^{+\infty} \sqrt{x_f(t)^2 + x_{Hf}(t)^2}\, e^{-j2\pi ft} dt \tag{2.69}$$

2.4.5 The Spectral Kurtosis

The present dissertation proposes the use of Spectral Kurtosis method so as to identify the filter characteristics, i.e. its central frequency, f_c and its bandwidth, f_r, used for the formation of the analytic signal. Before the description of the methodology, it is significant to mention that the use of higher-order statistics for the pattern recognition of non-stationary signals was firstly introduced by Dwyer (1981; 1983a; 1983b, 1984) and dealt with underwater noise measurements. During the statistical analysis of noise signals, Dwyer observed that kurtosis value deviated from the values of Gaussian distribution (Fig. 1.23, section 1.2.2.3). Dwyer also perceived that the representation of kurtosis moments in the frequency spectrum could provide the specific frequency band that is related with the non-Gaussian behaviour. These significant observations made by Dwyer on the field of underwater noise measurement, stimulated the scientists, who worked on the faults detection of rolling element bearings.

As it is discussed in section 1.2.2.3, the faults of rolling element bearing exhibit impulsive behaviour and excite the resonances of the machine. However, the resonances excited were significantly distorted in the frequency domain (Fig. 1.19d, section 1.2.2.3) due to the randomness introduced by the slip of the bearings and noises from other parts of the machine. In addition, the values of those resonances differed not only between the various testing configurations, but also in the same machine as the faults developed (Yiakopoulos, 2005). All

the above introduced significant difficulties towards the identification of the band that is excited from the fault and consequently towards the application of the adequate filter so as to demodulate the signal (section 2.4.4).

As it is already discussed, the observations made by Dwyer, reveal a significant characteristic of the kurtosis value; its ability to identify the frequency band of the spectrum that exhibits the most non-Gaussian behaviour. For this reason, Antoni (2006) along with Antoni and Randall (2006) investigated the prospect of using the bands that exhibit the most non-Gaussian behaviour so as to construct the band pass filter, neededd for the demodulation procedure. According to their results, the use of the spectrum's kurtosis was able to identify the resonance excited from the bearing fault (Fig. 1.24, section 1.2.2.3). Nevertheless, additional effort was needed so as to scan, efficiently and with low computational cost, the frequency spectrum and identify the optimum characteristics of the filter. The last difficulty was overcome with the development of the Fast Kurtogram (Antoni, 2007b) that followed the publication regarding the complete mathematical formulation of the Spectral Kurtosis (Antoni, 2006). Both of them are presented in this section.

The complete mathematical formulation for the Short Time Fourier Transformation (STFT) estimation of spectral kurtosis, $\hat{K}_Y(f)$, was given by Antoni (2006):

$$\hat{K}_Y(f) \triangleq \left\langle \left| Y_w(kP, f) \right|^{4n} \right\rangle_k \Big/ \left\{ \left\langle \left| Y_w(kP, f) \right|^{2n} \right\rangle_k \right\}^2 - 2 \tag{2.70}$$

where $Y_w(kP,f)^{xn}$ is the xn-th order empirical spectral moment of the STFT of a sampled process $Y(n)$, $w(n)$ is the analysis window, P is the temporal step and $\langle \ldots \rangle_k$ is the time averaged operator over index k, which denotes the number of temporal steps.

According to Eq. 2.70, the calculation of spectral kurtosis requires the computation of STFT, the resolution of which on the frequency domain has direct impact on the selected time window. In addition, the previous discussion highlighted the need to, efficiently and with low computational power, scan the frequency spectrum and identify the filters characteristics. In order to overcome this limitation, spectral kurtosis is calculated for different frequency resolutions and all the results are plotted as function of frequency. This calculation is accomplished with the use of Fast Kurtogram (FK) that utilises either a multirate filter bank approach or an STFT approach (Antoni, 2007b). In this study, the second approach is used, where STFT decomposition is made in divisions by two:

$$N_{\delta f} = 2^{(DL-1)}, \quad DL = 0,...,12 \tag{2.71}$$

where $N_{\delta f}$ is the number of sectors that the frequency domain is split and DL is the decomposition level (DL). Consequently, the frequency domain discretization, δf is provided from Eq. 2.72:

$$\delta f = \frac{f_s}{2N_{\delta f}} = \frac{f_N}{N_{\delta f}} = f_r \tag{2.72}$$

where f_N is the Nyquist frequency and f_r the bandwidth of the band pass filter. In practice, in the case of FK, the f_r value coincides with that of δf. The final outcome of the calculations is a two-dimensional map of the value of spectral kurtosis, as function of frequency versus frequency resolution, as presented in Fig. 2.15. The location and the maximum value of the spectral kurtosis for each DL changes as the original signal is divided in more and more segments. The Maximum Spectral Kyrtosis (MSK) can be finally obtained at a specific frequency range and decomposition level.

The FK of a vibration signal of a pump operating under normal conditions is drawn in Fig. 2.15. The FK reveals the frequency and frequency resolution of the maximum spectral kurtosis (MSK) value, which is information of crucial importance regarding the detection of non-stationarities. More specifically, these quantities correspond to the central frequency, f_c and the bandwidth, f_r of the band pass filter to be used for the isolation of the impulsive behavior hidden in the sampled signal. In the case of Fig. 2.15, the MSK=0.8 corresponds to a band pass filter with $f_c \cong 3.4$ kHz and $f_r \cong 0.1$ kHz. As a result, the calculations made for the construction of FK act as an optimiser of the band pass filter's characteristics (f_c, f_r) and allow the signal's demodulation with the procedure described in section 2.4.4.

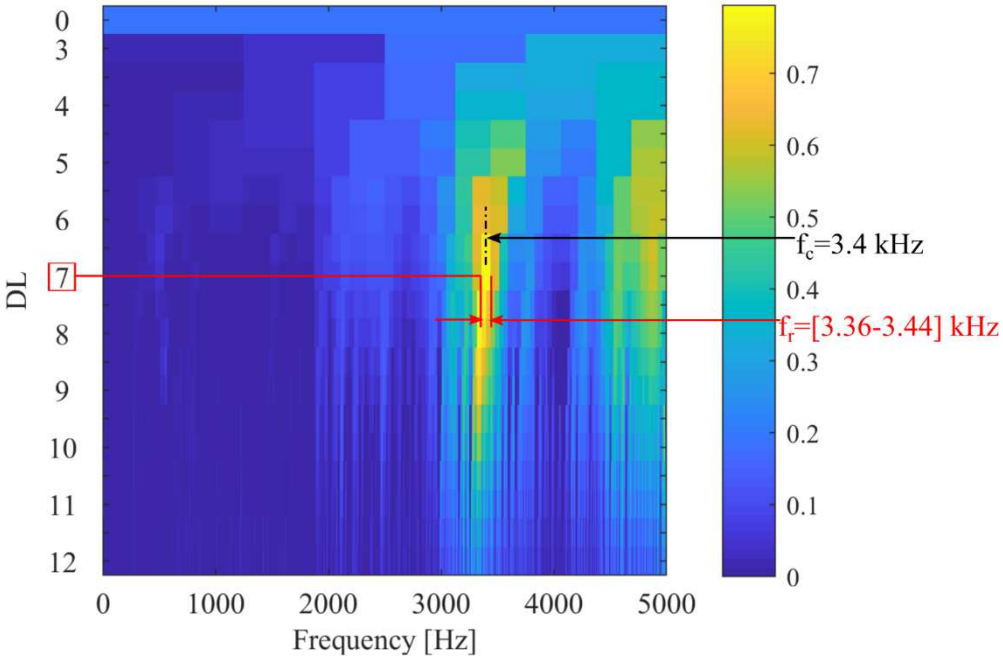

Figure 2.15 Fast Kurtogram at the vibration signal of a centrifugal pump.

2.5 Experimental configurations

Until this point, all the mathematical and theoretical background of the methodologies used during the testing of the centrifugal pumps was presented. The expressions that describe all the procedures in sections 2.2 to 2.4 include a number of operating, geometrical and acquisition parameters. Only the parameters that are necessary for the application of the aforementioned equations are presented below, along with the two test configurations and the sensors used in the present study. More specifically, the present section 2.5, includes:

- The geometrical and operational characteristics of each configuration that influence the calculation of the pump's performance.
- The geometrical characteristics of each impeller, which are used for the calculation of the non-dimensional variables.
- The systematic uncertainties of the sensors used to measure the mean flow and operating quantities during the testing of the pumps under normal and cavitating conditions.
- The data acquisition and the filter characteristics of each noise and vibration sensor used in both test configurations.
- The mechanical and hydraulic frequencies that are possible to affect the operation of the centrifugal pumps tested.

2.5.1 Lancaster University test rig

2.5.1.1 Experimental set up

The first test configuration is installed in the Engineering Department of Lancaster University and includes the laboratory pump manufactured by Turbine Technologies Ltd. The complete test rig has a compact design, and it is presented in Fig. 2.16. In practice, this handy configuration allows the user to complete the performance tests of the pump, which include the control of the motor's speed (13), the valves' regulation (6,8) and the data acquisition (14) by operating them from the same position.

The same figure highlights the main advantage of this test rig, in terms of the study of cavitation inception and development; the manufacturing of the volute, the front casing of the pump and all the piping system from Plexiglas material. In this way it is possible to visualise the flow conditions in the parts that are prone to cavitate, such as the pump impeller and the suction pipe system. In addition, the pump does not have its own bearings and all the mechanical and hydraulic loads are transferred to the bearings of the motor. This facilitates the detection of the cavitation phenomenon, since the noise and vibration emitted from the bearings is more difficult to surpass the cavitation noise and vibration in the impeller.

In that test rig, the water is pumped from the tank (7), passes through the suction valve (8), the elbow (10), the impeller (2), the flowmeter (5) and the discharge valve (6), and returns again to the tank (7). The points (e) and (α) correspond to the static pressure measurements points, similarly to Fig. 2.1. The pump is driven from a variable speed BALDOR induction motor with 3 horsepower rated output at n=1750 rpm and maximum n=1800 rpm. The details regarding the geometrical, operational and physical characteristics of the Lancaster University test rig are:

- geodetic pressure differential, $\Delta H_z = z_\alpha = 0.305$ m
- suction pipe diameter, $d_{p,e} = 0.047$ m,
- discharge pipe diameter, $d_{p,\alpha} = 0.041$ m,
- typical BALDOR motor efficiency, $\eta_{mot} = 87.5$ %, and
- water temperature, T=23 ºC.

One drawback of the compact design of this configuration is the use of one 90º bending pipe (No. 10 in Fig. 2.16) upstream of the impeller inlet, which does not comply with the practical guidelines of pumping station design (Jones, 2006), which require a part of straight line pipe with length $[5 - 10] \cdot d_{p,e}$, where $d_{p,e}$ is the diameter of suction pipe.

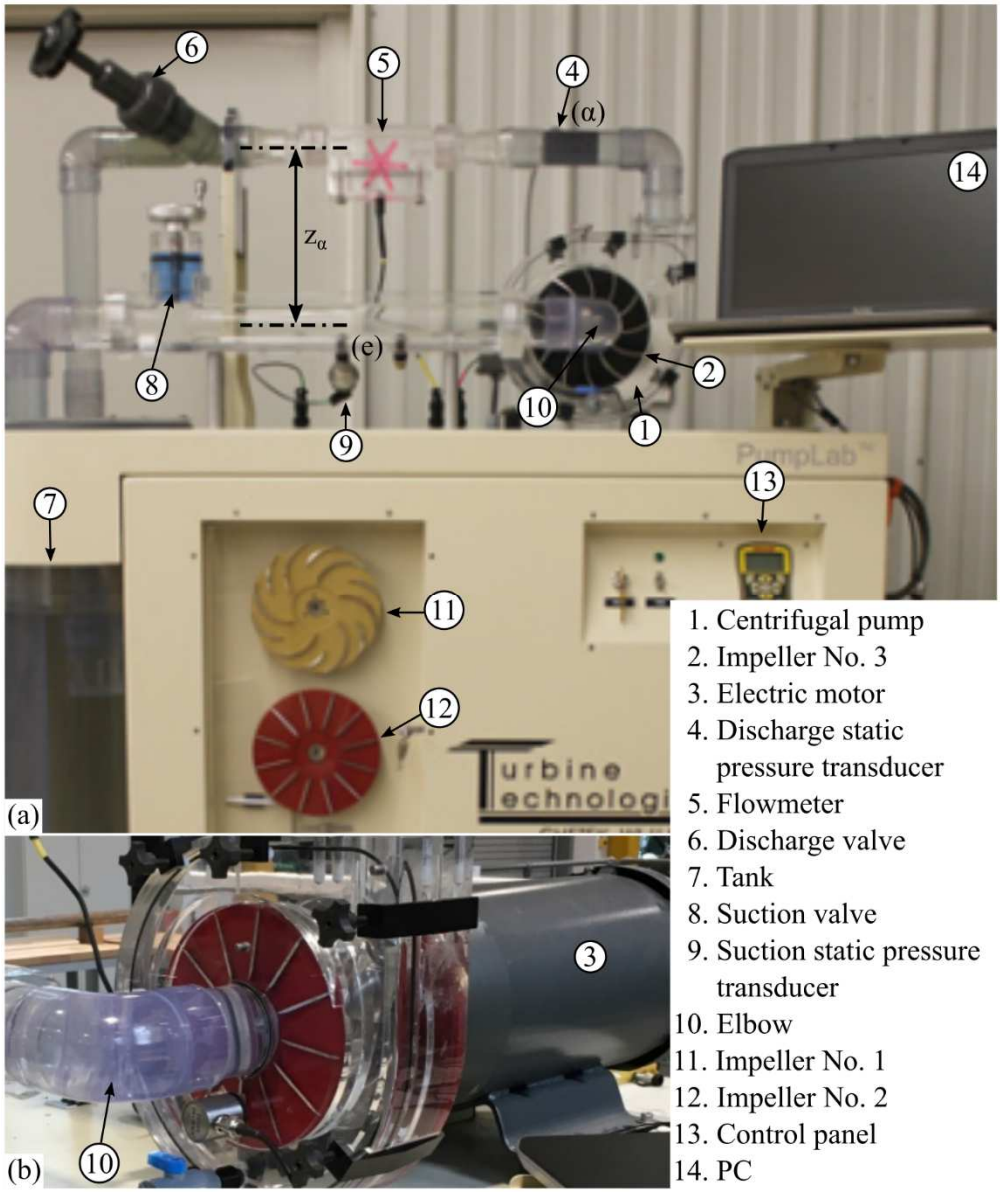

Figure 2.16 a) Front view of the general configuration of the Lancaster University pump laboratory, **b)** the centrifugal pump and its electric motor.

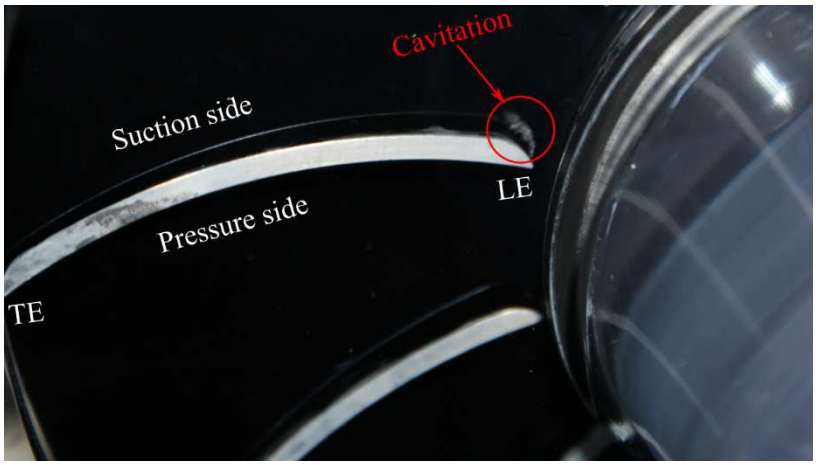

Figure 2.17 Non-axisymmetric appearance of vapour bubbles.

The existence of the 90º curvature, as also the presence of the spiral volute, disturb the axial symmetry of the flow in the pump. This results in a non-axisymmetric pressure and velocity field at the impeller inlet, and as a consequence, cavitation inception appears firstly on the left side of the impeller eye, as it is shown in Fig. 2.17, and also, its further development its faster there. As a consequence, in order to depict the onset and development of the phenomenon the camera takes pictures from the left side of each impeller, as it shown in the upcoming Fig. 2.19a.

The tests in the Lancaster University include the investigation of three impellers with different geometric design, one with curved main and splitter blades (impeller No. 1, Fig. 2.18a), a second with straight, radial blades (impeller No. 2, Fig. 2.18b), and a third with curved, forward blades (impeller No. 3, Fig. 2.18c). All are unshrouded , semi-open impellers, made from aluminum, and their main geometric and physical characteristics are tabulated in Table 2.2.

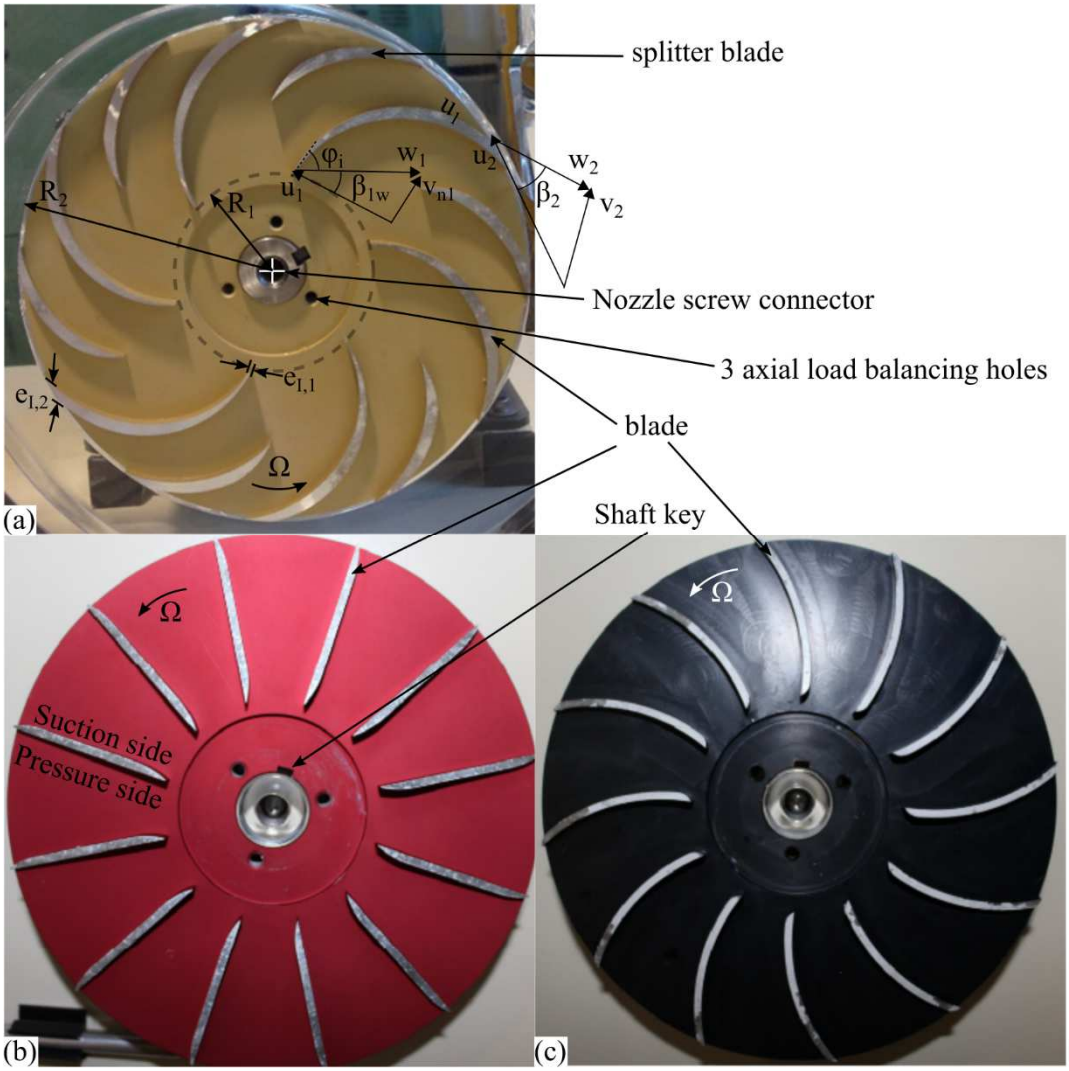

Figure 2.18 a) Impeller No. 1, **b)** impeller No. 2, **c)** impeller No. 3

Table 2.2 is split in two parts; i) the fist includes those characteristics that are common for the inlet (1) and outlet (2) of the three impellers, while ii) the second gives separately the geometric features between the inlet (1) and outlet (2) of each impeller (Fig. 2.18).

Table 2.2 Geometrical characteristics of the impellers at Lancaster University.

	Impeller No. 1		**Impeller No. 2**		**Impeller No. 3**	
z_s **[-]**	6		12		12	
$z_{s,s}$ **[-]**	6		-		-	
$b_{V,2}$ **[m]**	0.013		0.013		0.013	
	Inlet (1)	**Outlet (2)**	**Inlet (1)**	**Outlet (2)**	**Inlet (1)**	**Outlet (2)**
d **[m]**	0.0655	0.165	0.0655	0.165	0.0655	0.165
e **[mm]**	1.1	10.1	2.8	5.9	1	2.2
b_I **[mm]**	7.5	3	7.6	3.1	7.6	3.1
β **[deg]**	65	25	85	90	80	125

2.5.1.2 Transducers and measuring systems

The sensors used for the measurements in the Lancaster University test rig, in order to derive the performance curves of the pumps are as follows:

- a pressure transducer located at the suction side of the pump (No. 9 in Fig. 2.16a) that measures the gauge pressure (relative to the atmospheric pressure). In order to adequately conduct the cavitation experiments that deal with significantly low pressure values, the sensor is able to measure negative gauge pressure.
- a pressure transducer located at the discharge pipe of the pump (No. 4 in Fig. 2.16a) that also measures the gauge pressure. The gauge pressure measurements must be converted to absolute pressure for the NPSH calculation.
- a rotor flowmeter located at the discharge of the pump (No. 5 in Fig. 2.16a).
- an electric power and rotational speed sensor embedded in the electric motor.

The relative systematic uncertainty for each measured quantity is presented in Table 2.3. These uncertainties are taken from the sensor's manufacturer.

Table 2.3 Relative systematic uncertainties of the measured quantities of LU configuration.

	Measured quantities					
	Q	$\mathbf{p_e}$	$\mathbf{p_a}$	**T**	$\mathbf{P_{el}}$	**Ω**
(systematic) $\mathbf{F(\bar{\varphi},s)}$ **[%]**	1	0.25	0.25	1	1	0.5

Two piezoelectric accelerometers, B01_1 and A01, and one preamp AE sensor are mounted on the casing of the pump, the first and the third closer to the two-phase flow area, and the second on the volute. The positioning of each sensor relative to the pump, as well as their power supply and analog filter devices, are presented in Fig. 2.19.

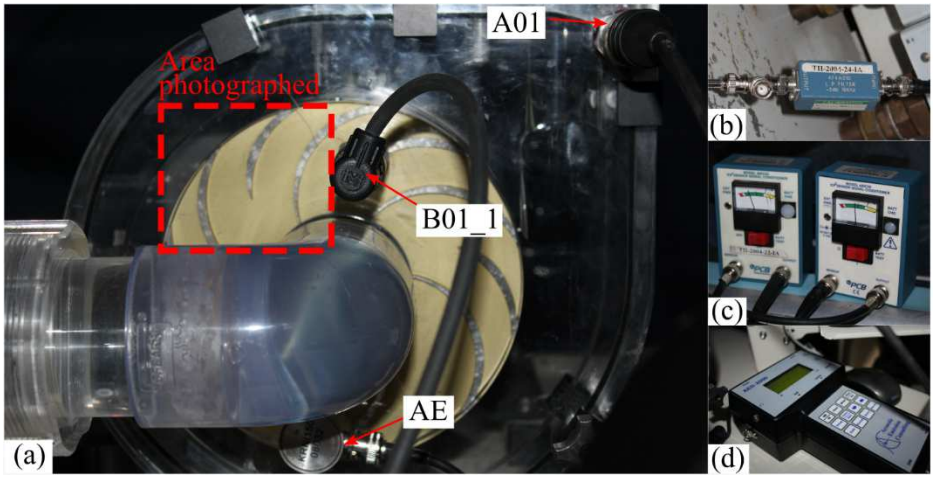

Figure 2.19 a) Sensors mounting position, **b)** accelerometers' analog low pass filter, **c)** accelerometers' power supply, **d)** AE's power supply, analog band-pass filter and acquisition device.

The sampling frequency, f_s, the cutoff frequency of the low pass filter, f_{cutoff}, the bandwidth of the analog band pass filter, f_r, the Nyquist frequency, f_N, the acquisition time, t_s and the frequency range that each sensor is able to measure are given in Table 2.4. The AE provides the RMS averaged value from Eq. 2.65 and uses 90 segments, ε, with 3400 values, p, at each segment, but does not provide the raw time series data. Consequently, the AE results obtained at LU test rig are not processed with additional signal processing tools.

Table 2.4 Noise and vibration sensors and acquisition characteristics of LU configuration.

	f_s [kHz]	f_{cutoff} [kHz]	f_r [kHz]	f_N [kHz]	t_s [sec]	$[f_{min}$-$f_{max}]$ [kHz]
B01_1	20	10	-	10	30	0-15
A01	10	5	-	5	30	0-10
AE	306	-	100-150	150	30	100-150

The camera used in this setup is a DSLR type with 4752 x 3168 recording pixel, CMOS image sensor and max shutter speed of 0.25 msec. For the stationary depiction of the two-phase flow formations in the pump, a stroboscope is used, and its frequency is regulated so as to comply with that of impeller's rotational speed. In order to reduce the effect of the environmental light and improve the photos quality, the entire test rig is placed inside a black tent. In the present study, flow visualization is used as a tool that confirms the existence of cavities, their onset, as well as their extent and position, but only from a macroscopic stationary perspective. In practice, this means that the photographs obtained at the various operting points examined, represent the behaviour of the above characteristics (extent and position) in the duration of each measurement (120 sec). This selection is made because, although the phenomenon is very dynamic, especially during its onset, after the stabilisation of the presence of vapour cavities in the impeller, their two dimensional visible extent, as well as their position, do not change significantly in time. The results regarding the inception and development of the phenomenon, are further discussed in Chapter 3.

Finally, the mechanical, electric and hydraulic frequencies and sideband frequencies, which are possible to appear in the pump-motor system are given in Table 2.5. The equations used for the calculation of each frequency component have been presented and discussed in the Chapter 1. The only exception deals with the splitter blade passing frequency that is given in Eq. 2.73 and is used only for impeller No.1.

$$TBPF = (z_s + N_{SB}) \cdot RF \tag{2.73}$$

The number of the corresponding equation is provided for each frequency of Table 2.5. The frequencies calculated are based on the nominal rotational frequency (RF) of the pump (n=1800 rpm), while the 6207 and 6203 denote the two bearings embedded on the electric motor's shaft. The details for the bearings characteristics are given in Table 2.6.

Table 2.5 Frequencies [Hz] excited by the pump-motor system of LU configuration.

	RF	**BPF**	**TBPF**	**RCF**	**RSF**	**SF**	**PPF**
Eq.	-	1.1	2.73	I.4	I.3	1.5	1.6
No. 1	30	180	360	33-36	15-27	5	100
No. 2	30	360	-	33-36	15-27	5	100
No. 3	30	360	-	33-36	15-27	5	100
	SBF_R	**SBF_L**	**6207/6203**				
			BPFO	**BPFI**	**FTF**	**BSF**	
Eq.	1.7	1.8	1.9	1.10	1.11	1.12	
No. 1, 2, 3	±20	±100	107/79	163/131	12/11	69/57	

Table 2.6 Bearing characteristics for the Lancaster University configuration.

	6207	**6203**
D_P [mm]	53.44	28.78
D_B [mm]	11.10	7.14
N_B [-]	9	7

2.5.2 NTUA Test Rig

2.5.2.1 Experimental set up

The second configuration is installed in the Laboratory of Hydraulic Turbomachines, of the National Technical University of Athens (NTUA), and includes an industrial pump manufactured from Drakos Polemis Group. The complete test rig is shown in Fig. 2.20.

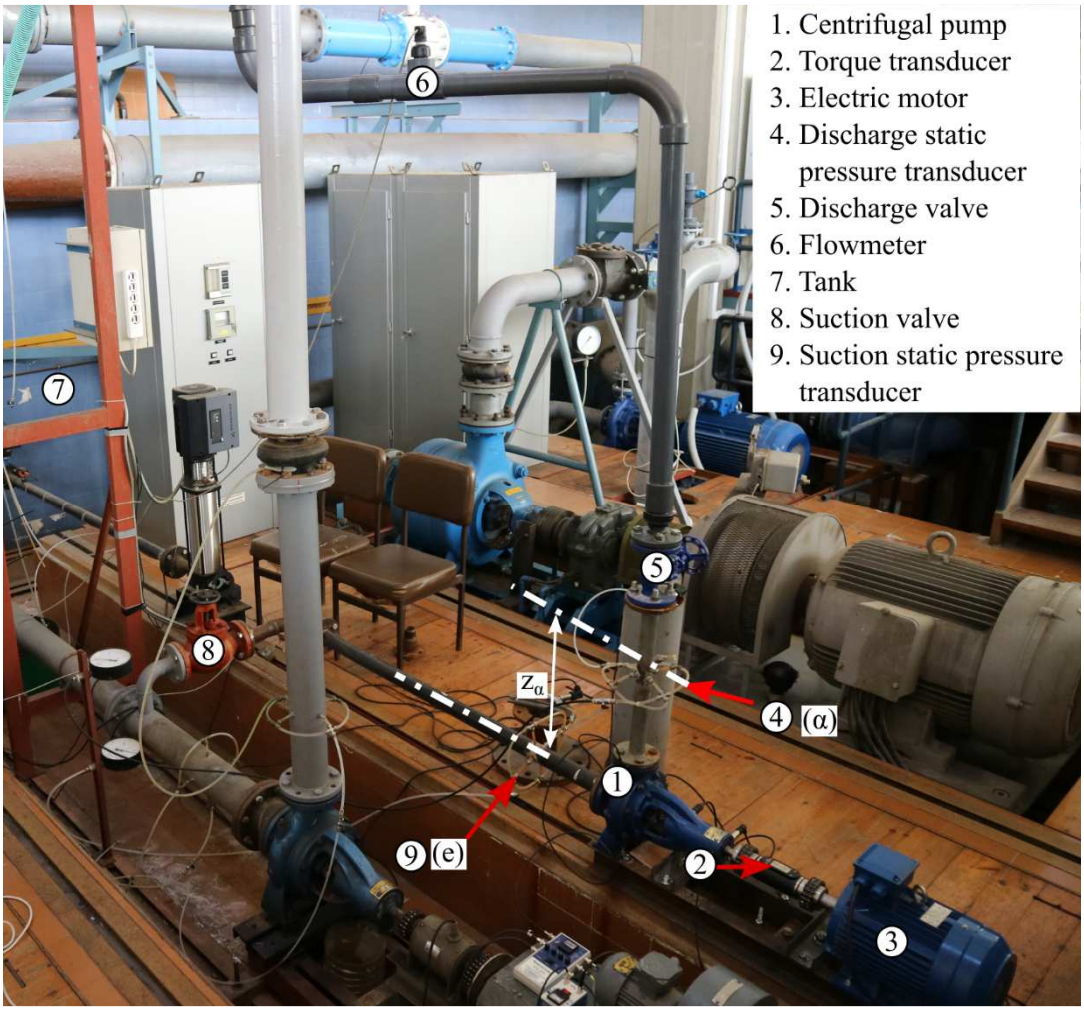

Figure 2.20 General configuration of the NTUA pump laboratory.

In contrast to the Lancaster University test rig, this of the NTUA uses typical steel pipes, a metallic closed impeller and volute, while the suction pipe is straight with a length that satisfies the prerequisite, $l_p > 10 \cdot d_{p,e}$ (Jones, 2006), in order to retain axisymmetric flow at the pump inlet. Also, this test rig is not autonomus but is adapted on one of the 10 parallel test sections of the laboratory, all of which are fed by the main water reservoir of the laboratory, of 320 m^3 capacity.

Another significant difference is that the industrial pump of NTUA has two radial load bearings of the same type (6206 2RS, Table 2.11), whose noise and vibration characteristics could interact with those of cavitation. The electric induction motor has also two radial bearings (6308), the characteristics of which are also given in theTable 2.11.

Similarly to the LU circuit, the water is pumped from the tank (7), passes through the suction valve (8), the impeller (1), the discharge valve (5) and the flowmeter (6), and returns again to the main tank (7) (Fig. 2.20). The points (e) and (α) correspond to the static pressure measurements points, similarly to Fig. 2.1. The pump is driven from a variable speed electric motor with P_{el}=5.5 kW rated power output at n=2900 rpm. The details regarding the geometrical, operational and physical characteristics of the NTUA test rig are:

- geodetic pressure differential, $\Delta H_z = z_\alpha$=0.53 m
- suction pipe diameter, $d_{p,e}$=0.0531 m,
- discharge pipe diameter, $d_{p,\alpha}$=0.0529 m,
- water temperature, T=20 ºC.

In order to visualise and take pictures of the vapour formation in the pump, the impeller had to be made again from scratch and the casing had to be modified. More specifically, the original impeller is digitised (Fig. 2.21a), and the new impeller is manufactured with the same design but in two parts (Fig. 2.21b): i) the hub with the five blades, and ii) the shroud. The first part is made from copper in a CNC machine, while the second is cut from an initial Plexiglas piece in a lathe. The copper and Plexiglas parts are then assembled with the use of screws that are tightened through the holes of the blades (Fig. 2.21c) and the Plexiglas shroud (Fig. 2.21d). The holes at the Plexiglas shroud are drilled at the thicker initial part (Fig. 2.21d) before the final cutting at the lathe. Henceforward, the impeller tested in NTUA will be called impeller No. 4, and it is the last impeller examined in this dissertation.

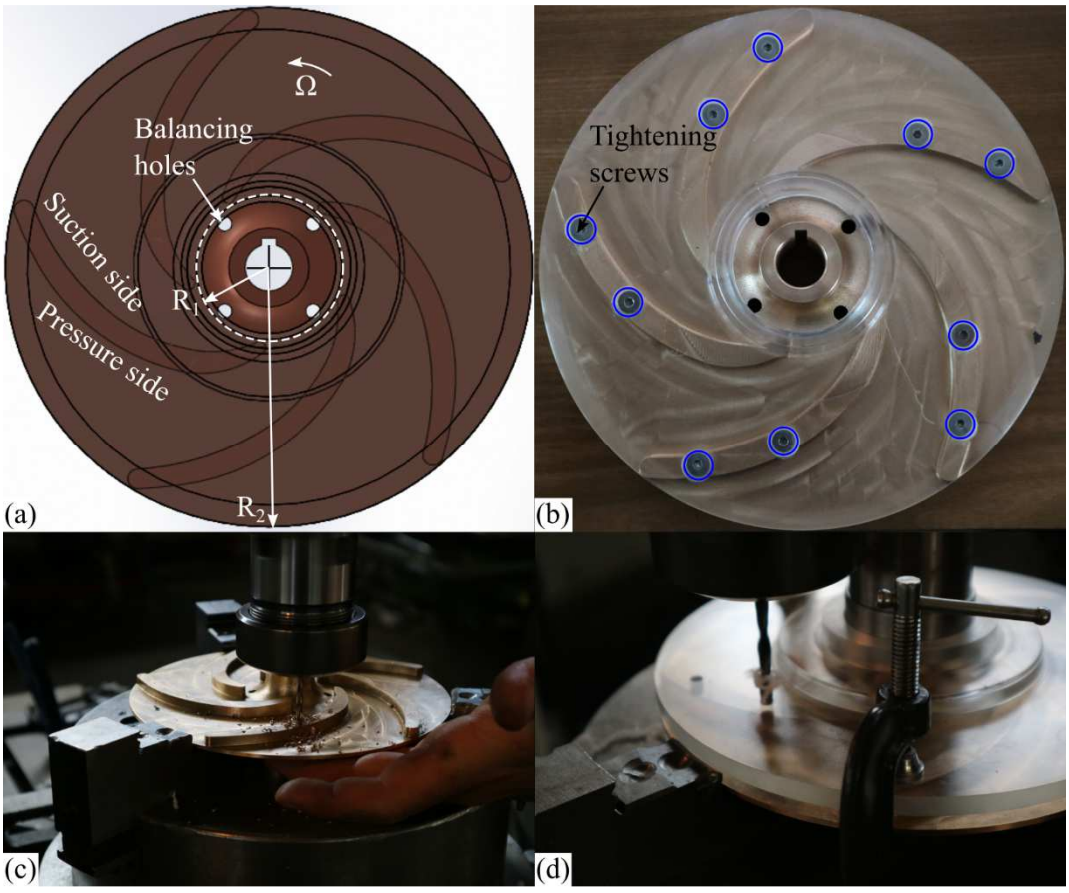

Figure 2.21 a) The impeller No. 4 3D model, **b)** the manufactured parts, **c)** drilling holes for thread manufacturing at the blade and **d)** Plexiglas shroud.

In addition, at the front side of the casing, a plane square piece is cut and replaced by a new transparent window of Plexiglas (Figs. 2.22a,b). Due to technical limitations regarding the strength of the casing, the window size is limited to a small distance from the internal diameter at the inlet of the pump (red curved line of Fig. 2.22a). As a consequence, it is not possible to visualise the blades' leading edge (Fig. 2.22c), and hence in this configuration the cavitation becomes observable after the first development phase. However, the purpose of this testing, which is to ensure the presence of cavitation at low σ OP and to compare the noise and vibration signals with those at maximum σ, is adequately served. Furthermore, in order to improve the understanding regarding the cavitation inception and development in this particular pump, a computational model is developed and presented in Chapters 4 and 5 respectively. In this way, it is possible to counterbalance the aforementioned test rig limitations and estimate the suction conditions that correspond to the onset of cavitation. Finally, the geometric characteristics of impeller No. 4 are presented in Table 2.7.

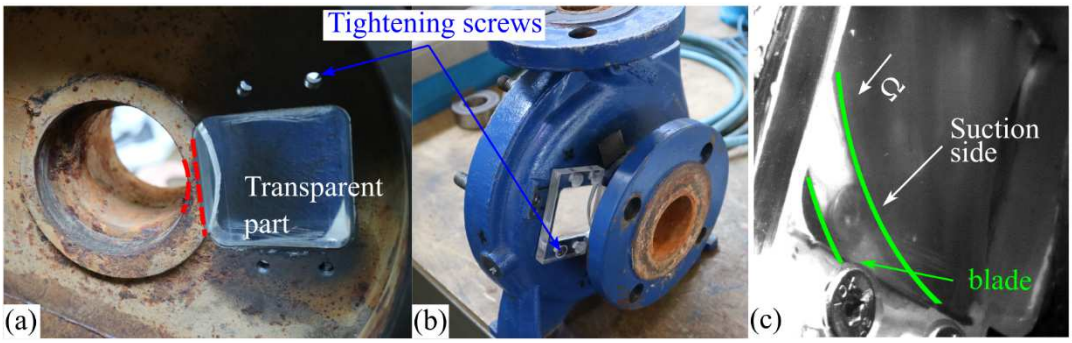

Figure 2.22 Transparent Plexiglas part at the casing of the pump a) inner side, b) outer side, and c) assembled part viewed from outside.

Table 2.7 Geometrical characteristics of the impeller at NTUA.

	z_s [-]	$b_{V,2}$ [m]	d [m]	e [mm]	b_I [mm]	β [deg]
Impeller	5	0.008	-	-	-	-
Inlet (1)	-	-	0.0516	3.5	7.3	25
Outlet (2)	-	-	0.177	6.7	5	40

2.5.2.2 Transducers and measuring systems

In order to derive the performance curves of the pump, similar sensors with those described in section 2.5.1.2 for the Lancaster University set up are used. The only exception is that in the NTUA test rig a torque-meter (No. 2, Fig. 2.20) is connected between the impeller's shaft and the shaft ofthe electric motor, in order to measure the mechanical power provided to the pump, as well as the rotation speed. The torque-meter incorporates two 6302 deep groove ball bearings that support the stator unit on the rotating shaft. The bearings geometrical characteristics and their kinematic frequencies are given in Table 2.10 and 2.11, respectively.

The relative systematic uncertainty for each measured quantity is presented in Table 2.8. The systematic uncertainties for the pressure, flowrate and torque sensors are obtained after the calibration procedure, presented in Appendix A.

Table 2.8 Relative uncertainties of the measured and calculated quantities of NTUA configuration.

	Measured quantities					
	Q	**p_e**	**p_a**	**T**	**M_m**	**Ω**
(systematic) **F($\bar{\varphi}$,s)** [**%**]	1.4	0.25	0.14	1	1	0.5

Two piezoelectric accelerometers, B01_1 and B01_2, and one preamp AE sensor are mounted on the pump, at the location of the 6206 bearing, and at the side and the front casing of the pump, respectively (Fig. 2.23a). The positioning of each sensor relative to the pump, as well as their power supply, the filtering and the pre-amplifier devices are shown in Fig. 2.23. In the NTUA test rig the analog signals of the vibration sensors are digitised in a NI USB-9233 DAQ device (Fig. 2.23b) that incorporates a low pass filter, the cutoff frequency of which is automatically adjusted to the half of the sampling frequency. This device is also used for the power supply of the accelerometers.

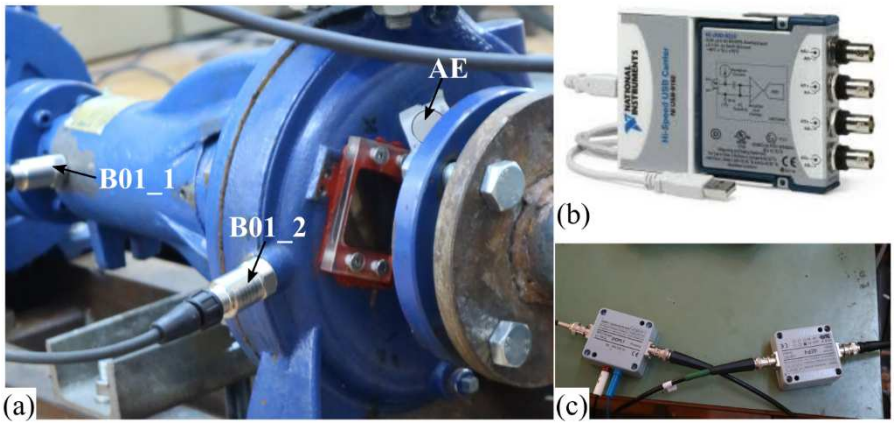

Figure 2.23 a) Sensors mounting position, **b)** NI USB-9233 DAQ device, **d)** AE's pre-amplifier and analog band-pass filter.

The sampling frequency, f_s, the cutoff frequency of the low pass filter, f_{cutoff}, the bandwidth of the analog band pass filter, f_r, the Nyquist frequency, f_N, the acquisition time, t_s and the frequency range that each sensor is able to measure are given in Table 2.9.

Table 2.9 Noise and vibration sensors and acquisition characteristics of NTUA configuration.

Sensor	**f_s [kHz]**	**f_{cutoff} [kHz]**	**f_r [kHz]**	**f_N [kHz]**	**t_s [sec]**	**[f_{min}-f_{max}] [kHz]**
B01_1	25	12.5	-	12.5	30	0-15
B01_2	25	12.5	-	12.5	30	0-15
AE	160	-	2.5-80	80	1	2.5-80

The camera used is a TSI Powerview Plus™ 4MP with a Nikon lens of 50mm. For the stationary depiction of the two-phase flow formation in the pump, a stroboscope is used, the frequency of which is regulated so as to be identical with that of impeller's rotational frequency (RF). In order to reduce the effect of the environmental light and improve the photos quality, the centrifugal pump is placed inside a black tent, similarly to the LU configuration.

Finally, all the possible discrete frequencies and sideband frequencies to be excited for the motor-pump system of NTUA configuration are presented in Table 2.10, for n=2900 rpm, similarly to those presented for Lancaster University configuration.

Table 2.10 Frequencies [Hz] excited by the pump-motor system in NTUA test rig.

	RF	**BPF**	**TBPF**	**RCF**	**RSF**	**SF**	**PPF**
Eq.	-	1.1	2.73	I.4	I.3	1.5	1.6
No. 4	48.3	241	-	53-58	24-43.5	1.7	100

	SBF_R	**SBF_L**	**6206/6308/6302**			
			BPFO	**BPFI**	**FTF**	**BSF**
Eq.	1.7	1.8	1.9	1.10	1.11	1.12
No. 4	±3.4	±100	172/149/123	263/234/213	24/19/24	117/99/90

Table 2.11 Bearing characteristics for the NTUA configuration.

	6206	**6308**	**6302**
D_P [mm]	45.92	70	29.49
D_B [mm]	9.52	15.08	7.92
N_B [-]	9	8	7

2.6 Synopsis

The present Chapter provides the theoretical background of the performance and testing of centrifugal pumps. All the mathematical expressions used for the experimental derivation of the characteristic curves of the pumps, discussed in Chapters 3, 4, 5, 6 and 7 are given in sections 2.2 and 2.3. In addition, the testing procedures followed for the derivation of the characteristic curves are given in detail, along with the mathematical formualtions used for the estimation of the total uncertainty of the measurements. Section 2.4 provides the theory behind the data acquisition approach followed for the collection of the noise and vibration measurements, as well as the mathematical formultions and the theoretical background of signal processing methodologies used. Finally, this Chapter closes with the detailed presentation of the two test configurations, the sensors and the pump impellers used for the conduction of the experiments of the present study.

3. Performance Tests & Flow Visualisation

3.1 Introduction

The experimental results of performance tests for all four impellers pump are presented in this Chapter 3. The laboratory set up and the measuring procedure is described in detail in Chaper 2. The aim of the experimental study is to investigate the behaviour of the engineering quantities that describe the pumps' performance, under normal operating conditions as a function of the flowrate and under cavitating conditions as a function of the suction state. The tests under normal contidions include the derivation of the characteristic operation curves of head, mechanical power and efficiency of the pump, where the best efficiency point (BEP) of the pump is determined.

On the other hand, the cavitation performance of the impellers is analyzed by the derivation of the characteristic curves (σ-Ψ) under cavitating conditions, at four different flowrates. These results are crucial for the present thesis, since they constitute the basis of all Chapters. In Chapter 3, the flow visualisation results of the cavitation formations are shown in different stages of their development and are presented with respect to the σ-Ψ curves. In addition, in Chapters 4 and 5, the numerical model is validated and evaluated with the use of those results. Finally, Chapters 6 and 7 utilise the noise and vibration measurements that are obtained in parallel to the σ-Ψ curves, so as to propose an experimental approach towards the prompt detection of the phenomenon. Consequently, the vast majority of the results of the present Thesis refers to the results of σ-Ψ curves that are given in the present Chapter.

3.2 Non-cavitating conditions

The cavitation experiments in hydraulic turbomachinery usually follow the drawing of characteristic curves of total head (H_{tot}), mechanical power (P_{mech}) and efficiency (η), as function of the pump flow rate, Q. The reason is the significant complexity associated with cavitation related problems that makes necessary the complete understanding of the machine's behavior under normal operation. As a consequence, the characteristic curves under non-cavitating conditions are firstly derived for all the impellers examined in this Thesis (Fig. 3.2).

The dimensional results of the total head and the mechanical power are given in Fig. 3.2, for a wide range of flowrates for each impeller (Fig. 3.1). The results are derived through the Eqs. 2.28 (H_{tot}) and 2.8-2.9 (P_{mech}). The tests are performed at four different rotation speeds, in order to cover a wide range of operation and to indicate the BEP for each impeller. Also, it is intented to test the pump at the maximum possible motor's speed of each test rig, because the higher rotation accelerates the flow field and makes more possible the formation of vapour bubbles during the forthcoming cavitation tests. The electric motor of the LU set up rotates at a maximum rotational speed n_{max}=1800 rpm (see Table 2.5), while the electric motor of the NTUA Laboratory has n_{max}=2900 rpm (see Table 2.10). The curves presented in Fig. 3.2 are the result of six repeated experiments; three set of measurements are performed for continuously increasing flowrates and other three for reducing flow rates. This procedure is adopted, in order to check and verify the repeatability of the measurements, and the possible

effect of the closing / opening of the discharge valve on the accuracy of the derived characteristic curves. As can be seen in the diagrams of Fig. 3.2, all the characteristic curves are repeatable and they are not affected by the way the testing procedure is performed.

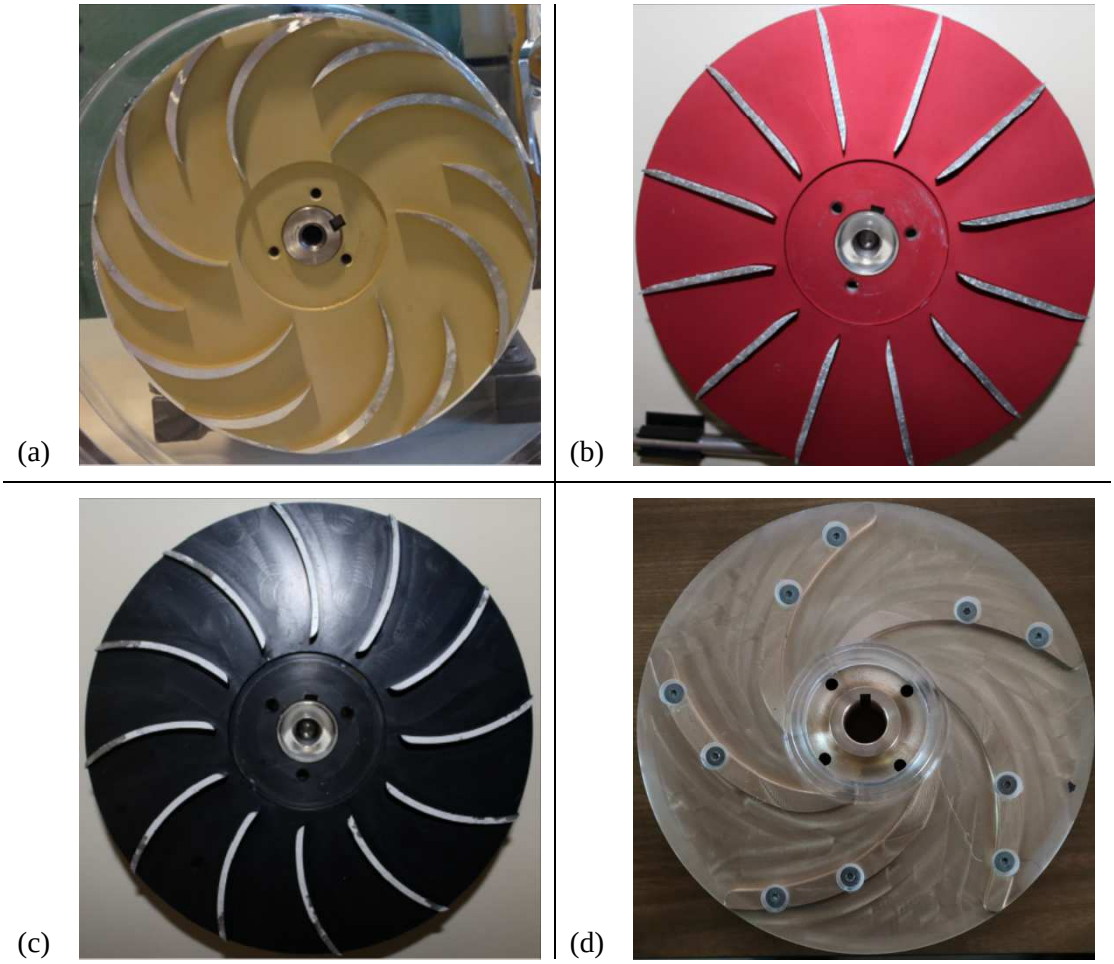

Figure 3.1 a) Impeller No. 1, **b)** No. 2, **c)** No. 3, **d)** No. 4.

Regarding the pattern of the curves, as it is expected, the change of the rotational speed at higher values increases the mechanical power transferred from the electric motor to the impeller (P_{mech}) and, subsequently, the power transferred from the impeller to the water (H_{tot}). This gradual increase of both characteristic curves that obeys to the affinity laws (Eqs. 2.10-2.12, section 2.2.1) is clear to all graphs of Fig. 3.2.

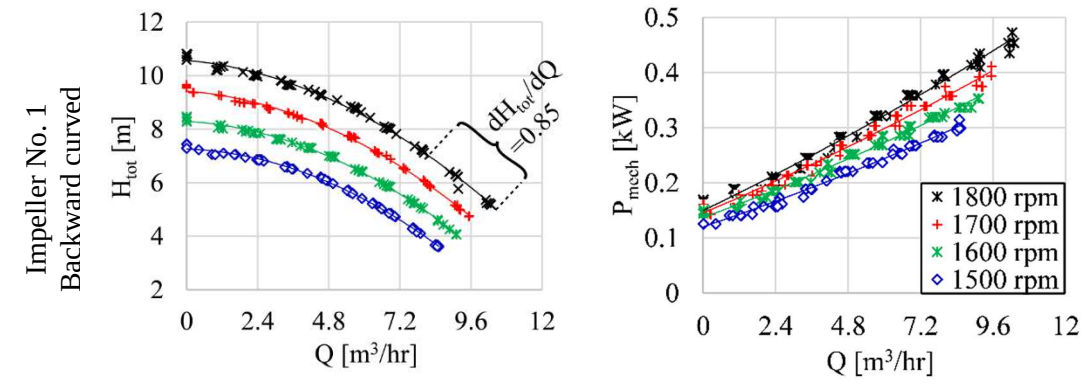

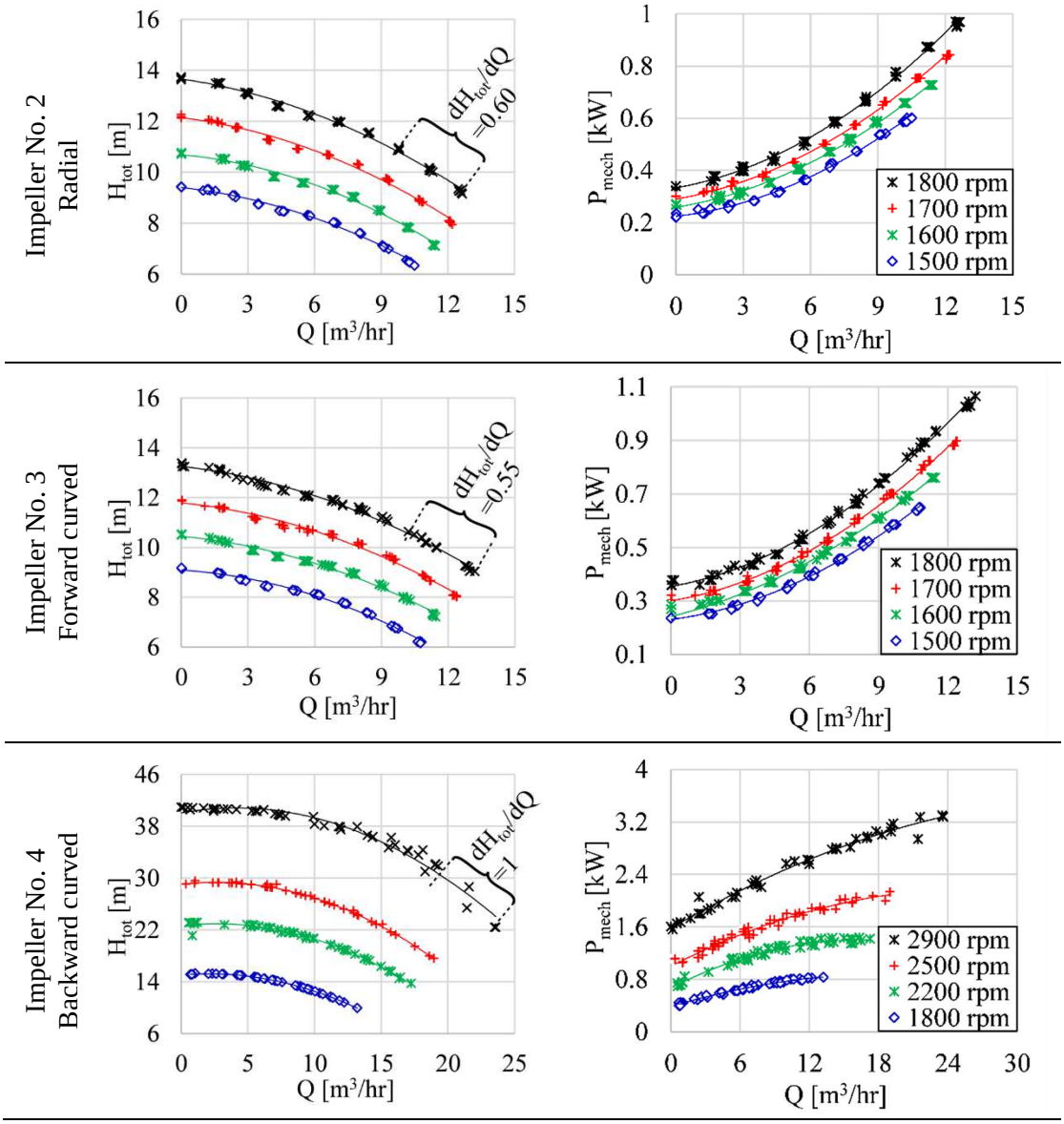

Figure 3.2 Dimensional experimental H_{tot} and P_{mech} characteristic curves for the four tested impellers.

The slope of the total head curves of Fig. 3.2 comply with the theoretical slope, where the slope dH_{tot}/dQ is expected to increase when the blade outlet angle, β_2 decreases. In the cases of the impellers tested, those with backward-curved blades, impeller No. 1 (β_2=25º) and impeller No. 4 (β_2=40º) exhibit ratios with $dH_{tot}/dQ > 0.8$, whereas for those with radial (No. 2, β_2=90º) and forward-curved blades (No. 2, β_2=125º) the ratio drops to $dH_{tot}/dQ < 0.6$.

Trends that also agree with those of the literature (TCF, 2018; Rahman, 2019 - Fig. 3.3) exhibit also the power curves, P_{mech} of all the impellers (Fig. 3.2), where their trend increases with Q. However, slight differences are observed at low flowrate values ($Q<6$ m^3hr^{-1}) between the shapes of P_{mech} curves of impellers No. 1, 4 and impeller No. 2, 3 (Fig. 3.2). For the impellers with the backward-curved blades, the shape is a straight line, while for the other two the shape is a curved line. The investigation of the plots presented in the literature (Karassik, 1960; Holland, 1966; Karassik, 2007; TCF, 2018; Rahman, 2019) confirms this differentiation (Fig. 3.3) that results from the velocity triangle at the outlet of the blade.

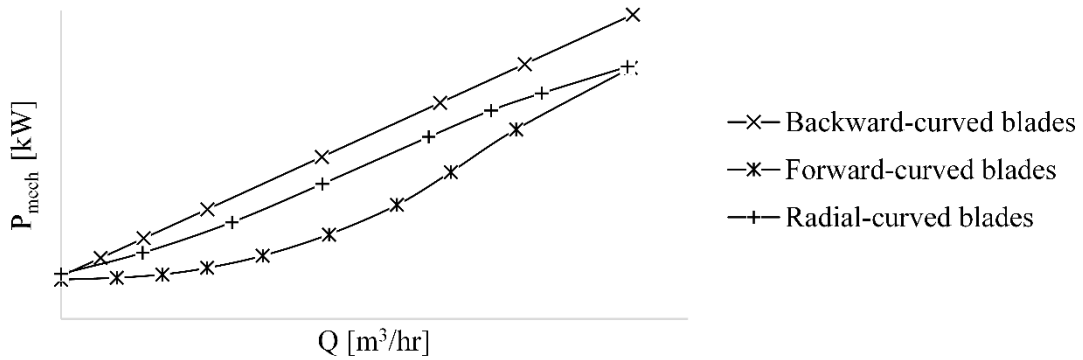

Figure 3.3 Typical P_{mech} curves for backward, forward and radial-curved blades found in the literature (TCF, 2018; Rahman, 2019).

The maximum absolute total uncertainty, $\delta(\varphi,t)$, and its corresponding relative uncertainty, $F(\varphi,t)$, of the measured (Q) and calculated quantities (H_{tot} & P_{mech}) for the plots of Fig. 3.2 are estimated from the procedure described in section 2.3.3, and they are presented in Table 3.1. The $\delta(\varphi,t)$ values are given, in order to highlight their value relative to the results of Fig. 3.2, while $F(\varphi,t)$ is given, in order to present the uncertainty propagation among the calculations.

Table 3.1 Uncertainty level for the results of Fig. 3.2.

	Lancaster University			**NTUA**		
φ →	**Q [m³/hr]**	**H_{tot} [m]**	**P_{mech} [kW]**	**Q [m³/hr]**	**H_{tot} [m]**	**P_{mech} [kW]**
δ(φ,t)	0.12	0.07	0.01	0.33	0.08	0.037
F(φ,t) [-]	1%	0.53%	1%	1.4%	0.19%	1.12%

The $F(Q,t)$ of both configurations shows that the total value of the uncertainty is mainly affected by its systematic component, since the $F(Q,t)$ values that are presented in Table 3.1 are almost equivalent with $F(Q,s)$ values presented in the Tables 2.3 and 2.8, for the LU and NTUA test rig, respectively. In addition, the differences between the $F(Q,t)$ and $F(H_{tot},t)$ values between the two configurations are analogous to the differences that present the $F(Q,s)$, $F(p_e,s)$ and $F(p_a,s)$ values in the Tables 2.3 and 2.8. In general, the uncertainty values presented in Table 3.1 are low and ensure the reliability of the conclusions drawn from the plots of Fig. 3.2.

The characteristic curves of the total efficiency, η are calculated through Eq. 2.7 and are shown in Fig. 3.4. Here, the maximum measured value of efficiency, η_{BEP}, depicts the BEP of the impeller for a specific rotation speed, which is the highest tested for all impelleres, and it is highlighted with a yellow circle. The industrial NTUA pump is designed, in order to operate with maximum efficiency at 2900 rpm (Chrysovergis, 2017).

On the other hand, the low rotational speed limit of laboratory pump, is justified by the use of Plexiglass back and front casing (Fig. 2.16, section 2.5.1) that limits the overal strength of the structure. A second limitation that justifies the low rotational speed of LU pump, is related with the use of high blade inlet angles, which limits cavitation performance of the impeller (Eq. 2.19, section 2.2.2). When such design is combined with high rotational speeds, the impeller becomes prone to vapour bubbles formation that deteriorate pump's performance. The aforementioned limitiations explain also the low efficiency value of this pump.

All the examined impellers have low specific speed ($n_{q,No1}$=844, $n_{q,No2}$=836, $n_{q,No3}$=816, $n_{q,No4}$=847, Q in $m^3 \cdot hr^{-1}$), and hence the impeller diameter is much larger than its width (radial flow impellers). The specific speed value is calculated with the use of Eq. 1.18 (section 1.3.2) This design is associated with higher flow velocities and increased hydraulic losses in the impeller, as also relatively high rotating disk losses (Papantonis, 2016). The η_{BEP} of the impeller No. 4 is closer to that of typical commercial pumps of the same specific speed and size (flow rate), as can be seen in the statistical curves of Fig. 3.5 by the Worthington Group (Papantonis, 2016). The thin green rectangle in this plot reveals the area, where the four impellers approximately lie.

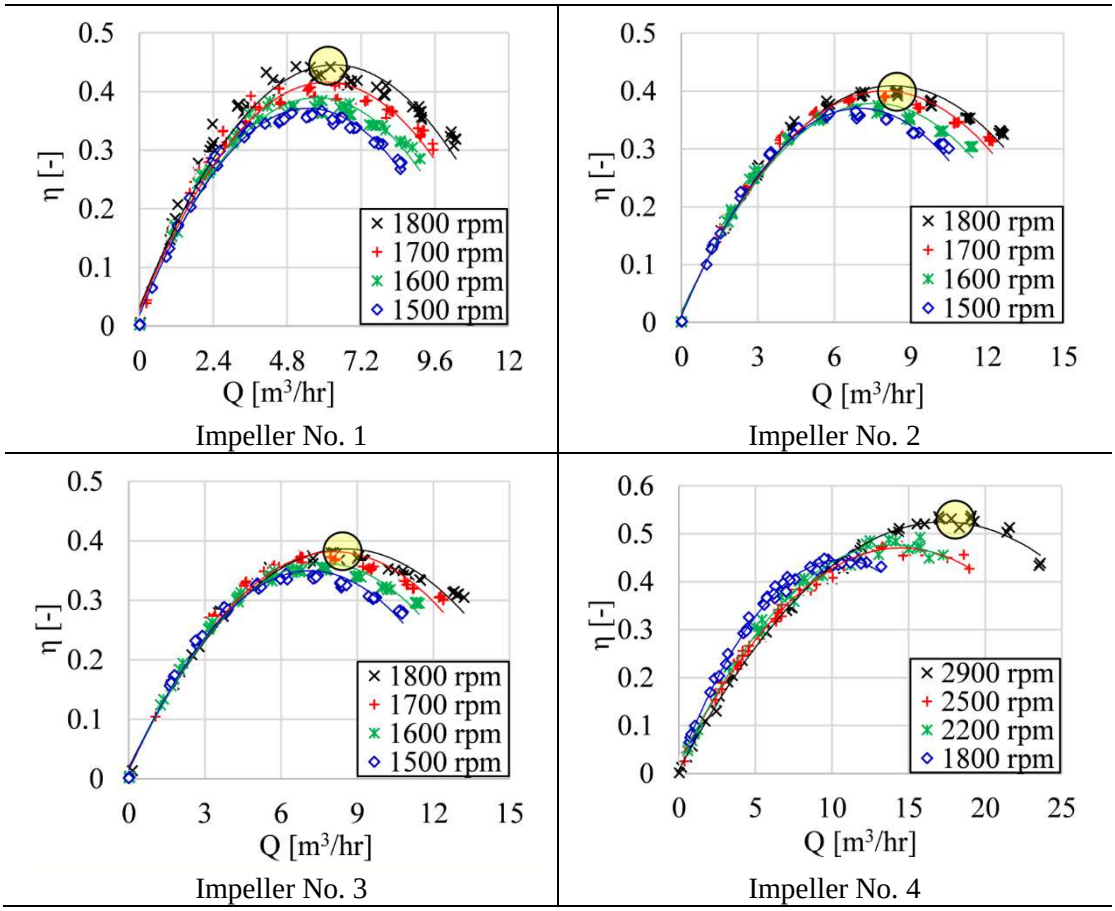

Figure 3.4 Total efficiency characteristic curves of all impellers.

The lowest η_{BEP} value (~38.5%) corresponds to the impellers No. 2 and 3, with twelve blades and the highest value of inlet and outlet blade angles (≥85°). The hydrodynamic design of these experimental impellers is rather poor to drive the flow efficiently (in purpose, to study the different behaviour and performance of these blades). Also, the larger area covered by the blades, as well as the high inlet blade angle introduce considerable hydraulic and shock losses, respectively, that reduce further the efficiency of the pump.

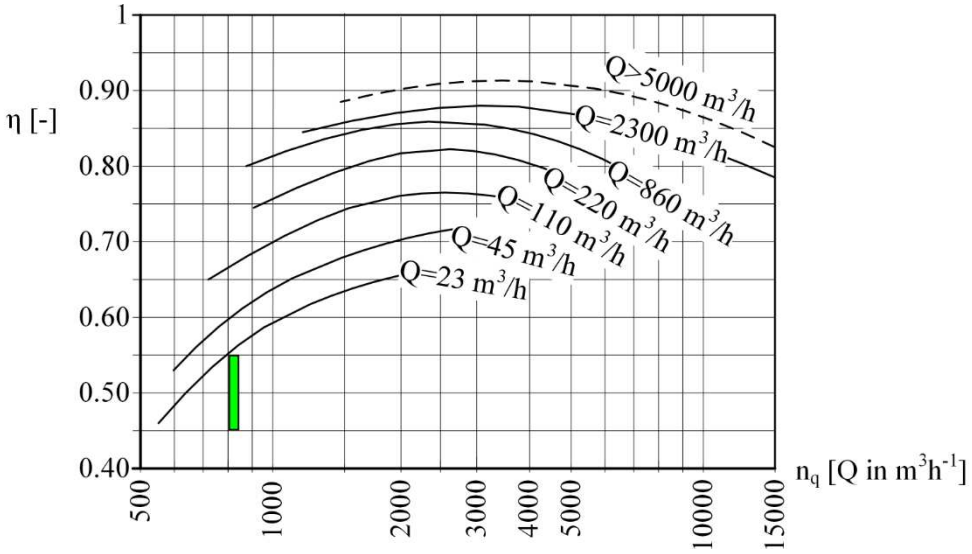

Figure 3.5 The total efficiency of the pump as a function of specific speed and flowrate (Papantonis, 2016).

In addition, the tip clearance causes higher volumetric losses in the open impellers No. 1, 2 and 3, and justifies their lower η_{BEP} compared to the closed impeller No. 4 of a commercial pump. The inlet shock and tip clearance losses are also examined with the use of numerical (CFD) tools, as will be discussed in Chapter 5. The level of uncertainty for the efficiency values presented in the plots of Fig. 3.4, is discussed below, along with the rest non-dimensional variables (Φ,Ψ & N).

Moreover, the results of Fig. 3.4 depict the shifting of maximum efficiency to larger flowrates with the increase of rotational speed. As it is expected, the BEPs of the rotational speeds are corresponding points on the characteristic curves, which highlights the applicability of affinity laws, Eqs. 2.10-2.12.

The efficiency and total head characteristic curves of all impellers are plotted with respect to the BEP in Fig. 3.6, along with the literature results (Papantonis, 2016) for similar specific speed value (n_q=1200). The discussion preceded in this section, as well as the comparison between the literature and measured curves of Fig. 3.6, confirms the proper behavior of the characteristic curves of all impellers tested.

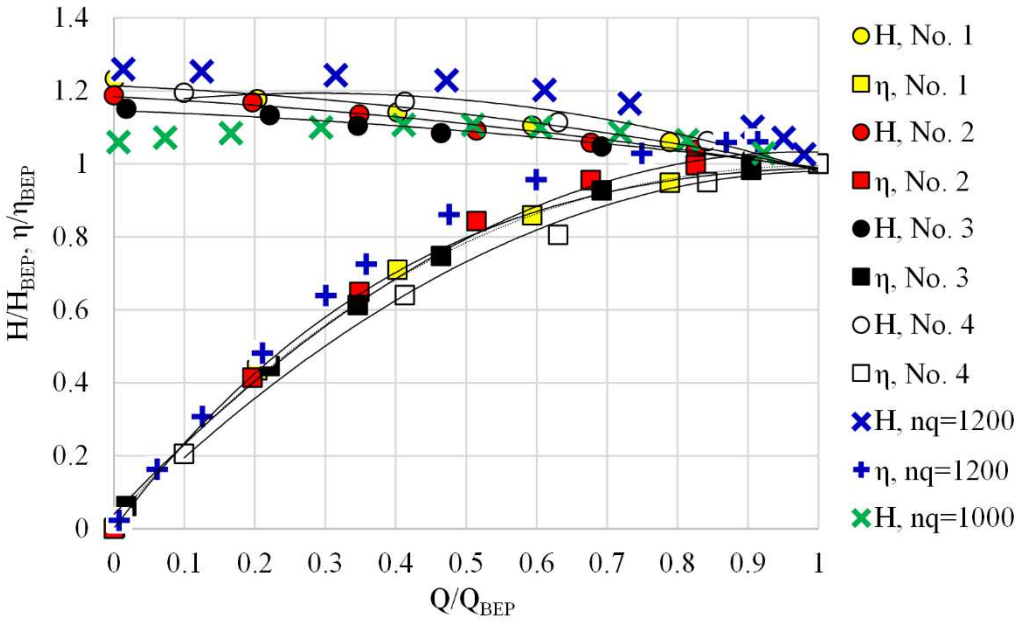

Figure 3.6 The normalised total head and efficiency characteristic curves of all impellers examined along with the typical results for n_q=1200 (Papantonis, 2016) and n_q=1000 (Stepanoff, 1957; Pöyhönen, 2019).

The non-dimensional characteristic curves for each impeller are calculated with use of Eqs. 2.13, 2.16 and 2.17, for Φ, Ψ and N, respectively. These results are presented in Fig. 3.7 along with the η_{BEP}, Φ_{BEP}, Ψ_{BEP} and N_{BEP} values at the best efficiency point (BEP) of the pumps. The non-dimensional characteric curves are used for the validation and discussion of the numerical results of Chapter 5.

The non-dimensional flowrate parameter (Φ) is expressed there as the ratio of the best efficiency point (BEP) flowrate (Φ/Φ_{BEP}). This convention is used for all the results presented in this Thesis, in Chapters 4, 5, 6 and 7. The corresponding dimensional BEP values of Φ, Ψ and n are used for the calculation of specific speed, n_q value (Eq. 1.18, section 1.3.2) that is also given in Fig. 3.7. The similar n_q values also justifies the similar values and trends of the Φ-Ψ characteristic curves.

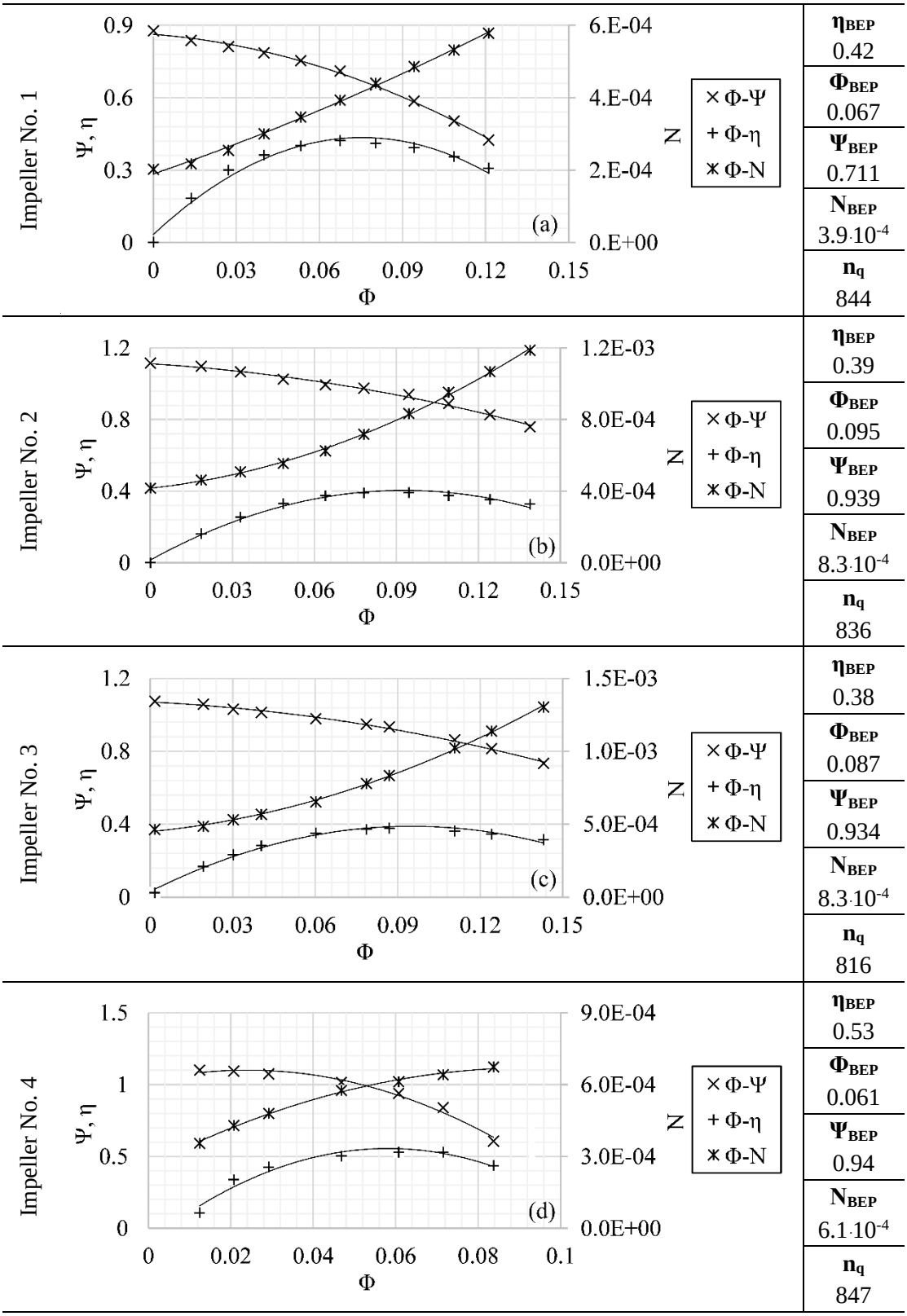

Figure 3.7 Non-dimensional characteristic curves for the four impellers along with the corresponding η_{BEP}, Φ_{BEP}, Ψ_{BEP}, N_{BEP} and n_q values.

The $\delta(\varphi,t)$ and $F(\varphi,t)$ values for the calculated non-dimensional quantities (Φ, Ψ, η & N) of Fig. 3.7 are estimated from the procedure described in section 2.3.3, and they are presented in Table 3.2. The results of the uncertainty are shown in a similar way with those of Table 3.1.

According to Table 3.2, the $F(\Phi,t)$, $F(\Psi,t)$ and $F(N,t)$ values are higher than the corresponding dimensional values of $F(Q,t)$, $F(H_{tot},t)$ and $F(P_{mech},t)$, which are shown in Table 3.1. This behaviour reveals the increasing effect of the uncertainty of the rotation speed (Ω) that is now included in the calculations of the non-dimensional quanities (Eqs. 2.13, 2.16 & 2.17). This effect is stronger for the case of N and Ψ, since N=f(Ω^3) and Ψ=f(Ω^2), and less significant for Φ since Φ=f(Ω). Nevertheless, the aforementioned increase of $F(\varphi,t)$, the $\delta(\varphi,t)$ values presented in Table 3.2 remains low, thus ensuring the reliability of the conclusions drawn in this section.

Table 3.2 Uncertainty level for the results of Fig. 3.7.

	Lancaster University				**NTUA**			
φ →	**Φ [-]**	**Ψ [-]**	**η [-]**	**N [-]**	**Φ [-]**	**Ψ [-]**	**η [-]**	**N [-]**
δ(φ,t) [-]	0.0017	0.01	0.007	$2\cdot10^{-5}$	0.0012	0.01	0.01	$1.2\cdot10^{-5}$
F(φ,t) [-]	1.12 %	1.13%	1.54%	1.8%	1.49%	1.02%	1.8%	1.8%

3.3 Cavitating conditions

3.3.1 Cavitation characteristic curves

After the investigation of impellers' performance under normal operating conditions, the derivation of the cavitation characteristic curves follows. The calculation of the value of the cavitation parameter, σ, is done through Eq. 2.24. The rotation speed remains constant during the tests, and it is adjusted at 1800 rpm for impellers No.1, 2, 3 and 2900 rpm for impeller No. 4, for which the pump efficiency maximises (Fig. 3.4). Four different flowrates for each impeller are selected, in order to represent a sufficient range of operating conditions. As discussed in section 2.3.2, the open sump with throttle valve (CTC, see Fig. 1.27, section 1.3.1.1) procedure (ISO 9906:2012) is followed for the derivation of σ-Ψ curves in both test rigs. During this procedure, the suction static pressure of the flow is progressively reduced by throttling the suction valve. In this way the suction losses are increased and the NPSH value decreases. However, the flowrate of the pump is also diminished, and hence the discharge valve has to be properly regulated, so as to restore the flowrate to its initial value. This really elaborate procedure is carefully carried out by hand, in order to regulate the flow rate with the desired accuracy.

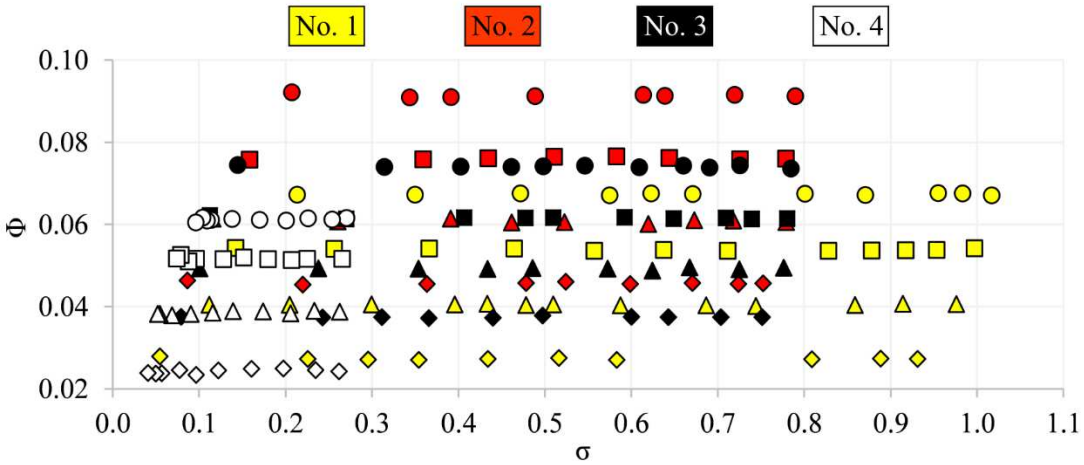

Figure 3.8 Flowrate as a function of σ for all operating conditions tested.

The satisfaction of this prerequisite is demonstrated in Fig. 3.8, where it can be observed that in all the sixteen different cases tested, the Φ values remain practically unaffected during the drop of σ. The aforementioned procedure introduces a limitation to the minimum attainable value of σ, when the discharge valve reaches its fully open position, because after that, any further throttling of the suction valve reduces the flowrate. Thus, none of the flowrates selected for this study take values above Φ_{BEP}.

The σ-Ψ cavitation characteristic curves are presented in Fig. 3.9, for the four flowrates examined for each impeller. The blue and the red colour circles in the plots depict the conditions of visual inception, σ_{VI} and of full cavitation, σ_{FC}, respectively. These conditions are identified from the examination of the flow visualization results, which are presented in section 3.3.2.

For all cases tested, the total head values remain unaffected from the reduction of σ value, even after the formation of the first visually observed cavities at σ_{VI} (blue area). However, the minimising of suction conditions (σ_{FC}, red area) results in the total head deterioration and confirms the general shape of the σ-Ψ curve that can be found in the results of the literature (Anderson, 1994; Gülich, 2008; Brennen, 2011; Papantonis, 2016). The concentration of vapour bubbles at the inlet of the impeller creates gas pockets that significantly reduce the area where the liquid fluid flows through, as well as spoils the hydrodynamic characteristics of the blade. Those conditions are usually followed by flow recirculation and constitute the main

reason for the total head collapse. In the present study, the total head drop for all the flowrates tested, except for Impeller No. 1 (Fig. 3.9a), for which the σ value cannot be further decreased, as it is discussed previously.

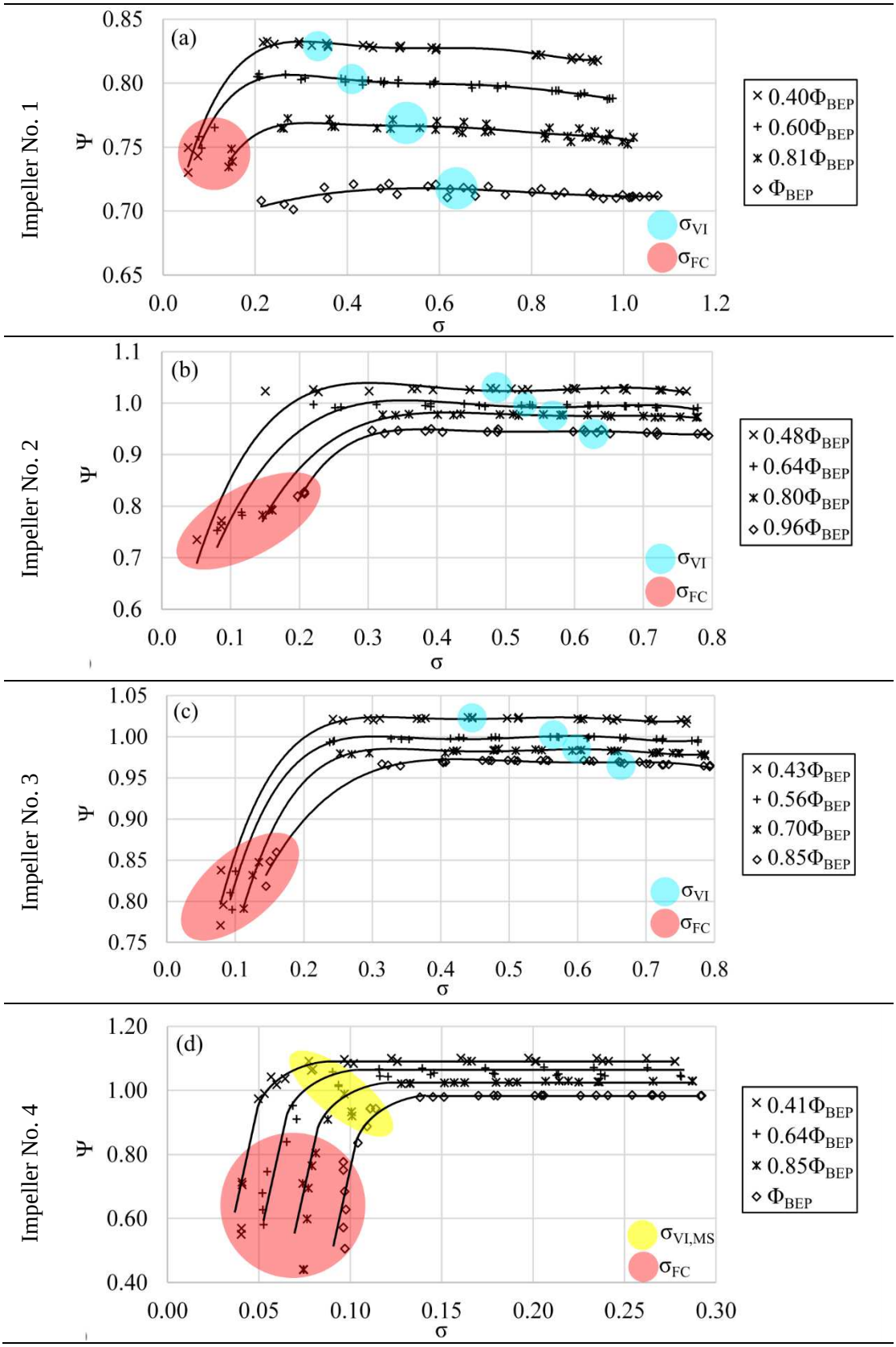

Figure 3.9 Cavitation characteristic curves (σ-Ψ) for four Φ values.

Another observation is that at the cavitating region of LU impellers, between the last two σ values, the slightest change of valve position results in a drastic drop of suction pressure, where the total head is collapsed. This very violent and instantaneous reaction of the impellers No. 1, 2, 3 does not allow to obtain measurements during the intermediate operating conditions. This behavior is probably related with the geometric characteristics of LU impellers. The significantly large inlet blade angles of all impellers (β_1>60º, Table 2.2 at section 2.5.1) could create an abrupt drop of pressure and consequently energy in the medium, which cannot be controlled. On the other hand, the interaction and balance between the rotation speed of the pump and the intense two phase flow could also be the reason for this behavior. When extreme cavitating conditions appear in low rotation speed machines, it is easier to dominate in the flow field and take deteriorate the machine operation. On the other hand, when similar conditions appear in high-speed machines, the mechanical power supplied is significantly higher and allow the user to control the suction and discharge valves, even though the total head eventually drops.

Impeller No. 4 exhibits lower σ_{VI} values due to the limitation discussed in section 2.5.2.1 and deals with the inability of the manufacturing process to extend the Plexiglas window of the casing until to the point, where the leading edge (LE) of the rotating blade is visible. Consequently, at this configuration the onset of the phenomenon is not visualised and the visual inception point, σ_{VI} corresponds to operating conditions, where cavitaties extend at the midspan of the blade. These operating conditions are highlighted with yellow colour (Fig. 3.9d) only for impeller No. 4.

Another observation from Fig. 3.9 is that, irrespective of the impeller tested, an increase of the flowrate results in higher value of both σ_{FC} and σ_{VI}. The reason for this behavior is that higher flowrates in the same impeller accelerate the flow and produce lower static pressure fields at the suction side of the pump, which favor the vapour formation.

For similar flowrate ranges [0.4·Φ_{BEP} – Φ_{BEP}], Impellers No. 2, 3 show higher σ_{VI} values (σ_{VI} ~[0.5 – 0.7]) compared to impellers No. 1 (σ_{VI} ~[0.3 – 0.6]) and No. 4 (σ_{VI} ~[0.06 – 0.11]) for two reasons, related to their geometrical characteristics; i) the larger number of blades (12, instead of 6 and 5) and ii) the higher inlet blade angle (80º, 85º instead of 65º, 25º) . More specifically, the larger number of blades reduces the net flow passage area and accelerates the flow at the impeller inlet. On the other hand, an even higher inlet blade angle than the relative flow incidence angle (see Fig. 2.2b), increases the flow impact losses and local recirculation at the suction side of the blade, that reduce the static pressure values there, thus making the impeller more prone to cavitation (Eq. 2.23).

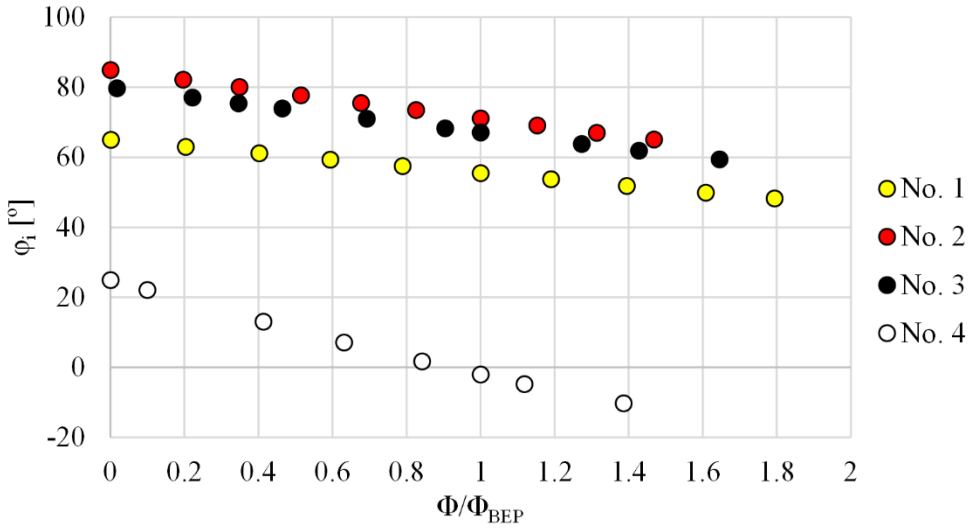

Figure 3.10 The deviation of incidence angle as function of flowrate, for the three impellers.

The effect of the incidence angle, φ_i, in the development of two phase flow formations can be quantified by estimating its value for the various flowrates tested. The value of $\varphi_i=\beta_1-\beta_{1w}$ can

be calculated, since the inlet blade angle, β_1, is known (Tables 2.2 & 2.7, section 2.5), and the inlet angle of the flow, β_{1w} can be calculated from $\beta_{1w}=\arctan(v_{n1}/u_1)$ (Fig. 2.2, section 2.2.1). Both velocity components, v_{n1} and u_1 are known, since the geometrical and operating characteristics of the impellers are given. The results of the calculation of φ_i values for all impellers are provided in Fig. 3.10.

The equation for the β_{1w}, assumes that the tangential component of the absolute velocity at the inlet of the blade (v_{u1}) is zero, which means that the medium enters the impeller with no pre-rotation. This is a crude assumption for the LU configuration, because the pump has a 90º elbow installed at its suction that introduces a significant amount of pre-rotation, which affects in a different way every blade. However, it is reasonable to assume that the impact of the elbow is similar to all the three impellers, since it is a characteristic of the configuration. Consequently, although the absolute values of φ_i for the LU impellers (Fig. 3.10) could deviate significantly from the real values, they can be seen from a comparative perspective.

More specifically, from the results of Fig. 3.10, it is concluded that the incidence angle is higher for impellers No. 2 and 3 compared to that of impeller No. 1, no matter the operating condition. Another observation deals with the significant lower φ_i value in the case of impeller No. 4. The results of Fig. 3.10 confirm the experimental definition of the BEP of the impeller, since the φ_i value minimises for the Φ_{BEP} flowrate. This fact highlights the strong effect that the incidence angle has on the flow field conditions, in the case of the closed impeller No. 4. On the other hand, the incidence angle for the semi-open impellers during optimum flowrate conditions is particularly high. Consequently, it is expected that the semi-open impellers suffer from strong recirculation even at their nominal flowrate conditions.

Finally, the σ-η cavitation curves are provided in Fig. 3.11, for the same σ values with those of Fig. 3.9. As expected, the efficiency curves follow Ψ trend and exhibit an abrupt reduction at σ_{FC}.

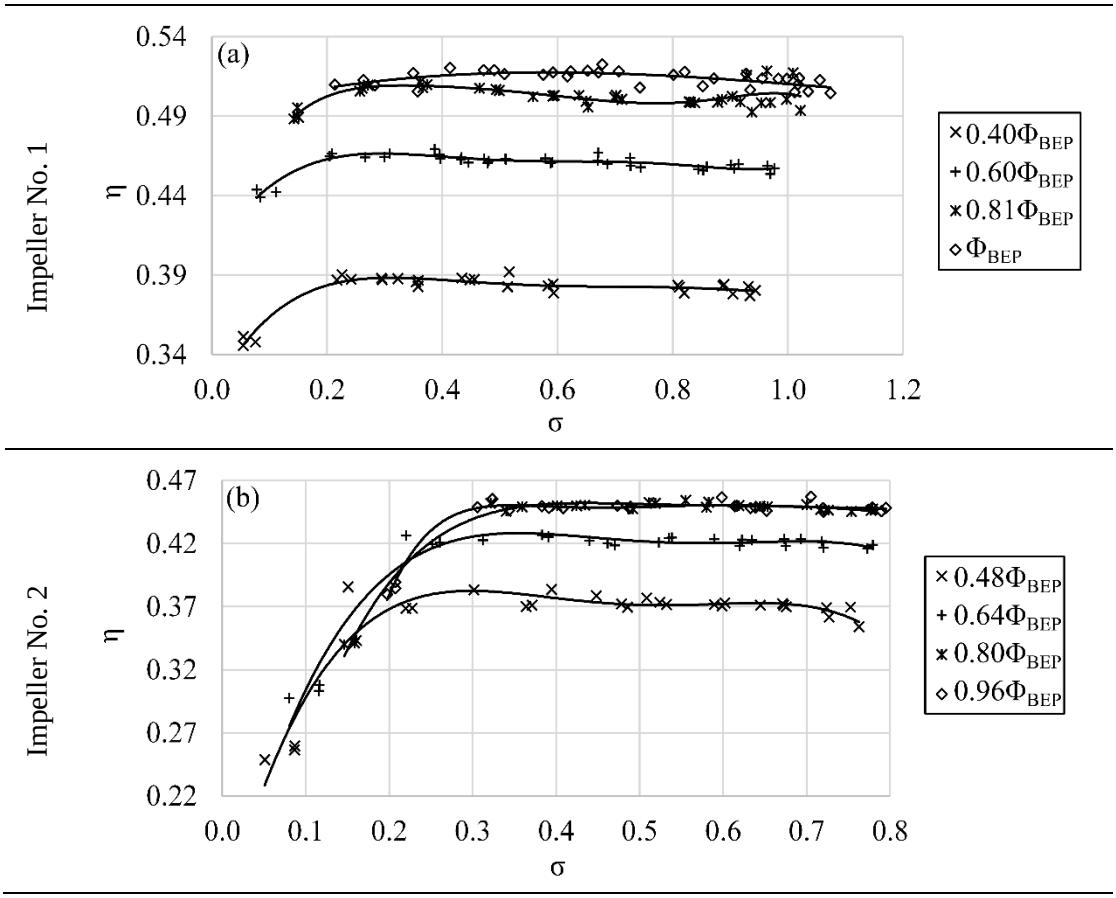

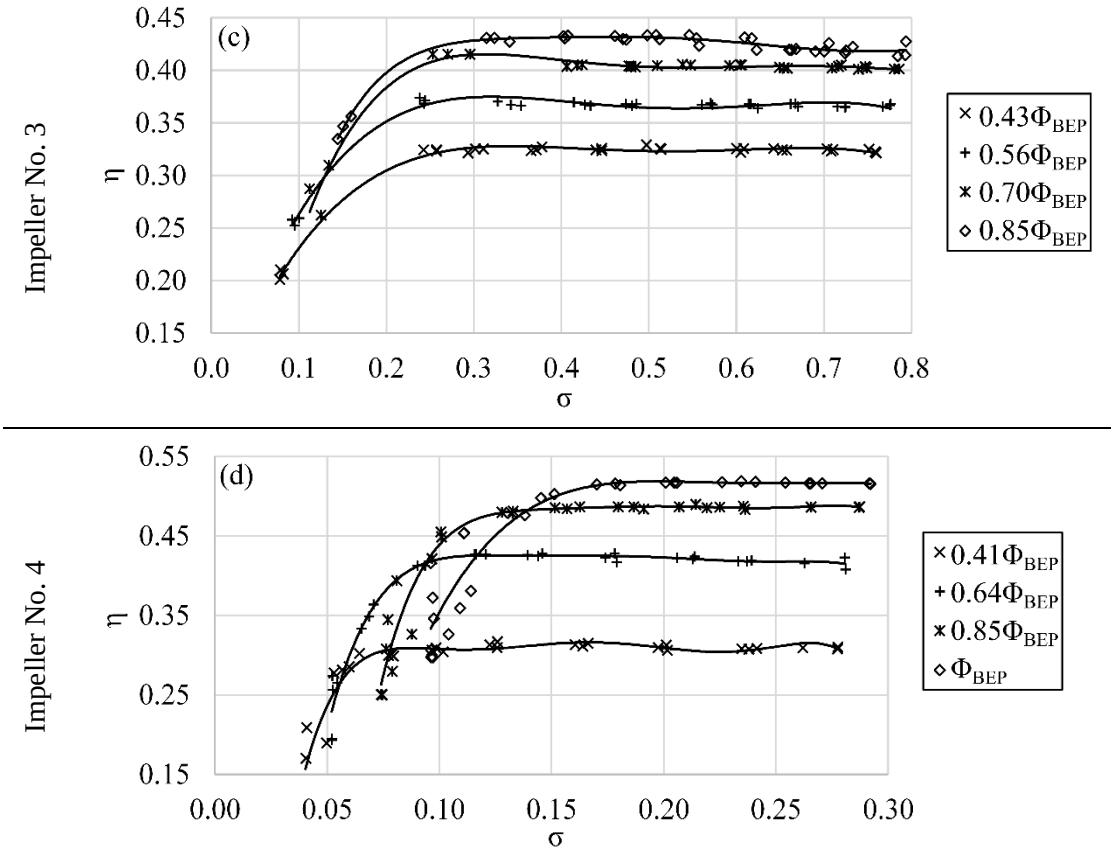

Figure 3.11 Efficiency as a function of σ for four Φ values.

Each curve presented in Figs. 3.9 and 3.11 contains experimental data that are taken by three repeated tests, conducted only for reducing σ value, in order to detect the onset and development of the phenomenon. In spite of the unstable flow conditions created due to the the vapour bubble formation and implosion during cavitating conditions, the σ-Ψ curves of Figs. 3.9, 3.11 are repeatable, thus confirming their accuracy and reliability.

The $\delta(\varphi,t)$ and $F(\varphi,t)$ values for the calculated σ values of Figs. 3.9 and 3.11 are estimated from the procedure described in section 2.3.3 and are presented in Table 3.3. The uncertainty results of the rest non-dimensional quantities (Φ, Ψ & η) have already been discussed in Table 3.2, and their values remain sufficiently low.

Table 3.3 Uncertainty level for σ.

	LU	**NTUA**
	σ [-]	**σ [-]**
δ(σ,t) [-]	0.006	0.001
F(σ,t) [-]	0.63%	0.32%

According to Table 3.3, the uncertainty level of σ is lower for the configuration of the NTUA compared to that of the LU. The behaviour of σ values follow this of H_{tot} that is presented in Table 3.1 for both configurations. The H_{tot} value is strongly affected by the lower values of the relative systematic uncertainty of the sensor that is located at the discharge of the pump, $F(p_a,s)$ and, according to Tables 2.3 and 2.8, it takes lower values for the NTUA configuration.

3.3.2 Visual observations

In this section, the flow visualization results of all impellers are given in Figs. 3.12 - 3.14, 3.16. For each operating point shown in Figs. 3.9 and 3.11, a set of photographs are taken from

the flow field between the rotating blades. The experimental photographs presented in all Chapters of the present Thesis are representative of the visually observed characteristics (location and shape) that the vapour phase exhibits during the 120 sec. of each measurement. As it is discussed at the end of this section, there are operating points (depending on the blade geometry and the σ value), where part of the cavitation area remains relatively unchanged. It is evident that the representation of the actual cavity shape and location improves for these conditions.

In order to present the most characteristic steps of cavitation development, operating conditions for four diffeent flow rates, Φ, and four different σ values are selected to be presented. In order to improve the referencing to the visualisation photos, an additional notation for each column (a→d) and row (e→h) is provided in the front and left limits of Fig. 3.12. In this way, the photograph, for instance, of σ=0.21 at Φ=0.60·Φ_{BEP} for impeller No. 1, is referenced as Fig. 3.12cf. The same notation applies for Figs. 3.13, 3.14 and 3.16.

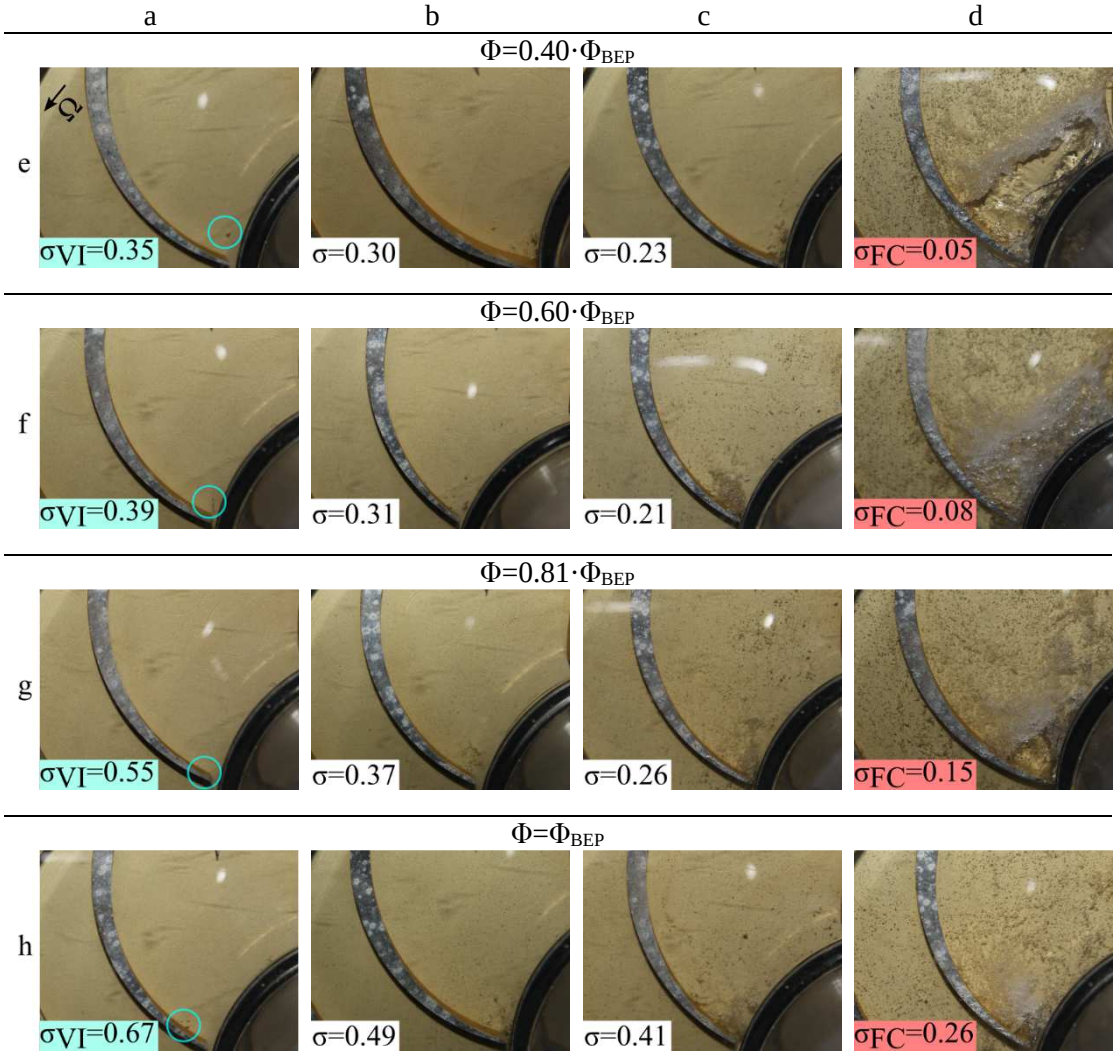

Figure 3.12 Flow visualization results for impeller No. 1.

For the LU impellers (Figs. 3.12 - 3.14) the first photograph in each row (column a) is taken at the visual cavitation inception point, σ_{VI}, while the last photograph of the row (column d) corresponds to fully cavitating conditions, at σ_{FC}. The second (column b) and third (column c) photographs refer to two intermediate conditions, with $\sigma_{VI} < \sigma < \sigma_{FC}$. The camera characteristics and the intense colours used for the painting of the hub of LU laboratory impellers makes easy to discern the appearance of the first bubbles. The discussion of flow visualisation results consists of two parts; i) the first deals with the discussion of the extent of the two-phase flow

development as a whole and as a function of flowrate and suction conditions, while ii) the second attempts to approach each stage of cavitation development for each impeller tested seperatelly, and to associate the photographed characteristics with the various types of cavitation introduced in section I.2.

For all flowrates, the first small bubbles always appear at the suction side of the leading edge (LE) of the blades, area that is more prone to develop minimum static pressures that may allow local evaporation according to the turbomachinery theory (Brennen, 2005; Gülich, 2008; Papantonis, 2016;). The two-phase flow zone at the onset of the phenomenon is shown with the blue circles drawn on Figs. 3.12 - 3.14.

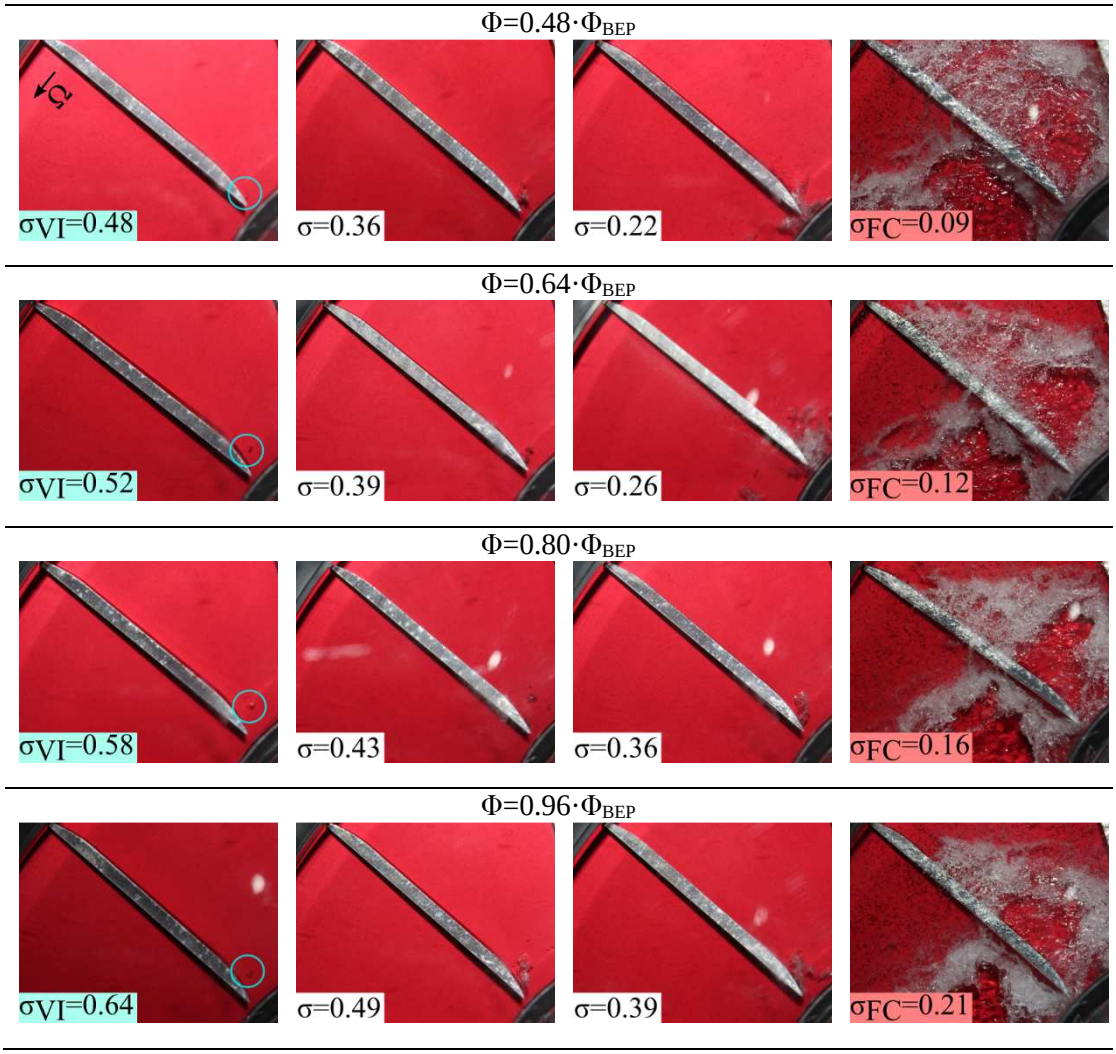

Figure 3.13 Flow visualization results for impeller No. 2.

For the industrial impeller No. 4 (Fig. 3.16) it is considered necessary to firstly show a photograph for non cavitating conditions ($\sigma>\sigma_{VI}$, column a of Fig. 3.16), in order to highlight the differences with the σ_{VI} OP in the second photograph. Similarly to LU impellers, the two-phase flow area appears at the suction side of the blades of impeller No. 4. For this impeller, cavitation is recognised from the colour change of the gray-scale to a lighter (white), colour compared to the non-cavitating pictures. As expected, the area covered from cavities is larger compared to those of LU impellers because, due to the previously mentioned delay (sections 3.3.1 & 2.5.2.1), the phenomenon has already been developed.

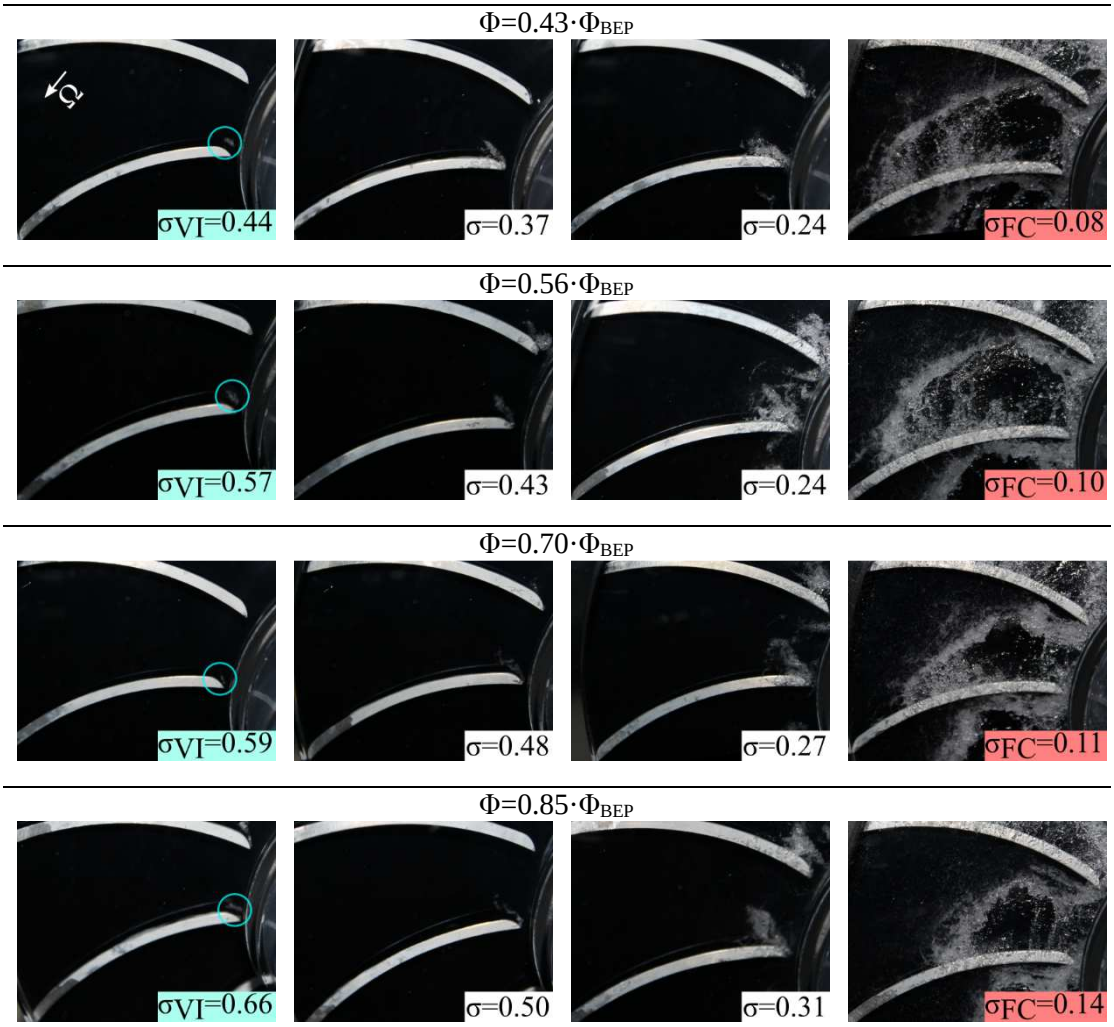

Figure 3.14 Flow visualization results for impeller No. 3.

Reduction of the cavitation coefficient value results in increased number of bubbles generated at the suction side of the blade, irrespective of the impeller design, as shown in the intermediate snapshots of Figs. 3.12 to 3.14 (columns b & c). In the end, further reduction to σ_{FC} values (column d) causes an abrupt and drastic head drop due to the extended size of cavitation area between the blades, that can be observed in the last photo of each row in these figures.

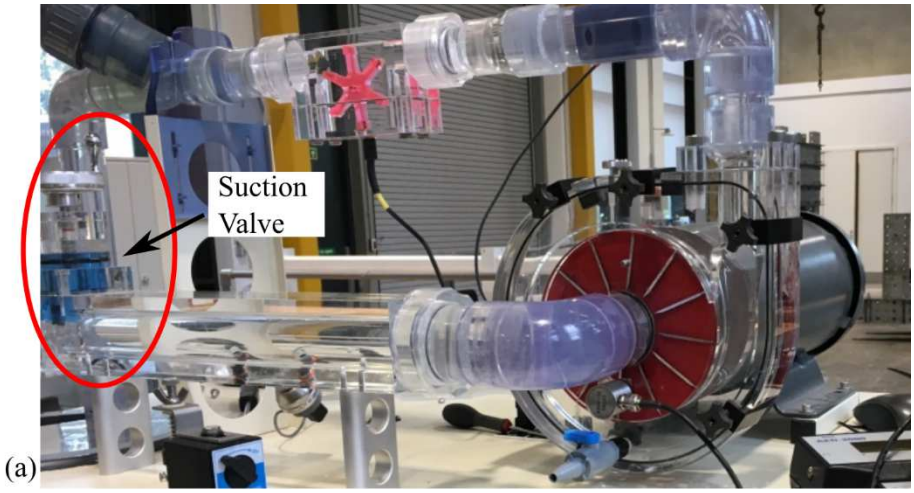

(a)

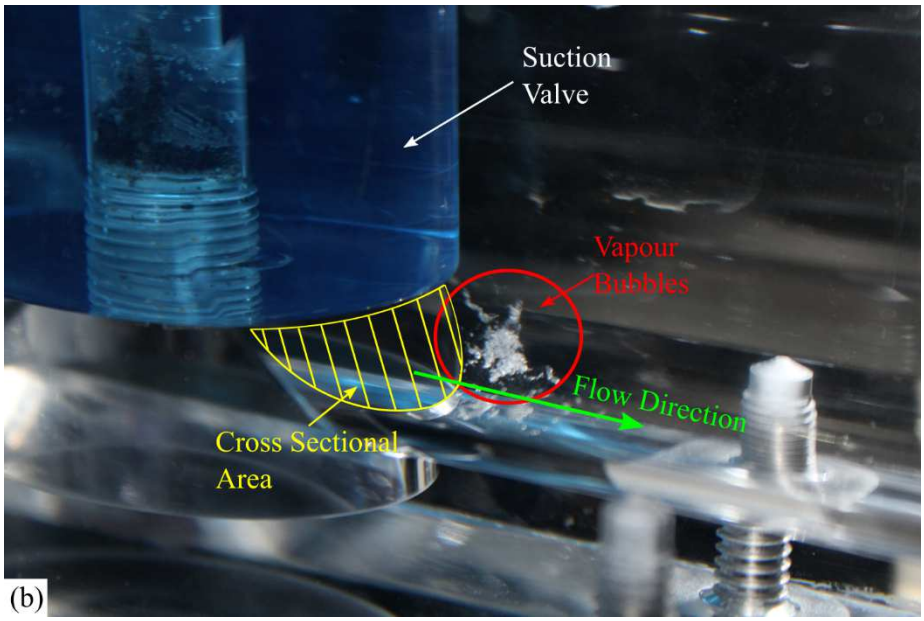

Figure 3.15 a) The suction valve in the LU establishment and **b)** Typical two-phase flow formation in the flow downstream the suction valve, during σ_{FC}, conditions.

The ability to obtain a significant number of measurements at the σ_{FC} area is the reason for the selection of both the third (column c) and fourth (colum d) photograph of impeller No. 4, which depict cavitation formation during the total head collapse (Fig. 3.16). At such operating conditions the flow becomes very unsteable and exhibits intensive recirculation and separation regions, a behavior also observed by other researchers (Baldassarre, 1998; Nelik, 1999; Hofmann, 2001; Friedrichs, 2002; Coutier-Delgosha, 2003b).

Cavitation development at σ_{FC} is violent and extended, and almost blocks the suction of LU impellers. In the LU configuration, it can be observed (Fig. 3.15b) that the vapour bubbles are created at the suction valve area and stronger the formation of cavities in the impeller. In the case of semi-open impellers, where the depiction of the two-phase flow area is clearer (Figs. 3.12-3.14), one interesting observation is made with respect to the flowrate conditions.

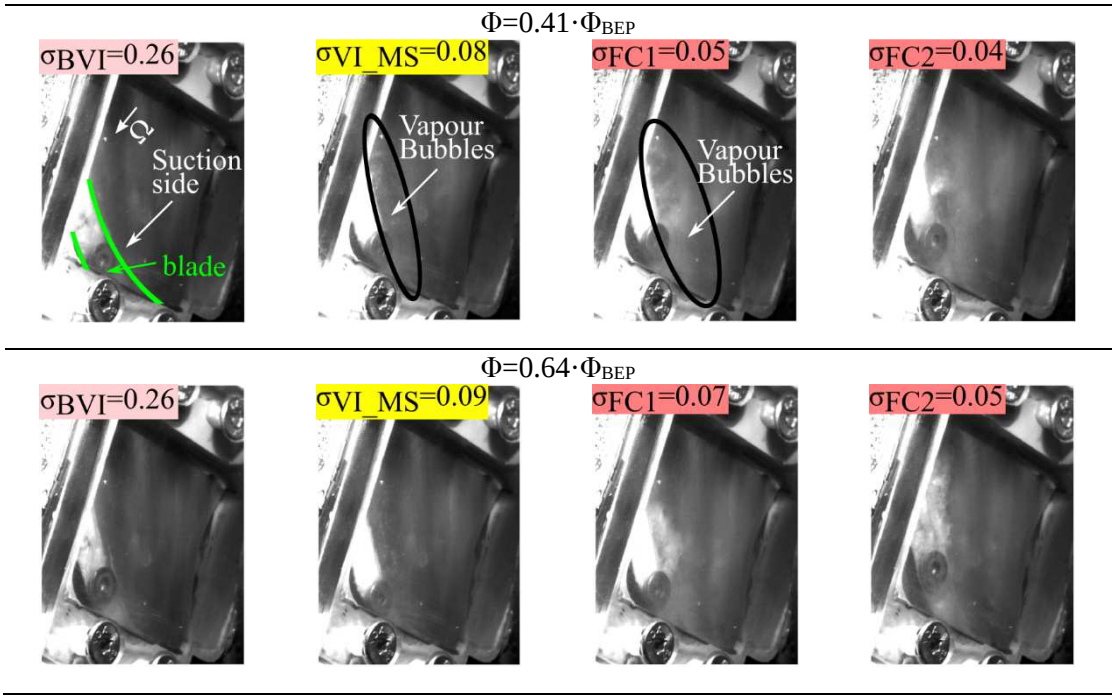

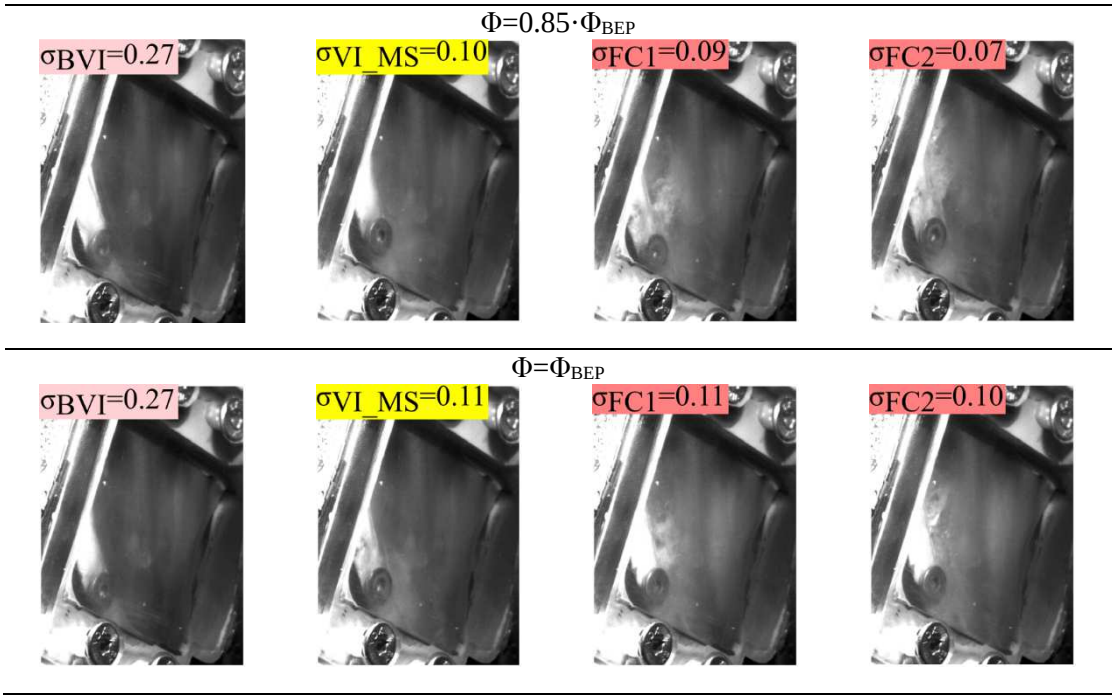

Figure 3.16 Flow visualization results for impeller No. 4.

As it has been shown in Figs. 3.9a,b,c. the total head of those pumps collapses at σ_{FC} point, when according to Figs. 3.12-3.14 the two-phase flow area extends until the neighbouring blade of the impeller. In the case of higher flowrates, such conditions are easier to be reached compared to lower flowrates, due to the flow acceleration that has already been discussed. In addition, when the pump reaches at σ_{FC} conditions it is not possible to further drop the pressure level of the configuration. As a result, the σ_{FC} is always higher for the higher flowrates, which in practice means that the total head drop happens earlier and for this reason the extent of the two-phase flow is narrower. The last observation can be made after the comparison of the d-collumn photographs of Figs. 3.12-3.14.

In addition, the comparison of cavitation extent inside the impellers at σ_{FC} values supports the previous discussion about the positive effect of smaller inlet blade angles and number of blades of the impellers No. 1 and 4. Even at such operating conditions, for relatively similar flowrates, the two-phase flow area of these impellers is less developed (Figs. 3.12 and 3.16), compared to the other two impellers (Figs. 3.13 and 3.14), where the unsteady area extends from the leading to trailing edge and forms a supercavitation area (Figs. 3.13de,df & 3.14de,df).

Although cavitation is considered a mechanism of intense unsteadiness, the macroscopic two-phase flow formations presented in this section show a combination of steady and transient behaviour. The degree of the presence of the macroscopic steady and unsteady behaviour is related with the type of cavitation (see section I.2), and is a function of the suction conditions and the geometrical characteristics (incidence angle and number of blades) of each impeller. Here, at the end of the flow visualisation section it is attempted to associate the visualised characteristics of the phenomenon with the various types of cavitation. In order to perform this association adequately, the photographed results, along with the practical experience gained through the execution of the experiments, are utilised.

During the initial stages of cavitation development, which are presented in column (a) of Figs. 3.12-3.14, the appearance of the first bubble formations is unquestionably dynamic. At these stages the bubbles are created almost seperately (Fig. 3.17a-c) and reliquified abruptly, due to the presence of pressure gradient in the impeller. This behaviour characterises a typical travelling bubble cavitation case. Passing to lower suction conditions during intermediate cavitation (columns b & c), the cavitation behaviour differentiates with respect to the value of incidence angle. On the one hand, impeller No. 1 with lower incidence angle (Fig. 3.10)

compared to impellers No. 2,3, exhibits behaviour similar to that during the onset of the phenomenon (Fig. 3.17d).

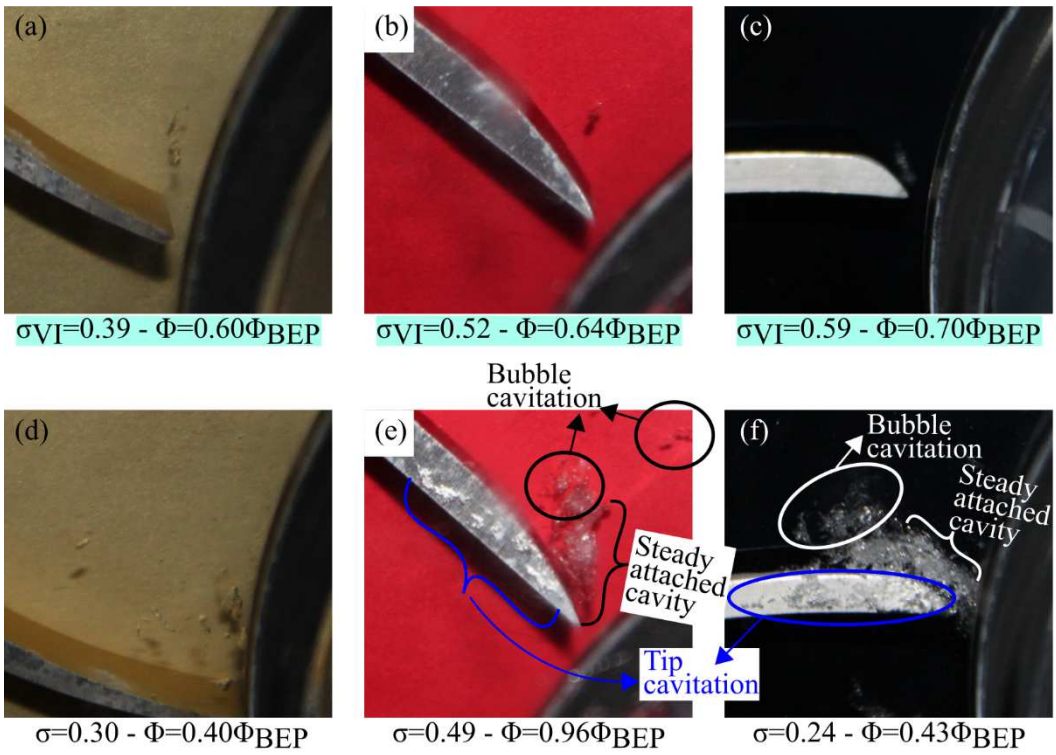

Figure 3.17 Association of photographed characteristics with various cavitation types during initial and intermediate cavitating conditions.

On the other hand, the cavitation formation in the impellers with the radial (impeller No. 2, Fig. 3.17e) and forward curved (No. 3, Fig. 3.17f) blades consists of two areas; i) one that behaves as a steady attached cavity, which does not change significantly over time (Figs. 3.17e,f), and ii) one second area at the limits, or even out of the limits of the attached cavity, which is made from travelling bubbles and presents unsteady behaviour (Figs. 3.17e,f). The appearance of the attached cavity is the result of the flow separation that is expected to appear due to the increased incidence angle (section I.2). In parallel, during intermediate cavitating conditions, large-scale vapour formations appear at the tip clearance of all the impellers (Figs. 3.17e,f). Unfortunatelly, the experimental tools used in the present study cannot illustrate the local flow conditions in the tip clearance of the impeller. Consequently, at this point it is not possible to associate the vapour formations at the tip (Fig. 3.17) with a particular type of large-scale cavitation (section I.2); tip vortex cavitation, backflow cavitation or a different type. For this reason, the numerical model that is developed and validated in Chapter 4, includes the narrow tip clearance area and attempts to provide an answer regarding the type of cavitation that is observed in Fig. 3.17. The results of the tip clearance flow conditions are presented in Chapter 5.

Finally, at σ_{FC} point, four different large-scale cavitation formations coexist; i) attached vapour cavities formed at the suction of the blade and forming a uniform single bubble area, ii) cloud bubble cavitation at and out of the limits of the attached cavitation area, iii) vapour cavities generated at the suction valve (Fig. 3.15), at the elbow pipe and the nozzle area at the inlet of the pump and transferred up to the entrance of the impeller; and iv) tip cavitation through the blade leakage area. All the aforementioned types are highlighted in photographs of Fig. 3.18. As it is mentioned again for the results of Fig. 3.17, the assosiation of the tip clearance cavitation with a specific type of a large-scale vapour formation requires additional clarification, which is provided by the numerical model in Chapter 5.

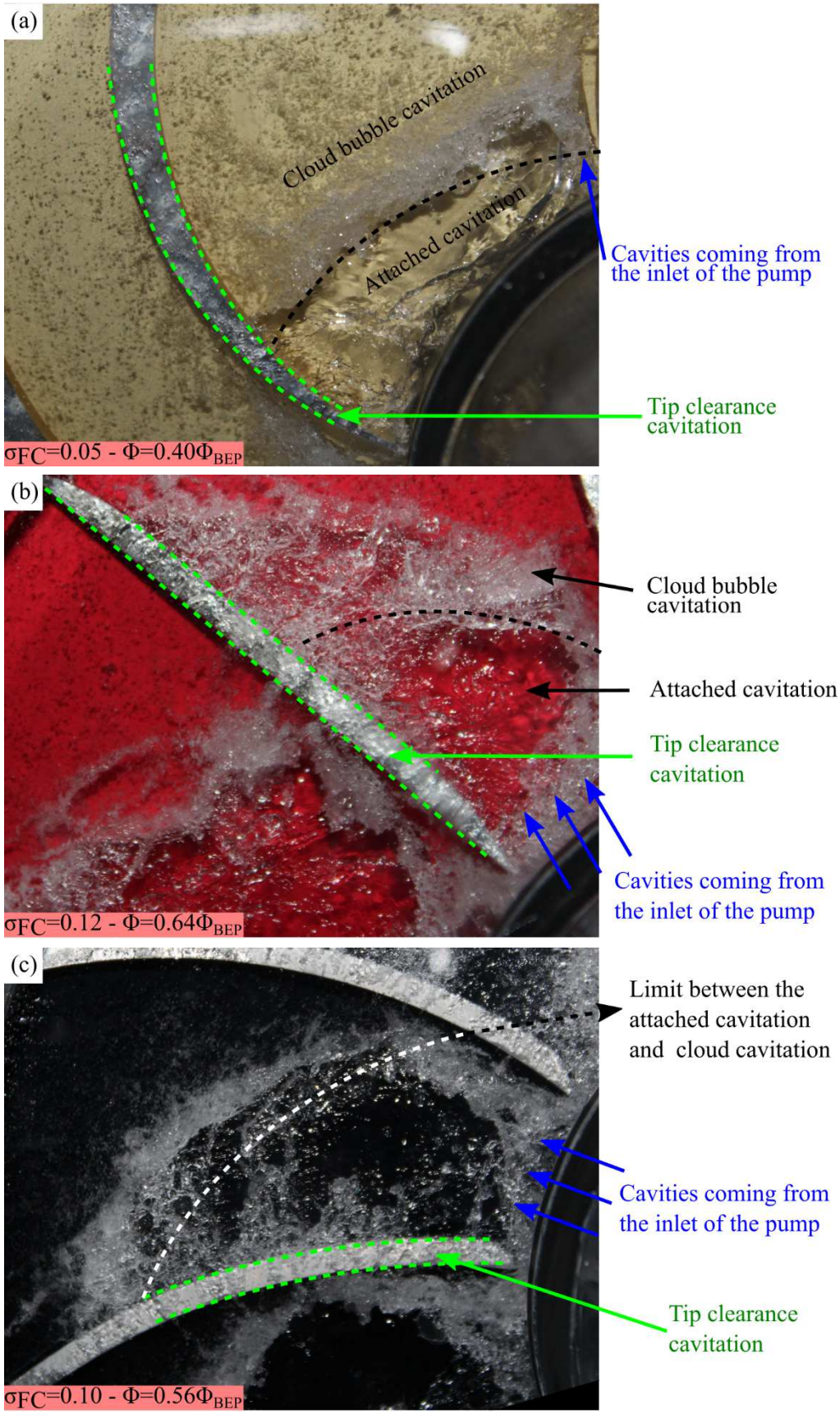

Figure 3.18 Association of photographed characteristics with various cavitation types during heavy cavitating conditions.

3.4 Synopsis

In this chapter, the performance of the four impellers examined in this Thesis is presented and discussed, for several operating points and cavitating or non-cavitating conditions. These same operating points will then be used for the presentation of the numerical results from the simulation of the flow in these impellers (Chapters 4 & 5), and for the analysis of the obtained noise and vibration data (Chapters 6 & 7).

The laboratory experiments carried out for the plotting of the characteristic operation curves (head, efficiency and power, as function of the flow rate) are found to be repeatable within adequate accuracy. The value of the measured maximum efficiency of the industrial impeller No. 4 is typical for centrifugal pumps in this specific speed and size range. The lower efficiency of the unshrouded impellers No. 1 to 3 is justified due to their hydrodynamic design and the increased frictional and shock losses at the rotating blades, as well as from the additional volumetric losses in the blades tip clearance.

For the vast majority of the tests under cavitating conditions, the total head value diminishes when the cavitation parameter, σ, drops at the minimum σ area. As expected, the first bubbles always appear at the suction side of the leading edge of the blades. The value of σ at visual inception of cavitation (σ_{VI}), and at total head drop (σ_{FC}) increases with the flowrate, due to the increased flow velocities that reduces the corresponding static pressure values. Impellers No. 2, No. 3 are more prone to two-phase flow development, as a result of their larger number of blades and higher inlet blade angle.

Further reduction of σ value clearly increases the number of bubbles generated at the suction side of the blades, irrespective of the impeller design. Reaching close to full cavitation conditions (σ_{FC}), the extent of the two phase flow area in the impeller maximises and causes a drastic drop of the total head and efficiency. At such operating conditions, the flow becomes very unsteable, and exhibits intensive recirculation and separation regions, while cavitation covers a significant part of flowpath between the blades. These impacts are the results of four vapour mechanisms; a) attached vapour cavities that are formed at the suction of the blade and form a uniform single vapour-filled area, b) bubble cavitation at and out of the limits of the attached cavitation area, c) vapour cavities generated at the suction valve (Fig. 3.15), at the elbow pipe and the nozzle area at the inlet of the pump and transferred to the entrance of the impeller; and d) tip cavitation through the blade leakage area. Impellers No. 1, 4 appear milder cavitation characteristic due to their improved geometrical characteristics.

In addition, the illustration of the cavitation area through the camera depicts the characteristics of the attached and tip clearance vapour formations, as well as the instantaneous characteristics of the dynamic bubble formations. The attached and tip cavitation results are considered that present steady state characteristics in terms of the area that cover, even though microscopically they exhibit transient features. It should be mentioned that flow visualization is used as a tool that confirms macroscopically the existence or absence of cavities, and its results are subjected to camera limitations. As a consequence, it is possible that micro-cavities exist microscopically before the optical visual inception but the resolution of the camera could not depict them.

In general, the observed cavitating flow and corresponding performance of the laboratory tested impellers can be explained based on their geometrical and operation characteristics. Consequently, the obtained experimental data can be used for further study of this phenomenon in the following chapters.

4. Computational Modelling

4.1 Introduction

In this chapter the development of the numerical tool that is used for the study and detection of cavitation of centrifugal pumps is described. Firstly, the mathematical formulation that govern mass and momentum conservation, turbulence modelling and two-phase flow formation is presented. Two impellers are selected to be modeled; the unshrouded impeller No. 2 and the closed impeller No.4. Impeller No. 2 is used, in order to develop and validate the model against the experimental measurements, under normal and cavitating conditions. The mesh and the boundary conditions for both impellers are presented in sections 4.3 and 4.4. For the pump with impeller No. 4, the computational domain and the mesh are taken from Kassanos et al. (2016a) and Chrysovergis (2017). In these studies, the same pump is simulated, in order to investigate its performance when it operates under direct (pump) and inverse (hydroturbine), non-caviating conditions. The evaluation includes the comparison of the computed operating points of the characteristic curves with the corresponding measurements, under normal (Φ-Ψ & Φ-η) and cavitating (σ-Ψ) conditions, as well as the location and extent of the visualised and simulated two-phase flow area. The experimental results have been already shown and discussed in Chapter 3. The extended evaluation of the numerical results, with respect to the vapour formation characteristics under various operating conditions, reveals the ability of the model to identify adequately the presence of cavitation. Finally, the present study examines the effect of the tip clearance thickness on the performance of the machine and on the cavitation development. For this reason, section 4.7, includes all the details regarding the numerical modelling of the additional tip clearance cases.

4.2 Mathematical formulation

4.2.1 Mass and momentum equations

Every isothermal problem in fluid dynamics, such as the flow inside a hydrodynamic turbomachinery, is governed by the equations of mass and momentum that are expressed in the unsteady, three dimensional form (Batchelor, 2000; Versteeg & Malalasekera, 2007) by Eqs. 4.1 and 4.2, respectively.

$$\frac{\partial \rho}{\partial t} + \nabla\left(\rho \vec{v}\right) = 0 \tag{4.1}$$

$$\frac{\partial}{\partial t}\left(\rho \vec{v}\right) + \nabla\left(\rho \vec{v}\vec{v}\right) = -\nabla p + \nabla\left(\bar{\bar{\tau}}\right) + \rho \vec{g} + \vec{F} \tag{4.2}$$

where ρ is the density, v the three dimensional velocity vector, p the static pressure, g the gravitational acceleration, and F the external forces. The stress tensor, τ, is calculated from Eq. 4.3:

$$\overleftrightarrow{\tau} \triangleq \begin{bmatrix} \tau_{xx} & \tau_{xy} & \tau_{xz} \\ \tau_{yx} & \tau_{yy} & \tau_{yz} \\ \tau_{zx} & \tau_{zy} & \tau_{zz} \end{bmatrix} = \mu \left[\left(\nabla \vec{v} + \nabla \vec{v}^{\mathrm{T}} \right) - \frac{2}{3} \nabla \vec{v} \; \overleftrightarrow{I} \right] \tag{4.3}$$

where μ is the dynamic viscosity and I is the unit tensor.

4.2.2 Turbulence modelling

The Reynolds number of flows in hydraulic turbomachinery is typically higher than 10^6 (Papantonis, 2016), therefore the flow is fully turbulent, and a turbulence model is required for the numerical simulation. Turbulence is the random, unsteady and three-dimensional motion of fluid particles in any kind of flow. These characteristics of the turbulent velocity field create disordered eddies of many different time and length scales that are self-preserving, diffusive and continuously mix the flow (Tsaggaris, 2005). Especially in internal flows, this behaviour is strongly related with the presence of solid boundaries (Wilcox, 1993b; Greitzer, 2007) and the formation of the boundary layer, where shear stress forces become significant due to turbulence and viscous effects. The aforementioned attributes make the simulation of turbulent flows a primary problem of the fluid mechanics. Depending on the accuracy required for a particular application, different simulation techniques have been proposed that could be classified in three main categories: direct numerical simulation (DNS), large eddy simulation (LES) and turbulence models for the Reynolds-averaged Navier-Stokes (RANS) equations (Versteeg & Malalasekera, 2007).

DNS methodology solves numerically the exact time-dependent Navier-Stokes (NS) equations, without modelling the turbulence. The very high computational cost that is required for the adjustment of the mesh and time step, in order to resolve the time and length scale of all eddies makes DNS non-applicable in industry related problems. On the other hand, DNS has been used for the in-depth study of eddy structures, and for the evaluation of current and new developed turbulence models.

LES approach focuses on resolving only the larger scale flow structures and models the interaction of the flow with the lower scale eddies. This is accomplished with the use of a filter function on the time-dependent NS equations that rejects the smaller eddies, whose effect is included in the simulation with the use of sub-grid scale models. In this way, although the unsteady equations have to be solved, larger mesh elements are used for the spatial discretization, thus resulting in relatively lower computation cost compared to DNS. Nowadays, LES tool is mainly used in the simulation of compressible flows at high Reynolds numbers, and like DNS, for the assessment of traditional and new turbulence models (Argyropoulos, 2015).

RANS equations, which are used in the present study, describe the turbulent fluid motion using the Reynolds decomposition (Eq. 4.4). The latter assumes that the flow property φ, consists of one mean $\overline{\Phi}$ and one fluctuating φ' component:

$$\varphi = \overline{\Phi} + \varphi' \tag{4.4}$$

Reynolds decomposition transforms mass (Eq. 4.1) and momentum (Eq. 4.2) equations to the Eqs. 4.5 and 4.6 that are presented with the use of Einstein notation and by dropping the overbar on the mean values:

$$\frac{\partial \rho}{\partial t}+\frac{\partial}{\partial x_i}\left(\rho v_i\right)=0 \tag{4.5}$$

$$\frac{\partial}{\partial t}\left(\rho v_i\right)+\frac{\partial}{\partial x_j}\left(\rho v_i v_j\right)=-\frac{\partial P}{\partial x_i}+\mu\frac{\partial^2 v_i}{\partial x_j \partial x_j}+\frac{\partial\left(-\rho\tau_{ij}\right)}{\partial x_j} \tag{4.6}$$

where τ_{ij} is the stress tensor derived from the fluctuating part of Reynolds decomposition, called Reynolds-stress tensor, shown in Eq. 4.7:

$$-\tau_{ij}=-\overline{v_i' v_j'} \tag{4.7}$$

At this point, the system of four Eqs. 4.5 and 4.6 contains ten unknowns: P, u_i and the six components introduced from the Reynolds-stress tensor. Turbulence models are used, in order to close this system of equations. In this study, the k-ω shear-stress transport (SST) turbulence model (Menter, 1994) is used, which applies the Boussinesq hypothesis (Eq. 4.8) that relates Reynolds stresses with the mean velocity gradients:

$$-\rho\overline{v_i' v_j'}=\mu_t\left(\frac{\partial v_i}{\partial x_j}+\frac{\partial v_j}{\partial x_i}\right)-\frac{2}{3}\left(\rho k+\mu_t\frac{\partial v_k}{\partial x_k}\right)\delta_{ij} \tag{4.8}$$

where μ_t is the turbulent viscosity, k is the turbulence kinetic energy and δ_{ij} is the Kronecker delta. In the k-ω SST model, two additional transport equations are solved, Eq. 4.9 for k and Eq. 4.10 for the specific turbulence dissipation rate, ω, while μ_t is calculated from 3.11.

$$\frac{\partial}{\partial t}\left(\rho k\right)+\frac{\partial}{\partial x_i}\left(\rho k v_i\right)=\frac{\partial}{\partial x_j}\left(\Gamma_k\frac{\partial k}{\partial x_j}\right)+\tilde{G}_k-Y_k \tag{4.9}$$

$$\frac{\partial}{\partial t}\left(\rho\omega\right)+\frac{\partial}{\partial x_i}\left(\rho\omega v_i\right)=\frac{\partial}{\partial x_j}\left(\Gamma_\omega\frac{\partial \omega}{\partial x_j}\right)+G_\omega-Y_\omega+D_\omega \tag{4.10}$$

$$\mu_t=\frac{\rho k}{\omega}\frac{1}{\max\left[\frac{1}{\alpha^*},\frac{S\cdot F_2}{0.31\omega}\right]} \tag{4.11}$$

where F_2 is the blending function, S is the strain rate magnitude, Γ is the effective diffusivity and G, Y and D represent the generation, dissipation and cross-diffusion terms, respectively. The expressions used for the calculation of the Γ, G, Y, D, α^*, S and F_2 are given in Appendix C.

The mean and fluctuating velocity characteristics change significantly close to the solid boundaries, where the no slip condition is applied. The area very close to the wall exhibits almost laminar flow characteristics, as both normal and tangential velocity fluctuations reduce due to kinematic blocking and viscous damping, respectively. On the other hand, turbulence increases at the outer part of near wall area because of the large gradient of the mean flow velocity (Versteeg & Malalasekera, 2007). This behaviour of the flow in the boundary layer is described from the Law of the Wall, where the non-dimensional velocity, u^+ is given as function of the non-dimensional wall distance for a wall-bounded flow, y^+ (Versteeg & Malalasekera, 2007). The definitions for the dimensionless u^+ and y^+ are given in Eqs. 4.12 and 4.15, respectively:

$$u^+ = \frac{u}{u_*} \tag{4.12}$$

$$u_* = \sqrt{\frac{\tau_w}{\rho}} \tag{4.13}$$

$$\tau_w = \tau(y=0) = \mu\left(\frac{\partial v}{\partial y}\right)_{y=0} \tag{4.14}$$

$$y^+ = \frac{u_* y}{\nu_v} \tag{4.15}$$

where u is the local tangential velocity, u_* the friction velocity, τ_w the shear stress at the wall, and ν_v the kinematic viscosity. According to the Law of the Wall, the value of u^+ close to the wall is estimated from Eq. 4.16 for the part of the flow that lies in the viscous sublayer ($y^+<5$) and from the Eq. 4.17 for the part that lies in the log-law region ($y^+>30$).

$$u^+ = y^+ \tag{4.16}$$

$$u^+ = \frac{1}{\kappa}\ln(y^+) + B \tag{4.17}$$

where κ is the von Karman's constant that equals 0.41 and B a constant that depends on the wall roughness and is taken equal to 5.1 for smooth walls. The distribution of u^+ in the area close to the wall is shown in Fig. 4.1. For the transitional area (buffer layer) between the two zones ($5 < y^+ < 30$), the viscous and turbulent stresses are of similar magnitude and the flow exhibits laminar and turbulent characteristics. For y^+ ~11 the two lines intersect and this value is considered as the limit for the application of both laws.

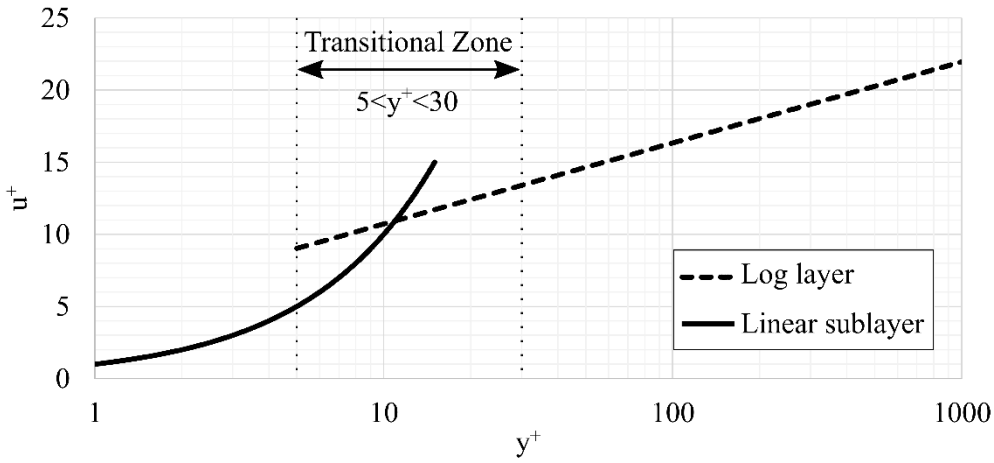

Figure 4.1 Velocity distribution in the near wall region (Humble, 2006).

The accurate modelling of the boundary layer area is of critical importance, in order to achieve reliable numerical results. The *k-ω* SST turbulence model combines the use of standard *k-ε* turbulence (Launder, 1974) in flow regions outside of the boundary layer with the use of its transformation to the *k-ω* turbulence model (Wilcox, 1988; 1993a; 1993b; 1994) in the near wall area, by applying the blending functions of Eqs. A.43 and A.59 (Appendix C). As a result,

the application of the *k-ω* SST turbulence model implies the resolution of the viscous sub-layer with the use of denser meshes in the near-wall area (FLUENT, 2009; Moukalled, 2016). In the present study, the estimation of the height of the first cell in the different parts of the computational domain of impeller No. 2 is described in the flowchart of Fig. 4.2.

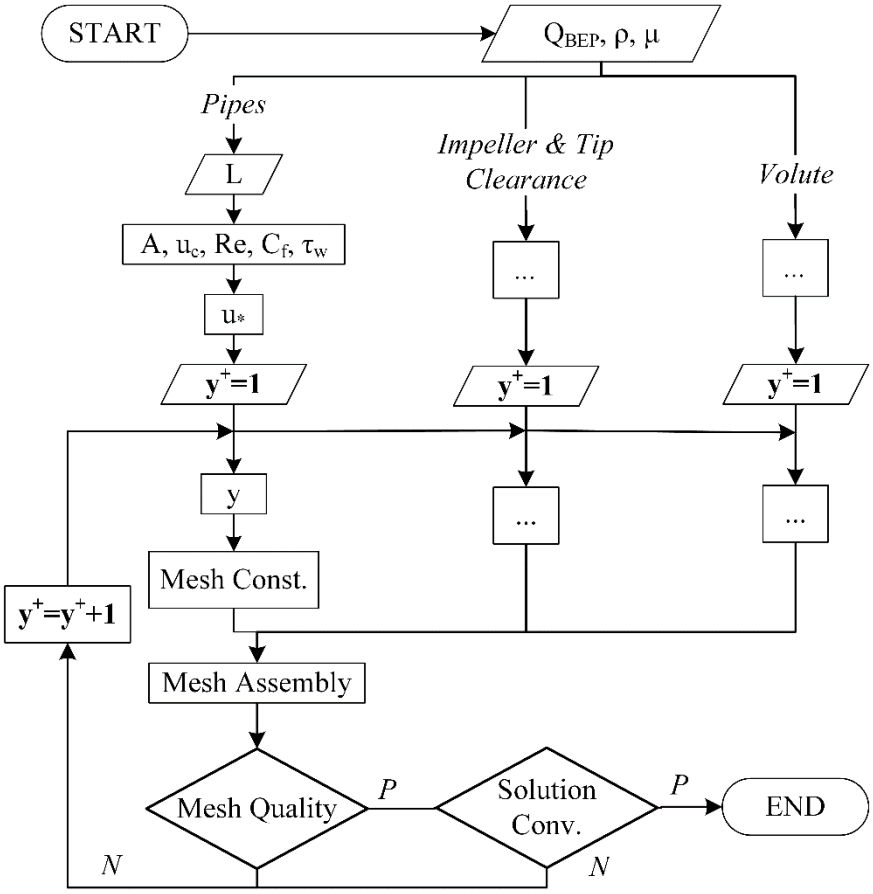

Figure 4.2 Flowchart of y^+ estimation and assessment during mesh construction procedure.

In Fig. 4.2, the L is the characteristic linear dimension, u_c the characteristic velocity of the corresponding part of the domain, *Re* the Reynolds number and C_f is the skin friction coefficient. Depending on circumstances, the L is assumed equal to the diameter of the pipes, the impeller and the volute. The measured best efficiency point (BEP) flowrate, Q_{BEP} is used for the calculation of u_c. The estimation of the shear stress at the wall is done through Eq. 4.18 (White, 2011) and the calculation of C_f and *Re* from Eqs. 4.19 and 4.20, respectively. Finally, the height of the first cell next to the wall is calculated from Eq. 4.15.

$$\tau_w = \frac{1}{2} C_f \rho u_c^{\,2} \tag{4.18}$$

$$C_f = 0.079\,\mathrm{Re}^{-0.25} \tag{4.19}$$

$$\mathrm{Re} = \frac{\rho u_c L}{\mu} \tag{4.20}$$

After the calculation of the height of the first cell at all wall boundaries of the domain (pipes, impeller and volute), the mesh is constructed and evaluated in terms of mesh quality and solution convergence. If these criteria are not satisfied the y^+ is increased by one unit ($y^+ = y^+ + 1$). The use of k-ω SST turbulence model restricts the y^+ to take values close to 1 but at the

same time, the mesh quality and computational power impose additional limitations. The consideration of these parameters concludes to an averaged value of $y^+ \sim 9$ on the rotating surfaces and the tip of the impeller No. 2.

4.2.3 Equations in the rotating reference frame

The adequate computational modelling of the flow in a centrifugal pump should incorporate the simulation of the stationary (inlet/outlet pipes and volute) and the rotating (impeller) parts of the pump. In order to satisfy this prerequisite, the present study uses the steady state approximation of multiple reference frame (MRF) approach (FLUENT, 2009). The latter accomplishes the adequate modelling of the flow in the pump by implementing the following steps:

i. The total computational domain is divided in zones that correspond to the rotating and stationary parts of the pump.
ii. For the first part the equations are solved in the rotating reference frame, in the form presented in this section (Eqs. 4.22 and 4.23).
iii. For the second part the equations are solved in the stationary domain with the use of Eqs. 4.1 and 4.2.
iv. Interface surfaces are defined between the rotating and stationary frames, with the MRF method (Fig. 4.3), which is used for the transformation of the equations between the rotating and stationary zones.

It is underlined that in MRF approach the computational mesh remains fixed during the numerical solution of the equations. Subsequently, the use of the term “rotating zone” in the present thesis, refers only to the type of the equations solved and does not imply that the zone is actually rotating.

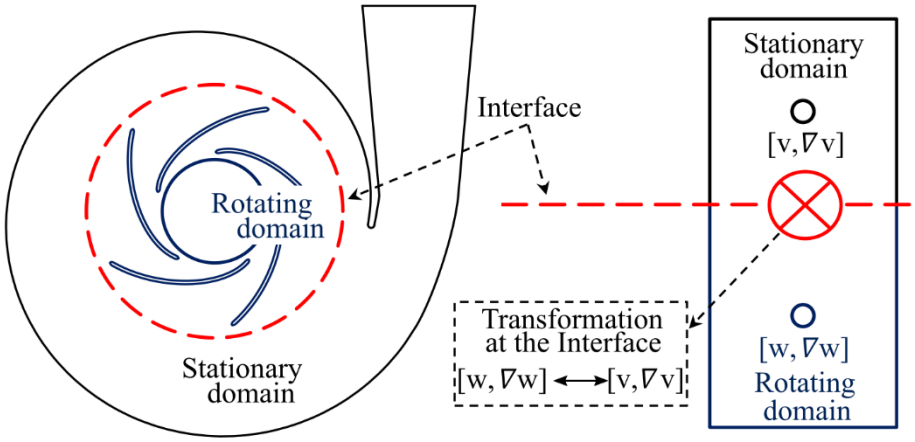

Figure 4.3 Schematic representation of the numerical domains of a typical centrifugal pump (Chrysovergis, 2017).

The mass and momentum equations presented in section 4.2.1 (Eqs. 4.1 & 4.2) are transformed from the Cartesian to the cylindrical coordinate system for the analysis of the flow in the rotating zones. This transformation is based on Eq. 4.21 that correlates the velocities in both coordinate systems:

$$\vec{w} = \vec{v} - \vec{\Omega} \times \vec{r} \tag{4.21}$$

where Ω is the rotation speed, w is the relative velocity (rotating system) and v is the absolute velocity. The corresponding mass and momentum equations that use the relative velocities as dependent variables (relative velocity formulation) become:

$$\frac{\partial \rho}{\partial t} + \nabla\left(\rho \vec{w}\right) = 0 \tag{4.22}$$

$$\frac{\partial}{\partial t}\left(\rho \vec{w}\right) + \nabla\left(\rho \vec{w}\vec{w}\right) + \rho\left(\underbrace{2\vec{\Omega}\times\vec{w}}_{Coriolis} + \underbrace{\vec{\Omega}\times\vec{\Omega}\times\vec{r}}_{Centripetal}\right) = -\nabla p + \nabla\left(\bar{\bar{\tau}}_r\right) + \vec{F} \tag{4.23}$$

4.2.4 Two-phase flow modelling

In this study the Zwart et al. (2004) model is used for the modelling of the vapour phase in the centrifugal pumps simulated. This is a homogeneous model, in which vapour and liquid phases are considered to behave as single medium (mixture) rather than two separate phases that interact with each other. Hence, only one set of governing equations is solved, and it is assumed that the two phases have the same dynamics, and there is no slip between them. The governing flow equations thus become:

$$\frac{\partial \rho_m}{\partial t} + \nabla\left(\rho_m \vec{v}\right) = 0 \tag{4.24}$$

$$\frac{\partial}{\partial t}\left(\rho_m \vec{v}\right) + \nabla\left(\rho_m \vec{v}\vec{v}\right) = -\nabla p + \nabla\left(\bar{\bar{\tau}}\right) + \rho_m \vec{g} + \vec{F} \tag{4.25}$$

where the mixture density ρ_m and the transfer equation that controls the mass transfer between the two phases are given by the following corresponding expressions (Zwart, 2004):

$$\rho_m = \rho_v \alpha_v + \rho_l \alpha_l \tag{4.26}$$

$$\frac{\partial}{\partial t}\left(\rho_l \alpha_l\right) + \nabla\left(\rho_l \alpha_l \vec{v}\right) = \dot{m}^+ + \dot{m}^- \tag{4.27}$$

where α_v, and α_l are the volume fractions of the vapour and liquid phase, respectively. The equations that describe the mass transfer evaporation rate, $\dot{m}^-$ and condensation rate, $\dot{m}^+$ are given by Eqs. 4.28 and 4.29, respectively.

$$\dot{m}^- = -C_{vap}\frac{3\alpha_v \rho_v}{R_B}\sqrt{\frac{2\left(p_{sat} - p\right)}{3\rho_l}} \tag{4.28}$$

$$\dot{m}^+ = C_{cond}\frac{3\alpha_v \rho_v}{R_B}\sqrt{\frac{2\left(p - p_{sat}\right)}{3\rho_l}} \tag{4.29}$$

where R_B is the radius related with the nucleation site, p_{sat} is the vapour saturation pressure, and C_{vap} and C_{cond} are vaporization and condensation coefficients, respectively.

These expresions (Eqs. 4.28 & 4.29) predict sufficiently condensation procedure ($\dot{m}^+$) but are not correct for the modelling of vaporization conditions $\dot{m}^-$ (Zwart, 2004). The reason is the assumption that vapour bubbles do not interact with each other, which only applies during the first stages of vaporization, where vapour bubble expands from the nucleation sites. However, passing to conditions with increased vapour volume fraction, this assumption is not valid and the nucleation site density should decrease. In order to include the correct physics for the

modelling of vaporization procedure, the term α_v in Eq. 4.28 is replaced with the term $\alpha_{nuc}(1-\alpha_v)$ and the final form of mass transfer evaporation is given in Eq. 4.30.

$$\dot{m}^- = -C_{vap}\frac{3\alpha_{nuc}\left(1-\alpha_v\right)\rho_v}{R_B}\sqrt{\frac{2\left(p_{sat}-p\right)}{3\rho_l}} \tag{4.30}$$

where α_{nuc} is the nucleation site volume fraction. The values for the model coefficients used in this study are: $R_B=10^{-6}$ m, $\alpha_{nuc}=0.0005$, $C_{vap}=50$ and $C_{cond}=0.01$. These values are proposed by Zwart et al. (2004) and have been found to work decently in studies related with two-phase flow modelling in semi-open radial hydraulic turbomachinery applications (Bakir, 2004; Liu, 2012; Zhang D., 2015a; Zhang D., 2015b; Zhang D., 2015c; Limbach, 2017).

4.3 Meshing strategy

In section 4.3, the strategy for the construction of the mesh of impeller No. 2 is described along with the presentation of the meshing details of impeller No. 4. In the present study, the numerical model is applied, so as to examine its effectiveness towards the identification of the cavitation formations in centrifugal pumps, for a wide range of flowrate and suction conditions. An additional reason for the development of the present numerical model is the need to improve the current understanding of the flow mechanisms that drive cavitating flows. A characteristic example is discussed regarding the flow visualisation results for the semi-open impellers of section 3.3.2, where it is not possible to perceive the type of cavitation in the tip clearance area, since the experimental configuration does not provide information for the local flow conditions. Such difficulties can be overcome with the use of the numerical model developed and validated in the present Chapter.

The intention to study and compare the two-phase flow development in two geometries that differ significantly in respect to; i) the shroud, ii) the inlet blade angle, β_1, and iii) the number of blades used, justifies the selection of impellers No. 2 and 4. More specifically, the geometrical similarities between the impellers of Lancaster University (LU), allowed the modelling of one out of the three impellers, so as to provide the characteristics needed from the numerical model. Impellers No. 1, 2 and 3 are all semi-open impellers of the same diameter and nominal rotation speed (see section 3.2). On the other hand, they present geometrical differences with respect to their blade shape and the number of blades.

Nevertheless, the selection to model also impeller No. 4 makes possible the consideration of the aforementioned geometrical differences. More specifically, impeller No. 2 is a semi-open impeller with β_1=85º and consists of twelve blades, while impeller No. 4 is a closed impeller with β_1=25º and is made with five blades. Also, the flow visualisation results of impeller No. 4, which are presented in Fig. 3.13 (section 3.3.2), reveal the limitation of the test configuration to identify the formation of the cavities during their initial stages of development. Consequently, the modelling of the NTUA impeller also allows to improve the estimation regarding the NPSH and σ values that correspond to the visual inception of cavitation.

The procedure followed for the mesh construction of impeller No. 2 is described in the following steps:

i. Geometry digitization in the solid modelling software.
ii. Extraction of the fluid domain that is modelled.
iii. Geometrical changes, in order to simplify the meshing procedure and reduce computational cost.
iv. Definition of the rotating and stationary zones, along with the interfaces.
v. Construction of four meshes (finer to coarser).
vi. Simulation of the four meshes under identical boundary conditions that correspond to intermediate cavitation development, so as to quantify the dependence of the results on the of spatial discretization.
vii. Selection of the final mesh used throughout the Thesis.
viii. Study of the relative blade position influence.

The geometry, the mesh, and the boundary conditions on the walls of the domain of impeller No. 4 are taken from the studies of Kassanos et al. (2016a) and Chrysovergis (2017). Consequently, the mesh convergence study (steps v & vi) and the study of the blade position influence (step viii) are not provided in this Thesis.

4.3.1 Impeller No. 2

4.3.1.1 Computational domain

The mathematical model presented in section 4.2, is used at first for flow simulations in the semi-open impeller No. 2. The non-axisymmetric flow conditions in the impeller, due to the spiral volute and the inlet bent pipe discussed in section 2.5.1, make necessary the modeling of

the entire impeller, along with the volute and the elbow (Fig. 4.4). In this way, the flow conditions are adequately represented and optimal comparisons could take place between the numerical and experimental results. Furthermore, the precise application of the boundary conditions at the inlet and outlet of the fluid domain entails the extension of the computational domain until the positions of static pressure measurement at the inlet and outlet pipes. The construction of the computational domain is done through the digitization of the geometry of that part of LU test rig, which is included between the inlet and outlet boundaries and depicted in Fig. 4.4a. The extraction of the fluid domain presented in Fig. 4.4b, is done by the adequate subtraction of bodies in SolidWorks computer-aided design software.

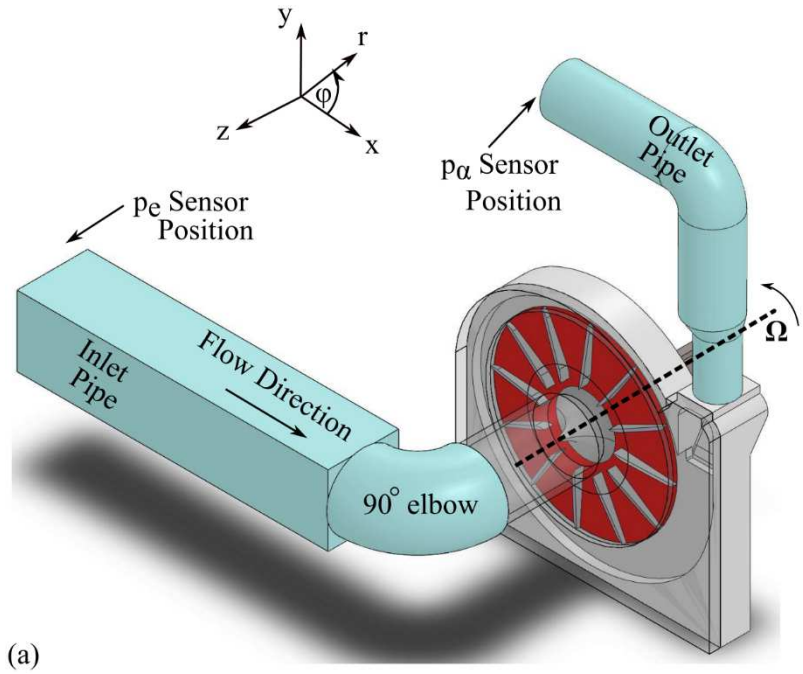

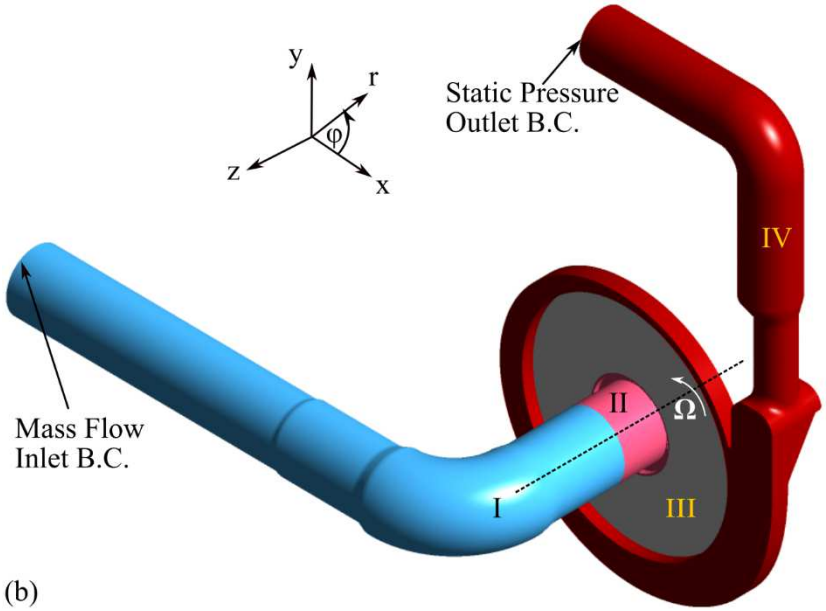

Figure 4.4 a) Digitised geometry and **b)** computational domain of impeller No. 2.

The computational domain is divided in four zones, as highlighted in Fig. 4.4b: the inlet pipe (I), the impeller inlet section (II), the impeller blades (III), and the volute with the outlet pipe (IV). Zones I and IV are stationary and the flow equations for zones II and III are solved in the rotating reference frame with n=1800 rpm, similar to the experimental conditions. The

imported geometry of zone III is shown in Fig. 4.5 and includes the twelve straight blades (grey colour), the hub of the impeller (dark blue colour) and the outer boundary of the tip clearance (transparent blue colour).

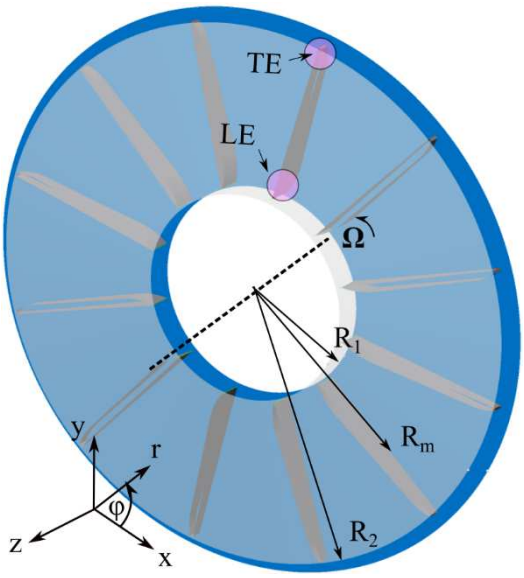

Figure 4.5 Imported geometry of zone III of impeller No.2 in ANSYS turbogrid.

In addition, zone III includes the original front tip clearance between the rotating blades and the stationary casing, with thickness t_{tc}=0.9 mm. The front tip clearance is presented in Figs. 4.6a (zoom in area A) and 3.6b. In Fig. 4.6a the axis origin position of the LU pump domain is highlighted. Zones I and IV are meshed with tetrahedral elements, except of the straight pipes, where the discretization is done with hexahedral elements. The impeller inlet section is meshed with tetrahedral elements, whereas the blades zone III is meshed as blade-to-blade topology in ANSYS Turbogrid with hexahedral elements. Three interface areas are defined between the four zones, and are presented in Figs. 4.6b, 4.8 and 4.12.

The reason that the impeller is split in two zones (II & III) is the inlet casing protuberance presented in Fig. 4.6 that introduces three angles of ~90° (red colour angles of Fig. 4.6b) in the flow direction. The presence of such an abnormal configuration in the suction of the impeller accelerates the flow and increases significantly the losses, hence making all the Lancaster University impellers prone to cavitation.

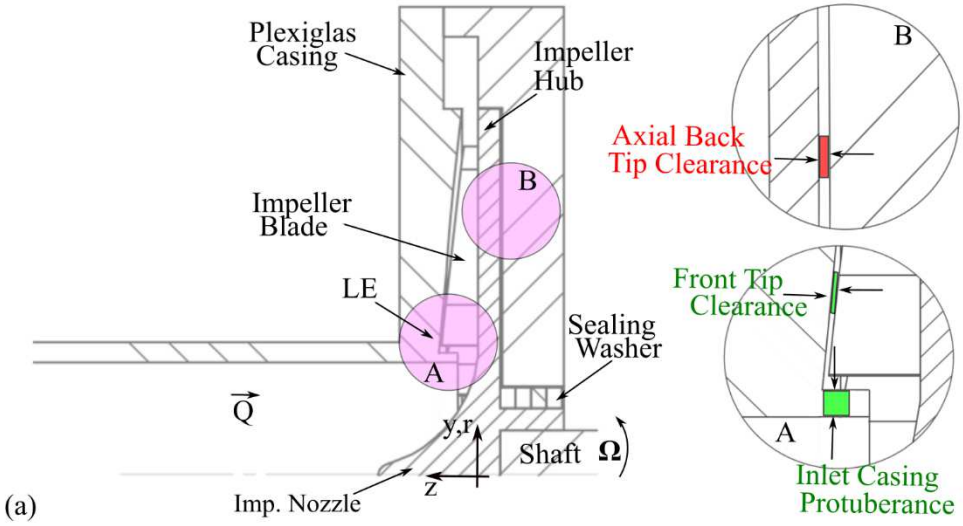

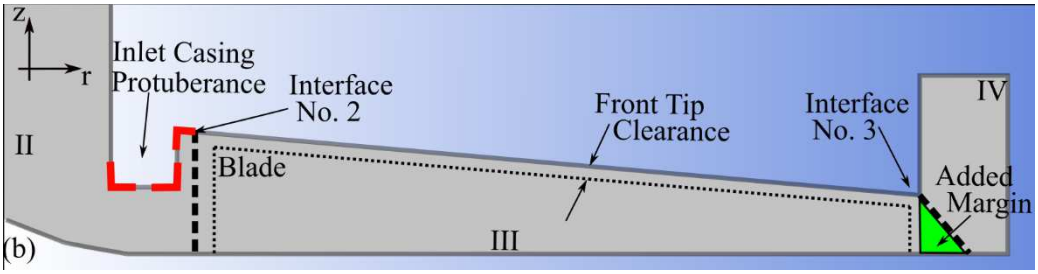

Figure 4.6 Meridional view of: **a)** the pump with two zoom in areas (A & B) that depict the two tip clearances and the protuberance at the inlet's casing and **b)** the computational domain of impeller No. 2.

By this way, the test configuration of Lancaster University achieves to create and visualise two phase flow development without throttling substantially the suction valve. In order to improve the quality of the mesh at the pump inlet, where the flow velocity exhibits strong variation in both magnitude and direction, the impeller domain is split in two parts (Fig. 4.6b); part II that includes the inlet part of the impeller form interface No. 1 (Fig. 4.8) until the impeller's nozzle (Fig. 4.6a) and is meshed with tetrahedral elements, and part III that includes the main body of the impeller, presented in Fig. 4.5 that is meshed with hexahedral elements.

Two geometrical modifications are introduced during the construction of the computational domain. Firstly, the effect of the axial load balance holes along with that of axial back tip clearance between the rotating hub and the stationary casing, presented in the zoom-in area B of Fig. 4.6a, are not included in the computational domain. This simplification is selected due to the large number of cells required to model the thin area of axial back tip clearance compared to its contribution to the efficiency of the pump. More specifically, impeller No. 2 does not have holes for the balancing of the axial loads, which results in negligible volumetric losses through this region behind the hub. In this pump, the axial back tip clearance mainly affects the rotating disc mechanical (power) losses, which are the result of the friction produced between the rotating hub and the fluid. The torque that corresponds to the rotating disc mechanical losses (M_s) is calculated by Eq. 4.31 (Papantonis, 2016) and added to the torque simulated, so as to adequately estimate the power and efficiency characteristic curves of the pump.

$$M_s = \left(c_M \rho \Omega^3 R^5\right)/4 \tag{4.31}$$

where R is the impeller's radius and c_M (Eq. 4.32) is a coefficient that is function of the peripheral Reynolds number (Eq. 4.33):

$$c_M = 0.0622 Re_p \tag{4.32}$$

$$Re_p = \Omega R^2 / \nu_v \tag{4.33}$$

The second modification deals with the added margin at the outer radious (R_2) of the rotating impeller, in order to increase the distance of the trailing edge of the blade from the interface No. 3. By increasing this distance, the effect of possible errors, introduced at the interface, to the calculation of the blade's flowfield, is eliminated. This area is depicted with the green colour triangle in Fig. 4.6b.

4.3.1.2 Mesh presentation

Four structured meshes are constructed for the impeller blades area (zone III), in order to study the convergence of numerical solution as spatial discretization becomes denser. All meshes are shown in Fig. 4.7, where emphasis is given at the LE area of the blade, the design of which is critical for the onset of cavitation. The green, white, blue and red coloured areas depict the hub, the blade, the tip clearance and the interface No. 2, respectively. The number of

elements used increases along the two directions depicted in Fig. 4.7 (mesh No. 1); e_1 refers to the number of cells used at the area between the two blades on x-y plane, and e_2 refers to the number of cells used at the area between the hub and the blade tip on yz plane.

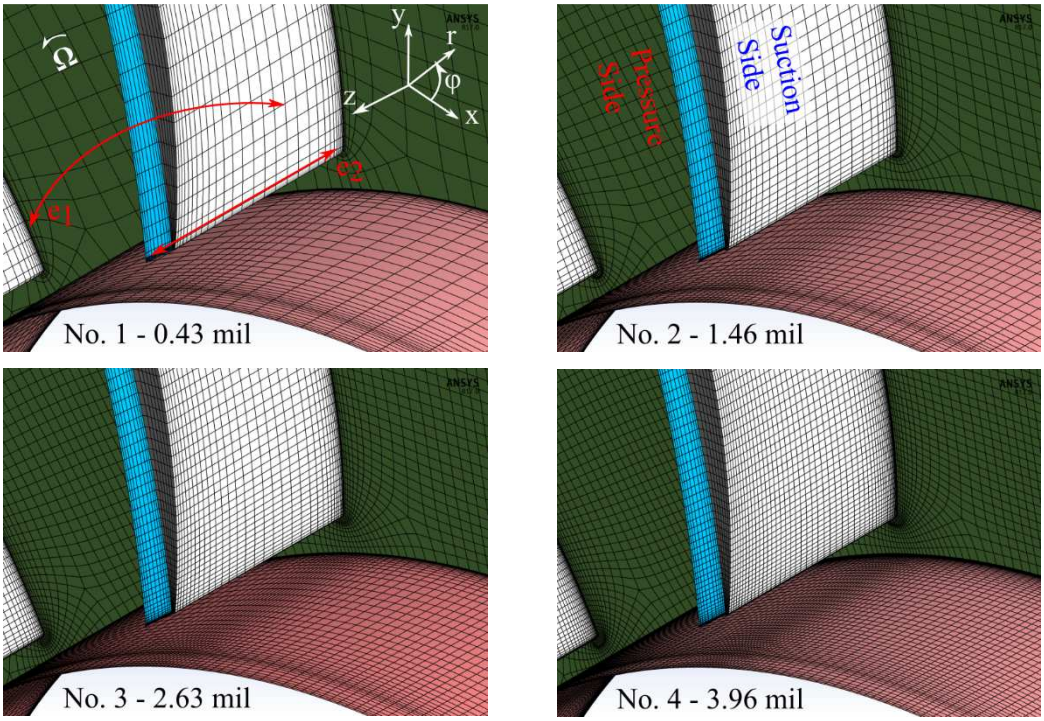

Figure 4.7 Various meshes at the leading area of the blade of zone III for impeller No. 2, with different number of elements.

On the other hand, three different meshes are constructed for zones I, II and IV, and their cross section at yz plane is shown in Fig. 4.8. In this figure, the hexahedral elements used for the pipes (zone I) and the tetrahedral elements used for the impeller inlet (zone II) and the volute (zone IV) can be observed. For these zones, the denser meshes are derived by decreasing the size of the cells. Special care is given in the handling of the protuberance surfaces (Fig. 4.6b), where smaller size elements are added on the 90º surfaces.

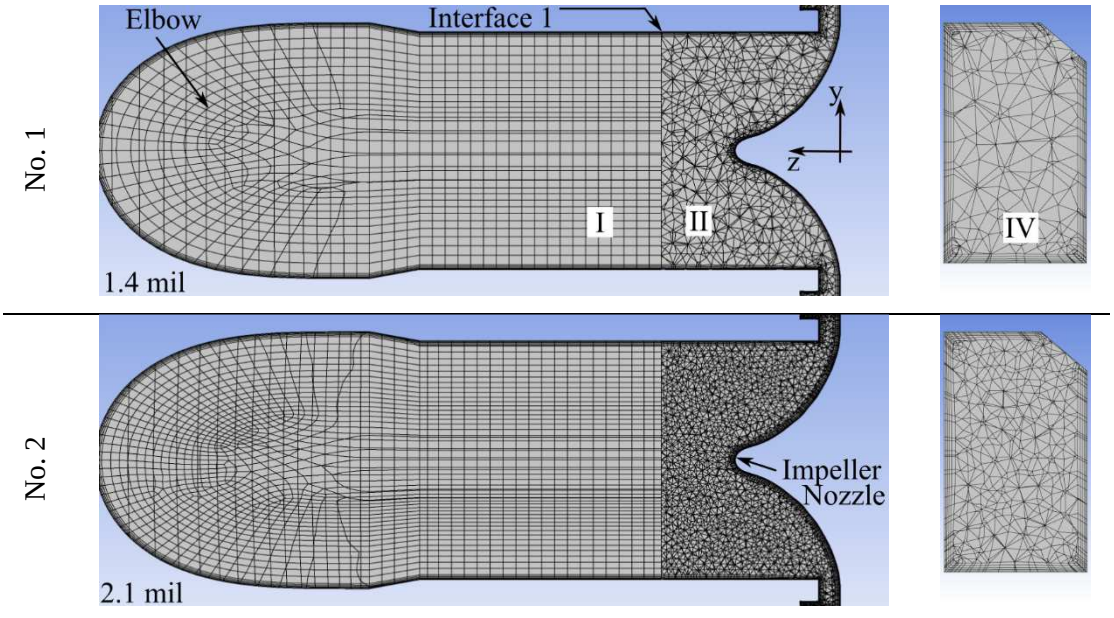

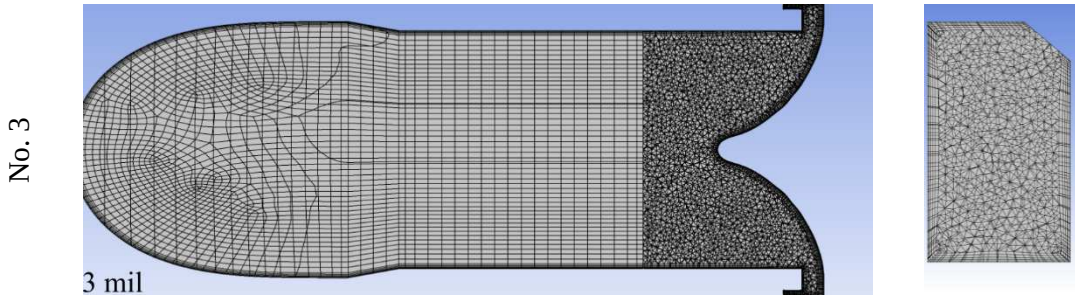

Figure 4.8 Meridional view of various meshes configuration at zones I, II, IV, for the impeller No. 2.

The complete meshes are made up from the individual meshes in the four zones (Fig. 4.9) that are merged in tmerge17.0 ANSYS tool and their cell size characteristics are provided in Table 4.1. In Fig. 4.9 it can be observed that meshes No. 2 and 3 have the same structure in zones I, II and IV. This is adopted, in order to further investigate the mesh convergence study in the most critical impeller area of the impeller.

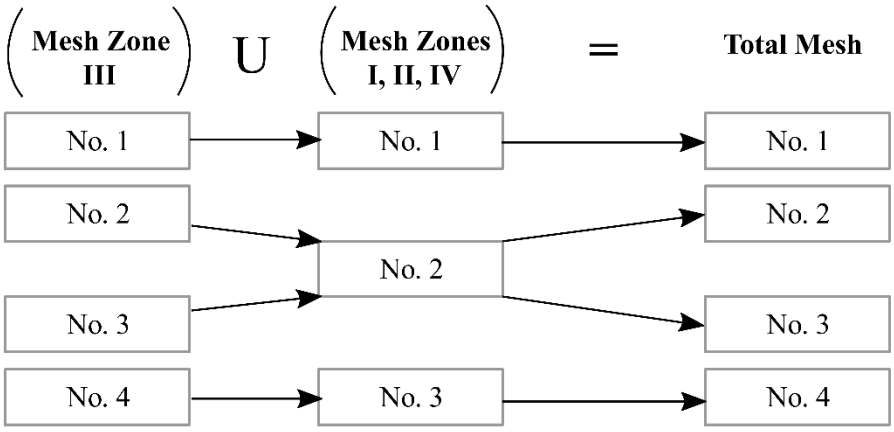

Figure 4.9 Mesh composition of the entire computational domain.

Table 4.1 Mesh characteristics for the impeller No. 2.

Total Mesh		**Mesh for Zone III**				**Mesh for Zones I, II, IV**				
No.	El. ($\times 10^6$)	No.	El. ($\times 10^6$)	e_1	e_2	No.	El. ($\times 10^6$)	Size of El. [mm]		
								I	II	IV
1	1.83	1	0.43	12	15	1	1.4	2.6	2.6	2.6
2	3.56	2	1.46	30	33	2	2.1	1.5	1	1.5
3	4.73	3	2.63	36	42	2	2.1	1.5	1	1.5
4	6.96	4	3.96	50	60	3	3	1.2	0.5	0.7

4.3.1.3 Mesh convergence study

The Mesh Convergence Study (MCS) is carried out for a compex flow field, obtained at partial flowrate $\Phi=0.076$ ($0.80\Phi_{BEP}$) and under CCs with outlet boundary condition $P_{out}=55.3$, using the four different density meshes of Table 4.1. The selection of a partial flowrate for the MCS is made because the vast majority of the cavitation tests of impeller No. 2 are executed in partial flowrates. The mesh independence of the above four quantities, which are important for the calculations in the Thesis, are studied; the non-dimensional variables of σ, Ψ and η are shown in Fig. 4.10a and the static pressure around the blade, from the leading edge to the trailing edge, are given in Fig. 4.10b. From the results presented in Fig. 4.10, it can be observed

that the aforementioned parameters are stabilised for meshes with resolution equal or higher than that of mesh No. 2.

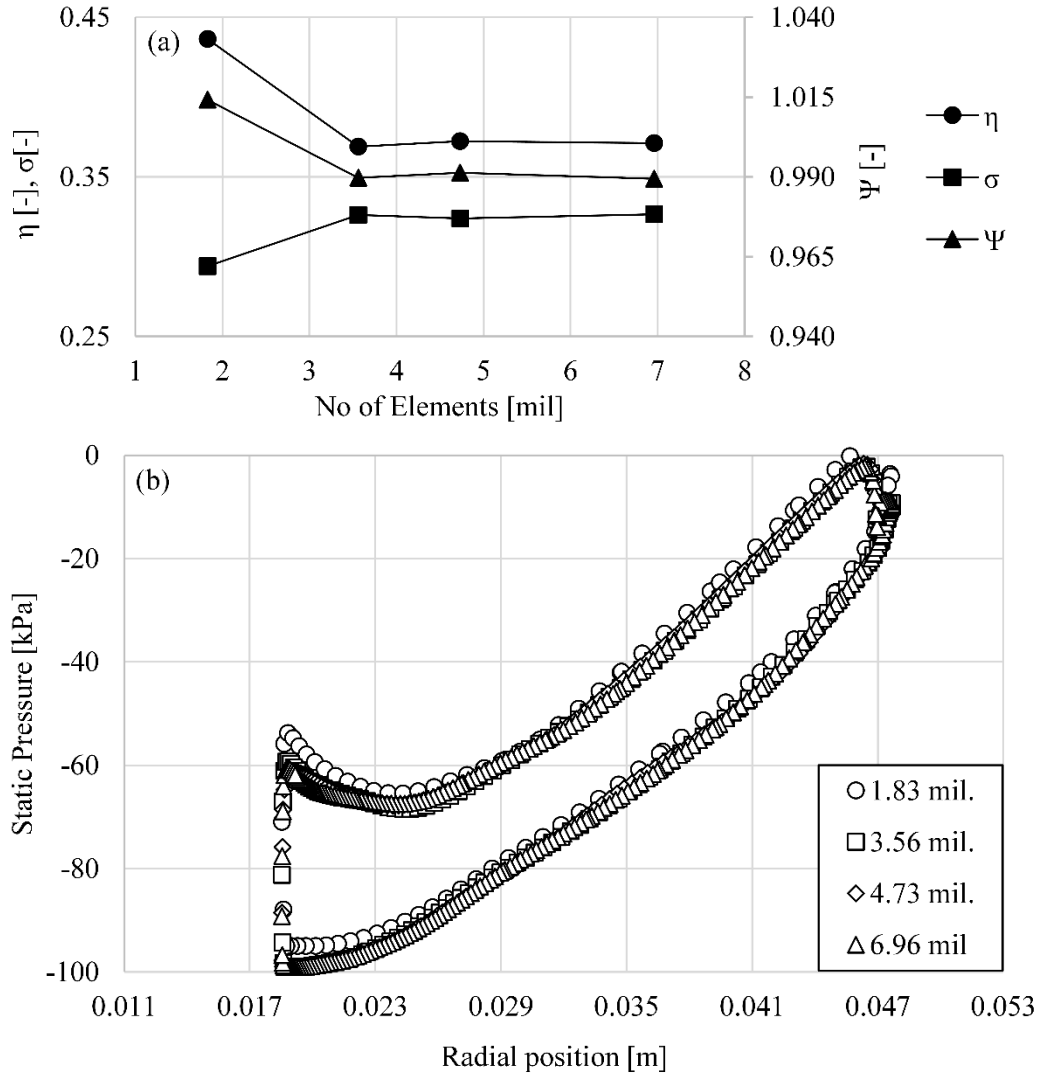

Figure 4.10 Mesh convergence study of **a)** σ, η and Ψ and **b)** of the static pressure around the blade on the x-y plane, for z=2mm.

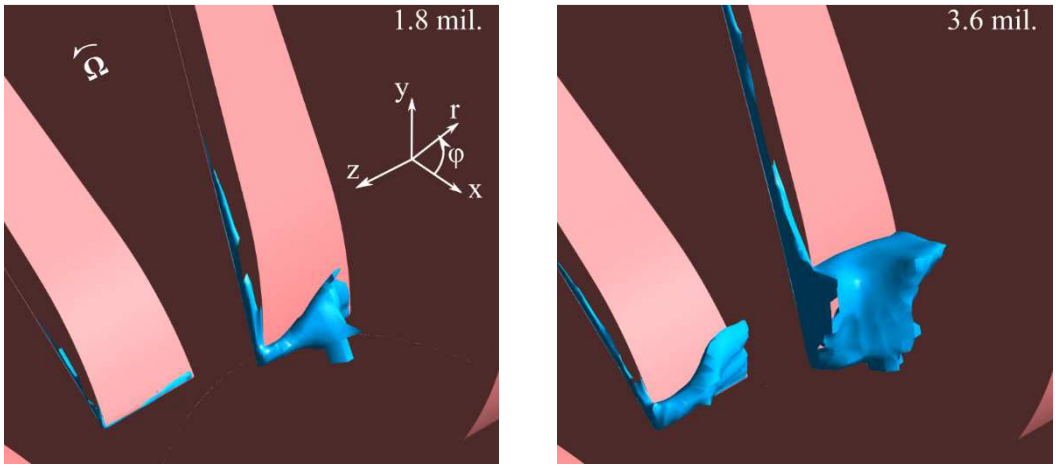

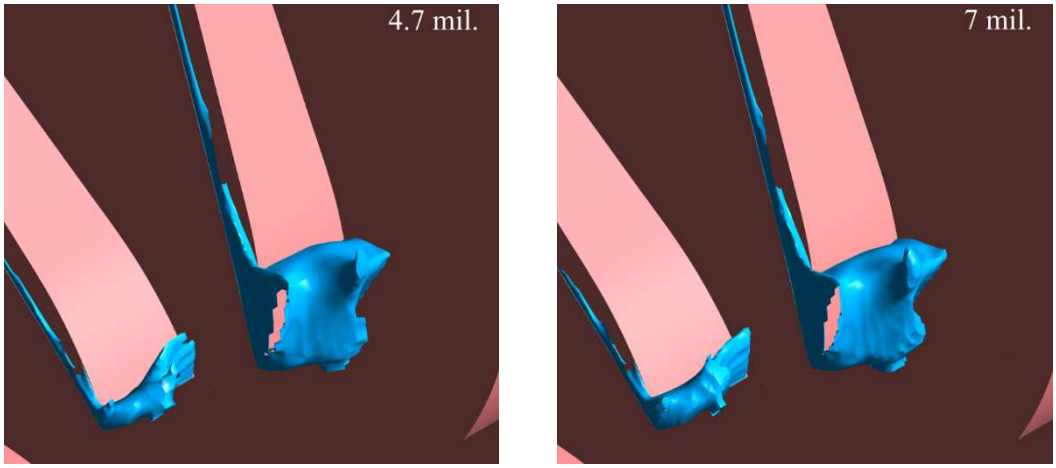

Figure 4.11 Isosurfaces of vapour pressure area at the LE of the blades.

The area covered by vapour at the suction side of the impeller is studied, in order to determine when its shape and extent become spatially independent. As a consequence, the isosurfaces of the vapour pressure area are plotted for the four meshes in Fig. 4.11, where it can be observed that the cavitation area computed by three finer meshes has similar shape and size. Consequently, the complete mesh No. 2, with 3.6 million elements in total is selected to be used throughout the present study. Its meridional view in the entire computational domain is shown in Fig. 4.12. The minimum orthogonal quality and the maximum skewness and aspect ratio of all elements used in this mesh are 0.16, 0.83 and 450, respectively.

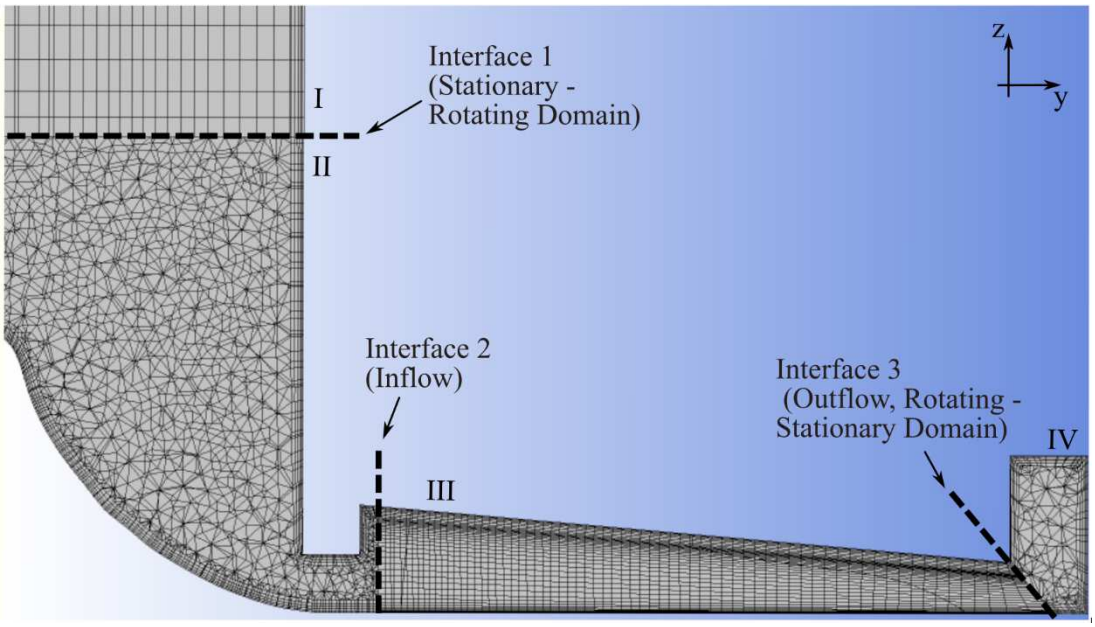

Figure 4.12 Section at yz plane for the total mesh of impeller No. 2.

4.3.1.4 Influence of blade position

After the selection of the final mesh, the effect of the impeller blades angular position relative to the volute is studied. In cases of steady state MRF simulations that include the total turbomachinery domain (impeller and volute), the interaction between the volute tongue and the impeller's blade should be investigated (Dick, 2001). For this reason, the impeller section is rotated in various different angles (θ_1, θ_2 & θ_3) relative to the reference position examined in the MCS in the oposite direction of φ, and the simulations are performed for the same OP (Φ=0.80·Φ_{BEP} and σ=*0.33*). The relative impeller rotation is shown in Fig. 4.13a and the corresponding angles are calculated from Eq. 4.34 (in degrees):

$$\theta_i = \theta_{i-1} + 0.25\left(\frac{360}{z_s}\right), \quad i = 1,2\,\&\,3, \quad \theta_0 = 0\,\text{deg} \tag{4.34}$$

where z_s is the number of blades.

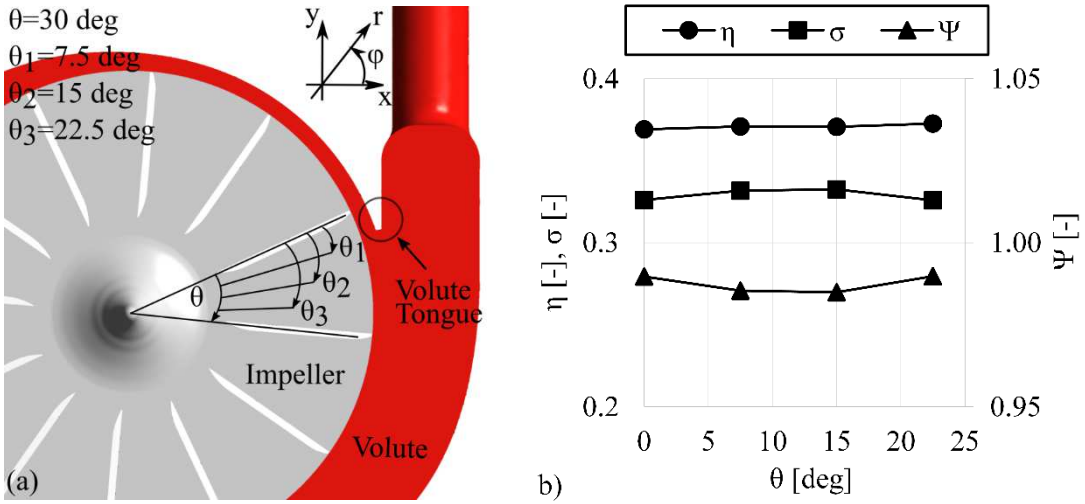

Figure 4.13 a) Impeller relative angular position, and **b)** its effect on the resulting values of η, σ and Ψ.

The simulation results of η, σ and Ψ values at four different angles are shown in Fig. 4.13b. The results for θ_0=0 deg correspond to those presented in the MCS in section 4.3.1.3. It can be seen that all these physical quantities are very slightly influenced by the exact impeller's position. Efficiency, cavitation Thoma number and the non-dimensional head, vary less than 1.5%, 2% and 0.5%, respectively. For this reason, the computational domain with the impeller at position θ=θ_0 is considered suitable and representative for the simulations of the present study.

4.3.2 Impeller No. 4

The computational domain and the final mesh of impeller No. 4 are taken from the studies of Kassanos (2016a) and Chrysovergis (2017), where single flow conditions have been discussed in detail for this pump. As a consequence, only the computational domain, its simplifications and the final mesh are presented in this section.

4.3.2.1 Computational domain and simplifications

The fluid domain of impeller No. 4 is constructed in the same way with impeller No. 2, and is given in Fig. 4.14. The domain is split into three zones; the inlet pipe (I – blue colour), the impeller (II – grey colour) and the volute (III – red colour). The flow equations in Zones I and III are solved in the stationary form, while those of zone II in the rotating reference frame with n=2900 rpm. Similarly to impeller No. 2, the inlet pipe and the impeller are meshed with hexaedral elements, whereas in the volute the discretization is done with tetrahedral elements.

The computational domain of impeller No. 4 does not include the two clearances shown in the mechanical drawing of Fig. 4.15 (enclosed with red colour dots); the areas between the shroud and the front casing (i), and between the hub and the back casing (ii). In the same figure, the recirculating flow pathlines from the high pressure area at the impeller exit to the low pressure inlet area are also drawn (blue streamlines).

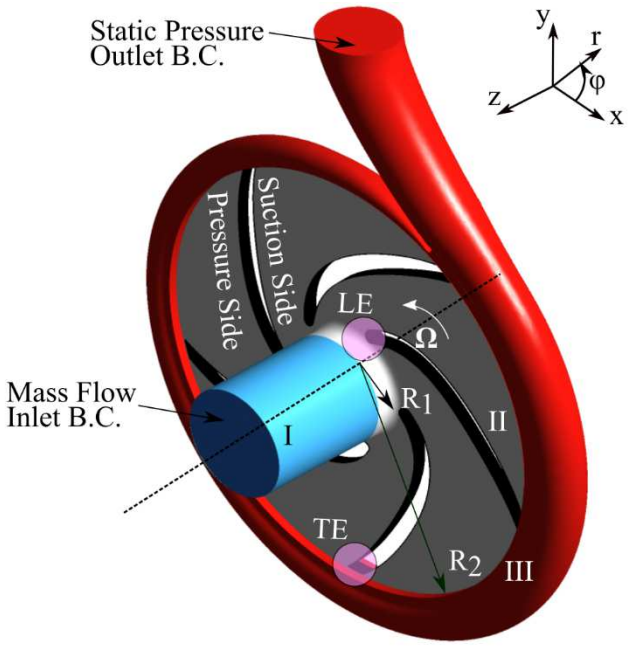

Figure 4.14 Computational domain of impeller No. 4.

The balance holes manufactured on the shroud at $r \sim R_{1h}$ allow some high pressure water to return at the inlet of the impeller, and hence the axial thrust on the impeller is reduced. The volumetric losses related with these two clearances are not modelled in the domain of Fig. 4.14, and consequently, the efficiency and head of the pump are expected to obtain higher values in the numerical results, compared to the experimental measurements. On the other hand, the torque that corresponds to the hydraulic losses due to the rotating flow friction developed here in both clearance areas (in front of the shroud and behind the hub) is calculated similarly to the impeller No.2, from Eq. 4.35, and it is added to the simulated torque of the impeller:

$$M_s = \left(c_M \rho \Omega^3 R^5 \right) / 2 \tag{4.35}$$

$$M_e = M_m \zeta_e \tag{4.36}$$

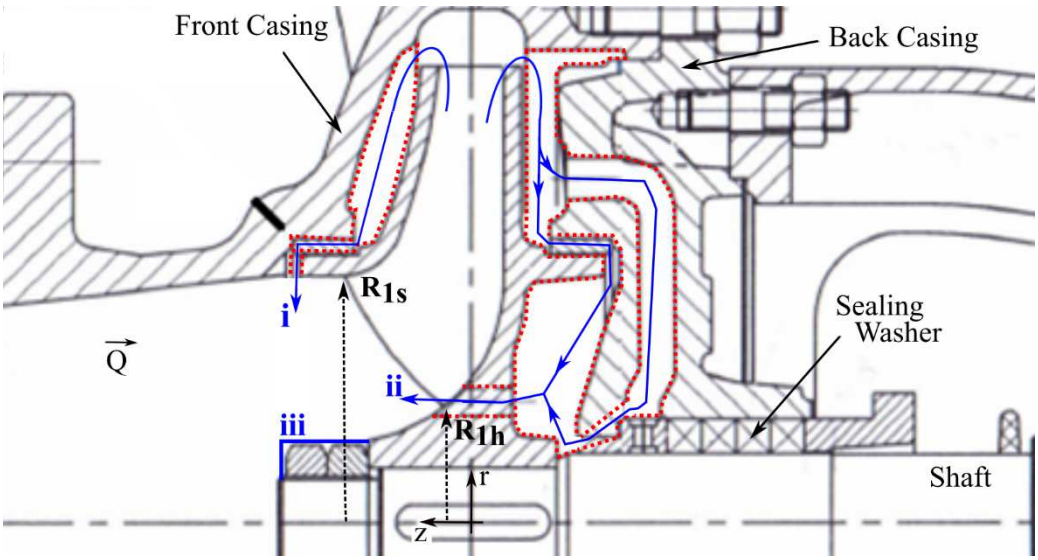

Figure 4.15 Backflows (i & ii) and tightening nuts (iii) of the simulated impeller LDP 32-160 (impeller No. 4).

The mechanical losses at the bearings of the pump are estimated from Eq. 4.36, using a bearing loss coefficient, ζ_e=0.04, proposed for small radial centrifugal pumps (Papantonis, 2016). Finally, a geometrical simplification with much lower impact on the simulation results is the replacement of the two nuts used for tightening the impeller at the pump's shaft, with a cylinder, as it shown in Fig. 4.15 (area iii).

4.3.2.2 Mesh presentation

A z-r section of the total mesh used in this study is shown in Fig. 4.16a, along with the two interface areas defined between the three zones. In the same figure the axis origin position of the NTUA pump domain is highlighted. A detailed view of the mesh at the inlet of the impeller domain (zone II) is presented in Fig. 4.16b, where the green, white and red coloured areas correspond to the hub, the blade and the interface No. 1, respectively. The mesh characteristics for the impeller No. 4 are given in Table 4.2. The minimum orthogonal quality and the maximum skewness and aspect ratio of all elements used in this mesh are 0.09, 0.83 and 300, respectively. The average y^+ value for the walls of impeller No. 4 computational domain, calculated for the nominal flowrate, is 10.

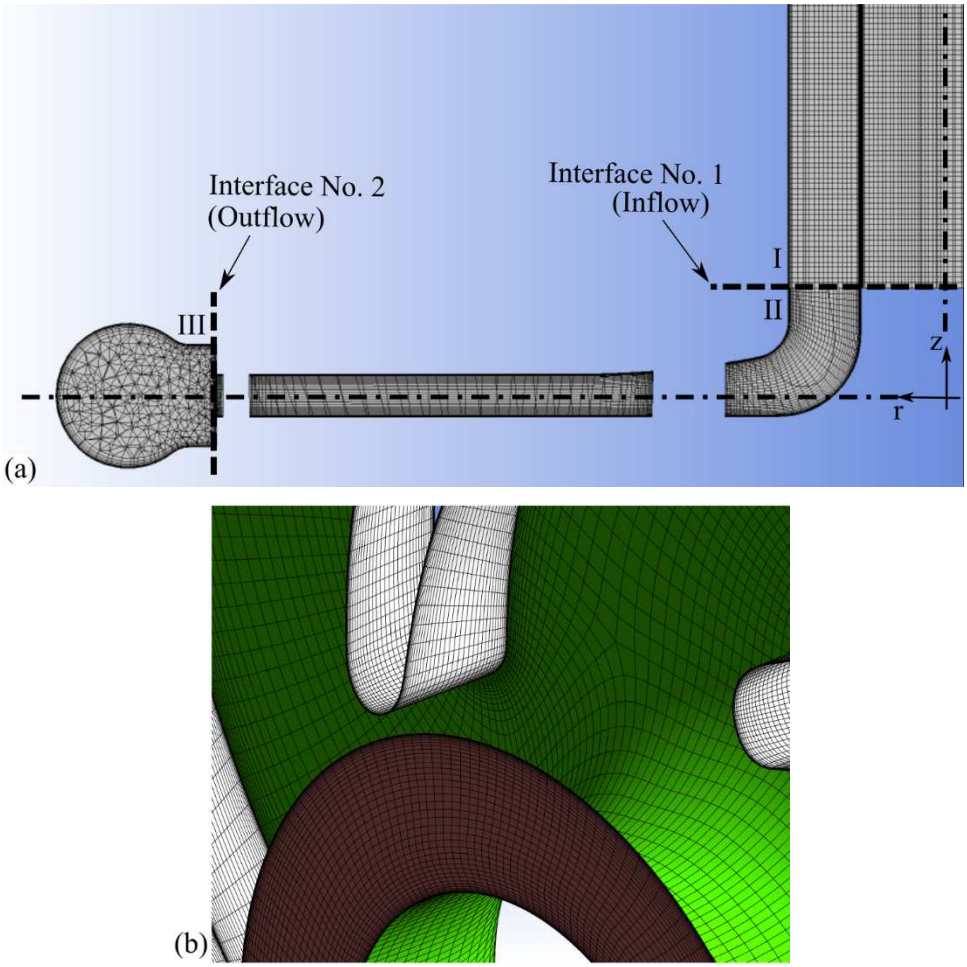

Figure 4.16 a) Mesh configuration at a z-r plane, and **b)** detailed view at the inlet section of impeller No.4.

Table 4.2 Mesh characteristics for impeller No. 4.

Total Mesh		**Mesh for Zone II**				**Mesh for Zones I, III**			
No.	El. ($\times 10^6$)	No.	El. ($\times 10^6$)	e_1	e_2	No.	El. ($\times 10^6$)	Size of El. [mm]	
								I	III
1	3.2	1	1	22	28	1	2.2	0.8	1

4.4 Boundary conditions

The modelling of the entire domain (all impeller blades with the inlet/outlet pipes and the volute) of a hydraulic turbomachinery requires the definition of the boundary conditions (BCs) at the inlet and outlet areas, as well as at the internal walls of the computational domain. The proper application of the wall boundaries requires the definition of the shear condition and the walls motion. The shear BCs are the same for all the walls of the domain, where the no slip condition is applied. A value of absolute roughness equal to 70 μm on the walls of the computational domain of closed impeller No. 4 (Kassanos, 2016a). In the case of semi-open impeller No. 2, the absolute roughness is set equal to 0 μm. The differences in the value of the absolute roughness reflects the use of different materials for the construction of the two pumps; on the one hand the LU pump is made of Plexiglas (pipes, volute) and aluminium (impellers), while the NTUA pump is made mainly by copper (hub and blades) and steel (volute and pipes).

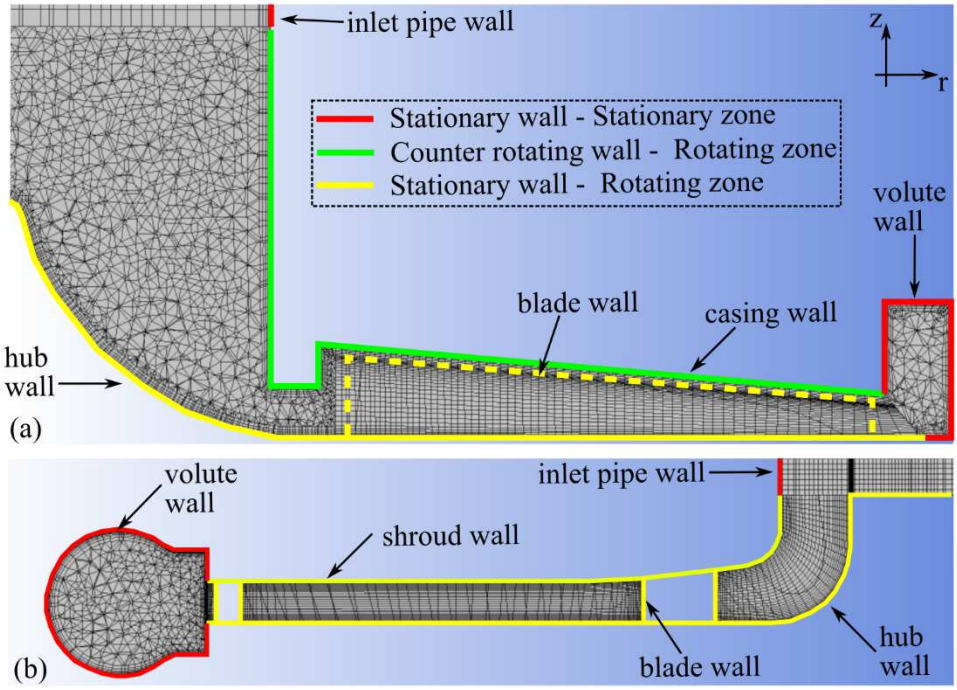

Figure 4.17 Wall motion BC at the meridional view of **a)** impeller No. 2 and **b)** impeller No. 4.

On the other hand, the flow simulations are carried out in the rotating (with the impeller) system of reference. Hence, the wall motion boundary takes one of the three conditions shown in Fig. 4.17a; stationary wall in a stationary zone (red colour), counter rotating wall in a rotating zone (green colour), and stationary wall in a rotating zone (yellow colour). For both impellers, the walls of the pipes and the volutes, which are located in stationary zones, and the walls of the hubs and the blades, which are located in rotating zones, are defined as stationary. The selection of the wall motion of the casing at impeller No. 2 and the shroud at impeller No. 4 highlights the modelling differences between semi-open and closed impellers. For impeller No. 2 the casing wall is considered as counter rotating wall on a rotating zone, while the shrouded wall of impeller No. 4 is defined as stationary wall on a rotating zone.

Mass flow inlet (MFI) and static pressure outlet (SPO) BCs are applied at the inlet and outlet areas of both impellers, as it is shown in Figs. 4.4b and 4.14. The values given at the inlet and outlet BCs are taken directly from the experimental measurements so as to reduce possible uncertainties introduced from the BC application and also to validate the model performance under identical operating conditions with those of the experiments.

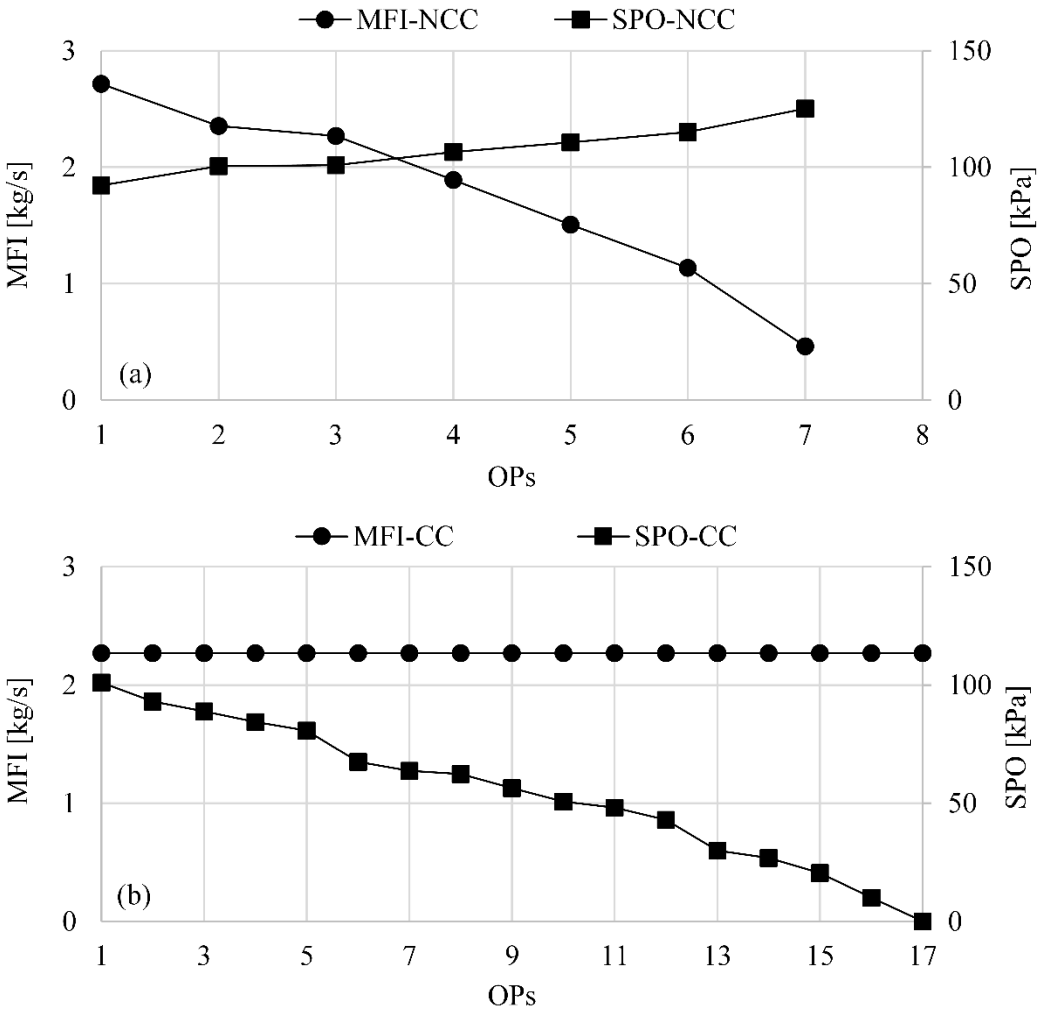

Figure 4.18 Inlet and outlet BCs for simulations of impeller No. 2, under **a)** NCCs and **b)** and CCs.

The BCs used for the derivation of performance curves under non-cavitating conditions (NCC) are depicted in Figs. 4.18a, for impeller No. 2. In Fig. 4.18b, the BCs for the simulations under CCs and for a typical Φ value are presented again for impeller No. 2. The pattern of boundary conditions at the different operating points is identical for impeller No. 4. The number of OPs is higher for CCs, because of the need to simulate a wide range of cavitating conditions, which will correspond to the conditions of the tested impeller. In addition, the simulations under CCs are performed at constant flowrate, similarly to the experiments, while the study of NCCs requires the computation of several flowrates. On the other hand, in both plots of Figs. 4.18, the SPO value decreases for CCs and increases for NCCs. This behaviour imitates the experimental procedure, where the static pressure level of the configuration is progressively reduced in the case of CCs. On the other hand, the decrease of MFI BC during the non-cavitating conditions drives the static pressure at the outlet to higher values.

The value of vertical distance z, between the inlet (e) and outlet (a) positions, is z=0.305 for impeller No. 2 and z=0.53 m for impeller No. 4. For cavitation simulations, no vapour is assumed at the inlet area (MFI of vapour phase is given equal to 0 kgs^{-1}). The vapour pressure for the water was set to p=2.8 kPa and to p=2.3 kPa that corresponds to T=23 °C and T=20 °C for impellers No. 2 and 4, respectively. Both vapour pressure values are absolute pressures. These are the temperatures that all the experiments were carried out at the two test rigs, respectively.

4.5 FLUENT solver

The computational meshes constructed in the above pump flow field domains are used for the numerical solution of the equations described at section 4.2 with the commercial software ANSYS Fluent (FLUENT, 2009). A control-volume-based technique is applied for the transformation of the differential transport equations to algebraic by integrating them at each control volume. The integral form of the transport equation for a scalar quantity, φ (Eq. 4.37) is written after discreetization in the form of Eq. 4.38:

$$\int_V \frac{\partial \rho\varphi}{\partial t} dV + \oint \rho\varphi\vec{v} d\vec{A} = \oint \Gamma_\varphi \nabla\varphi d\vec{A} + \int_V S_\varphi dV \tag{4.37}$$

$$\frac{\partial \rho\varphi}{\partial t} V + \sum_j^{N_{faces}} \rho_j \varphi_j \vec{v}_j \vec{A}_j = \sum_j^{N_{faces}} \Gamma_\varphi \nabla\varphi_j \vec{A}_j + S_\varphi V \tag{4.38}$$

where A is the surface vector, S_φ is the source of φ per unit volume, j symbolises the faces of the cell, N_{faces} is the number of faces that enclose the cell, φ_j is the value of φ convected through face j, and V is the cell volume. The solution of the discretised equation requires the calculation of the flow variables both at the center and the boundary faces of the cells. These values are interpolated from the cell center values with the use of upwind schemes. In this study, the second order upwind scheme (Eq. 4.39) is used for the discretization of momentum, α_v, k and ω equations and the calculation of the corresponding values at the cell faces.

$$\varphi_j = \varphi_{c0} + \nabla\varphi_{c0}\vec{r}_{c0} \tag{4.39}$$

$$\left(\nabla\varphi\right)_{c0} \delta r_i = \left(\varphi_{c1} - \varphi_{c0}\right) \tag{4.40}$$

where φ_{c0} is the value at the center of the upstream cell, $\nabla\varphi_{c0}$ is its gradient and r_{c0} is the displacement vector from the upstream cell centroid to the face centroid, as it is presented in Fig. 4.19. In addition, the second order central scheme (Eq. 4.41) is used for the pressure computation at the faces:

$$p_j = 0.5\left(p_{c0} + p_{c1}\right) + 0.5\left(\nabla p_{c0}\vec{r}_{c0} + \nabla p_{c1}\vec{r}_{c1}\right) \tag{4.41}$$

where p_{c0} and p_{c1} are the pressure values at the centers of upwind and downwind cells, respectively. The value of N_{faces} is equal to the number of the neighboring cells and the transport equation can be written in the linearised form of Eq. 4.42:

$$\alpha_p \varphi = \sum_{nb} \alpha_{nb} \varphi_{nb} + b \tag{4.42}$$

where nb subscript stands for the neighboring cells, b is the source term, α_p and α_{nb} are the linearised coefficients for φ and φ_{nb}.

The flow equations are all written in the form of Eq. 4.42 for every cell of the mesh, and constitute the final system of algebraic equations, which is iteratively solved. The integral form of the steady state mass (Eq. 4.43) and momentum equations (Eq. 4.45), along with their discretizated forms (momentum discretization in x-direction), are given below:

$$\oint \rho\vec{v} d\vec{A} = 0 \tag{4.43}$$

$$\sum_{j}^{N_{faces}} J_j A_j = 0 \tag{4.44}$$

$$\oint \rho \vec{v}\vec{v} d\vec{A} = -\oint pI d\vec{A} + \oint \vec{\tau} d\vec{A} + \int_V \vec{F} dV \tag{4.45}$$

$$a_p v_x = \sum_{nb} \left(a_{nb} v_{x_{nb}} \right) + \sum \left(p_j A_j \right) \hat{i} + S_m \tag{4.46}$$

where J_j is the mass flux through face j.

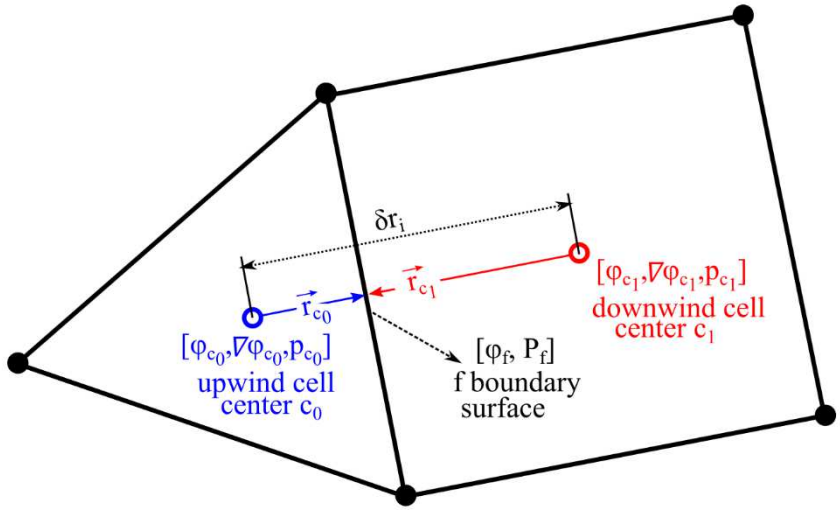

Figure 4.19 Schematic representation of the second order upwind scheme.

The pressure-based segregated solver (SIMPLE) is used in this study, by which the pressure field is calculated by a correction equation. SIMPLE solves the individual equations one after another and uses an equation that relates velocity and pressure corrections so as to enforce mass conservation and to obtain the pressure field. More specifically, the solver uses a guessed pressure value p^* for the estimation of the mass flux J_j^* through face j from Eq. 4.47, and corrects this value, in order that $J_j = J_j^* + J_j'$:

$$J_j^* = \hat{J}_j^* + d_j \left(p_{c_0}^* - p_{c_1}^* \right) \tag{4.47}$$

where d_j is related with the average coefficient $\overline{a_p}$ calculated from a_p coefficients of momentum equation that correspond to both sides of the face. Also, the algorithm presupposes that J_j' can be written as function of pressure correction p' and constructs its discrete equation in the cell:

$$J_j' = d_j \left(p_{c_0}' - p_{c_1}' \right) \tag{4.48}$$

$$a_p p' = \sum_{nb} a_{nb} p'_{nb} + \sum_{j}^{N_{faces}} J_j^* A_j \tag{4.49}$$

The corrected values for the pressure at the center of the cell, as well as the mass flux through face j are calculated from Eqs. 4.50 and 4.51, respectively, so as to satisfy the mass continuity equation:

$$p = p^* + \alpha_p p' \tag{4.50}$$

$$J_j = J_j^* + d_j \left(p_{c_0}^{'} - p_{c_1}^{'} \right) \tag{4.51}$$

Furthermore, second order spatial discretization is selected for the pressure, momentum, volume fraction and turbulence. In the present study, the steady state approach is considered for all simulations, with the use of the moving reference frame technique (MRF). The selection of such an approach in cavitation problems has been reported in several studies (Coutier-Delgosha, 2003; Sedlar, 2009; Harada, 2010), so as to model the attached cavity. This selection is also justified by the visual observations of the cavitation phenomenon, which are discussed in detail at Chapter 3 and confirm that the extent and the position of the two phase flow area does not vary significantly after the stabilisation of the appearance of vapour cavities in the impeller. These observations refer to the two dimensional macroscopic characteristics of the phenomenon, which are captured by the cameras.

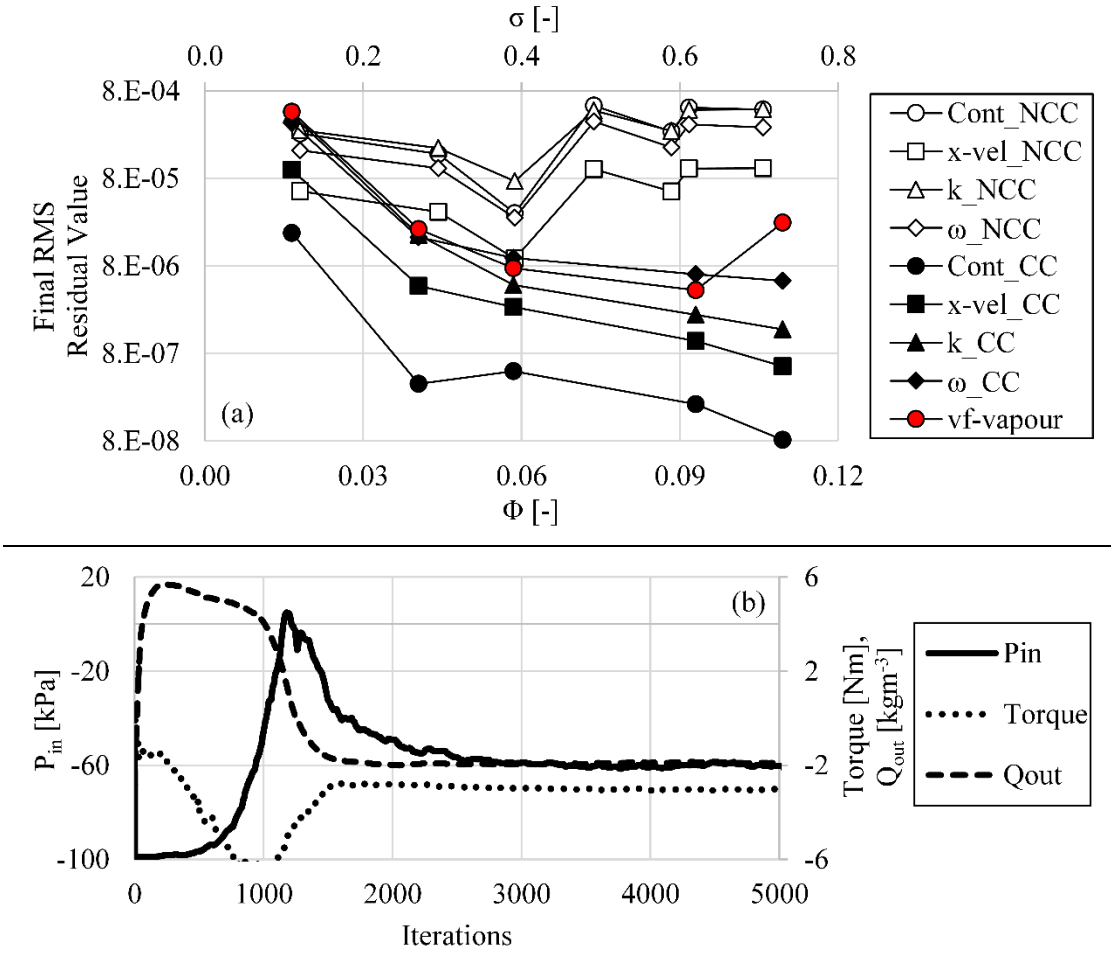

Figure 4.20 Typical plots of the **a)** residuals values at the final iteration of the simulation, **b)** monitored flow variables during simulations.

Finally, two convergence criteria are used (Limbach, 2017) for the termination of the iterative solution; i) the drop of the maximum normalised residual of the flow equations (continuity, u_x, k, ω, α_v) below ~10^{-4} and ii) the minimization of fluctuations of the averaged values of static pressure, flowrate and torque, calculated on the surface of the inlet, outlet and rotating solid boundaries of the domain. These values are important for the accurate simulation of the performance characteristics of the pump, under both normal and cavitating conditions, because they are involved in the calculation of σ (Eq. 2.24), Ψ (Eq. 2.16) and η (Eq. 2.7). In

Fig. 4.20a, the values of the RMS values of the residuals under normal (empty marker) and CCs (black marker) are given for seven Φ and five typical σ values, respectively. The vapour phase is also monitorerd and its corresponding RMS residuals are depicted with the use of a red marker, only for CCs (Fig. 4.20a).

The first convergence criterion of 10^{-4} is satisfied in all cases presented, for both normal and cavitating conditions. In two-phase flow conditions, the convergence is more satisfactory (RMS$<8\cdot 10^{-6}$) during the first stages of cavitation development ($\sigma > 0.2$), compared to extreme cavitating conditions. The curves correspond to NCCs do not present a specific trend with the change of flowrate. On the other hand, the static pressure at the inlet area, the torque on the impeller and the flowrate at the outlet are monitored, in order to control the convergence of the computation of σ, Ψ and η. In Fig. 4.20b the static pressure inlet, torque and outlet flowrate are plotted during the iterative procedure and stabilise after about 2500 iterations, where they fluctuate at ±1% of the mean value. The negative value for the outlet mass flowrate that leaves the computational domain is because the positive direction is used for the inlet flow. The results of all the simulations presented in this study satisfied both convergence criteria.

4.6 Validation of the numerical model

The model developed in sections 4.2-4.5 for the impeller No. 2 is validated before its application for the study and detection of cavitation in centrifugal pumps. The validation procedure includes:

i. The confirmation of the non-axisymmetric flow characteristics in the pump suction.
ii. The comparison of the numerically obtained performance curves under normal and cavitating conditions with the corresponding experimental curves, for all operating points of impeller No. 2, discussed in Chapter 3.
iii. The selection of the vapour volume fraction value that will be used to determine the interface between vapour and liquid phase.
iv. The evaluation of the extent and location of the computed two-phase flow area for a wide range of operating conditions.

4.6.1 Evaluation of the non-axisymmetric flow conditions

Regarding the non-axisymmetric flow pattern, in section 2.5.1 (Fig. 2.17) the effect of the inlet pipe bending on the suction flow conditions of the pump is discussed. According to the experimental photos taken from the flowpaths between the blades, cavitation does not develop axisymmetrically, but firstly appears at the left side ($90°<\varphi<180°$) of the impeller. In Fig. 4.21 the static pressure contour at the x-z plane (z=1 mm) under NCCs for a typical flowrate (Φ=0.80Φ_{BEP}) is drawn. The static pressure contours show that the lower static pressure area (blue colour area) indeed lies at the left side of the impeller eye and can be associated with the flow conditions downstream the elbow. This behaviour verifies the installation of the camera at the left side of the impeller (Fig. 4.21 & Fig. 2.19a, section 2.5.1), in order to detect the inception and early development of cavitation in the impeller.

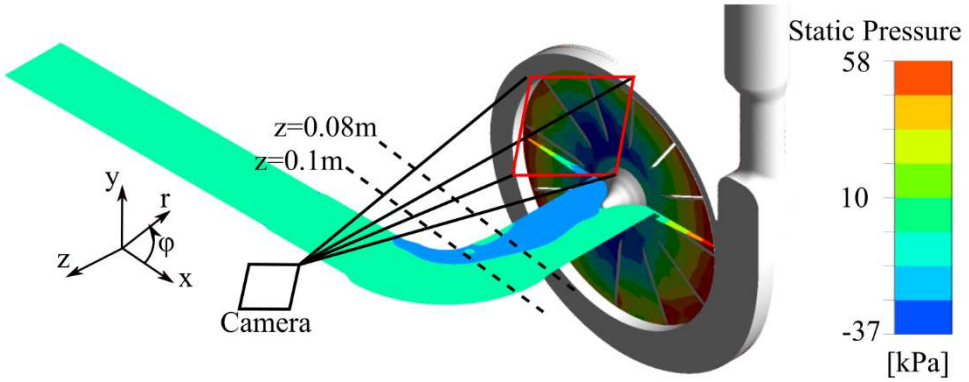

Figure 4.21 Static pressure field at the x-z plane of the pump, velocity vectors at x-y plane at distance.

4.6.2 Evaluation of the numerical characteristic curves

4.6.2.1 Under single-phase flow conditions

The numericaly obtained characteristic operation curves of total head, efficiency and power of the pump with the impeller No. 2, are plotted in normalised form in Fig. 4.22, against the experimental curves, presented in Fig. 3.7 for the same impeller. The boundary conditions and the results of these curves are also provided in Table 4.3, so as to navigate the reader during the presentation of the results of this Chapter. The flowrates selected as inlet boundary conditions (BCs) are in the range [0.20 – 1.2]·Φ_{BEP}, in order to include the flowrates tested during cavitation experiment (see section 3.3.1) for this impeller ([0.48-0.96]·Φ_{BEP}). By this way, the

numerical results extracted from the model under normal conditions could be useful in the discussion of the cavitation results under similar flowrates but lower values of the cavitation parameter σ.

Table 4.3 Boundary conditions and results of the numerical model along with the experimental characteristic curves for impeller No. 2.

	Numerical Model						**Experiment**			
	Boundary Conditions			**Results**			**Results**			
A/A	**Q_{in} [kg/s]**	**Φ/Φ_{BEP} [-]**	**P_{out} [kPa]**	**Ψ [-]**	**η [-]**	**N [-]**	**Φ/Φ_{BEP} [-]**	**Ψ [-]**	**η [-]**	**N [-]**
1	2.71	1.15	92	0.92	0.42	0.00088	1.46	0.76	0.33	0.00119
2	2.35	1.00	100	0.96	0.41	0.00082	1.31	0.83	0.35	0.00107
3	2.27	0.96	101	0.96	0.40	0.00080	1.15	0.89	0.38	0.00095
4	1.89	0.80	107	1.03	0.38	0.00076	1.00	0.94	0.39	0.00083
5	1.51	0.64	111	1.10	0.34	0.00071	0.82	0.98	0.39	0.00072
6	1.14	0.48	115	1.12	0.31	0.00063	0.67	0.99	0.37	0.00063
7	0.46	0.20	125	1.17	0.16	0.00049	0.51	1.02	0.33	0.00056
8							0.35	1.07	0.25	0.00051
9							0.20	1.10	0.16	0.00046
10							0.00	1.12	0.00	0.00042

According to the results of Fig. 4.22, all the numerical curves exhibit the typical behaviour of centrifugal pump impellers in this specific speed area, i.e. Ψ is a monotonically decreasing function of Φ, N increases with Φ and η reaches one global maximum. Satisfactory agreement for all variables (Ψ, N & η) is obtained between the numerical results and the experimental measurements. The discrepancies minimise close to the BEP of the pump (Fig. 4.22) and increase at partial load operating conditions. In general, the numerical total head results show higher values compared to the measurements because the model ignores the disturbances introduced by the interaction between the rotating and the stationary parts of the pump. A second reason for the increased total head values are the geometrical simplifications in the geometry of the LU pump (section 4.3.1). The aforementioned differences increase as the flowrate reduces, but remain below 10 % (Fig. 4.22).

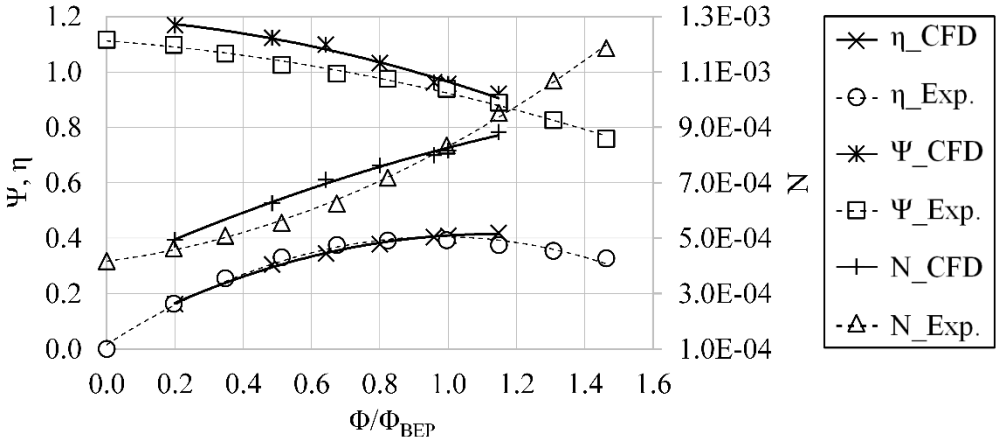

Figure 4.22 Numerical and experimental characteristic operation curves of impeller No. 2.

On the other hand, the differences that can be observed in Fig. 4.22 between the two power curves are probably the result of the estimation approach of the rotating disc mechanical losses (see Eq. 4.31). The differences between the power and the head curves counterbalance and this results in a very good agreement of the numerical and experimental results of efficiency, η that are also plotted in Fig. 4.22. Based on this overall satisfactory agreement, the numerical results

are considered acceptable to be used for further study of the flow cavitating conditions in this pump.

4.6.2.2 Under two-phase flow conditions

In Fig. 4.23, the computed cavitation characteristic curves (σ-Ψ) for four partial flowrates are presented along with the corresponding measured that were shown in Fig. 3.9 (section 3.3.1). The comparison covers the total range of suction conditions ($0<\sigma<0.8$) at n=1800 rpm for T=23 ºC. In the cavitating region, between the last two OPs measurements (left end of curves), the slightest change of valve position resulted in a drastic drop of suction pressure and the total head is collapsed, as discussed in section 3.3. On the contrary, in the numerical analysis it is possible to simulate the flow conditions between these two lowest experimental σ values, as shown in Fig. 4.23.

Under non-cavitating conditions, at the maximum σ value, the relative difference between the numerical and experimental values of total head is ~9% for the lowest flowrates (Φ=0.48·Φ_{BEP} and Φ=0.64·Φ_{BEP}), decreases to ~6% at Φ=0.80·Φ_{BEP} and minimises ~2.8% close to the nominal flowrate, Φ=0.96·Φ_{BEP}. The trend of these discrepancies follows the corresponding trend that is discussed during the derivation of total head curves under normal conditions (Fig. 4.22) in section 4.6.2.1.

In both plots of Fig. 4.23, the numerical model describes sufficiently the total head drop under fully developed cavitation (σ_{FC}), for all flowrates studied. Moreover, the model describes adequately the effect of the flowrate on the two-phase flow development, since the higher flowrate simulated, the sooner the total head collapses, similarly to the measurements.

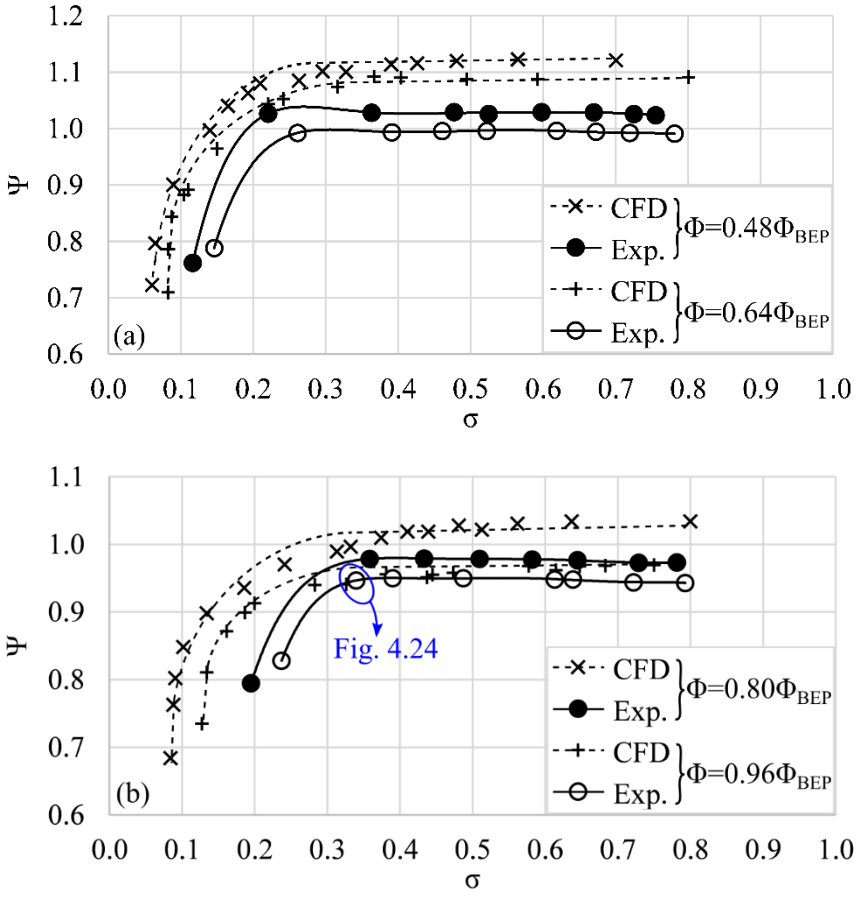

Figure 4.23 Cavitation characteristic curves computed and measured for impeller No. 2 at **a)** Φ=0.48·Φ_{BEP}, Φ=0.64·Φ_{BEP} and **b)** Φ=0.80·Φ_{BEP}, Φ=0.96·Φ_{BEP}.

Another observation from the comparison of the characteristic curves, deals with the fact that the numerical drop of the head occurs always at lower σ values, compared to the corresponding experimental values. For all the flowares examined, the model seems to overestimate the ability of the pump to provide hydraulic power to the fluid under heavy cavitating conditions. The main parameter responsible for this systematic deviation is the inability of the model to simulate the vapour formations created in the suction valve, as presented in Fig. 3.15b (section 3.3.2). The cavitation in the suction valve is developed only during the testing of the minimum σ values, (Fig. 3.18, section 3.3.2), and contributes to the vapour formations in the impeller. This part of the cavitation is not modelled numerically, since for all the cases simulated, the inlet boundary condition remains a_v=0. As a result, the numerically obtained vapour formations refer only to the static pressure drop in the areas of the domain. This is the reason that the model has to face a stronger σ drop so as to predict a similar pressure drop with the experiment. For instance, in the case of Φ=0.80·Φ_{BEP}, the Ψ=0.8 value is achieved for an experimental σ=0.2, which is two times larger than the corresponding numerical σ (σ=0.1).

Additional parameters that affect the differences of Fig. 4.23, are the values given to the vaporization and condensation constants of the cavitation model (Eqs. 4.57 and 4.58, section 4.2.4), and of course the assumptions regrading the isothermal and incompressible flow that this particular modeling approach incorporates. In view of these uncertainties, the agreement in all the cases of Fig. 4.23 is quite satisfactory.

4.6.3 Vapour fraction value for the representation of the cavitation area

The selection of the value of vapour volume fraction plays critical role in this study, since it is used for the depiction of two-phase flow area boundaries. In order to calibrate α_v, the contour plot of Fig. 4.24b is compared with the corresponding one of the flow visualisation results (Fig. 4.24a). That result refers to σ~0.34 at Φ=0.96·Φ_{BEP}, which is presented in Fig. 4.23b and corresponds to an intermediate point of cavitation development, before the drop of the total head of the pump.

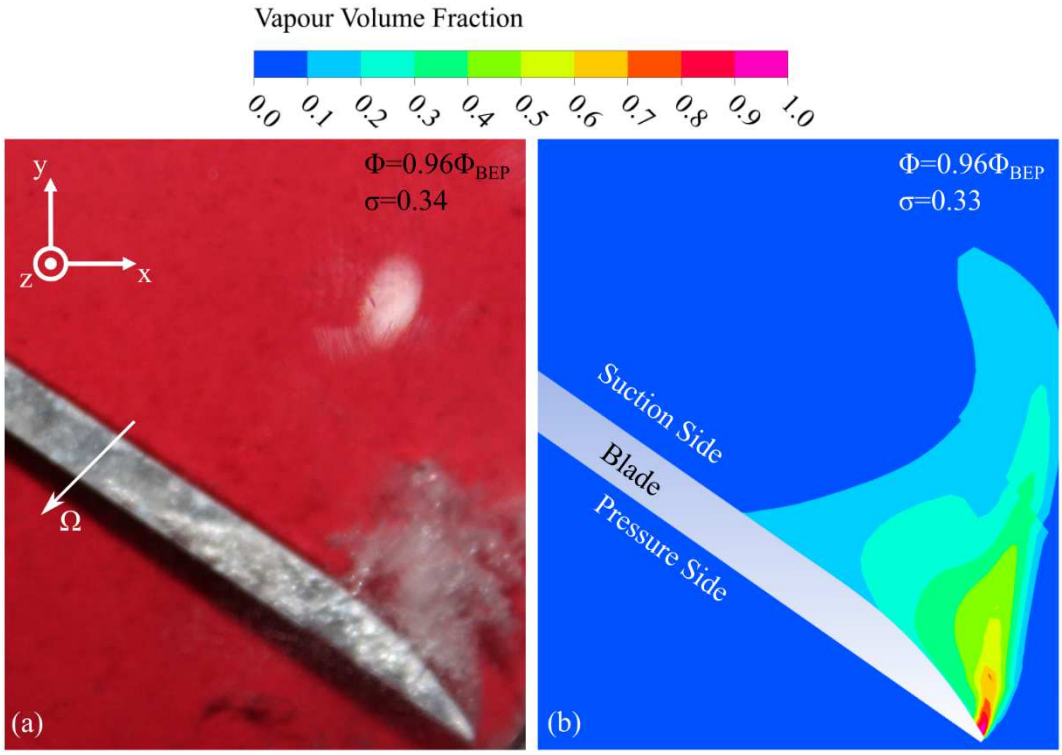

Figure 4.24 a) Flow visualization and **b)** vapour volume fraction contour at x-y plane, z=1 mm, simulated at σ~0.34, Φ=0.96·Φ_{BEP}.

From a general perspective, the numerical model successfully computes the cavitation area at the suction side of the blade, where the $\alpha_v \geq 0$. Moreover, the vapour area becomes denser as the pressure becomes lower towards the LE of the blade. This result confirms the literature (Karassik, 2007; Papantonis, 2016), as well as the experimental results at the identical geometry and operating conditions (Fig. 4.24a). As it is expected, the vapour volume area becomes larger with the decrease of the α_v value (Fig. 4.24b). From the study of Fig. 4.24, it can be deduced that a surface that includes the area with a value of $\alpha_v \geq 0.5$, provides a satisfactory representation of the macroscopically visible vapour area shown in Fig. 4.24a. The same value has also been adopted in similar simulations of hydraulic turbomachinery applications (Lindau, 2009; Li, 2011; Wack, 2019).

4.6.4 Extent and location of the numerically obtained vapour formations

All the computed curves of section 4.6.2.2 are put together in the plot of Fig. 4.25. The selected OPs, which lie in the red and green areas, will be used for further comparison with the flow visualization results. In the same plot, the area of the experimental (Exp. VI) and numerical (CFD. VI) visual inception are given along with the point of the experimental total head drop (Exp. σ_0). The numerical visual inception operating points correspond to the appearance of vapour areas with $\alpha_v \geq 0.5$. The results of Fig. 4.25 reveal the delay of the numerical model to detect cavitation during the early stages of cavitation development. This delay is related with three limitations of the selected modelling approach. The first deals with the assumption of the Zwart et. al (2004) model that the flow is a mixture of two fluids (vapour and water), without account for the effect of the non-condensable gas in the actual medium. As it is discussed in the Introduction (section I.1), the gas particles in the medium reduce the tension of the liquid and favour the formation of vapour cavities (Arndt, 1981; Best, 1993). Consequently, the inclusion of the non-condensable gas on the modelling procedure has been found to affect the visual inception of the phenomenon (Li, 2014; Yang, 2020).

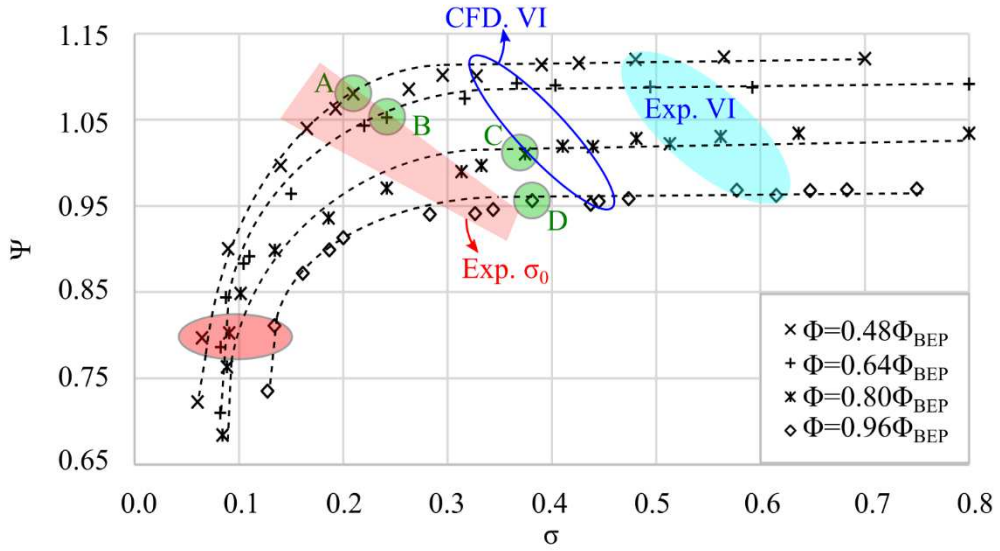

Figure 4.25 Computed σ-Ψ characteristic curves for impeller No. 2.

The second limitation is related with the intense dynamic behaviour of the vapour bubbles during the initial stages of cavitation development that is discussed in section 3.3.2. The selection to perform a steady state MRF simulation makes the model unable to predict accurately the dynamic behaviour of the travelling vapour bubbles during the initial stages of their development. However, when the attached mechanism becomes stronger, the model identifies the two-phase flow formations. It is significant to underline that the identification is achieved before the total head drop of the pump, which consequently makes the model able to

detect cavitation before the traditional performance monitoring approaches. Finally, a secondary reason that may affect the differences close to the cavitation inception, deals with the material imperfections at solid boundaries of the experimental configuration. These imperfections have been found to cause nucleition sites that favour two-phase flow development (Papantonis, 2016). However, in the case of Lancaster University test rig, the use of Plexiglas and aluminum for the manufacturing of the pump, is expected to decrease those effects, which are not included in the current model.

The next stage of the analysis, deals with the comparison between the numerically obtained vapour areas with the corresponding experimental. The operating points selected for this comparison are provided in Fig. 4.25 (green areas). The selection of the green OPs is made, in order to present a wide range of suction conditions relative to the experimental visual inception area. More specifically, the OPs A and B correspond to σ ~0.2-0.25, while the OPs C and D are close to σ ~0.4 and lie close to the visual inception area.

In Fig. 4.26, the comparison of the position and the size of the computed steady attached and tip clearance cavities against the total visualised vapour area is given for the operating conditions A, B, C and D. As concluded in section 4.6.3, the use of the iso-surface for a computed vapour volume fraction value of α_v=0.5 is proposed in this study. This area is computed and highlighted (blue colour surface area) in Fig. 4.26 along with the visualised vapour area that is depicted with the dashed curve and corresponds to the results presented in Fig. 3.13 (section 3.3.2). The values of σ that define the experimental OPs (written in the plots of Fig. 4.26), are selected as close as possible to the corresponding numerical ones (x coordinate of the operating points (OPs) in the graph of Fig. 4.25), in order to be comparable.

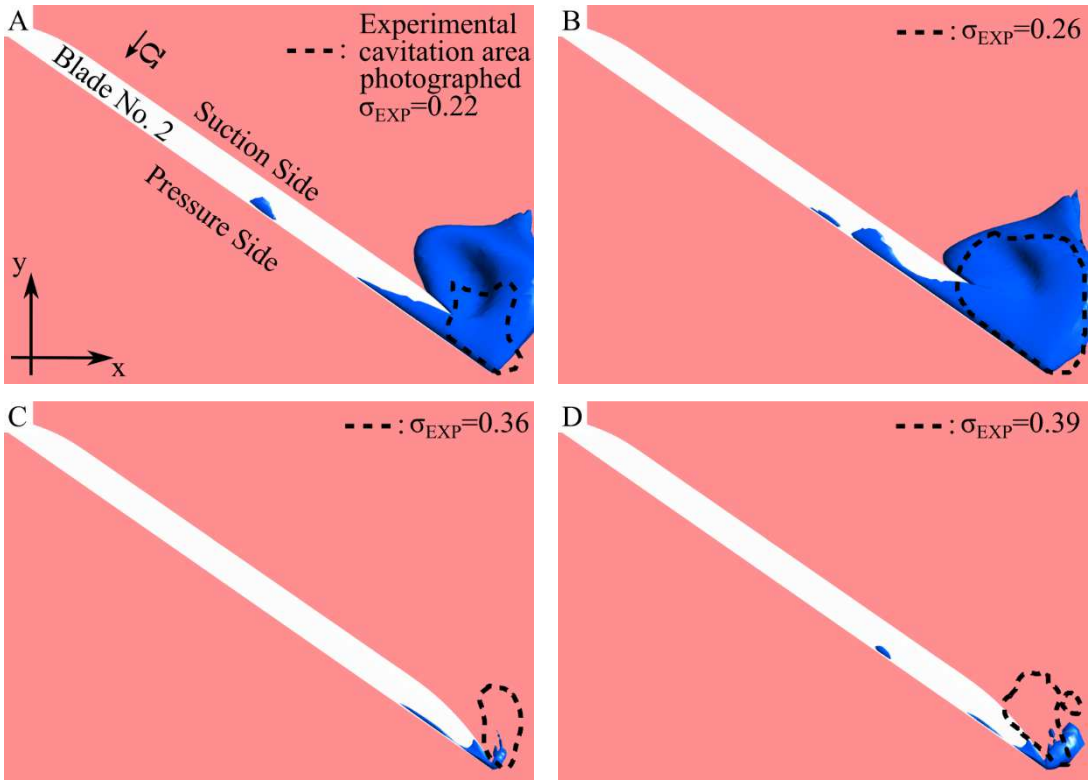

Figure 4.26 Comparison of the computed two phase flow area with the corresponding visualised during experimental measurements at initial and intermediate conditions.

For all the computational results of Fig. 4.26, cavitation area appears at the suction side of the blade close to the leading edge of the blade, similarily to the experimental results. In addition, the size of the two-phase flow becomes larger when the σ value decreases (OPs A and B). For the OPs with the largest σ values that lie closer to the visual inception point (OPs C and D) the model predicts significantly narrower cavitating area compare to the corresponding

experimental visual observations. This disagreement at the higher σ values has been discussed at the beginning of this section, and is justified from the fact that during initial conditions the attached mechanism of cavitation is relatively weak, as well as the modelling approach does not include the effect of gas particles in the mixture. When the σ value becomes lower, as in the case of OPs A and B, the steady part of the two-phase flow becomes stronger and the model improves the predictions regarding the extent and the shape of the two-phase flow area.

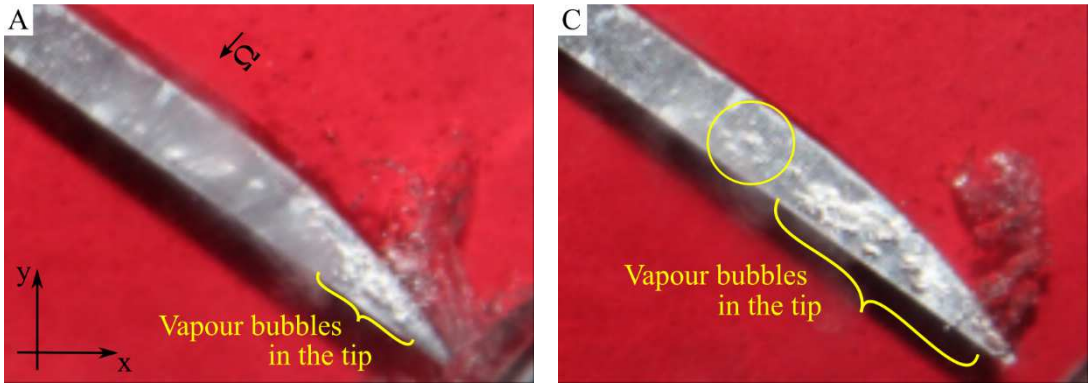

Figure 4.27 Visualization results for the experimental operating points A and C focused at the leading edge of the rotating blade of impeller No. 2.

Moreover, the numerical results in Fig. 4.26, show that cavitation also initiates in the tip clearance region of the blade, at the same time (e.g. point D), or even earlier (point C). This is also certified from the experiments in the real impeller, as it is discussed also in section 3.3.2. For this reason, the experimental photos taken at OPs A (σ_{EXP}=0.22) and C (σ_{EXP}=0.36) are provided again in Figs. 4.27 (they are also presented in Fig. 3.13), but this time they are both focused at the LE area of the blade. By this way it is possible to confirm the appearance of vapour bubbles in the area of the LE. More specifically, in both zoomed-in photos, the vapour area extends from the suction side of the blade until the line that defines the limit between the pressure side and the blade. This behaviour is also depicted in the simulation results of Fig. 4.26.

Finally, the numerical results for the OPs that lie in the red colour area of Fig. 4.25 and correspond to heavy cavitating conditions close to σ_{FC}, are given in Fig. 4.28. In this figure, the results for four flowrates are shown along with a dashed curve that illustrates the outer limits of the total vapour area obtained from the visual results. This limit is presented for one typical flowrate in Fig. 4.29. At these operating conditions the cavities block the entire path between the impeller blades, and the flow exhibits intensive recirculation and separation regions. In addition, the area of tip clearance is totally covered by vapour cavities that recirculate to the suction side of the blade and to the inlet of the impeller, a behaviour that is discussed in detail in Chapter 5. Also, for the case of minimum Φ, the two-phase flow extends from the LE to the TE and covers the entire area from the suction to the pressure side of the next blade (Fig. 4.28a).

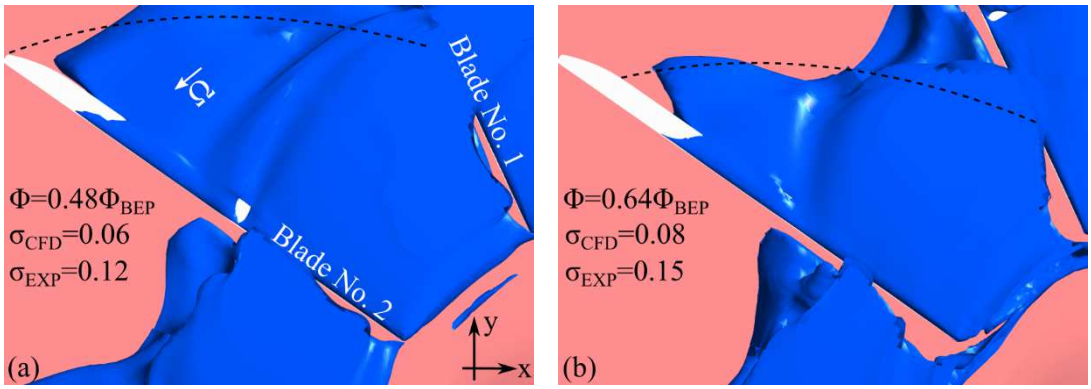

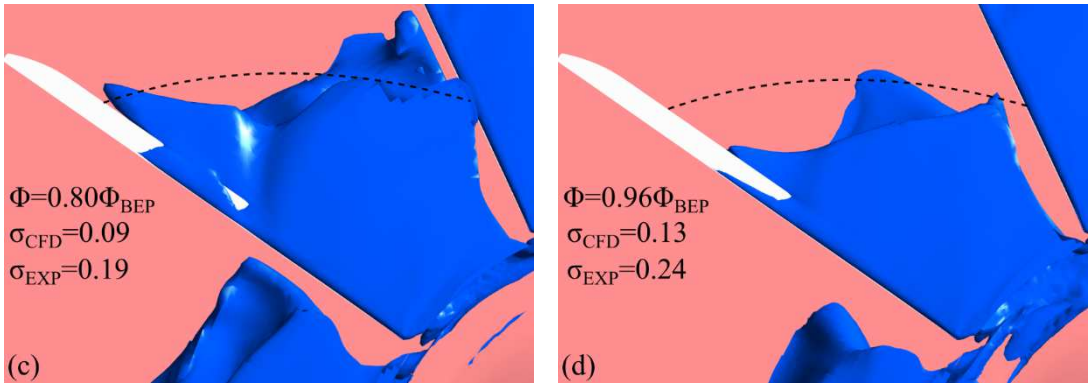

Figure 4.28 Comparison of the computed two-phase flow area with the outer separation limit of the corresponding visualised during experimental measurements at heavy cavitating conditions.

The cavitation area decreases with the increase of Φ, and for higher flow rates it covers smaller blade span to the radial direction (Fig. 4.28b to d). This behaviour appears also in the flow visualisation results of section 3.3.2 and is justified from the fact that at higher flowrates the blocking of the flowpath (tangential area between two blades, Fig. 4.28), which drives the total head drop of the pump, is achieved earlier, at higher σ values (Fig. 4.25). Consequently, this results in the narrower extent of two phase flow formations in the radial direction.

The non-periodic flow can be observed at this OP for all flowrates, where the extent of the two-phase region is different at neighboring flow passages.

In general, for the case of minimum σ value the model calculates an extended attached cavity (blue colour area) that covers an area similar to this of the total vapour area of the experimental results shown with the dashed line in Fig. 4.28. The agreement between the numerical and experimental results of Fig. 4.28 is achieved only under the comparison of similar Ψ but different σ values. In order to highlight the differences of suction conditions, the corresponding numerical (σ_{CFD}) and experimental (σ_{EXP}) σ values are given in each plot of Fig. 4.28. The latter comment further confirms the conclusion drawn after the comparison of σ-Ψ characteristic curves regarding the effect of the cavitation created at the suction valve during heavy cavitating conditions. As a consequence, from the σ perspective, the model needs to sustain significantly lower suction conditions, compared to the experimental, so as to exhibit vapour formations that extent over the midspan of the radial blade.

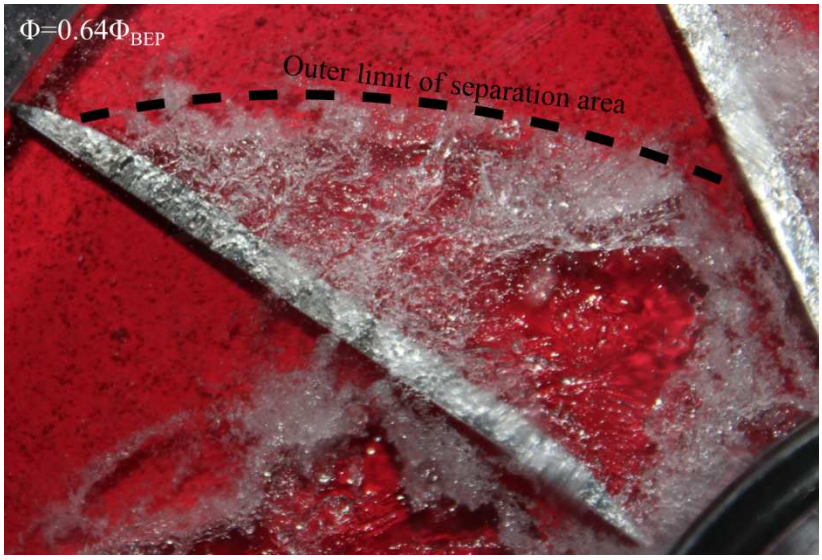

Figure 4.29 Outer limit of the separation area, photographed during σ_{FC} conditions.

The results of section 4.6 confirm that the model of impeller No. 2 simulates decently the single and two phase flow conditions in the pump. Moreover, the results presented in section 4.6.4 are of increased significance, because they show the ability of the proposed modelling approach to identify the vapour formations in the impeller promptly, far before the drop of the total head. This ability of the model is evaluated for various operating conditions, and for all the tested flowrates of the impeller No. 2. For this reason, the two phase flow model is applied also to the impeller No. 4, so as to provide additional information regarding the cavitation development in the NTUA pump. These results are provided in Chapter 5.

4.7 Modelling of additional tip clearance cases

One of the objectives of the present work is to study numerically the effect of the blades tip clearance on the onset and development of cavitation in the impeller. For this reason, the computational domain presented in section 4.3.1 includes the area between the stationary casing of the pump and the rotating blades. In order to carry out this parametric study, two modified geometries are generated with different than the original tip clearance (t_{tc}=0.9 mm), one with t_{tc}=0.5 mm and a second with t_{tc}=1.5 mm.

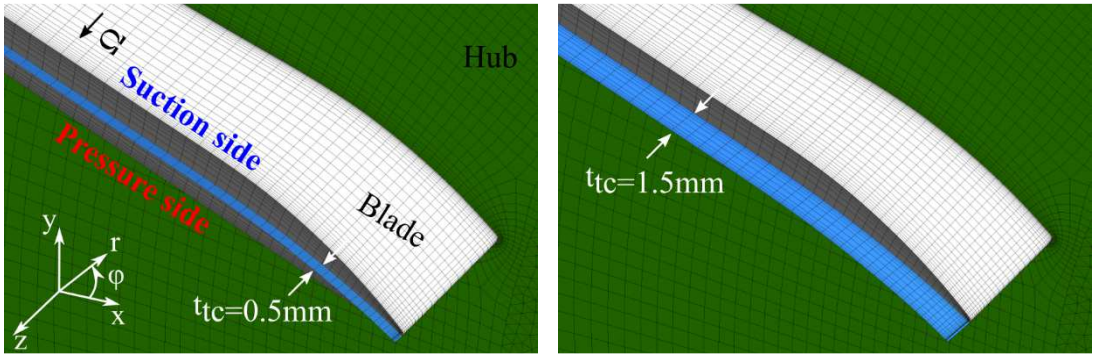

Figure 4.30 Geometry and mesh of the two additional tip clearance cases.

In both these new cases the same meshing strategy is followed, as it is presented in section 4.3. The two additional tip cases are shown in Fig. 4.30, so as to demonstrate the mesh differences and similarities. The study of the tip clearance size contains two stages: i) the derivation of the characteristic performance curves of the pump, namely the total head, torque and efficiency curves, and ii) the comparison of the numerical results for three OPs with particular σ values that correspond to intermediate (σ_{INT}) and heavy cavitating conditions (σ_{FC}) for one flowrate (Φ=0.80·Φ_{BEP}.). For the derivation of Φ-Ψ, Φ-N and Φ-η curves the same inlet and outlet boundary conditions are applied as in the original tip clearance case, as described in Fig. 4.18a. For the comparison of the different tip geometries under CCs it is necessary to keep the same σ and Φ values. To achieve this, the outlet boundary value of the static pressure must be appropriately regulated for the case of intermediate cavitation, as can be seen in Table 4.4. Under fully cavitating conditions (σ_{FC}). the computed σ, reaches the same value for all tip clearance cases, and no regulation is needed.

Table 4.4 Pressure outlet BCs and σ value for the three different t_{tc} modeled at Φ=0.80·Φ_{BEP}.

OP	t_{tc}=0.5 mm		t_{tc}=0.9 mm		t_{tc}=1.5 mm	
	σ	Pout [kPa]	σ	Pout [kPa]	σ	Pout [kPa]
σ_{INT}	0.31	63.6	0.33	55.3	0.33	45.2
σ_{FC}	0.13	-10.0	0.13	-10.0	0.13	-10.0

4.8. Synopsis

In this chapter, a detailed description of the numerical model used for the simulation of the two-phase flow formation in the impellers No. 2 and 4 is presented. The modelling approach incorporates the solution of the steady state mass and momentum RANS equations along with the transport equations used for the turbulence (k-ω SST) and the two-phase flow modelling (Zwart, 2004). Furthermore, the rotating parts of the domain are solved at the rotating reference frame and the rotor-stator interfaces are handled with the use of MRF method.

The meshing procedure for impeller No. 2 initiates with the derivation of the computational domain. Few changes are applied in the geometry of the domain, in order to simplify the mesh generation, improve the solution convergence, and reduce the computational power needed for the simulations. The total flow domain of impeller No. 2 is separated in four zones, two of them are solved based on the equations in the stationary frame and two with the equations in the rotating frame of reference. Each zone is meshed with either hexaedral or tetrahedral elements and the total mesh is the result of a merging procedure. Four total meshes of different density are constructed, in order to perform the grid dependence study. The final mesh selected is then used to study the influence of the blade position with respect to the volute tongue. The mesh of impeller No. 4 is taken from the studies of Kassanos (2016a) and Chrysovergis (2017), and only a brief description of the geometry and the mesh details is given here.

The solid wall boundary conditions for semi-open and closed impellers are provided in section 4.4, where emphasis is given to the modelling of the tip clearance walls. Furthemore, typical inlet and outlet boundary conditions are given for normal and cavitating conditions. These values are taken directly from the corresponding experimental measurements.

The numerical model is validated against the experimental measurements in terms of: i) the non-axisymmetric flow conditions in the impeller, ii) the characteristic curves of Φ-Ψ, Φ-N, Φ-η, σ-Ψ and iii) the visualization results of two phase flow development. According to the results, the strong asymmetric characteristics of the flow field in the impeller No. 2, which pushes the low static pressure field at the $90^o<\varphi<270^o$ region, are in agreement with the experimental visualisation results that confirm the onset of two phase flow in the same region. In addition, the model is able to predict the characteristic curves of the pump with the impeller No. 2, under single-phase and two-phase flow conditions. The largest differences on the σ-Ψ curves are observed at the total head breakdown operating point, which is reached systematically earlier (at higher cavitation numbers) in the experimental than in the numerical results, due to the fact that the model does not include the effect of vapour bubbles generated in the suction valve during the cavitation tests.

The comparison of the numerically obtained two-phase flow area with the corresponding experimental visual observations of section 4.6 prove the ability of the model to calculate the location of the cavitation correctly, at the leading edge of the suction of the radial blades. Moreover, these comparisons highlight the difficulties that the model experiences towards the calculation of the shape of the vapour area, especially during initial cavitating conditions, when its attached part is relatively weak. Under such conditions, the numerically calculated cavity is significantly smaller than this of the experiment. For lower σ values, where the attached cavity becomes stronger, the numerically obtained results exhibit significant improvement towards the prediction of the cavity shape.

On the other hand, for $\sigma=\sigma_{FC}$ conditions, the observed differences increase again, since the model overpredicts the ability of the pump to provide hydraulic power to the fluid. More specifically, the simulation results exhibit similar two-phase flow extent with the experiment, only when numerical σ values take values that are almost half of the corresponding measured, σ_{FC}. This behaviour reflects more the already discussed effects of the cavitation formations that are created at the suction valve area, which are not taken into account in the modelling procedure.

Beyond the aforementioned difficulties of the model, the results presented in section 4.6 are of increased significance, because they reveal the ability of the proposed modelling approach

to identify the vapour formations in the impeller promptly, before the drop of the total head. This ability of the model is evaluated for various operating conditions, for all the tested flowrates of the impeller No. 2. For this reason, the two-phase flow model is applied also in impeller No. 4 so as to provide additional information regarding the cavitation development in NTUA pump. These results are provided in Chapter 5.

5. Application of the Numerical Tool

5.1 Introduction

The results of the application of the numerical tool, presented in Chapter 4, for the study of the internal flow conditions in the centrifugal pumps under examination are given and discussed in this Chapter. As it explained in Chapter 4, two impellers are selected for the simulation of the internal flow field: i) the semi-open impeller No. 2 of the Lancaster University Laboratory and ii) the closed impeller No. 4 of the NTUA Laboratory. The numerical model is firstly used for the analysis of the characteristics of the flow when the pumps operate under non-cavitating conditions. The study of semi-open impeller is focused on the tip clearance area and includes the effect of the different thickness geometries presented in section 4.7. The flow pattern at the blades tip clearance region is significant because it is related with secondary flows that recirculate and influence the vapour formations presented in the flow visualisation results of section 3.3.2. In case of impeller No. 4, the discussion of the internal flow conditions is accompanied with the comparison of the numerically obtained characteristic curves of Φ-Ψ, Φ-N and Φ-η with the correspondig measurements that are presented in section 3.3.1.

After the examination of the performance of the pumps at normal conditions, the cavitation investigation follows. The assessment of the ability of the model to simulate two phase flow conditions in the impeller No. 2, has already been presented in the validation section of Chapter 4. The present Chapter focuses on the tip clearance area and the association of backflow recirculation with cavitation development, as well as on the effect of the tip clearance thickness in the two phase flow patterns. Finally, the results after the application of the Zwart et al. (2004) model in the case of the closed impeller are presented. These results are evaluated against the visual observations of section 3.3.2 and provide the σ values that correspond to the numerically obtained visual inception point.

5.2 Non-cavitating conditions

5.2.1 Impeller No. 2

The analysis of the internal flow conditions of the semi-open impeller No. 2 is based on the numerically obtained characteristic curves, which are shown in Fig. 4.22, of section 4.6.2.1. In Fig. 5.1 the simulated static pressure contours at the x-y plane for z=1 mm are shown for six different flowrates. The distance z is measured from the hub surface of the impeller, where the x-y plane has z=0 mm (Fig. 5.2). The static pressure of the flow increases in the radial direction within the impeller, and even more in the spiral casing towards the volute exit, as the kinetic energy of the flow at the impeller outlet is progressively transformed to potential energy. As expected, the higher the flowrate, the lower is the computed static pressure field values.

A non-axisymmetric behaviour of the flow can be observed in the contours of static pressure for all cases of Fig. 5.1, which is more obvious in the impeller inlet area, between the leading edge (LE) and the midspan (MS) of the blades, where $R_1 \leq r \leq R_m$. These flow irregularities that

appear at the lowest static pressure regions (p<50 kPa) are of significant interest regarding the two-phase flow development when the pump operates under cavitating conditions.

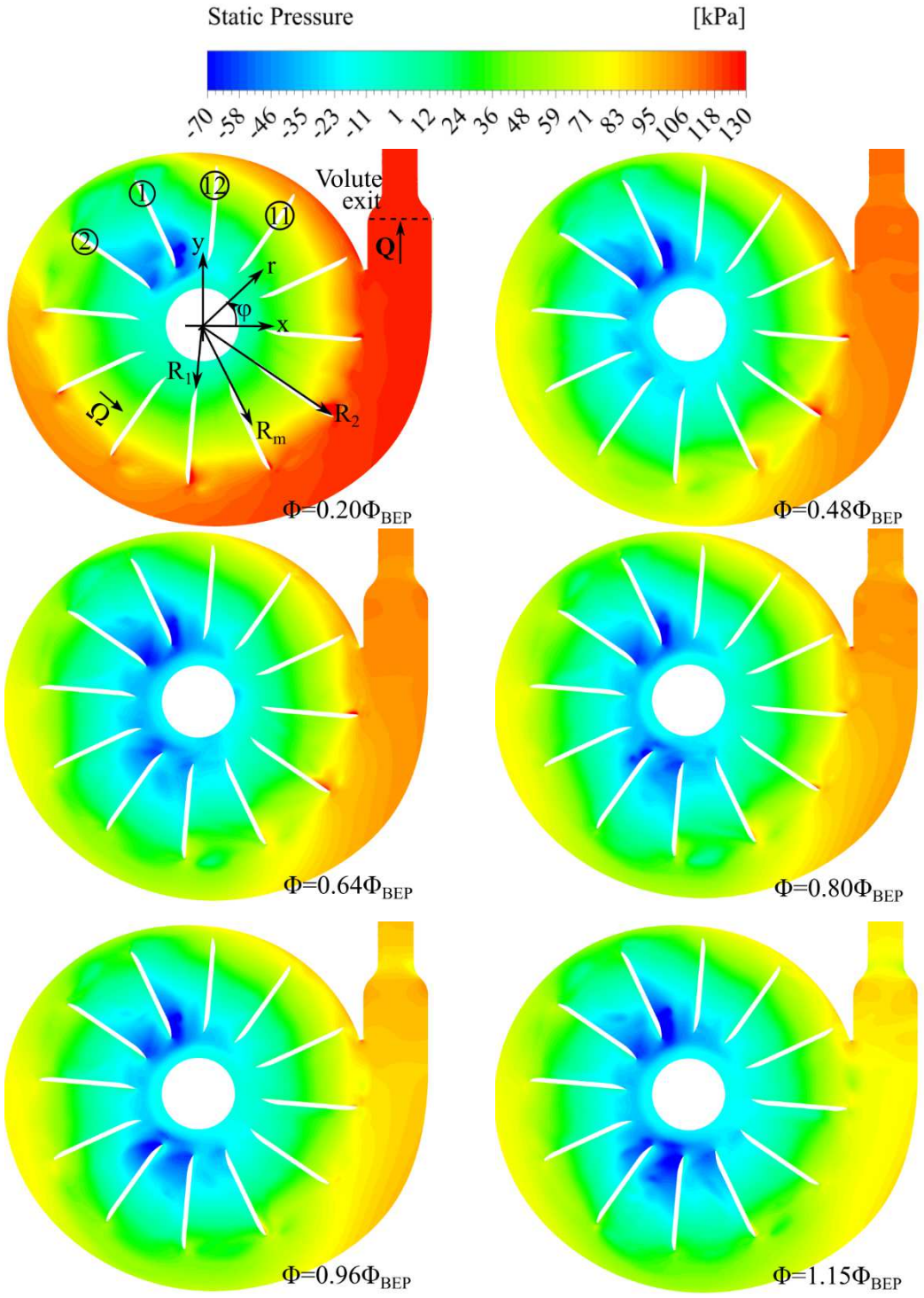

Figure 5.1 Static pressure contours at different flowrates, at z=1mm of impeller No. 2.

In order to clarify their location, the blades of impeller No. 2 are numbered in the φ direction from 1 to 12 in the first contour plot of Fig. 5.1 (Φ=0.20·Φ_{BEP}). The first blade (No. 1) is that where appears the minimum static pressure area in the impeller. The flow field asymmetries of Fig. 5.1, even at the best efficiency point (BEP), are the result of the elbow at the suction of the pump, and of the existence of the volute. The non-axisymmetric flow field has been also discussed during the presentation of the LU test configuration (Fig. 2.17, section 2.5.1), as well

as in the validation procedure of Chapter 4 (Fig. 4.21, section 4.6.1). There are three main mechanisms that drive the low pressures in the suction area of a centrifugal pump impeller. The first deals with the flow rate; when the pump operates under high Φ values the flow field is accelerated and hence the static pressures in the impeller is reduced. This effect is clear in the static pressure plots of Fig. 5.1, as the values and the extent of the negative pressure areas enlarge with the increase of the flowrate.

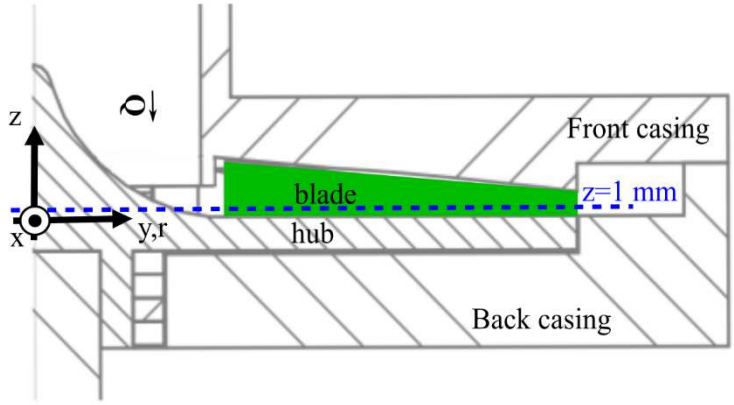

Figure 5.2 Position, where the x-r plane with z=1 mm intersects z-r plane.

The second mechanism is related with the development of secondary flow and recirculation at the suction side of the blade when the pump operates at partial flowrate conditions. A theoretical representation of the second mechanism is illustrated in Fig. 5.3a (Papantonis, 2016), where a change of flow inlet angle, β_{1w} relative to the blade inlet angle, β_1 is shown, due to which a recirculation zone can be created at the blade leading edge region. In the same figure, the vectors of relative flow velocity are plotted for various flow rates, at the flowpath between the first and the second blade at the leading edge area.

According to these results, strong recirculation appears at the suction side of the blades not only for the partial flowrates ($\Phi<\Phi_{BEP}$, Fig. 5.3b,c), but also close to the BEP flow conditions (Fig. 5.3d). This behaviour of the relative velocity vectors leads in a different way to the same conclusions drawn from Fig. 3.10 (section 3.3.1), i.e. the fact that the incidence angle (φ_i) for all the semi-open impellers of LU (impellers No. 1, 2 & 3) during optimum flowrate conditions is very high, close to 90 deg. The high incidence angle demonstrates the poor impeller design, especially at leading edge, and justifies the low efficiency of this pump measured in section 3.2, similarly to other works related to impellers with radial blades (Anagnostopoulos, 2005 & 2009). In addition, carefull examination of Fig. 4.26 (section 4.6.4) reveals that the two phase flow development in the present geometry initiates and develops in the recirculated area highlighted by the relative velocity vectors of Figs. 5.3. As a result, this mechanism introduces significant losses and influences the static pressure contours of Fig. 5.1, and consequently, the cavitation development in the impeller.

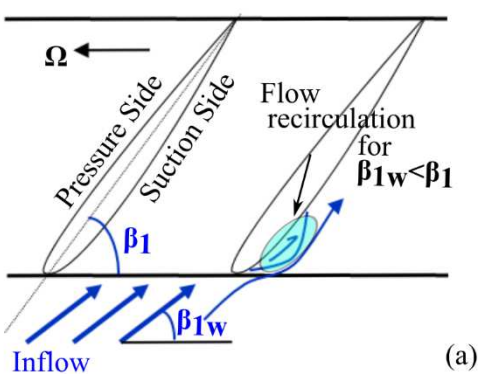

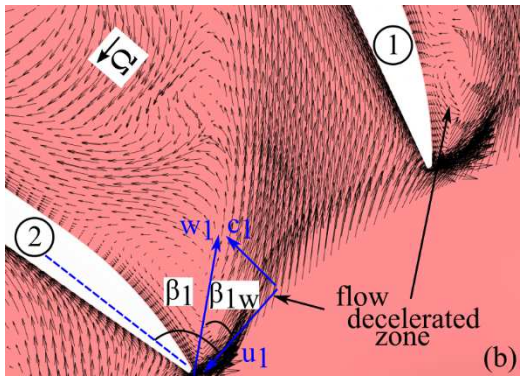

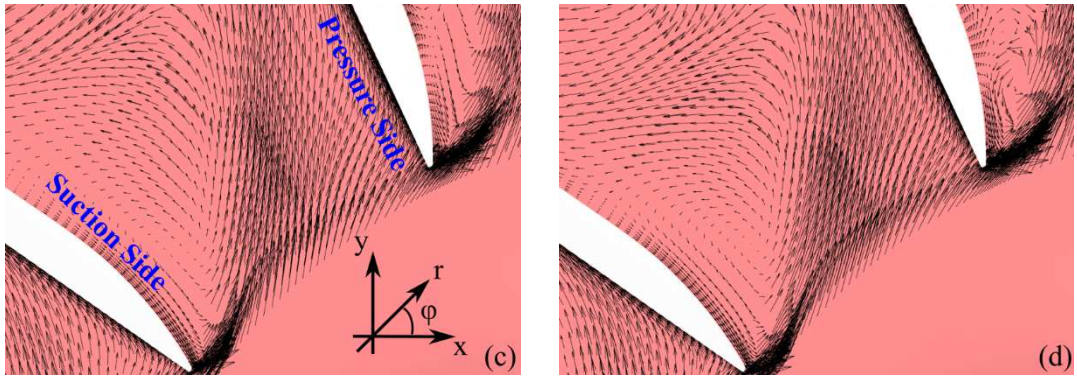

Figure 5.3 a) Theoretical depiction of flow recirculation in the suction side of impeller's blade (Papantonis, 2016), **b)** Vectors of relative velocity at z=1mm for $\Phi=0.46\cdot\Phi_{BEP}$, **c)** $\Phi=0.80\cdot\Phi_{BEP}$ and **d)** $\Phi=0.96\cdot\Phi_{BEP}$.

A third mechanism that affects the overall efficiency and the low static pressure areas of the semi-open impellers is the tip clearance flow that is developed between the rotating blades tip and the stationary casing. The sketch of Fig. 5.4 depicts tip clearance area of the blades and qualitatively represents the complex flow conditions at the inlet of this particular impeller. The flow in the narrow area of the tip clearance consists of two parts; one component that is directed radially, towards the exit of the impeller, $Q_{tc,TE}$ (blue colour vector, Fig. 5.4b)), and the areas of extended three-dimensional recirculation (red colour vectors), $Q_{tc,bfr}$, where fluid leaks to the suction side of the blade. The driving force of these recirculations is the pressure differential between the high static pressure at the tip clearance area and the blade inlet and suction side (Yokota, 2004; Kimura, 2008; Yamamoto, 2009).

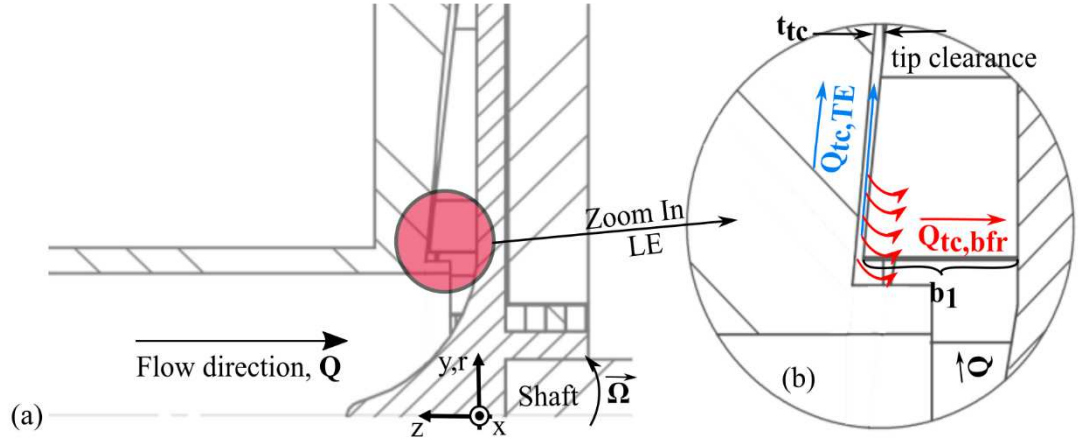

Figure 5.4 Sketch of the meridional plane of impeller No. 2 **(a)**, and detailed view of the blade leading edge and the direction of the secondary flows related with the tip clearance **(b)**.

In order to adequately depict and represent the effect of both relative velocity components on the local flow pattern, the tangential component of the relative velocity vectors are plotted on two different planes, as shown in Fig. 5.5; plane A_1 (blue colour) is perpendicular to this page and intersects the mean distance of the blade's tip clearance, and plane A_2 (red colour) that is the meridional *z-r* plane. The last plane is located in an angular position so as to allow the depiction of flow conditions in the second blade. All the results of this chapter that focus on the tip clearance, refer to the area close to the second blade (blade No. 2, Fig. 5.1) of impeller No. 2. This area is critical for the investigations carried out in the present Thesis, because it is the location where the static pressure firstly drops below the vapour pressure value, and the first vapour bubbles appear in the experimental observations (section 2.5.1.1).

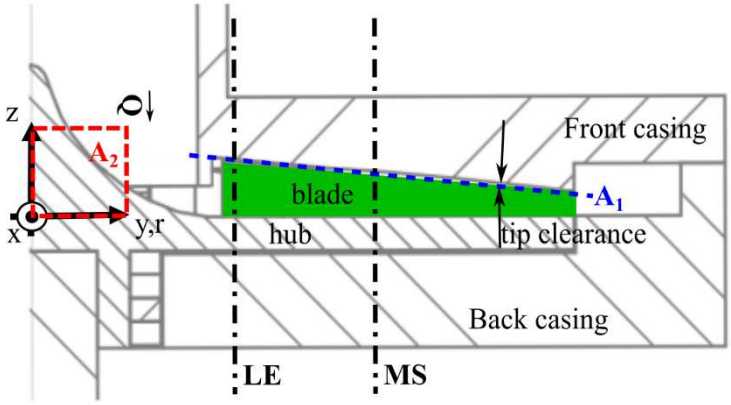

Figure 5.5 Planes and blade positions for the velocity vector plots.

In addition, for the appropriate representation of the tip leakage flowrates along the blade-span, the vectors are given in two areas: i) at the blade LE, and ii) at the MS of the blade. The position of these areas is also highlighted in the sketch of Fig. 5.5 (black centerlines). The tangential component of the relative velocity is given for two flowrates (Φ=0.96·Φ_{BEP} & Φ=0.48·Φ_{BEP}), and for all planes and areas, in Fig. 5.6.

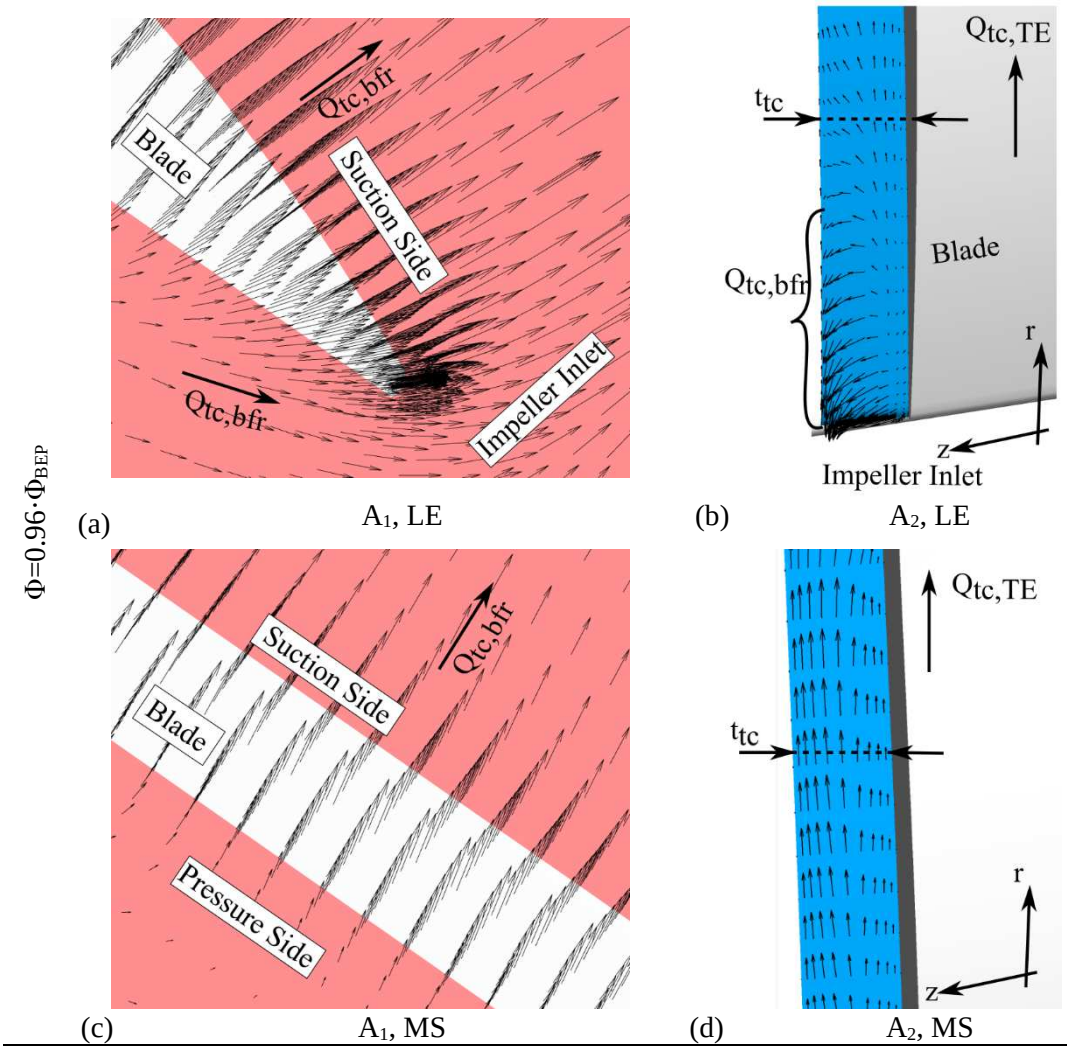

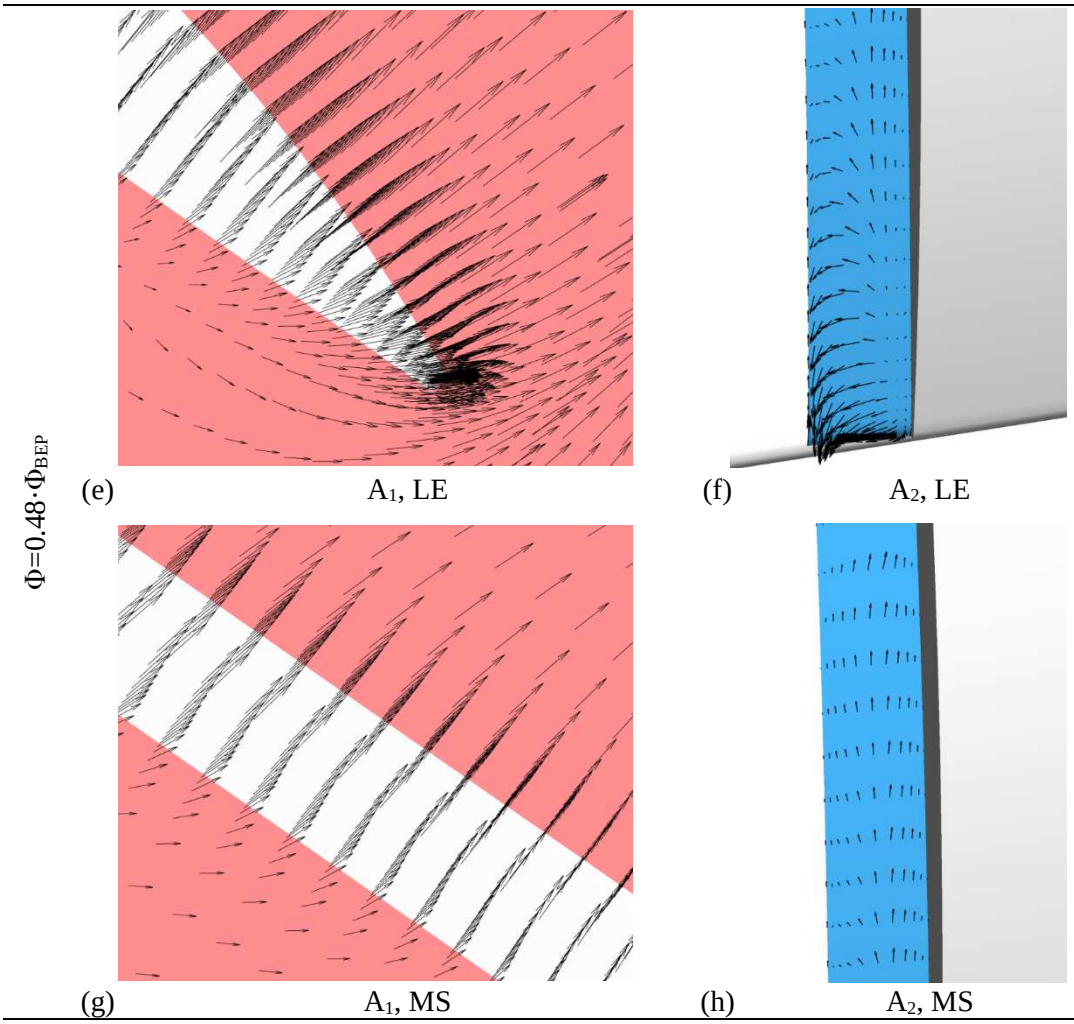

Figure 5.6 Tangential component of the relative velocity vectors in the blade tip clearance region, at the midspan and the leading edge area of blade No.2, for $\Phi=0.96\cdot\Phi_{BEP}$ and $\Phi=0.48\cdot\Phi_{BEP}$.

Both components of the tip leakage flowrate, which are qualitatively described in Fig. 5.4b, are presented in the results of Fig. 5.6. According to the relative velocity vectors shown in the A_1 plane at the LE area (Fig. 5.6a), the flow recirculates towards the suction, low pressure side of the blade and to the impeller inlet (see both vectors of $Q_{tc,bfr}$). In the same plane, at the MS of the blade, the leakage recirculation directs the flow only towards the suction side of the blade (Fig. 5.6c).

On the other hand, the flow in the A_2 plane at the LE area (Fig. 5.6b,f) consists of two components: $Q_{tc,bfr}$ that recirculates the flow towards the inlet of the pump, and the part that flows towards the TE, $Q_{tc,TE}$, which is due to the centrifugal action of the rotating impeller, and resembles to flow between parallel plates (Fig. 5.6d,h). These conclusions also apply for the partial flowrates modelled.

The results of Fig. 5.6 are important for the present study, since they reveal the internal flow conditions at the tip clearance area of the impeller No. 2. According to the results, the flow recirculation dominates the flow conditions along the tip clearance and drives the flow towards the suction side of the blades and the inlet of the pump. If this recirculation of the flow is accompanied with the formation of vapour cavities, the backflow phenomenon described in Fig. 5.6 is converted to backflow cavitation, which is described in the Introduction (section I.2). In addition, the relative velocity vectors of Fig. 5.6 provide the answer regarding the type of cavitation (backflow cavitation) that is illustrated in the flow visualisation photos of Fig. 3.17e (section 3.3.2).

The end of this section highlights the fact that the tip clearance recirculation plays significant role to the performance of the pump and the possible development of cavitating formations (Tani, 2012; Kang, 2019). For this reason the effect of its thickness is examined in the next section 5.2.1.1.

5.2.1.1 Effect of the tip clearance thickness on the performance of the pump

The effect of the change of tip clearance thickness, t_{tc}, to the performance of impeller No. 2 under normal conditions is investigated in this section. The results of the two additional tip clearances modeled (t_{tc} =0.5 mm and t_{tc} =1.5 mm) are presented along with the results of the original geometry (t_{tc} =0.9 mm), which were shown in section 5.2.1.

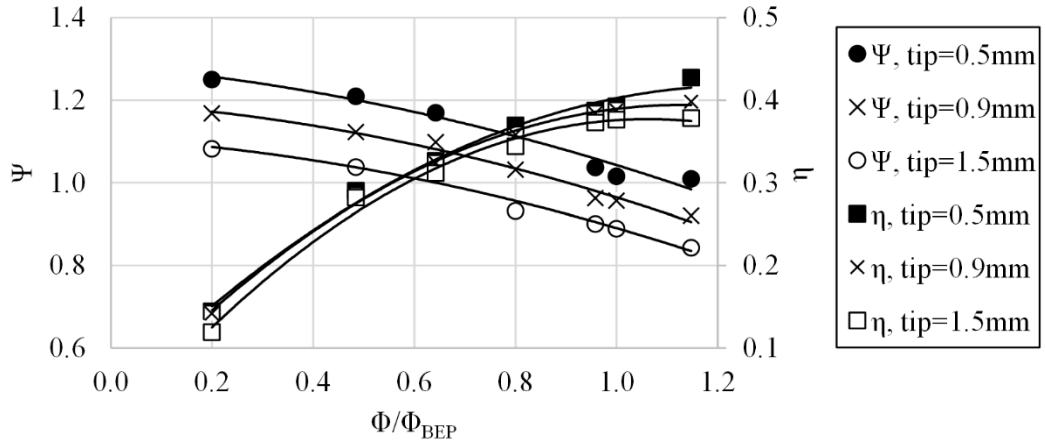

Figure 5.7 Total head and efficiency characteristic curves for different tip clearance thicknesses.

The numerically obtained characteristic curves for Ψ, η and N of the pump for the three tip clearance cases are plotted in Figs. 5.7 and 5.8. Here, the values of nondimensional head Ψ increase with the decrease of tip clearance thickness, and maximise for the case with the minimum tip clearance, due to the minimization of leakage flow through the tip clearance, which does not exchange much energy with the rotating impeller (see also: Wood, 1965; Hong, 2006; Ayad, 2015; Boitel, 2016; Kim, 2017).

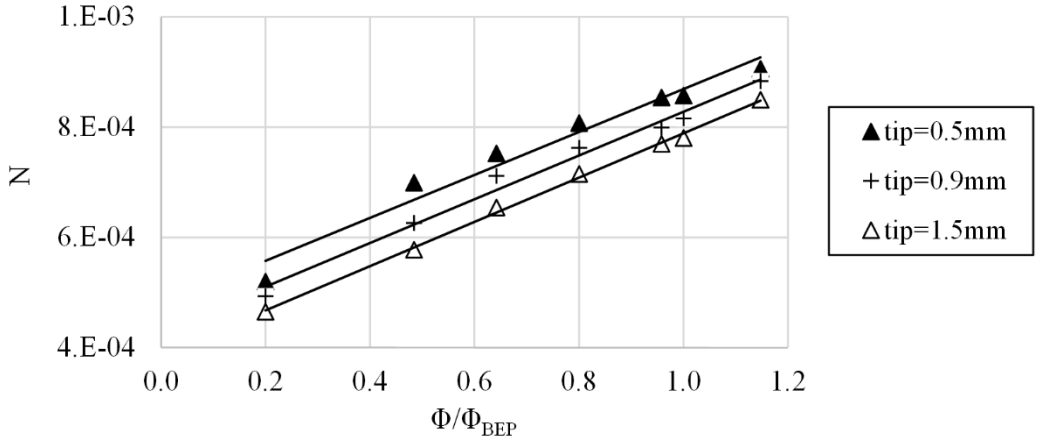

Figure 5.8 Power characteristic curves for various different tip clearance thicknesses.

The corresponding differences in the efficiency curve are significantly smaller and are mainly observable at large flowrates. This behaviour is very similar with that presented from Ayad et al. (2015), and it is justified by the power characteristic curves given in Fig. 5.8. An increase of the area of the blade surface due to the use of smaller tip clearance increases the

shaft power transffered to the fluid, and hence the energy efficiency, which is analogous to the ratio of Ψ to N, is balanced.

In Fig. 5.9 the total energy (pressure) of the fluid, averaged at various cross section areas along the flow in the pump is plotted for four different flowrates and for the three tip clearances simulated here. The positions are the inlet and outlet of the computational domain, as well as the three interfaces that are shown in Fig. 4.12. The plot presents the increase of total pressure along the flow path, together with the differences observed in total pressure value when the tip clearance changes. In Fig. 5.9, the total pressure differences between the three tip clearances is developed up to the second interface (impeller inlet). Then, the total pressure does not change significantly until the exit of the pump, because the outlet boundary conditions are the same for all cases, as it is mentioned in section 4.7. Hence, the different energy exchange in the impeller is represented by the energy difference between the exit and the inlet of the impeller (interface 3 – interface 2).

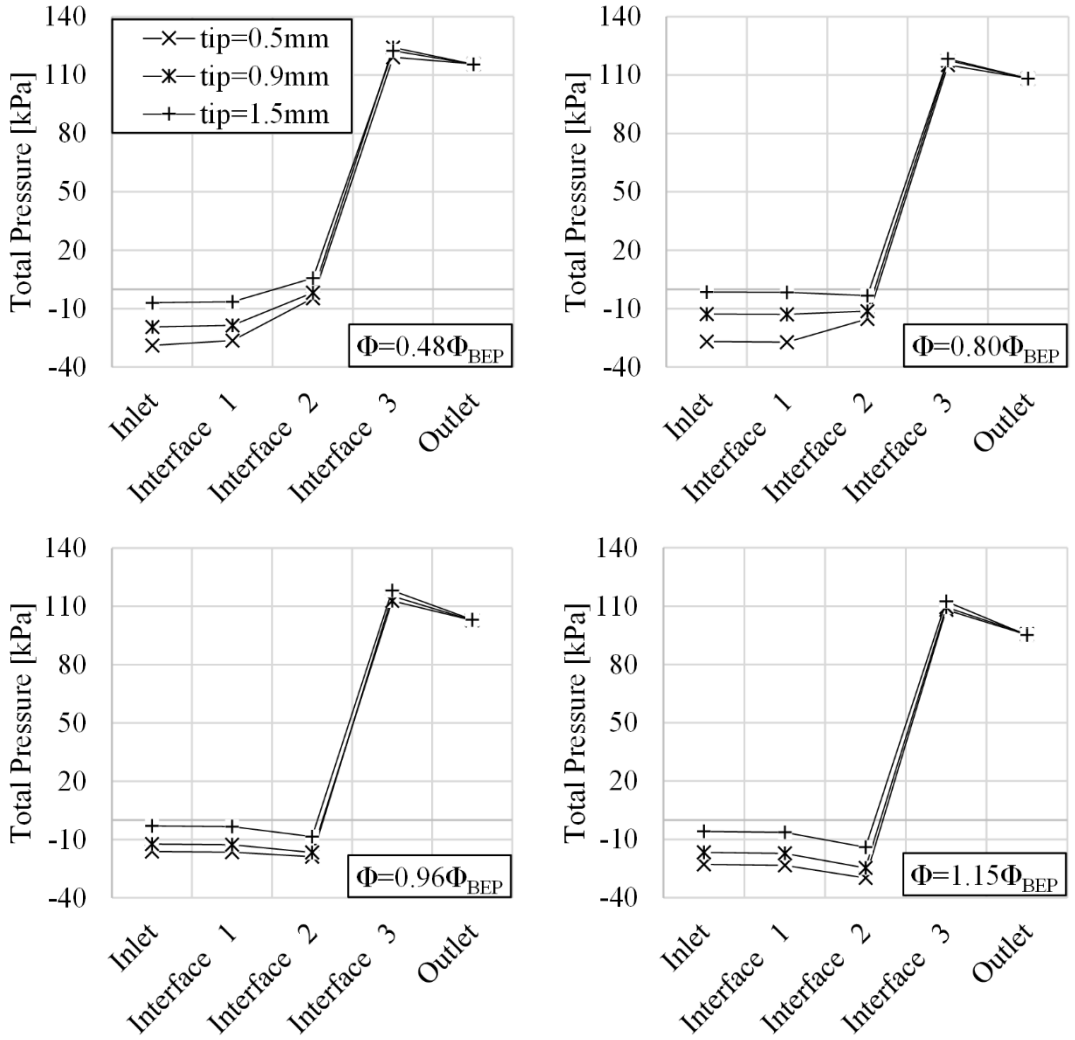

Figure 5.9 The value of total pressure area at different positions in the computaional domain.

This behaviour is also confirmed by the contours of the static pressure at z=1mm, presented in Fig. 5.10 for the two additional tip clearances studied, and at two flowrates. The plotted area includes zone III (see section 4.3.1.1, Figs. 4.4b and 4.5). The selection of five contour levels is done on purpose so as to clearly highlight the limits between the areas of low, medium and high pressure fields.

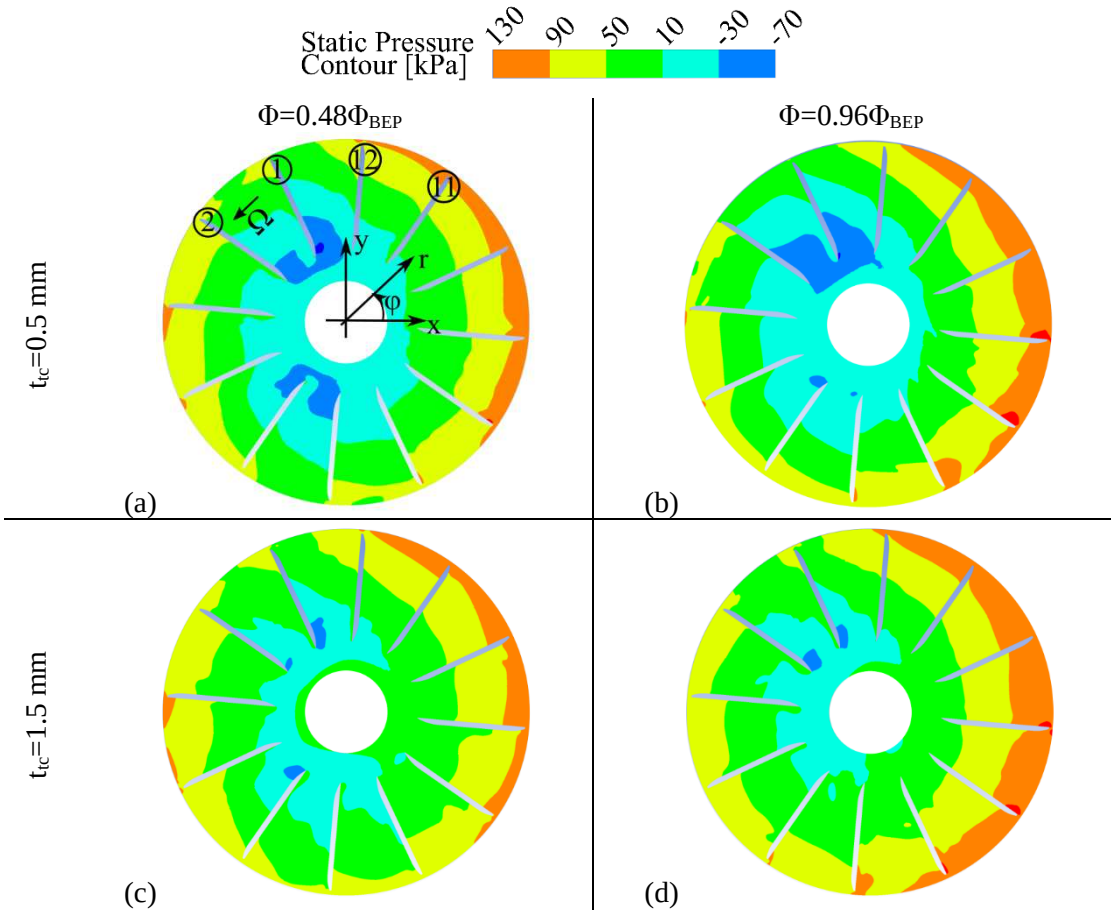

Figure 5.10 Static pressure contour at z=1mm for different tip clearance thicknesses of impeller No. 2.

For the smallest tip clearance case, the low pressure area (<10 kPa) occupies a wider part of the domain at the inlet of the impeller, compared to t_{tc}=1.5 mm. More specifically, for t_{tc}=0.5 mm, the low pressure area covers the entire impeller inlet (Fig. 5.10a,b), whereas for t_{tc}=1.5 mm it is restricted to the area $45^o \leq \varphi \leq 285^o$ for $\Phi=0.48\Phi_{BEP}$ and to $60^o \leq \varphi \leq 270^o$ for $\Phi=0.96\Phi_{BEP}$. (Fig. 5.10c and d). On the other hand, in all cases the radial span of this low pressure area is influenced by the aforementioned non-symmetries of the inlet flow (see section 5.2.1) and it is more extended at the left side of the impeller (Fig. 5.10). As a result, the closest area to cavitation lies at the leading edge of blades No. 1, 2, 5 and 6 (Fig. 5.10a). A more detailed discussion for the effects of tip clearance in the two-phase flow (cavitation) development is given in section 5.3.

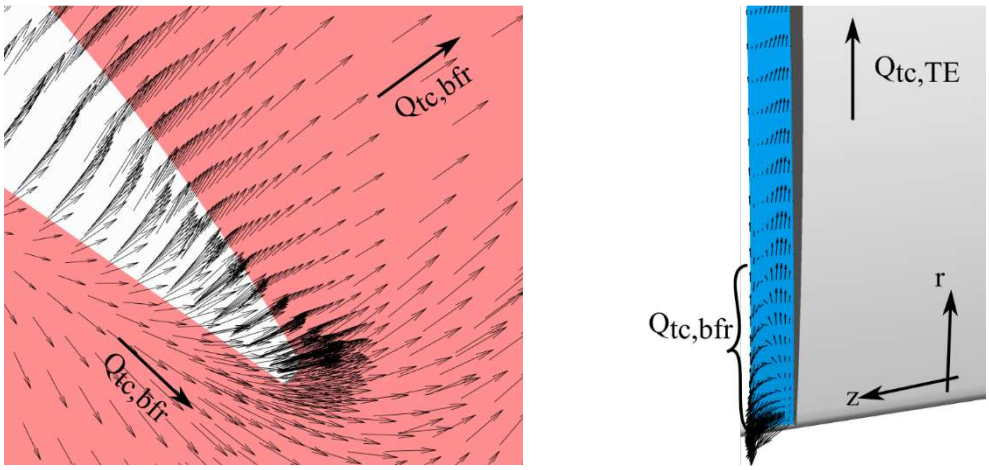

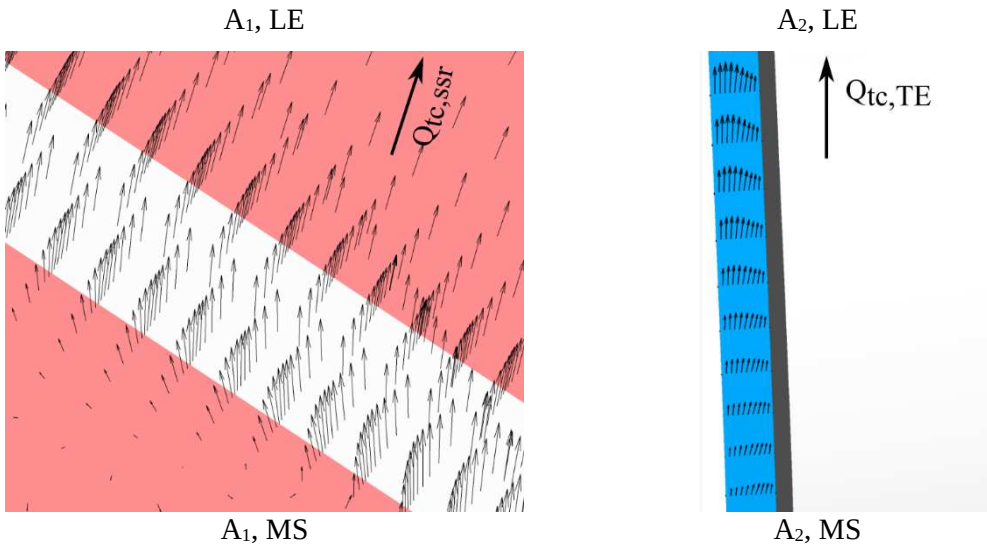

Figure 5.11 Tangential component of the relative velocity vectors for t_{tc}=0.5 mm, $\Phi=0.96\cdot\Phi_{BEP}$ at A_1 and A_2 areas at the midspan and the leading edge area of the blade.

Finally, the effect of tip clearance thickness at the backflow phenomenon is also examined, and presented with the velocity vector plots of Figs 5.11 and 5.12, at the same planes and areas with the original tip clearance case shown in Fig. 5.6. According to the results in these figures, the direction of the back flow recirculation, $Q_{tc,bfr}$, remains similar with those presented in Fig. 5.6 for the original geometry. On the A_1 plane, the tip clearance flow recirculates to the suction side of the blade and to the impeller inlet, whereas on plane A_2 the main part of the flow is directed towards the trailing edge of the blade, except of the area close to the LE, where flow recirculates to the inlet area of the impeller.

Few differences can be observed in the velocity direction of the recirculating flow between the plots of the tip clearances. More specifically, at the MS of the blade at A_1 plane, the direction of the relative velocity vectors of t_{tc}=1.5 mm is similar with that presented for t_{tc}=0.9 (Fig. 5.6c) mm but different than the corresponding one of t_{tc}=0.5 mm (Fig. 5.11). In the latter case, the vectors appear to be affected less from the recirculation and their direction is closer to that of the blade. However, when the study focus on the LE area, those differences minimise.

Similar conclusions are drawn from the comparison of the velocity vectors at the A_2 plane at the MS of the blade. Here the tip with the narrowest clearance appear to be more alligned with those presented for the largest tip clearance cases, where even recirculations in the radial directions are observed (Fig. 5.12). Moreover, when the examination focuses at the LE of the blades, recirculation zones appear in all cases of Figs. 5.11 and 5.12, the extend of which decreases significantly in case of t_{tc}=0.5 mm (Fig. 5.11), which highlights the better behaviour of the narrowest tip clearance case.

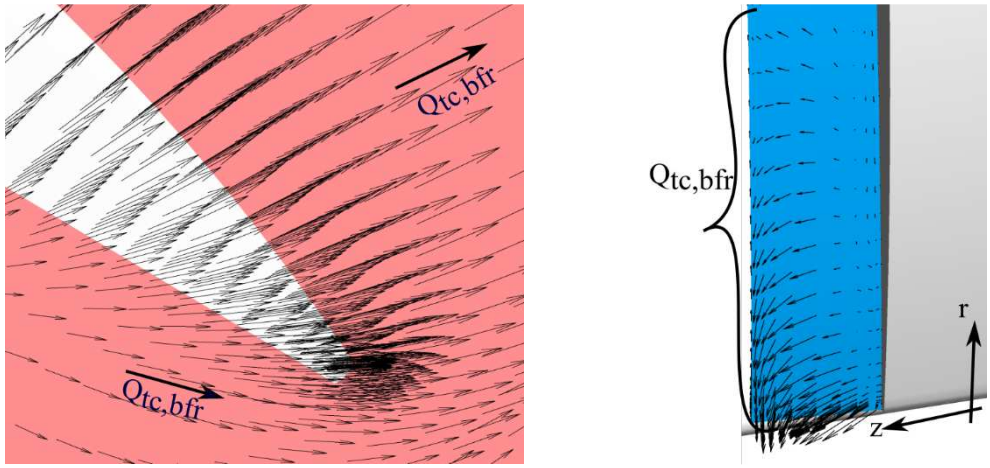

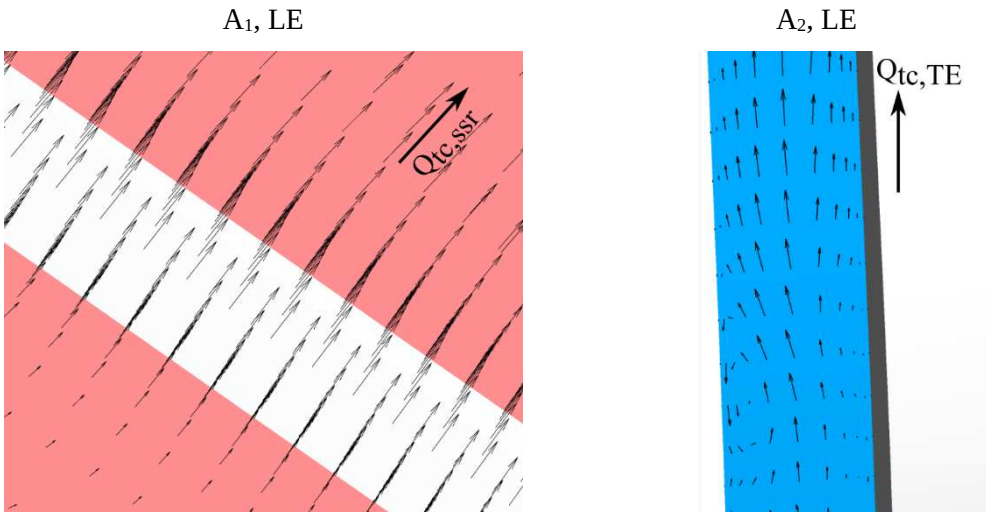

Figure 5.12 Tangential component of the relative velocity vectors for t_{tc}=1.5 mm, $\Phi=0.96\cdot\Phi_{BEP}$ at A_1 and A_2 areas at the midspan and the leading edge area of the blade.

5.2.2 Impeller No. 4

The numerically obtained non-dimensional characteristic curves of the total head, power and efficiency, for the pump with the impeller No. 4 are plotted in Fig. 5.13, against the corresponding experimental results, presented in Fig. 3.7 for the impeller No. 4. Along with the characteristics curves, Table 5.1 is provided, where the boundary conditions and the results that constitute the characteristic curves are shown. The flowrate range selected for the modelling of the non-cavitating conditions ($[0.4 - 1.2]\cdot\Phi_{BEP}$, Table 5.1) includes the flowrates that are studied under two-phase flow conditions ($[0.4 - 1]\cdot\Phi_{BEP}$).

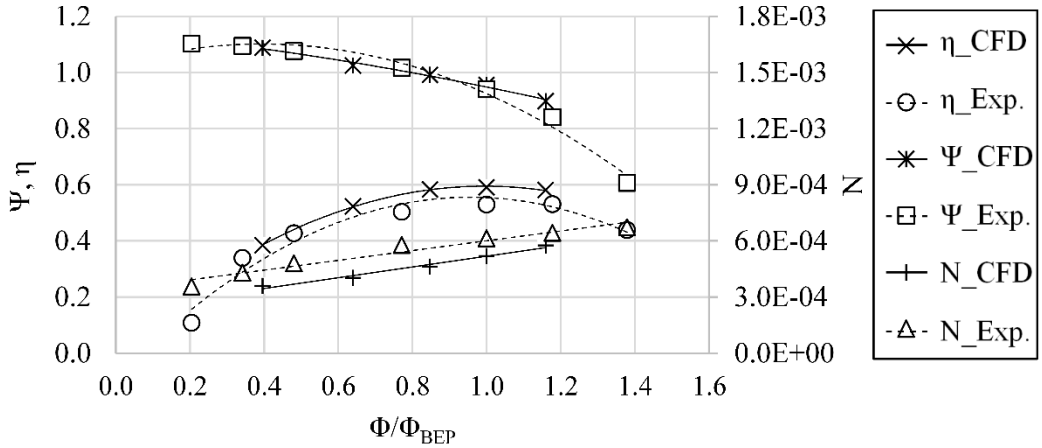

Figure 5.13 Numerical and experimental characteristic curves of impeller No. 4.

The numerical results of the total head agree well with the measurements, however, a systematic difference is observed between the power curves, where the numerical model underestimates the pump power in the entire loading range (Fig. 5.13). This divergence can be attributed to the present modelling of the bearing (Eq. 4.36) and rotating disc losses (Eq. 4.35), that is difficult to be estimated with adequate accuracy. The computed lower power values leads in turn to a corresponing overestimation of the pump efficiency values in the entire loading range of Fig. 5.13.

Table 5.1 Boundary conditions and results of the numerical model along with the experimental characteristic curves for impeller No. 4.

	Numerical Model						Experiment			
	Boundary Conditions			Results			Results			
A/A	Q_{in} [kg/s]	Φ/Φ_{BEP} [-]	P_{out} [kPa]	Ψ [-]	η [-]	N [-]	Φ/Φ_{BEP} [-]	Ψ [-]	η [-]	N [-]
1	5	1.16	317	0.90	0.58	0.00058	1.38	0.61	0.44	0.00067
2	4.32	1.00	342	0.96	0.59	0.00052	1.18	0.84	0.53	0.00064
3	3.66	0.85	361	0.99	0.58	0.00046	1.00	0.94	0.53	0.00061
4	2.76	0.64	377	1.03	0.52	0.00040	0.77	1.02	0.50	0.00058
5	1.71	0.40	398	1.09	0.38	0.00036	0.48	1.08	0.43	0.00048
6							0.34	1.09	0.34	0.00043
7							0.20	1.10	0.11	0.00036

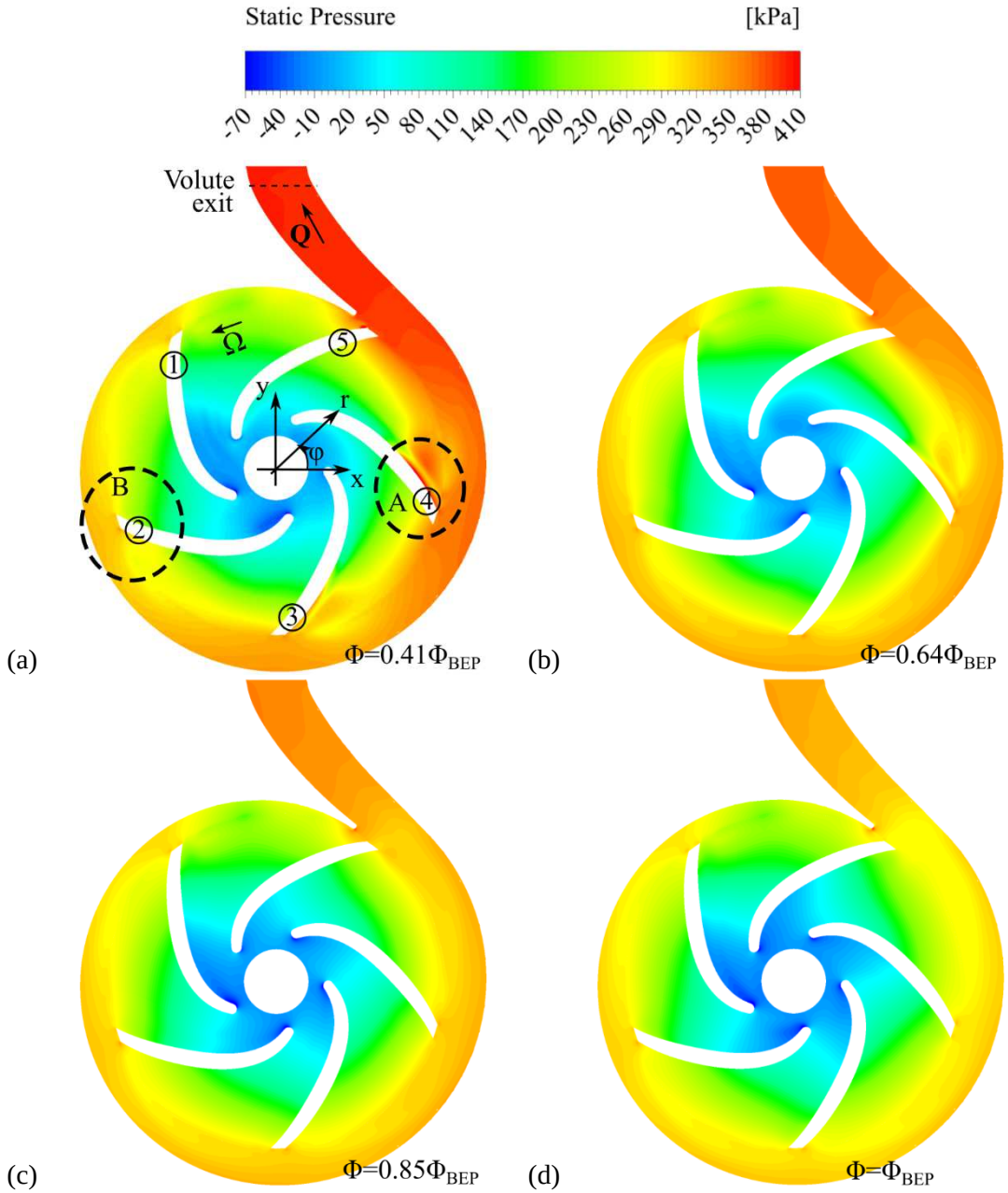

Figure 5.14 Static pressure contours at different flowrates at the midspan of impeller No. 4.

The static pressure plots at a *x*-*y* plane at *z*=0 mm of impeller No. 4 are given in Fig. 5.14, for four different flowrates. The axis origin positions in shown in Fig. 5.15a, so as to illustrate the exact position of the plane. In Fig. 5.14a the five blades are numbered in the direction of rotation. As it is expected, the pressure increases along the radial direction and, likewise impeller No. 2, it takes maximum values at the volute exit. The static pressure at the pump exit increases as the flowrate takes lower values (Fig. 5.14a to d), since the inlet pressure is kept constant in these simulations.

Moreover, the range of static pressure values is wider here ([-70, 410] kPa), compared to that presented in Fig. 5.1 ([-70 – 130] kPa) for impeller No. 2, due to the higher rotation speed of the impeller No. 4. The static pressure field in the impeller No. 4 appears to be more periodically symmetric than that of impeller No. 2, because the inlet pipe of the computational domain (Fig. 5.15a) is straight and does not include an elbow close to the pump, as in the case of impeller No. 2 (Fig. 5.15b).

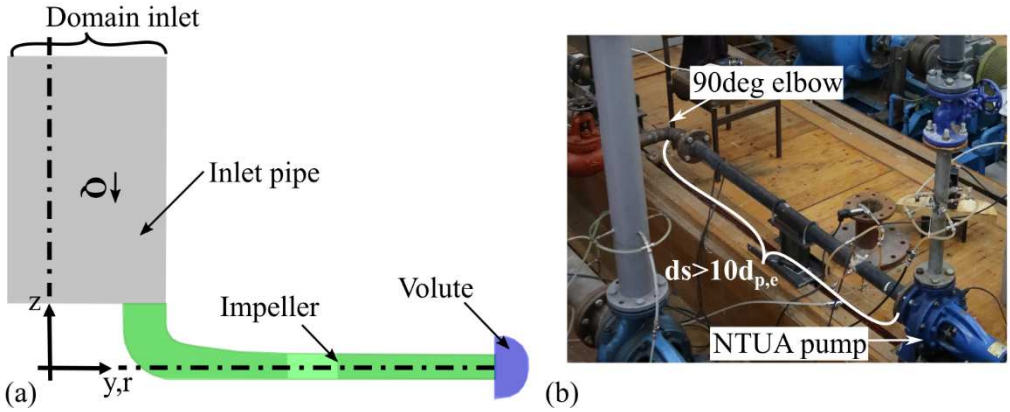

Figure 5.15 a) Axis origin position for the NTUA pump domain, **b)** location of elbow with respect to the pump's position.

Nevertheless, the volute configuration causes the differences in the pressure field at the TE of the five blades and introduces non-uniformities like the ones depicted in Fig. 5.14a with the dashed line circles A and B. Moreover, the pressure field around the TE of blade No. 4 that is closer to the volute exit is quite different than that at the TE of the other blades. However, these differences are eliminated towards the BEP (Fig. 5.14d), where the flow field in the entire casing approaches the free vortex rotation pattern.

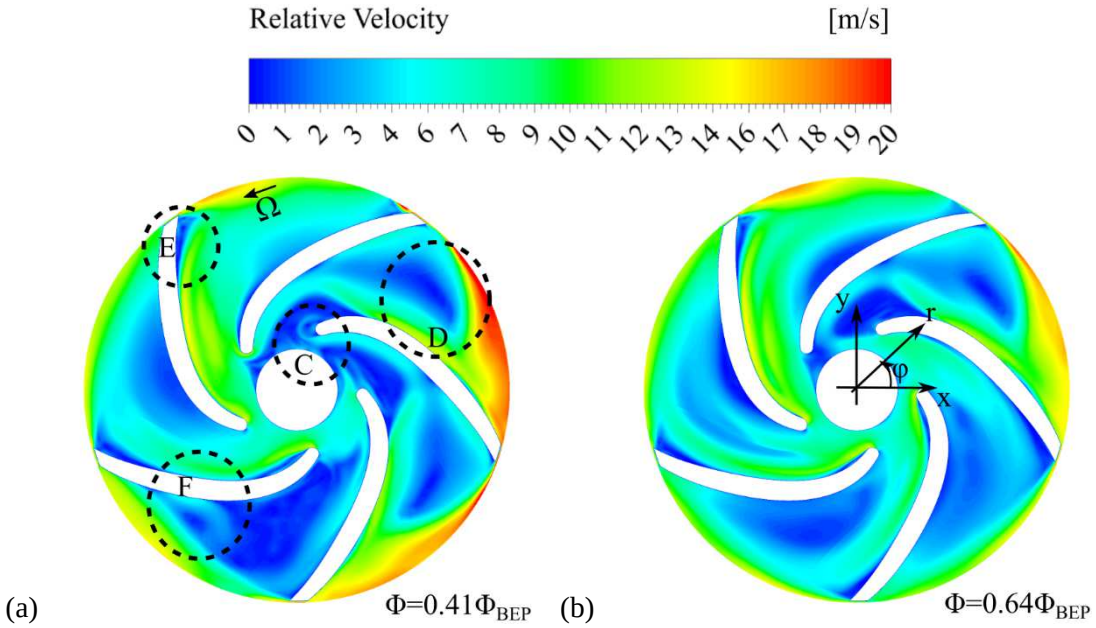

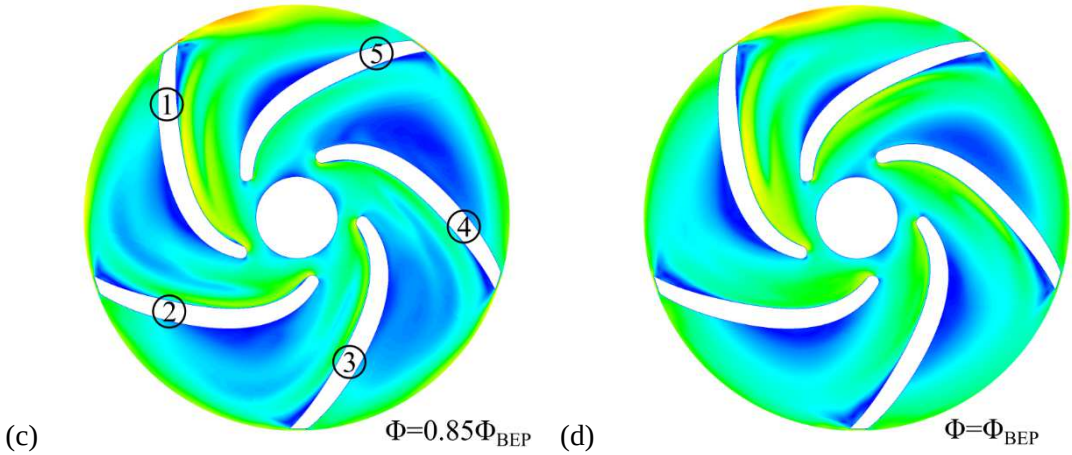

Figure 5.16 Relative velocity magnitude contours for various flowrates at the midspan of impeller No. 4.

The contours of the relative velocity magnitude are given in Fig. 5.16 for the same flowrates presented in Fig. 5.14 at the midspan of impeller No. 4. Additional non-uniformities and non-periodic regions of the flow appear in these contours at the suction and pressure sides of blades No. 3 and 4, which are much different than those at the other blades, especially for low flowrates (Fig. 5.16a), which are weaken at Φ_{BEP} (Fig. 5.16d).

Furthermore, four new areas (C, D, E and F in the dashed line circles) are highlighted in Fig. 5.16, at the lowest flowrate, where local recirculation and typical partflow losses appear (Anagnostopoulos, 2006). These areas are located at the LE of the blades (area C), in the flowpath between the blades (area D), at the TE of the blades (area E), and at the midspan of the pressure side of the blades (area F).

In order to examine and analyse the flow conditions in these areas, the vectors of relative velocities for Φ_{BEP} are plotted and compared with the corresponding ones for Φ_{MIN}, in Fig. 5.17. The detrimental effect on the efficiency of the reduced loading of the pump is obvious in all these areas. Strong recirculation zones are created not only at the blade edges (areas C and E, Fig. 5.16a), but also in the flowpath between the blades (areas D and F, Fig. 5.16a).

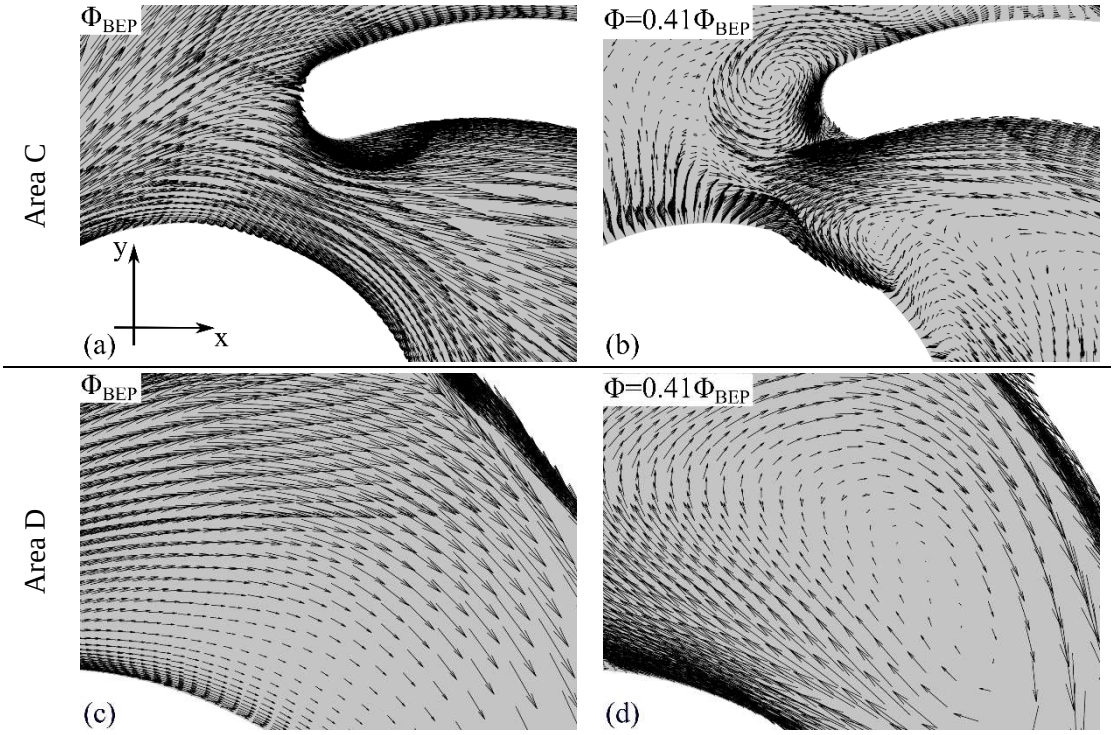

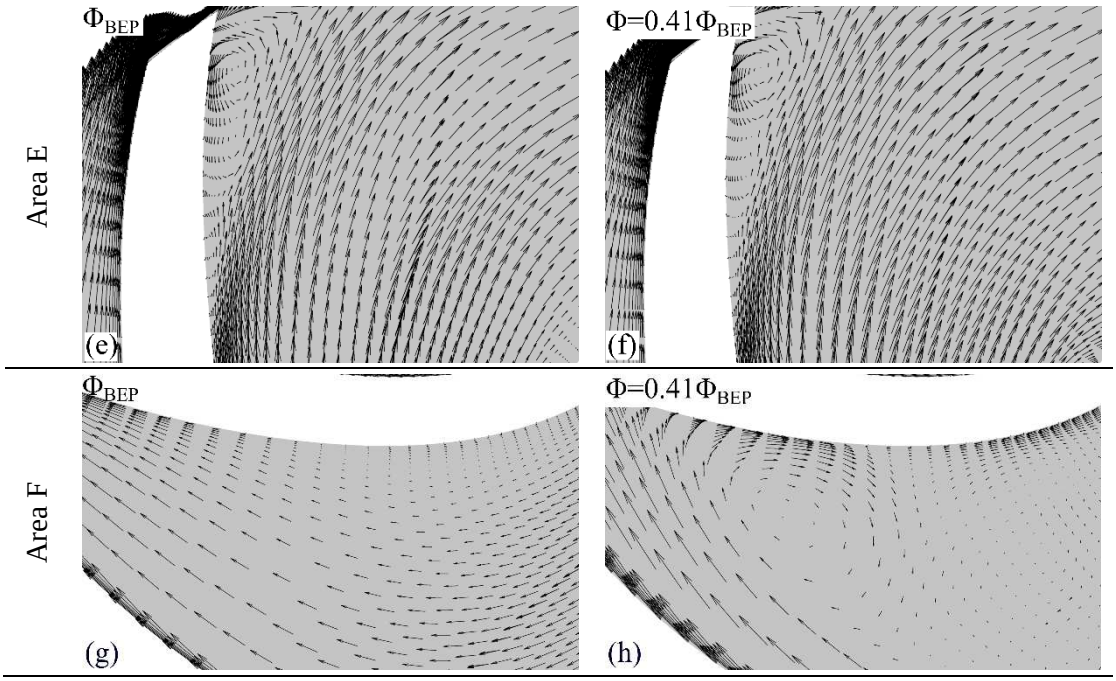

Figure 5.17 Relative velocity magnitude vectors at the areas C, D, E, and F (see Fig. 5.16) at the midspan of impeller No. 4.

In addition, the flow recirculation at the leading edge of the blade when the pump operates under partial loading (Fig. 5.17b) illustrates the effect the flow incidence angle increase. As concluded in the discussion of Fig. 3.10 (section 3.3.1), the incidence angle dominates the internal flow conditions in the case of the closed impeller, and it minimises at the BEP conditions of the pump (Fig. 5.17a). The numerical model can provide clear views of the the incidence angle effect on the local flow filed developed in both impellers presented in this Chapter.

On the other hand, the flow becomes smoother at the BEP, both at the LE (area C, Fig. 5.17a), in the flowpath (area D, Fig. 5.17c) and at the midspan of the blade (area F, Fig. 5.17g), and hence the suction performance of the impeller regarding cavitation is improved. However, the reverse flow area at the suction side of the blades TE persists (Fig. 5.16d and 5.17ed), as also the low to zero velocity region at the pressure side of the blades (Fig. 5.16d). This flow picture reveals that the hydrodynamic design of the blades is not optimised, and can explain the relatively low attained efficiency of this pump (Fig. 5.13).

5.3 Cavitating conditions

After the detailed investigation of the performance of the pumps at normal operating conditions, the cavitation study follows. In the case of impeller No. 2, its performance under cavitating conditions it has been already discussed in the validation section 4.6. Consequently, this section presents the effect of the cavitation in the pressure distribution on the blade surfaces, the cavitating flow details at the tip of the impellers, and the influence of the tip's thickness on the cavitation performace of the pump. Finally, the results of the two phase flow simulations, for the geometry of the closed impeller No. 4, are shown.

5.3.1 Impeller No. 2

The significant drop of pressure in the impeller that operates under cavitating conditions can be depicted with the static pressure distribution on the surface of the blade No. 2 for z=1 mm, presented in Fig. 5.18. The static pressure is represented from Ψ_{ST} non-dimensional number, calculated from Eq. 5.1, where p is the static pressure computed and u_2 is the tangential velocity of the TE of impeller No. 2.

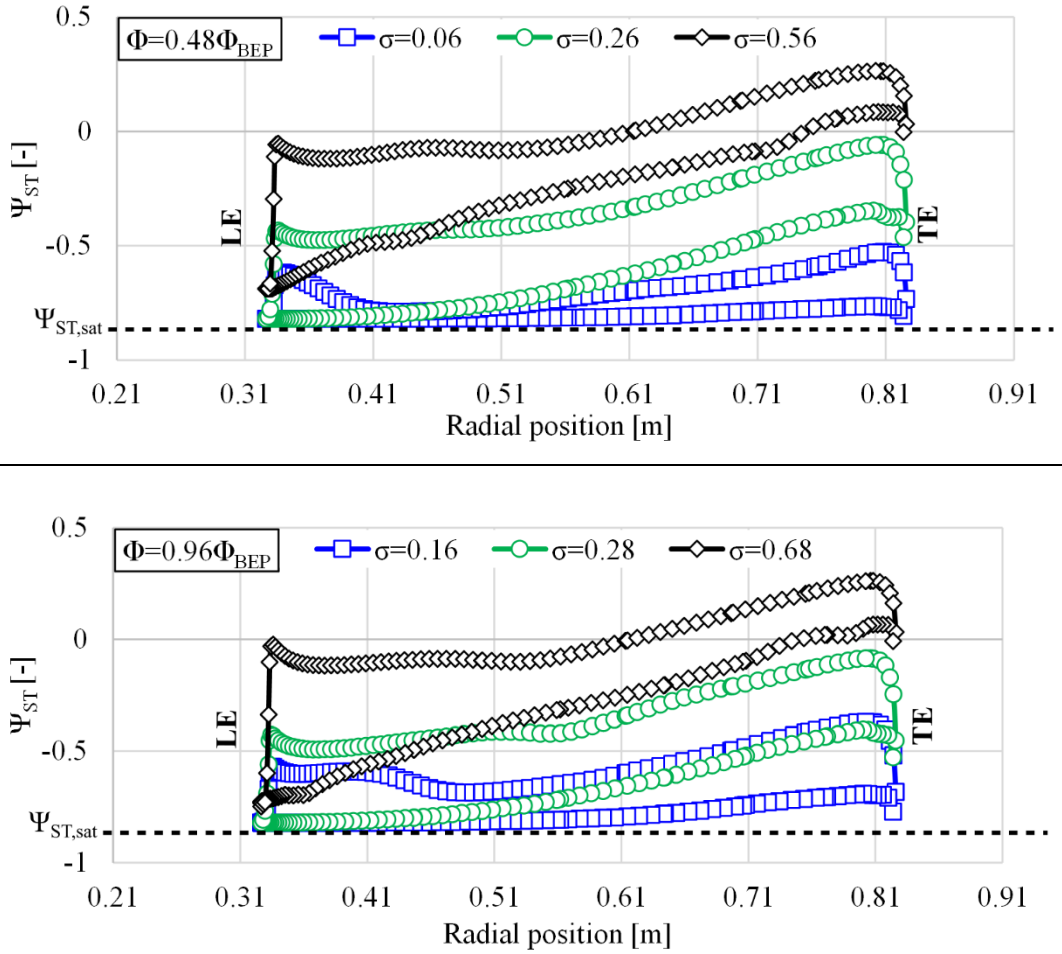

Figure 5.18 Static pressure distribution of the streamline on the surface of the blade No. 2 at impeller No. 2.

$$\Psi_{ST} = \frac{2p}{\rho u_2^2} \tag{5.1}$$

In the plots of the two Φ numbers shown in Fig. 5.18, is clear that Ψ_{ST} value is reduced progressively as σ takes lower values for both suction and pressure side. At intermediate σ values (green line) Ψ_{ST} is minimised, by obtaining the vapour pressure value, $\Psi_{ST,sat}$=-0.84, at the LE of the suction side, demonstrating the existence of two-phase flow at this area. Only the maximum σ values (black colour rhombus line) ignore vapour pressure values and cavitation at the blade surface.

For the minimum σ values (blue colour square line) presented, the Ψ_{ST} value is minimised along the total span of suction side of the blade. Furthermore, at Φ=0.48·Φ_{BEP}, where σ values are the lowest, even the pressure side of the blade takes values close to the $\Psi_{ST,sat}$. For the minimum σ numbers (σ=0.06 for Φ=0.48·Φ_{BEP} & σ=0.16 for Φ=0.96·Φ_{BEP}), the shape of the distribution at the pressure side shows a sudden drop that is not visible to the other σ values.

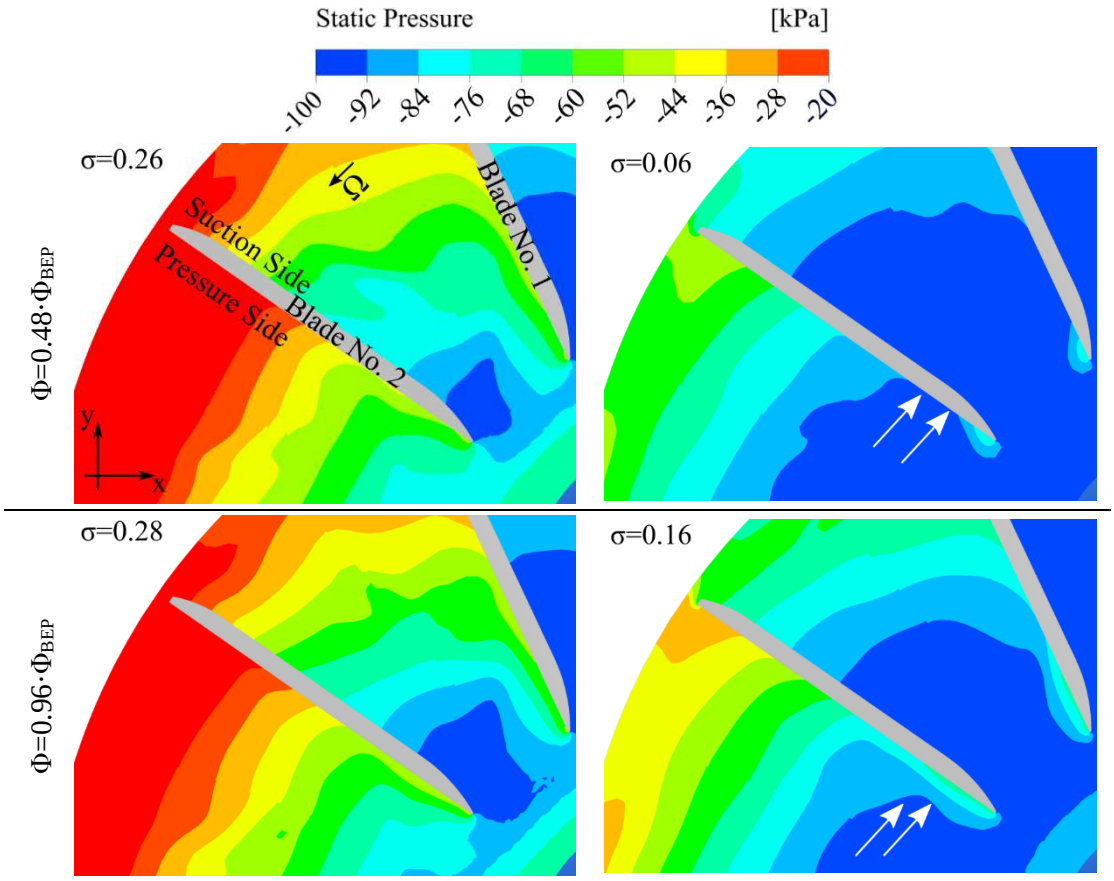

Figure 5.19 Static pressure at blade No. 2 at x-y plane with *z*=1 mm for impeller No. 2.

This strange shape can be explained by the static pressure contours on the *x-y* plane at *z*=1 mm, which are shown in Fig. 5.20 for the two lowest σ values of all flowrates presented in Fig. 5.18. At the point of severe cavitation, low static pressure area blocks the inflow of this impeller path and reach the pressure side of the next coming blade (white arrows, Fig. 5.19).

The performance of the present pump is significantly affected by the absence of impeller shroud. In Section 5.2.1, it is concluded that backflow recirculation from the tip is important close to the LE of the blade. This could strongly affect cavitation development at lower σ values and possibly create conditions that favor backflow cavitation. For this reason, the analysis of tip clearance effect on cavitation focuses on the comparison of the tangential component of the

relative velocity vectors at the LE for three different OPs; $\sigma=0.62$ that is close to the onset of the first bubbles, $\sigma=0.34$ at an intermediate stage of development, and $\sigma_{FC}=0.16$ at the total head breakdown, for flowrate close to the nominal ($\Phi=0.96\cdot\Phi_{BEP}$).

The results of the tangential components of the relative flow velocity are shown in Fig. 5.20, together with the static pressure contours for the two different planes discussed in section 5.2.1: A_1 (x-y) and A_2 (y-z). The static pressure decreases gradually in the entire LE region with the reduction of σ value, while low static pressure zone (cavitation) grows and captures larger volumes at the suction side of the blade, at the impeller inlet and in the tip clearance area (Fig. 5.20a to c). As expected, at σ_{FC} the low pressure cavitating flow (absolute pressure of 2.8 kPa), dominates the entire tip clearance.

The results of Figs. 5.20b,e at $\sigma=0.34$ illustrate the backflow cavitation mechanism, that transfers fluid from the low static pressure area of the tip towards the suction side of the blades and the inlet of the impeller.

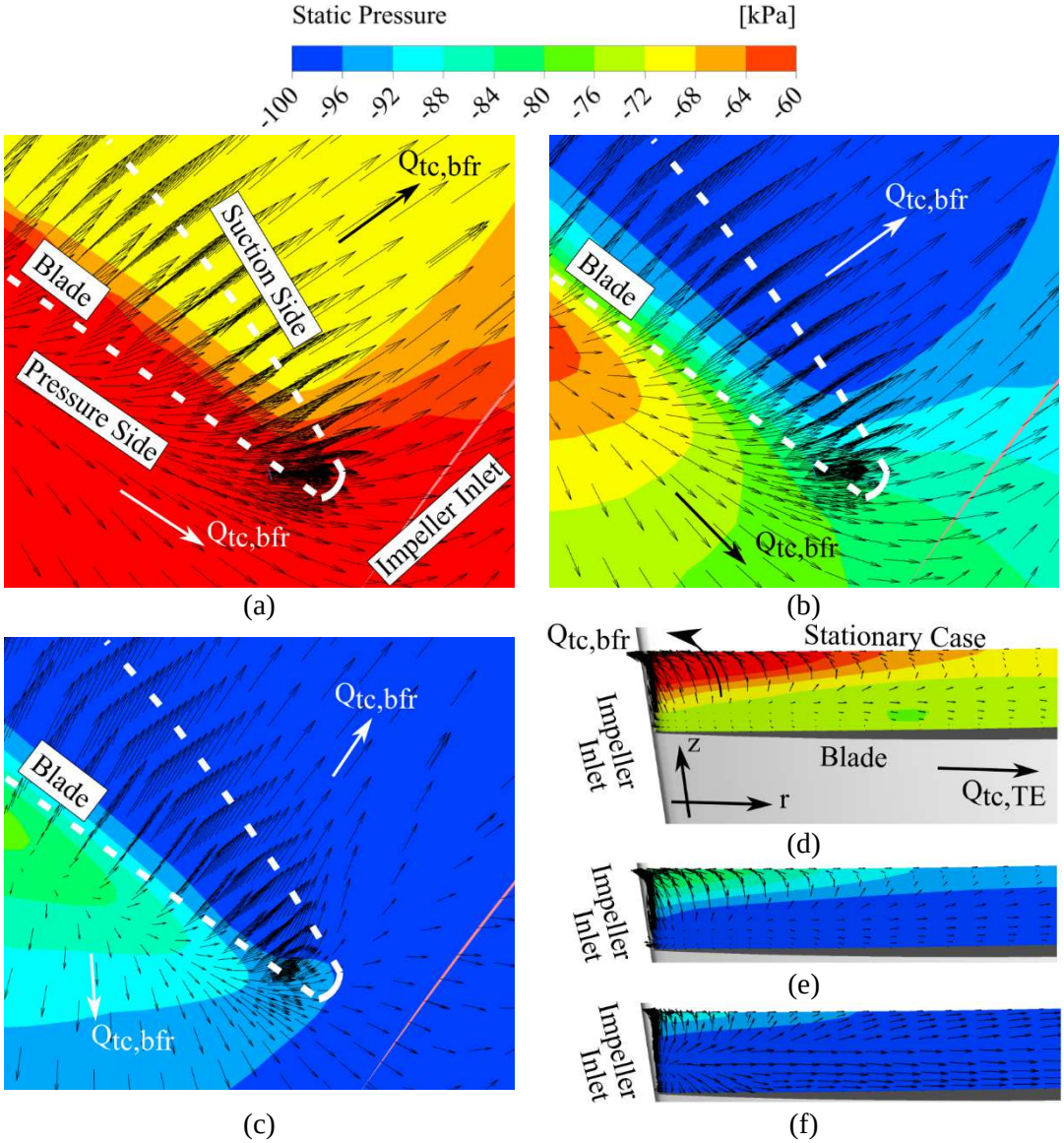

Figure 5.20 Static pressure contour and tangential component of therrelative velocity vectors for $\Phi=0.96\cdot\Phi_{BEP}$ at **a)** A_1, $\sigma=0.62$, **b)** A_1, $\sigma=0.34$, **c)** A_1, $\sigma_{FC}=0.16$, **d)** A_2, $\sigma=0.62$, **e)** A_2, $\sigma=0.34$, **f)** A_2, $\sigma_{FC}=0.16$.

However, when σ takes its lowest value, and Ψ is collapsed, both recirculation flows appear to decrease (Figs. 5.20c, f). This is because the static pressure continues to decrease only at the

pressure side of the blade, and hence the pressure differences which drive backflow recirculation become smaller. As a result, the backflow cavitation weakens as σ decreases and hence this flow mechanism seems to affect more the OPs at intermediate values of σ. Hence it is confirmed that the drop of total head, presented in the σ-Ψ curves of impeller No. 2 (Fig. 3.9b - section 3.3.1 & Fig. 4.23 - section 4.6.2) is related mainly to the vapour formations developed in the flowpath between the blades rather than those developed at the area of the tip clearance.. This behaviour is also observed in the study of Kim (S., 2013), where a similar numerical investigation (CFD code and two-phase model) is carried out in a turbopump inducer.

5.3.1.2 Effect of the tip clearance thickness on the cavitation development

The effect of tip clearance thickness on the two-phase flow development in the impeller No. 2 is investigated with the simulation of two additional geometries of tip clearance (t_{tc}=0.5 mm and t_{tc}=1.5mm) at Φ=0.80Φ_{BEP}. Two σ values are simulated for the two-phase flow analysis, which correspond to intermediate (σ_{INT}~0.32) and intense cavitating conditions (σ_{FC}=0.13). The static pressure contours at the x-y plane for all cases listed in Table 4.4, are presented in Fig. 5.21, where a representative view from inside the impeller can be observed at z=1 mm. The general behaviour of the flow is relatively similar for the three simulated tip clearance cases presented in the plots of Fig. 5.21, because two important mechanisms that affect cavitation development, counteract.

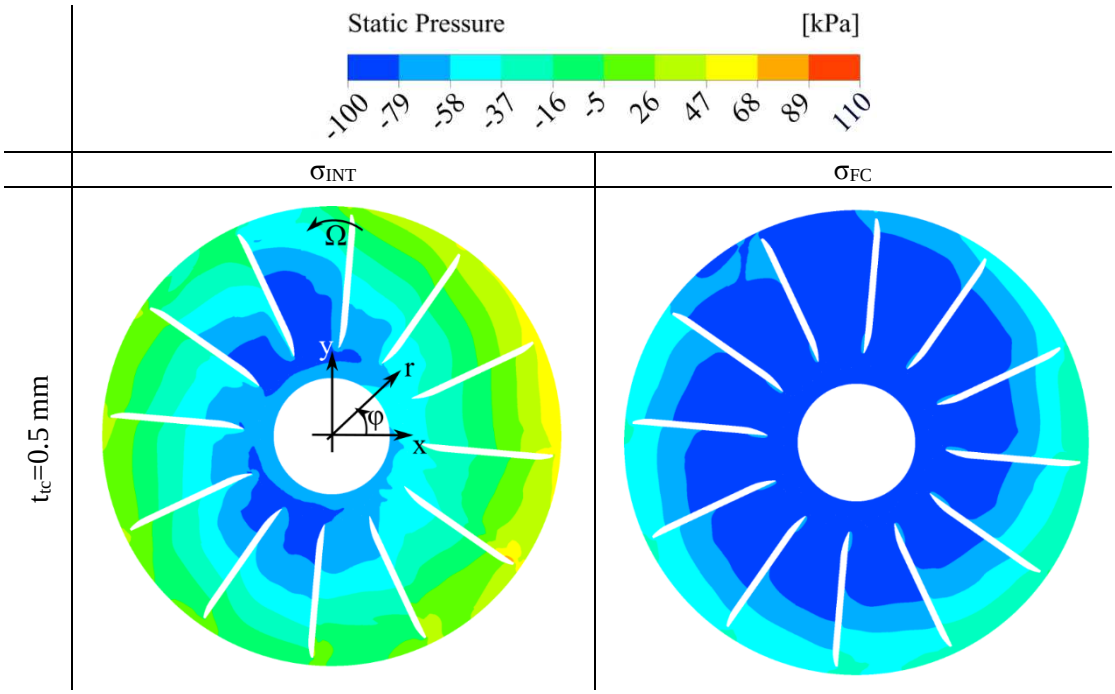

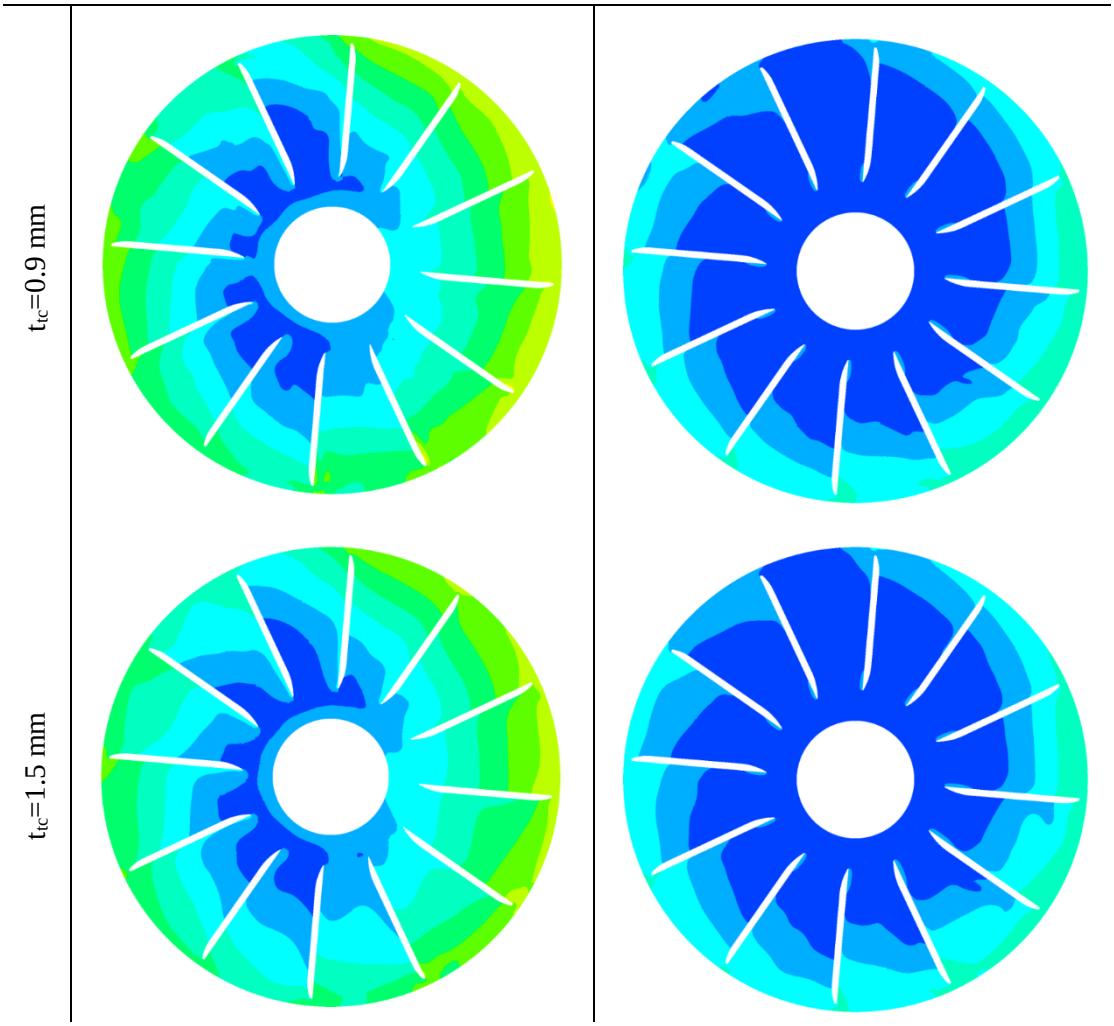

Figure 5.21 Pressure contour at x-y plane, z=1mm for $\Phi=0.80\Phi_{BEP}$, for σ_{INT} and σ_{FC} at the three tip clearance case.

On the one hand, the increase of tip clearance thickness results in stronger recirculations (presented in Fig. 5.12 under non-cavitating conditions) that localy decrease static pressure and force the flow to cavitate, while simultaneously decreases the rotating surface and decelerates the flow. This similarity is more evident for the area of total head drop (Fig. 5.21 σ_{FC}), since for intermediate conditions, a closer examination of the pressure fields in Fig. 5.21, shows that the extent of lower pressure area ([-79 – -100] kPa) in the suction side of the blades appears in more blades when t_{tc} increases (Hong, 2006; Luo, 2008; Xu, 2017). In addition, the changes introduce in t_{tc}, do not affect the flow asymmetries in the impeller, however the non-axisymmetric behaviour weakens at σ_{FC}.

Finally, the results of relative velocity vectors and static pressure on the planes A_1 and A_2 at the LE of the second blade are plotted for σ_{INT}~0.32, $\Phi=0.80\cdot\Phi_{BEP}$ in Fig. 5.22. In the static pressure plots of A_1 plane (Figs. 5.22a,b,c) the low static pressure zone (cavitation) occupies larger area at the suction side of the LE of the blade, for the minimum thickness tip clearance (t_{tc}=0.5 mm - Fig. 5.22a). In the same contour, the maximum static pressure value is obtained (-60kPa) at the pressure side of the blade (Figs. 5.22a,b,c). The vectors of relative velocity on the A_1 plane do not change significantly with the value of t_{tc}, where the flow recirculates to the suction side of the blade, as well as towards the impeller's inlet.

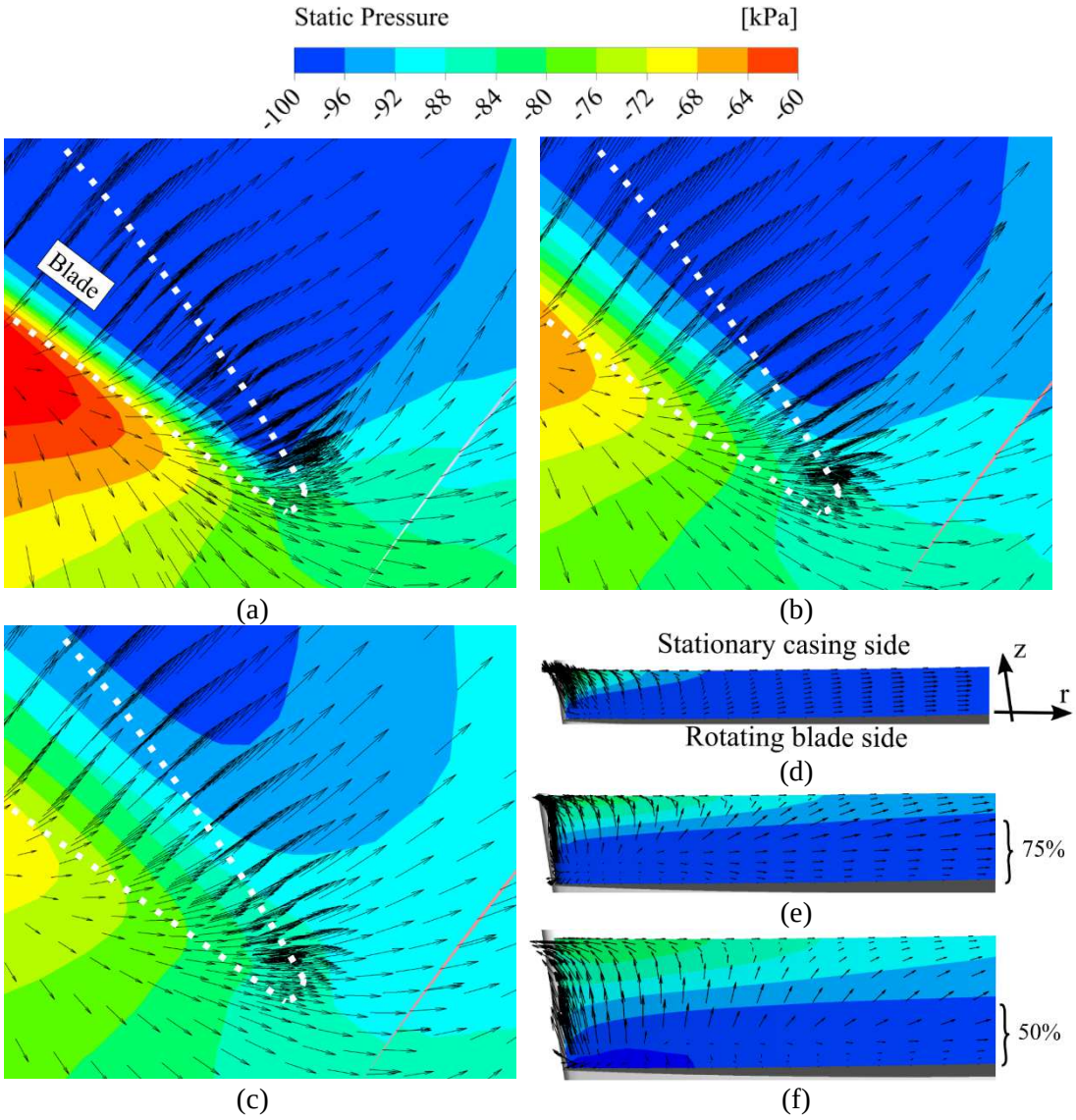

Figure 5.22 Static pressure contour and tangential component of the relative velocity vectors for σ_{INT}, $\Phi=0.80\cdot\Phi_{BEP}$ at **a)** A_1, t_{tc}=0.5 mm, **b)** A_1, t_{tc}=0.9 mm, **c)** A_1, t_{tc}=1.5 mm, **d)** A_2, t_{tc}=0.5 mm, **e)** A_2, t_{tc}=0.9 mm, **f)** A_2, t_{tc}=1.5 mm.

Furthermore, in the results of plane A_2 of Fig. 5.22d-f, it can be observed that the low pressure area covers the largest part of the tip and extends towards the stationary casing side of the numerical domain, especially in the case of t_{tc} =0.5 mm (Fig. 5.22d). For larger thicknesses, the size of the low static pressure zone decreases, thus it covers less portion of the tip clearance space (75% of t_{tc}=0.9mm and 50% of t_{tc}=1.5mm). However, the flow recirculation area, depicted from the relative velocity vectors in Fig. 5.22d,e,f, increases with the increase of t_{tc} and strengthens backflow cavitation at the impeller's inlet. This behaviour agrees with the conclusions made after the comparison of Figs. 5.6, 5.11 and 5.12, under non-cavitating conditions.

5.3.2 Impeller No. 4

The simulated cavitation characteristic curves (σ-Ψ) for four different flowrates are given in Fig. 5.23 together with the corresponding measurements that were shown in Fig. 3.9 for the impeller No. 4. In Fig. 5.23a the results for partial flow conditions ($\Phi=0.41\cdot\Phi_{BEP}$ and $\Phi=0.64\cdot\Phi_{BEP}$) are given, while Fig. 5.23b presents the curves for the flowrates close to nominal

conditions (Φ=0.85·Φ_{BEP} and Φ=Φ_{BEP}). The selection of these operating points is made, in order to include the total range of suction conditions (0<σ<0.4) at n=2900 rpm for T=20 ºC. According to the results of Fig. 5.23, the simulated curves reproduce successfully the performance of the pump under various cavitating conditions.

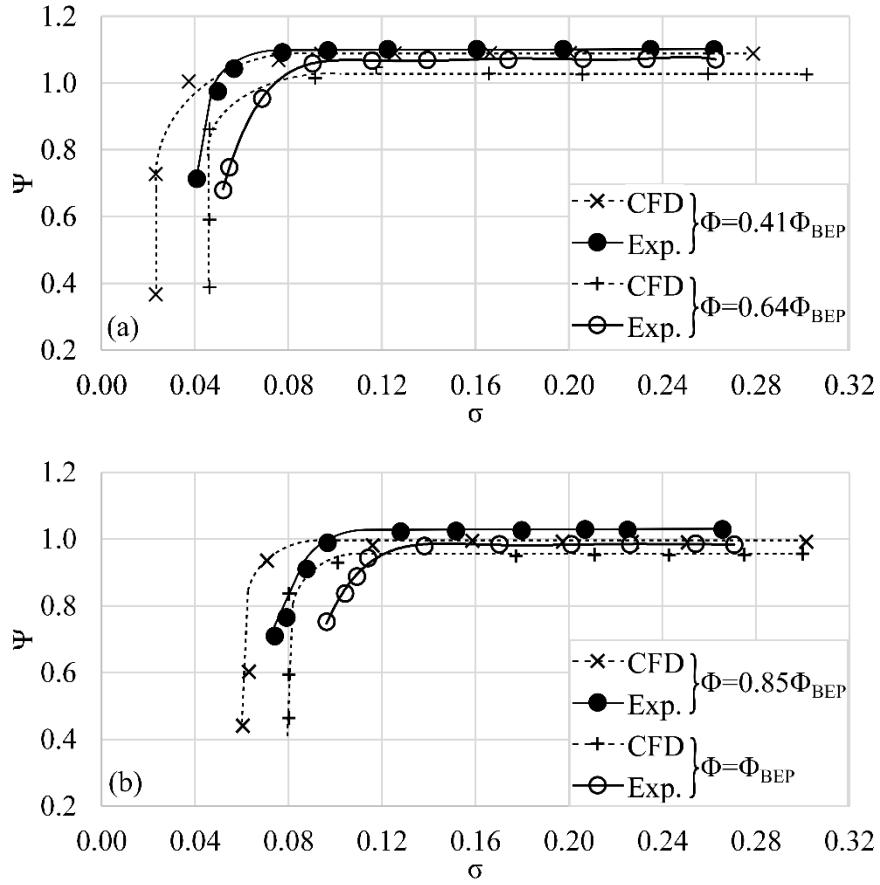

Figure 5.23 Cavitation characteristic curves computed and measured for impeller No. 4 at **a)** Φ=0.41·Φ_{BEP}, Φ=0.64·Φ_{BEP} and **b)** Φ=0.85·Φ_{BEP}, Φ=Φ_{BEP}.

Similarly to impeller No. 2, the model overestimates the ability of the machine to pump at extreme suction conditions, because it does not consider the effect of the two-phase flow formations created before the suction of the pump.

All the numerical σ-Ψ characteristic curves are summarised in Fig. 5.24, together with the experimental (yellow colour similarly to Fig. 3.9, Exp.VI) and numerical (dark blue colour rectangular, CFD.VI) visual inception cavitation area. Regarding the operating points selected for the two-phase flow analysis, OPs A, B lie in the CFD onset area at high σ values, while OPs C and D are close to the experimental visual inception area. Finally, the OPs encircled in the red colour area represent the total head drop conditions, similarly with the impeller No. 2 (Fig. 4.25, section 4.6.4). The selected operating point for visualization cover a wide range of suction conditions and flow coefficients, from 40% to 100% of the nominal flowrate.

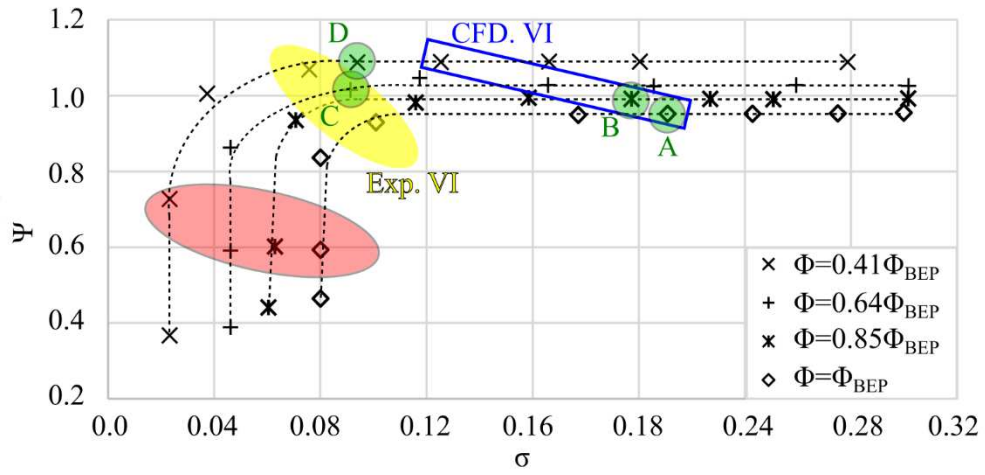

Figure 5.24 Computed σ-Ψ characteristic curves for impeller No. 4.

In Fig. 5.25 the two-phase flow area developed in the impeller No. 4 at the operation points A, B, C and D is shown. In all plots, the cavitation area is given along with the location of the Plexiglas window of this particular pump. The results of the OPs A and B represent the onset of two-phase flow formation at σ~0.2. Under such conditions, steady attached cavities are formed close to the LE of the suction side of the blade and exhibit the lowest growth compared to the results of OPs C, D in the same figure. At these early stages of two-phase flow development, the shape of the narrow vapour phase is elliptic. The computed cavitation area at σ~0.2 does not expand until the MS of the blade, which agrees with the observations made in Fig. 3.16, where no vapour is observed in the flow visualisation photographs. Weak asymmetries are also evident for point B, where the vapour phase is developed only close to the blades No. 1, 2 and 3, while for point A, which lies at the nominal flowrate, it appears at the LE of all blades.

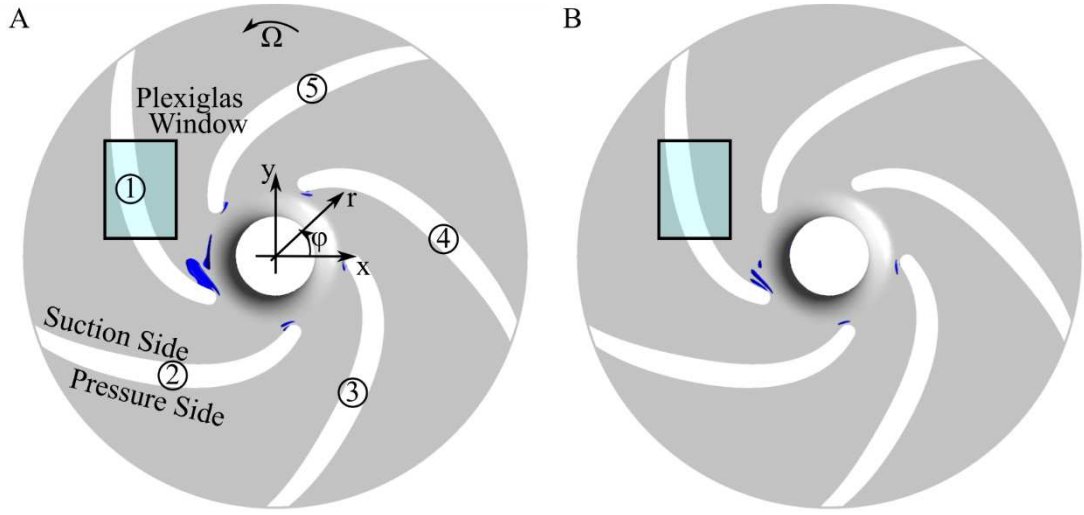

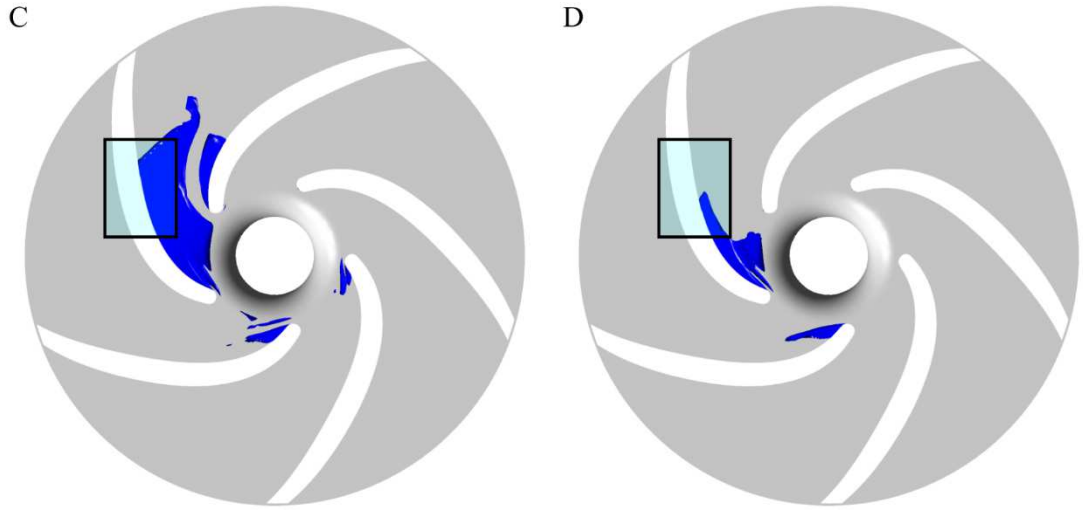

Figure 5.25 Development of vapour phase in the operating points A, B, C and D for impeller No. 4.

The plots of the OPs C and D in Fig. 5.25 represent the intermediate stages of cavitation development at σ~0.1. Under these conditions, asymmetries regarding the cavitation area clearly appear. For point C, the cavities occupy part of the suction of blades No. 1, 2 and 3, and for point D, which lies at a slighter larger σ value, the vapour phase lies only at the suction of blades No. 1 and 2. According to the plots for C and D OPs, the attached vapour area enlarges and especially for blade No. 1, it reaches the MS of the blade, in the area of the Plexiglas window. The vapour area at blade No. 1, is thinner and shorter for the OP D compared to that for OP C because $\sigma_C<\sigma_D$ and $\Phi_C>\Phi_D$. The flow visualizations during the experimental measurements of impeller No. 4, presented in Fig. 3.16, confirm the appearance of vapour bubbles at the intermediate cavitating conditions (OP C and D) of Fig. 5.25, and further validate the modelling approach proposed in this study. In addition, the results of Fig. 5.24 and 5.25 confirm the ability of the modelling approach towards the prompt detection of the cavitation phenomenon, far before the total head drop of the pump, even for the case of the closed impeller No. 4.

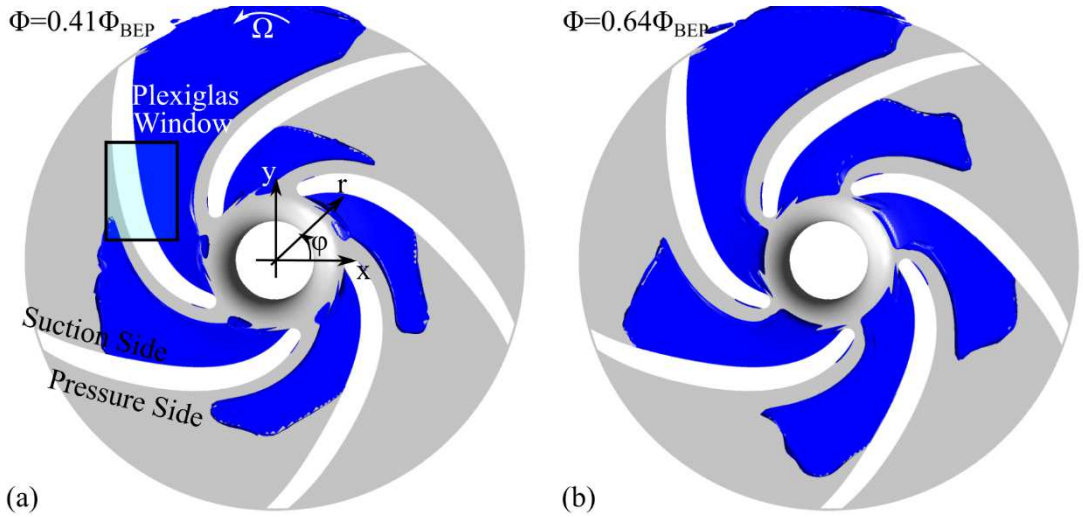

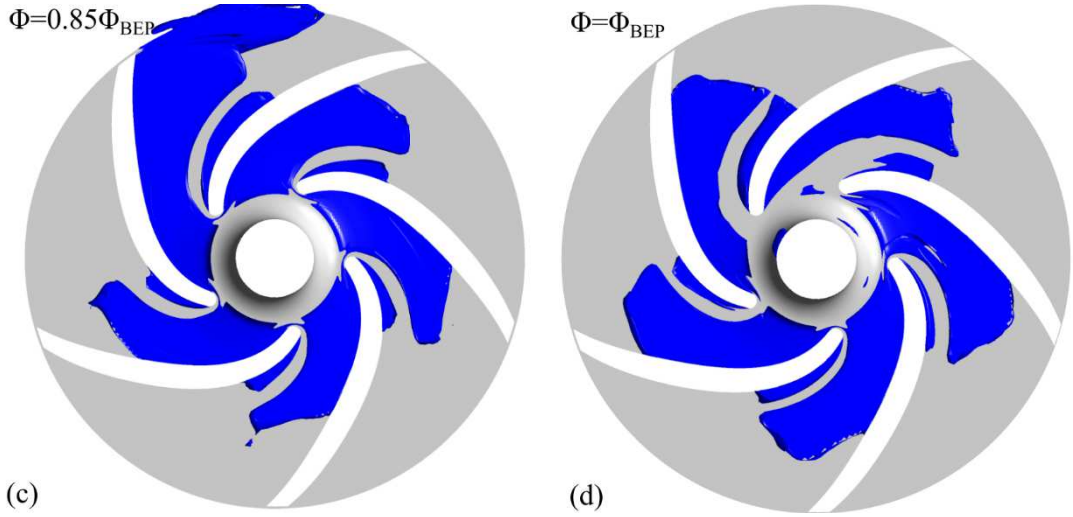

Figure 5.26 Development of vapour phase under σ_{FC} suction conditions for impeller No. 4.

Finally the results at the total head drop OPs for the four flowrates are shown in Fig. 5.26. At such conditions the size of the steady attached vapour cavities maximises, and thy block the inflow area of the flowpath between the blades, making the pump unable to provide power to the fluid. In case of partial flowrates, the cavities reach the trailing edge of blade No. 1 and spread in the volute area (Fig. 5.26a to c). The asymmetries observed in Figs. 5.25 and 5.26 are presumably the result of the volute's asymmetric shape, and the additional losses introduced by its tongue that are increased at lower flowrates (Pouffary, 2008; Fu, 2015). When the flow conditions become optimum at Φ_{BEP}, the asymmetries are minimised (OP A in Fig. 5.25, and Fig. 5.26d).

5.4 Synopsis

In this section the results from the application of the numerical model for the simulation of the performance of impellers No. 2 (semi-open) and No. 4 (closed), under single-phase and cavitating flow conditions are presented. For the simulation of the steady two-phase flow, the homogeneous model of Zwart et al. (2004) is used. Impeller No. 4 is shrouded (closed), while impeller No. 2 is semi-open and the computational domain includes the blades tip clearance area. By this way, the effect of steady tip leakage flow in the performance and suction behaviour of the pump is investigated.

In the case of impeller No. 2, three are the basic mechanisms that drive the low static pressure area in the pump; i) the amount of flowrate that passes through the blade channels, ii) the inlet blade angle, which for impeller No. 2 is radial (β_1=90º), and iii) the recirculations due to the tip clearance flow. Optimum flow conditions appear only for the Φ_{BEP} of impeller No. 4, since the high blade angle of impeller No. 2 and its tip clearance introduce significant recirculations in the entire range of flowrates simulated.

The semi-open impeller faces additional volumetric and hydraulic losses due to the three-dimensional flow in the tip clearance. More specifically, the flow in this narrow area consists of two parts; i) the main radial component that flows towards the trailing edge (TE) of the blade at the exit of the impeller and ii) the areas of strong backflow recirculation, where the water flows towards the suction of the blade and the inlet of the impeller.

These recirculations are of significant importance, because they are responsible for the backflow cavitation phenomenon, when the static pressure drops and approaces the vapour saturation pressure value. Under two phase flow conditions, the flow recirculates from the tip cavitating area and brings cavities towards the already cavitated impeller suction side. The recirculation, no matter the suction conditions, occurs throughout the total tip clearance. The phenomenon is also highlighted experimentaly in the photographs of the visualised vapour flow in Chapter 3. The effect of backflow cavitation in the suction performance of the pump is significant until the σ_{FC} OP, where the pressure differences that drive this recirculation are minimised, following the total head breakdown.

The flow visualization and measurements performed in the NTUA test rig for the impeller No. 4 confirm the ability of the numerical model to predict the extent of the cavitation zone under intermediate cavitating conditions. In addition, the proposed numerical approach detects the development of cavitation before the total head drop of the pump, similarly to the semi-open impeller case. The comparison cannot be made for initial cavitating conditions since the transparent window does not allow the observation of the flow close to the LE of the blade. However, the decent performance of the simulation results under intermediate condition, and the sufficient agreement of the predicted and measured σ-Ψ curves allow the use of the model, in order to estimate the suction conditions that correspond to the onset of cavitation. For this reason, the results at the visual inception point as computed for impeller No. 4, are used in the following Chapters 6, 7, in order to provide additional information regarding the onset of the cavitation mechanism.

Finally, the effects of the thickness of tip clearance on the performance of the semi-open impeller No. 2 are examined, under both normal and cavitating conditions. According to the results, increase of this thickness causes further reduction of the total head of the pump under single-phase conditions. Moreover, under cavitating conditions, the tip clearance thickness does not affect considerably the absolute size of the two-phase flow region in the pump, but a larger thickness creates stronger back recirculation flow, which enhances the backflow cavitation behaviour of the impeller.

6. Noise & Vibration Measurements

6.1 Introduction

In this chapter, the flow visualizations and the performance measurements for the derivation of the cavitation characteristic curves in the four impellers, described in Chapter 3, are supplemented with the results of the mechanical vibration and Acoustic Emission (AE) measurements (Fig. 6.1). The characteristics and the position of the noise and vibration sensors for both test rigs are provided in section 2.5. The aim of this Thesis is to identify an experimental signal processing procedure that is able to detect vapour phase at early cavitation stages in hydraulic turbomachinery. In order to achieve it, the noise and vibration signal characteristics are studied both in time and frequency domain. The behaviour of the signal properties as a function of Thoma cavitation number, σ, at different stages of cavitation development, is also examined and presented in this chapter.

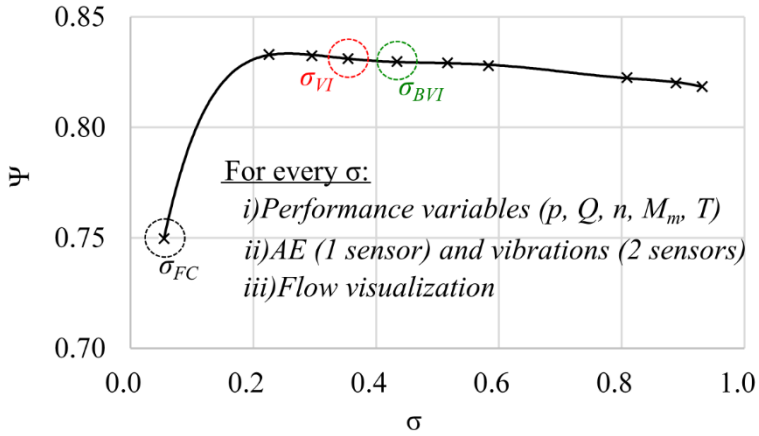

Figure 6.1 Cavitation characteristic curve, for the first test of impeller No. 1, at $\Phi=0.40\cdot\Phi_{BEP}$.

Initially, the results are presented in the time domain, where the raw time series of the vibration and the AE signals are given along with the study of their distribution and the patterns of their statistical moments; the mean, the variance, the skewness and the kurtosis. The next stage of analysis includes different processing techniques that describe signal's behaviour in the frequency spectrum and are presented in section 2.4. These are:

i. The velocity of vibration root mean square (RMS) tool, provided from the International Standards Organization (ISO 10816-1) for the mechanical vibration measurements.
ii. The Power Spectral Density (PSD) and the powerband tool for the vibration measurements.
iii. The AE_{RMS} calculation for the noise measurements.

The cavitation tests include the investigation of four different flowrates for each impeller (Fig. 3.9), each of which consists of an average of ten operating points (OPs). The reduction of the number of data presented at each stage of analysis is done by selecting typical operating conditions, usually one non-cavitating point, the visual inception point, σ_{VI} and the total head drop point, σ_{FC}. For the Lancaster University (LU) impellers (No. 1, No. 2 & No. 3) the non-

cavitating point is represented from the point that lies next to σ_{VI}, the so-called: before visual inception, σ_{BVI}, with $\sigma_{BVI} > \sigma_{VI}$ (see Fig. 6.1). On the other hand, the limitations in the experimental visual observations of National Technical University (NTUA), discussed in Chapter 2, make unsafe a similar comparison for impeller No. 4. For this reason the σ_{BVI} OP is the one with the maximum measured σ (Fig. 6.2b).

Henceforward, the study focuses on the detection of cavitation phenomenon by the monitoring of its dynamic characteristics that are transmitted from the bubbles implosion to the vibration and AE sensors. For the analysis of Chapters 6 and 7, the two-phase flow area is not treated as a combination of different types of cavitation (i.e. attached, travelling bubble, cloud cavitation, tip clearance etc.) but as a single (unified) dynamic mechanism that creates shock pressure waves. As a consequence, the various types of vapour formations that are used for the description of the phenomenon until this point, will be included in the term cavitation.

6.2 Time domain results

The first stage of the signal processing analysis refers to the measured noise and vibration time series. By this way, it is possible to compare the raw and evident characteristics of the signals, such as their amplitude and the behaviour of abnormal components. The second step of the analysis examines the distribution characteristics of the signals, while the final step includes the study of the pattern of the statistical moments of the measured data as function of suction conditions.

6.2.1 Measured signals

In Fig. 6.2 two typical three-dimensional graphs of measured signals in time for all σ values are shown. The first (Fig. 6.2a) corresponds to the vibration sensor (A01) of impeller No. 1 for Φ=0.40·Φ_{BEP} and the second to the AE sensor of impeller No. 4 for Φ=Φ_{BEP}.

For all vibration measurements, the vibration signal is converted from Volts to acceleration values by dividing Volts with the sensitivity of the vibration sensors (0.0102 V/m·s^2). The time series of Fig. 6.2 are focused in a short timespan, as it can be seen in the x-axis (time), because it is easier to illustrate details, such as the signal amplitude or possible impulses.

The higher sampling rate, f_s, for the AE sensor (160 kHz), compared to that of the vibration measurements (20 kHz), presented also in Table 2.9, (section 2.5.2.2), results in a denser signal. For this reason, the time axis that corresponds to the AE measurements (Fig. 6.2b) is one order of magnitude smaller.

The y-axis (σ) of Fig. 6.2b, is logged in, so as to make more discernable the AE time series that correspond to σ values close to the σ_{FC} region (σ~0.1). The logged in of the y-axis is used only for three-dimenional plots that refer to impeller No. 4. The reason is that only during the testing of impeller No. 4 (Fig. 3.9d, section 3.3.1), it was possible to take more than one measurements close to the total head drop operating point, at the minimum σ value. The more measurements close to minimum σ value, the denser the three-dimenional plot is expected at the minimum σ value. The latter justifies the logged in of the y-axis.

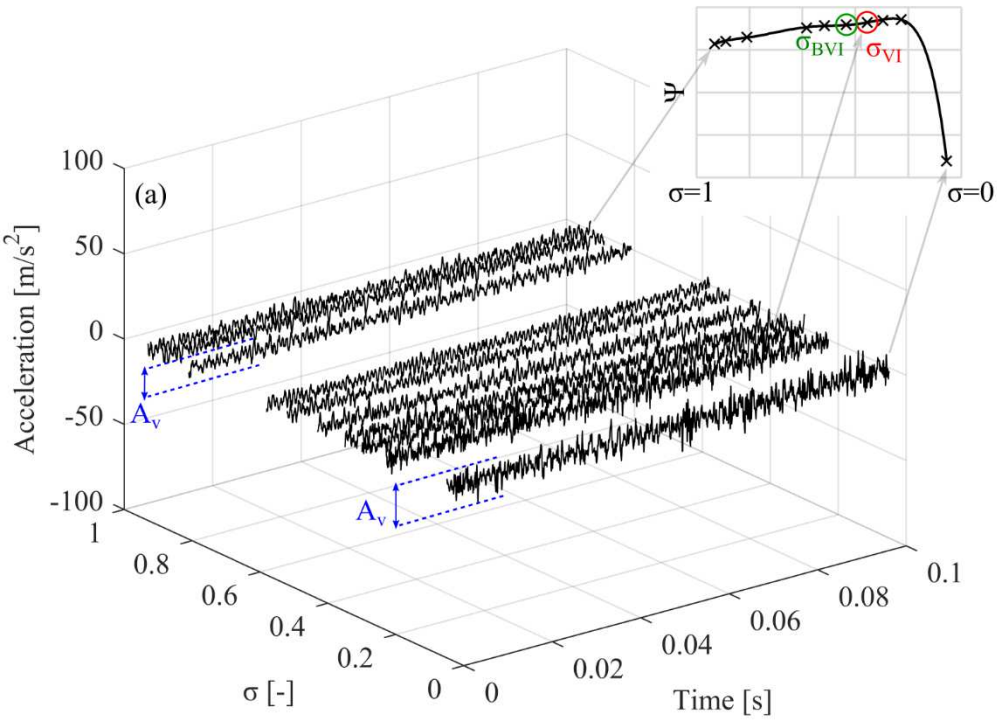

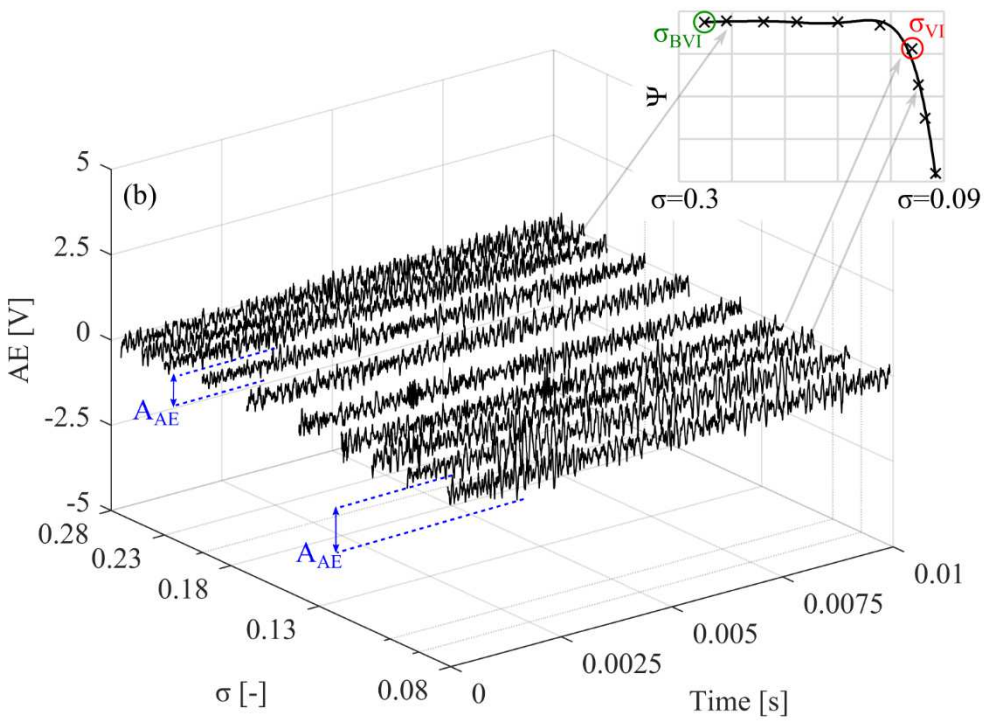

Figure 6.2 Measured time series of **a)** impeller No. 1, A01 sensor, $\Phi=0.40\cdot\Phi_{BEP}$, **b)** impeller No. 4, AE sensor, $\Phi=\Phi_{BEP}$.

Along with the measured signals, the corresponding σ-Ψ curves are also given in Fig. 6.2, in order to depict the suction conditions of the signals in the cavitation characteristic curve. The σ values in these curves are flipped in the opposite direction compared to the curves of Fig. 3.9 (section 3.3.1) due to illustration purposes.

From the three-dimensional representation, one general conclusion is that, no matter the suction conditions, the combination of processes that compose the signals exhibit stationary characteristics in terms of their mean value. The mean value of all signals remains constant and does not change during the sampling time.

In the same graphs of Fig. 6.2, a first observation regarding the changes in the signal pattern when pumps operate at cavitating conditions can be made. This is related with the increase of the vibration (A_v) and noise (A_{AE}) amplitudes at operating points where, $\sigma<\sigma_{VI}$. This behaviour is further highlighted in the time series of all sensors used in this study and are presented in Figs. 6.3 (LU impellers) and 6.4 (NTUA impeller). The selected operating points (OPs) refer to one flowrate per impeller and, in terms of suction conditions, follow the convention introduced in section 6.1. The flowrate and σ values of each OP are given in Table 6.1, along with the inlet blade angles and the type of the blade for each impeller tested that assists the forthcoming analysis.

Table 6.1 Flowrate, Thoma cavitation number of the selected operating conditions and blade characteristics for each impeller.

	Φ/Φ_{BEP}	σ_{BVI} [-]	σ_{VI} [-]	σ_{FC} [-]	β_1 [°]	Blade type
Impeller No.1	0.4	0.43	0.35	0.05	65	Backward curv.
Impeller No.2	0.64	0.62	0.52	0.12	85	Radial str.
Impeller No.3	0.7	0.65	0.59	0.11	80	Forward curv.
Impeller No.4	1	0.27	0.114	0.096	25	Backward curv.

According to the results of Fig. 6.3, the overall amplitude of all signals increases and exhibits impulse characteristics during heavy cavitating conditions, for σ_{FC}. The impulses in the time

series are depicted as areas of thin timespan with increased amplitude. This increase is stronger as the inlet blade angle of the impellers becomes more radial and is maximised for the impeller No. 3 with the forward curved impeller blades (Figs. 6.3e,f).

The vibration results at σ_{FC} for the sensor located on the volute (A01) take systematically larger values compared to the sensor located close to the impeller inlet (B01_1). On the other hand, during initial and non-cavitating conditions, vibration range amplitude remains in similar levels at both sensors.

At this stage of analysis, slight differences arise from the comparison of the time series between σ_{BVI} and σ_{VI}, according to the results of impellers No. 1 and 2. The main reason for this similarity is that the two-phase flow for $\sigma \sim \sigma_{VI}$ is, according to the photographs of Figs. 3.12ae and 3.13af (section 3.3.2), at its very early development stages. Under such conditions, it covers a very small part of the blade's suction and consequently the overal vibration of the machine prevails that of the noise of the pressure waves. One of the aims of this study is to process the signal in a way to extract the information of these pressure waves even during the initial stages of the phenomenon, in both the laboratory and the industrial pumping set-ups.

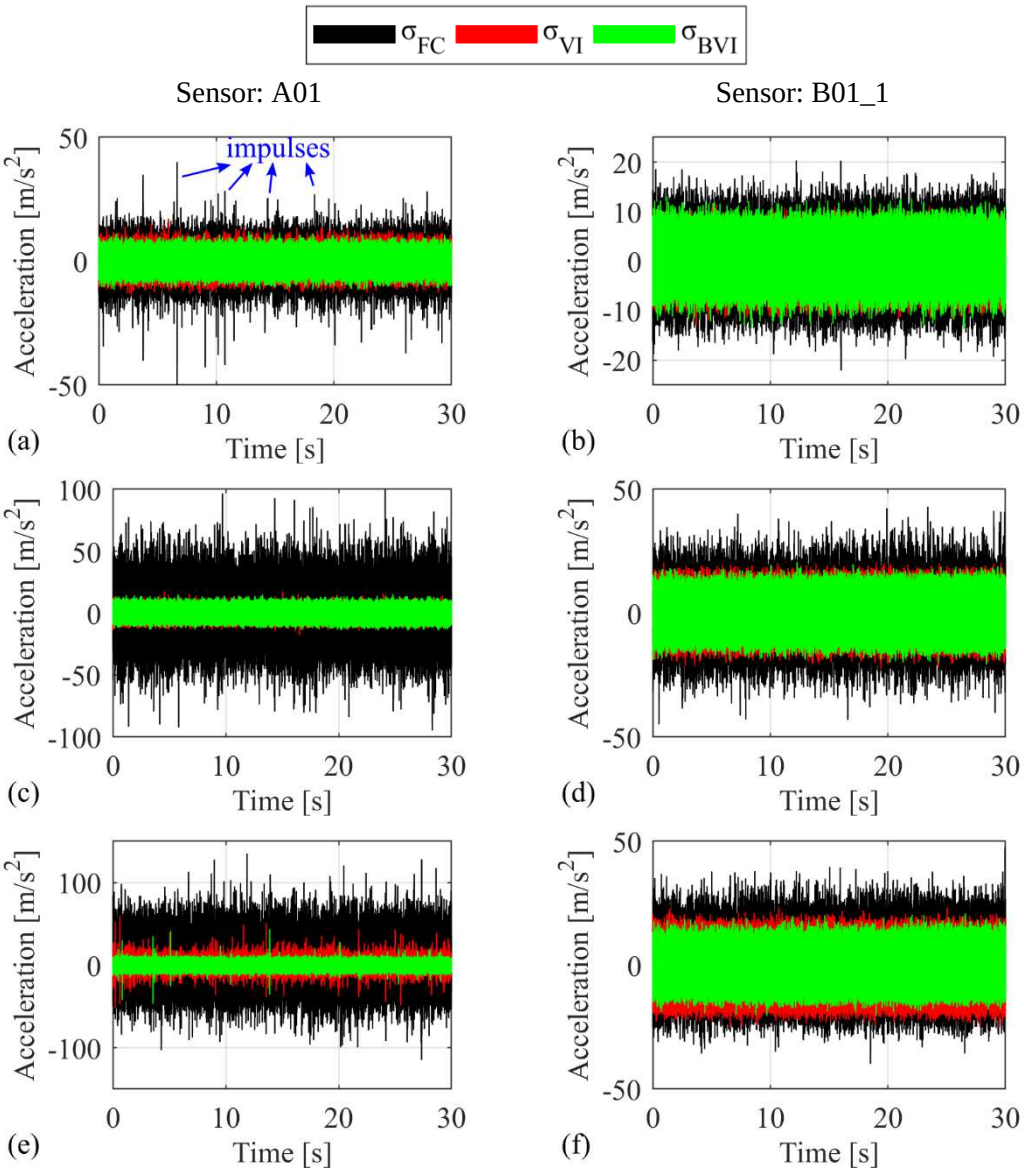

Figure 6.3 Sampled time series for non-cavitating, visual inception and for heavy cavitating conditions for **a,b)** impeller No. 1, $\Phi=0.40\cdot\Phi_{BEP}$, **c**,**d)** impeller No. 2, $\Phi=0.64\cdot\Phi_{BEP}$, **e**,**f)** impeller No. 3, $\Phi=0.70\cdot\Phi_{BEP}$.

The vibration results of impeller No. 3 (Fig.6.3e,f) are different than those of No. 1 and 2, since the signal during visual inception point displays narrow areas of increased amplitude, similar similar with those discussed for σ_{FC}. This irregular behaviour of impeller No. 3 is met in various stages of the analysis of this chapter, however is finally clarified in Chapter 7.

The corresponding results of impeller No. 4 are presented in Fig. 6.4, where the raw data of AE sensor are also provided (Fig. 6.4c). The mounting positions of the noise and vibration sensors used in the NTUA test configuration are shown in Fig. 2.23a (section 2.5.2.1). Here, the amplitude of the vibration is generally higher compared to the corresponding of the LU pump, because the pump in the NTUA test rig; i) operates under significantly higher rotation speed (2900 rpm compared to 1800 rpm), ii) embeds two ball bearings in its casing, which are considered as a significant source of mechanical noise, and iii) has casing and pipe system made from metallic material, whereas the LU pump is made mainly from Plexiglas.

The examination of the characteristics of the time signal as function of Thoma parameter concludes that the vibration results of the NTUA impeller show similar behaviour with those of LU at σ_{FC}, where the amplitude range increases and impulses emerge. As it is expected, the delayed visual onset of two-phase flow at σ=0.114 is again confirmed, as the results at σ_{VI} present analogies with those at fully developed at σ_{FC}. In this impeller, the sensor located closer to the cavitation region (B01_2) develops stronger characteristics (Fig. 6.4b). However, the fact that the sensor installed on the pump's bearings (B01_1) presents also impulse behaviour with an increase in its vibration range, is of significant interest. This sensor is located at the back of the pump, away from the impeller's inlet, and it is expected that the mechanical vibration sources of the bearing would prevail over a pressure wave mechanism of hydrodynamic nature, like cavitation.

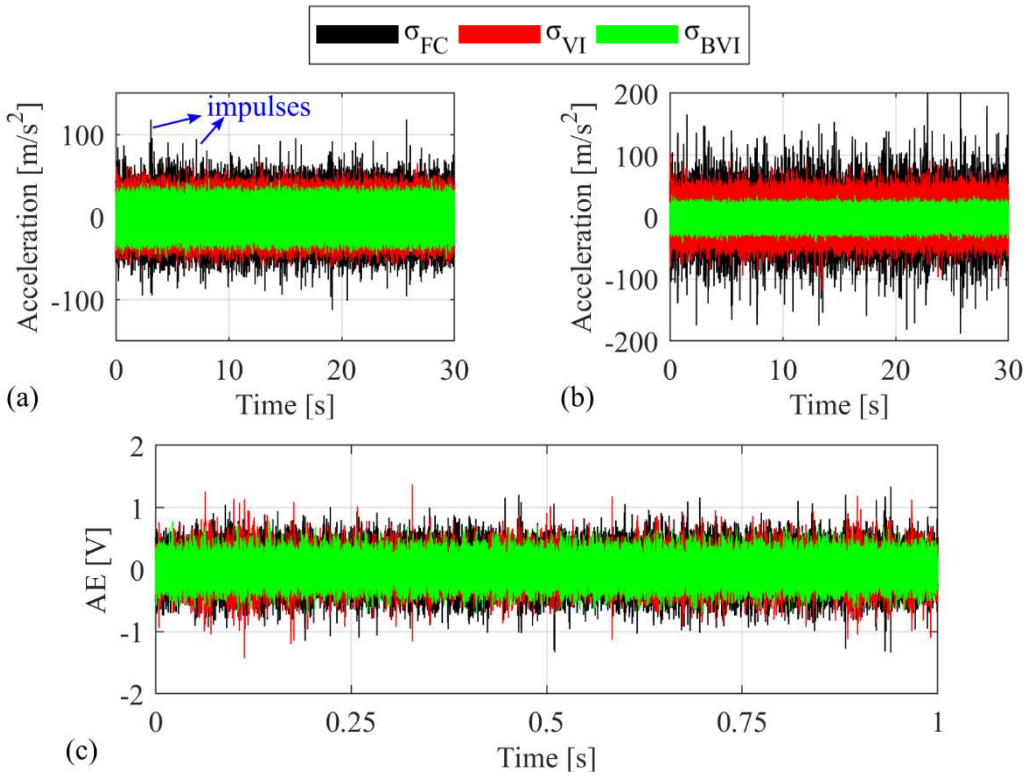

Figure 6.4 Sampled time series for non-cavitating, visual inception and heavy cavitating conditions for impeller No. 4, at $\Phi=\Phi_{BEP}$: **a)** sensor B01_1, **b)** sensor B01_2, **c)** sensor AE.

Moreover, the bubble implosion also changes the time series of the AE sensor, but the impact in terms of the amplitude range is significantly smaller than that of vibration sensors for both test rigs. This trend depicts the effect of the lower limit of band pass filter used in the AE measurements, which does not allow to pass (filters out) frequencies with $f \leq$2500 Hz, a range

that could be excited from cavitation. The conclusions drawn from the vibration and AE of Figs. 6.3 and 6.4, do not change when the pumps operate at different loading conditions.

Finally, the analysis of the measured signals focuses on the short time span of some of the time series presented in Figs. 6.3 and 6.4, in order to clarify the nature of the signals and to extract additional information for the occurring impulses. The time span presented in the following figures, is δt =0.06 sec, and it is large enough to include the main low mechanical frequency components of the vibration signals, such as the rotating frequency of the shaft (RF) and the blade passing frequency. The periods of all mechanical frequencies for LU and NTUA impellers can be calculated from the data of the Tables 2.5, 2.10 (section 2.5), respectively.

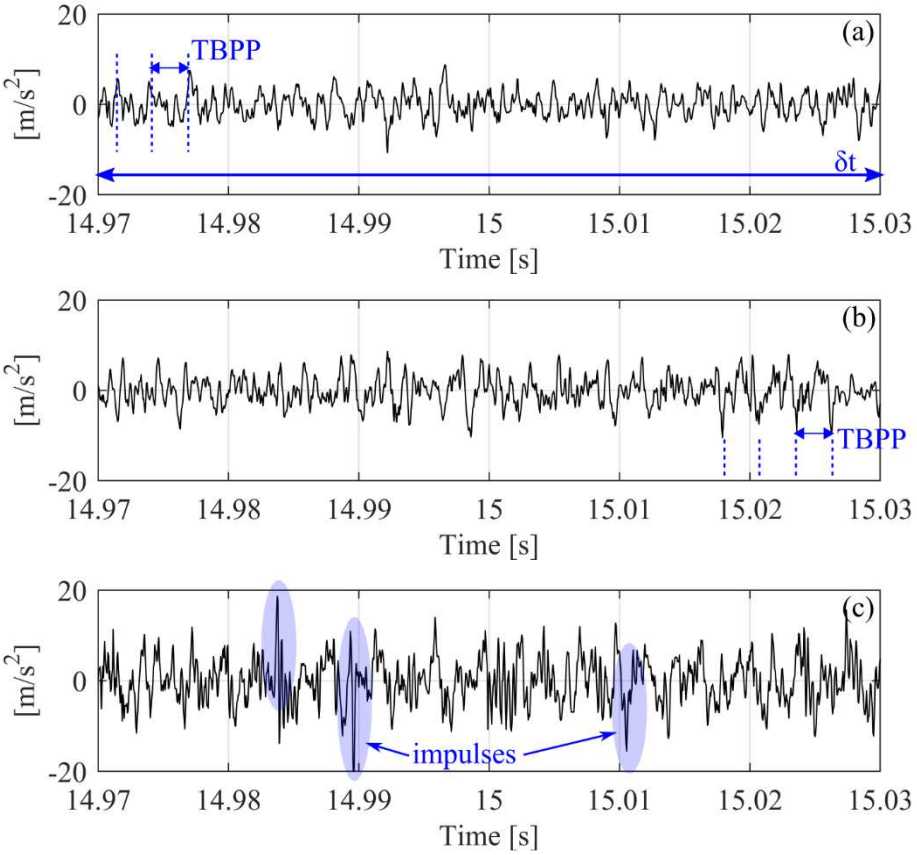

Figure 6.5 Time series of impeller No. 1 for sensor A01, $\Phi=0.4\cdot\Phi_{BEP}$ at: **a)** σ_{BVI}, **b)** σ_{VI}, **c)** σ_{FC}.

The results for impellers No. 1, 2, 3 and 4 are given in Figs. 6.5, 6.6, 6.7, 6.8, respectively. The time series of impeller No. 1 during non-cavitating conditios (σ_{BVI}) include mainly the sinusoidal component introduced from the blades passing, and its repeatable trend is highlighted in Fig. 6.5a and b. The signature of the vibration signal in centrifugal pumps is expected to be modulated from the rotational and blade passing frequency (Fig. 1.2 - Taylor, 2005; Scheffer, 2008) and consequently, to be a kind of sinusoidal, especially in machines such as the LU pump that does not have embedded bearings.

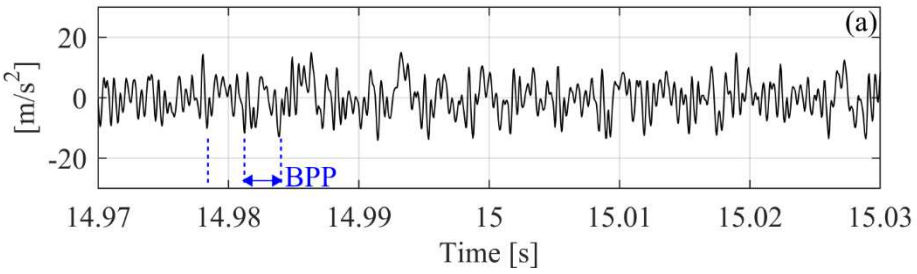

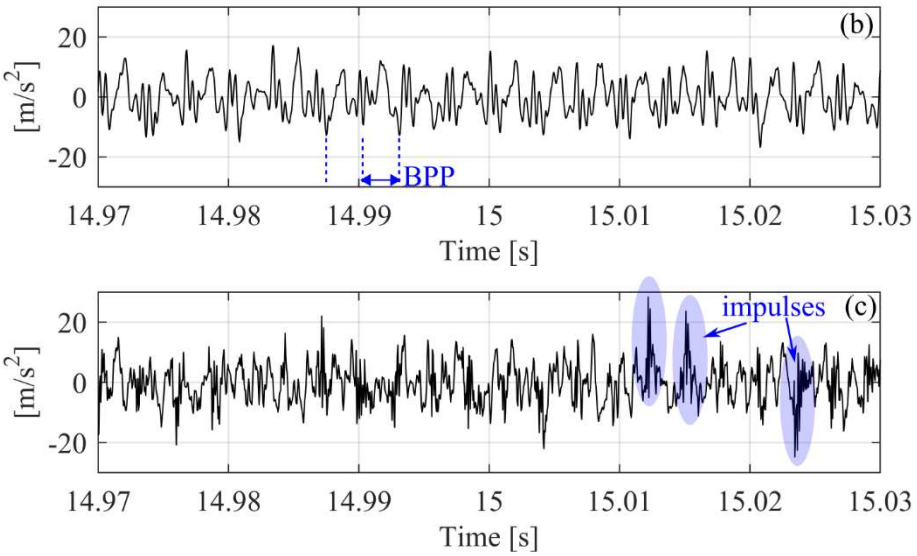

Figure 6.6 Time series of impeller No. 2 for sensor B01_1, $\Phi=0.64\cdot\Phi_{BEP}$ at: **a)** σ_{BVI}, **b)** σ_{VI}, **c)** σ_{FC}.

It is noted that the hydraulic and mechanical loads of LU pump are handled from the motor bearings, which until this point do not affect the results discussed. For the same reason, the behaviour of the vibration results for impellers No. 2 (Fig. 6.6a) and No. 3 (Fig. 6.7a), at σ_{BVI}, exhibits the same trend with those of impeller No. 1.

As it is shown also in Figs. 6.3a and 6.3d, the passing from non-cavitating to early stage cavitating conditions, at σ_{VI}, does not change the signal form of impellers No. 1 (Fig. 6.5b) and No. 2 (Fig. 6.6b), compared to σ_{BVI}. On the other hand, the results of impeller No. 3 at σ_{VI} (Fig. 6.7b) reveals the appearance of few impulses that increase the amplitude range shown in Fig. 6.3e.

The dynamic interaction of these impulses with the mechanical vibration of the pump-motor system mask the useful information that could be used, in order to establish possible detection cavitation criteria. This observation is of significant importance, as it manifests one main objective of the present work, which is the development of tools that can separate low frequency mechanical noise sources from the vibration signal and reveal the two-phase flow formation at its early stages, close to σ_{VI}.

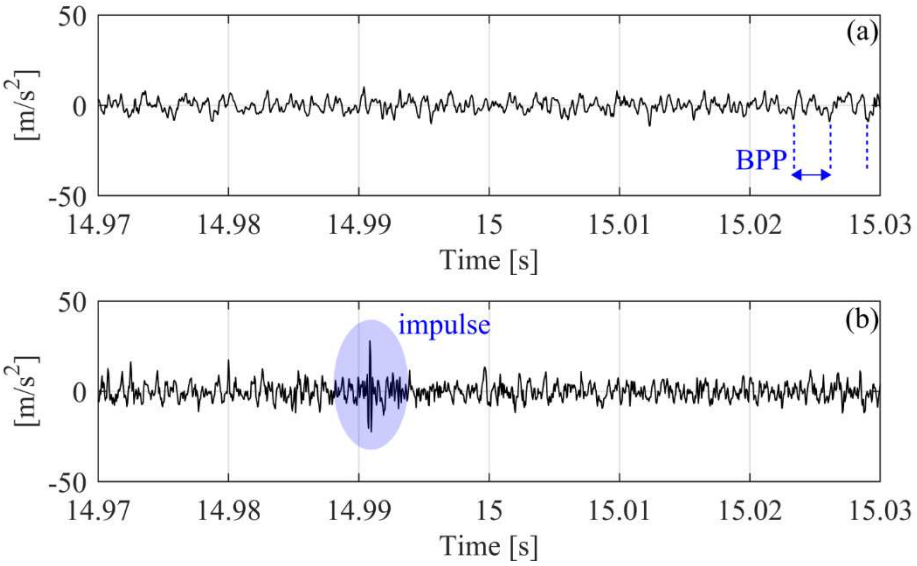

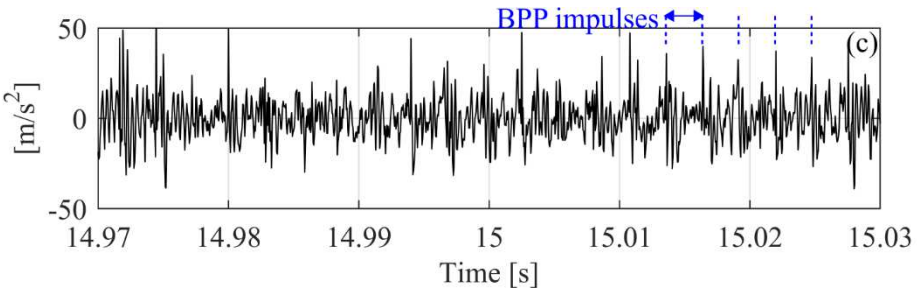

Figure 6.7 Time series of impeller No. 3 for sensor A01, $\Phi=0.7\cdot\Phi_{BEP}$ at: **a)** σ_{BVI}, **b)** σ_{VI}, **c)** σ_{FC}.

When the LU pump operates under heavy cavitating conditions, the vibration signature exhibits impulses of increased amplitude that are described in Fig. 6.3. More specifically, for impellers No. 1 and 2 (Figs. 6.5c and 6.6c) the signal presents few sharp edges that exhibit a relatively random behaviour. Similar knocks occur also for impellers No. 3 (Fig. 6.7c), however in that case they clearly follow the passing of the blades (BPP). Nevertheless, the association of BPP with extensive vapour formation, could be an additional evidence for the cavitation appearance, only in the case that similar behaviour appears for all the pumps under investigation.

In the end, the raw vibration data of industrial NTUA impeller are given in Fig. 6.8. The differences in this signal with the corresponding of LU impellers, can be attributed to the location of the sensor (B01_1) that for these measurements is at the bearings. Nevertheless, the passing to σ_{FC} operating points introduces impulses (Fig. 6.8c), similar to the semi-open impeller results of Figs. 6.5c, 6.6c and 6.7c. These impulses at σ_{FC} (Fig. 6.8c) are significantly weaker compared to the corresponding ones of the LU impellers (Figs. 6.5c, 6.6c & 6.7c) for two reasons; i) the effect of the bearing noise, and ii) the effect of shroud of the closed impeller No. 4 that acts as an additional obstacle for the pressure wave transmission from the suction side of the blade through the casing of the pump and to the sensors.

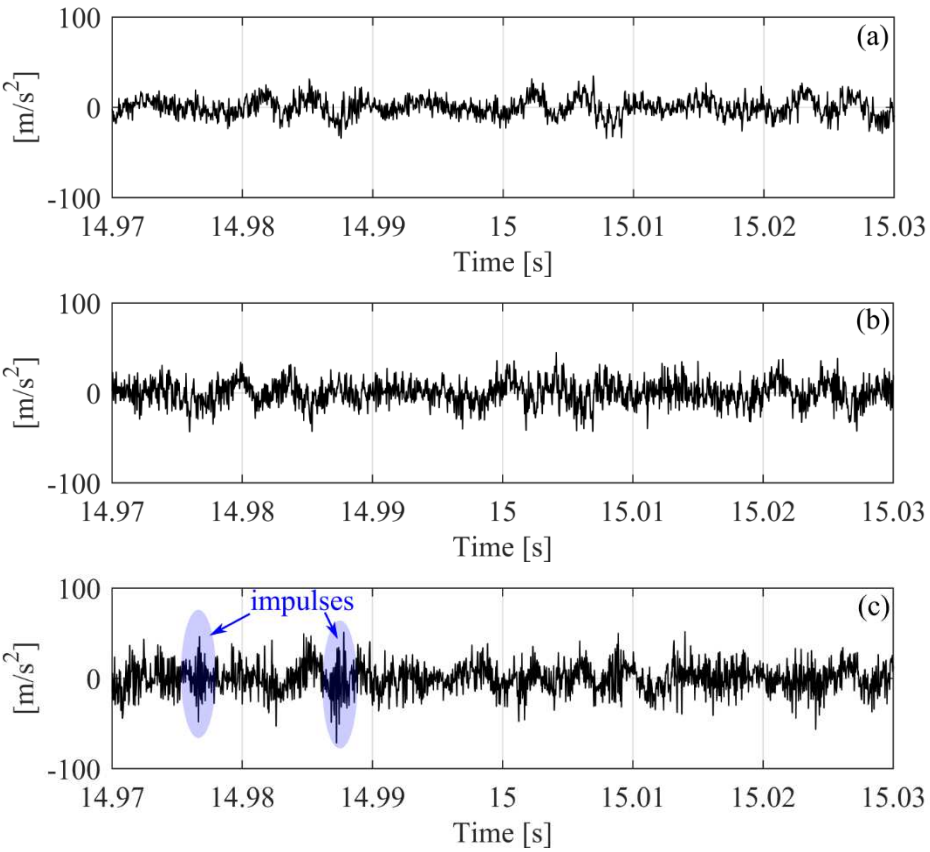

Figure 6.8 Time series of impeller No. 4 for sensor B01_1, $\Phi=\Phi_{BEP}$ at: **a)** σ_{BVI}, **b)** σ_{VI}, **c)** σ_{FC}.

The analysis of the raw measured data provides some first indications that reveal the presence of cavitation, like the increase of vibration amplitude due to the impulses at σ_{FC}. However, at this stage, these indications cannot form a robust prompt cavitation detection criterion, because they are valid mainly at heavy cavitating conditions, when the phenomenon is fully developed and already deteriorates the machine's performance. From the above it is concluded that additional analysis in the signal properties should be made, in order to extract new information and improve our understanding on the mechanisms that govern the interaction of the phenomenon with the machine components.

6.2.2 Statistical properties of the measured signals.

The second level of the analysis of the signals includes the study of the statistical properties of the measured time series and their variation with cavitation development. The most common way to begin the statistical analysis is to approximately display the distribution of the measured data in a histogram. The behaviour of the normalised density frequency of the measured time series under the three different suction conditions (σ_{BVI}, σ_{VI}, σ_{FC}) is illustrated in Figs. 6.9a,b,c, respectively. The histograms presented in Fig. 6.9 refer to the time series obtained from the vibration sensor A01, of impeller No. 1. The values of the flowrate and Thoma cavitation number used in Fig. 6.9, are taken again from Table 6.1. The width of the bins used for the construction of the histograms is calculated (0.24 m/s^2) for the non-cavitating condition case (σ_{BVI}) from the procedure descibed in section 2.4.2, and it is kept as reference for the presentation of the other histograms (σ_{VI}, σ_{FC}).

According to the results of Figs. 6.9a,b,c, the populations described from the histograms have in general normal Gaussian distributions, since they are all symmetric arround the mean value, the probability maximises at the mean value $\bar{\varphi}$ and they are distributed in the range of ±3s. The effect of the cavitation development in the standard deviation, *s*, of the histograms is clear, since its value increases and differentiates the shape of the histogram. The increase of *s* begins during the first stages of cavitation development (Fig. 6.9b) and becomes even higher at heavy cavitating conditions (Fig. 6.9c). Similar changes in the shape of the distribution due to the two-phase flow development exhibit all the measurements made in the present study, as well as the vibration results presented from Al Hashmi (2009), in Fig. 1.29, of section 1.3.1.3. These differences are created from the increased amplitude values, after the formation of vapour bubbles in the impeller area, presented in Figs. 6.3-6.8.

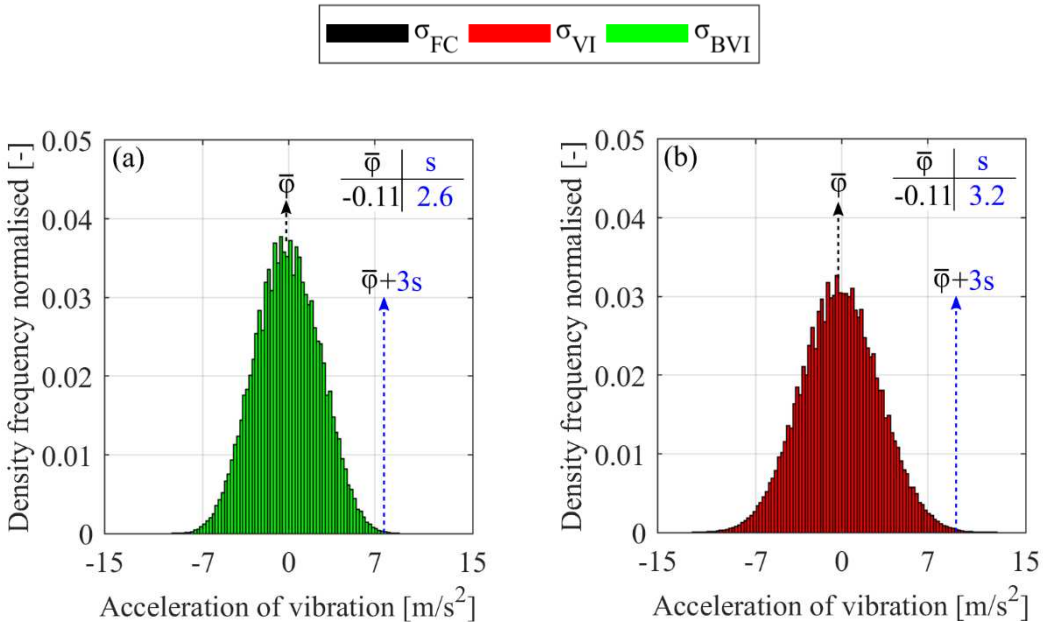

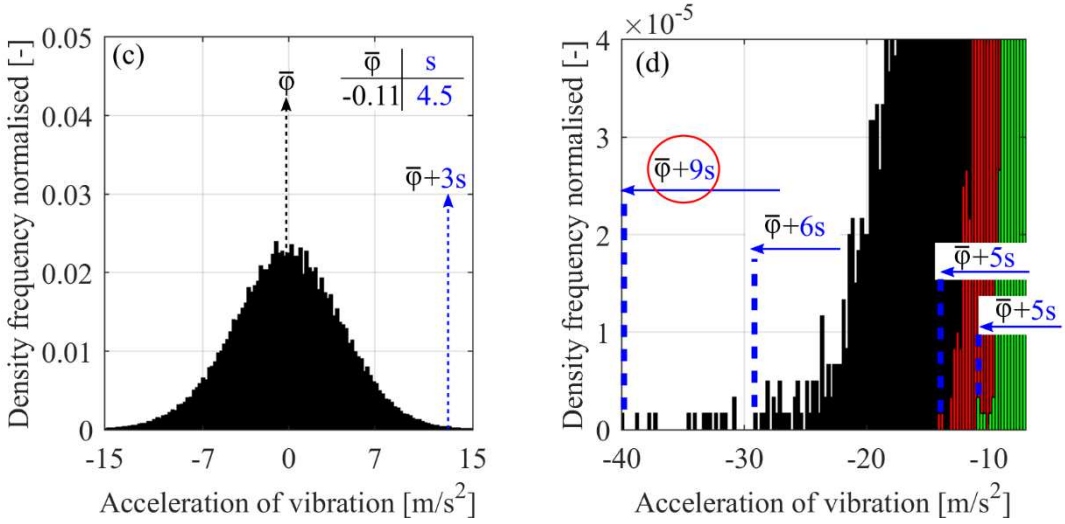

Figure 6.9 Histograms of raw vibration measurements at Impeller No. 1, sensor A01, $\Phi=0.40\cdot\Phi_{BEP}$, **a)** non-cavitating conditions, **b)** visual cavitation inception, **c)** heavy cavitating conditions, and **d)** limits of the three histograms a, b, and c.

Nevertheless, interesting observations are also made after the examination of the distributions in the area that lies out of the limit of ±3s, and is presented in Fig. 6.9d, where all the histograms are plotted together. Here, in the case of σ_{BVI} and σ_{VI} operating conditions, a small part of the raw data lies until a value of ±5s. This behaviour is generaly expected, when the data follow the normal distribution. On the other hand, the raw data obtained under heavy cavitating conditions (black colour bars) exhibit values that lie in the area out of the ±6s and reach the ±9s. These values clearly correspond to the extreme values presented in Figs. 6.3-6.8 and are the result of the appearance of cavitation impulses.

The last observation is noticed systematically under cavitating conditions, especially at σ_{FC}, for all the impellers examined and arises questions regarding the effect of cavitation development in normality of the calculated distributions. A way to examine the differences of the measured data with the normal distribution under normal and cavitating conditions is with the use of normal probability plots that are introduced in section 2.4.2. The results of six representative cases, that include all four impellers, are shown in Fig. 6.10. Similarly to Figs. 6.3, 6.4 and 6.9, three suction conditions are presented, all of them taken from Table 6.1. The increased number of samples, N_s (Eq. 2.52, section 2.4 & Tables 2.4, 2.9, section 2.5) results in normal probability plots that although made from markers, they look more similar to solid lines.

According to Fig. 6.10, when the pump operates at σ_{BVI}, the distribution values exhibit Gaussian characteristics, as their normal probability plots are aligned with the straight center-lines of normal distribution. When vapour is formed in the impeller, the shape of the markers becomes curved at the limits of the distribution curves. These limits of the curves of Fig. 6.10 coincide with the extreme values of the noise and vibration measurements due to the impulses of Figs. 6.3-6.8. The higher the aplitude of the impulse the stronger is the deviation from the normal probability straight line, as for example in the case of σ_{FC} value of Fig. 6.10c, where the impulse takes values close to 60 m/s^2.

The normal probability plots reveal that the high amplitude impulses due to vapour formation in the pump introduce non-Gaussian characteristics in the noise and vibration signals. These characteristics are not very intense at σ_{VI} but rise significantly at σ_{FC}. This observation is important, because it adds a second aspect on the conclusions made in section 6.2.1, by characterising statistically the impulses generated during the two-phase flow development, as non-Gaussian with respect to the density frequency of both the raw noise and vibration data. However, the aforementioned nature of the raw measurements can not be directly related with cavitation, as similar statistical characteristics may appear due to various faults related with

rotating machinery (Al Hashmi, 2009; Lin, 2017). As a result, additional work is made for the identification of the statistical moments' effect in the non-Gaussian nature of the present data.

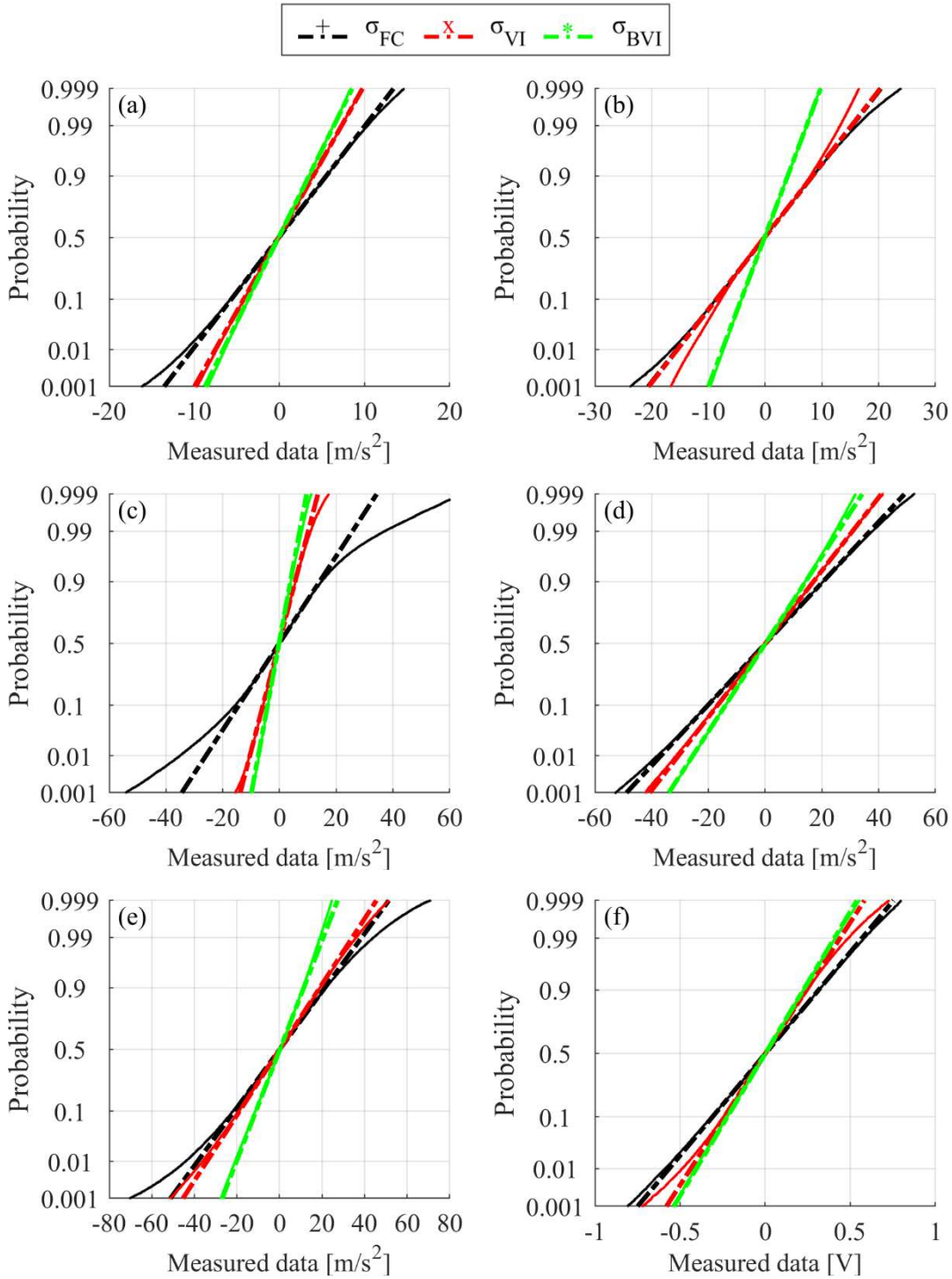

Figure 6.10 The normal probability plots of measured time series for non-cavitating, initial cavitating and fully cavitating conditions for **a)** impeller No. 1, sensor A01, $\Phi=0.40\cdot\Phi_{BEP}$ **b)** impeller No. 2, sensor B01_1, $\Phi=0.64\cdot\Phi_{BEP}$ **c)** impeller No. 3, sensor A01, $\Phi=0.70\cdot\Phi_{BEP}$ and impeller No. 4, $\Phi=\Phi_{BEP}$, sensors **d)** B01_1 **e)** B01_2, **f)** AE.

The next step of the analysis include the examination of the behaviour of all the statistical moments as function of suction conditions (σ). From the analysis preceded above, and the results of Figs. 6.3, 6.4 and 6.9, it can be deduced that the first (mean) and the third (skewness) moments are not affected from the two-phase flow development. More specifically, the mean

value of the time series remains at the center of the range (Figs. 6.3, 6.4) and distribution (Fig. 6.9), no matter the cavitation parameter σ value is. In addition, the histograms presented in Fig. 6.9 exhibit a symmetric shape for all suction conditions examined, which reveals that the skewness of the distribution remains relatively unchanged. These observations made for the mean and the skewness values are further confirmed with the use of the results of Fig. 6.11, where the two moments are plotted as a function of all σ values for the vibration and noise measurements of impellers No. 1 and 4, respectively. The results include all the flowrates tested and highlights that both moments remain relatively constant, and are not affected from the cavitation development.

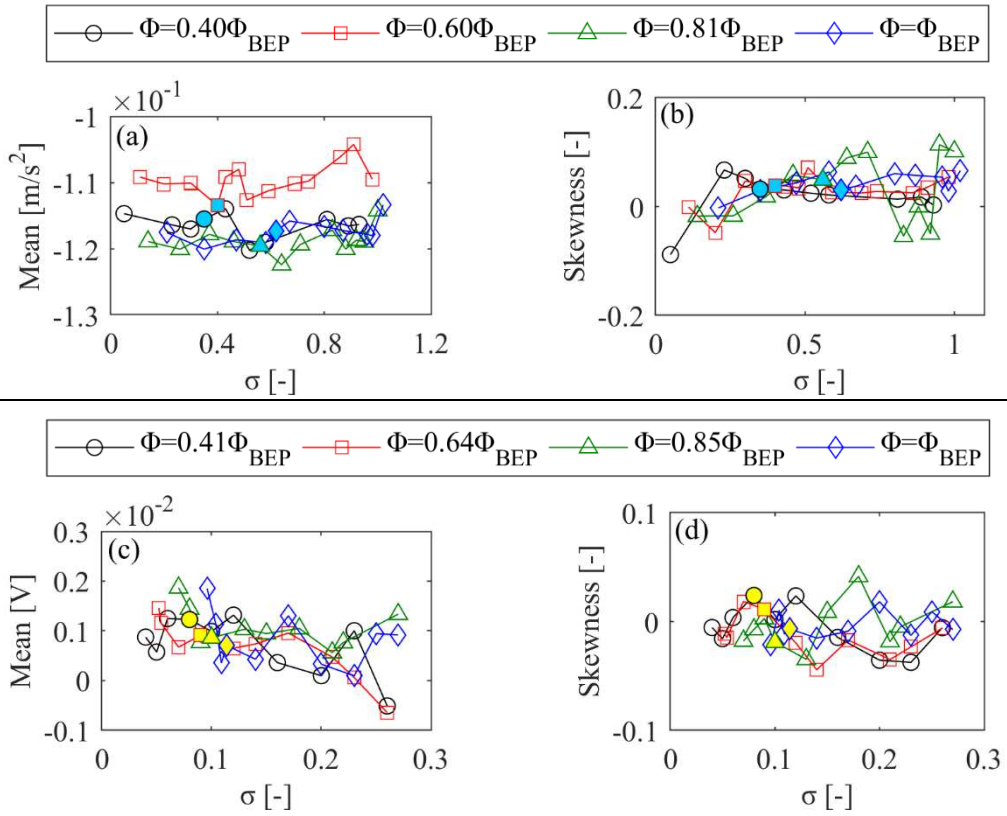

Figure 6.11 Mean and skewness values under various suction conditions for impeller No. 1, sensor A01 **(a, b),** and impeller No. 4, sensor AE **(c, d)**.

In the plots of Figs. 6.11, as well as in the following Figs. 6.12 to 6.15, the marker filled with blue and yellow colours coincide with the experimental visual inception (σ_{VI}) point for the LU and the NTUA impellers, respectively. The name and colours for σ_{VI} are defined in section 3.3.1 and are according to Fig. 3.9.

On the other hand, the changes in the values of the second (standard deviation, *s*) and the fourth (kurtosis) moment with the cavitation development are exhibit more interesting behaviour, and they are presented in Figs. 6.12-6.15 for impellers No. 1-4, respectively. The selection to provide the total results is based on the fact that for the first time, at this stage, differences occur between the different machines and flowrates, in contrast to the previous results, where the time series, the histograms and the normal probability plots are quite similar.

The pattern of standard deviation, *s*, of the sensor A01, at impeller No. 1 (Fig. 6.12a), as Thoma cavitation number, σ, decreases are contradicting. For the lowest flowrate tested, the *s* value remains relatively low (s~2.5 m·s^{-2}) until σ~0.4>σ_{VI}, where it starts to increase until a maximum value (s_{MAX}~4.5 m·s^{-2}) at σ_{FC}=0.05. This early increase could be the effect of a mechanical mechanism or even the appearance of vapour bubbles at very initial stages, which could not be captured from the visual observation system. Interestingly, the corresponding kurtosis behaviour, along with the point of its increase, is similar with that of *s*.

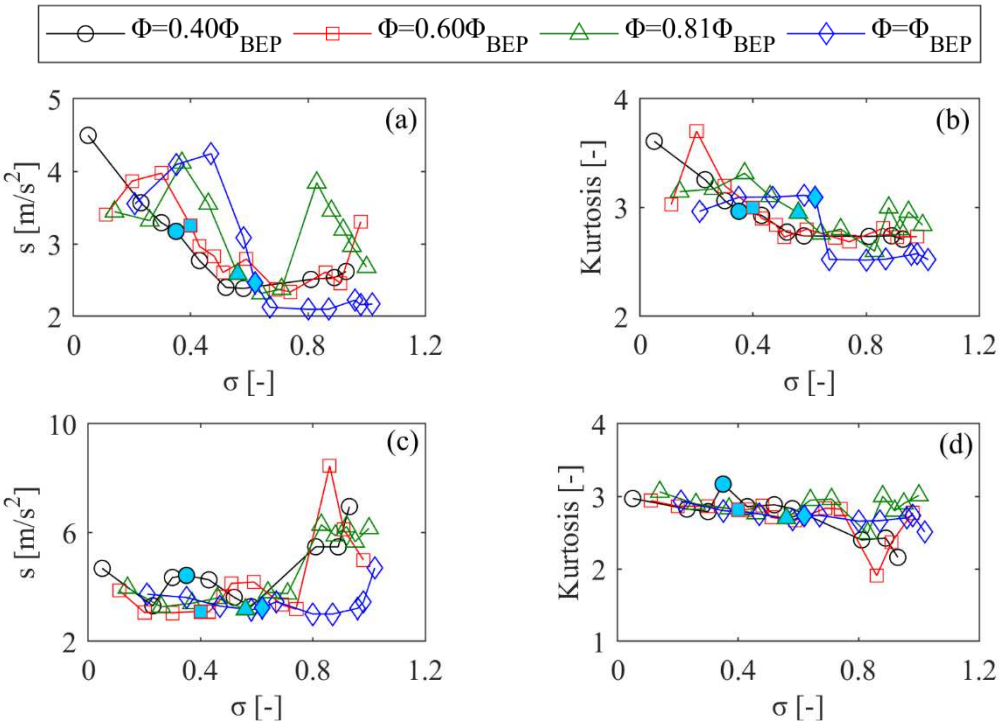

Figure 6.12 Standard deviation **(a, c)** and kurtosis **(b, d)** values under various suction conditions for impeller No. 1, sensor A01 **(a, b)** and sensor B01_1 **(c, d)**.

The passing to higher flowrates (Φ=0.60·Φ_{BEP} & Φ=0.81·Φ_{BEP}) increases perceptibly the values of *s* under non-cavitating conditions (σ>0.6) that drop at σ~0.6 and increase again for σ<0.6. The pattern at Φ=0.60·Φ_{BEP} is similar with that at Φ=0.40·Φ_{BEP}, as *s* increases when σ>σ_{VI}, while for Φ=0.81·Φ_{BEP}, *s* value increases at σ=σ_{VI}. On the other hand, kurtosis values behave similarly with these of *s* at σ<0.8, but they exhibit a more reasonable trend, as their values remain low at σ>0.8. At optimum flow conditions (Φ=Φ_{BEP}) the results show a more robust pattern in the standard deviation and kurtosis values.

Here, both moments take their minimum value under non-cavitating conditions, increase at σ=σ_{VI} and remain at high values until σ_{FC}. One possible explanation for this optimum behavior, is that under partial flow conditions possible noise from hydrodynamic sources, such as the flow separation at the leading edge of the blades, may introduce vibrations that spoil standard deviation pattern. Finally, the corresponding results of the second sensor, B01_1 (Fig. 6.12c,d) do not present a justifiable behaviour; kurtosis value remains relatively constant and close to the Gaussian kurtosis value (kurtosis=3), while *s* decreases with cavitation development, which reveals the effect of sensor position in the results.

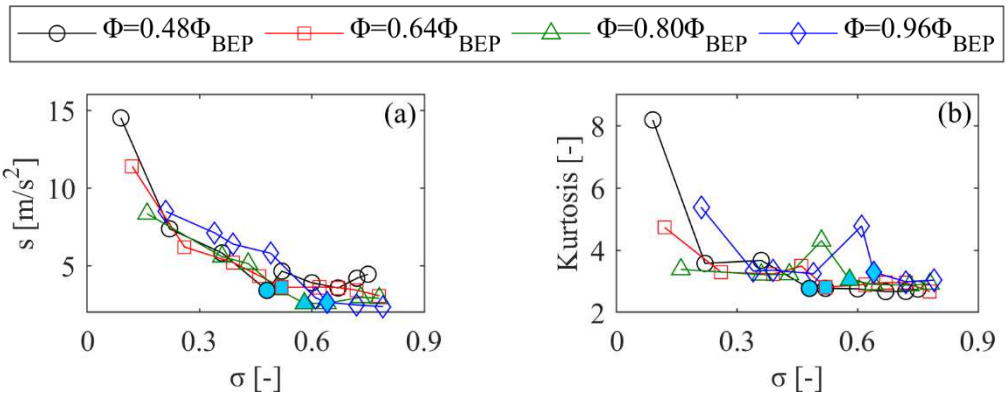

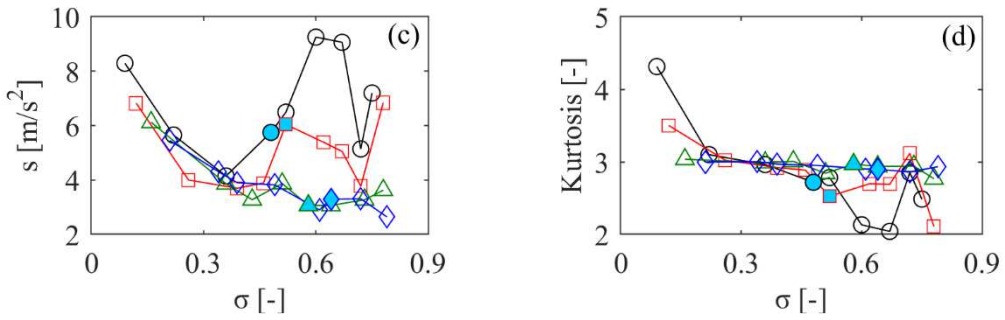

Figure 6.13 Standard deviation **(a, c)** and kurtosis **(b, d)** values under various suction conditions for impeller No. 2, sensor A01 **(a, b)** and sensor B01_1 **(c, d)**.

The corresponding plots of the second impeller are given in Fig. 6.13. For the sensor A01 (Fig. 6.13a,b), the patterns of standard deviation are almost identical for all flowrates, as their values start to increase exactly after σ_{VI}. The values of kurtosis exhibit similar behavior for the two lowest flowrates, but the trends change significantly for $\Phi=0.80\cdot\Phi_{BEP}$ and $\Phi=0.96\cdot\Phi_{BEP}$. In these cases, although the value of kurtosis increases after cavitation onset, it decreases again and stabilises at a higher level than $\sigma>\sigma_{VI}$. Only for the largest flowrate, kurtosis value increases again for σ_{FC}, where it maximises, similarly to $\Phi=0.48\cdot\Phi_{BEP}$ and $\Phi=0.64\cdot\Phi_{BEP}$.

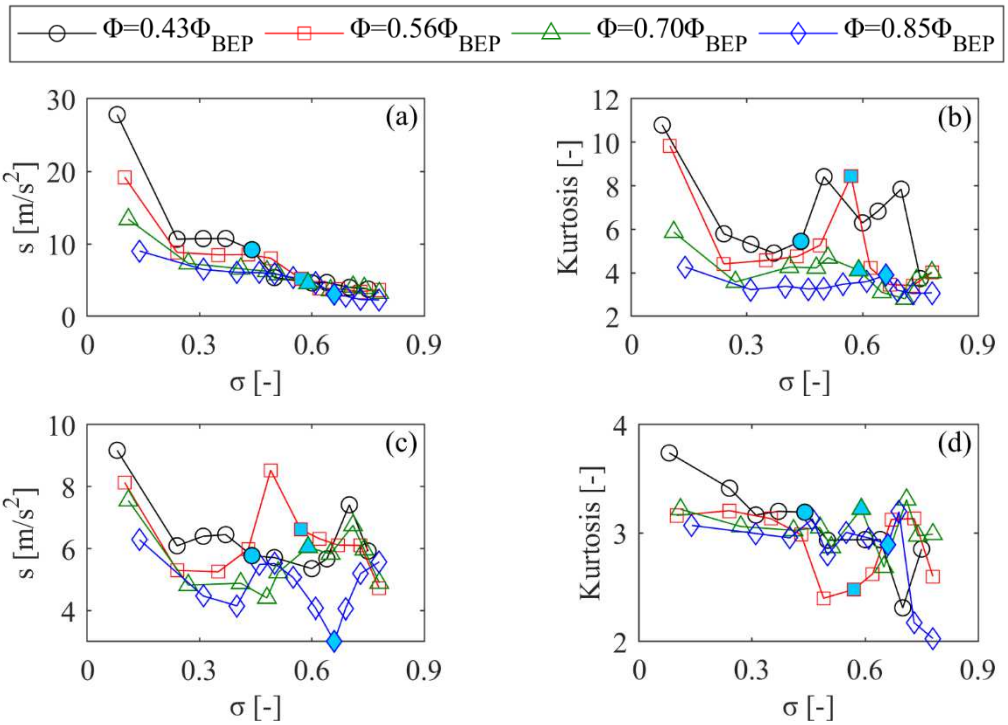

Figure 6.14 Standard deviation **(a, c)** and kurtosis **(b, d)** values under various suction conditions for impeller No. 3, sensor A01 **(a, b)** and sensor B01_1 **(c, d)**.

On the other hand, the values calculated from the data obtained from B01_1 sensor (Fig. 6.13c,d) do not show a robust pattern. Especially for the two lowest flowrates and similarly to the results presented for impeller No. 1, the *s* value is maximised under non cavitating conditions. The kurtosis value of these flowrates, takes values close to the normal (3), except from the minimum σ, where it rises over 3. The kurtosis results for $\Phi=0.80\cdot\Phi_{BEP}$ and $\Phi=0.96\cdot\Phi_{BEP}$ remain constant close to 3 for all suction conditions. Only the standard deviation of $\Phi=0.80\cdot\Phi_{BEP}$ and $\Phi=0.96\cdot\Phi_{BEP}$ exhibit a reasonable pattern, which also agrees with that of A01, as *s* takes low values (s~3 m·s^{-2}) until σ~0.6, and after this point it increases to s~6 m·s^{-2}.

The graphs of standard deviation for the sensor A01 of impeller No. 3, are similar to those of impeller No. 2 (Figs. 6.13a,b), as they start to increase at σ_{VI} and maximise for σ_{FC}. Similarly to *s*, the kurtosis value begins to increase at σ_{VI}, except from the lowest flowrate, where it increases early (σ~0.8). The position of the sensor affect also the results of impeller No. 3, as the behaviour of both moments for B01_1 sensor do not present a meaningful pattern.

Finally, the results, of the industrial impeller No. 4 are plotted in Fig. 6.15. Here, in addition to the graphs of the two vibration sensors (Fig. 6.15a-d), the corresponding results from the AE sensor are also given (Fig. 6.15e,f). The patterns of the standard deviation and kurtosis moments of the two sensors are identical. The standard deviation of the flowrates close to the best efficiency point (Φ=0.85·Φ_{BEP} and Φ=Φ_{BEP}) increases at σ_{VI}, while decreases slightly at the same σ for the two lowest flowrates. The only difference in the plots of kurtosis is that for Φ=0.41·Φ_{BEP} and Φ=0.64·Φ_{BEP} the value remains constant until its increase for σ~0.05.

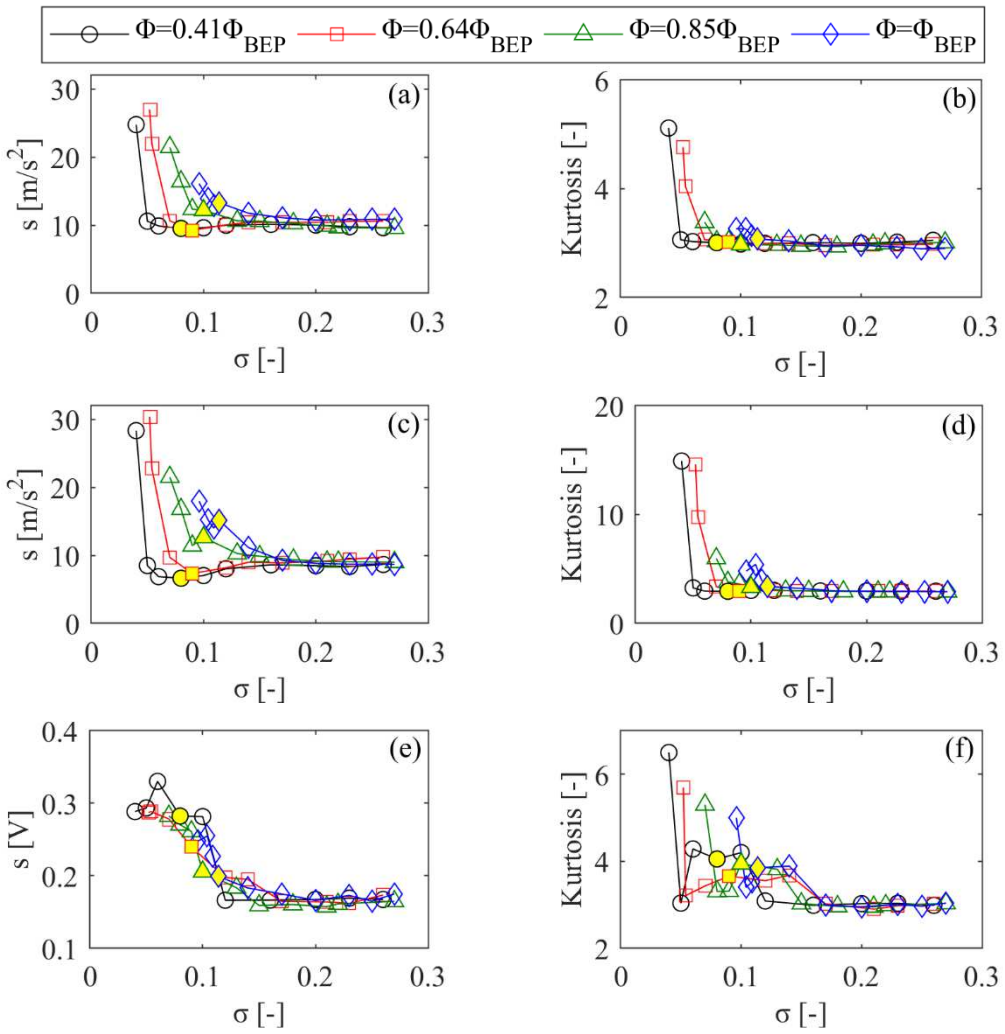

Figure 6.15 Standard deviation **(a, c)** and kurtosis **(b, d)** values under various suction conditions for impeller No. 4 and for sensor B01_1 **(a, b),** sensor B01_2 **(c, d)**, and sensor AE **(e,f)**.

In addition, the maximum value of kurtosis for the sensor B01_2, which is located closer to two-phase flow formation area is three times larger than that of sensor B01_1, which is mounted on the pump's bearing. The pattern of noise measurements (Fig. 6.15e,f) changes relative to those of vibration. More specifically, for most flowrates the increase of *s* and kurtosis precedes visual inception. This tendency of both moments to rise before σ_{VI}, is justified from the fact that in this impeller the visual inception point does not coincide with the onset of cavitation. After the first increase, the pattern of the two moments becomes different. The

standard deviation increases monotonically until minimum σ, whereas kurtosis value decreases after σ_{VI} and increases again at the minimum σ.

The ability of the standard deviation and kurtosis moments to perceive the onset and development of cavitation is summarised in Table 6.2. All the calculations presented in Figs. 6.12-6.15 are evaluated and noted with a success (✓) or failure (×) sign. Successful is considered the case where the behaviour of the moment satisfies two criteria; i) the moment value is low for $\sigma>\sigma_{VI}$ and increases close to σ_{VI}, and ii) it maximises for $\sigma<\sigma_{VI}$. These criteria are developed and discussed during the review of the powerband studies in section 1.3.1.3 of this Thesis. By this way it is possible to decide which of the used moments, sensors and mounting locations are more capable to discern the two-phase flow formation.

Table 6.2 Summary of the ability of standard deviation and kurtosis moments of the noise and vibration raw data to identify cavitation appearance.

Impeller	Φ/Φ_{BEP}	Standard Deviation			Kurtosis		
		A01/ B01_2	B01_1	AE	A01/ B01_2	B01_1	AE
No. 1	0.40	✓	×		✓	×	
	0.60	×	×		✓	×	
	0.81	×	×		✓	×	
	1.00	✓	×		✓	×	
No. 2	0.48	✓	×		✓	×	
	0.64	✓	×		✓	×	
	0.80	✓	✓		✓	×	
	0.96	✓	✓		✓	×	
No. 3	0.43	✓	×		×	×	
	0.56	✓	×		✓	×	
	0.70	✓	×		✓	×	
	0.85	✓	×		✓	✓	
No. 4	0.41	×	×	✓	×	×	✓
	0.64	×	×	✓	×	×	✓
	0.85	✓	✓	✓	✓	✓	✓
	1.00	✓	✓	✓	✓	✓	✓

According to Table 6.2, the behaviour of both moments can contribute to cavitation identification. The main factor that affects the detection capability is the sensor position for the LU and the sensor type for the NTUA test rig. More specifically, the sensor located close to the area of cavitation in the LU pump fails to distinguish cavitation onset, systematically, for all the impellers used. In addition, only the AE sensor satisfies the aforementioned criteria for all flowrates of impeller No. 4, since the two vibration sensors manage to succeed only for the largest flowrates, that lie close to the BEP of the pump, at the optimum operating conditions.

From the above discussion it is implied that, although both moments exhibit encouraging behavior, they cannot constitute a robust criterion for cavitation detection. However, this conclusion is based on the analysis of the raw data measured from the machines. The investigation of non-stationarities of the statistical moments, along with the study of the signal properties in the frequency domain, could provide useful information for the construction of digital filters that will be able to remove possible noise sources, which now complicate the two-phase flow identification. As a result, none of the moments, sensors or locations examined until this point is rejected.

The last step of the study of statistical properties deals with the investigation of possible non-stationarities of the two moments and their association with the results of Fig. 6.10 that question the Gaussian behavior of the extreme noise and vibration values. Non-stationary processes can be described from a signal that exhibits statistical characteristics that are time-varying (Cardona-Morales, 2018). The graphs of Figs. 6.12-6.15 present only the averaged values of standard deviation and kurtosis, and how these are affected by the onset and development of vapour formation.

A practical way to examine the non-stationary behavior of the moments, is through the splitting of the AE and vibration signals in sampled groups that include the same number of raw data. In the present study the signals are put in groups of 1000 raw data. For each group, the standard deviation and the kurtosis is calculated, and in this way it is possible to illustrate their deviation in time that is now expressed in number of samples. After this prcocessing, it is possible to examine whether their values remain constant (the moments describe a stationary process) or deviate in time (the moments describe a non-stationary process). The results of standard deviation and kurtosis, for various typical cases are shown in Figs. 6.16 and 6.17, respectively.

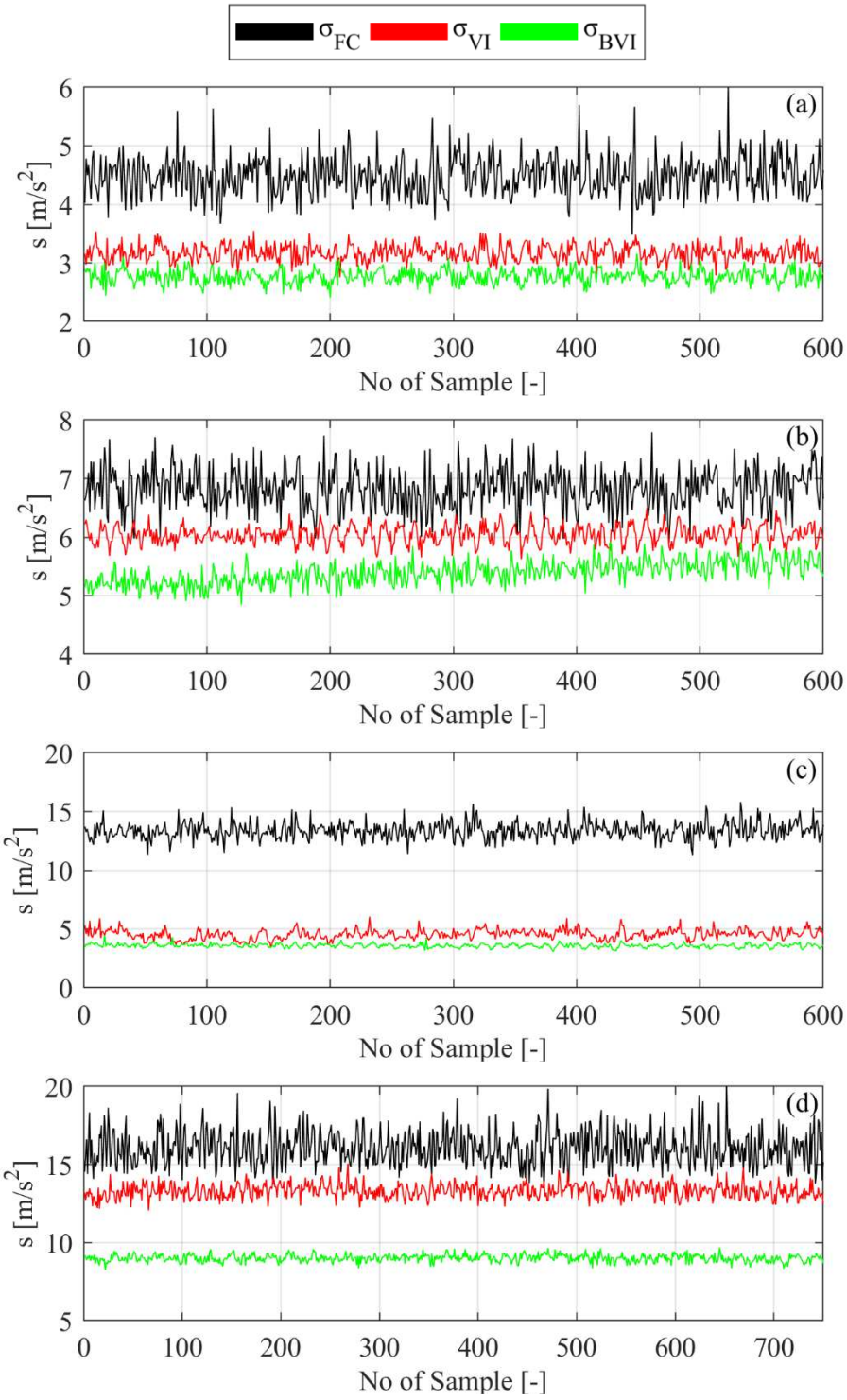

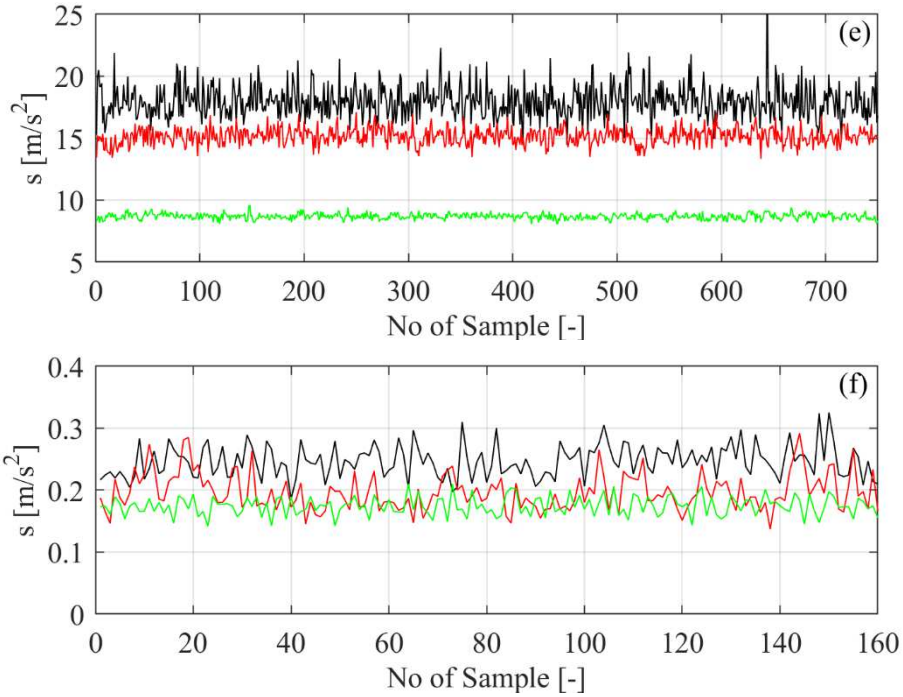

Figure 6.16 Standard deviation of the grouped data for **a)** impeller No.1, sensor A01, $\Phi=0.40\cdot\Phi_{BEP}$, **b)** impeller No.2, sensor B01_1, $\Phi=0.64\cdot\Phi_{BEP}$, **c)** impeller No.3, sensor A01, $\Phi=0.70\cdot\Phi_{BEP}$, **d)** impeller No.4, sensor B01_1, $\Phi=\Phi_{BEP}$, **e)** No.4, sensor B01_2, $\Phi=\Phi_{BEP}$, **f)** No.4, sensor AE, $\Phi=\Phi_{BEP}$.

According to the results of Fig. 6.16, the standard deviation value for all cases presented, does not change significantly as function of the number of samples (time) during constant suction conditions. Differences are only observable between the different σ values examined, and confirm the general pattern of *s*, presented in the histograms of Fig. 6.9 and the patterns of Figs. 6.12-6.15, where cavitation development increases its value.

On the contrary, the kurtosis graphs in Fig. 6.17, no matter the sensors and the impeller, reflect the highly transient behavior of this quantity, when the impellers operate under initial and heavy cavitation conditions. More specifically, for non-cavitating conditions (σ_{BVI}), in most of the cases of Fig. 6.17, the kurtosis values remain close to the normal distribution value (kurtosis=3). The only exception comes from impeller No. 3 (Fig. 6.17c), where the signal exhibits non-stationary characteristics at σ_{BVI}, a behaviour possibly related with the few impulses presented in Fig. 6.3. The transition to cavitating conditions (σ_{VI} & σ_{FC}) generate significant number of kurtosis peaks that in most cases of Fig. 6.17, at least double the normal kurtosis value.

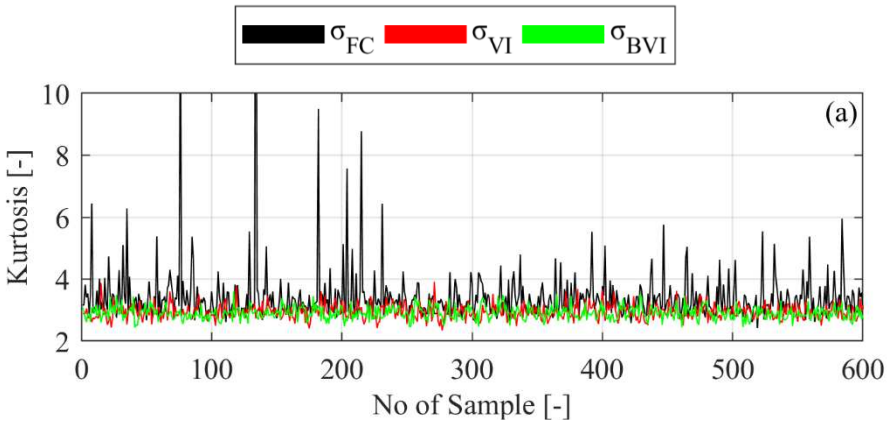

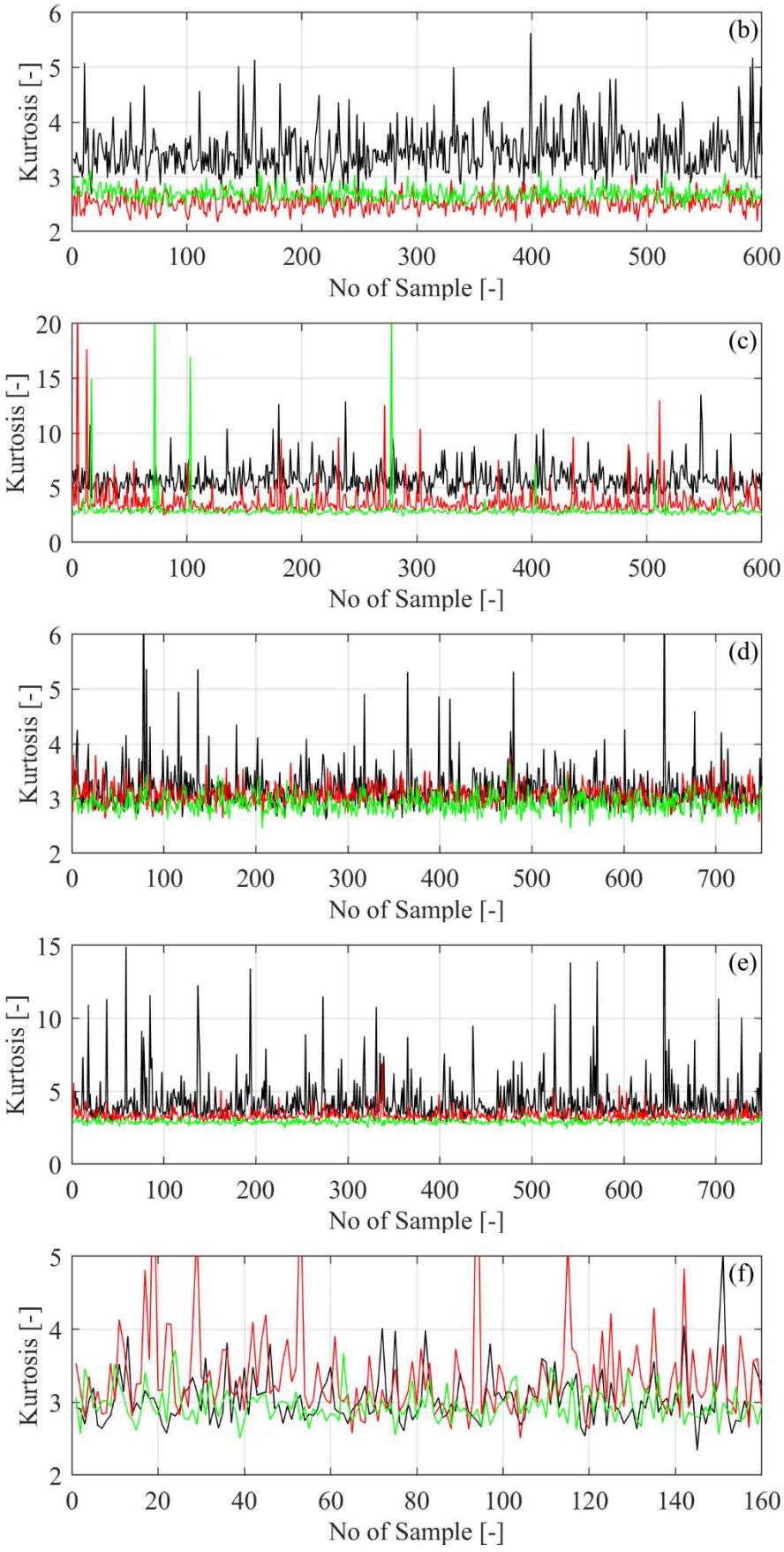

Figure 6.17 Kurtosis of the grouped data, a) to f) operating points are the same with those given in the caption of Fig. 6.16**.**

For σ_{FC} conditions, the areas outside of these peaks take kurtosis values close to 3 for the impellers No. 1, 4 (Figs. 6.17a,d,e,f), whereas for impellers No. 2, 3 (Figs. 6.17b,c) the average kurtosis value is also increased to ~3.5 and ~5, respectively. The reason for this behavior is that impellers 2 and 3 are those with the poorest design in terms of number of blades and inlet blade angle (see section 3.3.1 and Table 6.1), and consequently exhibit the most intense cavitation characteristics, as presented also in the visual observations of Figs. 3.11 and 3.12. High local kurtosis value (>10) is also calculated for the vibration sensor (B01_2, Fig. 6.17e) located close to impeller of the NTUA pump. Finally, the calculated kurtosis value of the AE sensor for impeller No. 4 (Fig. 6.17f) exhibits to be more sensitive during the onset of the phenomenon (σ_{VI}) compared to σ_{FC}.

The results of Figs. 6.12 to 6.17 prove that cavitation influences the standard deviation and the kurtosis values of the measured noise and vibration signal in two directions. On the one hand, standard deviation is affected from a stationary perspective, since its averaged values increase for the majority of the cases examined (Figs. 6.12-6.15 & Table 6.2), when two-phase flow develops. At the same time its value remains constant when it is studied from a transient perspective (Figs. 6.16).

On the other hand, the kurtosis value is affected from a non-stationary perspective, as it is shown in the results of Fig. 6.17 that highlight the significant increase of its value relative to the kurtosis value of the Gaussian distribution (3). The latter behaviour reveals the effect of the non-stationary impulses, whose appearance is strongly related with cavitation development and also influence the curved normal probability plots of Fig. 6.10. The last conclusion is of crucial importance since it reveals the similarities of the cavitation detection with the results (Fig. 1.23, section 1.2.2.3) presented from Dwyer (1981 & 1983b) and constituted the basis (Antoni, 2006) of the modern tools used for the extraction of non-stationary characteristics from measured time series. The further investigation of kurtosis-related detection tools is presented in Chapter 7.

6.3 Frequency spectrum analysis

The examination of signal characteristics in time domain is followed from the analysis of the frequency spectrum. The tool selected for the study of frequency distribution of the noise and vibration signals is the Welch estimate (Welch, 1967), described in section 2.4.3 (Eq. 2.58). The investigation of the frequency spectrum is divided in two parts; i) one that is focused on the low frequency content, related with the mechanical frequencies and ii) one focused on the high frequency content. The study of the first includes only the vibration signals, since the AE low frequency content is filtered out from the band pass filter that is embedded in the preamplifier and has a lower cut-off of 2.5 kHz, as it is presented in Table 2.9 (section 2.5.2.2).

Furthermore, the low frequency analysis deals with the identification of the peaks presented at the area with f <1200 Hz, as well as with the calculation of velocity vibration RMS [mm·s^{-1}] and its presentation as function of Thoma cavitation number, σ. The examination of the high frequency part of the signal is performed through the averaging of the power content in specific frequency ranges. The justification of the frequency range selection precedes the final graphs that depict the high frequency power content as a function of suction conditions, for all the operating points, sensors and impellers tested in the present Thesis.

6.3.1 The power spectral density

The distribution of the power at each frequency, for the estimation of power spectral density is done with the Welch's tool. Before the application of the estimator, the selection of the number of segments (ε) used in this study is analysed in section 6.3.1.1. After, the selection of this parameter (ε), which plays significant role in the calculations according to Eq. 2.58, the frequency spectra of the signals are provided in section 6.3.1.2. At this stage, the frequencies with the stronger intensity are associated with the mechanical components of the pumps, and the differences observed during the development of vapour phase are discussed.

6.3.1.1 Selection of the number of segments

The calculations of Welch estimator involve the sectioning, the recorded data, and the averaging of the modified periodograms of the sections. The use of large number of sections optimises the estimation of the power at each discrete frequency component, since the number of observations increase the sample used. However, the use of many observations decrease the actual value of t_s, which consequently spoils the frequency domain discretisation, δf defined in Eq. 2.50 (section 2.4.1). In order to avoid any of the aforementioned consequences, the effect of the number of segments is investigated in some of the typical noise and vibration signals discussed in the present study.

The indicative results are given in the frequency domains of Fig. 6.18; the first (Fig. 6.18a) account for the non-cavitating conditions (σ_{BVI}=0.43) measured by the A01 sensor located at impeller No. 1 for Φ=0.40·Φ_{BEP}, while the second (Fig. 6.18b) is the AE spectrum during fully cavitating conditions (σ_{FC}=0.096) from impeller No. 4 for Φ=Φ_{BEP}. The x-axis (frequency) of both plots are adjusted, in order to highlight the strong components of frequency domain; i) for the vibration signal corresponds to the area with f<50 Hz that includes mainly the rotational frequency (RF) of 30 Hz and ii) for the noise signal represents the high frequency area with f=[5500 – 6500] Hz. The effect of four different number of segments is examined; 1, 5, 50 and 500 segments, that divide the signals of 600000 (vibration signal) and 160000 (AE signal) data in reasonable numbers of sections.

The results for only 1 segment represent the estimation of spectrum without averaging of segments and without loss of information in the frequency discretisation, whereas the results for 500 segments depict the maximum averaging selected, with the poorest δf. The poor performance of the estimation using 500 segments is evident in both power spectra of Fig. 6.18, where the power of the peaks can not be highlighted at all. Better desciption achieves the estimation using 50 segments, which depicts roughly the power concentration of the peaks.

However, the corresponding green line of 50 segments is enveloping the frequencies excited in the spectrum and, consequently, it cannot provide detailed information regarding possible sidebands, which are considered significant in the present study. As a result, the sectioning of data in 5 segments is preferred than that of 1 segment, since it provides a better estimation of the frequency spectrum (after the averaging of 5 segments) and, simultaneously, preserves an adequent discretisation in the frequency domain. The sectioning of data in 5 segments is used to describe the frequency estimation in all the results presented in section 6.3.

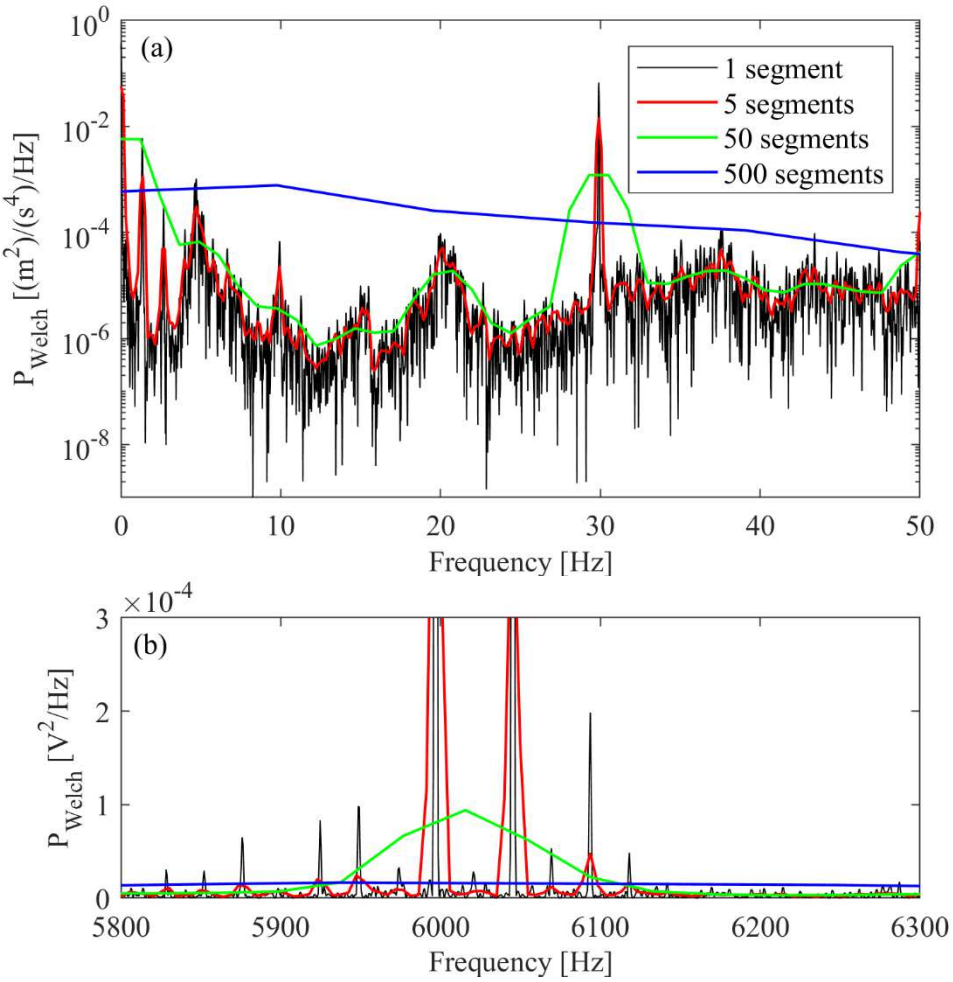

Figure 6.18 Effect of the number of segments in the application of Welch estimator to: **a)** the vibration signal of impeller No. 1, sensor A01, σ_{BVI}, $\Phi=0.40\cdot\Phi_{BEP}$ and **b)** the AE signal of impeller No. 4, σ_{FC}, $\Phi=\Phi_{BEP}$,.

6.3.1.2 Frequency spectrum of the results

The estimated frequency domains, for each sensor, are calculated for all OPs tested in the present study. In Fig. 6.19, two of them that correspond to the time series of Fig. 6.2, are plotted again, as function of suction conditions, in three-dimensional graphs. The x-axis (σ) of Fig. 6.19b, is logged in, so as to make more discernable the AE frequency spectra that correspond to σ values close to the σ_{FC} region (σ~0.1), similarly to Fig. 6.2b. In the first graph (Fig. 6.19a) the highest amplitude of the vibration spectra, that coincides with the third harmonic of the total blade passing frequency (TBPF) of impeller No.1 (~1 kHz) seems to decrease when passing to cavitating conditions. This pattern has been reported in similar experiments (Abdulaziz, 2017; Lu, 2017) but contradicts with the results of other researchers (Ganeriwala, 2011; Kotb, 2015), where the low frequency vibration amplitude increased. This odd behavior is due to the fact that the low frequency components of a pump-motor system are strongly dependent from the

structural characteristics of each pump under investigation and could not be generalised. The expected low frequency mechanical and hydraulic components for all the pumps discussed in this study, are given in Tables 2.5 and 2.10 (section 2.5), and their effect is discussed in Fig. 6.20.

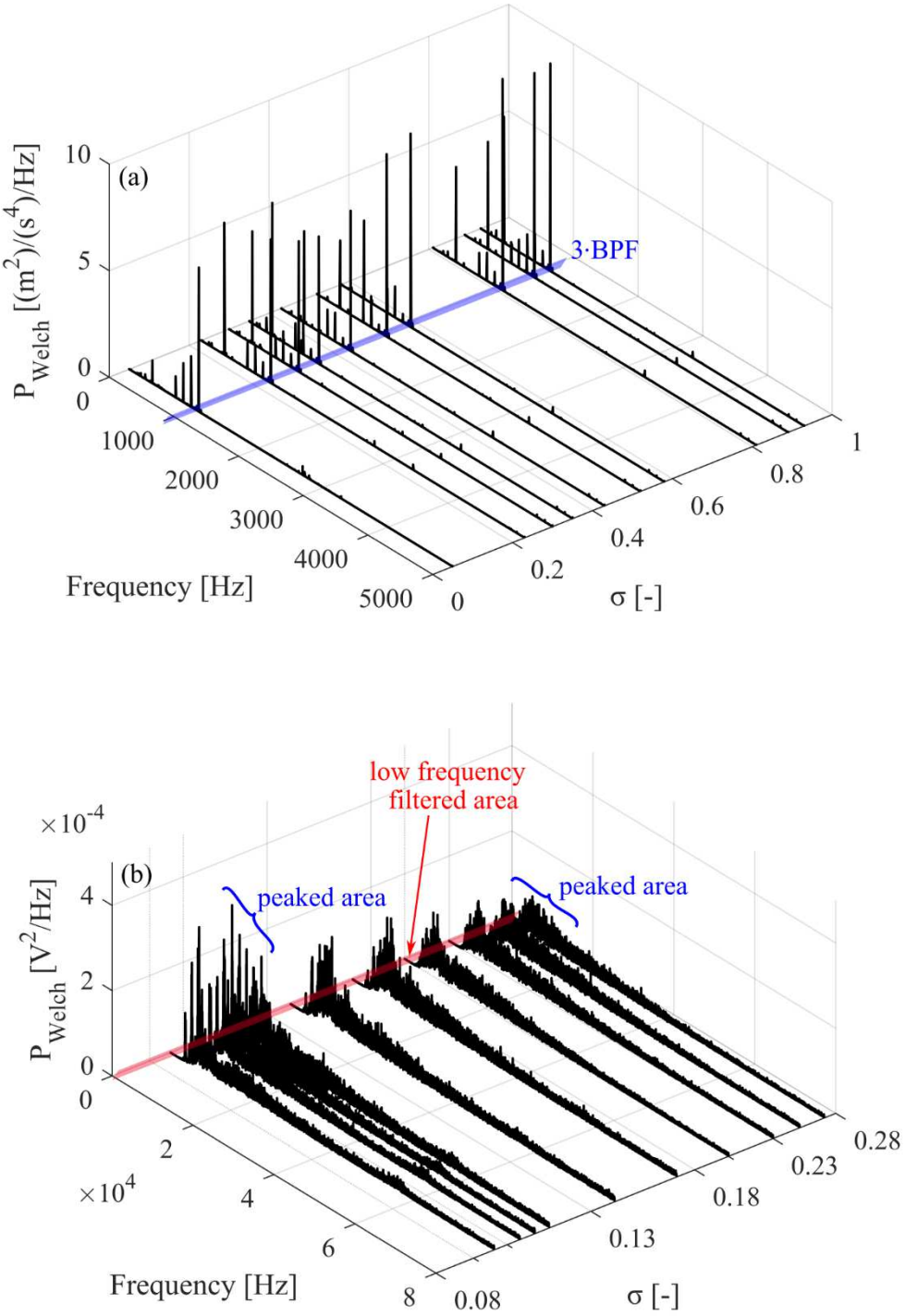

Figure 6.19 Frequency spectrum under various suction conditions for: **a)** impeller No. 1, sensor A01, $\Phi=0.40\cdot\Phi_{BEP}$ and for **b)** impeller No. 4, sensor AE, $\Phi=\Phi_{BEP}$.

In contrast to the vibration results, the AE spectrum (Fig. 6.19b) is made only from high frequency sources, due to the filtering of frequencies lower that 2.5 kHz (see Table 2.9, section

2.5.2.2). Here, noise seems to excite the total frequency range, until 60 kHz. The range above the 60 kHz and until the upper limit of 80 kHz does not show significant differences with respect to two-phase flow development. Nevertheless, the largest frequency amplitudes lie in the audible frequency range (f<20 kHz), and form relatively uniform power peaks. Interestingly, this area exhibits increased amplitudes when passing from large cavitation numbers (σ>0.20) to lower (σ<0.13), where vapour bubbles are formed. According to the pump monitoring literature (Chudina, 2003b; Gulich, 2008, Lobanoff; 2013), the high frequency, widely distributed, "broadband" vibration and noise content is related with hydrodynamic sources, such as turbulence and cavitation. The aforementioned amplitude increase of Fig. 6.19b, that seems to confirm this conclusion, is further studied in section 6.3.3, where it is quantified and presented again as a function of suction conditions, for all the flowrates and impellers tested.

The frequency domain results of Fig. 6.19a manifest the appearance of low frequency vibrations. At this stage of analysis, the sources that contribute to these peaks are examined and clarified. As it was previously commented, the vibration signals obtained from all sensors and impellers show similar characteristics with those of Fig. 6.19a. The low part of frequency spectrum of the vibration signals of all impellers under non-cavitating conditions, σ_{BVI} (see Table 6.2) is given in the results of Fig. 6.20.

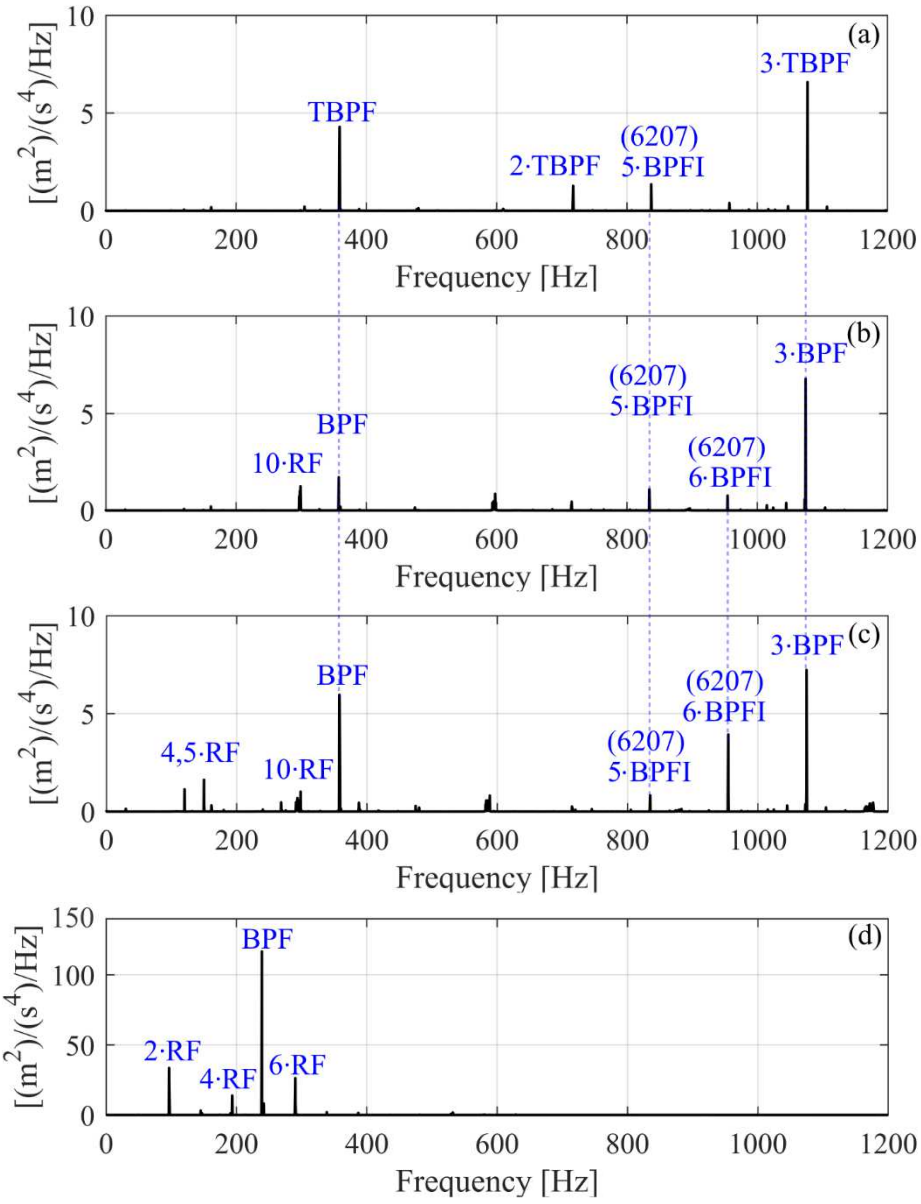

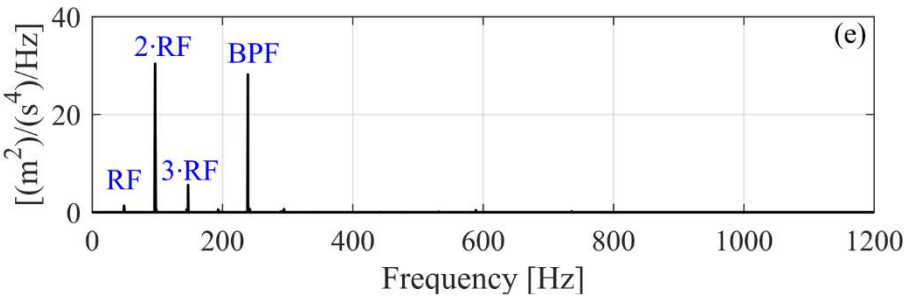

Figure 6.20 Low frequency spectrum (f <1200 Hz) representation for non-cavitating conditions (σ_{BVI}) for: **a)** impeller No.1, sensor A01, $\Phi=0.40\cdot\Phi_{BEP}$ **b)** impeller No.2, sensor B01_1, $\Phi=0.64\cdot\Phi_{BEP}$ **c)** impeller No.3, sensor A01, $\Phi=0.70\cdot\Phi_{BEP}$, **d)** impeller No.4, sensor B01_1, $\Phi=\Phi_{BEP}$, **e)** impeller No.4, sensor B01_2, $\Phi=\Phi_{BEP}$.

According to these graphs, the stronger vibration amplitude (~100 $m^2\cdot s^{-4}\cdot Hz^{-1}$) is calculated for the NTUA pump (Figs. 6.20d,e) and more specifically, for the sensor located at the pump bearings (B01_1). This is a reasonable result that follows the trend of the time series presented in Figs. 6.3 and 6.4, where the amplitude during σ_{BVI} (green colour line) has its strongest value for this particular sensor and impeller, and can be justified by; i) the particular operating conditions (rotation speed), ii) the metallic material used for the manufacturing of the general configuration, and iii) the fact that the strongest low-frequency vibration is expected on the gathering point of all forces of the pump. In addition, examination of Fig. 6.20 demonsrtates the strong correlation that exists between the results of LU impellers (Figs. 6.20a,b,c). This is the result of the identical rotational speed and test rig configuration, since all the rotating components remain the same except from the change of the impeller. As a consequence, the rotation frequency (RF), the (total) blade passing frequency (TBPF), and the motor (MF) and bearing frequencies (BPFI) coincide in the results of impeller No. 1, No. 2 and No. 3.

Furthermore, in the spectrum of the LU impellers (Figs. 6.20a,b,c) the blade passing frequency and its third harmonic dominate the spectrum. The total blade passing frequency is used only for impeller No. 1 and denotes the effect of both the blades and the splitter blades in the passing frequency. The appearance of different harmonics of blade passing frequency (BPF) in the frequency spectrum has been observed in various similar experimental and numerical studies (Lu, 2015; Wang, 2018; Ma, 2019) and in case of turbomachinery could be dependent on the volute casing design and the pump's type, i.e. whether it uses an open, semi-open or closed impeller (Chudina, 2009a). The fact that the third harmonic appears systematically only for the semi-open impellers of Lancaster University and not for this of NTUA, could be used as a confirmation of the above literature's conclusions. Along with them, the harmonics of the rotational frequency and the ball pass frequency (BPF) of the inner ring of the 6207 bearing are present.

A smaller number of frequencies appear in the spectra of impeller No. 4 sensors (Figs. 6.20 d,e), where the rotational and the blade passing frequency dominate the power distribution. This deals with the significantly stronger amplitude of these components relative to the corresponding of impellers No. 1,2,3, where their frequency plots are focused in lower vibration amplitudes that make secondary components to look stronger.

The last part of section 6.3.1 deals with the investigation of possible differences observed in the low amplitude area of the vibration spectrum. This approach is used by several researchers (Neill, 1997; Chudina, 2003a,b, 2009a,b; Cernetič, 2008), in order to highlight possible divergences in the areas that are not visible in plots such as those in Figs. 6.19 and 6.20. The analysis makes use of semi-log plots, where only the y-axis of the power distribution is shown in logarithmic scale. The results for all impellers are presented in Fig. 6.21 and include the spectra of non-cavitating, initial cavitation, and fully cavitated conditions, for typical flowrates and sensors, the same with those used for the normal probability plots in Fig. 6.10.

For all operating points, it is clear that fully developed cavitation excites wide areas of the frequency spectrum, regardless of the particular impeller and sensor mounting position. It is important to underline that the excitations due to cavitation development do not refer to the

increase of discrete frequency components. The descrete components of the high frequency range, which are amplified with the use of the semi-log plot, appear before the cavitation development. This is concluded from the carefull examination of the spectrum and the observation of the existence of green peaks in the majority of the high frequency discrete components (Fig. 6.21). Some of these peaks are highlighted with the grey colour ellipse in the plots of Fig. 6.21.

On the other hand, the excitation due to cavitation refers to wide ranges of the spectrum, and is highlighted with the use of the blue broken lines in Fig. 6.21. These lines are located in representative parts of the spectrum, where these excitations maximise. It is important to notice that in case of total head drop (black line) the excitation almost covers the total band of the measured spectrum, similarly to the noise (Fig. 1.32d, section 1.3.1.3) and vibration (Fig. 1.32b) results, presented by Cernetič (2008) and Chudina (2009a) for plastic semi-open impellers. In general, the changes in the characteristics of frequency spectrum due to cavitation development follow the trend of the published literature for centrifugal pumps (Neill, 1997; Chudina, 2003a,b, 2009b; Cernetič, 2012) and hydroturbines (Escaler, 2003, 2004 - Fig. 1.34, section 1.3.1.3). In fact, the similarities with the results of Escaler (2003, 2004) spectra that refer to Francis hydroturbine prototypes of 10MW, reveal the analogies of the cavitation effect between the different types and magnitude of hydaulic machines.

The amplitude divergences with cavitation development are more obvious for the impeller No. 4 (Figs. 6.21d,e), starting since the visual onset, at σ_{VI}. On the other hand, the differences between σ_{VI} and non-cavitating (σ_{BVI}) conditions are less distinguishable for the LU impellers. This is an expected difference in the results of the two test rigs, since the σ_{VI} OP for the NTUA pump is lower than the non-visible, actual inception point. More specifically, the increase of the spectrum amplitude becomes apparent only for frequencies f >1 kHz for impellers No. 1 (Fig. 6.21a) and No. 3 (Fig. 6.21c), and for f >6 kHz for impeller No. 2 (Fig. 6.21b).

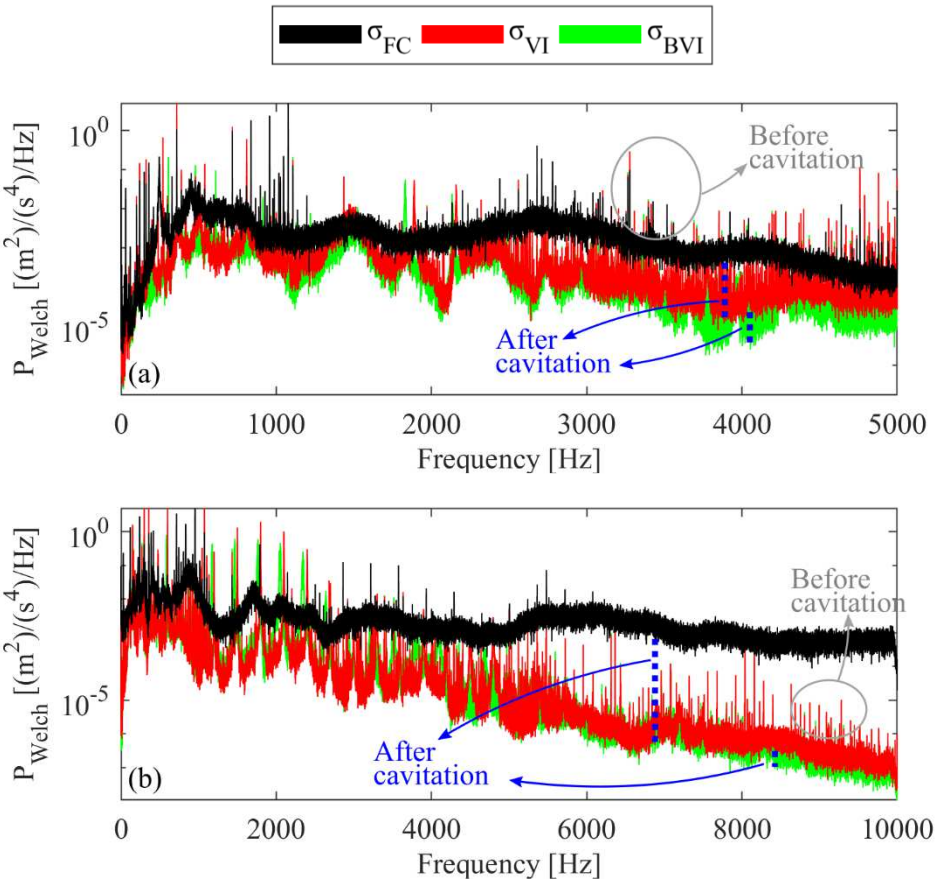

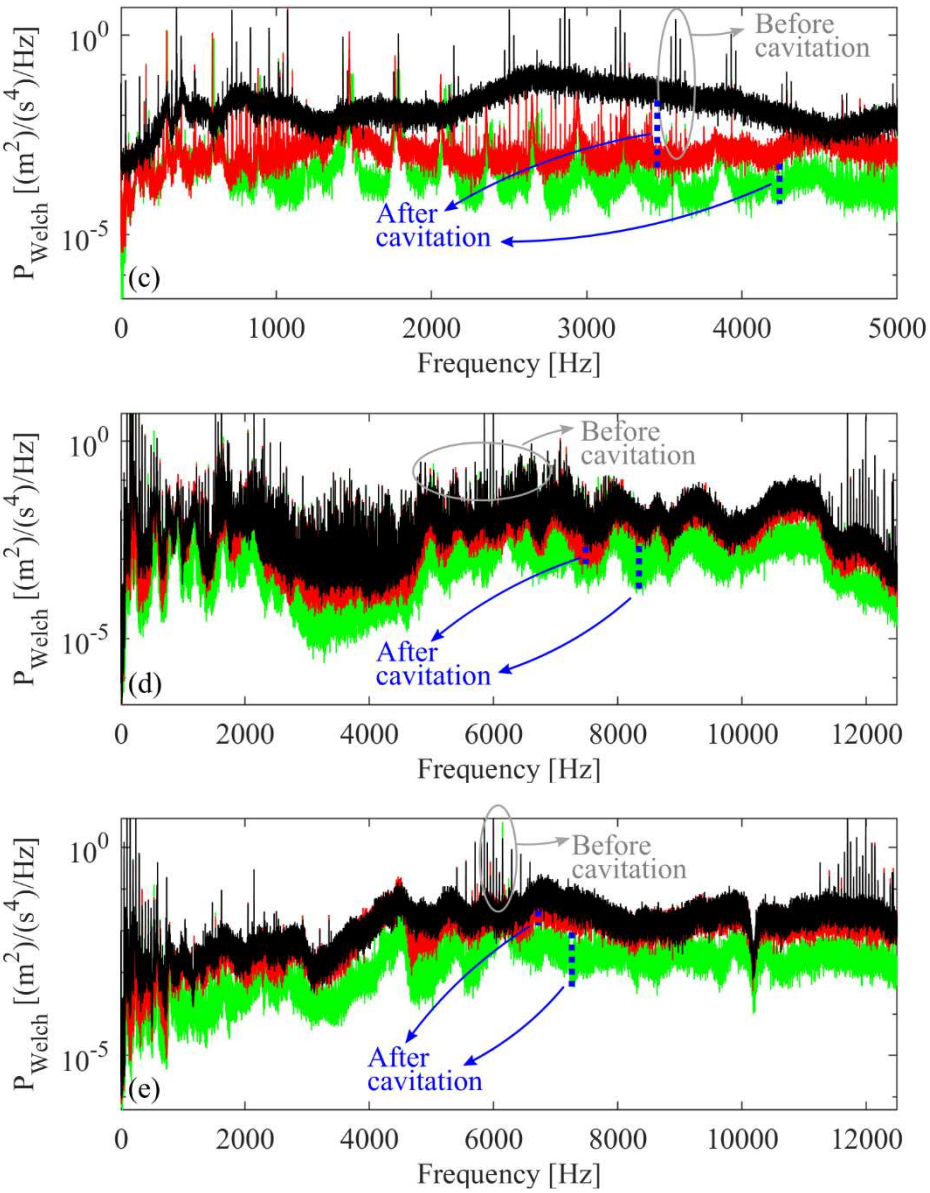

Figure 6.21 Semi-log frequency spectra for various cavitation conditions of: **a)** impeller No. 1, sensor A01, $\Phi=0.40\cdot\Phi_{BEP}$, **b)** impeller No. 2, sensor B01_1, $\Phi=0.64\cdot\Phi_{BEP}$, **c)** impeller No. 3, sensor A01, $\Phi=0.70\cdot\Phi_{BEP}$, **d)** impeller No. 4, sensors B01_1, $\Phi=\Phi_{BEP}$ and **e)** impeller No. 4, sensors B01_2, $\Phi=\Phi_{BEP}$.

The excitations produced by two-phase flow development (Fig. 6.21) are strongly related with the fault mechanism of cavitation, and more specifically, with the shock pressure waves created during the bubble's implosion. The effect of the implosions can be observed in the time signals presented in the time series of Fig. 6.3 and 6.8, for heavy cavitating conditions. This association of the cavitation impulses with the excitations seen in Fig. 6.21, is equivalent with the association of the impulses created from faults related with the rolling element bearings (Figs. 1.19a,c & 1.24 section 1.2.2.3) and the resonances excited in the frequency spectrum (Fig. 1.19b,d, 1.20, 1.21b, section 1.2.2.3).

Comparison of these spectra with those of Fig. 6.21 reveals the common characteristics of the frequencies that could be excited from bearing and cavitation fault mechanisms. In the literature, there have been reported resonances that excited either a narrow part of the spectrum (Figs. 1.20a, section 1.2.2.3) or a wider range (Figs. 1.20b, 1.21b), similarly to cavitation in Fig. 6.21. In general, the resonances created from the bearing faults are strongly dependent on

the randomness introduced by the slip of the bearings (Fig. 1.19d, section 1.2.2.3), and by the changes created in the geometrical shape of the structure due to the bearing wear (Yiakopoulos, 2005; Randal 2007). For this reason, the prediction of the resonance area was not possible and its identification in the frequency spectrum was an open problem until recently (Randal & Antoni, 2011). The difficulty to locate the part of the frequency spectrum or the resonance excited from cavitation is evident also in the results of Fig. 6.21, where the location and magnitude of the resonance changes among the different impellers and cavitating conditions. The last observation manifests an additional similarity of the cavitation's and bearing's impulsive mechanism.

The results presented in Fig. 6.21 are of critical importance regarding the development of the experimental tool for cavitation detection. In these plots, the increase of the high frequency vibration amplitude caused by the two-phase flow development is apparent in all cases examined. The next step is to advance from the qualitative spectrum comparison to more quantified methods. This is achieved with the calculation of the vibration velocity RMS method, v_{RMS} (see Eq. 2.62, section 2.4.3) that is discussed in section 6.3.2 and the use of powerbands (Eq. 2.61, section 2.4.3) and AE_{RMS} (Eq. 2.65, section 2.4.3) so as to integrate the power of high frequency spectra, which is discussed in section 6.3.3.

6.3.2 Low frequency content of the vibration signals

The low frequency range characteristics are discussed in detail in the previous section, with the aid of the results of Figs. 6.19 and 6.20. In Fig. 6.20 the mechanical vibration sources that mainly contribute in the low frequency spectrum are successfully provided, while in Fig. 6.19a it is not possible to highlight a specific trend for their amplitude variation with the change of suction conditions. In order to provide a clear answer regarding the last issue, it is attempted to quantify the vibration power at low ranges and present it as a function of Thoma cavitation number, σ, similarly to the statistical moments in Figs. 6.11-6.15. The velocity RMS [mm/s] methodology, proposed by ISO 10816-1, ISO 4413 for the evaluation of machine vibration by measurements on non-rotating parts, described by Eq. 2.62 in section 2.4.3 is used for the performance of this examination.

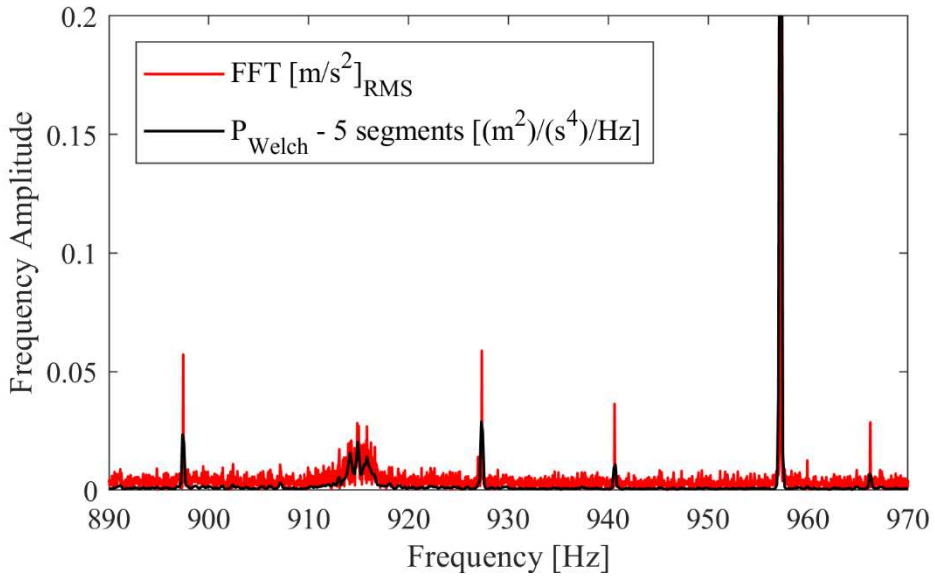

Figure 6.22 Comparison of FFT and Welch estimation of the frequency spectrum for impeller No.1, sensor A01, $\Phi=0.40\cdot\Phi_{BEP}$.

One difference from those discussed in section 6.3.1 is that the application of the ISO tool proposes the use of popular Fast Fourier Transformation (FFT) for the calculation of frequency

spectrum, instead of the Welch estimator. However, although, the absolute value will be of a different quantity (velocity instead of acceleration of vibration), the calculated patterns are expected to be similar. This conclusion is based on the results of Fig. 6.22, where the zoomed-in frequency spectrum of Fig. 6.20a is shown along with the FFT calculation for the same signal. Both tools calculate the same peaks, even at the very week amplitudes of $<0.2\ m^2 \cdot s^{-4} \cdot Hz^{-1}$.

An additional advantage of the ISO methodology is that in the seventh part of the same ISO (10816-7) the acceptable levels of vibration is $5.1\ mm \cdot s^{-1}$ for rotordynamic pumps with unrestricted long-term operation (see section 2.4.3). As a consequence, the application of this tool, reveals the low frequency behaviour of the vibration as a function of σ and simultaneously, it is possible to compare the absolute value calculated for each σ with the vibration limits.

Table 6.3 Corresponding flowrates for each impeller, as a function of their Φ_{BEP}.

Impeller	Φ_1	Φ_2	Φ_3	Φ_4
No.1	0.40	0.60	0.81	1
No.2	0.48	0.64	0.80	0.96
No.3	0.43	0.56	0.70	0.85
No.4	0.41	0.64	0.85	1

The results of all sensors, flowrates and impellers are presented in the plots of Fig. 6.23, with the use of a common flowrate legend. The tested flowrates are not exactly the same for all impellers, and their exact values are matched with the Φ values in Table 6.3. According to the results, the velocity vibration RMS, in general, does not increase during the first stages of cavitation, for $\sigma \sim \sigma_{VI}$. One observation of critical importance is that in most of the cases (Figs. 6.23a,b,c,d,e,g) the behavior of v_{RMS} is pretty similar with that of standard deviation, shown in Figs. 6.12-6.15. This observation higlights the association of the v_{RMS}, and consequently this of low frequency vibration range, with the stationary characteristics of the time series.

Only after passing to heavy cavitating conditions, at the minimum σ values, the v_{RMS} value seems to be excited from the phenomenon, especially in the results of sensor A01 (Figs. 6.23a,c,e - impellers No. 1,2,3) and B01_1 (Fig. 6.23g - impeller No. 4). At this stage, cavitation dominates the performance operation and, consequently, impacts on the steady characteristic of the vibration signal, such as the standard deviation and the v_{RMS}. However, the detection of the phenomenon at these operating conditions could be done more efficiently by simply monitoring the total head or efficiency performance of the machine, as it is presented in section 3.3.1 (Figs. 3.9 & 3.11). A modern detection tool must be able to detect the presence of cavitation during early stages of its development, in order to provide sufficient time to the operator take actions to decrease its consequences related with the performance and material wear.

The overall vibration value for the LU impellers does not exceed the vibration limit for unrestricted long-term operation, which is $5.1\ mm \cdot s^{-1}$ (section 2.4.3). Similar behavior shows also the B01_2 sensor of NTUA test configuration, which is located on the casing of the pump. Only the sensor mounted at the bearings of the NTUA pump (Fig. 6.23g) exhibits high vibration levels, which exceed the acceptable vibration limits, for the lowest σ value at partial loading. However, since the increased level of vibration is limited only during minimum σ and does not influence the flowrate value (Fig. 3.8, section 3.3.1), the testing even at such severe conditions is considered reliable.

To sum up, the v_{RMS} and the standard deviation of the vibration results could be applied as a supplementary tool in cases where the detection is based in the total head or the efficiency measurements, in order to confirm the development of heavy cavitating conditions. The observed trend of these results highlights the association of low frequency mechanical vibrations with the steady behavior of standard deviation (Fig. 6.16). Both conclusions are significant, as they practically exclude the use of velocity vibration RMS for early cavitation detection purposes and drive the research to investigate for additional information in the study of high frequency vibrations, presented in the following section.

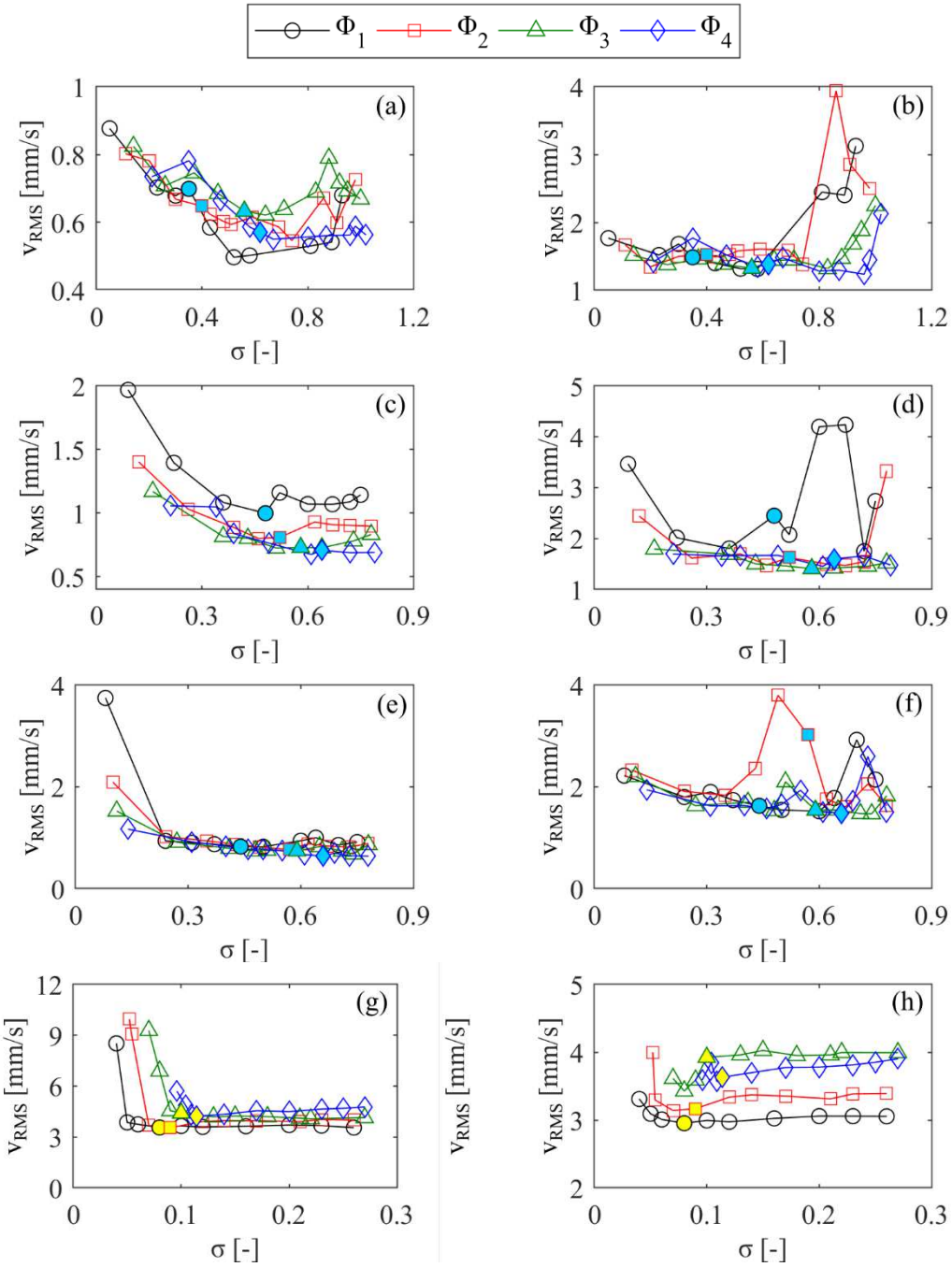

Figure 6.23 Velocity of vibration RMS [mm·s^{-1}] as a function of σ for: **a)** impeller No. 1, sensor: A01, **b)** impeller No. 1, sensor: B01_1, **c)** impeller No. 2, sensor: A01, **d)** impeller No. 2, sensor: B01_1, **e)** impeller No. 3, sensor: A01, **f)** impeller No. 3, sensor: B01_1, **g)** impeller No. 4, sensor: B01_1, **h)** impeller No. 4, sensor: B01_2.

6.3.3 High frequency content of noise and vibration signals

The study of the high frequency characteristics includes the analysis of AE and vibration signals with the use of RMS and powerband tools, respectively. The RMS value for the AE measuring system is considered that represents the high frequency spectrum, since the band pass filters of both test rigs remove the low frequency components. On the other hand, the ability to control the range included in the powerband ensures the representation of the high frequency vibration spectrum. The only concern regarding the use of powerband pertains to the

range selection and its effect on the obtained results. Consequently, the presentation of high frequency noise and vibration results in section 6.3.3.2, follows the study for the selection of the powerband range, in section 6.3.3.1.

6.3.3.1 Selection of powerband range

The influence of the range in the powerband calculation is shown in Fig. 6.24 for the LU (Fig. 6.24a,b) and the NTUA (Fig. 6.24c,d) pumps. One flowrate per test rig is depicted and the effect on both accelerometers is investigated. The ranges examined are given in the legends of these figures, where the higher limit equals to the cut off frequency (f_{cutoff}) of the low pass filters used (see Tables 2.4, 2.9, section 2.5) for all cases. As a result, the change of range width is controlled only by the lower limit values.

In the previous sections (6.2.1 & 6.3.2) it have been discussed the effects of rotation speed, the material and the bearings on the overal vibration level of the pumps tested. These effects also justify the y-axis differences observed between the LU (Fig. 6.24a,b) and NTUA (Fig. 6.24c,d) impellers. However, in contrast to Fig. 6.20, the powerbands of Fig. 6.24 for the sensor installed on the casing of the pump (B01_2) take higher values relative to the sensor mounted at the bearings (B01_1).

This behaviour depicts the effect of the application of the powerband ranges, which in practice act as a digital high pass filter. More specifically, in this section the low frequency components that dominate Fig. 6.20, are not taken into account, because they lie in frequency range below 2 kHz, that is the lowest limit of the range applied. The results of Fig. 6.24c,d provide a first indication that the high frequency vibration results of B01_2 sensor will be more excited than those of B01_1 sensor due to the positioning of the former closer to the two-phase flow formation area.

As expected, in the results of Fig. 6.24, the wider ranges produce higher powerband values, since they include larger amount of signal power. Furthermore, the results of A01 sensor (Fig. 6.24a) demonstrate that the pattern of the powerbands remains relatively constant for [3 – 5] kHz or less range width. The wider ranges of [2 – 5] and [2.5 – 5] kHz are affected from low frequency noise sources that exist for f <2.5 kHz.

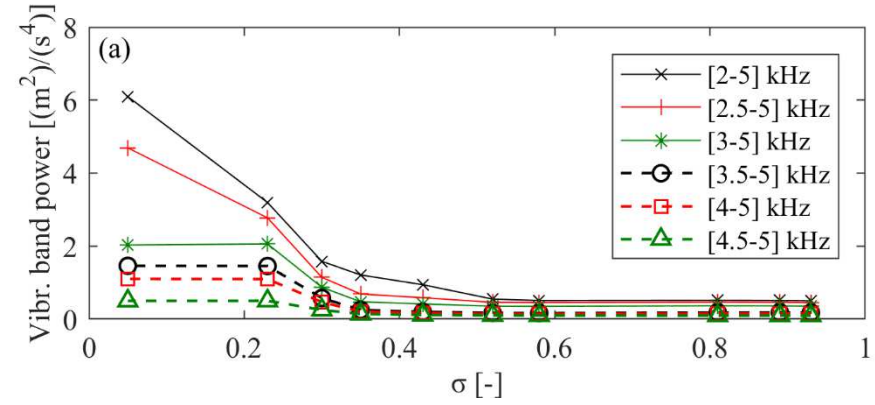

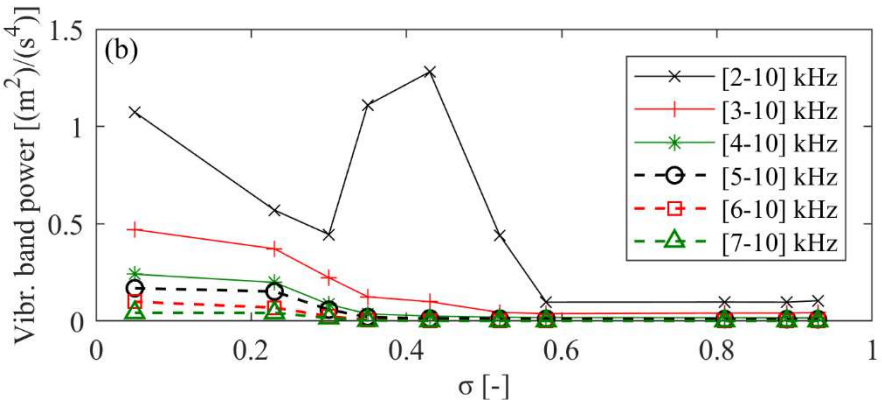

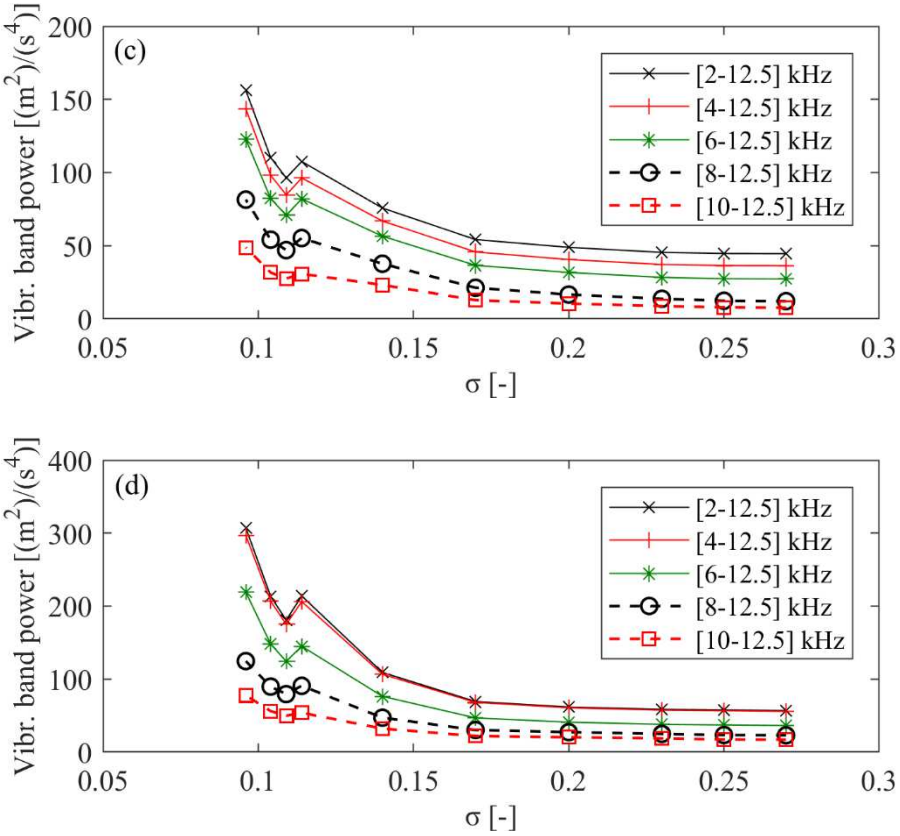

Figure 6.24 The effect of range in the results of impeller No. 1, $\Phi=0.40\cdot\Phi_{BEP}$, for sensors: **a)** A01, **b)** B01_1 and of impeller No. 4, $\Phi=\Phi_{BEP}$, for sensors: **c)** B01_1, **d)** B01_2.

As a consequence, the [3 – 5] kHz range is selected for the powerband calculations of the vibration measurements of the A01 sensor, for all LU impellers. Similarly to A01 sensor, the powerband power for B01_1 sensor stabilises for about the same lower limit (3 or 4 kHz, Fig. 6.24b), hence the [4 – 10] kHz range is selected for the powerband of this sensor.

Finally, the powerbands of the results of both sensors at the NTUA test rig (Figs. 6.24c,d) depict an increase of the powerband value as σ value decreases. The further reduction of σ is decreases the powerband value, before its maximisation at minimum σ. The patterns under different ranges are not affected, therefore, the wider range of [2 – 12.5] kHz is used for the powerband analysis, in order to be benefited from the inclusion of larger signal information.

6.3.3.2 High frequency noise and vibration as a function of σ

The analysis in the present chapter is completed with the presentation of the high frequency noise and vibration results, as a function of suction conditions. The noise results for all impellers tested are given in Fig. 6.25, while those of vibration sensors are provided in Figs. 6.26 to 6.29 for the impellers No. 1 to 4, respectively. Every graph in each of the Figs. 6.26-6.29 refers to a different flowrate. The blue (LU) and yellow (NTUA) markers coincide with the experimental visual onset of cavitation (σ_{VI}), while the black marker used only for the results of impeller No. 4, denotes the numerical estimation regarding the inception of the phenomenon, so as to provide an additional indication of the onset of the phenomenon.

The presentation of the results starts with the discussion of AE_{RMS} (Fig. 6.25) behaviour for all the pumps. One first observation from the plots of Fig. 6.25 is that the noise increase occurs in higher σ values, as the flowrate increases. That tendency of the AE_{RMS} value agrees with the conclusions drawn in Chapter 3, regarding the changes in the σ_{VI} and σ_{FC} values as function of the flowrate conditions. These conclusions refer to the earlier onset and total head drop of the pump during its operation at higher flowrates due to the accelerated flow field.

The incremental trend of AE_{RMS} at the point of visual inception is sharper for the first (Fig. 6.25a) and third (Fig. 6.25c) impeller, than for the second impeller (Fig. 6.25b). However, in the latter, the appearance of the first bubble is difficult to be captured by the camera, because the vapour area was extremely small and the first bubbles are not stable. Nevertheless, when σ value decreases further, cavitation appearance is stabilised and the AE_{RMS} values increase more sharply (Fig. 6.26a). In addition, impellers No. 1 and 4 exhibit the lowest AE ranges for similar flowrates compared to impellers No. 2 and 3, due to the effect of the smaller number of blades and the lower incidence angle.

In general, the high frequency range energy captured by the AE sensor shows a remarkable sensitivity and capability to detect the first bubbles implosion of LU impellers (Figs. 6.25a,b,c) in accordance with Gulich's (2008) findings.

Also, for $\Phi=0.43\cdot\Phi_{BEP}$ and $\Phi=0.85\cdot\Phi_{BEP}$ at impeller No. 3 (Fig. 6.25c) a very slight increase in AE_{RMS} is noticed for σ values higher than σ_{VI}. This behavior agrees with the results of the corresponding vibration measurements shown in Figs. 6.3e and 6.17c, and it is also found in the results shown in similar studies (McNulty, 1982; Boccazzi, 1989; Gulich, 2008). The reason behnid this early increase of noise and vibration measurement is the fact the cavities are possibly created and implode in the impeller in microscopic formations before they become visually observable.

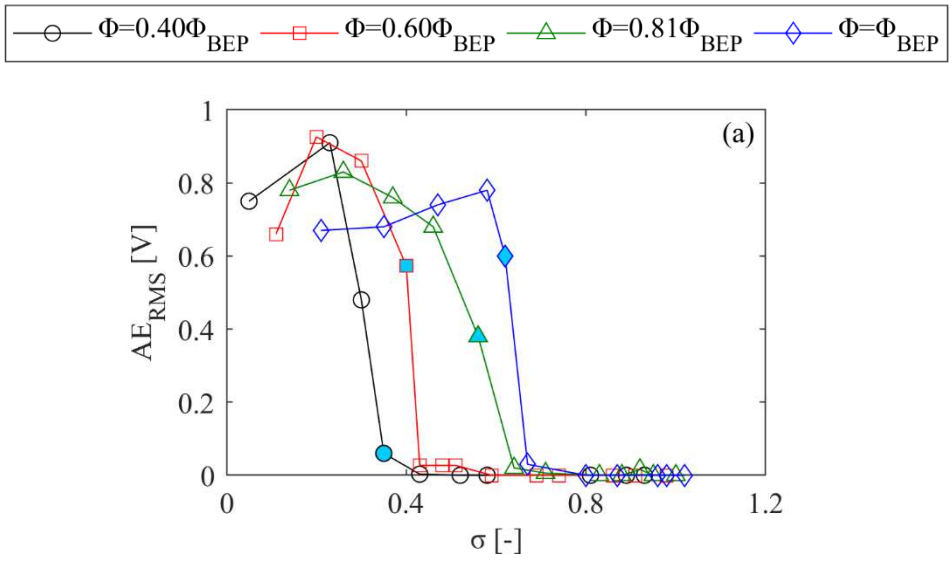

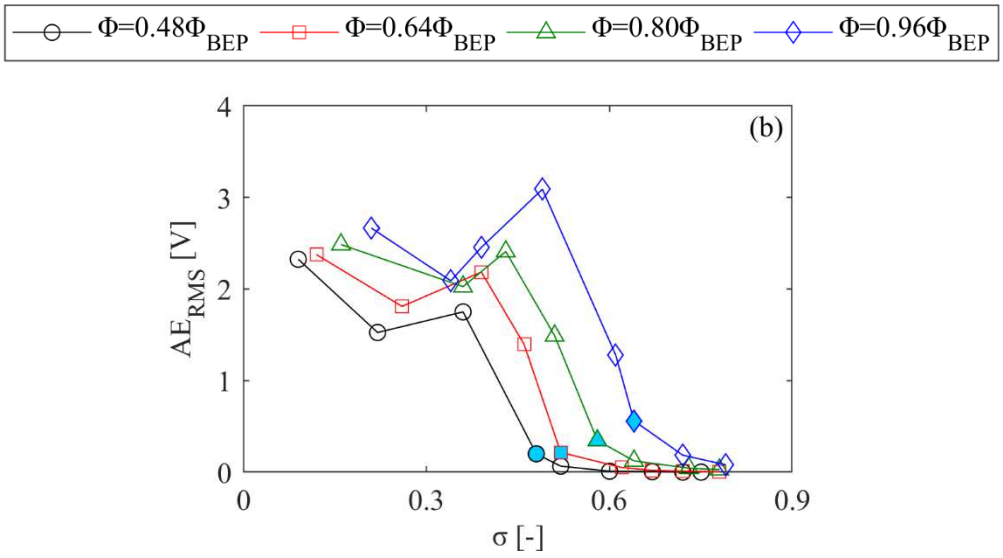

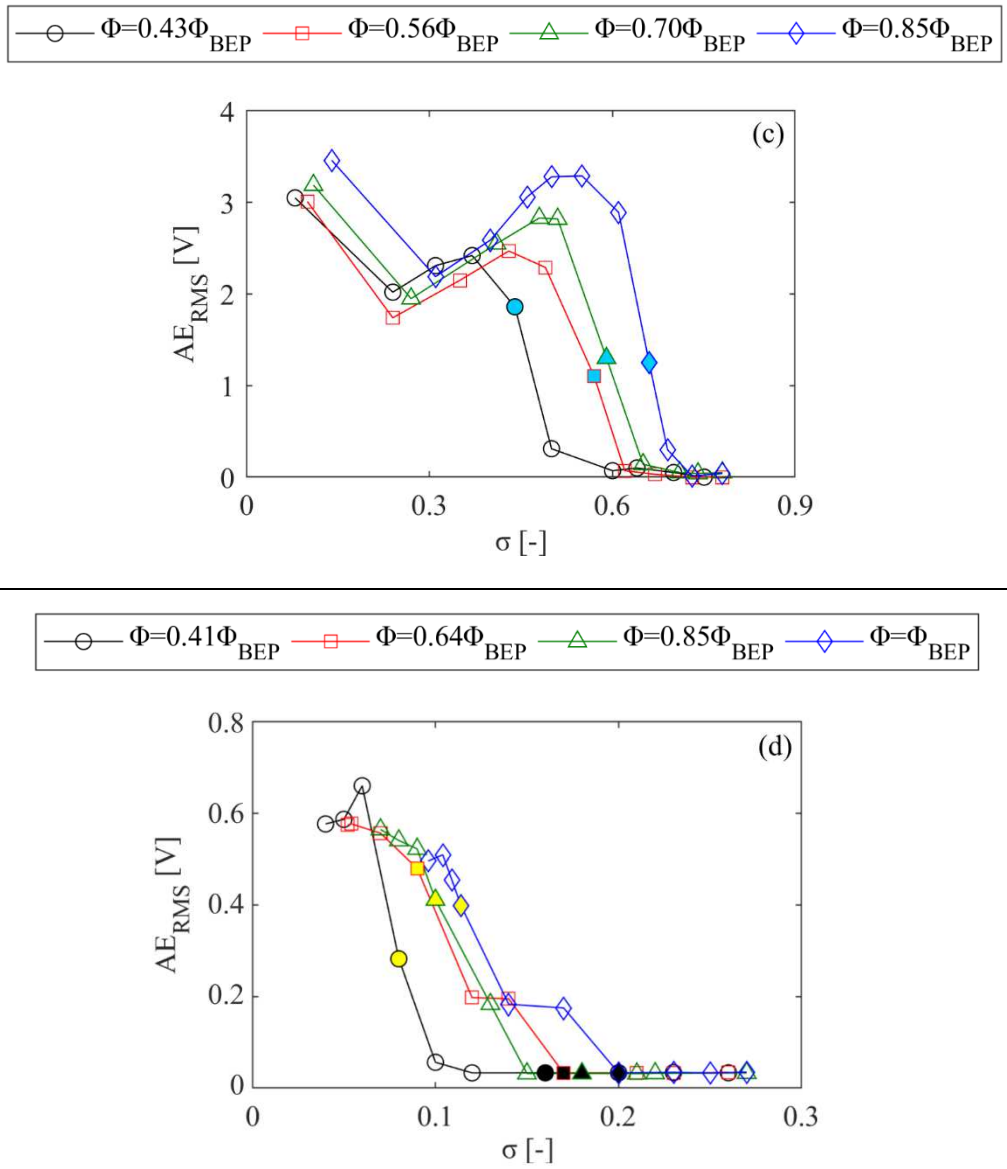

Figure 6.25 AE_{RMS} results under various flowrates for **a)** impeller No. 1, **b)** impeller No. 2, **c)** impeller No. 3, **d)** impeller No. 4.

Another reason, could be the presence of cavities that are created outside from the camera focusing area, such as the pipe elbow before the pump inlet. However, until this point, the signal processing methodology does not provide a well-rounded justification towards this behaviour. For this reason, this tedency of impeller No. 3 is further analysed and discussed in the results of Chapter 7.

The AE results present reasonable pattern also for the industrial closed impeller No. 4 (Fig. 6.25d). Here the increase initiates in the area between the experimental and numerical visual inception point,where the actual onset of bubble formation occurs. However, the AE sensor fails to promptly detect the cavitation in case of the lowest flowrate examined (Φ=0.41·Φ_{BEP}), since the increase of sensor's RMS occurs for σ<0.1, where the total head of the pump has already begin to collapse, according to the results of Fig. 3.9 shown in the section 3.3.1. The reason for this delay of the AE sensor in the NTUA test configuration is related with the lower frequency range ([2.5 – 80] kHz) that measures, compare with the AE sensor of LU ([100 – 150] kHz), which could be affected from the noise due to pump operation under partial loading, and the effect of the shroud that acts as an obstacle between the implosions and the sensor.

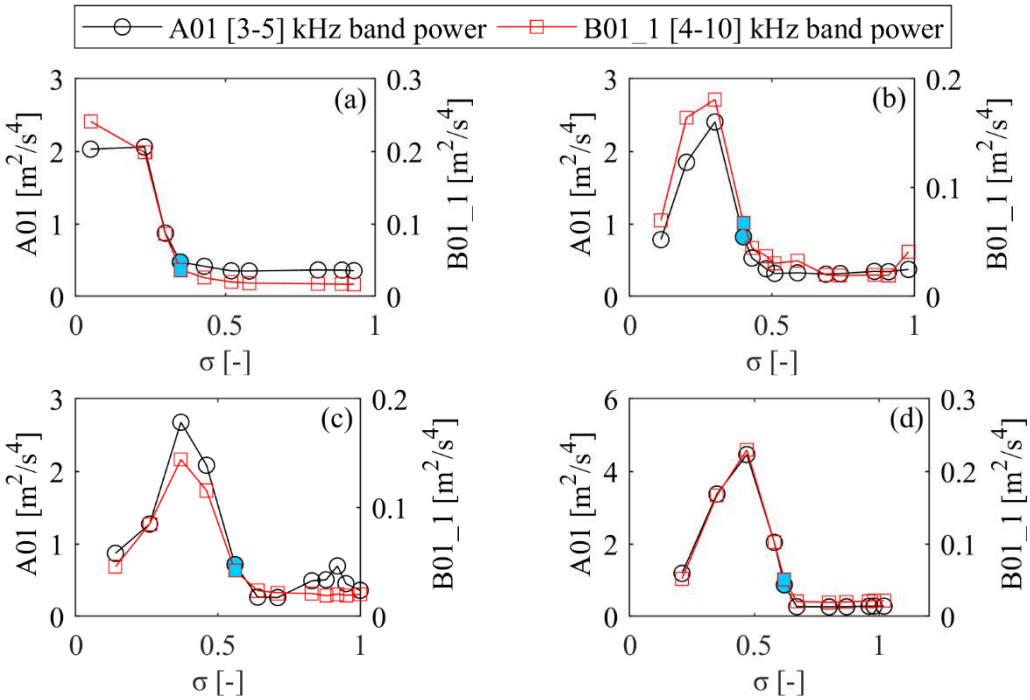

Figure 6.26 High frequency vibration results for impeller No.1, for: **a)** $\Phi=0.40\cdot\Phi_{BEP}$, **b)** $\Phi=0.60\cdot\Phi_{BEP}$, **c)** $\Phi=0.81\cdot\Phi_{BEP}$, **d)** $\Phi=\Phi_{BEP}$.

After the presentation of the AE_{RMS} results for all the impellers, the discussion focuses on the vibration powerbands for the semi-open impellers. A first observation confirms the conclusion extracted from the AE_{RMS} results that the vibration band power increases for higher σ values, when the flowrate increases (Figs. 6.26-6.29). Moreover, in all cases presented, the vibration powerband value increases close to the σ_{VI} conditions and maximises for $\sigma<\sigma_{VI}$, and this makes the use of vibration powerbands able to identify the presence of cavitation development. The satisfactory behavior of the noise and vibration trends in the case of semi-open impellers allows the further penetration of results and their comparison with the visual observations made for each impeller in Figs. 3.12-3.14 of Chapter 3.

One interesting observation of all the vibration results of Figs. 6.26-6.29 is that the behaviour of both accelerometers is identical, no matter the impeller and the flowrate examined. This observation occurs for the first time here, as a result of this signal processing technique, and it is opposed to the trends of Figs. 6.11-6.15 and 6.23, where the plotted results are sensitive to the position of the vibration sensor.

The vibration band power, drawn in the same figures close to σ_{VI} for the LU impellers (Figs. 6.26-6.28), exhibits a very similar trend to the AE_{RMS} values for the majority of the operating conditions tested. However, the increase of the band power starts at slightly lower σ values than σ_{VI} in the plots of Figs. 6.26b, 6.27b,c,d,e and 6.28d,e. This delay compared to AE_{RMS} could be the result of the lower frequency range used for the vibration analysis. Further reduction of σ value results in increased number of bubbles, though the cavitation area remains small and restricted. This behavior is clear in the flow visualization photos of intermediate cavitation Figs. 3.12-3.14 of section 3.3.2.

The enlargement of the two-phase flow area is accompanied with an increase in noise and vibration signals, irrespective of the impeller and the flowrate (Figs. 6.26-6.28). The vibration band power curve follows in most cases the trend of the AE curve and reaches a local maximum point. This point behaves, as a function of flowrate, differently in AE and in vibration measurements, as also for the various impellers, and hence, it is difficult to extract some specific correlations.

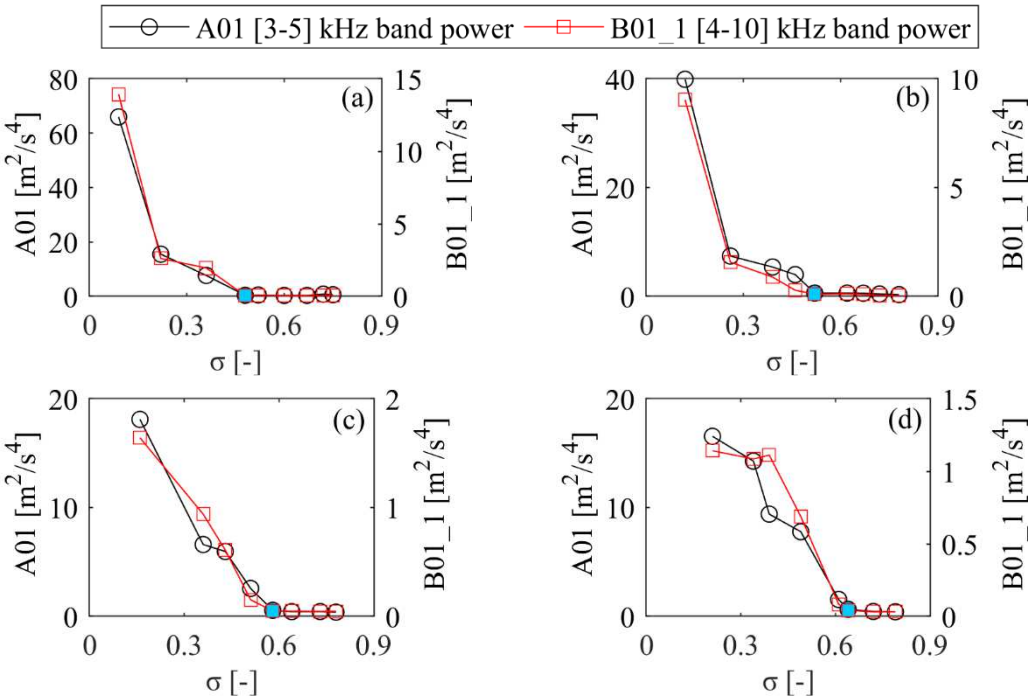

Figure 6.27 High frequency vibration results for impeller No.2, for **a)** $\Phi=0.48\cdot\Phi_{BEP}$, **b)** $\Phi=0.64\cdot\Phi_{BEP}$, **c)** $\Phi=0.80\cdot\Phi_{BEP}$, **d)** $\Phi=0.96\cdot\Phi_{BEP}$.

From this operating point, as σ takes even smaller values, the cavitation area enlarges and increases the amount of vapour bubbles that implode and collapse in the flow stream. At these conditions that correspond to the third column (c) of Figs. 3.13-3.15 (section 3.3.2) at the operating point just before σ_{FC}, the AE_{RMS} and the vibration powerband results start to significantly deviate between the different impellers, as well as between the different frequency ranges used in their calculation. It is important to note at this point that the AE_{RMS} results are treated similarly to the powerband, because their results illustrate the power included in specific ranges of the frequency spectrum. The only difference compared to the powerbands is that in their case the limits (f_r) are set from the analog band pass filters used during their acquisition, as they are described in Tables 2.4, 2.9 of section 2.5. The formation of various patterns in the plots of AE_{RMS} and the vibration powerbands reveals the similarities with the results discussed in the literature review section 1.3.1.3 of the present Thesis. In order to simplify the discussion of those results, the notation applied in the Fig. 1.35, which is given in the second column of Table 1.1 (section 1.3.1.3), is also followed here.

The results of Figs. 6.25a-c, 6.26-6.8, confirm the conclusion that the higher the frequency range used for the calculation of the powerband (and the AE_{RMS}) the sooner their value is maximised. More specifically, the noise results of the impellers No.1 (Fig. 6.25a - Pattern/$\sigma_{PB,M}$: 2/E) and No. 2 (Fig. 6.25b - Pattern/$\sigma_{PB,M}$: 1/E) that include high frequency bands, maximise their values during early stages of cavitation development, between the visual inception (σ_{VI}) and the point where the total head collapses (σ_o). This area is marked in Fig. 1.35 (section 1.3.1.3) with the letter E. The AE_{RMS} results of impeller No. 3 (Fig. 6.25c) are similar with those of No. 2 (Fig. 6.25b), however they maximise at the total head drop point, which manifests the additional effect of the geometrical characteristics.

The early increase of the high frequency measurements is followed by a strong decrease of the noise (Fig. 6.25a-c). As it has already been discussed in the review section 1.3.1.3, according to Gulich (2008), the main cause of this decrease is the drop of the pressure differential between the surrounding liquid and vapour at lower σ values, as well as the fact that the formation of large cavities at the suction of the impeller acts as an additional surface between the sensor and the implosion area, which absorbs part of the noise emitted. This noise and vibration behavior has also been observed and discussed by several authors (McNulty, 1982; Neill, 1997; Chudina, 2003b; Alfayez, 2004; Cernetič, 2008; Brennen, 2011).

The results of the vibration powerbands for impellers No. 2 (Fig. 6.27 - Pattern/$\sigma_{PB,M}$: 3/A) and No. 3 (Fig. 6.28 - Pattern/$\sigma_{PB,M}$: 1/A), which integrate lower frequency ranges, maximise for all the examined cases close to the minimum suction conditions. This area is marked in Fig. 1.35 (section 1.3.1.3) with the letter A. Intrestingly, the vibration powerbands of impeller No. 1 presents a similar pattern with that of the AE_{RMS} and maximises its value relatively earlier. The main reason for this behaviour is probably related with the better suction characteristics of this impeller, discussed also in sections 3.2 and 3.3.

The differences that are discussed between the noise pattern of impeller No. 3 and the vibration powerband of impeller No. 1, reveal the additional effect of the blade design on the behaviour of powerbands. Unfortunatelly, the studies reviewed in section 1.3.1.3 do not provide the characteristics of the blades and it is not possible to compare the present results with those of the literature.

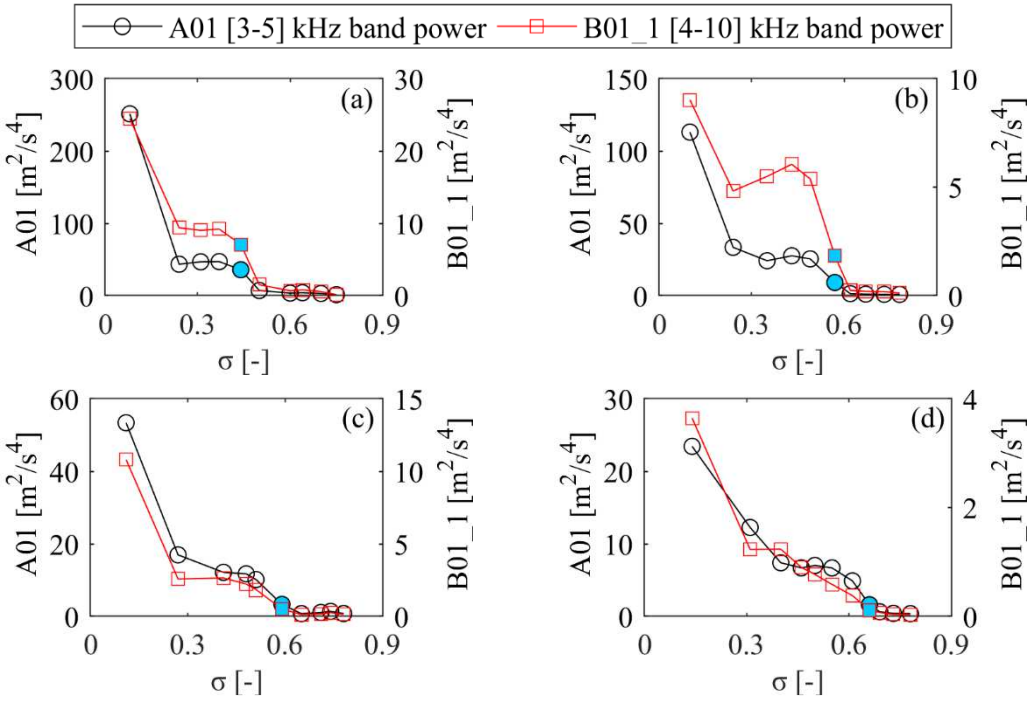

Figure 6.28 High frequency vibration results for impeller No.3, for **a)** $\Phi=0.43\cdot\Phi_{BEP}$, **b)** $\Phi=0.56\cdot\Phi_{BEP}$, **c)** $\Phi=0.70\cdot\Phi_{BEP}$, **d)** $\Phi=0.85\cdot\Phi_{BEP}$.

Another intresting observation that deals with the majority of the vibration powerband results of the semi-open impellers, is that the flowrates closer to the BEP results in a general decrease of the powerband. According to the classic pump theory (Hergt, 1985; Nelik, 1999; Gulich, 2008; Lobanoff, 2013; Papantonis; 2016) and experimental investigations (Alfayez, 2004; Zhang N., 2015a) the flow in low specific speed machines operating at part load conditions becomes three dimensional, and strong recirculation regions are created in the impeller flow path. The large eddies formed in those recirculation areas excite pressure pulsations that rise the overall energy of the vibration signal, even for non-cavitating conditions, with σ higher than σ_{VI}. The vibration sensors appear to be more sensitive in the recording of this behaviour, probably due to the lower frequency range selected during the calculation of the vibration powerbands. This behaviour is also confirmed in the vibration powerband results of the closed impeller of NTUA, presented in Fig. 6.29.

Finally, the vibration powerband results in the case of impeller No. 4 (Fig. 6.29) question the ability of the discussed methodology to promptly detect cavitation. This is revealed from the results of the two lowest flowrates examined (Figs. 6.29a,b), where the vibration powerband exhibits its first increase only when $\sigma<0.1$, when the total head of the pump has already collapsed. This observation agrees with the inability also of the AE_{RMS} to promptly detect cavitation development in the same impeller at the lowest flowrate tested. The reasons for the

failure of vibration powerbands to detect cavitation before the total head drop, deals with the same reasons discussed for the case of AE sensor (shroud effect & increased hydraulic noise at partial loading conditions).

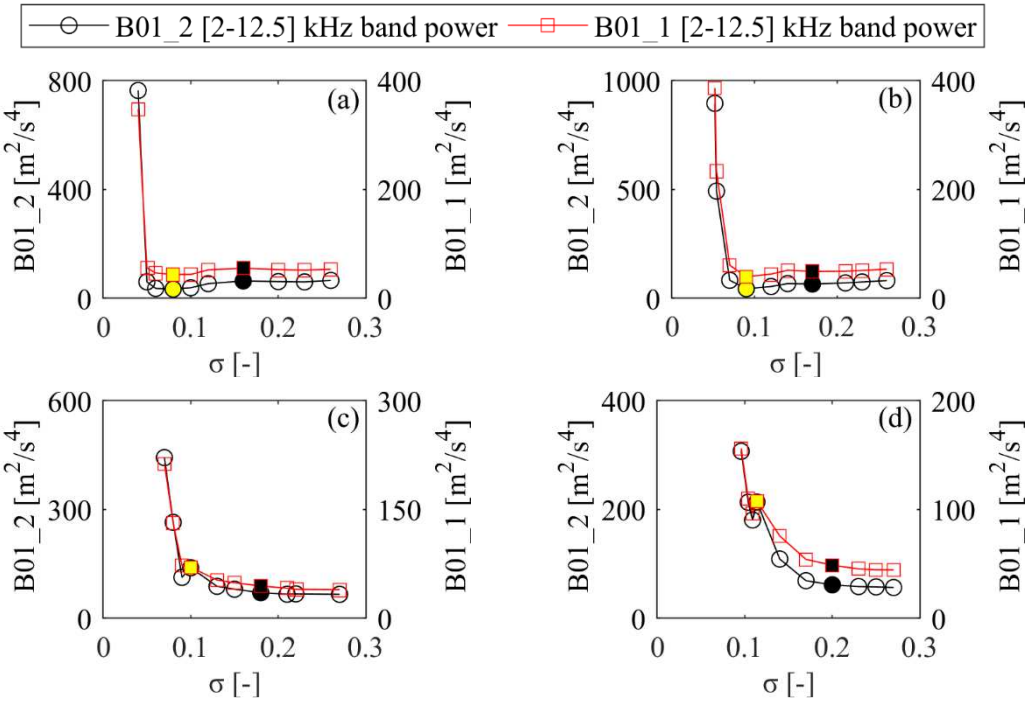

Figure 6.29 High frequency vibration results for impeller No.4, for **a)** $\Phi=0.41\cdot\Phi_{BEP}$, **b)** $\Phi=0.64\cdot\Phi_{BEP}$, **c)** $\Phi=0.85\cdot\Phi_{BEP}$, **d)** $\Phi=\Phi_{BEP}$.

6.4 Synopsis

This chapter studies and discusses the capability of noise and vibration signals to detect the cavitation onset and development in the four impellers tested in the present Thesis. The study starts with the examination of the measured time series, plotted in non-cavitating, initial cavitation, and fully cavitating conditions. The observation of the raw signals, especially during heavy cavitating conditions, reveals the presence of impulses that increase the vibration amplitude range. The increase of amplitude is a typical symptom of fault in rotating machinery and the appearance of shock characteristics in the signals is usually related with damaged bearings (Yiakopoulos, 2011; Chang, 2017; Hu, 2019). Nevertheless, in the controlled tests of this study, the impulses appeared only after passing into fully developed cavitation operating points and makes them the first significant indication of vapour development in the machine.

However, during such intense cavitating conditions, even the performance (total head and efficiency) of the pump deteriorates, as it is shown in detail in Chapter 3. Consequently, the aforementioned conclusion can not be used for detecting vapour formation at early stages, and further analysis is done on the statistical characteristics on the signals. According to these results, the impulses of the raw measurements during σ_{VI} and σ_{FC} affect the Gaussian distribution of the data, under non-cavitating conditions. This outcome is highlighted in the calculated histograms and normal probability plots for all impellers. Furthermore, the examination of the statistical moments associates the cavitation impulses and the signals' non-Gaussian behavior with the kurtosis of the population. The steady behavior of standard deviation is related with the velocity vibration RMS value but both are found unable to detect systematically the development of cavitation promptly, as well as their values are found to be affected by the sensor location.

The next step of the signal processing includes the study of the frequency spectrum. At first glance, only the results of AE spectrum of impeller No. 4 change with the drop of σ, since the vibration spectrum is dominated by the low mechanical frequencies. Nevertheless, the use of logarithmic plots in the vibration amplitude brings out significant differences between the normal and cavitating conditions. More specifically, in the logged graphs the excitation of the high frequency spectrum is clearly shown, no matter the operating point, the location of the sensor or the impeller tested. In order to quantify the spectrum excitation, the use of powerbands at high frequency ranges is qualified in parallel with the AE_{RMS} measurements that include only the high frequency content of the noise signal. All the AE_{RMS} and powerband results are plotted as a function of suction conditions, and significant conlcusions are drawn.

According to them, both the AE sensor and the accelerometers are able to identify cavitation far before the total head drop point, in the case of semi-open impellers. The AE sensor and the majority of the vibration powerband results are able to detect the appearance of the first visible bubble inside every impeller. Some of the vibration trends, which use lower frequency range, show a delayed detection, yet this is achived close to the visual inception and far from the total head drop conditions.

Further decrease of σ value results in an increasing number of bubbles and, consequently, intensifies the noise and vibration of the machine. Nevertheless, after some point, the reduction of σ is found to temporarily reduce the noise and vibration emitted, because the vapour phase absorbs part of the sound. At the fully developed cavitation point the total pump head drops and the flow becomes very turbulent, with large separation and cavitating regions, which makes the majority of noise and vibration results to rise.

Intresting conclusions can be drawn regarding the behaviour of the AE_{RMS} and the vibration powerbands that confirm and enrich those obtained from the litarature review. The first deals with the fact that the higher frequencies included in the calculations of the AE_{RMS} and the vibration powerbands results in their maximisation at higher σ values. On the other hand, the results of the vibration powerbands, which integrate lower frequency bands, maximise close to the minimum suction conditions.

The comparisons between the three LU impellers produce interesting conclusions for the effect of geometrical characteristics on the behaviour of powerbands and AE_{RMS}. More specifically, in the impeller No. 1, the use of backward curved blades along with the splitter blades result in milder noise and vibration characteristics. In addition, those geometrical characteristics differentiate the behaviour of the vibration powerband that appear to be similar with that of AE_{RMS}. In the same direction, the use of backward-curved blades for impeller No. 3 is found to affect the point where the noise maximises.

An additional conclusion made from the investigation of the powerband plots is that their patterns (against the Thoma number) remain identical between the two vibration sensors, in contrast to all the other signal processing techniques applied in this section, where the results are dependent on the sensor mounting position. This reveals the decisive effect of the filtering of low frequency mechanical components for the adequate detection of two phase flow development in a hydraulic turbomachine.

The application of the vibration powerband tools is proved to be ineffective towards the prompt detection of cavitation in the closed impeller No. 4, when the pump operates under extremely small flowrates. In such conditions, the hydraulic and the bearing noise, along with the presence of the shroud, mask the noise due to the bubble implosion and prevent its prompt detection. However, further reduction of σ value close to the the total drop head of the pump, increases significantly the vibration level of the pump.

The present study delves into the application of powerband tools and identifies additional disadvantages of this approach. More specifically, the wide range excitations, attempted to be integrated from those tools, are a symptom rather than the actual fault mechanism. The fault mechanism in case of cavitation is the bubble implosion close to the rotating and stationary solid surfaces, and is the same for every pump. On the other hand, the symptom (high frequency excitation) reveals the interaction of the fault mechanism with the pump structural characteristics, and consequently, it varies between various configurations.

Furthermore, the fact that the the vibration powerbands quantify the excitation of high frequency spectrum, introduces additional questions regarding their applicability towards the detection of cavitation. The literature provides several examples (McFadden, 1984b, Prashad, 1985; Saidi, 2014), where mechanical faults at some stage of their evolution seem to excite wide range of high frequencies, up to 20 kHz, in a similar manner with cavitation. From the latter, it can be concluded that for measurements that quantify frequency ranges over the audible frequency range (> 20 kHz), as in the case of AE sensor, the influence of such mechanical faults decreases. One way to distinguish the cavitation among the mechanical faults is to operate the hydraulic turbomachine in lower (or higher) σ values, to study the development of this excitation, either in the frequency spectrum or in a powerband. However, this procedure is not practical when dealing with industrial hydraulic turbomachines and consequently the use of such tools can not provide a clear answer regarding cavitation development.

From a combination of the above conclusions it can be deduced that a reliable cavitation detection tool has to be based on the fault mechanism rather than its symptoms, in order to be of general applicability and practical use. As a consequence, additional effort is needed for a well-rounded characterization of cavitation that will include the identification of the phenomenon signature in time, and its correlation with a discrete or a range of frequencies that will not change in different machines. In this direction, the results presented in Chapter 6, especially those that refer to the kurtosis and to the high frequency vibration spectrum, are not ignored or undervalued. On the contrary, both constitute the basis of the finally applied methodology for cavitation detection, the Spectral Kurtosis (SK), that is introduced in section 2.4.5 and will be thoroughly discussed in the next Chapter 7.

7. The Spectral Kurtosis

7.1 Introduction

This chapter contains the investigation of the application of the Spectral Kurtosis (SK) methodology, in order to calculate the characteristics of the filter, which is applied for the unmasking of cavitation characteristics in the measured signal. In addition, the results of the filtering procedure are demodulated so as to examine the possible low frequency periodicities that may modulate cavitation characteristics. As it is presented in section 1.3.1.4, there are few authors (Bourdon, 1994; Escaler, 2002, 2004) that attempted to use signal's demodulation towards the detection of cavitation phenomena that are developed in reaction hydroturbines. Although their results are promising, the demodulation methods have not attracted particular attention from researchers in the field of cavitation detection in hydraulic turbomachines. To the author's opinion, the reason is the difficulty to efficiently define the characteristics of the filter that is applied to the signal before the demodulation procedure.

In the aforementioned studies, these characteristics are taken from the strongest excitation in the frequency spectra. Nevertheless, this Thesis reveals the difficulty to define those characteristics with the use of the spectrum analysis by illustrating the excitation of a wide range of frequencies (Fig. 6.21, section 6.3). The last observation has been found to apply in a large number of studies also reviewed in this Thesis (Figs. 1.32, 1.33, section 1.3.1.3). As presented is section 2.4.5, the SK methodology has been developed in order to provide the filter's characteristics based on the kurtosis value of the spectrum. The SK method has been found to work decently in the case of bearing faults, which present an impulsive fault mechanism, similar to cavitation. Consequently, this Chapter implements and evaluates the SK method towards the detection of cavitation in the four impellers tested in this Thesis (Fig. 7.1).

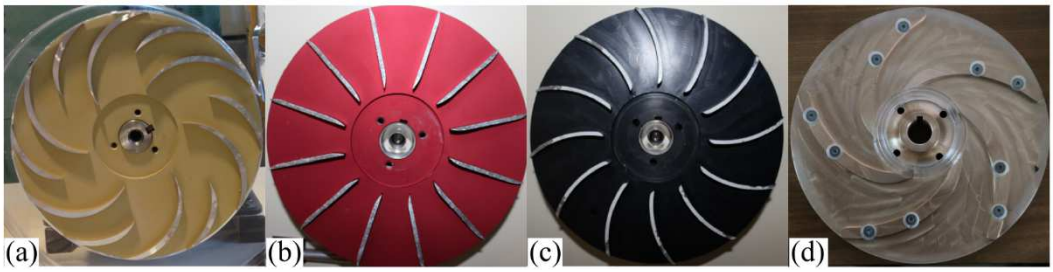

Figure 7.1 a) Impeller No. 1, **b)** No. 2, **c)** No. 3, **d)** No. 4.

Before the application of SK, the selection the decomposition level (DL) value used for the representation of Fast Kurtograms (FK) is justified. The final results are presented at first for the laboratory pump of Lancaster University (LU) and then for the industrial pump of the Laboratory of Hydraulic Turbomachines, at the National Technical Univesity of Athens (NTUA). These results include the presentation of typical FKs under normal and cavitating conditions along with the Maximum Spectral Kurtosis (MSK) value and its corresponding Decomposition Level (DL) as function of Thoma number, σ.

Moreover, the time series (TS) of the filtered signals, $x_f(t)$ and the frequency spectrum (FS) of the envelope, $e_d(f)$ for various operating points (OP) of the pumps are discussed. The study focuses on the initial and intermediate cavitating conditions, where the effective and reliable

detection of two phase flow formation is a challenge. Measurements taken at intense cavitation conditions and pump head collapse OPs are also presented in order to confirm the specific patterns of the filtered results due to bubble implosion in the impellers.

The SK method focuses to the vibration signals, because the acquisition characteristics for the majority of the noise measurements do not provide the access to the raw data time series and due to the fact that their measurement frequency range limits them to include frequencies that may be affected from the presence of other impulsive mechanical faults, such as those discussed in sections 1.2.2.3, 6.3 and 6.4.

7.2 Decomposition level selection

The DL value specifies the discretization of the frequency domain, δf, as it is defined by Eqs. 2.71 and 2.72 (section 2.4.5), where the statistical study of kurtosis is implemented and its maximum value is calculated. In practice, the higher DL value results in increased number of calculations that enlarge the FK extent and band pass filters of narrower range, f_r. In Table 7.1 all the possible filter ranges, δf (Eq. 2.72, section 2.4.5), are provided as a function of the decomposition level for each sampling frequency, f_s, used in the sensors of the present study (Tables 2.4 & 2.9, section 2.5). The f_s=25 kHz refers to both NTUA vibration sensors, while those of f_s=20 kHz and f_s=10 kHz refere to B01_1 and A01 sensor of the LU set up.

Table 7.1 The effect of decomposition level value on δf and f_r.

DL	**$N_{\delta f}$**	**f_s [kHz]**		
		25	***20***	***10***
		δf, f_r [Hz]		
0	2	6250	5000	2500
3	4	3125	2500	1250
4	8	1563	1250	625
5	16	781	625	313
6	32	391	313	156
7	64	195	156	78
8	128	98	78	39
9	256	49	39	20
10	512	24	20	10
11	1024	12	10	5

The appropriate selection of the DL value used for FK representation is made after considering the spectrum characteristics of cavitation phenomenon, made in Fig. 6.21 of section 6.3.1.2. In those plots the wide excitation (resonances) of the frequency spectrum is observed for all the examined cases. This is a conclusion that agrees with the published literature (Neill, 1997; Chudina, 2003a,b, 2009a,b; Cernetič, 2003, 2012; Escaler, 2003, 2004) and depicts the impulsive nature of cavitation. As a result, there is high limit of DL value, over which the range of the calculated digital band pass filter has a very narrow range. For instance, if the implementation of FK results in a MSK value that corresponds to a DL value of 11, according to Table 7.1, the band pass filter should have a range of 5 Hz. It is obvious that in the case of impulsive phenomena, which excite wide frequency ranges (remember also Figs. 1.19b,d, 1.20 & 1.21 of section 1.2.2.3, for bearing faults), a band pass filter with 5 Hz range would be impractical to be used.

Considering the above characteristics of cavitation, along with the proposed values in the literature (Antony, 2006 & 2007b), the high limit for the DL value is set equal to 7 in the present study. This value corresponds to a minimum band pass filter range of 78 Hz (Table 7.1) in case of sensor A01 that has the lowest sampling frequency, f_s=10 kHz.

7.3 Lancaster University pump

The SKT is firstly applied to the pump of the LU test rig (Figs. 7.1a-c), which has two advantages compared to the industrial pump of NTUA (Fig. 7.1d); i) the lack of bearings on the pump's casing results in less mechanical noise sources close to cavitation formation areas, and ii) the Plexiglas casing and the semi-open impellers enable the visualization and monitoring of cavitation inception and development in the entire flow path between the blades. No matter the test rig discussed, the results of the present Chapter include:

i) The MSK value and the corresponding level as function of σ.
ii) The time series (TS) of the filtered signal.
iii) The frequency spectrum (FS) of the envelope.

The time series (TS) of the filtered signal are presented in typical suction conditions (σ) for each flowrate, so as to investigate the cavitation fault signature, if the result of the filtering procedure allows it. The suction conditions correspond to; i) non-cavitating conditions, σ_{BVI}, namely the OP just before the visual inception of the phenomenon, ii) initial cavitating conditions, close to the onset of the phenomenon, (σ_{IN}), and iii) intermediate cavitating conditions, σ_{INT} that lie before the total head drop. The study focuses on the initial and intermediate cavitating conditions, where the efficient and reliable detection of two-phase flow formation is a challenge. In order to reduce the amount of the time series presented, the results at this point are presented by using each sensor alternately. The measurements obtained at σ_{FC} OP, which depict intense cavitating behavior, are only used, in order to provide additional evidence that the suggested methodology can identify efficiently the vapour formation.

Finally, the results of the demodulation procedure are presented in the frequency spectrum (FS) of the vibration envelope. The same suction conditions (σ_{BVI}, σ_{IN}, σ_{INT}) are selected so as to present the FS results and illustrate the effect of cavitation at its early stages of development. In that case, the spectrum allows the simultaneous plotting of the three suction conditions and consequently, the results of all sensors for every flowrate can be provided.

7.3.1 Fast Kurtogram results

The Fast Kurtogram (FK) results are used, in order to reveal the frequency with the most intense non-stationary behavior and, as a result, to effectively select the central frequency and the range of the band pass filter that will be applied to the original signal. This procedure is repeated for all the OPs that constitute the σ-Ψ characteristic curves discussed in Chapter 3 (Fig. 3.9). The results of the Maximum Spectral Kurtosis (MSK - red colour marker) and the Decomposition Level (DL - white colour marker) values as function of σ, for the LU impellers are shown in Figs. 7.2 to 7.4. This kind of representation of the filter's characteristics is selected, in order to illustrate and discuss the effect of cavitation development on those characteristics. On the other hand, the results of the central frequency of the band pass filter are totally random in all the examined cases (impellers No.1-4), and do not form patterns that are worth to discuss. The only comment that could be made is that this randomness confirms the observations made in Fig. 6.21 (section 6.3.1.2) regarding the stochastic behaviour of the excited frequencies and the association of the cavitation phenomenon with other impulse fault mechanisms, such as the bearing faults. The circle and triangle markers of Figs. 7.2-7.4 correspond to sensors B01_1 and A01, respectively. The mounting positions of the vibration sensors are given in Fig. 2.19a (section 2.5.1.1). The blue marker symbolises the onset of cavitation at σ_{VI} OP, where the vapour phase area becomes visible in the impeller area, according to the results of Chapter 3 (Figs. 3.12 to 3.14).

Similarly to the results of high frequency noise and vibration (Figs. 6.25 to 6.27), where the low frequency bands are ignored, the data of the two sensors show very similar behavior, no matter the flowrate and impeller tested. The MSK values (red marker curves) do not exhibit certain trend in the graphs of impeller No. 1 (Fig. 7.2). Although for the lowest flowrate tested (Φ=0.40·Φ_{BEP}) the MSK shows an increase for both sensors at σ_{VI}, and then declines for further

decrease of σ (Fig. 7.2a), its trend remains relatively unchanged for the other three Φ values examined (Fig. 7.2b,c,d).

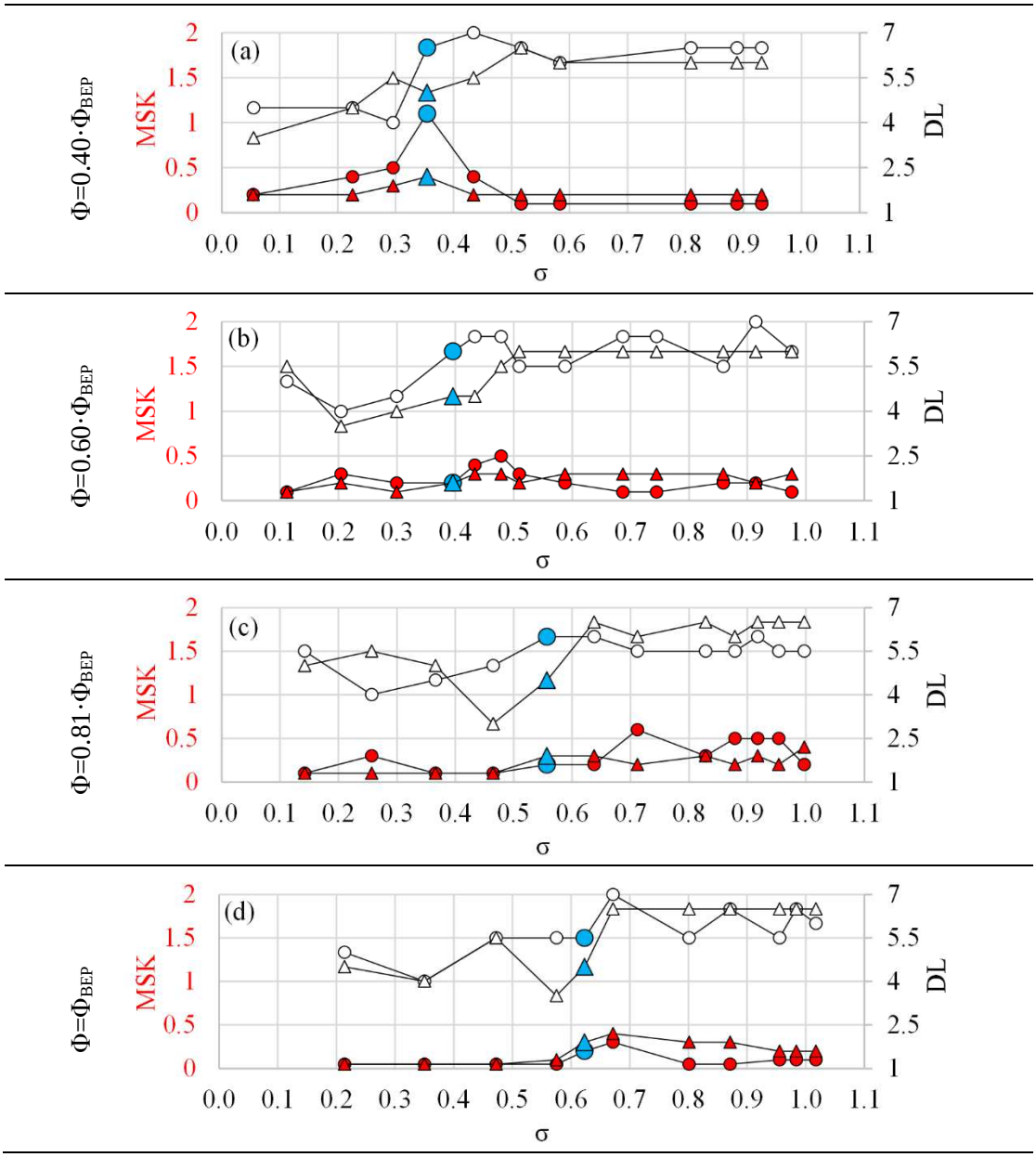

Figure 7.2 MSK value (red color) and its corresponding DL (white color) as a function of σ, for sensor B01_1 (circle marker) and A01 (triangle marker), and for impeller No. 1.

On the contrary, the DL presents a more systematic trend as it is takes values in the range of [6 – 7] under non cavitating conditions, and decreases to [3 – 5] when cavitation develops, and this behavior is identical for all the flowrates and sensors used. This drop of DL value after the development of two-phase flow conditions, is in agreement with the conclusions made in section 6.3.1.2 (Fig. 6.21) regarding the wide range excitations from cavitation, and confirm the selection made in section 7.2 over the DL value.

The results of the MSK and its corresponding DL for impeller No. 2 are shown in Fig. 7.3, and in this case both quantities present interesting behaviour. In contrast to the first impeller, the maximization of MSK value coincides with σ_{VI} for all sensors and flowrates tested, albeit the first steps of its increase already exhibit slightly higher values of $\sigma>\sigma_{VI}$. For smaller σ values, the MSK maximization is followed by a decrease to the level during non-cavitating conditions.

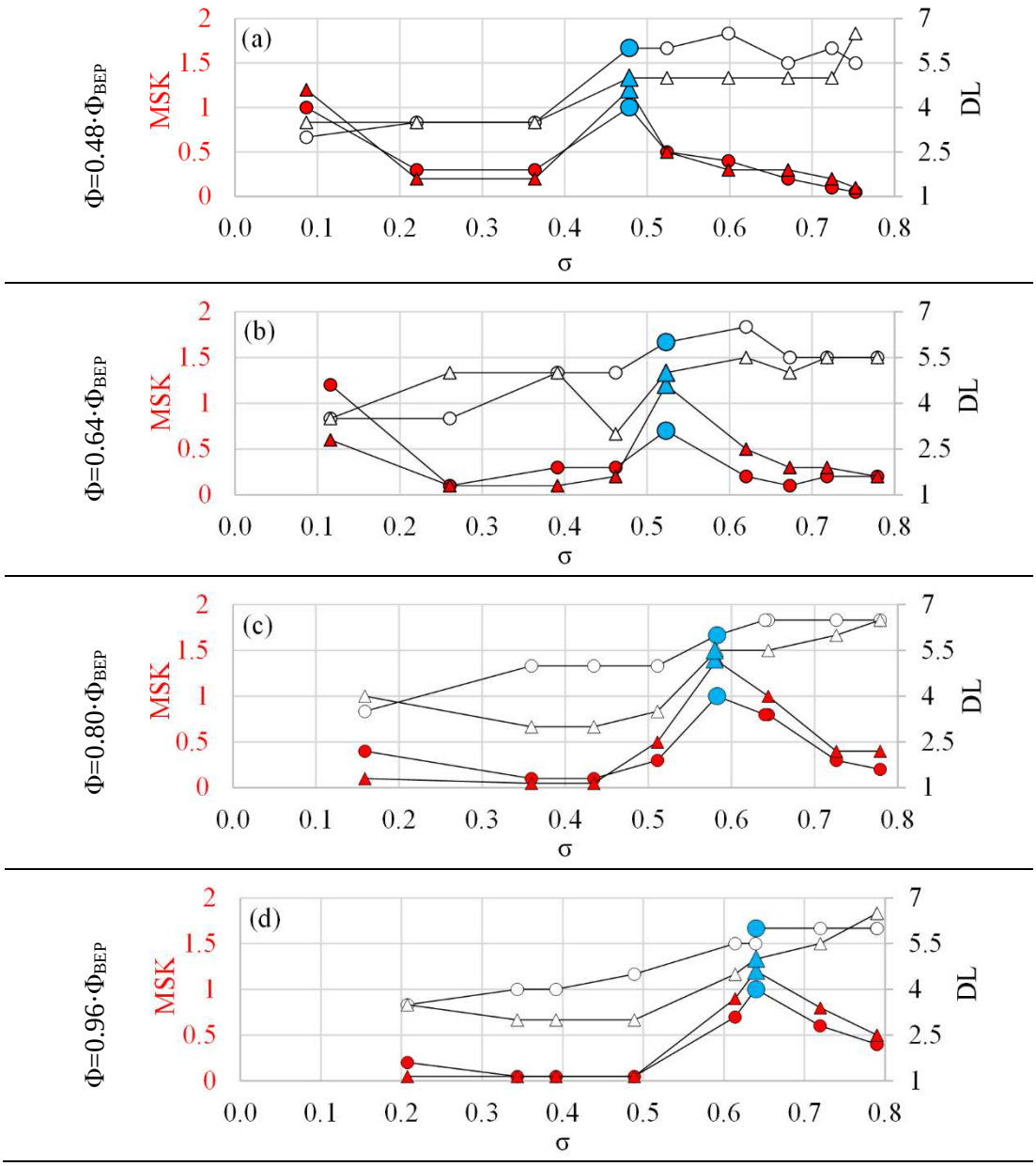

Figure 7.3 MSK value (red color) and its corresponding DL (white color) as a function of σ, for sensor B01_1 (circle marker) and A01 (triangle marker), and for impeller No. 2.

This behaviour is observed for all flowrates, and could be the result of the same mechanism discussed in section 6.3.3.2, regarding the high frequency power trends of noise and vibration results of this Thesis, as well as in some other works (Cernetič, 2008; Gulich, 2008; Brennen, 2011), which damps the pressure waves created from bubble implosion at low σ values. The low MSK values remain relatively unchanged until $\sigma \approx 0.2$ for all flowrates, and rises again at heavy cavitating conditions, for $\sigma < 0.2$.

With respect to the DL behaviour, it behaves as for impeller No. 1, and drops with the appearance of cavitation from [5.5 – 6.5] to [3 – 5] at lower σ values, indicating the use of a wider range for the applied band pass filter. The differences in the band pass filter range as a function of DL value are depicted in the results of Table 7.1, where the range for DL=4 is four times larger than the corresponding range at DL=6.

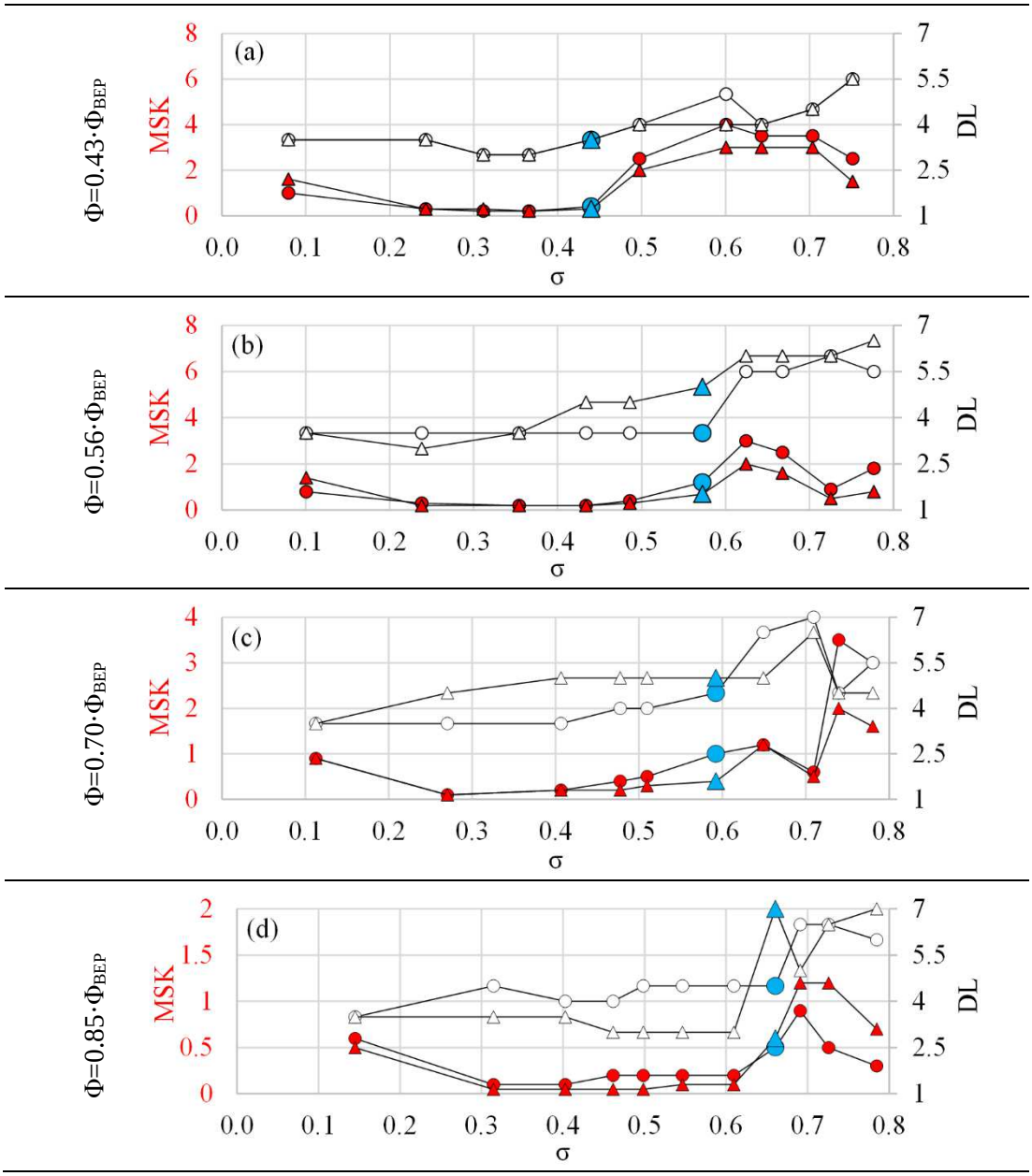

Figure 7.4 MSK value (red color) and its corresponding DL (white color) as a function of σ, for sensor B01_1 (circle marker) and A01 (triangle marker), and for impeller No. 3.

Finally, the FK results for impeller No. 3 are given in Fig. 7.4. For this impeller, the MSK starts from remarkably higher values for $\sigma>\sigma_{VI}$, which are then drastically reduced after the onset and during the development of cavitation, until the σ_{FC} OP, where they rise again to about 1, as in the impeller No. 2 (Fig. 7.3). These differentiations are related with those presented in Figs. 6.3e (section 6.2.1), 6.17c (section 6.2.2) and 6.25c (section 6.3.3.2) for the same impeller, and it is attempted to be explained by using the results of the frequency spectrum of the envelope and the time domain of the filtered signal, in the forthcoming section.

On the other hand, the DL results follow the consistent trend of the other impellers, as its value decreases with the appearance of vapour bubbles. More specifically, for $\Phi=0.56\cdot\Phi_{BEP}$ (Fig. 7.4b) its value declines exactly at σ_{VI} for both sensors, and the same happens for B01_1 sensor at $\Phi=0.70\cdot\Phi_{BEP}$ and $\Phi=0.85\cdot\Phi_{BEP}$ (Fig. 7.4c,d). For the rest cases, this decrease slightly precedes visual inception, like in case of both sensors of $\Phi=0.43\cdot\Phi_{BEP}$ (Fig. 7.4a), and of A01 sensor for $\Phi=0.70\cdot\Phi_{BEP}$ (Fig. 7.4c) and $\Phi=0.85\cdot\Phi_{BEP}$ (Fig. 7.4d).

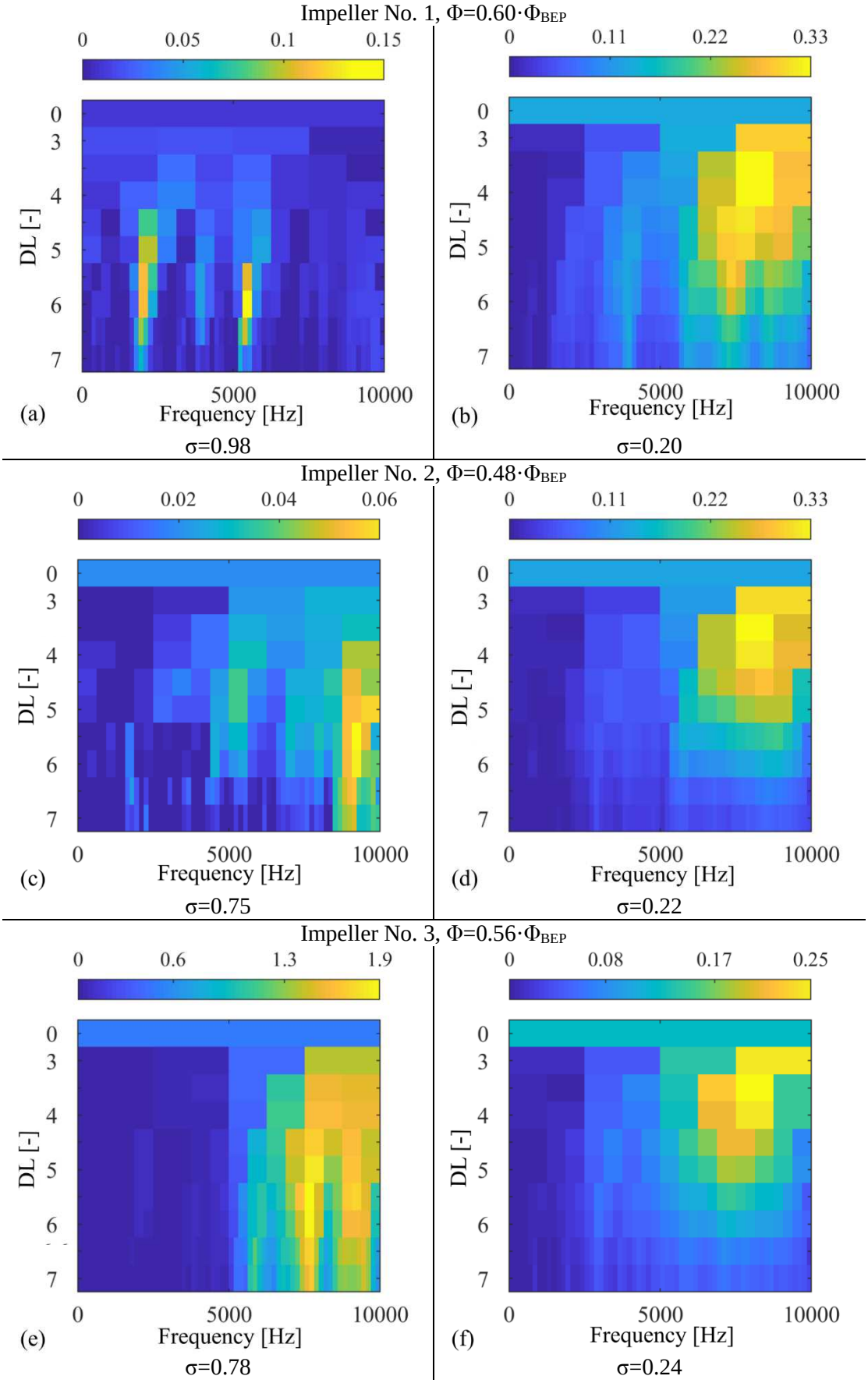

Figure 7.5 Comparison of FKs between normal (left) and cavitating (right) conditions for sensor B01_1.

In order to provide an interpretation of the FKs under normal and cavitating conditions, their results are presented in Figs. 7.5 and 7.6, for sensors B01_1 and A01, respectively. The left FK charts correspond to normal, and the right ones to cavitating flow conditions, for which the systematic shifting to lower DLs can be observed in all cases. This consistent pattern of the DL values is obtained for all flowrates and hence it could be related with cavitation. However, since other faults that exhibit impulsive behaviour, such as those related with bearings, are expected to excite wide ranges of the spectrum (see Fig. 1.25d, 1.26b & 1.27), leads to the conclusion that such a drop of DL value occurs also during their development (Antoni, 2007b; Zhang X, 2015; Li, 2016). Consequently, the decrease of DL value could be a strong sign that an impulsive fault develops in the machine (bearing or cavitation related). Nevetheless, in order to identify the exact type of fault further analysis on the signal is required.

The aforementioned DL shifting is accompanied with a wider range of frequency-DL pairs with increased spectral kurtosis value. This behavior is mainly depicted in the FKs of impellers No. 1 (Figs. 7.5a,b & 7.6a,b) and No. 2 (Figs. 7.5c,d & 7.6c,d), where a relatively narrow area of normal conditions enlarges significantly after vapour formation.

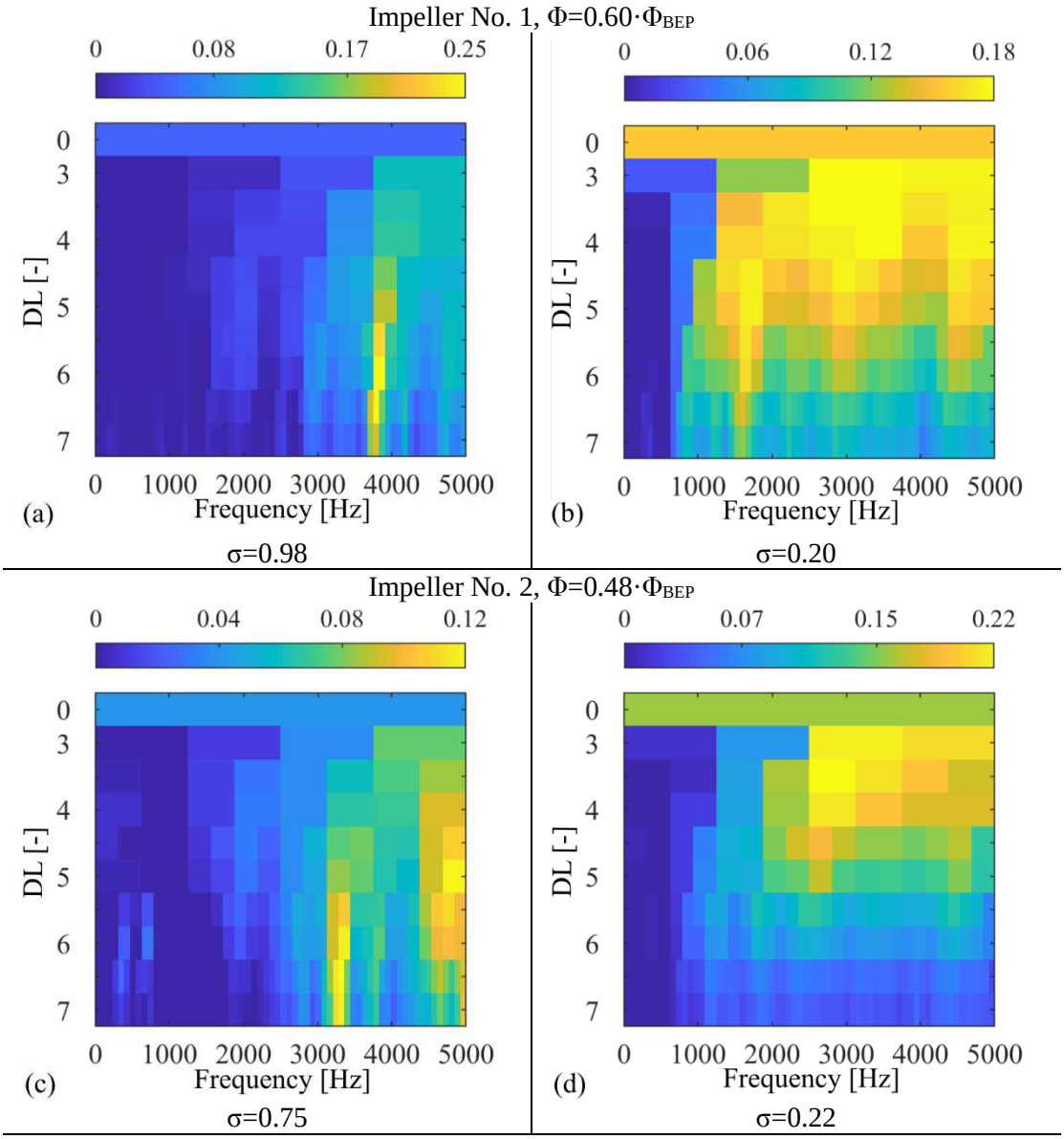

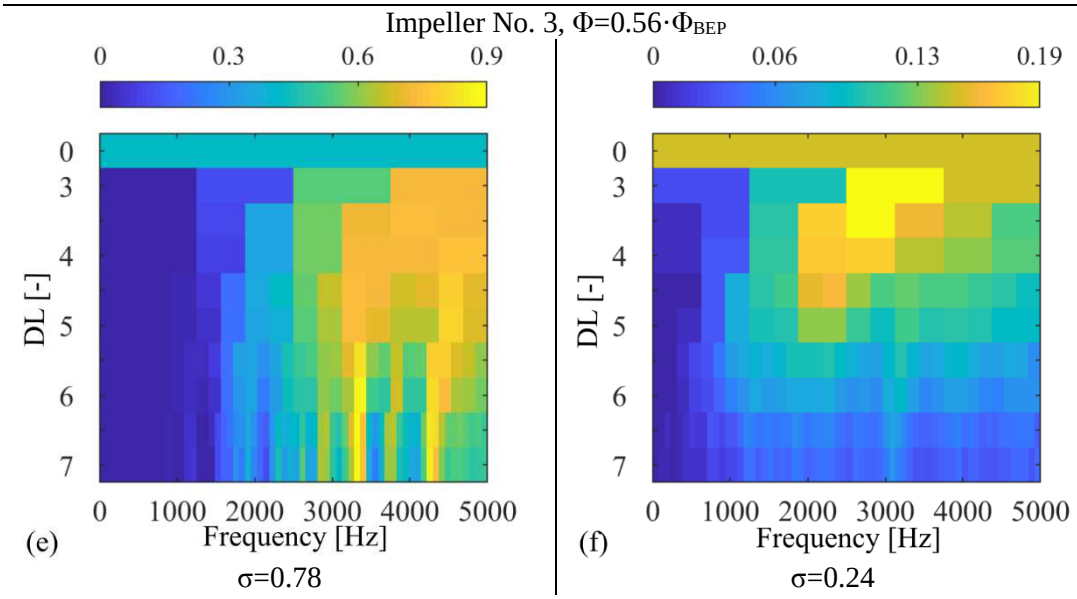

Figure 7.6 Comparison of FKs between normal (left) and cavitating (right) conditions for sensor A01.

This trend is related with the already discussed cavitation symptom, which deals with the excitation of wide resonances, as depicted in Fig. 6.21 (section 6.3.1.2). These differences weaken in the results of impeller No. 3 (Figs. 7.5e,f & 7.6e,f), where the areas of high kurtosis cover a large frequency range under both normal and cavitating conditions.

The changes in the frequency domain and in the value of central filter frequency, f_c are not commented, since they do not present a systematic pattern. This is also depicted, even in the plots of the few cases presented in Figs. 7.5 and 7.6, where the frequency value remains constant for the impeller No. 3 of B01_1 and A01 sensors (Figs. 7.5e→f, 7.6c→d and 7.6e→f), or increases (Figs. 7.5a→b) or decreases (Figs. 7.5c→d, 7.6a→b) when passing to cavitating conditions.

From the above Figs.7.5 and 7.6, the pairs dyads (f_c, δf) of the MSK value appearance provide the band pass filter's central frequency and range, which can be used to filter the original signal, so as to isolate the cause of non-gaussian behavior. For example, in the case of Fig. 7.6d the values for the filter's f_c=2.8 kHz and δf=f_r=0.63 kHz. The results the filtered signals in the time domain and the envelope's frequency spectrum are given in sections 7.3.2 and 7.3.3, respectively.

7.3.2 The filtered time series (TS)

The filters obtained from the application of the FK tool are applied in the raw measured time series. These are the same time series used from the FK tool for the calculation of the filter's characteristics. As it is shown in section 7.3.1, every operating point (OP) has a different filter, and this depicts the dynamic nature of the cavitation mechanism. The filtering procedure is evaluated from the results of the time series and those of the envelope's frequency spectrum. The reason for the presentation of the filtered results in the time domain is to examine its characteristics and investigate the possibility to segregate cavitation from other possible faults.

The filtered time series (TS), for the three Lancaster University (LU) impellers, are presented in Figs. 7.7 to 7.9, during cavitating conditions. The TS include also the results during non-cavitating conditions at σ_{BVI}, only for the lowest flowrate, so as to compare it with the corresponding TS under cavitating conditions. The plots at σ_{BVI} represent all the filtered time series under normal conditions, no matter the flowrate examined. The timespan, δt, of the filtered series is 0.06 sec and equals to ~2·RP. Consequently, the passing of each blade is included two times in the timespan.

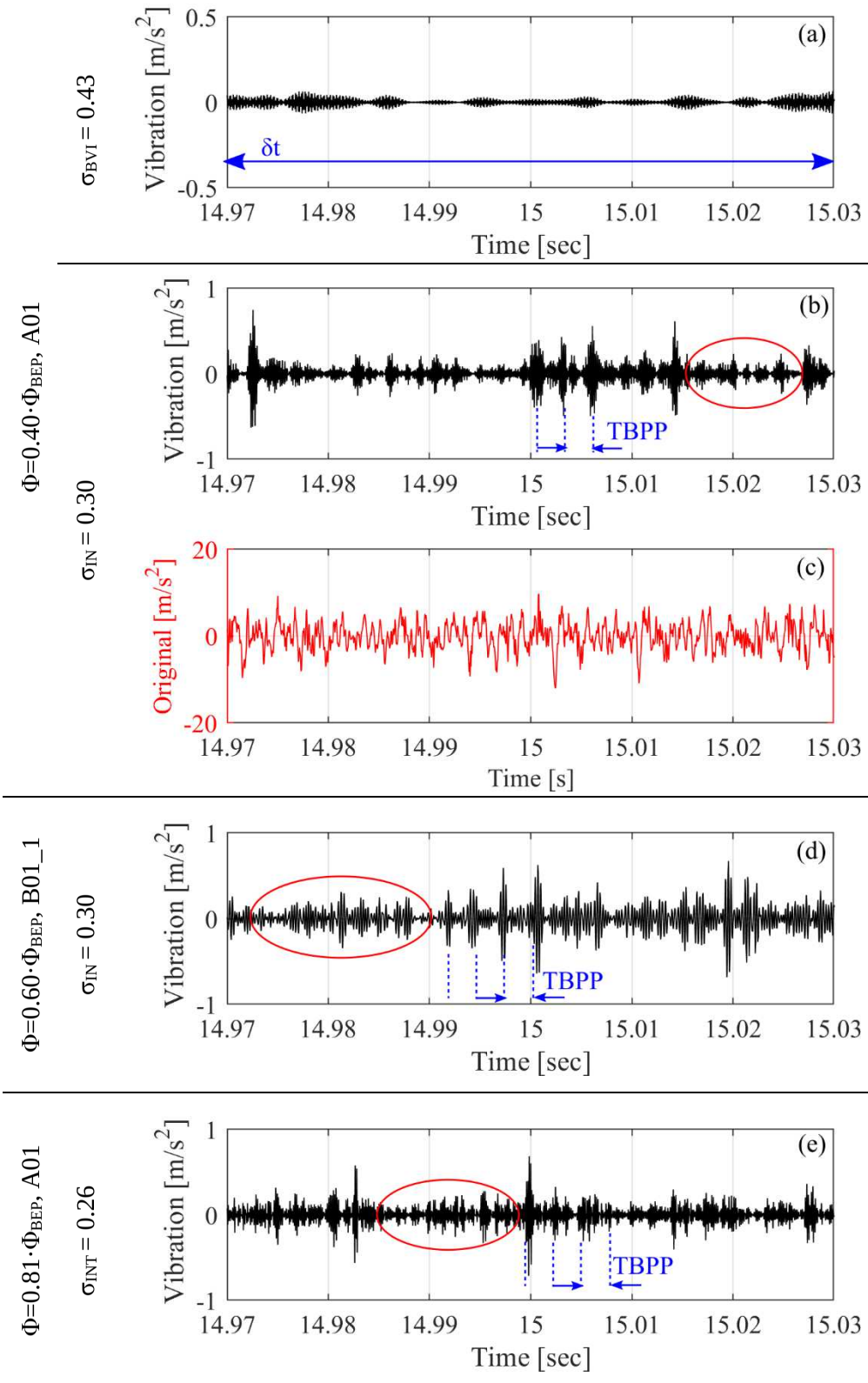
σBVI = 0.43
Vibration [m/s2]
(a)
δt
Time [sec]
Φ=0.40·ΦBEP, A01
σIN = 0.30
(b)
TBPP
(c)
Original [m/s2]
Time [s]
Φ=0.60·ΦBEP, B01_1
σIN = 0.30
(d)
TBPP
Time [sec]
Φ=0.81·ΦBEP, A01
σINT = 0.26
(e)
TBPP
Time [sec]

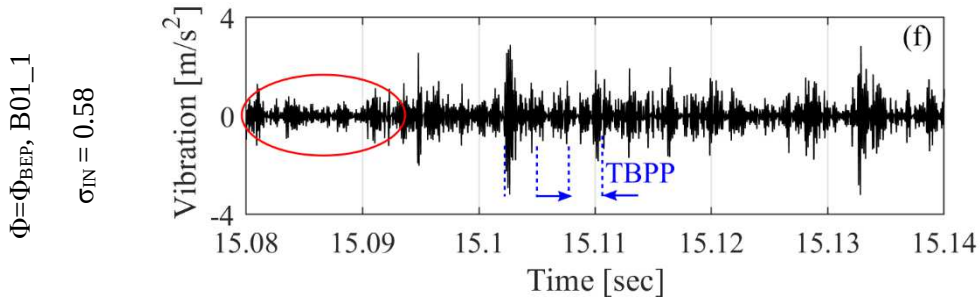

Figure 7.7 Filtered **(a,b,d,e,f)** and original **(c)** time series during: non-cavitating conditions **(a)** and cavitating conditions **(b,c,d,e,f)** for impeller No. 1.

The results of Figs. 7.7a and 7.8a depict the filtered signal when the pump operates under non-cavitation conditions. These signals take the minimum amplitude value compared to cavitating conditions (Figs. 7.7b-f & 7.8b-e) and they do not present distinctive characteristics. In practice, at such conditions the application of the filter made from the FK tool fails to reveal a particular pattern in the filtered signal, since for $\sigma=\sigma_{BVI}$ the machine is expected to operate under faultless conditions.

The first significant observation regarding the formations of the filtered signal is that the passing to cavitating conditions changes unquestionably the pattern of the filtered vibration time series, for impellers No. 1 (Figs. 7.7b,d-f) and No. 2 (Fig. 7.8b-e). The application of band pass filter with f_c and f_r calculated from the FK, reveals the existence of clear strikes in the filtered signal.

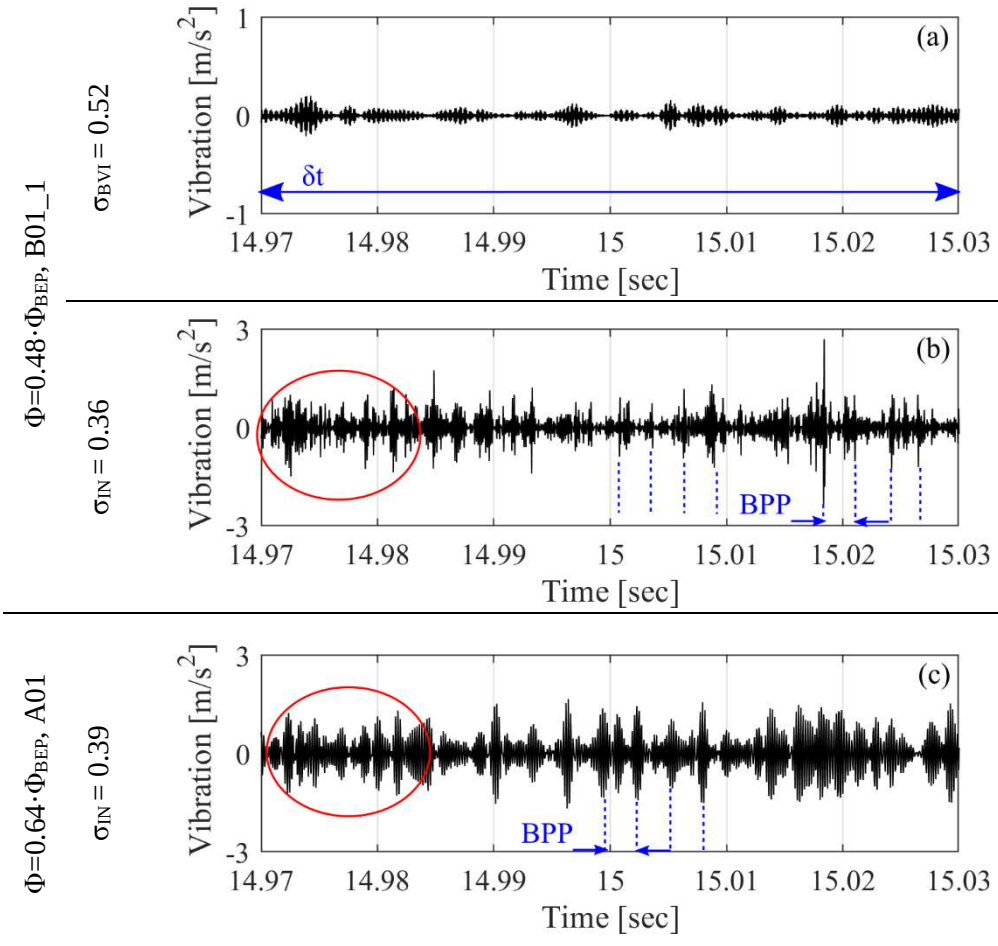

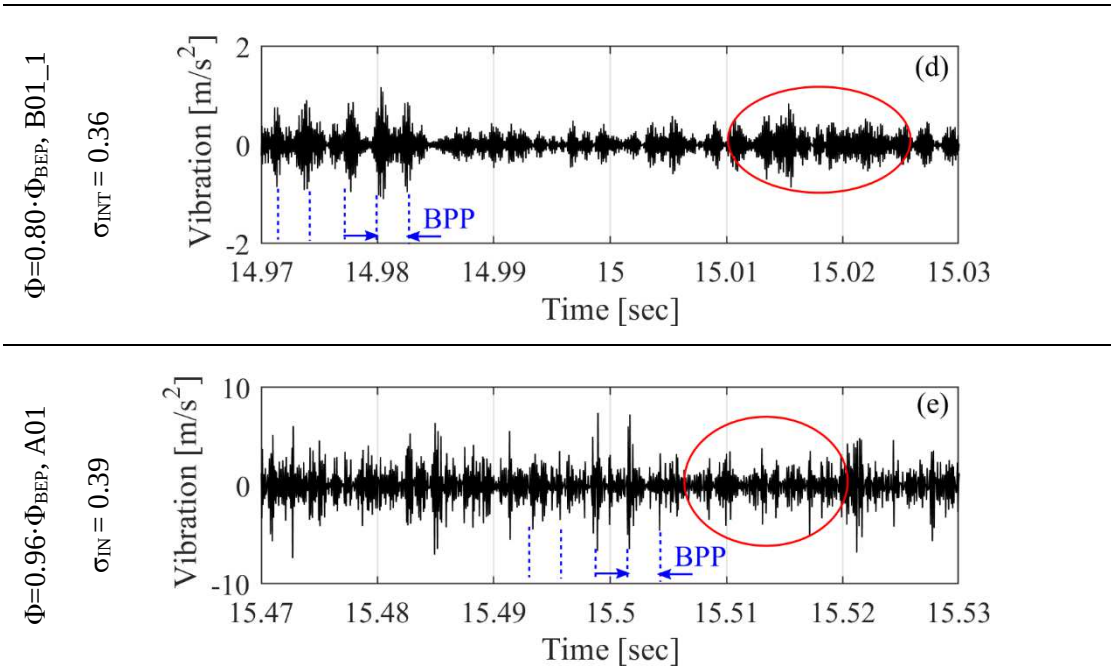

Figure 7.8 Filtered time series during: **a)** non-cavitating conditions, **b**,**c**,**d**,**e)** early stages of cavitation development for impeller No. 2.

The comparison of the filtered signal of Fig. 7.7b with its corresponding original time series, presented in Fig. 7.7c (red colour), confirms the successful application of the filter, since the impulses are not observable in the raw measured vibration data. This observation is of paramount importance, since it reveals the impulsive pattern of cavitation mechanism that is masked in the original raw measured signal from the various other noises of the pump. The decrease of the amplitude after filtering of the signal, is justified considering the significant amount of noise and vibration sources removed from the band pass filter.

Similar conclusions are drawn also for impeller No. 3, since the development of cavitation at $\sigma \leq \sigma_{IN}$ presented in Figs. 7.9c-f, creates similar impulses with those discussed for impellers No. 1,2. Nevertheless, impeller No. 3 is discussed separately, because under σ_{BVI} conditions (Fig. 7.9b), where the vapour bubbles have not been visually observable, the filtered vibration signal contains also strikes of strong amplitude. From the results of Fig. 7.9b, it can be concluded that the sensor located on impeller No. 3 identify vapour bubble implosion even at the very early stages of cavitation development, before their visual inception. In order to present results that correspond to non-cavitating conditions for impeller No. 3, the filtered time series under maximum suction conditions (σ) are presented in Fig. 7.9a. Here, it is clear that the signal does not contain impulses and is very similar with the filtered signals presented in Figs. 7.7a, 7.8a.

The amplitudes of the filtered signals of Figs. 7.7b,d-f, 7.8b-e, 7.9b-f, do not present a clear dependence on the flowrate. The signals are formed by two main parts: one with low amplitude between the impulses (~0.1 $m \cdot s^{-2}$), and one that includes the impulses' amplitudes that range from [0.4 – 3], [1.5 – 9] and [3 – 15], for the impellers No. 1, 2, 3, respectively. The largest values for the impellers No. 1 and 2 are obtained during the testing of the highest flowrate (Figs. 7.10f & 7.11e), while these of impeller No. 3 are taken for the minimum flowrate.

One additional observation regarding the TS presented in the filtered signals of Figs. 7.7-7.9, is that the area where the strikes are formed, consists from random and periodic impulses. The latter follow mainly the blade passing frequency (BPF) of the impeller, and they are highlighted with the use of blue broken lines in the plots of Figs. 7.7-7.9. On the other hand, typical impulses that are aperiodic are featured with red ellipses. This behaviour of the filtered signal is the result of the distortion introduced by random noise sources and the filtering

process, which is attempted to be overcome with the enveloping of the filtered signals that is discussed in the next section 7.3.3.

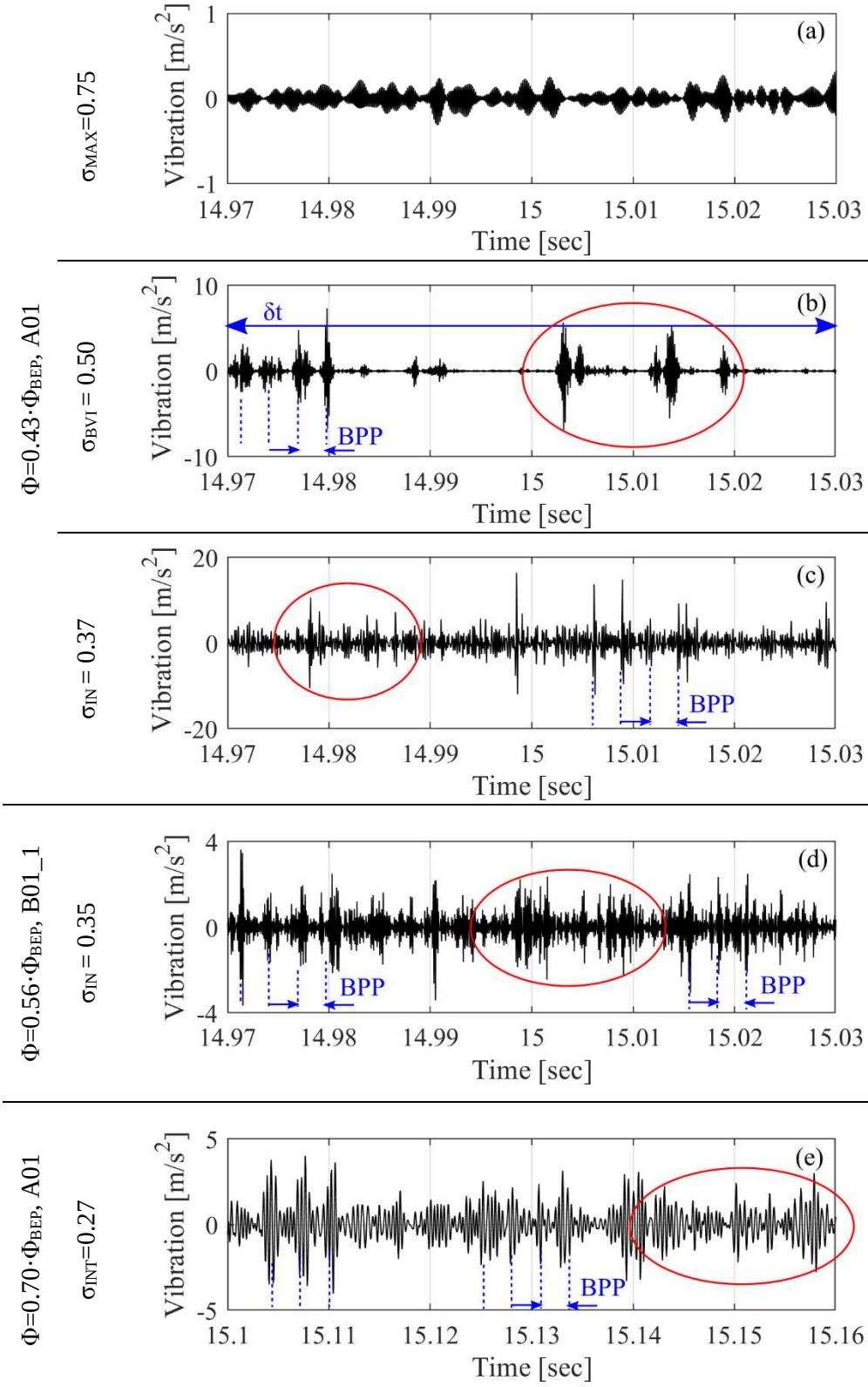

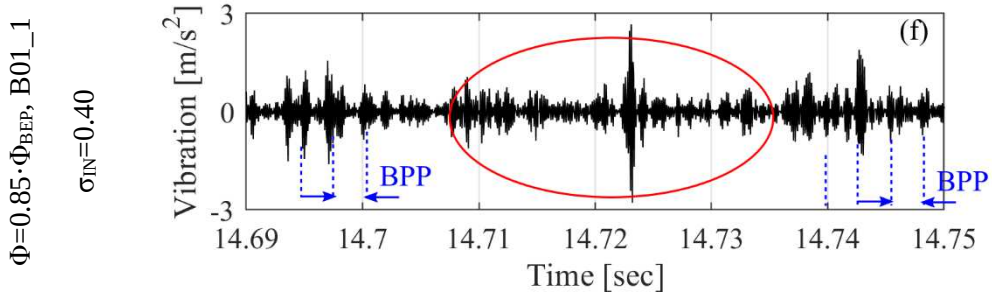

Figure 7.9 Filtered time series during: **a)** σ_{MAX}, **b)** σ_{BVI}, and **c,d,e,f)** early stages of cavitation development for impeller No. 3.

The correlation of the aforementioned impulses with cavitation phenomenon is further validated by studying the TS at even lower σ, such as at σ_{FC} (Fig. 7.10). At such operating conditions the cavitation area is expanded and covers large part of the flow path between the blades, as it is depicted in Figs. 3.12-3.14 (section 3.3.2) and dominates the vibration signal. In the plots of Fig. 7.10, the periodic with the blade passing frequency and, simultaneously, the impulsive behavior of TS can be clearly observed.

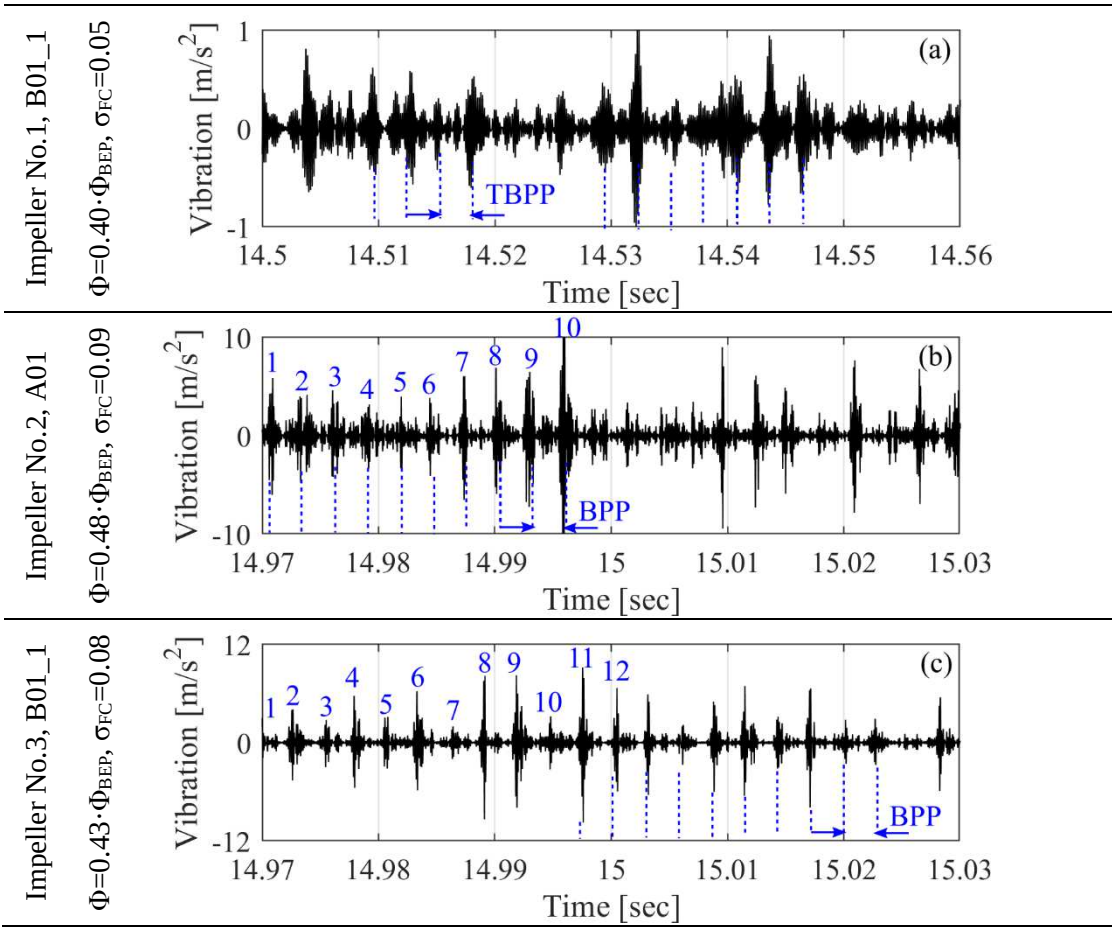

Figure 7.10 Filtered time series at σ_{FC} for impellers: **a)** No. 1, **b)** No. 2, **c)** No. 3.

In addition, the strikes of Fig. 7.10 are clearly continuous relative to those presented in Figs. 7.7-7.9, under initial and intermediate cavitating conditions. Especially for the impellers No. 2 and 3 (Figs 7.10b,c), at the half time span of the presented δt, the illustration of each of the 12 blades' contribution is highlighted. The impulsive shape of the strikes of these plots is so clear that resembles the shape of the filtered vibration signal, presented in Figs. 1.24b of section

1.2.2.3, which corresponds to bearings suffering from an outer race fault (Sawalhi, 2004; Antoni & Randall, 2006). In order to be able to discriminate the bearing and the cavitation impulsive faults, the use of the periodicity of the impulses is proposed, since the fundamental defect frequencies of the bearings follow Eqs. 1.9-1.12 (section 1.2.2.3), while those of cavitation follow the blade passing frequency. However, as it is shown in the impulses of Figs. 7.7-7.9, especially during the initial stages of cavitation development, the BPF periodicity is not always so clear due to the distortion created from the random noise sources and the filtering process. For this reason additional processing is done on the filtered signal with the calculation of the envelope's frequency spectrum so as to overcome those difficulties of the filtered time domain.

7.3.3 The frequency spectrum (FS) of the envelope

The frequency spectrum (FS) of the envelope from the LU impellers No. 1 to 3 is calculated from Eq. 2.69 and is presented in Figs. 7.11 to 7.13, for three different σ values and four flowrates. The green colour corresponds to non-cavitating conditions (σ_{BVI}), the red to initial cavitating conditions (σ_{IN}) and the black to intermediate cavitating conditions (σ_{INT}). These plots include the spectra of both accelerometers, A01 and B01_1, used in the cavitation tests.

The results of the FS demonstrate the decent applicability of the digital band pass filter, achieved after the calculation of MSK value in the FK and the decomposition of the filtered signal. More specifically, no matter the impeller, the sensor, and the flowrate examined (Figs. 7.11 to 7.13), the FS of the envelope exhibits significant differences when comparing non-cavitating with cavitating conditions. These differences are systematically related with the appearance of strong BPF (impellers No. 2 & 3, Figs. 7.12, 7.13) or TBPF (impeller No. 1, Fig. 7.11) components, when the pump operates under initial (σ_{IN}) and intermediate (σ_{INT}) two-phase flow conditions. As it is stated in section 2.5.1, the TBPF for impeller No. 1 acts as BPF that includes the effect of the splitter blades passing frequency.

These observations are critical, since not only differentiate the envelope's characteristics after the cavitation development, but also associate them with the BPF of the impeller and further confirm the results of the filtered signal analysed in section 7.3.2. The latter characteristics of the envelope confirm the observations made on the filtered signals (section 7.3.2). However, their clear depiction in the envelope's frequency spectrum makes them utilizable in case of a system that automatically aims to detect cavitation development.

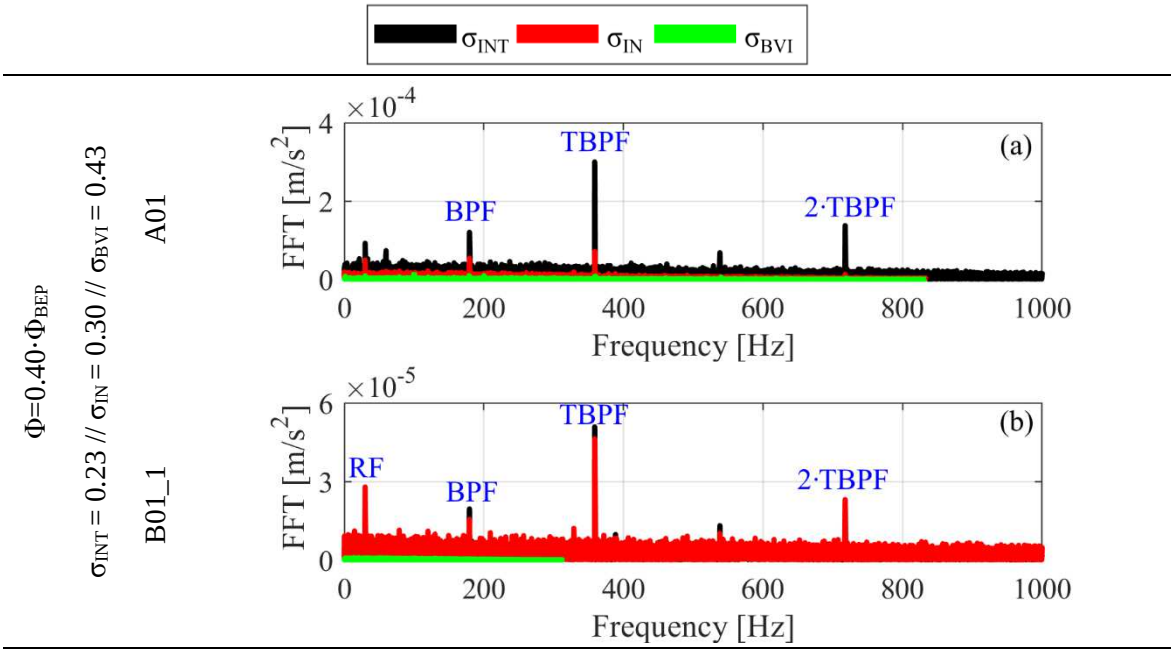

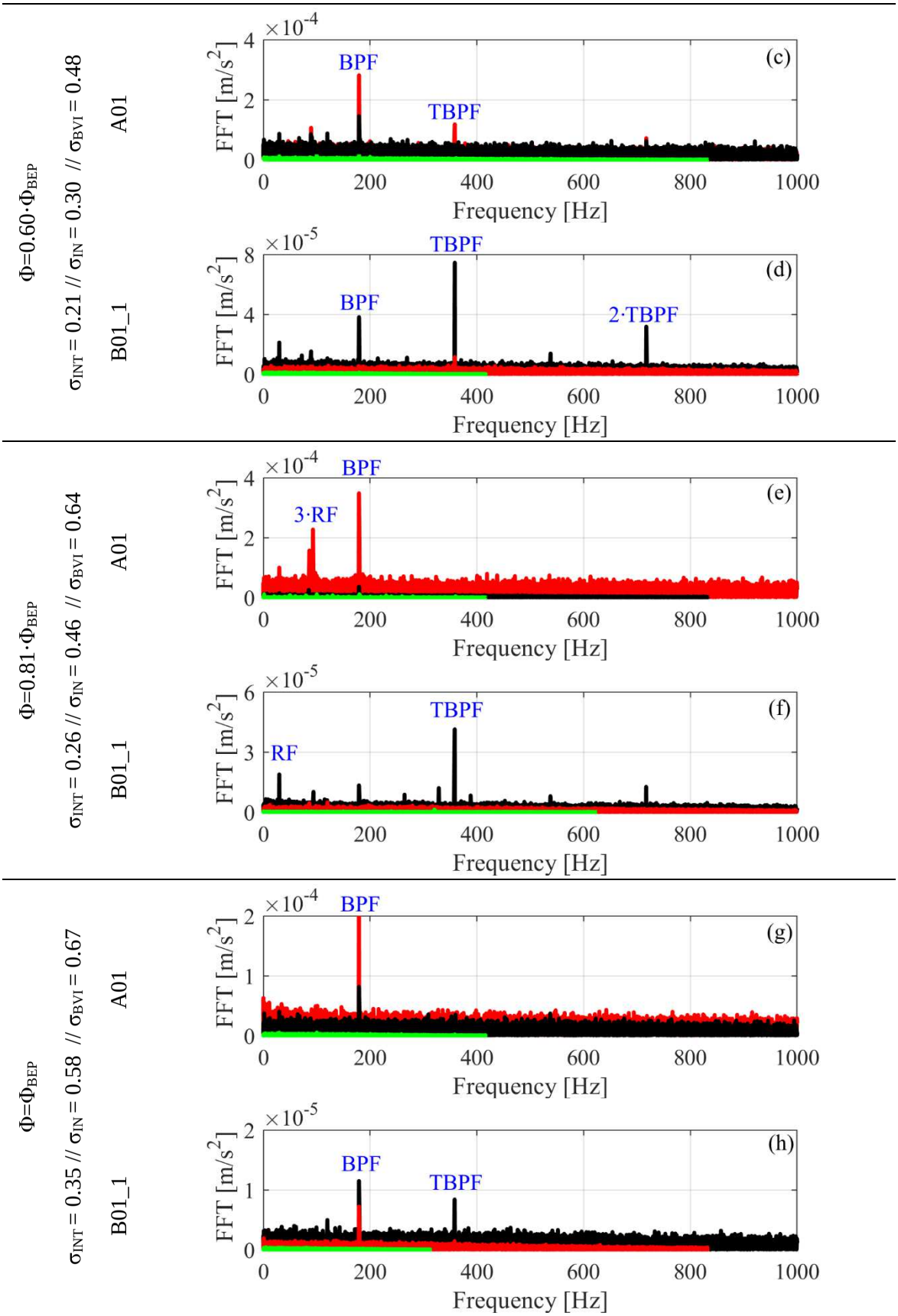

Figure 7.11 Frequency domain of the envelope of the vibration signal of both accelerometers of impeller No. 1.

The only exception with respect to the general trend of FS, is the minimum flowrate of impeller No. 3, for which a slight peak at BPF is also observed at σ_{BVI}, as it is highlighted for both sensors in the corresponding plots of Figs.7.13a,b. This peculiar behaviour has been already discussed and explained in the previous section, with the use of the filtered time series of Fig. 7.9.

The BPF modulation resembles the envelope characteristics, presented from Escaler et al. (2002, 2004) during the testing of reaction hydroturbines (see Figs. 1.38 and 1.39). More specifically, in these studies the vortex rope cavitation in the draft tube is associated with the 0.27·RF discrete frequency component, while the cavitation in the runner have been associated with the blade and guide vane passing frequencies. However, in these cases the characteristics of the filters are taken from the examination of the measured signal's spectrum, an approach that has been proved to be complicated for a large number of cases (Fig. 6.21, section 6.3 & Figs. 1.32, 1.33, section 1.3.1.3). The successful implementation of SK method with the FK tool overcomes the aforementioned difficulties and achieves to define the filter's characteristics efficiently, in cases where it would be impossible to define them otherwise.

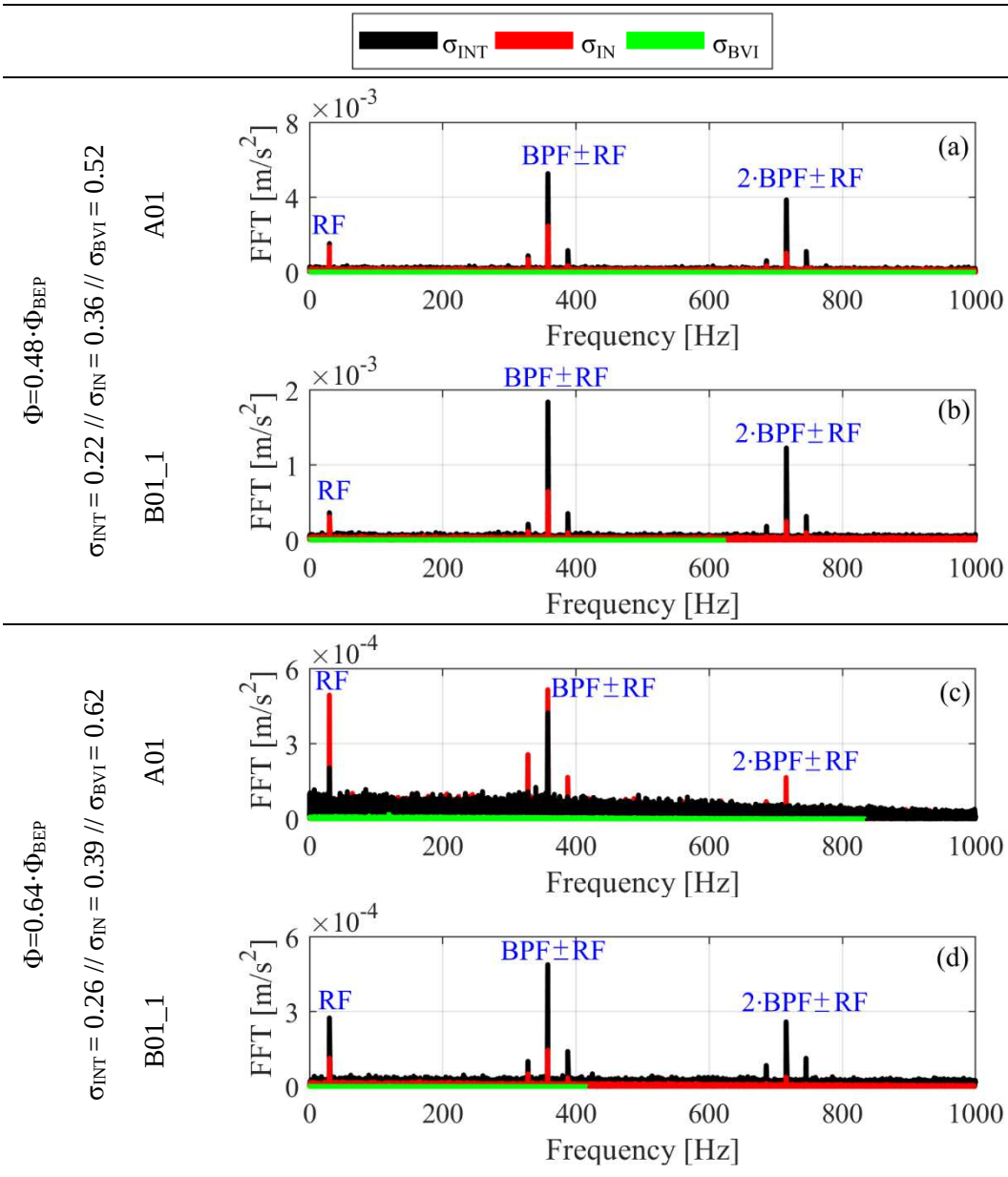

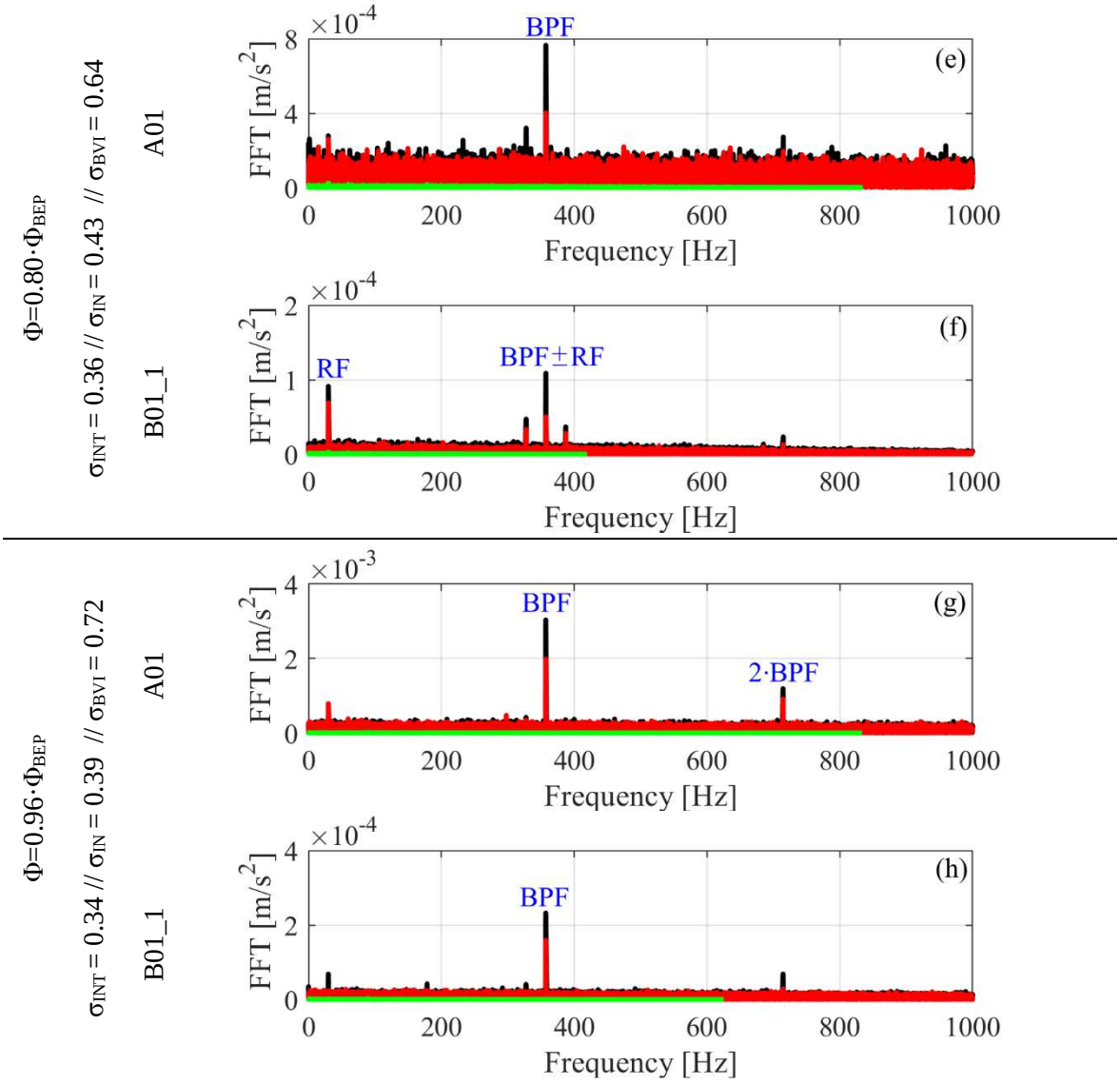

Figure 7.12 Frequency domain of the envelope of the vibration signal of both accelerometers of impeller No. 2.

The comparison of the amplitudes of the same sensor between the different impellers, depicts a rise of vibration intensity, from the lowest values of impeller No. 1 [$10^{-5} – 4 \cdot 10^{-4}$], and intermediate values of impeller No.2 [$10^{-4} – 8 \cdot 10^{-3}$], to the maximum values of impeller No. 3 [$2 \cdot 10^{-4} – 2 \cdot 10^{-2}$]. Therefore, this is the result of the geometric differences of the three impelleres. More specifically, the amplitutes minimise for impeller No. 1 due to: i) the use of splitter blades that increases the cross section area of the flow path between the blades and, consequently, reduces the flow velocity at the impeller inlet, and ii) the smaller blade inlet angle that reduces the inlet flow shock losses.

A decrease in BPF and TBPF vibration levels is observed in the majority of the cases examined, as the flow rate increases. This is because the flow conditions are improved close to the BEP flowrate, as well as because the σ_{INT} takes larger values for higher compared to lower flow rates, as can be seen in Figs. 7.11 to 7.13.

Furthermore, the discrete amplitudes for the same suction conditions increase for sensor A01 and follow the trend of the raw signal amplitude presented in the time series of Fig. 6.3 (section 6.2.1). In the same figure (Fig. 6.3) the values of A01 sensor are higher compared to those of B01_1, a trend that also appears in the differences between the FFT amplitudes of the two sensors in the results of Fig. 7.7 to 7.9. These differences reach up to one order of magnitude, and they are clearer for impellers No. 1, 3 compared to those of impeller No. 2.

A second harmonic appears for the majority of the cases examined, especially for impellers No. 2 and 3, which could be associated with the stronger characteristics of cavitation in these pumps, due to the aforementioned reasons. In addition, for the majority of the spectra of all impellers, a weaker RF component is observed that highlights the relation of the phenomenon with the rotational periodicity. Another observation is that the peaks for σ_{INT} (black line) are not always higher than those of σ_{IN} (red line). This can be related with the conclusions made in Chapter 6, regarding the noise reduction during intermediate stages of cavitation development.

To sum up, the appearance of the passing frequency of the impeller blades is clear after the inception of cavitation. This behaviour is observed in the filtered time series of section 7.3.2 and is further confirmed after their demodulation. Therefore, the identification of the impulses in the filtered signal, which are modulated from the blade passing frequency can be used to detect cavitation from the initial stages of its development, but also they highlight the physical mechanism of the fault, which is the implosion of the vapour bubbles. More specifically, the bubbles are formed at the suction side of the impeller's blade (Fig. 3.12-3.14, section 3.3.2) and their implosion is followed by the creation of shock pressure waves. The waves hit the neighbouring solid surfaces, which for the impeller are the rotating blades. The latter rotate and due to the machine's non-uniformities, create blade passing frequency noise (section 1.3.1.1) that modulates the shock pressure waves. Consequently, the raw vibration signal measured on the solid boundaries of the pump includes the above information, along with additional noise from the pump-motor system. The application of the procedure described in this chapter, achieves the unmasking of the noise sources and reveals the interaction of cavitation with the rotation of the blades.

The combination of the systematic characteristics in the filtered signal and the spectrum of the envelope with the physical meaning of the fault mechanism forms a unique detection criterion. To our knowledge, there have not been reported any fault mechanisms related with centrifugal pumps and reaction hydroturbines that excite an impulsive, BPP periodic behaviour. In the published literature, there are mechanisms (rotor-stator interaction) related with a BPP periodic behaviour, discussed in detail in section 1.3.1.1, which take sinusoidal form but they could not be impulsive (Barrio, 2008; Yao, 2011). On the other hand, in the case of faulty bearings the pattern of fault mechanism is strongly impulsive (Antoni & Randall, 2006; Randall, 2007), however its periodicity does not follow BPP, but the kinematic bearing frequencies (see section 1.3.2.3).

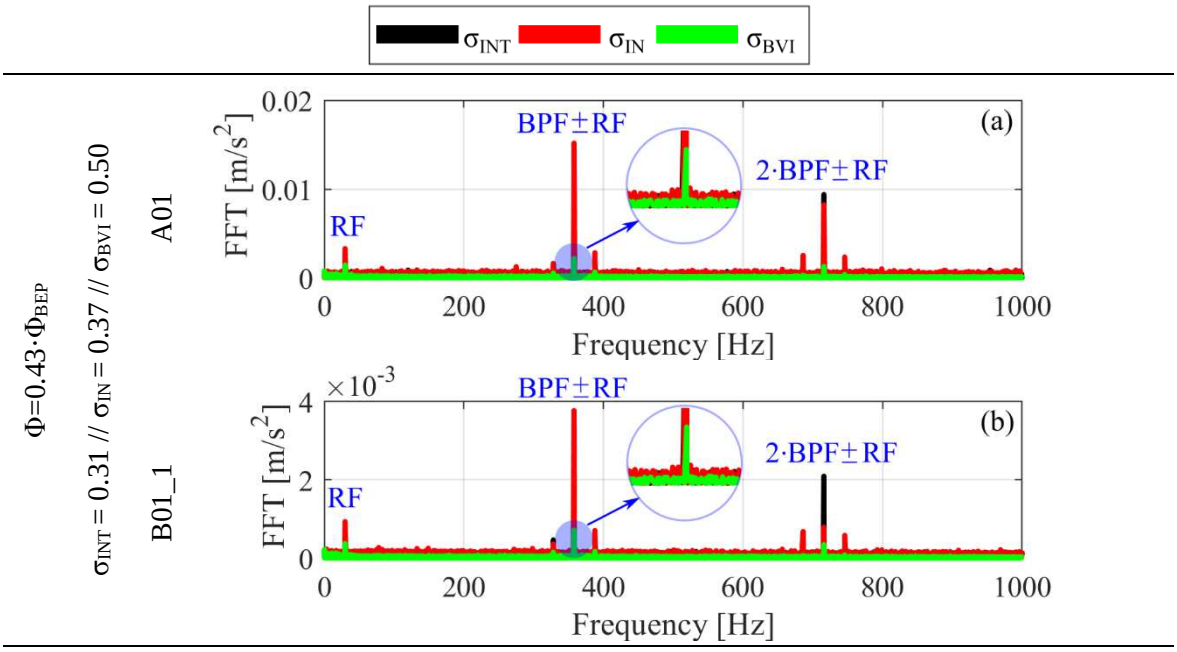

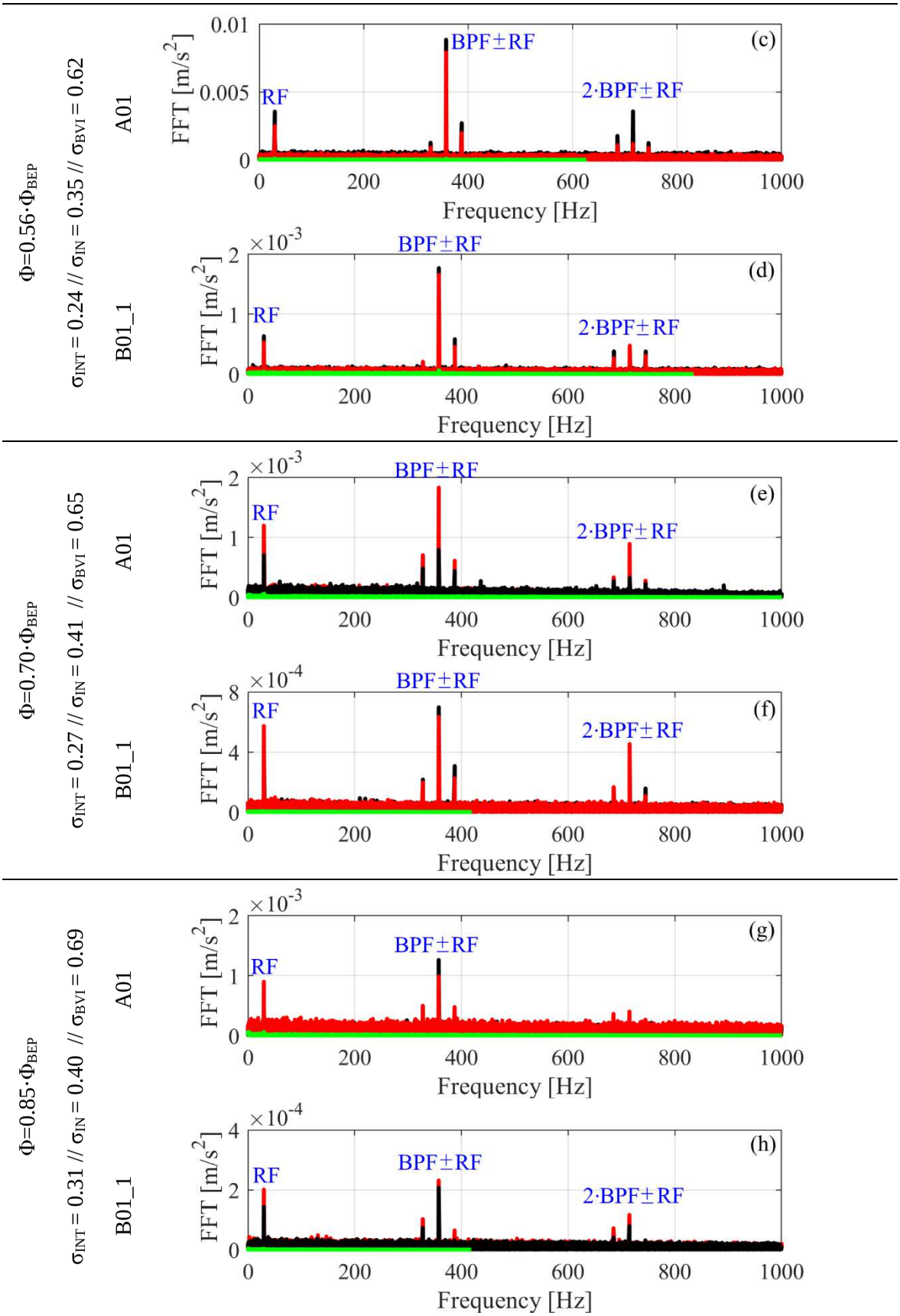

Figure 7.13 Frequency domain of the envelope of the vibration signal of both accelerometers of impeller No. 3.

7.4 NTUA pump

The results of the previous section are very important, because they link the results of the envelope's frequency spectrum with those of the filtered time series and confirm the imprint of vibration induced from cavitation appearance. Those encouraging results derived in the LU test rig indicate that the SKT method can constitute an efficient tool for cavitation detection in centrifugal pumps. Thus, the next step is to examine the applicability of this tool in an industrial centrifugal pump with a closed impeller, impeller No. 4.

7.4.1 Fast Kurtogram results

The FK results for various flowrates are shown for both sensors in Fig. 7.14. The yellow and the black markers illustrate the experimental and numerical visual inception operating point (OP), similarly to Fig. 6.28 (section 6.3.3). The MSK retains low values (~0.1) until the experimental visual inception point (yellow marker), and starts to increase for lower σ values until σ_{MIN}, where the total head collapses (Fig. 3.9d, section 3.3.1). The rise of MSK is stronger for the minimum flowrates (Figs. 7.14a,b), where it reaches values close to 1, and becomes weaker during the testing of flowrates closer to the BEP (Figs. 7.14c,d), where it takes values close to 0.25. This pattern is similar with that discussed during the presentation of vibration powerbands (section 6.3.3) and flow visualization results (section 3.3.2), and illustrates the narrower extent of cavitation area when the hydraulic turbomachine operates close to the best efficiency point (BEP).

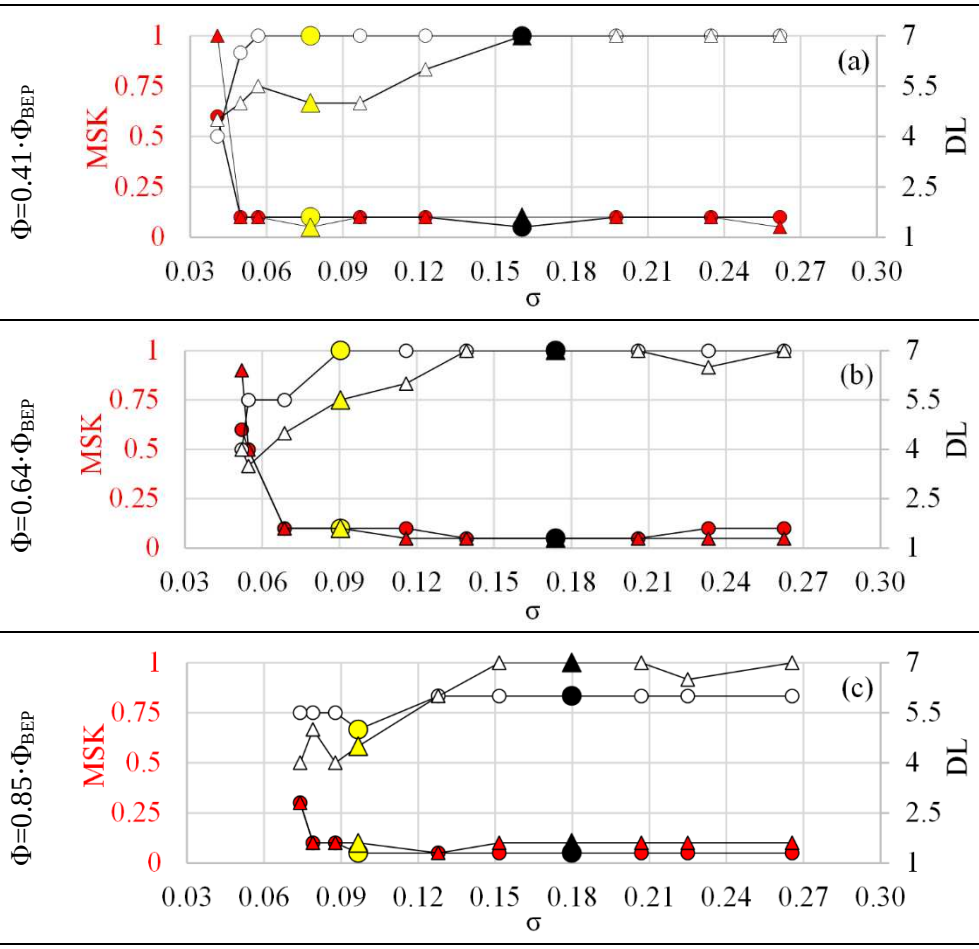

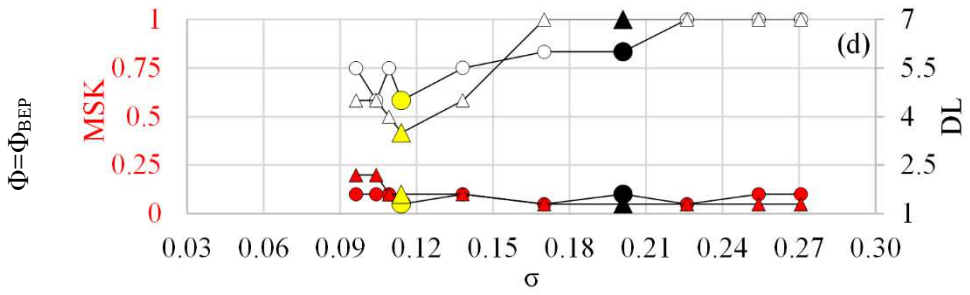

Figure 7.14 MSK value (red color) and its corresponding DL (white color) as a function of σ, for sensor B01_1 (circle marker) and B01_2 (triangle marker) for impeller No. 4.

Another observation deals with the systematically lower MSK value, relative to the LU impellers (Figs. 7.2-7.4). Two are the possible causes for this behavior, and they are related with the geometrical characteristics of impeller No. 4. The first deals with the fact that this is a shrouded impeller and the additional surface that intervenes between the developed two phase flow and the sensors makes harder the identification of cavitation onset. Moreover, the bearings, which are now located on the pump shaft, also contribute with supplementary noise sources that influence MSK behavior. A third reason probably deals with the geometrical characteristics of the blade at the inlet of the impeller. More specifically, the numerical results of Fig. 5.17a (section 5.2.2) prove the appropriate design of the inlet of the NTUA impeller that especially under BEP conditions, causes minimum recirculations. In addition, in section 3.3.1 it is shown that impeller No. 4 has the lowest relative flow incidence angle among the tested impellers (Fig. 3.10) in the entire range of flowrates examined in the present study. The effect of flow conditions at the inlet of the blade in the NPSH value is highlighted in Eq. 2.19 (section 2.2.2) and can justify the low values of MSK.

Similarly to the MSK and to the results of LU impellers, the DL value starts to diminish with cavitation inception (Fig. 7.14). Only few differences are noticed between the two sensors, with the DL value of sensor B01_2 starting to decrease before or during the experimental initial cavitating conditions, while for B01_1 sensor, and for the lowest flowrates, this happens at smaller σ values ($\sigma<\sigma_{VI,exp}$) (Figs. 7.14a,b). These differences are due to the positioning of the latter sensor at the pump bearings, where the mechanical sources of vibration can prevail over cavitation signals In general, the DL results agree with those presented in Figs. 7.2-7.4 and confirm the tendency of the phenomenon to excite wider parts of the frequency spectrum.

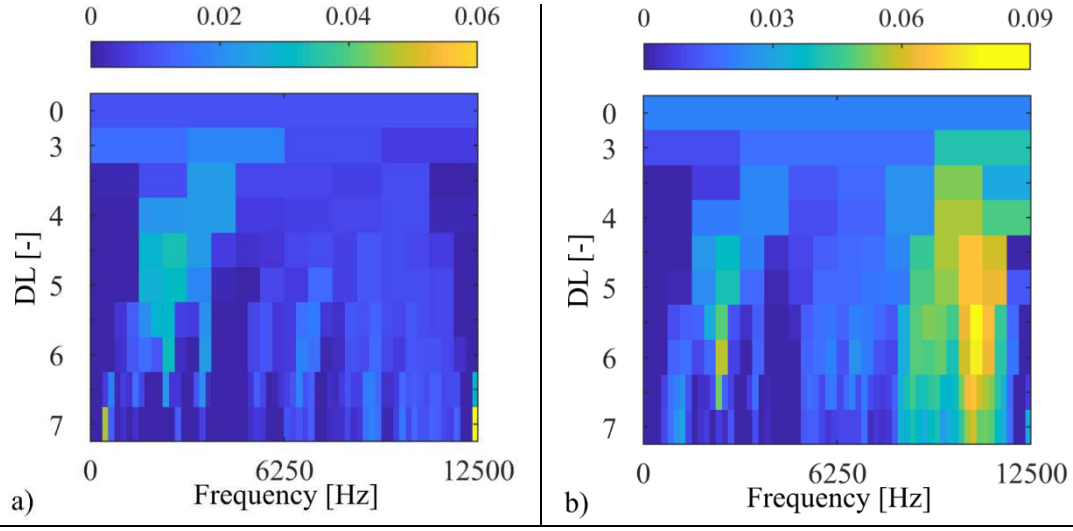

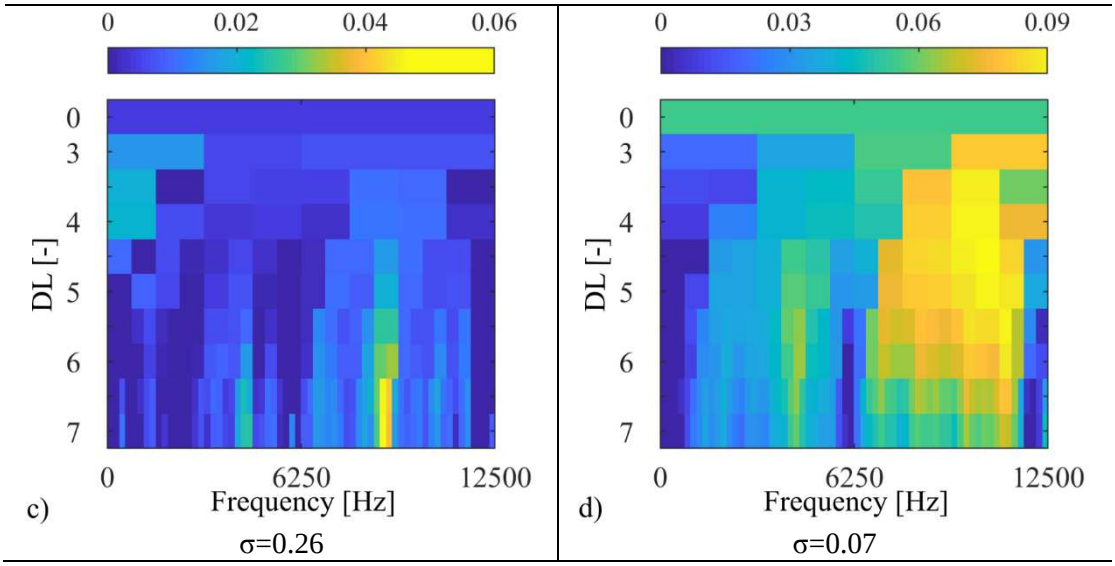

Figure 7.15 Comparison of FKs between normal (left) and cavitating (right) conditions for impeller No. 4, at $\Phi=0.64\cdot\Phi_{BEP}$. **a**,**b)** sensor B01_1, and **c**,**d)** sensor B01_2.

The FK maps for two σ values, at $\Phi=0.64\cdot\Phi_{BEP}$, are plotted in Fig. 7.15 for both sensors, in order to compare their pattern in different measuring points. As in Figs. 7.5 and 7.6, the left FK corresponds to normal and the right FK to cavitating conditions. According to these results, high spectral kurtosis values (yellow area) cover larger area at cavitating conditions and at the same time they move towards lower DL values, similarly to the semi-open impellers results in Figs. 7.2-7.6.

This behavior is more apparent for sensor B01_2, which is located on the casing of the pump, since the area that the increased MSK value covers, extends in larger frequency (6-12 kHz) and DL (3-7) range than that of the B01_1 sensor mounted at the bearing of the pump (f:10-12 kHz, DL:5-7). The results of the FK, are followed from the presentation of the filtered signals in the time domain and the envelope's frequency spectrum, in sections 7.4.2 and 7.4.3, respectively.

7.4.2 The filtered time series (TS)

The filtered time series (TS) of B01_1 and B01_2 sensors is presented in Fig. 7.16 for four different flowrates, during initial and intermediate cavitating conditions. The sensor B01_1 is mounted at the bearing (6206 RS) of the pump and the sensor B01_2 on its casing, closer to the suction of the pump (Fig. 2.23a, section 2.5.2.1). In this case, the σ_{IN} is defined between the experimental and the numerical visual inception OP, in order to present the filtered vibration results for suction conditions that lie closer to the actual onset of the phenomenon.

Similarly to LU impellers, the results are presented by using each sensor alternately, in order to reduce the amount of the time series presented. In addition, the blade passing frequency (BPF) of the NTUA impeller (BPF=241) is decreased relative to that of the LU impellers (BPF=TBPF=360 Hz), nevertheless the δt of the TS of Fig. 7.16 remains the same with that used in the plots of Figs. 7.7-7.9. The lower BPF of NTUA configuration increases the distance (BPP=1/BPF) between the spikes and reduces the number of times that the spikes appear in the TS. However, these changes are adequatelly illustrated in the plots of Fig. 7.16 and, consequently, the value of δt is kept the same.

During the non-cavitating conditions (σ_{BVI}) the TS of B01_2 (Fig. 7.16a) is identical with the corresponding one of impellers No. 1, 2, 3, presented in Figs. 7.7a, 7.8a and 7.9a. During non-cavitating conditions the filtering of the measured signal cannot provide reasonable results and the time series has the pattern of Fig. 7.16a. This behaviour is similar to the results of both sensors used in the present study.

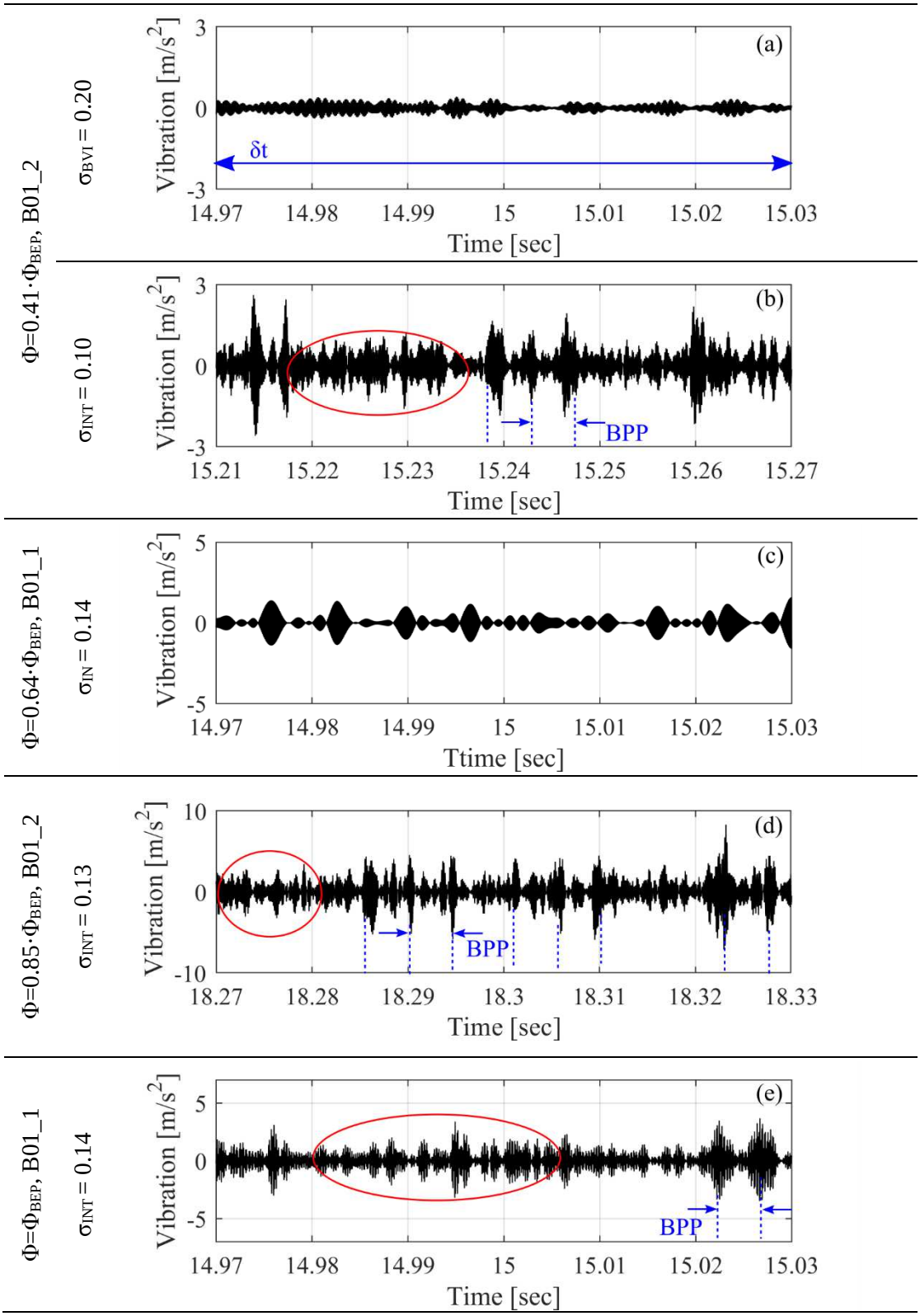

Figure 7.16 Filtered time series for impeller No. 4, sensor: B01_2, during: **a)** non-cavitating conditions, and **b**,**c**,**d**,**e)** early stages of cavitation development.

The passing to cavitating conditions differentiates the produced results, with respect to the location of the acceleremeter. More specifically, the results that correspond to the sensor located at the casing of the pump (B01_2) exhibit similar characteristics with those of the LU impellers, when the pump operates under cavitating conditions (Figs. 7.16b,d). Clear impulses

are formed in the filtered signal, which in some cases present random pattern (red ellipses), while in other cases they follow the blade passing frequency (blue broken lines). This behaviour of the results of B01_2 sensor is consistent for all filtered signals obtained under the initial and intermediate cavitating conditions.

On the other hand, the results of sensor B01_1 that is located at the bearings of the pump are contradicting. For the lower flowrate (Fig. 7.16c) the times series is similar with those presented under non-cavitating conditions (Figs. 7.16a, 7.7a, 7.8a, 7.9a). This peculiar pattern of the results of sensor B01_1 is also confirmed by the examination of initial and intermediate suction conditions for $\Phi=0.41\cdot\Phi_{BEP}$. Nevertheless, the method appears to work for all the other cases examined (σ_{IN} & σ_{INT} for $\Phi=0.81\cdot\Phi_{BEP}$ & $\Phi=\Phi_{BEP}$), as this of σ_{IN} for $\Phi=\Phi_{BEP}$ that is presented in Fig. 7.16e. Here, the filtered signal contains some random and some periodic spikes, as in Figs. 7.16b,d. This behavior of the TS results of B01_1 sensor demonstrates the impact of the distance of the sensor from the actual fault (cavitation in the impeller), as well as the effect of the additional bearing noise in the detection of two phase flow development in the pump. Nevertheless, the ability of the sensor to identify the cavitation is further evaluated with the examination of the envelope's frequency spectrum results.

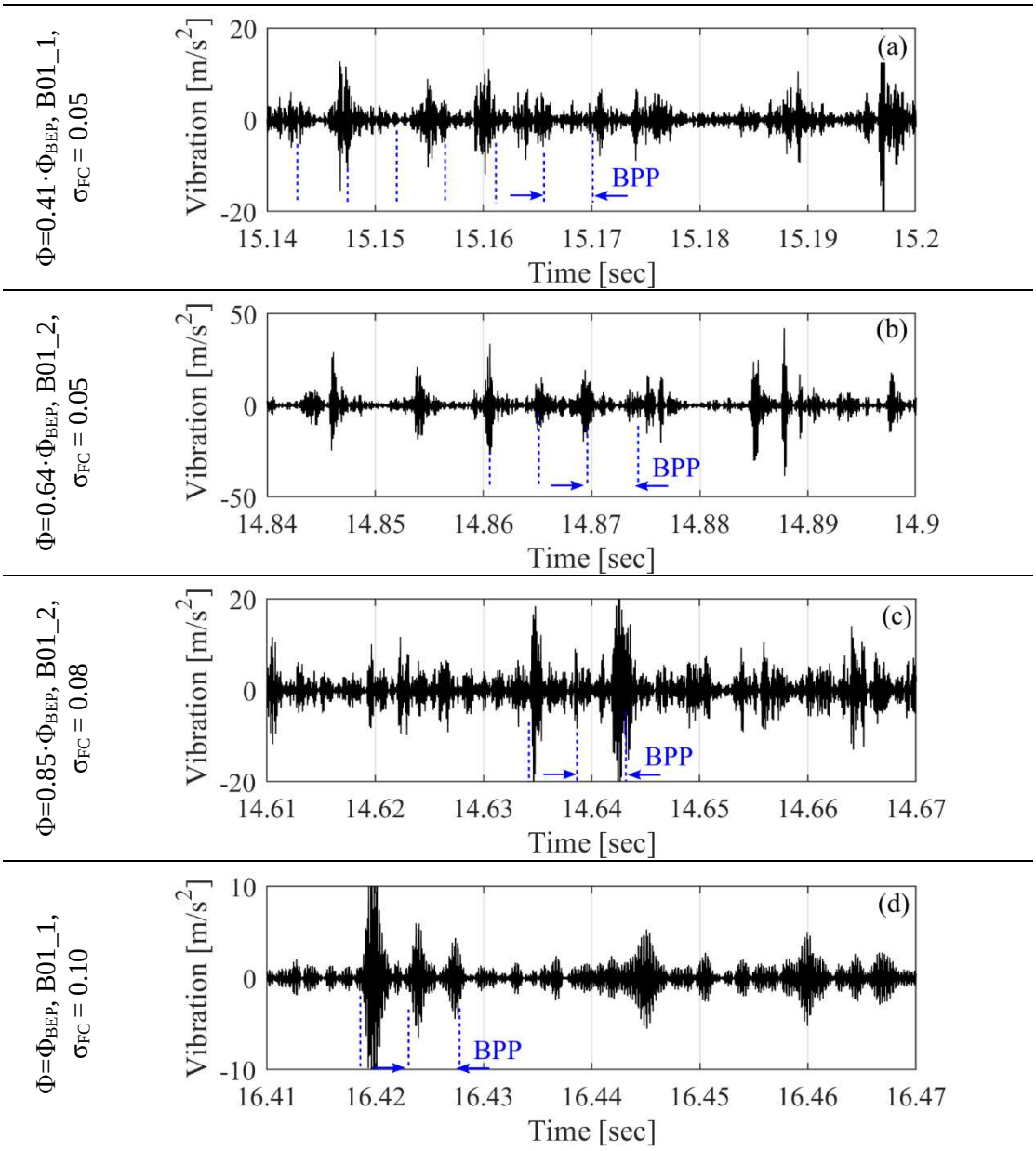

Figure 7.17 Time domain of the filtered vibration signal at σ_{FC} for impeller No. 4.

Similarly to the procedure followed for the semi-open impellers of LU pump, the results for the filtered vibration signal are given under minimum suction conditions (σ_{FC}), in order to examine the changes in their pattern from the two-phase flow development. The results are presented in Fig. 7.17 and refer to both accelerometers. According to Fig. 1.17, under heavy cavitating conditions, strong impulses appear to the filtered time domain. The strikes exhibit increased amplitude compared to the results of Fig. 1.16, no matter the flowrate conditions and the sensor examined.

Consequently, the observable impulses presented in Fig. 7.16 for both initial and intermediate cavitating conditions, verify that the band pass filters constructed from the application of the FK tool and the SK methodology identify the presence of cavitation. However, the prompt detection of the impulses it done systematically only for the sensor located at the casing of the pump, while further procesing of the signals need to be done, in order to clarify their periodicity. Towards this direction, section 7.4.3 provides the results obtained after the calculation of the envelope's frequency spectrum.

7.4.3 The frequency spectrum (FS) of the envelope

The frequency spectrum (FS) of the envelope of the NTUA impeller is given in Fig. 7.18, for both sensors at all flowrates tested. The results of the envelope's FS of sensor B01_2 are encouraging, since they agree with the observations made in section 7.3.3 for the semi-open impellers of LU. More specifically, the BPF exhibits a strong discrete component in the FS of all flowrates (Figs. 7.18b,d,f,h), after passing to intermediate cavitating conditions, at σ_{INT}. For conditions close to the onset of the phenomenon, σ_{IN}, the BPF component of sensor B01_2 only appears for the minimum flowrate (Fig. 7.18b), where its value is larger even for the intermediate conditions. For higher flowrates (Figs. 7.19d,f,h), the BPF amplitude diminishes, while the RF component and its harmonics become discernible.

The BPF component also appears in the FS of B01_1 sensor, for the three largest flowrates examined (Figs. 7.18c,e,g) during σ_{INT}. However, during the testing of minimum flowrate (Fig. 7.19a), the spectrum contains the BPFO frequency component of the electric motor's bearing (6308), no matter the stage of cavitation formation. The same frequency excites the envelope's FS of B01_1 sensor for the σ_{BVI} and σ_{IN} of Φ=0.64·Φ_{BEP} (Fig. 7.19c), while for the σ_{BVI} of Φ=0.85·Φ_{BEP} the BPFI component of the pump's bearing can be observed (6206 2RS). This behavior of the FS of B01_1 sensor demonstrates the impact of the bearing noise in the detection of cavitation. During the initial stages of two-phase flow development, before the drop of total head, the band pass filter made from the FK results isolates the bearing frequencies, as they comprise a low but the most evident source of transient behavior close to the sensor position.

The designation of bearing frequencies in the FS of the envelope does not signify a developed bearing fault, which if existed, it would had been also illustrated in the results of Figs. 6.20 d,e (section 6.3.1.2) and 6.23g,h and (section 6.3.2), where the vibration RMS value is given. These FSs depict the problematic results obtained after the application of Spectral Kurtosis methodology in the vibration signal measured by a sensor mounted at the bearing of the hydraulic turbomachine.

In the case of the NTUA pump, the amplitude of the BPF component unter intermediate cavitating conditions does not present a specific trend. In contrast to the semi-open impeller cases (section 7.3.3), the noisy bearing environment and the presence of the shroud complicate the analysis of the envelope's frequency spectrum amplitudes.

To conclude with, the results of sensor B01_2 for both initial and intermediate cavitating conditions, verify that that the SK methodology can be applied in closed industrial impellers too for the detection of cavitation. The drop of DL value proves the ability of the FK tool to detect the presence of excited resonances and long with the combination of the FS of the envelope and the TS of the filtered signal, can be used for efficient detection of cavitation in centrifugal pumps.

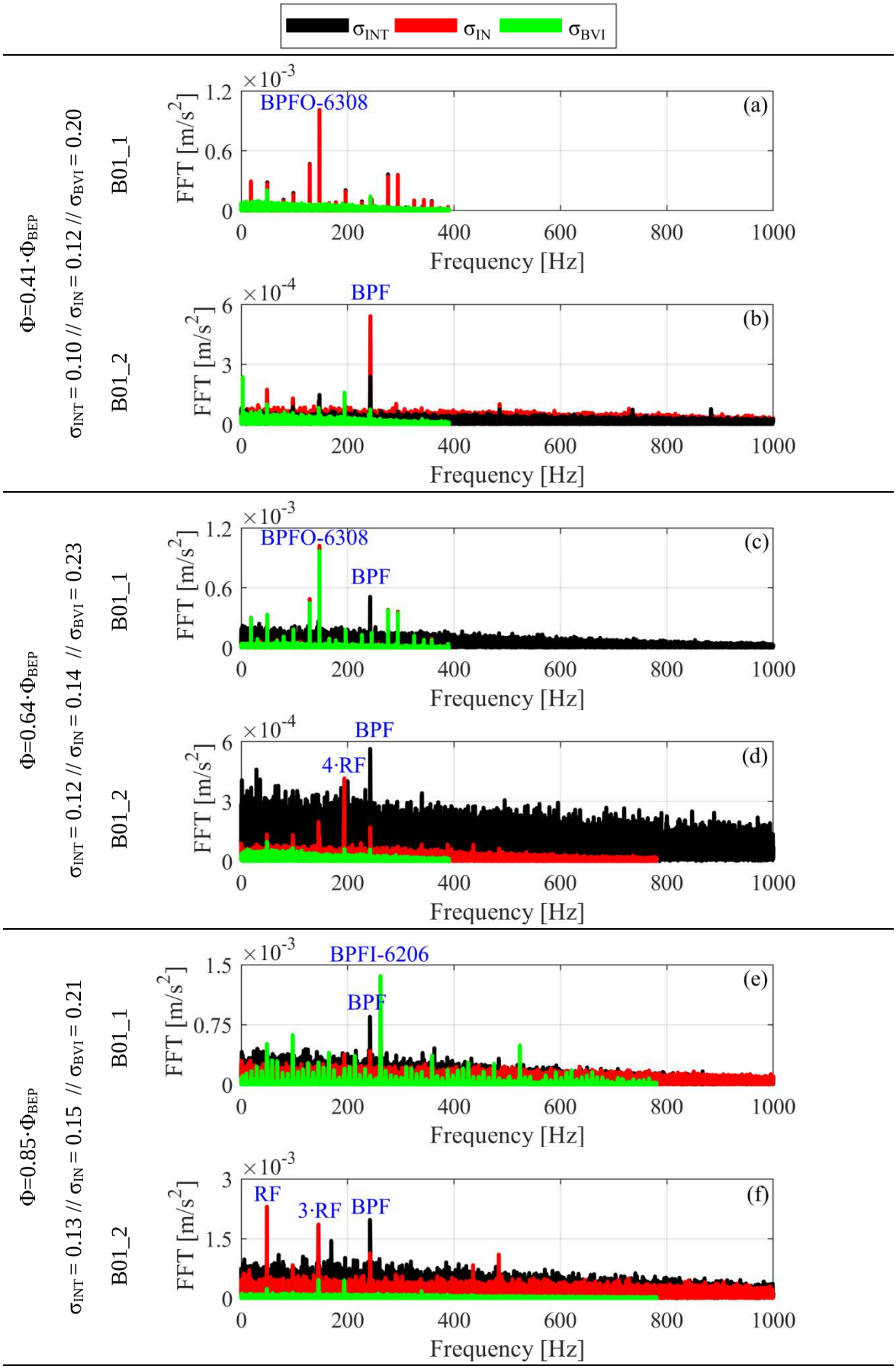
σINT
σIN
σBVI
Φ=0.41·ΦBEP
σINT = 0.10 // σIN = 0.12 // σBVI = 0.20
B01_1
B01_2
BPFO-6308
BPF
(a)
(b)
Φ=0.64·ΦBEP
σINT = 0.12 // σIN = 0.14 // σBVI = 0.23
4·RF
(c)
(d)
Φ=0.85·ΦBEP
σINT = 0.13 // σIN = 0.15 // σBVI = 0.21
BPFI-6206
RF
3·RF
(e)
(f)
FFT [m/s²]
Frequency [Hz]

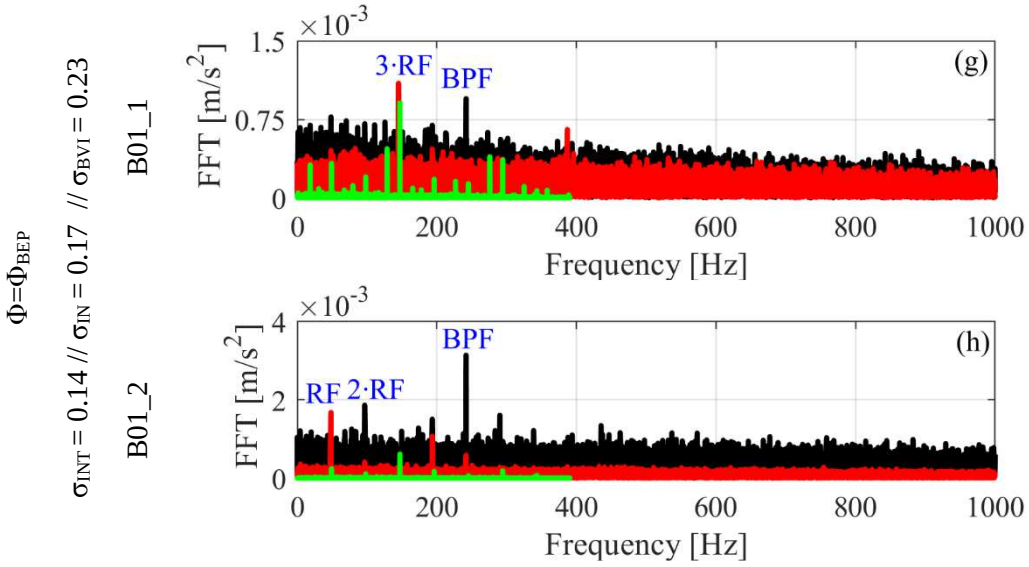

Figure 7.18 Frequency domain of the envelope of the vibration signal of both accelerometers used in impeller No. 4.

7.5 Synopsis

In this chapter, the spectral kurtosis methodology is applied for the detection of cavitation in the centrifugal pumps of two experimental set-ups studied in the present Thesis, namely in the three laboratory semi-open pump impellers of the LU and in the closed impeller of the industrial pump of the NTUA. The method is applied on the vibration signal of several operating points that consist the cavitation characteristic curve in each pump. The research focuses on the fault detection at the initial stages of cavitation development, where the processed signals are analysed both in frequency and time domain.

The results show that the Spectral Kurtosis methodology is capable to correlate vapour formation in the impeller with the appearance of BPF at the frequency spectrum of the envelope, and also to identify the impulsive signature of cavitation in the filtered time domain. The filtered signal in time is formed from random and periodic impulses, which are masked from various noise sources in the original signal. Nevertheless, the successful implementation of SK method allows their extraction. The periodic impulses of the signal follow for the pumps tested, the blade passing frequency. Moreover, the examination of the envelope's frequency spectrum illustrates the excitation of the blade passing frequency (BPF) discrete component, from the cavitation development, since the last appears only during $\sigma<\sigma_{VI}$. The aforementioned behavior of FS and TS is accompanied by the drop of signal Decomposition Level, observed in all examined cases. This drop confirms, from the filter construction perspective, the excitation of wider frequency bands after the development of cavitation.

It is underlined that the clarity and discernibility of the results of this approach depend on the sensors' mounting position. More specifically, sensors mounted on the pump casing close to the cavitating impeller region measure more intense and periodic impulses in the filtered signals, thus allowing to detect cavitation at early development stages. On the other hand, sensors positioned at the pump's bearings produce less intense signals, by which cavitation can be detected at more developed stages.

The appearance of the aforementioned characteristics in the time signal and the spectrum of the envelope are systematic for all the impellers tested, no matter the flowrate conditions and manifests the modulation of the filtered signal from the periodicity of the rotating blades. The combination of the identification of the strikes that appear in the filtered signal that are periodic with the BPF, along with the appearance of BPF discrete frequency in the envelope's spectrum, constitutes a general and robust cavitation detection criterion that can be used in centrifugal pumps. This behaviour of the filtered vibration signal is unique, since in the motor-coupling-pump system only the bearings could excite impulses, however they are modulated by different frequencies. Moreover, the fault mechanism (vapour bubble implosion) and the motor-pump system is analogous to that of the hydroturbine-generator, and this enables the application of the same criterion towards the detection of cavitation in hydroturbines.

In conclusion, the proposed methodology for the detection of cavitation in the rotating components of a centrifugal pump and hydroturbine consists of the following steps:

i. Application of the Spectral Kurtosis method in order to define the characteristics of the band pass filter. Cavitation phenomenon should increase the kurtosis value in a wide range of frequencies, which qualifies the use of wide range filters.
ii. Application of the band pass filter in the measured signal and identification of its impulsive characteristics in the time domain, which are periodic with the blade passing frequency.
iii. Demodulation of the filtered signal and extraction of the discrete low frequency that characterises the envelope. Cavitation phenomenon is modulated from the rotor-stator interaction frequencies.

8. Concluding Remarks

8.1 Summary of the Thesis conclusions

The present research work examines the capability of different experimental and numerical methodologies, in order to detect cavitation phenomenon in hydraulic turbomachines. The conclusions of the Thesis are grouped in three parts. The first deals with the analysis of the experimental performance of the pumps and the investigation of cavitation development with the use of flow visualisation results. The second part refers to the numerical analysis of the flow characteristics in semi-open and closed impellers under normal and cavitating conditions, and the use of the modelling results from a detection perspective. Finally, the third part contains the evaluation of signal processing techniques of different complexity, applied on the signals of noise and vibration measurements for the prompt and reliable detection of cavitation.

8.1.1 Performance of the centrifugal pumps and flow visualisation results

Four centrifugal pump impellers are tested under normal and cavitating conditions. The three of them are semi-open (unshrouded), and they are tested in the Lancaster University (LU) pump laboratory, while the fourth is a closed impeller, and it is tested in the Laboratory of Hydraulic Turbomachines (LHT) of the National Technical University of Athens (NTUA). Both test configurations allowed the flow visualisation of two-phase flow development in the impellers, since critical parts of the machines are manufactured from transparent material. Although all impellers are radial, with low specific speed values, they present significant differences in the geometrical characteristics of their blades. The effect of those characteristics is highlighted on their performance under single-phase and two-phase flow conditions.

A. The results of the performance characteristic curves under single-phase conditions confirm the theoretical predictions and obtain values close to the those expected for radial impellers of low specific speed. Moreover, the results of total head curves reveal the effect of the blade's shape on their trends, since the slope of the measured total head curves (Q-H_{tot}) increases with the decrease of the outlet blade angle.

B. The cavitation characteristic curves (σ-Ψ) are derived for each impeller operating at four different loading conditions (flow rates). The behaviour of the cavitation curves, regardless of the impeller and the operating conditions, is in line with the theory and the various similar data from the literature. Consequently, the normalised total head (Ψ) remains unaffected by the decrease of static pressure (σ) until a specific point, beyont which further decrease in suction pressure results in pump head break down.

C. For σ values that correspond to the total head deterioration, the flow visualisation photos illustrate the dominant characteristics of two-phase flow development, where cavitation area extends to all directions and practically blocks the flow path between the impeller blades. At such conditions, four different types of cavitation appear in the flowpath:

i. Attached vapour cavities at the suction (low pressure) side of the blades, which take the form of a single bubble area that remains macroscopically constant in terms of location and size.
ii. Cloud bubble cavities that are created at the downstream edges of the attached cavitation area.
iii. Vapour cavities that are generated before the impeller, at the suction valve and at the inlet pipe elbow.
iv. Tip cavitation that is formed at the tip clearance of semi-open impellers.

D. Furthermore, the flow visualisation photos allow the identification of the particular σ_{VI} operating points, where the phenomenon initiates. As a result, the visual onset of the formation of small vapour bubbles:
   i. Takes place far before the total head drop point.
   ii. Takes place at the suction side of the blades close to their leading edge.
   iii. Has dynamic and unstable characteristic, since the bubbles are created in a very small region where the static pressure is at the vapour saturation limit, and reliquified abruptly as the flow drives them to higher pressure points downstream in the impeller.

E. The flow visualisation tool enables the examination of the change of σ_{VI} value relative to the geometrical characteristics of each impeller and the flowrate conditions. According to the results:
   i. The increase of the flowrate accelerates the velocity field and drives the σ_{VI} at higher values.
   ii. The increased number of blades used in the impeller, accelerates the flow field, reduces the static pressures (for same flowrate) and makes the impeller more prone to cavitate.
   iii. The increased incidence angle of the incoming flow to the impeller results in stronger recirculation and vortices after the impeller inlet that reduce further the static pressure field at the suction side of the blades.

F. Finally, the operation of the pump under intermediate cavitating conditions, for cavitation coefficient values that lie between the σ_{FC} (the full cavitation extreme) and σ_{VI}, allowed to draw some interesting conclusions:
   i. The size of the visually observable area increases at lower σ values.
   ii. For the impellers that consist of backward-curved blades, the area covered by the vapour bubbles presents very dynamic behaviour, similarly to that discussed for the onset.
   iii. For the impellers that consist of radial and forward-curved blades the vapour area macroscopically consists of two sections that exhibit different behaviour: The core of the vapour phase area shows a macroscopically steady behaviour, similar to that of the attached cavity, while the outer limits of this area present dynamic, unsteady patterns.

8.1.2 Numerical modelling and detection of cavitation development

The numerical modelling approach includes the flow simulation of impellers No. 2 and 4 under normal and cavitating conditions. Impellers No. 2 and 4 appear significant geometrical differences with respect to their incidence angles, the number of blades used and the presence of tip clearance. The two phase flow modelling is carried out with the application of Zwart et al. cavitation model. Both computational domains include all the parts of the pumps and the boundary conditions are taken directly from the experimental measurements.

A. The model is validated against the experimental data obtained for impeller No. 2 under single and two-phase flow conditions and includes the comparison of the numerical and

experimental characteristic curves of the pump, as well as the comparison of the numerically obtained location and extent of two-phase flow area with the macroscopical observations made from the flow visualisation results. According to the simulation results under normal and cavitating conditions, the characteristic curves follow sufficiently the trend of the corresponding experimental data for both impellers. The differences between the various characteristic curves are attributed to:

i. The assumption of steady state, incompressible flow conditions.
ii. The modelling of the bearing and rotating disc losses.
iii. The assumption of a homogeneous mixture that consists only of vapour and water and does not account for the effect of non-condensable gas.
iv. The inability of the model to simulate the vapour bubbles that are formed in the suction valve during the tests.

B. The examination of the static pressure contours and the relative velocity vectors of the impeller No. 2 reveals the non-axisymmetric behaviour of the flow and the presence of strong irregularities (i.e. recirculations due to high incidence angle and the tip clearance), no matter the flowrate conditions, as a result of:

i. The elbow used close to the suction of the pump.
ii. The high incidence angle of the radial impeller.
iii. The recirculations produced from the tip clearance.

The above characteristic of the pump affect significantly its performance under normal conditions and justify the low total efficiency of this pump.

C. Moreover, the high incidence angle and the tip clearance influence also the performance of the pump under cavitating conditions. The latter exhibit the following characteristics:

i. During the numerical onset of cavitation, the vapour phase is initially formed at the suction side of the leading edge into the flow separation area, due to the high flow incidence angle. Under such conditions, the proposed simulations compute a significantly narrower cavitating area compared to the experimental.
ii. Under the lower σ values, the numerically obtained two-phase flow area increases and the steady mechanism of the attached cavity is predicted adequately.
iii. During extreme cavitating conditions, at the σ_{FC}, the numerical results illustrate the blocking of the flowpath from the vapour phase area that appears intensive recirculation and separation regions. However, the model achieves to depict this behaviour in significantly lower σ values than the experimental, since the latter is affected from the formation of vapour bubbles in the suction valve.

D. The present study also focuses on the extensive flow recirculations at the tip clearance area and reveals the following features:

i. The tip clearance recirculation is driven from the pressure difference between the pressure and the suction side of the blades.
ii. One part of the tip clearance flow directs the flow towards the exit of the impeller.
iii. A second part of the tip clearance flow creates an area of extended three-dimensional recirculation where the fluid leaks towards the suction side of the blade and the inlet of the impeller.
iv. Under initial and intermediate cavitating conditions, the vapour phase developed also in the tip clearance area, while the flow recirculation transfers it towards the impeller inlet and suction side and forms backflow cavitation.
v. Under heavy cavitating conditions, where the total head drops, the driving pressure differencel decreases and weakens the backflow cavitation phenomenon.

E. Moreover, the effect of tip clearance thickness on the performance of the pump No.2 is investigated and the following conclusions are drawn:

i. Under non-cavitating conditions, the torque on the impeller and the total energy transferred to the fluid increases when the tip clearance thickness reduces, due to reduction of internal flow recirculation.
ii. Under cavitating conditions, a larger tip thicknesses results in stronger recirculations that strengthen backflow cavitation at the impeller's inlet, however, it simultaneously decelerates the tip clearance flow

F. Impeller No. 4 is a shrouded (closed) impeller that presents lower incidence angles compared to impeller No. 2 and its configuration does not include an elbow close to its suction. The conclusions extracted from the numerical simulation of impeller No. 4 are listed below:
   i. Under the best efficiency point flowrate, the low incidence angle and the absence of elbow make the flow conditions to be more periodically symmetric.
   ii. Under partial flowrates, the incidence rises, which now results in local recirculations in the flowpath between the blades.
   iii. Under cavitating conditions, the model predicts the formation of an attached cavity at the suction side of the blade.
   iv. The cavity enlarges with the reduction of σ and reaches the area where the transparent window is manufactured for a σ value that is close to the experimentally obtained σ_{VI}.
   v. Under heavy cavitating conditions the vapour area maximises and blocks the inflow of the flowpath, in a similar way to that of impeller No. 2.

The ability of the developed model to predict sufficiently the various cavitating conditions in both closed and semi-open impellers, before the total head drop, reveals its capability to detect cavitation and enables its use as a primary or auxialiary tool during either the design stage or the operation of hydraulic turbomachines.

8.1.3 Detection of cavitation with the use of noise and vibration measurements

The derivation of the characteristic curves of the four impellers and the flow visualisations are followed from noise and vibration measurements. At first, the signals are analysed in the time domain along with their statistical properties that are plotted as function of the suction conditions. The second part includes the study of the frequency domain and the investigation of AE_{RMS} and powerbands capability to detect cavitation phenomenon. Finally, the last part of this thesis proposes the application of the Spectral Kurtosis (SK) along with the Hilbert Transformation so as to examine the pattern of the filtered signals in time and the envelope's frequency domain. The most interesting conclusions drawn are summarised in this section.

A. The depiction of the noise and vibration signals in time and concludes that:
   i. The vapour bubble implosions does not affect the signal's amplitude during its initial stages of development close to the visual inception point, σ_{VI}.
   ii. During heavy cavitating conditions, when the phenomenon reaches σ_{FC}, a clear increase of its amplitude is highlighted, which has the form of impulses.

B. The examination of the histograms and the normal probability plots reveal that the onset of the strikes after the development of cavitation spoil the Gaussian shape of the measured data. The obtained signals are processed in order to find an association between this behaviour and the statistical moments, and the following conclusions are drawn:
   i. The mean and the skewness moments are not affected by the development of cavitation in the pump.
   ii. The standard deviation and kurtosis moments present patterns that satisfy some basic detection criteria, such as the increase and the maximisation of their value for $\sigma<\sigma_{VI}$.
   iii. The results for the standard deviation and the kurtosis are not systematic and they are dependent on the sensor position and the flowrate.

iv. The development of cavitation increases the transient non-Gaussian behaviour of the kurtosis value and reveals its association with the impulses presented in the raw signal.

C. The study of the noise and vibration signals in the frequency domain, reveal some significant characteristics:
   i. Cavitation excitates a wide range of frequencies (resonances) that mainly lie in the high part of the spectrum.
   ii. The intensity and the location of those resonances are significantly affected by the geometrical and structural characteristics, and the operating conditions of each machine tested.
   iii. The shape of the excitations is similar with that presented in case of faults of rolling element bearings, since the latter also appear strong impulsive bheaviour.

D. An approximate way to quantify the excitations of the noise and vibration measurements is with the use of AE_{RMS} and powerbands, respectively. The conclusions after the application of these tools on the raw data are:
   i. In the case of semi-open impellers, the AE_{RMS} results detect promptly the appearance of cavitation, since its value increase coincides with the σ_{VI} and maximises for lower σ values.
   ii. Similar behaviour exhibit also the vibration powerbands for the semi-open impellers, even though they manage to detect the phenomenon at slighter lower σ values.
   iii. In the case of the closed impeller, the applicability of those tools is questioned, since they do not identify the two phase flow development promplty; especially in the case of vibration results their value increases when the total head of the pump has totally collapsed.
   iv. The difficulties in the detection of cavitation of closed impellers are related with the additional surface of the shroud and the effect of the rolling element bearings of the closed impeller.

E. The conclusions drawn from the examination of AE_{RMS} and vibration powerbands feature the strengths and weaknesses of AE_{RMS} and the (vibration) powerbands towards the prompt detection of cavitation in closed impellers. However, the closer study of their patterns for all the examined impellers, along with the review of other studies that implement similar tools, leads to some additional conclusions:
   i. The AE_{RMS} and the powerbands results present different patterns as function of suction conditions. Those irregularities are also confirmed in the published works reviewed in this thesis, and they are related with the selection of the integrated frequencies and the operating conditions.
   ii. The review of bearing-related faults reveals that due to their impulsive nature they excite resonances that possibly lie in the high frequency range of the spectrum, in a similar manner with that of cavitation signals. Moreover, the integration of the power of high frequency spectrum could include the resonances excited by a defected bearing rather than cavitation. As a consequence, the vibration powerbands could be applicable only in the case of a pump that operates with healthy bearings. Measurements that quantify frequency ranges over the audible frequency range (> 20 kHz), as in the case of AE sensor, are influences less from such mechanical faults.

G. The conclusions drawn for the application of AE_{RMS} and the vibration powerbands tools indicate their weaknesses towards the development of a robust and general cavitation detection criterion. The latter should:
   i. Be independent from the specific characteristics of the testing procedure (i.e. the test configuration, the geometrical characteristics of each pump, the flowrate conditions and the frequency range that the analysis focuses).

ii. Presents characteristics in the noise and vibration signal that differentiate cavitation fault signature from other faults related with the hydraulic machine.

H. The present research proposes the use of Spectral Kurtosis for the calculation of the characteristics of the band pass filter that will effectively unmask cavitation characteristics from the raw measured vibration signal. In addition, the identification of possible periodicities in the cavitation characteristic can be easily observed with the use of amplitude demodulation techniques, such as Hilbert Transformation. Consequently, this study examines the changes in the filtered signal in time, as well as the frequency spectrum of the envelope and associates them with the development of cavitation. The justification for the selection of Spectral Kurtosis method is based on two significant observations:
   i. The transient non-Gaussian behaviour of the kurtosis moment due to the cavitation development. As a consequence, it is expected that the implementation of SK method will be able to locate the resonances excited by the cavities formation by using the criterion of spectral kurtosis maximisation.
   ii. The differences in the location and the band of the resonances excited: i) in different test configurations, due to the geometrical and structural characteristics, as well as for different operating conditions, and ii) in the same machines under different stage of cavitation development. Similar differences have been reported in the case of faults of rolling element bearings, and this complicates the selection of the band pass filter's characteristics used for the demodulation procedure. The minimisation of the effect of such differences in the location and the range of the resonances was the main reason behind the development of SK method. The SK method is found to be able to regulate the filter's characteristics for each specific case and operating conditions by using the criterion of the maximisation of spectral kurtosis. The consideration of the similiraties between the cavitation and bearing detection problems justifies the selection of SK method.

I. The application of the SK methodology on the measured vibration data results in the following conclusions:
   i. The value of the central frequency of the band pass filter deviates in the different configurations, impellers and operating conditions and, consequently, it confirms the observations regarding the random position of the resonances excited by the two phase flow development.
   ii. The SK detects the appearance of impulses in the vibration filtered signal, which are modulated by the blade passing frequency (BPF) component. The latter is also highlighted after the demodulation of the signal and the presentation of envelope's frequency spectrum. The results obtained from the use of SK methodology are systematic for all the impellers and flowrates tested, and become clearer when the cavities extent increases.
   iii. According to the author's opinion, there is a clear analogy between the impulsive behaviour of the filtered signal and the shock pressure mechanism, as well as between the BPF modulation of the impulses with the fact that the shock pressure waves occur in the rotating impeller. More specifically, the bubbles are formed in the impeller at the suction side of the blade close to the leading edge and they implode as the flowpath drives them to higher pressure areas in the rotor. The implosion of the vapour bubbles is followed from the creation of shock pressure waves that hit the neighbouring solid surfaces that in this case are the blades of the impeller. The last rotate and due to the machine's non-uniformities, create blade passing frequency noise that dominates the flowfield and modulates the shock pressure waves.
   iv. The results are similar for those sensors located on the casing of the pump, close to the phenomenon, and differentiate for the sensor located at the bearing position, where the mechanical noises affect the ability of SK method to efficiently calculate

the envelope. Consequently, the present work proposes the use of the pump's casing for the appropriate mounting of the dynamic sensors.

v. The application of Spectral Kurtosis methodology towards the calculation of the band pass filter's characteristics is of increased significance because they disengage the detection of cavitation from the particular characteristics of the testing configuration and the impeller under examination. In addition, the simultaneous existence of the BPF at the envelope's frequency spectrum, along with the impulses in the filtered signal in time, are unquestionably related with the cavitation development, since there have not been reported any cases, where other faults present those characteristics.

8.2 Thesis contribution

The contribution and the novelties of the present Thesis refer to the testing configurations, to the identification and the study of complex flow mechanisms in the semi-open impellers of centrifugal pumps, and to the development and evaluation of experimental methodologis that detect cavitation in hydraulic turbomachinery. More specifically, the novel elements and contributions of the present study to the research in this field deal with:

1. The establishment at the LHT of the NTUA of a testing configuration that allows the performance of cavitation tests in centrifugal pumps, along with the flow visualisation of the phenomenon. The present set up can be used for the examination of both semi-open and closed impellers. Furthermore, the construction of a portable noise and vibration measuring system (toolkit) that could be used on site for monitoring and detection of cavitation and other faults in hydraulic turbomachines installed in various sectors (e.g. industrial pumps, hydroturbines etc.).

2. The conduction of cavitation experiments in impellers with different geometrical characteristics in the testing configuration of Lancaster University that are accompanied by dynamic (noise & vibration) measurements and visual observations of the phenomenon. This set up allows for the association of the visualised cavitation behaviour with the geometrical characteristics of the impellers, as also with the pattern of the noise and vibration measurements. The obtained results and conclusions contribute to a better understanding of the formation and the various development stages of cavitation in centrifugal pumps.

3. Application and extended evaluation of a numerical model for the simulation of pumps operation under normal and cavitating conditions. The detailed comparison of simulations with the corresponding experimental measurements and flow visualization data obtained for the same pumps, proves that the numerical model can be used as an additional tool for cavitation detection in hydraulic turbomachines, either in case of poor performace characteristics or intensive noise and vibrations or to verify a normal, non-cavitating performance. Moreover, this tool can be applied during the design and development stages of a hydraulic machine, as well as to study more elaborate mechanisms that are difficult or impossible to be measured, like the backflow cavitation studied in the present Thesis.

4. The extended evaluation of the AE_{RMS} and vibration powerband tools. Their application in the noise and vibration signals of three semi-open and one closed impeller in the tested pumps, reveals their strengths towards the detection of cavitation, but also their weaknesses towards the formation of a general robust two phase flow identification criterion.

5. The selection and application of Spectral Kurtosis (SK) methodology, so as to obtain the adequate band pass filter to be used for the extraction of the cavitation characteristics from the vibration measured data. The novelty refers to the justification of this selection in detection problems related with cavitation, which is based on two significant observation made in this work; i) the transient, non-Gaussian behaviour of the kurtosis moment, and ii) the ability of the SK method to regulate the filter's characteristics for each specific case and operating conditions, using the criterion of spectral kurtosis maximisation.

6. The successful implementation of Spectral Kurtosis (SK) method, which results in a filtered signal that significantly differentiates after the development of cavitation, far before the total head drop of the pump. This differentiation is also depicted in the frequency spectrum of the envelope and allows the formation of a general and robust two phase flow identification criterion. More specifically, the appearance of the impulsive behaviour in the filtered signal that is periodic with the frequency of the passing blades are the characteristics that this study proposes for the fast and reliable detection of cavitation in centrifugal pumps. In hydraulic turbomachinery, the mechanisms that could result in signals of impulsive behaviour are not modullated from the rotor-stator interaction, which makes the proposed tool adequate for the detection of two phase flow development. Moreover, this criterion could be generalised and applied for the detection of cavitation in all hydraulic turbomachines, including hydroturbines, since they all consist of similar mechanical components, and the hydrodynamic mechanism of cavitation development in them does not differentiate.

7. The association of the proposed detection features, i.e. the impulsive behaviour of the filtered signal in time and the blade passing frequency with the physical mechanism of the fault under investigation, i.e. the implosion of the vapour bubbles that occur in the rotor of the hydraulic turbomacinery.

8.3 Publications

In international journals

Mousmoulis, G., Karlsen-Davies, N., Aggidis, G., Anagnostopoulos, I., & Papantonis, D. (2019). Experimental analysis of cavitation in a centrifugal pump using acoustic emission, vibration measurements and flow visualization. European Journal of Mechanics-B/Fluids, 75, 300-311.

Mousmoulis, G., Anagnostopoulos, I., & Papantonis, D. (2019). A Review of Experimental Detection Methods of Cavitation in Centrifugal Pumps and Inducers. International Journal of Fluid Machinery and Systems, 12(1), 71-88.

Mousmoulis G., Kassanos I., Aggidis G., Anagnostopoulos I., (Under Review). Numerical simulation of the performance of a centrifugal pump with a semi-open impeller under normal and cavitating conditions.

Mousmoulis, G., Yiakopoulos, C., Aggidis, G., Antoniadis, I., & Anagnostopoulos, I., (Under Review). The application of spectral kurtosis at vibration signals for the detection of cavitation in centrifugal pumps.

In conferences

Mousmoulis G., Kassanos I., Anagnostopoulos I., Papantonis D., 'Experimental and Numerical Investigation of the Cavitating Draft Tube Vortex in a Francis Model Turbine', 6th IAHR International Meeting of the Workgroup on Cavitation and Dynamic Problems in Hydraulic Machinery and Systems, September 9-11, 2015, Ljubljiana.

Mousmoulis G., Karlsen-Davies N., Aggidis G., Anagnostopoulos I., Papantonis D., 'Experimental analysis of the onset and development of cavitation in a centrifugal pump', 7th IAHR International Meeting of the Workgroup on Cavitation and Dynamic Problems in Hydraulic Machinery and Systems, February 1, 2017, Porto.

Mousmoulis G., Kassanos I., Aggidis G., Papantonis D., Anagnostopoulos I., 'Study of cavitation development in centrifugal pumps with experimental and numerical tools', 11th Panhellenic Conference for Fluid Flow Phenomena, Kozani, 23-24 November, 2018, University of Western Macedonia, School of Mechanical Engineering.

Mousmoulis, G., Yiakopoulos, C., Kassanos, I., Antoniadis, I., & Anagnostopoulos, I. (2019, December). Vibration and acoustic emission monitoring of a centrifugal pump under cavitating operating conditions. In IOP Conference Series: Earth and Environmental Science (Vol. 405, No. 1, p. 012003). IOP Publishing.

8.4 Suggestions for future work

The present study manages to associate the two phase flow development in centrifugal pumps with the specific characteristics of the measured signals. The significance of these results is supported by the systematic detection of the formation of cavitaties during their early stage of development, and by the direct relation of the processed signal's characteristics with the physical mechanism of the fault (bubble implosion) and the operation of the machine (BPF). However, the completion of this work leaves several open issues referring to the applicability of the tool in different hydraulic turbomachines and configurations, and to a possible correlation between the results of the proposed methodology and the identification of the location of the phenomenon and its corresponding impact on the wear of the machine. In addition, there is a need for further improvements of the numerical approach, the experimental instrumentation and the testing configuration. These proposals for future work are summarised below:

i. The use of a modelling approach of higher fidelity that will include the modelling of the unsteady compressible characteristics of two phase flow development. Moreover, the assumption for a mixture of three fluids (vapour, liquid and gas) could improve the prediction for the cavitation inception. Finally, the transient modelling of the pump's performance with the use of a sliding mesh approach will allow to investigate the effect of rotor-stator interraction in the development of two-phase flow formations in the impeller, and the head break down point.

ii. Study of the effect of turbulence modelling in the effectiveness of the model to simulate the two phase flow formations in the hydraulic turbomachinery. Towards the same direction, calibration of the two phase flow model constants is proposed, with the use of experimental flow visualisation data, which may improve the predictions made for the vapour cavities, especially during the onset of the phenomenon. Finally, testing of cavitation modells that make use of a transport equation that contains only physical terms and parameters, and does not involve empirical constants.

iii. Performance of cavitation experiments in hydraulic turbomachines installed in experimental configurations that allow the implementation of the CTA methodology with the use of a closed tank, a vacuum pump and a heat exchanger. This will make the testing of the machines a faster procedure, with better control of the static pressure level, as well as of the medium's temperature and quality. In addition, the CTA methodology, will allow the more accurate determination of the total head drop point, since the effect of cavitation generated at the suction valve will not influence the results. In this way, the evaluation of the developed numerical model wil be improved.

iv. Further improvements on the selection of band pass filter characteristics, so as to obtain a clearer illustration of the impulsive behaviour of the bubble's implosion. Additional work should be done towards the association of the intensity of the impulses with the different levels of cavitation development.

v. Application of the proposed methodology in the noise and vibration signals obtained from different types of hydraulic turbomachinery, such as mixed flow and axial flow pumps and hydroturbines, so as to confirm its general applicability in a wide range of hydraulic turbomachines and to reveal and address its possible weaknesses.

vi. Use of the proposed methodology for the identification of the number of sensors and their mounting locations on the machine, so as to successfully determine the exact location of the phenomenon's inception.

vii. Association of envelope's characteristics at different stages of cavitation development with the wear made from bubble implosion on the material of the solid surfaces and the bearings, as function of the operating hours of the hydraulic turbomachinery. Such investigations on several machine types could be used for the development of a non-dimensional noise and vibration index that will define the appropriate time for the maintenance of the machine, and thus will minimise its downtime.

viii. Examination of the ability of the proposed methodology to detect cavitation in a hydraulic turbomachinery that suffers from an additional fault component or operates under faulty conditions (defective bearing, motor, unbalance, etc.). The conduction of such experiments would test the ability of the methodology to identify the phenomenon under severe conditions of increased complexity.

References

Abdulaziz, A. M., & Kotb, A. (2017). Detection of pump cavitation by vibration signature. *Australian Journal of Mechanical Engineering*, 15(2), 103-110.

Al Hashmi, S. A. (2009). Statistical analysis of vibration signals for cavitation detection ISIEA 2009. In 2009 IEEE Symposium on Industrial Electronics & Applications (Vol. 1, pp. 78-82). IEEE.

Al Hashmi, S. A. (2012). Spectrum analysis of acoustic signals for cavitation detection. *In 2012 IEEE Symposium on Industrial Electronics and Applications* (pp. 321-325). IEEE.

Al Obaidi, A. R. (2019). Investigation of effect of pump rotational speed on performance and detection of cavitation within a centrifugal pump using vibration analysis. Heliyon, 5(6), e01910.

Al Thobiani, F., Gu, F., & Ball, A. (2010). The monitoring of cavitation in centrifugal pumps based on the analysis of vibro-acoustic measurements. The Seventh International Conference on Condition Monitoring and Machinery Failure Prevention Technologies, 22-24 June 2010, Stratford-upon-Avon, UK.

Alfayez, L., Mba, D., & Dyson, G. (2004). Detection of incipient cavitation and the best efficiency point of a 2.2 MW centrifugal pump using Acoustic Emission. *Journal of Acoustic Emission*, 22, 77-82.

Allen, R. L., & Mills, D. (2004). Signal analysis: time, frequency, scale, and structure. John Wiley & Sons.

Anagnostopoulos, J. S. (2005). A numerical simulation methodology for hydraulic turbomachines. In *5th GRACM International Congress on Computational Mechanics, Limassol, Cyprus* (Vol. 29).

Anagnostopoulos, J. S. (2006). CFD analysis and design effects in a radial pump impeller. *Wseas Transactions on fluid mechanics*, *1*(7), 763.

Anagnostopoulos, J. S. (2009). A fast numerical method for flow analysis and blade design in centrifugal pump impellers. *Computers & Fluids*, *38*(2), 284-289.

Anderson, H. H. (1994). Centrifugal pumps and allied machinery. Elsevier.

Andersson, O. (2012). Experiment!: planning, implementing and interpreting. John Wiley & Sons.

Antoni, J., Bonnardot, F., Raad, A., & El Badaoui, M. (2004). Cyclostationary modelling of rotating machine vibration signals. *Mechanical systems and signal processing*, 18(6), 1285-1314.

Antoni, J. (2006). The spectral kurtosis: a useful tool for characterising non-stationary signals. *Mechanical systems and signal processing*, 20(2), 282-307.

Antoni, J., & Randall, R. B. (2006). The spectral kurtosis: application to the vibratory surveillance and diagnostics of rotating machines. *Mechanical systems and signal processing*, 20(2), 308-331.

Antoni, J. (2007a). Cyclic spectral analysis in practice. *Mechanical Systems and Signal Processing*, 21(2), 597-630.

Antoni, J. (2007b). Fast computation of the kurtogram for the detection of transient faults. *Mechanical Systems and Signal Processing*, 21(1), 108-124.

Argyropoulos, C. D., & Markatos, N. C. (2015). Recent advances on the numerical modelling of turbulent flows. *Applied Mathematical Modelling*, *39*(2), 693-732.

Arndt, R. E. (1981). Cavitation in fluid machinery and hydraulic structures. Annual Review of Fluid Mechanics, 13(1), 273-326.

Athavale, M. M., Li, H. Y., Jiang, Y. U., & Singhal, A. K. (2002). Application of the full cavitation model to pumps and inducers. *International Journal of Rotating Machinery*, 8(1), 45-56.

Ayad, A. F., Abdalla, H. M., & Aly, A. A. E. A. (2015). Effect of semi-open impeller side clearance on the centrifugal pump performance using CFD. *Aerospace Science and Technology*, *47*, 247-255.

Bakir, F., Rey, R., Gerber, A. G., Belamri, T., & Hutchinson, B. (2004). Numerical and experimental investigations of the cavitating behavior of an inducer. *International Journal of Rotating Machinery*, *10*(1), 15-25.

Baldassarre, A., De Lucia, M., & Nesi, P. (1998). Real-time detection of cavitation for hydraulic turbomachines. *Real-Time Imaging*, 4(6), 403-416.

Barkov, A. V., & Barkova, N. A. (1996). Diagnostic of gearing and geared couplings using spectrum methods. *In Proc. of the 20th Annual Meeting of the Vibration Institute*, Saint Louis, Missouri, USA.

Barre, S., Rolland, J., Boitel, G., Goncalves, E., & Patella, R. F. (2009). Experiments and modeling of cavitating flows in venturi: attached sheet cavitation. *European Journal of Mechanics-B/Fluids*, 28(3), 444-464.

Barrio, R., Blanco, E., Parrondo, J., González, J., & Fernández, J. (2008). The effect of impeller cutback on the fluid-dynamic pulsations and load at the blade-passing frequency in a centrifugal pump. *Journal of fluids engineering*, 130(11).

Batchelor, G. K. (2000). An introduction to fluid dynamics. Cambridge university press.

Bechhoefer, E., Kingsley, M., & Menon, P. (2011). Bearing envelope analysis window selection using spectral kurtosis techniques. *In 2011 IEEE Conference on Prognostics and Health Management* (pp. 1-6). IEEE.

Best, J. P. (1993). The formation of toroidal bubbles upon the collapse of transient cavities. Journal of Fluid Mechanics, 251, 79-107.

Blume, M., & Skoda, R. (2015). Numerical 3D analysis of cloud cavitation shedding frequency on a circular leading edge hydrofoil with a barotropic cavitation model. *In Journal of Physics: Conference Series* (Vol. 656, No. 1, p. 012146). IOP Publishing.

Boccazzi, A., Perdichizzi, A., Schiavello, B., & Tabacco, U. (1989). Cavitation Behaviour and Internal Flow Measurements by Laser Doppler Anemometry in a Low Solidity Inducer. *Proceedings of the XXth Hydraulics Open Days on Hydraulic Machinery*, Lyon, France.

Boitel, G., Fedala, D., & Myon, N. (2016). Tip clearance effects on loads and performances of semi-open impeller centrifugal pumps at different specific speeds. *IOP Earth Environ. Sci*, *49*, 032013.

Botero, F., Hasmatuchi, V., Roth, S., & Farhat, M. (2014). Non-intrusive detection of rotating stall in pump-turbines. *Mechanical Systems and Signal Processing*, 48(1-2), 162-173.

Bourdon, P., Simoneau, R., & Dorey, J. M. (1994). Accelerometer and pit counting detection of cavitation erosion on a laboratory jet and a large Francis turbine. *In 17th IAHR Symposium on Hydraulic machinery and cavitation (No. CONF).* International Association For Hydraulic Research.

Braun, S. (Ed.). (1986). Mechanical signature analysis: theory and applications.

Brennen, C. E. (2005). Fundamentals of multiphase flow. Cambridge university press.

Brennen, C. E. (2011). Hydrodynamics of pumps. Cambridge University Press.

Brennen, C. E. (2014). Cavitation and bubble dynamics. Cambridge University Press.

Cardona-Morales, O., Sierra-Alonso, E. F., & Castellanos-Dominguez, G. (2018). Bearing Fault Identification Based on Blind Extraction of Cyclostationary Signals Using Order Tracking. *In Advances in Condition Monitoring of Machinery in Non-Stationary Operations* (pp. 191-201). Springer, Cham.

Cernetič, J., Prezelj, J., & Čudina, M. (2008). Use of noise and vibration signal for detection and monitoring of cavitation in kinetic pumps. *The Journal of the Acoustical Society of America*, 123(5), 3316-3316.

Cernetič, J., & Chudina, M. (2012). Cavitation noise phenomena in centrifugal pumps. *In 5th Congress of Alps-Adria Acoustics Association (Vol. 1)*.

Chang, Y., Jiang, F., Zhu, Z., & Li, W. (2017). Fault diagnosis of rotating machinery based on time-frequency decomposition and envelope spectrum analysis. *Journal of Vibroengineering*, 19(2), 943-954.

Chen, Y., & Heister, S. D. (1994). A numerical treatment for attached cavitation. *J. Fluids Eng*. 116(3): 613-618.

Chen, Y., & Heister, S. D. (1996). Modeling hydrodynamic nonequilibrium in cavitating flows. *J. Fluids Eng*. 118(1): 172-178 (7 pages)

Chrysovergis, M., "Parametric Design, Computational Simulation & Investigation of Improvement Margins in Direct & Inverse Operation of Centrifugal Pumps", PhD, School of Mechanical Engineering, National Technical University of Athens, (in Greek), p. 378, (2017).

Chu, S., Dong, R., & Katz, J. (1995). Relationship between unsteady flow, pressure fluctuations, and noise in a centrifugal pump—part B: effects of blade-tongue interactions. *J. Fluids Eng.*, 117(1), 30-35.

Chudina, M. (2003a). Detection of cavitation phenomenon in a centrifugal pump using audible sound. *Mechanical systems and signal processing*, 17(6), 1335-1347.

Chudina, M. (2003b). Noise as an indicator of cavitation in a centrifugal pump. *Acoustical physics*, 49(4), 463-474.

Chudina, M. (2007). Pumps and pumping system noise and vibration prediction and control. Handbook of Noise and Vibration Control, 897-909.

Chudina, M., & Prezelj, J. (2009a). Detection of cavitation in operation of kinetic pumps. Use of discrete frequency tone in audible spectra. *Applied Acoustics*, 70(4), 540-546.

Chudina, M., & Prezelj, J. (2009b). Detection of cavitation in situ operation of kinetic pumps: effect of cavitation on the characteristic discrete frequency component. *Applied acoustic*s, 70(9), 1175-1182.

Ćorić, D., Aleksandrov, T., & Trstenjak, S. (2010). Significance of preload in the testing machine calibration procedure. *Transactions of FAMENA*, 34(2), 59-70.

Coutier-Delgosha, O., Fortes-Patella, R., & Reboud, J. L. (2003a). Evaluation of the turbulence model influence on the numerical simulations of unsteady cavitation. J. Fluids Eng., 125(1), 38-45.

Coutier-Delgosha, O., Fortes-Patella, R., Reboud, J. L., Hofmann, M., & Stoffel, B. (2003b). Experimental and numerical studies in a centrifugal pump with two-dimensional curved blades in cavitating condition. *J. Fluids Eng.*, 125(6), 970-978.

Coutier-Delgosha, O., Stutz, B., Vabre, A., & Legoupil, S. (2007). Analysis of cavitating flow structure by experimental and numerical investigations. *Journal of Fluid Mechanics*, 578, 171-222.

Cunha, M. A. R., & Nova, H. F. V. (2013). Cavitation modelling of a centrifugal pump impeller. *In 22nd International Congress of Mechanical Engineering*, Ribeirao Petro, Sao Paulo, Brazil.

Darlow, M. S., Badgley, R. H., & Hogg, G. W. (1974). Application of high-frequency resonance techniques for bearing diagnostics in helicopter gearboxes (No. MTI-74TR25). *Mechanical Technology Inc Latham NY*.

Dauby, D., Queutey, P., Leroyer, A., & Visonneau, M. (2006). Computation of 2D cavitating flows ant tip vortex flows with an unstructured RANSE solver.

Daugherty, R. L. (1915). Centrifugal pumps. McGraw-Hill Book Company, Incorporated.

Dellanoy, Y., & Kueny, J. L. (1990). Two phase flow approach in unsteady cavitation modeling. *ASME FED*, 98, 153-158.

Deshpande, M., Feng, J., & Merkle, C. L. (1994). Cavity flow predictions based on the Euler equations. *J. Fluids Eng*. 116(1): 36-44 (9 pages).

Dick, E., Vierendeels, J., Serbruyns, S., & Voorde, J. V. (2001). Performance prediction of centrifugal pumps with CFD-tools. *Task quarterly*, 5(4), 579-594.

Ding, H., Visser, F. C., Jiang, Y., & Furmanczyk, M. (2011). Demonstration and validation of a 3D CFD simulation tool predicting pump performance and cavitation for industrial applications. *Journal of fluids engineering*, 133(1).

Dong, G., & Chen, J. (2012). Investigation into various techniques of cyclic spectral analysis for rolling element bearing diagnosis under influence of gear vibrations. *In Journal of Physics: Conference Series* (Vol. 364, No. 1, p. 012039). IOP Publishing.

Dong, L., Zhao, Y., & Dai, C. (2019). Detection of inception cavitation in centrifugal pump by fluid-borne noise diagnostic. Shock and Vibration, 2019.

Dörfler, P. (1982). System dynamics of the Francis turbine half load surge. *IAHR section hydraulic machinery, equipment, and cavitation. In 11th Symposium* (Amsterdam, 1982) (Vol. 2).

Dörfler, P., Sick, M., & Coutu, A. (2012). Flow-induced pulsation and vibration in hydroelectric machinery: engineer's guidebook for planning, design and troubleshooting. Springer Science & Business Media.

Duplaa, S., Coutier-Delgosha, O., Dazin, A., Roussette, O., Bois, G., & Caignaert, G. (2010). Experimental study of a cavitating centrifugal pump during fast startups. *Journal of Fluids Engineering*, 132(2).

Dwyer, R. F. (1981). FRAM 2 Single Channel Ambient Noise Statistics. *In Presented at the 101st Meeting of the Acoust. Soc. of Am. Ottawa (Canada)*.

Dwyer, R. (1983a). Detection of non-Gaussian signals by frequency domain kurtosis estimation. In ICASSP'83. *IEEE International Conference on Acoustics, Speech, and Signal Processing* (Vol. 8, pp. 607-610). IEEE.

Dwyer, R. F. (1983b). A technique for improving detection and estimation of signals contaminated by under ice noise. *The Journal of the Acoustical Society of America*, 74(1), 124-130.

Dwyer, R. (1984). Use of the kurtosis statistic in the frequency domain as an aid in detecting random signals. *IEEE Journal of Oceanic Engineering*, 9(2), 85-92.

Escaler, X., Egusquiza, E., Mebarki, T., Avellan, F., & Farhat, M. (2002). Field assessment of cavitation detection methods in hydropower plants. *In Proceedings of the 21st IAHR Symposium on Hydraulic Machinery and Systems*, Lausanne, Switzerland (Vol. 1, No. CONF, pp. 483-490). International Association For Hydraulic Research.

Escaler, X., Egusquiza, E., Farhat, M., & Avellan, F. (2003). Vibration cavitation detection using onboard measurements. *In fifth international Symposium on Cavitation* (Vol. 5).

Escaler, X., Egusquiza, E., Farhat, M., & Avellan, F. (2004). Cavitation erosion prediction in hydro turbines from onboard vibrations. *In Proceedings of the 22nd IAHR Symposium on Hydraulic Machinery and Systems*, Stockholm, Sweden (Vol. 1, No. CONF, pp. 1-10). International Association For Hydraulic Research.

Escaler, X., Farhat, M., Ausoni, P., Egusquiza, E., & François, A. (2006). Cavitation monitoring of hydroturbines: tests in a francis turbine model. *Sixth International Symposium on Cavitation.*

Escaler, X., Ekanger, J. V., Francke, H. H., Kjeldsen, M., & Nielsen, T. K. (2015). Detection of draft tube surge and erosive blade cavitation in a full-scale Francis turbine. *Journal of Fluids Engineering*, 137(1).

Farokhzad, S. (2013). Vibration based fault detection of centrifugal pump by fast fourier transform and adaptive neuro-fuzzy inference system. *Journal of mechanical engineering and technology*, 1(3), 82-87.

Farrance, I., & Frenkel, R. (2012). Uncertainty of measurement: a review of the rules for calculating uncertainty components through functional relationships. *The Clinical Biochemist Reviews*, 33(2), 49.

Figliola, R. S., & Beasley, D. E. (2001). Theory and design for mechanical measurements. John Wiley & Sons, Inc.

FLUENT, ANSYS (2009). 12.0 Theory Guide. Ansys Inc, 5(5).

Frikha, S., Coutier-Delgosha, O., & Astolfi, J. A. (2008). Influence of the cavitation model on the simulation of cloud cavitation on 2D foil section. *International Journal of Rotating Machinery*, 2008.

Friedrichs, J., & Kosyna, G. N. (2002). Rotating cavitation in a centrifugal pump impeller of low specific speed. *J. Fluids Eng.*, 124(2), 356-362.

Fu, Y., Yuan, J., Yuan, S., Pace, G., d'Agostino, L., Huang, P., & Li, X. (2015). Numerical and experimental analysis of flow phenomena in a centrifugal pump operating under low flow rates. *Journal of Fluids Engineering*, *137*(1).

Ganeriwala, S. N., & Kanakasabai, V. (2011). Using vibration signatures analysis to detect cavitation in centrifugal pumps. *In Rotating Machinery, Structural Health Monitoring, Shock and Vibration*, Volume 5 (pp. 499-507). Springer, New York, NY.

German Calibration Service 2014, Calibration of Pressure Gauges, DKD-R 6-1, German Calibration Service, Braunschweig.

Gohil, P. P., & Saini, R. P. (2016). Numerical Study of Cavitation in Francis Turbine of a Small Hydro Power Plant. Journal of Applied Fluid Mechanics, 9(1).

Gopalakrishnan, S. (1985). Modern cavitation criteria for centrifugal pumps. *In Proceedings of the 2nd International Pump Symposium. Turbomachinery Laboratories*, Department of Mechanical Engineering, Texas A&M University.

Gopalan, S., & Katz, J. (2000). Flow structure and modeling issues in the closure region of attached cavitation. *Physics of fluids*, 12(4), 895-911.

Greitzer, E. M., Tan, C. S., & Graf, M. B. (2007). Internal flow: concepts and applications (Vol. 3). Cambridge University Press.

Gryllias, K., Yiakopoulos, C., & Antoniadis, I. (2008). Application of morphological analysis for gear fault detection and trending. Diagnostyka, 37-42.

Gryllias, K. C., Antoniadis, I. A. (2012). A Support Vector Machine approach based on physical model training for rolling element bearing fault detection in industrial environments. Engineering Applications of Artificial Intelligence, 25(2), 326-344.

Gülich, J. F. (1989). Guidelines for prevention of cavitation in centrifugal feedpumps (No. EPRI-GS-6398). Electric Power Research Inst., Palo Alto, CA (USA); Sulzer Bros. Ltd., Winterthur (Switzerland).

Gülich, J. F. (2008). Centrifugal pumps (Vol. 2). Berlin: Springer.

Gummer, J. H., & Hensman, P. C. (1992). A review of stayvane cracking in hydraulic turbines. *International Water Power and Dam Construction IWPCDM*, 44(8), 32-42.

Harada, I., Kobayasi, K., & Ono, S. (2010). Prediction of axial thrust for mixed-flow pumps with vaned diffuser by using CFD. *International Journal of Fluid Machinery and Systems*, 3(2), 160-168.

Hasegawa, Y., Kikuyama, K., Maeda, T., & Murakami, M. (1990). Unsteady pressure distributions and forces on the impeller blades of a centrifugal pump. *In Proc. of 15th IAHR Symposium*, Belgrade, Yugoslavia (pp. 11-14).

Hatano, S., Kang, D., Kagawa, S., Nohmi, M., & Yokota, K. (2014). Study of cavitation instabilities in double-suction centrifugal pump. *International Journal of Fluid Machinery and Systems*, 7(3), 94-100.

Hejranfar, K., Ezzatneshan, E., & Fattah-Hesari, K. (2015). A comparative study of two cavitation modeling strategies for simulation of inviscid cavitating flows. *Ocean Engineering*, 108, 257-275.

Hergt, P., & Starke, J. (1985). Flow patterns causing instabilities in the performance curves of centrifugal pumps with vaned diffusers. *In Proceedings of the 2nd International Pump Symposium*. Turbomachinery Laboratories, Department of Mechanical Engineering, Texas A&M University.

Heskestad, G., & Olberts, D. R. (1960). Influence of trailing-edge geometry on hydraulic-turbine-blade vibration resulting from vortex excitation. *Transactions of the ASME Journal of Engineering for Power*, 82A, 103–110.

Hirschi, R., Dupont, P., Avellan, F., Favre, J. N., Guelich, J. F., & Parkinson, E. (1998). Centrifugal pump performance drop due to leading edge cavitation: numerical predictions compared with model tests. *J. Fluids Eng*. 120(4): 705-711 (7 pages).

Hofmann, M., Stoffel, B., Coutier-Delgosha, O., Fortes-Patella, R., & Reboud, J. L. (2001). Experimental and numerical studies on a centrifugal pump with 2D-curved blades in cavitating condition. *http://resolver. caltech. edu/cav2001: sessionB7. 005*.

Holland, F. A., & Chapman, F. S. (1966). Pumping of liquids. Reinhold, New York.

Hong, S. S., Kim, J. S., Choi, C. H., & Kim, J. (2006). Effect of tip clearance on the cavitation performance of a turbopump inducer. *Journal of Propulsion and Power*, *22*(1), 174-179.

Hu, A., Xiang, L., Xu, S., & Lin, J. (2019). Frequency loss and recovery in rolling bearing fault detection. *Chinese Journal of Mechanical Engineering*, 32(1), 35.

Humble, R. A., Scarano, F., Van Oudheusden, B. W., & Tuinstra, M. (2006). PIV measurements of a shock wave/turbulent boundary layer interaction. In *Thirteenth Intl Symp. on Laser Techniques to Fluid Mechanics, Lisbon, Portugal, Paper* (Vol. 14).

Iliescu, M. S., Ciocan, G. D., & Avellan, F. (2008). Analysis of the cavitating draft tube vortex in a Francis turbine using particle image velocimetry measurements in two-phase flow. *Journal of Fluids Engineering*, 130(2).

International Electrotechnical Commission 2019, Hydraulic turbines, storage pumps and pump-turbines - Model acceptance tests, IEC 60193:2019, International Electrotechnical Commission, Geneva.

International Organization for Standardization 1995, Hydraulic fluid power - General rules and safety requirements for systems and their components, ISO 4413:1995, International Organization for Standardization, Geneva.

International Organization for Standardization 2009, Mechanical vibration - Evaluation of machine vibration by measurements on non-rotating parts - Part 1: General guidelines, ISO 10816-1, International Organization for Standardization, Geneva.

International Organization for Standardization 2009, Mechanical vibration - Evaluation of machine vibration by measurements on non-rotating parts - Part 7: Rotodynamic pumps for industrial applications, including measurements on rotating shafts, ISO 10816-7, International Organization for Standardization, Geneva.

International Organization for Standardization 2012, Rotodynamic pumps: Hydraulic performance acceptance tests: Grades 1, 2 and 3, ISO 9906:2012, International Organization for Standardization, Geneva.

Jacob, T., & Prénat, J. E. (1996). Francis turbine surge: discussion and data base. *In Hydraulic Machinery and Cavitation* (pp. 855-864). Springer, Dordrecht.

Jain, S. V., Patel, N. K., & Patel, R. N. (2017). Experimental investigations of cavitation characteristics of pump running in turbine mode. *Journal of Energy Engineering*, 143(1), 04016034.

Jese, U., Fortes-Patella, R., & Antheaume, S. (2014). High head pump-turbine: Pumping mode numerical simulations with a cavitation model for off-design conditions. *In IOP Conference Series: Earth and Environmental Science* (Vol. 22, No. 3, p. 032048). IOP Publishing.

Ji, B., Luo, X., Peng, X., Wu, Y., & Xu, H. (2012). Numerical analysis of cavitation evolution and excited pressure fluctuation around a propeller in non-uniform wake. *International Journal of Multiphase Flow*, 43, 13-21.

Jones, G. M., Sanks, R. L., Bosserman, B. E., & Tchobanoglous, G. (Eds.). (2006). Pumping station design. Gulf Professional Publishing.

Jošt, D., Morgut, M., Škerlavaj, A., & Nobile, E. (2015). Cavitation prediction in a Kaplan turbine using standard and optimized model parameters. *In Proceedings of the 6th IAHR Meeting of the Working Group on Cavitation and Dynamic Problems in Hydraulic Machinery and Systems*.

Kamiel, B. P. (2015). Vibration-based multi-fault diagnosis for centrifugal pumps (Doctoral dissertation, Curtin University).

Kamijo, K., Shimura, T., & Watanabe, M. (1977). An experimental investigation of cavitating inducer instability. *ASME Paper* 77-WA/FW-14

Kamijo, K., Yoshida, M., & Tsujimoto, Y. (1992). Hydraulic and mechanical performance of LE-7 LOX pump inducer. *Proc. 28th Joint Propulsion Conf.*, Paper AIAA-92-3133.

Kang, D., Watanabe, T., Yonezawa, K., Horiguchi, H., Kawata, Y., & Tsujimoto, Y. (2009). Inducer design to avoid cavitation instabilities. *International Journal of Fluid Machinery and Systems*, 2(4), 439-448.

Kang, D., Arimoto, Y., Yonezawa, K., Horiguchi, H., Kawata, Y., Hah, C., & Tsujimoto, Y. (2010). Suppression of cavitation instabilities in an inducer by circumferential groove and explanation of higher frequency components. *International Journal of Fluid Machinery and Systems*, 3(2), 137-149.

Kang, W. Z., Zhou, L. J., Wang, Z. W., & Wang, W. (2019). Analysis of backflow effect in a centrifugal pump. In *IOP Conference Series: Earth and Environmental Science* (Vol. 240, No. 3, p. 032007). IOP Publishing.

Karassik, I. J. & Carter, R. (1960). Centrifugal pumps: Selection, Operation and Maintenance. McGraw-Hill, New York.

Karassik, I. J. (2007). Pump Handbook Fourth Edition. McGraw-Hill, New York.

Kassanos, I., Chrysovergis, M., Anagnostopoulos, J., Papantonis, D., & Charalampopoulos, G. (2016a). Numerical performance evaluation of design modifications on a centrifugal pump impeller running in reverse mode. In *AIP Conference Proceedings* (Vol. 1738, No. 1, p. 480084). AIP Publishing.

Kassanos, I., Papantonis, D. (2016b). Calibration of the Pelton test rig pressure transducer PTR8 (Nr.1). *Laboratory of hydraulic turbomachines (LHT) calibration documentation*.

Kassanos, I., Papantonis, D. (2016c). Calibration of the ABB electromagnetic flow meter. *Laboratory of hydraulic turbomachines (LHT) calibration documentation*.

Kassanos, I., Papantonis, D. (2016d). Calibration of TTR6 M425 500Nm torque meter. *Laboratory of hydraulic turbomachines (LHT) calibration documentation*.

Kaya, M., & Ayder, E. (2017). Prediction of cavitation performance of radial flow pumps. *Journal of Applied Fluid Mechanics*, *10*(5), 1397-1408.

Kermeen, R. W. (1956). Water tunnel tests of NACA 4412 and Walchner Profile 7 hydrofoils in noncavitating and cavitating flows.

Khalifa, A. E., Al-Qutub, A. M., & Ben-Mansour, R. (2011). Study of pressure fluctuations and induced vibration at blade-passing frequencies of a double volute pump. *Arabian journal for science and engineering*, 36(7), 1333-1345.

Kim, C., Kim, S., Choi, C. H., & Baek, J. (2017). Effects of inducer tip clearance on the performance and flow characteristics of a pump in a turbopump. *Proceedings of the Institution of Mechanical Engineers, Part A: Journal of Power and Energy*, *231*(5), 398-414.

Kim, H. Y. (2013). Statistical notes for clinical researchers: assessing normal distribution (2) using skewness and kurtosis. Restorative dentistry & endodontics, 38(1), 52-54.

Kim, K. H., Chahine, G., Franc, J. P., & Karimi, A. (2014). Advanced experimental and numerical techniques for cavitation erosion prediction (Vol. 106). Springer.

Kim, M. J., Jin, H. B., & Chung, W. J. (2012). A study on prediction of cavitation for centrifugal pump. World academy of science, engineering and technology, 6, 12-22.

Kim, S., Choi, C., Kim, J., Park, J., & Baek, J. (2013). Tip clearance effects on cavitation evolution and head breakdown in turbopump inducer. *Journal of Propulsion and Power*, *29*(6), 1357-1366.

Kimura, T., Yoshida, Y., Hashimoto, T., & Shimagaki, M. (2008). Numerical simulation for vortex structure in a turbopump inducer: Close relationship with appearance of cavitation instabilities. *Journal of fluids engineering*, *130*(5).

Kobayashi, K., & Chiba, Y. (2010). Computational fluid dynamics of cavitating flow in mixed flow pump with closed type impeller. *International Journal of Fluid Machinery and Systems*, 3(2), 113-121.

Kotb, A., & Abdulaziz, A. M. (2015). Cavitation detection in variable speed pump by analyzing the acoustic and vibration spectrums. *Engineering*, 7(10), 706.

Kunz, R. F., Boger, D. A., Stinebring, D. R., Chyczewski, T. S., Lindau, J. W., Gibeling, H. J., Venkateswaran S. & Govindan, T. R. (2000). A preconditioned Navier–Stokes method for two-phase flows with application to cavitation prediction. Computers & Fluids, 29(8), 849-875.

Launder, B. E., & Spalding, D. B. (1974). The Numerical Computation of Turbulent Flows, *Comput. Methods Appl. Mech. Eng.*, Vol. 3, pp. 269–289.

Lennemann, E., & Howard, J. H. G. (1970). Unsteady flow phenomena in rotating centrifugal impeller passages. *J. Eng. Power*. Jan 1970, 92(1): 65-71.

Li, D. Q. (2011). Prediction of non-cavitating and cavitating performance of a SVA Potsdam propeller. In *Second International Symposium on Marine Propulsors*. Hamburg University of Technology Hamburg.

Li, L., Li, M., & Chen, F. (2016). A Fast Kurtogram Demodulation Method in Rolling Bearing Fault Diagnosis. *In MATEC Web of Conferences* (Vol. 77, p. 01003). EDP Sciences.

Li, W. G. (2014). Validating full cavitation model with an experimental centrifugal pump. *Task Quarterly*, 18(1), 81-100.

Li, X. R. (1999). Probability, random signals, and statistics. CRC press.

Liang, D., Yuqi, Z., Cui, D., & Yong, W. (2018). Research on cavitation acoustic characteristics of centrifugal pump based on fluid-acoustic field coupling method. *Advances in Mechanical Engineering*, 10(5), 1687814018773665.

Limbach, P., Müller, T., & Skoda, R. (2015). Application of a compressible flow solver and barotropic cavitation model for the evaluation of the suction head in a low specific speed centrifugal pump impeller channel. *In Journal of Physics: Conference Series* (Vol. 656, No. 1, p. 012065). IOP Publishing.

Limbach, P., & Skoda, R. (2017). Numerical and experimental analysis of cavitating flow in a low specific speed centrifugal pump with different surface roughness. *Journal of Fluids Engineering*, 139(10), 101201.

Lin, S. C., & Huang, Y. (2017). A histogram statistical method for the detection of localized faults in deep groove ball bearing. *In MATEC Web of Conferences* (Vol. 123, p. 00009). EDP Sciences.

Lindau, J. W., Moody, W. L., Kinzel, M. P., Dreyer, J. J., Kunz, R. F., & Paterson, E. G. (2009). Computation of cavitating flow through marine propulsors. In *Proceedings of the 1st International Symposium on Marine Propulsors*.

Liu, H. L., Liu, D. X., Wang, Y., Wu, X. F., & Wang, J. (2013). Application of modified k-ω model to predicting cavitating flow in centrifugal pump. Water Science and Engineering, 6(3), 331-339.

Liu, J., Liu, S., Wu, Y., Jiao, L., Wang, L., & Sun, Y. (2012). Numerical investigation of the hump characteristic of a pump–turbine based on an improved cavitation model. *Computers & Fluids*, 68, 105-111.

Liu, L., Li, J., & Feng, Z. (2006). A numerical method for simulation of attached cavitation flows. *International journal for numerical methods in fluids*. 52(6), 639-658.

Liu, S., Wu, Y., & Luo, X. (2005). Numerical simulation of 3D cavitating turbulent flow in Francis turbine. *In ASME 2005 Fluids Engineering Division Summer Meeting* (pp. 1551-1556). American Society of Mechanical Engineers Digital Collection.

Lobanoff, V. S., & Ross, R. R. (2013). Centrifugal pumps: design and application. Elsevier.

Lorusso, M., Capurso, T., Torresi, M., Fortunato, B., Fornarelli, F., Camporeale, S. M., & Monteriso, R. (2017). Efficient CFD evaluation of the NPSH for centrifugal pumps. *Energy Procedia*, 126, 778-785.

Lu, G. C., Zuo, Z. G., Liu, S. H., Fan, Y. Z., & Wu, Y. L. (2014). Numerical studies of the influence of casing shape on the hydraulic performance of a centrifugal boiler circulating pump. *2014 ISFMFE - 6th International Symposium on Fluid Machinery and Fluid Engineering*.

Lu, J., Yuan, S., Parameswaran, S., Yuan, J., Ren, X., & Si, Q. (2017). Investigation on the vibration and flow instabilities induced by cavitation in a centrifugal pump. *Advances in Mechanical Engineering*, 9(4).

Lu, J., Liu, X., Zeng, Y., Zhu, B., Hu, B., Yuan, S., & Hua, H. (2019). Detection of the Flow State for a Centrifugal Pump Based on Vibration. *Energies*, 12(16), 3066.

Luo, X., Liu, S., Zhang, Y., & Xu, H. (2008). Cavitation in semi-open centrifugal impellers for a miniature pump. *Frontiers of Energy and Power Engineering in China*, *2*(1), 31-35.

Ma, X., Lyu, K., Zhang, S., Zhou, P., & Huang, L. (2019). Numerical Simulation of Unsteady Flow in A Centrifugal Pump. *E3SWC*, 136, 03027.

Mancuso, G., Langone, M., & Andreottola, G. (2020). A critical review of the current technologies in wastewater treatment plants by using hydrodynamic cavitation process: principles and applications. *Journal of Environmental Health Science and Engineering*, 1-23.

MATLAB (2015a). Statistics and Machine Learning Toolbox.

Maxwell, J. H. (1983). Induction motor magnetic vibration. *In Proceedings of the Vibration Institute, Machinery Vibration Monitoring and Analysis Meeting*, Houston, Texas (pp. 213-218).

McFadden, P. D., & Smith, J. D. (1984a). Model for the vibration produced by a single point defect in a rolling element bearing. Journal of sound and vibration, 96(1), 69-82.

McFadden, P. D., & Smith, J. D. (1984b). Vibration monitoring of rolling element bearings by the high-frequency resonance technique—a review. Tribology international, 17(1), 3-10.

McNulty, P. J., Pearsall, I.S. (1982). Cavitation Inception in Pumps, *Journal of Fluids Engineering*, Vol. 104(1), 99-104.

Medvitz, R. B., Kunz, R. F., Boger, D. A., Lindau, J. W., Yocum, A. M., & Pauley, L. L. (2002). Performance analysis of cavitating flow in centrifugal pumps using multiphase CFD. *J. Fluids Eng.*, 124(2), 377-383.

Menter, F. R. (1994). Two-equation eddy-viscosity turbulence models for engineering applications. *AIAA journal*, 32(8), 1598-1605.

Mostafa, N. H., & Boraey, M. A. (2006). Numerical and experimental investigation of cavitation in axial pumps. *In 2006 8th International Congress of Fluid Dynamics and Propulsion* (pp. 14-17).

Moukalled, F., Mangani, L., & Darwish, M. (2016). The finite volume method in computational fluid dynamics (Vol. 113). Berlin, Germany. Springer.

Neale, M.J., Woodley, B.J. (1978). A guide to the condition monitoring of machinery. *Report TRD 223 for the British Department of Industry*.

Neill, G. D., Reuben, R. L., Sandford, P. M., Brown, E. R., & Steel, J. A. (1997). Detection of incipient cavitation in pumps using acoustic emission. *Proceedings of the Institution of Mechanical Engineers, Part E: Journal of process mechanical engineering*, 211(4), 267-277.

Nelik, L. (1999). Centrifugal & rotary pumps: fundamentals with applications. CRC Press.

Niedźwiedzka, A., Schnerr, G. H., & Sobieski, W. (2016). Review of numerical models of cavitating flows with the use of the homogeneous approach. Archives of Thermodynamics, 37(2), 71-88.

Nikolaou, N. G., & Antoniadis, I. A. (2002). Demodulation of vibration signals generated by defects in rolling element bearings using complex shifted Morlet wavelets. *Mechanical systems and signal processing*, 16(4), 677-694.

Papantonis, D. (2016). Hydrodynamic machines, hydrodynamic transmissions. Symeon. Athens. Greece (in Greek).

Parikka, R., & Helle, A. (2006). Monitoring of grease lubrication. *Tribologia*, 25(3), 3-13.

Pascarella, C., & Salvatore, V. (2001, June). Numerical Study of Unsteady Cavitation on a Hydrofoil Section Using a Barotropic Model. *In 4th International Symposium On Cavitation*.

Pearsall, I. S. (1966). Acoustic detection of cavitation. *In Proceedings of the Institution of Mechanical Engineers*, Conference Proceedings (Vol. 181, No. 1, pp. 1-8). Sage UK: London, England: SAGE Publications.

Pennacchi, P., Borghesani, P., Chatterton, S., & Vania, A. (2012a). Hydraulic instability onset detection in Kaplan turbines by monitoring shaft vibrations. *In International Design Engineering Technical Conferences and Computers and Information in Engineering Conference* (Vol. 45004, pp. 715-722). American Society of Mechanical Engineers.

Pennacchi, P., Vania, A., Chatterton, S., & Tanzi, E. (2012b). Detection of unsteady flow in a Kaplan hydraulic turbine using machine mechanical model and rotor measured vibrations. *In ASME Turbo Expo 2012: Turbine Technical Conference and Exposition* (pp. 739-748). American Society of Mechanical Engineers Digital Collection.

Peterson, A. (1933). Twenty years progress in centrifugal water works pumps. Journal (American Water Works Association), 25(10), 1372-1386.

Peyton, A., Walsh, V., & Walsh, Y. (1993). Analog Electronics with Op-amps: A Source Book of Practical Circuits. Cambridge University Press.

Pouffary, B., Patella, R. F., Reboud, J. L., & Lambert, P. A. (2008). Numerical simulation of 3D cavitating flows: analysis of cavitation head drop in turbomachinery. *Journal of Fluids Engineering*, *130*(6).

Pöyhönen, S., Ahonen, T., Ahola, J., Punnonen, P., Hammo, S., & Nygren, L. (2019). Specific speed-based pump flow rate estimator for large-scale and long-term energy efficiency auditing. Energy Efficiency, 12(5), 1279-1291.

Prashad, H., Ghosh, M., & Biswas, S. (1985). Diagnostic monitoring of rolling-element bearings by high-frequency resonance technique. *ASLE transactions*, 28(4), 439-448.

Psoinos, D. (1999). Statistics. Publications Zitis. Thessaloniki, Greece (In Greek).

Qin, Q., Song, C. C., & Arndt, R. E. (2003). A numerical study of the unsteady turbulent wake behind a cavitating hydrofoil. *Bulletin of the American Physical Society*, 48(10), 107.

Rahman, M. T. N., Turzo, M. M., Billah, A. M., Akanda, M. M., & Rahman, M. R. (2019). Repairing and commissioning of an AC motor speed controller for a centrifugal pump. *Journal of Physics and Its Applications*, *1*(2), 47-52.

Randall, R. B. (2004). State of the art in monitoring rotating machinery-part 1. *Sound and vibration*, 38(3), 14-21.

Randall, R. B. (2007). Noise and vibration data analysis. Handbook of Noise and Vibration Control, 549-564.

Randall, R. B. (2011). Vibration-based condition monitoring: industrial, aerospace and automotive applications. John Wiley & Sons.

Randall, R. B., & Antoni, J. (2011). Rolling element bearing diagnostics—A tutorial. Mechanical systems and signal processing, 25(2), 485-520.

Rapposelli, E., & d'Agostino, L. (2003, November). A barotropic cavitation model with thermodynamic effects. *In 5th International Symposium on Cavitation CAV2003*, Osaka, Japan.

Ren, Y., Li, W., Zhang, B., Zhu, Z., & Jiang, F. (2019). Fault Diagnosis of Rolling Bearings Based on Improved Kurtogram in Varying Speed Conditions. *Applied Sciences*, 9(6), 1157.

Romero, D. T., & Jovanovic, G. (2012). Digital FIR Hilbert transformers: fundamentals and efficient design methods. *MATLAB-A Fundam. Tool Sci. Comput. Eng. Appl*, 1, 445-482.

Ruiz-Cárcel, C., Hernani-Ros, E., Cao, Y., & Mba, D. (2014). Use of spectral kurtosis for improving signal to noise ratio of acoustic emission signal from defective bearings. Journal of Failure Analysis and Prevention, 14(3), 363-371.

Saidi, L., Ali, J. B., & Fnaiech, F. (2014). The use of spectral kurtosis as a trend parameter for bearing faults diagnosis. In 2014 15th International Conference on Sciences and Techniques of Automatic Control and Computer Engineering (STA) (pp. 394-399). IEEE.

Saito, Y., Nakamori, I., & Ikohagi, T. (2003). Numerical analysis of unsteady vaporous cavitating flow around a hydrofoil. *In Proc. 5th Int. Symp. Cavitation* (CAV2003), Osaka.

Sawalhi, N., & Randall, R. B. (2004). The application of spectral kurtosis to bearing diagnostics. *In Proceedings of ACOUSTICS* (pp. 3-5).

Scheffer, C. (2008). Pump condition monitoring through vibration analysis. *In Pumps: Maintenance, Design, and Reliability Conference* (pp. 1135-1146).

Schiavello, B., & Visser, F. C. (2009). Pump Cavitation: various $NPSH_R$ criteria, $NPSH_A$ margins, impeller life expectancy. *In Proceedings of the 25th international pump users symposium*. Texas A&M University. Turbomachinery Laboratories.

Schmidt, H., Kirschner, O., Riedelbauch, S., Necker, J., Kopf, E., Rieg, M., Arantes G., Wessiak M. & Mayrhuber, J. (2014). Influence of the vibro-acoustic sensor position on cavitation detection in a Kaplan turbine. *In IOP Conference Series: Earth and Environmental Science* (Vol. 22, No. 5, p. 052006). IOP Publishing.

Schnerr, G. H., & Sauer, J. (2001). Physical and numerical modeling of unsteady cavitation dynamics. In Fourth international conference on multiphase flow (Vol. 1). ICMF New Orleans.

Sedlar, M., Zima, P., & Muller, M. (2009). CFD Analysis of cavitation erosion potential in hydraulic machinery. *In Proc. 3rd IAHR WG Meeting* (pp. 205-214).

Sheen, Y. T. (2009). On the study of applying Morlet wavelet to the Hilbert transform for the envelope detection of bearing vibrations. *Mechanical Systems and Signal Processing*, 23(5), 1518-1527.

Shen, Y., & Dimotakis, P. E. (1989). The influence of surface cavitation on hydrodynamic forces. In American towing tank conference, 22nd.

Shengcai, L. (Ed.). (2000). Cavitation of hydraulic machinery (Vol. 1). World Scientific.

Shimazaki, H., & Shinomoto, S. (2007). A method for selecting the bin size of a time histogram. Neural computation, 19(6), 1503-1527.

Singhal, A. K., Athavale, M. M., Li, H., & Jiang, Y. (2002). Mathematical basis and validation of the full cavitation model. J. Fluids Eng., 124(3), 617-624.

Sloteman, D. P. (2007). Cavitation in high energy pumps-Detection and assessment of damage potential. *In Proceedings of the 23rd International Pump Users Symposium*. Texas A&M University. Turbomachinery Laboratories.

Stepanoff, A. J. (1957). Centrifugal and axial flow pumps. Theory, Design, and Application.

Stopa, M. M., Cardoso Filho, B. J., & Martinez, C. B. (2013). Incipient detection of cavitation phenomenon in centrifugal pumps. IEEE Transactions on industry applications, 50(1), 120-126.

Tani, N., Yamanishi, N., & Tsujimoto, Y. (2012). Influence of flow coefficient and flow structure on rotational cavitation in inducer. *Journal of fluids engineering*, *134*(2).

Taylor, J. I. (2005). The vibration analysis handbook, Vibration Consultants.

Taylor, J. R. (1997). Introduction to error analysis, the study of uncertainties in physical measurements.

TCF (2018). Performance Characteristics of Centrifugal Fans, Twin City Fan.

Teng, W., Ding, X., Zhang, Y., Liu, Y., Ma, Z., & Kusiak, A. (2017). Application of cyclic coherence function to bearing fault detection in a wind turbine generator under electromagnetic vibration. *Mechanical Systems and Signal Processing*, 87, 279-293.

Thoma, D. (1935). "Bericht zur Weltkraftkonferenz London 1924," *Zeitschrift des Vereines deutscher Ingenieure*, vol. 79, p. 329

Thornycroft, J. I., & Barnaby, S. W. (1895). Torpedo boat destroyers. In Minutes of the Proceedings of the Institution of Civil Engineers (Vol. 122, No. 1895, pp. 51-69). Thomas Telford-ICE Virtual Library.

Toebes, G. H., & Eagleson, P. S. (1961). Hydroelastic vibrations of flat plates related to trailing edge geometry. *J. Basic Eng*. 83(4): 671–678.

Torbjørn, K. Nielsen, T. K. & Antonsen, Ø. (2001). CFD simulation of von Karman vortex shedding. *IAHR Work Group on The Behaviour of Hydraulic Machinery under Steady Oscillatory Conditions*, Trondheim,Norway, June 26-28, 2001.

Tsaggaris, S. (2005). Fluid Mechanics, Symeon, Athens, Greece (in Greek).

Turbine Technologies Ltd. http://www.turbinetechnologies.com/

Valero, C., Egusquiza, M., Valentín, D., Presas, A., & Egusquiza, E. (2019). Behavior of Francis turbines at part load. Field assessment in prototype: Effects on the hydraulic system. *In IOP Conference Series: Earth and Environmental Science* (Vol. 240, No. 5, p. 052029). IOP Publishing.

Varga, J. J., Sebestyen, G., & Fay, A. (1969). Detection of cavitation by acoustic and vibration-measurement methods. *La houille blanche*, (2), 137-150.

Versteeg, H. K., & Malalasekera, W. (2007). An introduction to computational fluid dynamics: the finite volume method. Pearson education.

Wack, J., & Riedelbauch, S. (2015). Numerical simulations of the cavitation phenomena in a Francis turbine at deep part load conditions. In Journal of Physics: Conference Series (Vol. 656, No. 1, p. 012074). IOP Publishing.

Wack, J., & Riedelbauch, S. (2019). Cavitation Simulations of a Tip Leakage Vortex for a NACA0009 Hydrofoil and a Francis Turbine at Stable Full Load Operating Point. In *High Performance Computing in Science and Engineering'18* (pp. 351-365). Springer, Cham.

Wang, F., Zhu, Y., Li, X., Ma, J., Wang, L., & Tang, X. (2007). Experimental investigation of pressure fluctuation and vibration in a large Francis turbine. *In ASME/JSME 2007 5th Joint Fluids Engineering Conference* (pp. 879-884). American Society of Mechanical Engineers Digital Collection.

Wang, K., Zhang, Z., Xia, C., & Liu, Z. (2018). Experimental investigation of pressure fluctuation, vibration, and noise in a multistage pump. *Shock and vibration*, 2018.

Wang, Y., Liu, H., Liu, D., Yuan, S., Wang, J., & Jiang, L. (2016). Application of the two-phase three-component computational model to predict cavitating flow in a centrifugal pump and its validation. *Computers & Fluids*, 131, 142-150.

Welch, P. (1967). The use of fast Fourier transform for the estimation of power spectra: a method based on time averaging over short, modified periodograms. *IEEE Transactions on audio and electroacoustics*, 15(2), 70-73.

White, F. (2011). Fluid Mechanics. McGraw-Hill, New York.

Wilcox, D. C. (1988). Reassessment of the Scale-determining Equation for Advanced Turbulence Models, *AIAA J.*, Vol. 26, No. 11, pp. 1299–1310.

Wilcox, D. C. (1993a). Comparison of Two-equation Turbulence Models for Boundary Layers with Pressure Gradients, *AIAA J.*, Vol. 31, No. 8, pp. 1414– 1421.

Wilcox, D. C. (1993b). Turbulence Modelling for CFD, DCW Industries Inc., La Canada, CA.

Wilcox, D. C. (1994). Simulating Transition with a Two-equation Turbulence Model, *AIAA J.*, Vol. 32, pp. 247–255.

Wood, G. M., Welna, H., & Lamers, R. P. (1965). Tip-clearance effects in centrifugal pumps.

Wu, Y., Li, S., Liu, S., Dou, H. S., & Qian, Z. (2013). Vibration of hydraulic machinery (pp. 978-94). Springer Netherlands.

Xiang, J., Zhong, Y., & Gao, H. (2015). Rolling element bearing fault detection using PPCA and spectral kurtosis. *Measurement*, 75, 180-191.

Xu, Y., Tan, L., Liu, Y., & Cao, S. (2017). Pressure fluctuation and flow pattern of a mixed-flow pump with different blade tip clearances under cavitation condition. *Advances in Mechanical Engineering*, *9*(4), 1687814017696227.

Yamamoto, K., & Tsujimoto, Y. (2009). A backflow vortex cavitation and its effects on cavitation instabilities. *International Journal of Fluid Machinery and Systems*, *2*(1), 40-54.

Yamamoto, K., Müller, A., Favrel, A., Landry, C., & Avellan, F. (2016). Numerical and experimental evidence of the inter-blade cavitation vortex development at deep part load operation of a Francis turbine. *In Proceedings of the 28th IAHR symposium on Hydraulic Machinery and Systems* (Vol. 49, No. CONF, pp. 1-8). International Association For Hydraulic Research.

Yang, J., Zhou, L., & Wang, Z. (2016). The numerical simulation of draft tube cavitation in Francis turbine at off-design conditions. *Engineering Computations*.

Yang, H. M., Lee, K. Y., Kim, J. H., & Choi, Y. S. (2019). Vibration and flow characteristics near cavitation occurrence in mixed-flow pump. *In IOP Conference Series: Earth and Environmental Science* (Vol. 240, No. 6, p. 062032). IOP Publishing.

Yang, S., & Habchi, C. (2020). Real-fluid phase transition in cavitation modeling considering dissolved non-condensable gas. *Physics of Fluids*, 32(3), 032102.

Yao, Z., Wang, F., Xiao, R., He, C., & Liu, Z. (2011). Experimental investigation of relationship between pressure fluctuations and vibrations for a double suction centrifugal pump. *In ASME-JSME-KSME 2011 Joint Fluids Engineering Conference* (pp. 61-68). American Society of Mechanical Engineers Digital Collection.

Yiakopoulos, C., Gryllias, K., & Antoniadis, I. (2005). Spectral effects of the slip motion in defective rolling element bearings. *Advances in Vibration Engineering*, 4, 199-211.

Yiakopoulos, C. T., Gryllias, K. C., & Antoniadis, I. A. (2011). Rolling element bearing fault detection in industrial environments based on a K-means clustering approach. *Expert Systems with Applications*, 38(3), 2888-2911.

Yokota, K., Mitsuda, K., Tsujimoto, Y., & Kato, C. (2004). A study of vortex structure in the shear layer between main flow and swirling backflow. *JSME International Journal Series B Fluids and Thermal Engineering*, *47*(3), 541-548.

Yoshida, Y. (1991). Rotating stalls in centrifugal impeller/vaned diffuser systems. *In Proc. First ASME/JSME Joint Fluids Eng.*, Conf., Portland, 1991.

Yu, A., Tang, Q., Wang, X., Zhou, D., & Liu, J. (2019). Investigation of the pressure fluctuation alleviation in a hydraulic turbine by runner modification. *Water*, 11(7), 1332.

Zhang, D., Shi, L., Shi, W., Zhao, R., Wang, H., & van Esch, B. B. (2015a). Numerical analysis of unsteady tip leakage vortex cavitation cloud and unstable suction-side-perpendicular cavitating vortices in an axial flow pump. *International Journal of Multiphase Flow*, 77, 244-259.

Zhang, D., Shi, W., Pan, D., & Dubuisson, M. (2015b). Numerical and experimental investigation of tip leakage vortex cavitation patterns and mechanisms in an axial flow pump. *Journal of Fluids Engineering*, 137(12), 121103.

Zhang, D., Shi, W., van Esch, B. B., Shi, L., & Dubuisson, M. (2015c). Numerical and experimental investigation of tip leakage vortex trajectory and dynamics in an axial flow pump. *Computers & fluids*, 112, 61-71.

Zhang, F., Yuan, S., Fu, Q., Pei, J., Böhle, M., & Jiang, X. (2017). Cavitation-induced unsteady flow characteristics in the first stage of a centrifugal charging pump. Journal of Fluids Engineering, 139(1), 011303.

Zhang, H., & Zhang, L. (2012). Numerical simulation of cavitating turbulent flow in a high head Francis turbine at part load operation with OpenFOAM. Procedia Engineering, 31, 156-165.

Zhang, N., Yang, M., Gao, B., & Li, Z. (2015a). Vibration characteristics induced by cavitation in a centrifugal pump with slope volute. *Shock and Vibration*.

Zhang, N., Yang, M., Gao, B., Li, Z., & Ni, D. (2015b). Experimental investigation on unsteady pressure pulsation in a centrifugal pump with special slope volute. *Journal of Fluids Engineering*, 137(6).

Zhang, R., & Chen, H. X. (2013). Numerical analysis of cavitation within slanted axial-flow pump. Journal of Hydrodynamics, Ser. B, 25(5), 663-672.

Zhang, X., Kang, J., Xiao, L., Zhao, J., & Teng, H. (2015). A new improved kurtogram and its application to bearing fault diagnosis. Shock and Vibration, 2015.

Zhou, L., Wang, Z., Luo, Y., & Peng, G. (2008). Numerical simulation of cavitating flow in a Francis turbine. *In ASME 2008 Fluids Engineering Division Summer Meeting collocated with the Heat Transfer, Energy Sustainability, and 3rd Energy Nanotechnology Conferences* (pp. 1193-1197). American Society of Mechanical Engineers Digital Collection.

Zielke, W., & Hack, H. P. (1972). Resonance frequencies and associated mode shapes of pressurized piping systems. *In lnternational Conference Pressure Surges*, Paper G-1, Brit,. Hydromech. Ites. Assoc., Cranfield, England, GI-1-13.

Zuo, Z., Liu, S., Liu, D., Qin, D., & Wu, Y. (2013). Numerical predictions of the incipient and developed interblade vortex lines of a model Francis turbine by cavitation calculations. *Advances in Mechanical Engineering*, 5, 397583.

Zuo, Z., Liu, S., Liu, D., & Qin, D. (2014). Numerical predictions and stability analysis of cavitating draft tube vortices at high head in a model Francis turbine. *Science China Technological Sciences*, 57(11), 2106-2114.

Zwart, P. J., Gerber, A. G., & Belamri, T. (2004). A two-phase flow model for predicting cavitation dynamics. In *Fifth international conference on multiphase flow, Yokohama, Japan* (Vol. 152).

Appendices

Appendix A - Systematic uncertainty from calibration procedure

As it is stated in section 2.3.3, the systematic uncertainty can be estimated from the calibration procedure of the transducers. In the present study, this procedure is applied in the static pressure, level pressure, flowrate and mechanical torque sensors of National Technical University of Athens (NTUA). In order to calibrate a sensor of any kind, it is necessary to be able to compare the sensor's measuring value with the corresponding one, measured by an accurate device. In the NTUA, the accurate devices for pressure, flowrate and torque sensor calibrations, are a dead weight tester (Fig. A.1a), a volumetric tank (Fig. A.1b) and a calibration beam (Fig. A.1c), respectively. In this section, a brief description of each calibration configuration is firstly given. Afterwards, the main part of the calibration procedure along with its theoretical background, which is common, no matter the type of sensor calibrated, is presented. Finally, the modifications applied for each type of transducer are discussed. The aim of this section is to provide all the expressions used during calibration procedure, along with a detailed description of the steps followed. The values of the relative systematic uncertainty for each sensor that result from the calibration procedure of the Laboratory of Hydraulic Turbomachines (LHT) of NTUA are shown in section 2.5.2.

Accurate devices

The dead weight tester is consider as a primary tool (GKS, 2014; IEC 60193, 2019) for the calibration of static pressure transducers. Its configuration (Fig. A.1a) consists of a closed oil (ST25) circuit, where the fluid medium is used to transfer the pressure applied from a hydraulic screw compressor (5) to the one end of the set up that is used for fitting of the pressure sensor (1). The second end of the configuration consists of a piston/cylinder system that is able to compress the closed circuit with the use of reference weights (4). After the placement of the reference weights on the piston, the circuit is compressed from the user by the hydraulic screw compressor until the reference weights to raise. At this point, the known pressure exerted from the reference weight mass is balanced from the uniform pressure of the oil circuit that excites the pressure sensor.

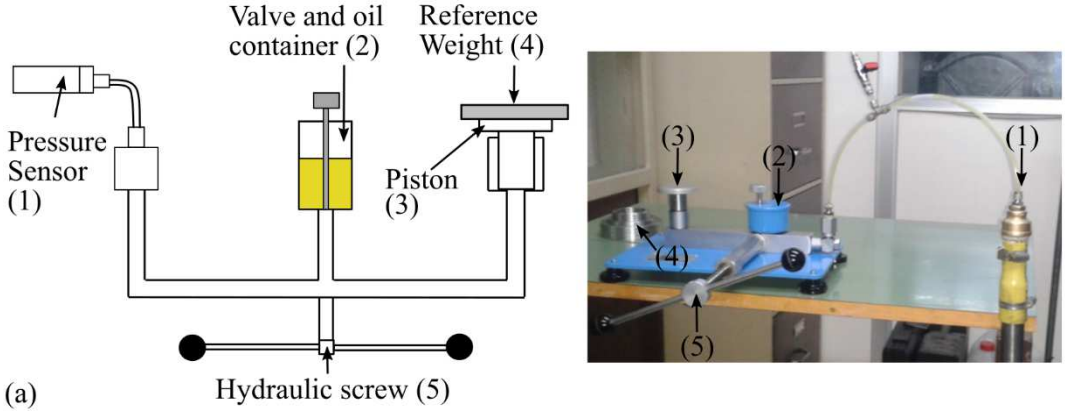

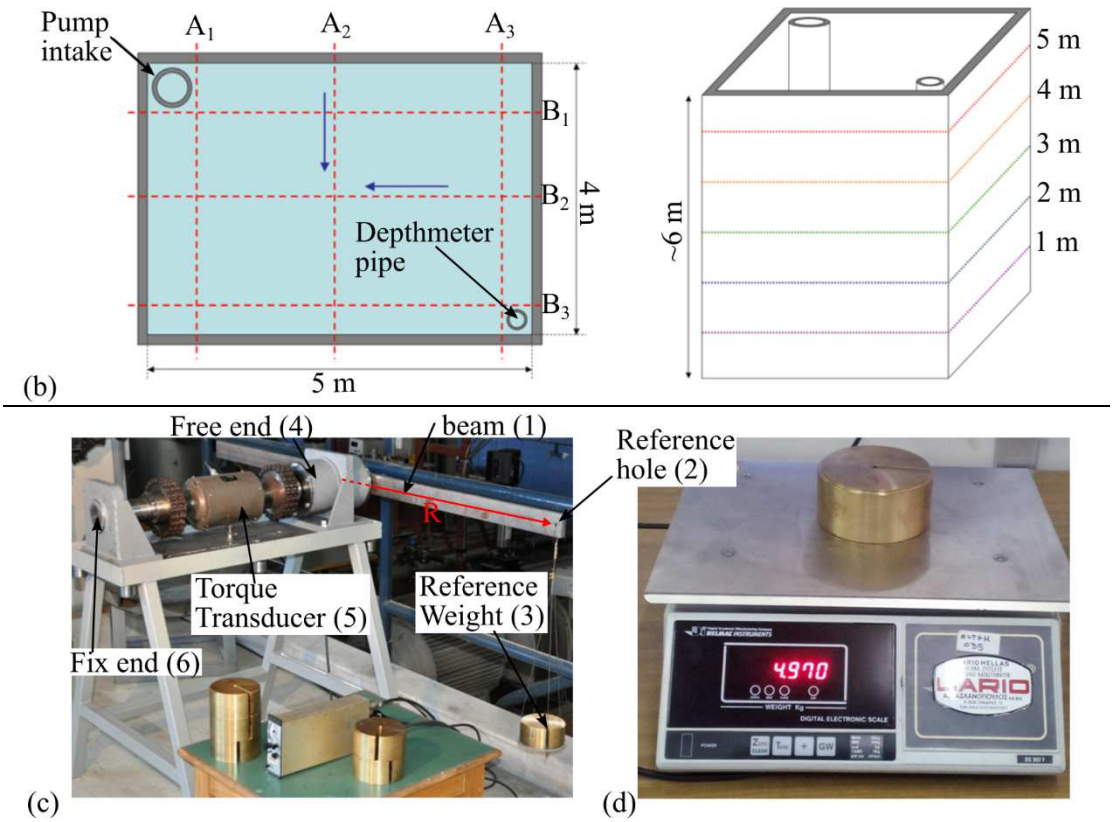

Figure A.1 a) Dead weight tester, **b)** volumetric tank **c)** torque calibration beam **d)** high accuracy scale (Kassanos, 2016b,c,d).

In this way and after the examination of multiple reference weights, it is possible to calibrate the volt raw data of the sensor with the corresponding pressure exerted from the reference weight mass on the cross sectional area of the piston. The reference weights corresponding pressure is provided from the manufacturer and is of high accuracy.

The volumetric tank method configuration (Fig. A.1b) consists of the main pump used to transfer the water from the main tank through the flow transducer to the volumetric tank and the secondary pump that transfers the water from the volumetric tank back to the main tanks so as to empty the first. In addition, a pressure level transducer is located in the volumetric tank, in order to measure the level of the water. The pressure level transducer has been already calibrated with the dead weight tester and its uncertainty is transferred to the uncertainty calculation of the flow meter. The uncertainty related with the cross sectional area of the volumetric tank as a function of its level is also transferred to the calculations. The aim of this calibration procedure is to relate the increase of the volumetric tank's level at a finite time span with the raw volt data of the sensor. In order to change the flowrate of the system, the rotational speed, *n* of the main pump or its discharge valve is adjusted. The waiting time introduced in sections 2.3.1 and 2.3.2 is also used here, in order to certify the steady flow conditions in the system.

The torque calibration beam set up (Fig. A.1c) is made up by a beam (1) that has a reference hole (2) at R=0.7785 m, where the reference weights (3) are suspended from. The the torque transducer (5) is installed and connected with the use of a geared chain coupling at the free end (4) of a shaft that is fixed on the calibration bead. The other end of the sensor is coupled with the same way in a shaft with a fixed end (6) in the configuration. Consequently, when the sensor is coupled in the axis system, the set up is motionless. In addition, the application of the weights (3) at the reference hole (2) creates a moment at the fixed end of the system that is transferred to the torque sensor. In this way, and after the examination of multiple reference weights, it is possible to calibrate the volt raw data of the sensor with the corresponding moment exerted from the reference weight mass at radial position, R. The reference weights are calibrated with

the use of high accuracy scale of the Laboratory of Thermal Turbomachines of NTUA (Fig. A.1d).

Main phase of calibration procedure

The main phase of the calibration procedure is common for all configurations. After the installation of the sensors and their warm up for 30 minutes, the procedure for a variable φ, can be described with the aid of Fig. A.2. The first part of the procedure ($0<t<720$ sec) deals with the full range preload cycle of the sensor, which includes the examination of sensor response at its extreme conditions for three times, alternately (GKS, 2014). In this way, the error of repeatability and the error of reversibility (hysteresis) are reduced (Ćorić, 2010) and also the residual forces, stresses and pressure, which may remain in the transducer after removing the load, are minimised.

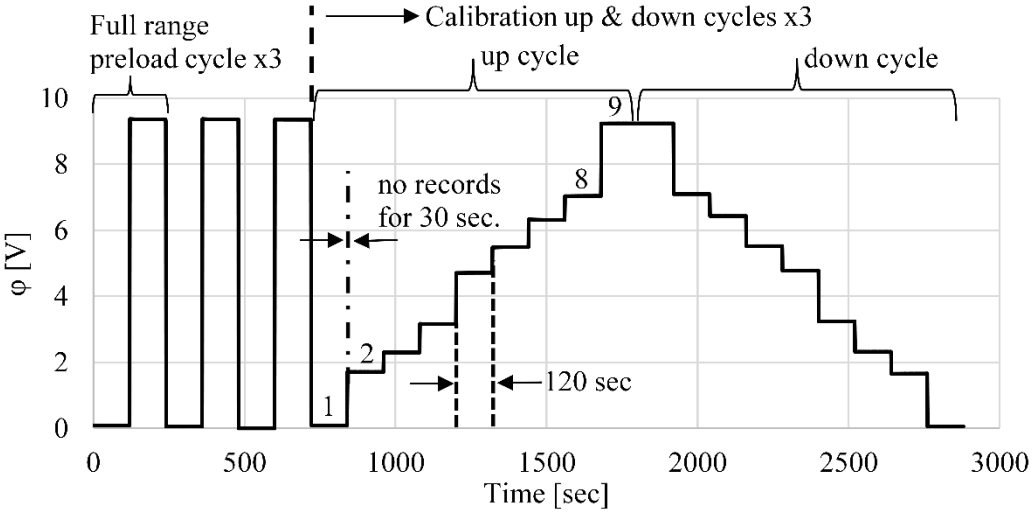

Figure A.2 Procedure of calibration of a typical variable φ.

After the three preload cycles, the calibration up cycle begins at t=720 sec, which includes the testing of 9 known values of the calibrated variable (Fig. A.2). After the end of the up cycle, the down cycle begins, where the same values are examined in the opposite direction, in order to calculate the hysteresis error. Both up and down cycles are repeated three times so as to calculate the repeatability error.

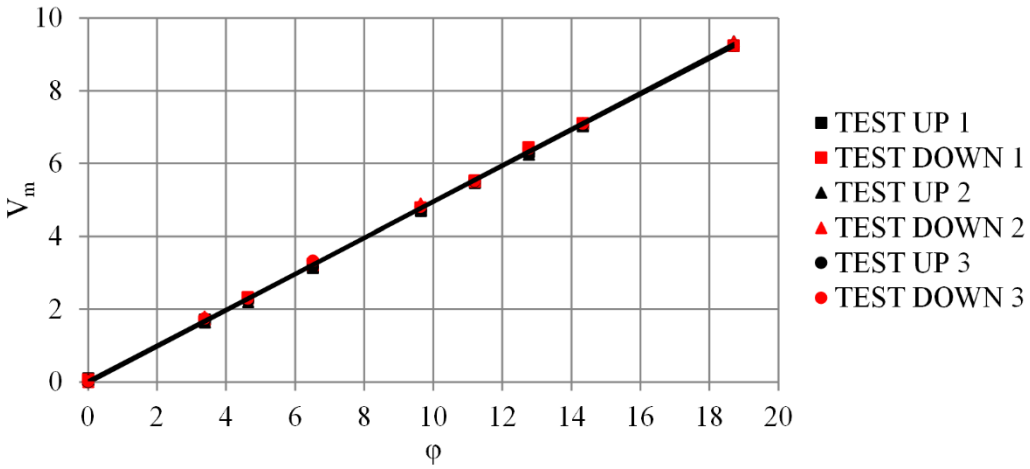

Figure A.3 The six calibration curves of φ variable.

The time span (δt= 120 s), the pausing time span (δt=30 s) and the averaging (Eqs. 2.29 & 2.30) for each calibration measurement is the same with those presented in sections 2.3.1 and 2.3.2. The result of the calibration procedure is the creation of of six curves (3 pairs of up and down tests), like the ones inticatively plotted for a typical φ value in Fig. A.3.

For each point of each curve corresponds a random (Eq. A.2), $F(\bar{\varphi},s,r)$ and a linearity error (Eq. A.3), $F(\bar{\varphi},s,l)$, while each point of the down test, along with its corresponding pair of the up test, show a hysteresis error (Eq. A.5), $F(\bar{\varphi},s,h)$. In addition, the calibration procedure results in six pairs of linear coefficients, where the application of φ to each pair results in the V_c (Eq. A.4). After obtaining the calibration data, V_m, the calculation of the level of systematic uncertainty, $F(\bar{\varphi},s)$, can be done by Eq. A.1:

$$F\left(\bar{\varphi},s\right)=\sqrt{F\left(\bar{\varphi},s,r\right)^2+F\left(\bar{\varphi},s,l\right)^2+F\left(\bar{\varphi},s,h\right)^2+F\left(\bar{\varphi},s,m\right)^2+\ldots}$$
$$\sqrt{\ldots+F\left(\bar{\varphi},s,c\right)^2+F\left(\bar{\varphi},s,s\right)^2+F\left(\bar{\varphi},s,Add\right)^2} \quad \text{(A.1)}$$

$$F\left(\bar{\varphi},s,r\right)=max\left(\frac{\delta\left(\bar{\varphi},s,r\right)}{\bar{\varphi}}\right) \quad \text{(A.2)}$$

$$F\left(\bar{\varphi},s,l\right)=\frac{max\left(V_c-V_m\right)}{max\left(V_c\right)} \quad \text{(A.3)}$$

$$V_c=\varphi_{p,Q,M_m}\cdot a_c+b_c \quad \text{(A.4)}$$

$$F\left(\bar{\varphi},s,h\right)=\frac{max\left(V_{m,up}-V_{m,down}\right)}{max\left(V_c\right)} \quad \text{(A.5)}$$

$$F\left(\bar{\varphi},s,s\right)=0.5\frac{\left(V_{max}-V_{min}\right)}{2^r}=0.5\frac{\left(V_{max}-V_{min}\right)}{2^{16}} \quad \text{(A.6)}$$

$$F\left(\bar{\varphi},s,m\right)=0.15\% \text{ (for p calibrations)}$$
$$F\left(\bar{\varphi},s,m\right)=1\% \text{ (for Q calibrations)} \quad \text{(A.7)}$$
$$F\left(\bar{\varphi},s,m\right)=0.10\% \text{ (for } M_m \text{ calibrations)}$$

where $F(\bar{\varphi},s,s)$ is the resolution error (Eq. A.6), r the data acquisition system's resolution, $F(\bar{\varphi},s,m)$ the error of the calibration methodology (Eq. A.7), $F(\bar{\varphi},s,c)$ the average error of the linear calibration coefficients, α_c and b_c, and $F(\bar{\varphi},s,Add)$ the additional error terms related to each calibration procedure, separately.

Modifications for each configuration

During the pressure calibration methodology, three corrections, provided from the dead weight tester manufacturer, are applied sequentially in the known $\bar{p}$ value before the derivation of calibration curves of Fig. A.3; i) z correction Eq. (A.8), ii) T correction Eq. (A.9) and iii) g correction Eq. (A.10).

$$\overline{p_c}=\overline{p_{c,z}}=\overline{p_{c,T}}+0.00085\left[\text{abs}\left(z-z_{DWT}\right)\right] \quad \text{(A.8)}$$

$$\overline{p_{c,T}}=\overline{p_{c,g}}+\text{abs}\left(20-T\right)\cdot 0.00002\cdot\overline{p_{c,g}} \quad \text{(A.9)}$$

$$\overline{\overline{p_{c,g}}} = \frac{g_{LHT}}{g_{DWT}} \overline{p} \tag{A.10}$$

where the z_{DWT} and g_{DWT} are the reference level and gravitational acceleration values of the dead weight tester.

Finally, two additional terms are added in the *F($\overline{\varphi}$,s)* equations (*F($\overline{\varphi}$,s,Add)* in Eq. A.1) for the flowrate and torque, respectively. On the one hand, the uncertainty of the volumetric tank area (0.5%) is added in the flowrate's equation, *F($\overline{Q}$,s)*, while the errors of the beam length (0.013%) and the beam's hole (0.063%) are added in the torque's, *F($\overline{M_m}$,s)*, equation.

Appendix B - Equations for error propagation

In Appendix B the derivation procedure of the equations used for the uncertainty propagation of each calculated quantity in section 2.3.3.2 is shown. The dash symbol that denotes the mean value of each measured and calculated quantity drops so as to simplify the equations.

The total head equation

The application of Eq. 2.39 (section 2.3.3.2) to Eq. 2.28 (section 2.3.1) that expresses the total head as a function of the measured static pressure at the suction (p_e) and the discharge (p_a) of the pump, as well as of the flowrate (Q), gives Eq. A.11:

$$\delta\left(H_{tot}\right)=\sqrt{\left[\frac{\partial H_{tot}}{\partial p_a}\cdot\delta\left(p_a\right)\right]^2+\left[\frac{\partial H_{tot}}{\partial p_e}\cdot\delta\left(p_e\right)\right]^2+\left[\frac{\partial H_{tot}}{\partial Q}\cdot\delta\left(Q\right)\right]^2} \tag{A.11}$$

The calculations of the partial derivatives of Eq. A.11, result in Eq. A.12:

$$\delta\left(H_{tot}\right)=\sqrt{\left[\frac{1}{\rho g}\cdot\delta\left(p_a\right)\right]^2+\left[\frac{1}{\rho g}\cdot\delta\left(p_e\right)\right]^2+\left[\frac{16Q}{\pi^2 g}\left(\frac{1}{d_{p,a}{}^4}-\frac{1}{d_{p,e}{}^4}\right)\cdot\delta\left(Q\right)\right]^2} \tag{A.12}$$

Finally, the application of Eq. 2.36 (section 2.3.3.1) to Eq. A.12, gives the equation used for the uncertainty of the total head:

$$\delta\left(H_{tot}\right)=\sqrt{\left[\frac{p_a}{\rho g}\cdot F\left(p_a\right)\right]^2+\left[\frac{p_e}{\rho g}\cdot F\left(p_e\right)\right]^2+\left[\frac{16Q^2}{\pi^2 g}\left(\frac{1}{d_{p,a}{}^4}-\frac{1}{d_{p,e}{}^4}\right)\cdot F\left(Q\right)\right]^2} \tag{A.13}$$

The mechanical power equation

The application of Eq. 2.39 (section 2.3.3.2) to Eq. 2.8 (section 2.2.1) that expresses the mechanical power as a function of the measured mechanical torque (M_m) and rotation speed (Ω), gives Eq. A.14:

$$\delta\left(P_{mech}\right)=\sqrt{\left[\frac{\partial P_{mech}}{\partial M_m}\cdot\delta\left(M_m\right)\right]^2+\left[\frac{\partial P_{mech}}{\partial \Omega}\cdot\delta\left(\Omega\right)\right]^2} \tag{A.14}$$

The calculations of the partial derivatives of Eq. A.14, result in Eq. A.15:

$$\delta\left(P_{mech}\right)=\sqrt{\left[\Omega\cdot\delta\left(M_m\right)\right]^2+\left[M_m\cdot\delta\left(\Omega\right)\right]^2} \tag{A.15}$$

The application of Eq. 2.36 (section 2.3.3.1) to Eq. A.15, gives Eq. A.16:

$$\delta\left(P_{mech}\right)=\sqrt{\left[\Omega\cdot M_m\cdot F\left(M_m\right)\right]^2+\left[M_m\cdot\Omega\cdot F\left(\Omega\right)\right]^2} \tag{A.16}$$

Finally, the application of Eq. 2.8 (section 2.2.1) to Eq. A.16, gives the equation used for the uncertainty of the mechanical power:

$$\delta\left(P_{mech}\right) = P_{mech} \cdot \left[\sqrt{F\left(M_m\right)^2 + F\left(\Omega\right)^2}\right] \tag{A.17}$$

The efficiency equation

The application of Eq. 2.39 (section 2.3.3.2) to Eqs. 2.7 and 2.8 (section 2.2.1) that expresses the total efficiency of the pump as a function of the calculated total head (H_{tot}) and the measured flowrate (Q), mechanical torque (M_m) and rotation speed (Ω) gives Eq. A.18:

$$\delta(\eta) = \sqrt{\left[\frac{\partial\eta}{\partial H_{tot}} \cdot \delta\left(H_{tot}\right)\right]^2 + \left[\frac{\partial\eta}{\partial Q} \cdot \delta\left(Q\right)\right]^2 + \left[\frac{\partial\eta}{\partial M_m} \cdot \delta\left(M_m\right)\right]^2 + \ldots} \sqrt{\ldots + \left[\frac{\partial\eta}{\partial\Omega} \cdot \delta\left(\Omega\right)\right]^2} \tag{A.18}$$

The calculations of the partial derivatives of Eq. A.18 result in Eq. A.19:

$$\delta(\eta) = \sqrt{\left[\frac{\rho g Q}{M_m \Omega} \cdot \delta\left(H_{tot}\right)\right]^2 + \left[\frac{\rho g H_{tot}}{M_m \Omega} \cdot \delta\left(Q\right)\right]^2 + \left[\frac{\rho g H_{tot} Q}{{M_m}^2 \Omega} \cdot \delta\left(M_m\right)\right]^2 + \ldots} \sqrt{\ldots + \left[\frac{\rho g H_{tot} Q}{M_m \Omega^2} \cdot \delta\left(\Omega\right)\right]^2} \tag{A.19}$$

The application of Eq. 2.36 (section 2.3.3.1) to Eq. A.19, gives Eq. A.20:

$$\delta(\eta) = \sqrt{\left[\frac{\rho g H_{tot} Q}{M_m \Omega} \cdot F\left(H_{tot}\right)\right]^2 + \left[\frac{\rho g H_{tot} Q}{M_m \Omega} \cdot F\left(Q\right)\right]^2 + \ldots} \sqrt{\ldots + \left[\frac{\rho g H_{tot} Q}{M_m \Omega} \cdot F\left(M_m\right)\right]^2 + \left[\frac{\rho g H_{tot} Q}{M_m \Omega} \cdot F\left(\Omega\right)\right]^2} \tag{A.20}$$

Finally, the application of Eq. 2.7 (section 2.2.1) to Eq. A.20, gives the equation used for the uncertainty of the efficiency of the pumps:

$$\delta(\eta) = \eta\sqrt{F\left(H_{tot}\right)^2 + F\left(Q\right)^2 + F\left(M_m\right)^2 + F\left(\Omega\right)^2} \tag{A.21}$$

The non-dimensional flowrate equation

The application of Eq. 2.39 (section 2.3.3.2) to Eqs. 2.13-2.15 (section 2.2.1) that expresses the non-dimensional flowrate of the pump as a function of the measured flowrate (Q) and rotation speed (Ω) gives Eq. A.22:

$$\delta(\Phi)=\sqrt{\left[\frac{\partial\Phi}{\partial Q}\cdot\delta(Q)\right]^2+\left[\frac{\partial\Phi}{\partial\Omega}\cdot\delta(\Omega)\right]^2} \tag{A.22}$$

The calculations of the partial derivatives of Eq. A.22 result in Eq. A.23:

$$\delta(\Phi)=\sqrt{\left[\frac{1}{(\pi d_2-z_s e_2)b_{I,2}}\frac{1}{\Omega R_2}\cdot\delta(Q)\right]^2+\left[\frac{Q}{(\pi d_2-z_s e_2)b_{I,2}}\frac{1}{\Omega^2 R_2}\cdot\delta(\Omega)\right]^2} \tag{A.23}$$

The application of Eq. 2.36 (section 2.3.3.1) to Eq. A.23, gives Eq. A.24:

$$\delta(\Phi)=\sqrt{\left[\frac{Q}{(\pi d_2-z_s e_2)b_{I,2}}\frac{1}{\Omega R_2}\cdot F(Q)\right]^2+\left[\frac{Q}{(\pi d_2-z_s e_2)b_{I,2}}\frac{1}{\Omega R_2}\cdot F(\Omega)\right]^2} \tag{A.24}$$

Finally, the application of Eqs. 2.13-2.15 (section 2.2.1) to Eq. A.24, gives the equation used for the uncertainty of the non-dimensional flowrate of the pumps:

$$\delta(\Phi)=\Phi\cdot\left[\sqrt{F(Q)^2+F(\Omega)^2}\right] \tag{A.25}$$

The non-dimensional total head equation

The application of Eq. 2.39 (section 2.3.3.2) to Eqs. 2.16 and 2.15 (section 2.2.1) that expresses the non-dimensional total head of the pump as a function of the calculated total head (H_{tot}) and the measured rotation speed (Ω) gives Eq. A.26:

$$\delta(\Psi)=\sqrt{\left[\frac{\partial\Psi}{\partial H_{tot}}\cdot\delta(H_{tot})\right]^2+\left[\frac{\partial\Psi}{\partial\Omega}\cdot\delta(\Omega)\right]^2} \tag{A.26}$$

The calculations of the partial derivatives of Eq. A.26 result in Eq. A.27:

$$\delta(\Psi)=\sqrt{\left[\frac{2g}{\Omega^2 {R_2}^2}\cdot\delta(H_{tot})\right]^2+\left[\frac{2gH_{tot}}{{R_2}^2}\frac{2}{\Omega^3}\cdot\delta(\Omega)\right]^2} \tag{A.27}$$

The application of Eq. 2.36 (section 2.3.3.1) to Eq. A.27, gives Eq. A.28:

$$\delta(\Psi)=\sqrt{\left[\frac{2gH_{tot}}{\Omega^2 {R_2}^2}\cdot F(H_{tot})\right]^2+\left[\frac{2gH_{tot}}{{R_2}^2}\frac{2}{\Omega^2}\cdot F(\Omega)\right]^2} \tag{A.28}$$

Finally, the application of Eqs. 2.16-2.15 (section 2.2.1) to Eq. A.28, gives the equation used for the uncertainty of the non-dimensional total head of the pumps:

$$\delta(\Psi) = \Psi \cdot \left[\sqrt{F\left(H_{tot}\right)^2 + \left[2 \cdot F\left(\Omega\right)\right]^2} \right] \tag{A.29}$$

The non-dimensional mechanical power equation

The application of Eq. 2.39 (section 2.3.3.2) to Eq. 2.17 (section 2.2.1) that expresses the non-dimensional mechanical power of the pump as a function of the mechanical power (P_{mech}) and the measured rotation speed (Ω) gives Eq. A.30:

$$\delta(N) = \sqrt{\left[\frac{\partial N}{\partial P_{mech}} \cdot \delta\left(P_{mech}\right)\right]^2 + \left[\frac{\partial N}{\partial \Omega} \cdot \delta\left(\Omega\right)\right]^2} \tag{A.30}$$

The calculations of the partial derivatives of Eq. A.30 result in Eq. A.31:

$$\delta(N) = \sqrt{\left[\frac{1}{\rho \Omega^3 {d_2}^5} \cdot \delta\left(P_{mech}\right)\right]^2 + \left[\frac{P_{mech}}{\rho {d_2}^5} \frac{3}{\Omega^4} \cdot \delta\left(\Omega\right)\right]^2} \tag{A.31}$$

The application of Eq. 2.36 (section 2.3.3.1) to Eq. A.31, gives Eq. A.32:

$$\delta(N) = \sqrt{\left[\frac{P_{mech}}{\rho \Omega^3 {d_2}^5} \cdot F\left(P_{mech}\right)\right]^2 + \left[\frac{P_{mech}}{\rho {d_2}^5} \frac{3}{\Omega^3} \cdot F\left(\Omega\right)\right]^2} \tag{A.32}$$

Finally, the application of Eq. 2.17 (section 2.2.1) to Eq. A.32, gives the equation used for the uncertainty of the non-dimensional mechanical power of the pumps:

$$\delta(N) = N \cdot \left[\sqrt{F\left(P_{mech}\right)^2 + \left[3 \cdot F\left(\Omega\right)\right]^2} \right] \tag{A.33}$$

The Net Positive Suction Head (NPSH) equation

The application of Eq. 2.39 (section 2.3.3.2) to Eqs. 2.31 and 2.32 (section 2.3.2) that expresses the NPSH as a function of the measured static pressure at the suction (p_e) of the pump, the flowrate (Q) and the temperature (T), gives Eq. A.34:

$$\delta(NPSH) = \sqrt{\left[\frac{\partial NPSH}{\partial p_e} \cdot \delta\left(p_e\right)\right]^2 + \left[\frac{\partial NPSH}{\partial Q} \cdot \delta\left(Q\right)\right]^2 + \left[\frac{\partial NPSH}{\partial T} \cdot \delta\left(T\right)\right]^2} \tag{A.34}$$

The calculations of the partial derivatives of Eq. A.34 result in Eq. A.35:

$$\delta(NPSH) = \sqrt{\left[\frac{1}{\rho g}\cdot\delta(p_e)\right]^2 + \left[\frac{16Q}{g\pi^2 d_{p,e}{}^4}\cdot\delta(Q)\right]^2 + \left[\frac{0.1907}{\rho g}\cdot\delta(T)\right]^2} \quad \text{(A.35)}$$

Finally, the application of Eq. 2.36 (section 2.3.3.1) to Eq. A.35, gives the equation used for the uncertainty of the NPSH:

$$\delta(NPSH) = \sqrt{\left[\frac{1}{\rho g}p_e\cdot F(p_e)\right]^2 + \left[\frac{16Q^2}{g\pi^2 d_{p,e}{}^4}\cdot F(Q)\right]^2 + \left[\frac{0.1907T}{\rho g}\cdot F(T)\right]^2} \quad \text{(A.36)}$$

The Thoma cavitation number equation

The application of Eq. 2.39 (section 2.3.3.2) to Eq. 2.24 (section 2.2.2) that expresses the σ as a function of the calculated NPSH and the total head (H_{tot}) of the pump, gives Eq. A.37:

$$\delta(\sigma) = \sqrt{\left[\frac{\partial\sigma}{\partial H_{tot}}\cdot\delta(H_{tot})\right]^2 + \left[\frac{\partial\sigma}{\partial NPSH}\cdot\delta(NPSH)\right]^2} \quad \text{(A.37)}$$

The calculations of the partial derivatives of Eq. A.37, result in Eq. A.38:

$$\delta(\sigma) = \sqrt{\left[\frac{NPSH}{H_{tot}{}^2}\cdot\delta(H_{tot})\right]^2 + \left[\frac{1}{H_{tot}}\cdot\delta(NPSH)\right]^2} \quad \text{(A.38)}$$

The application of Eq. 2.36 (section 2.3.3.1) to Eq. A.38, gives Eq. A.39:

$$\delta(\sigma) = \sqrt{\left[\frac{NPSH}{H_{tot}}\cdot F(H_{tot})\right]^2 + \left[\frac{NPSH}{H_{tot}}\cdot F(NPSH)\right]^2} \quad \text{(A.39)}$$

Finally, the application of Eq. 2.24 (section 2.2.2) to Eq. A.39, gives the equation used for the uncertainty of σ:

$$\delta(\sigma) = \sigma\cdot\left[\sqrt{F(H_{tot})^2 + F(NPSH)^2}\right] \quad \text{(A.40)}$$

Appendix C - Turbulence model equations

The following Eqs. A.41 to A.59 are used for calculation of all quantities involved in the *k-ω* SST turbulence (FLUENT, 2009).

For the Eq. 4.9:

$$\Gamma_k = \mu + \frac{\mu_t}{\sigma_k} \tag{A.41}$$

$$\sigma_k = \frac{1}{\frac{F_1}{1.176} + (1 - F_1)} \tag{A.42}$$

$$F_1 = \tanh\left\{\min\left[\max\left(\frac{\sqrt{k}}{0.09\omega y}, \frac{500\mu}{\rho y^2 \omega}\right), \frac{4\rho k}{\sigma_{\omega,2} D_\omega^+ y^2}\right]\right\} \tag{A.43}$$

$$D_\omega^+ = \max\left(2\rho \frac{1}{1.168}\frac{1}{\omega}\frac{\partial k}{\partial x_j}\frac{\partial \omega}{\partial x_j}, 10^{-10}\right) \tag{A.44}$$

$$\tilde{G}_k = \min\left(-\rho \overline{v_i' v_j'} \frac{\partial v_j}{\partial x_i}, 0.9\rho k\omega\right) \tag{A.45}$$

$$Y_k = 0.09\rho k\omega \tag{A.46}$$

For the Eq. 4.10:

$$\Gamma_\omega = \mu + \frac{\mu_t}{\sigma_\omega} \tag{A.47}$$

$$\sigma_\omega = \frac{1}{\frac{F_1}{2} + \frac{(1 - F_1)}{1.168}} \tag{A.48}$$

$$G_\omega = -\frac{a_\infty}{\nu_{v,t}} \rho \overline{v_i' v_j'} \frac{\partial u_j}{\partial x_i} \tag{A.49}$$

$$a_\infty = 0.553F_1 + 0.44(1 - F_1) \tag{A.50}$$

$$\nu_{v,t} = \frac{\mu_t}{\rho} \tag{A.51}$$

$$Y_\omega = \rho\omega^2\left[0.075F_1 + 0.0828(1 - F_1)\right] \tag{A.52}$$

$$D_\omega = 2(1 - F_1)\rho \frac{1}{1.168\omega}\frac{\partial k}{\partial x_j}\frac{\partial \omega}{\partial x_j} \tag{A.53}$$

For the Eq. 4.11:

$$\alpha^{*} = \frac{ß_i / 3 + \mathrm{Re}_t / 6}{1 + \mathrm{Re}_t / 6} \tag{A.54}$$

$$ß_i = F_1 ß_{i,1} + \left(1 - F_1\right) ß_{i,2} \tag{A.55}$$

$$\mathrm{Re}_t = \frac{\rho k}{\mu \omega} \tag{A.56}$$

$$S = \sqrt{2 S_{ij} S_{ij}} \tag{A.57}$$

$$S_{ij} = \frac{1}{2}\left(\frac{\partial v_i}{\partial x_j} + \frac{\partial v_j}{\partial x_i} \right) \tag{A.58}$$

$$F_2 = \tanh\left\{ \left[\max\left(\frac{2\sqrt{k}}{0.09 \omega y}, \frac{500 \mu}{\rho y^2 \omega} \right) \right]^2 \right\} \tag{A.59}$$

where y is the distance from the wall and $v_{v,t}$ the turbulent kinematic viscosity.

ΕΘΝΙΚΟ ΜΕΤΣΟΒΙΟ ΠΟΛΥΤΕΧΝΕΙΟ
ΣΧΟΛΗ ΜΗΧΑΝΟΛΟΓΩΝ ΜΗΧΑΝΙΚΩΝ
ΤΟΜΕΑΣ ΡΕΥΣΤΩΝ
ΕΡΓΑΣΤΗΡΙΟ ΥΔΡΟΔΥΝΑΜΙΚΩΝ ΜΗΧΑΝΩΝ

ΑΝΑΠΤΥΞΗ ΜΕΘΟΔΟΛΟΓΙΑΣ ΔΙΑΓΝΩΣΗΣ ΣΠΗΛΑΙΩΣΗΣ ΣΕ ΥΔΡΟΔΥΝΑΜΙΚΕΣ ΜΗΧΑΝΕΣ ΜΕ ΠΕΙΡΑΜΑΤΙΚΑ ΚΑΙ ΥΠΟΛΟΓΙΣΤΙΚΑ ΕΡΓΑΛΕΙΑ

Γεώργιος Μουσμούλης

Διδακτορική Διατριβή

Ιούνιος 2020
Αθήνα

ΕΘΝΙΚΟ ΜΕΤΣΟΒΙΟ ΠΟΛΥΤΕΧΝΕΙΟ
ΣΧΟΛΗ ΜΗΧΑΝΟΛΟΓΩΝ ΜΗΧΑΝΙΚΩΝ
ΤΟΜΕΑΣ ΡΕΥΣΤΩΝ
ΕΡΓΑΣΤΗΡΙΟ ΥΔΡΟΔΥΝΑΜΙΚΩΝ ΜΗΧΑΝΩΝ

ΑΝΑΠΤΥΞΗ ΜΕΘΟΔΟΛΟΓΙΑΣ ΔΙΑΓΝΩΣΗΣ ΣΠΗΛΑΙΩΣΗΣ ΣΕ ΥΔΡΟΔΥΝΑΜΙΚΕΣ ΜΗΧΑΝΕΣ ΜΕ ΠΕΙΡΑΜΑΤΙΚΑ ΚΑΙ ΥΠΟΛΟΓΙΣΤΙΚΑ ΕΡΓΑΛΕΙΑ

Διδακτορική Διατριβή

Γεώργιος Μουσμούλης

Τριμελής Συμβουλευτική Επιτροπή
Ι. Αναγνωστόπουλος, Καθηγητής, ΕΜΠ, (Επιβλέπων)
Δ. Παπαντώνης, Ομότιμος Καθηγητής, ΕΜΠ
Ν. Αρετάκης, Αναπληρωτής Καθηγητής, ΕΜΠ

Examination Committee
Ι. Αναγνωστόπουλος, Καθηγητής, ΕΜΠ, (Επιβλέπων)
Γ. Αγγίδης, Καθηγητής, Lancaster University
Ν. Αρετάκης, Αναπληρωτής Καθηγητής, ΕΜΠ
Ι. Αντωνιάδης, Καθηγητής, ΕΜΠ
Δ. Μπούρης, Αναπληρωτής Καθηγητής, ΕΜΠ
Δ. Μαθιουλάκης, Καθηγητής, ΕΜΠ
Σ. Βουτσινάς, Καθηγητής, ΕΜΠ

Ιούνιος 2020
Αθήνα

Περιεχόμενα

Περίληψη

Από τις πιο συχνά απαντώμενες μηχανές στις διάφορες βιομηχανικές εγκαταστάσεις και τεχνικά έργα είναι οι φυγοκεντρικές αντλίες, ενώ οι υδροστρόβιλοι λειτουργούν σε ένα μεγάλο αριθμό υδροηλεκτρικών έργων, σε όλο τον κόσμο, παράγοντας σημαντικό μέρος της καταναλώμενης ηλεκτρικής ενέργειας. Συνεπώς, η ομαλή και αποτελεσματική επιτέλεση μιας πληθώρας τεχνικών λειτουργιών, βιομηχανικών διεργασιών και παραγωγικών δραστηριοτήτων βασίζεται στην αξιόπιστη και αποτελεσματική λειτουργία αυτών των υδροδυναμικών μηχανών. Ένας από τους ροϊκούς μηχανισμούς που μπορεί να διαταράξει τη λειτουργία αυτών των μηχανών, είναι η σπηλαίωση, δηλαδή η τοπική εξάτμιση του υγρού (συνήθως νερού), η οποία δημιουργείται όταν η πίεση σε κάποια σημεία εντός του ρότορα μειωθεί σε τιμές κάτω από την πίεση ατμοποίησης στη θερμοκρασία λειτουργίας. Η επανυγροποίηση των φυσαλίδων ατμού σε περιοχές όπου η στατική πίεση επανέρχεται σε υψηλότερες τιμές, γίνεται μέσω της ενδόρρηξης τους, μια απότομη μεταβολή φάσης, η οποία ακολουθείται από την ανάπτυξη τοπικών κρουστικών κυμάτων πίεσης, προκαλώντας διάβρωση των στερεών εσωτερικών επιφανειών της μηχανής. Λειτουργία μιας υδροδυναμικής μηχανής υπό συνθήκες σπηλαίωσης, ακόμη και σε σύντομο διάστημα, μπορεί να προκαλέσει εκτεταμένες φθορές που συνοδεύονται από αύξηση των μηχανικών ταλαντώσεων και πτώση του βαθμού απόδοσης. Η παρούσα Διατριβή, ασχολείται με την ανάλυση των χαρακτηριστικών της ροής σε φυγοκεντρικές αντλίες, στις οποίες αναπτύσσεται το φαινόμενο της σπηλαίωσης, και έχει ως στόχο την ανάπτυξη εργαλείων που να μπορούν να διαγνώνουν έγκαιρα τον σχηματισμό φυσαλίδων ατμού.

Το πρόβλημα προσεγγίζεται τόσο πειραματικά όσο και υπολογιστικά. Πιο συγκεκριμένα, χρησιμοποιούνται δύο εργαστηριακές διατάξεις, οι οποίες επιτρέπουν την οπτική παρατήρηση του φαινομένου εντός των εξεταζόμενων μηχανών: μια διάταξη εγκατεστημένη στο Τμήμα Μηχανικών του Πανεπιστημίου του Λάνκαστερ (LU - Ην. Βασ.) και μία στο Εργαστήριο Υδροδυναμικών Μηχανών του ΕΜΠ. Η αντλία που βρίσκεται εγκατεστημένη στο LU έχει το κέλυφος της κατασκευασμένο από διαφανές υλικό, ενώ στη συγκεκριμένη διάταξη χρησιμοποιούνται τρεις πτερωτές ακτινικής ροής ημι-ανοικτού τύπου (χωρίς στεφάνη), με οπισθοκλινή, με ακτινικά και με εμπροσθοκλινή πτερύγια. Από την άλλη, η πειραματική διάταξη του ΕΜΠ περιλαμβάνει μια τυπική βιομηχανική φυγοκεντρική αντλία, με κλειστού τύπου πτερωτή, με οπισθοκλινή πτερύγια. Στην αντλία του ΕΜΠ έγιναν σημαντικές τροποποιήσεις, ώστε να επιτραπεί η διενέργεια οπτικών παρατηρήσεων εντός της πτερωτής, που περιλαμβάνουν ανακατασκευή της πτερωτής με στεφάνη κατασκευασμένη από διαφανές υλικό, και διάνοιξη διαφανούς παραθύρου στην εμπρόσθια πλευρά του κελύφους.

Οι πειραματικές μετρήσεις περιλαμβάνουν τις χαρακτηριστικές καμπύλες λειτουργίας των τεσσάρων πτερωτών, οι οποίες συνοδεύονται από μέτρησεις θορύβου και μηχανικών ταλαντώσεων, καθώς επίσης και από οπτικές παρατηρήσεις εντός της ροής. Σε κάθε διάταξη, χρησιμοποιούνται δύο επιταχυνσιόμετρα και ένας αισθητήρας ακουστικών σημάτων (acoustic emission), ενώ οι χρονοσειρές που λαμβάνονται αναλύονται και μελετώνται με στόχο την αναγνώριση των χαρακτηριστικών του φαινομένου και την ανάπτυξη ενός γενικού κριτηρίου διάγνωσης της σπηλαίωσης. Πιο συγκεκριμένα, τα σήματα επεξεργάζονται στα πεδία χρόνου και συχνοτήτων με χρήση εργαλείων στατιστικής, μέσης τετραγωνικής τιμής (RMS) και φασματικής πυκνότητας ισχύος (PSD). Επιπλέον, δοκιμάζεται η εφαρμογή της μεθόδου Φασματικής Κύρτωσης (SK) για την κατασκευή ζωνοπερατών φίλτρων, τα οποία διαχωρίζουν τα χαρακτηριστικά της σπηλαίωσης από το μετρούμενο σήμα.

Παράλληλα με τις πειραματικές μετρήσεις, μοντελοποιείται η ροή εντός της μηχανής σε συνθήκες με και χωρίς σπηλαίωση, με χρήση εμπορικού λογισμικού υπολογιστικής ρευστοδυναμικής. Η υπολογιστική προσέγγιση περιλαμβάνει την επίλυση των εξισώσεων Reynolds Averaged Navier Stokes Equations (RANS), μαζί με μια πρόσθετη εξίσωση μεταφοράς, για τον υπολογισμό του ρυθμού μεταφοράς μάζας μεταξύ της υγρής φάσης και του ατμού. Το μοντέλο k-ω SST επιλέγεται για την μοντελοποίηση της τύρβης, ενώ για τις περιοχές του υπολογιστικού χωρίου που ανήκουν στην περιστρεφόμενη πτερωτή επιλέγεται η επίλυση των εξισώσεων της ροής στο στρεφόμενο σύστημα αναφοράς.

Οι χαρακτηριστικές καμπύλες λειτουργίας των αντλιών κατασκευάζονται για όλες τις πτερωτές των δύο διατάξεων και η συμπεριφορά τους προέκυψε απόλυτα συμβατή με τη θεωρητική φυγοκεντρικών αντλιών παρόμοιου ειδικού αριθμού στροφών. Για τις μετρήσεις σε συνθήκες σπηλαίωσης, η ρύθμιση της πίεσης στην είσοδο της αντλίας επιτυγχάνεται μέσω στραγγαλισμού της βάνας αναρρόφησης. Καθώς μειώνεται η πίεση, αρχίζει να εξελίσσεται το φαινόμενο της σπηλαίωσης στην πτερωτή, με την εμφάνιση φυσαλίδων ατμού και την προοδευτική αύξηση της περιοχής διφασικής ροής. Η τιμή του ολικού ύψους της αντλίας παραμένει σταθερή, μέχρι το σημείο όπου η περιοχή του ατμού αρχίζει να καλύπτει σχεδόν όλο το εύρος της ροής μεταξύ των πτερυγίων, μειώνοντας τη δυνατότητα πρόσδοσης ισχύος στο εργαζόμενο μέσο και προκαλώντας απότομη πτώση του ολικού ύψους. Τα αποτελέσματα των οπτικών παρατηρήσεων εντός των πτερωτών του LU, απεικονίζουν την εμφάνιση των πρώτων φυσαλίδων ατμού και τη σταδιακή ανάπτυξη τους, όσο τα επίπεδα στατικής πίεσης εντός της διάταξης μειώνονται. Επιπλέον, οι φωτογραφίες των οπτικών παρατηρήσεων, αναδεικνύουν τη συνύπαρξη διαφόρων ειδών σπηλαίωσης εντός της πτερωτής, όπως ‘travelling bubble’, ‘cloud’, ‘tip clearance’, και ‘attached’ σπηλαίωσης.

Τα αποτελέσματα των οπτικών παρατηρήσεων και οι πειραματικές μετρήσεις πιστοποιούν τη δυνατότητα του αριθμητικού μοντέλου να προβλέψει την πτώση του ολικού ύψους της αντλίας. Το μοντέλο δυσκολεύεται να αναγνωρίσει την εμφάνιση των πρώτων φυσαλίδων ατμού, καθώς στα πρώτα στάδια ανάπτυξης το φαινόμενο παρουσιάζει ιδιαίτερα ασταθή συμπεριφορά. Ωστόσο, η ικανότητα του μοντέλου να προβλέψει τη θέση, την έκταση και το σχήμα της ατμοποιημένης περιοχής βελτιώνεται αισθητά στα ενδιάμεσα στάδια ανάπτυξης του φαινομένου και πριν την πτώση του υδραυλικού ύψους. Επομένως, η προτεινόμενη υπολογιστική μεθοδολογία μπορεί να χρησιμοποιηθεί για τη διάγνωση του φαινομένου, αλλά προϋποθέτει την ακριβή γνώση όλων των γεωμετρικών χαρακτηριστικών της μηχανής και της εγκατάστασης, καθώς και τα δεδομένα λειτουργίας της. Επιπρόσθετα, στην περίπτωση της πτερωτής ημι-ανοικτού τύπου, τα αριθμητικά αποτελέσματα φανερώνουν τα περίπλοκα χαρακτηριστικά της ροής στο διάκενο μεταξύ του πτερυγίου και του κελύφους, απεικονίζοντας μια κυκλοφορία της ροής μέσω του διακένου προς την πλευρά υποπίεσης του πτερυγίου (‘backflow’). Όταν η μηχανή λειτουργεί σε συνθήκες πρόκλησης σπηλαίωσης, η κυκλοφορία αυτή μεταφέρει και φυσαλίδες ατμού που δημιουργούνται στο στενό διάκενο (‘backflow tip cavitation’).

Οι μετρήσεις θορύβου και κραδασμών λαμβάνονται από τα επιταχυνσιόμετρα και τον ακουστικό αισθητήρα, όργανα που τοποθετούνται στο σώμα (κέλυφος) των δύο φυγοκεντρικών αντλιών. Οι πρωτογενείς μετρήσεις σε συνθήκες πτώσης του ολικού ύψους λόγω σπηλαίωσης αναδεικνύουν την ύπαρξη κρουστικών σημάτων, που σχετίζονται με την ενδόρρηξη των φυσαλίδων ατμού. Η στατιστική ανάλυση των δεδομένων επιτυγχάνει να συσχετίσει τις προαναφερθείσες διαφοροποιήσεις με το μέγεθος της κύρτωσης του σήματος (τέταρτη ροπή), η τιμή της οποίας αποκλίνει σημαντικά από την κανονική κατανομή. Η μελέτη του πεδίου συχνοτήτων των δυναμικών μετρήσεων απεικονίζει τη διέγερση μεγάλου εύρους συχνοτήτων. Επομένως, προκρίνεται η χρήση ‘RMS’ και ‘powerband’ εργαλείων, με στόχο την ποσοτικοποίηση της έντασης των διεγέρσεων και την αποτύπωσή τους σε σχέση με τις συνθήκες αναρρόφησης. Τα αποτελέσματα καταδεικνύουν την επιτυχή χρήση των παραπάνω εργαλείων για την έγκαιρη διάγνωση της σπηλαίωσης, στην πλειονότητα των υπό εξέταση συνθηκών λειτουργίας. Ωστόσο, η δυσκολία τους να αναγνωρίσουν το φαινόμενο σε μερικές παροχές της κλειστού τύπου πτερωτής, σε συνδυασμό με τον κίνδυνο να εκληφθεί ένας άλλος τύπος σφάλματος (π.χ. σε έδρανα κύλισης, που προκαλεί επίσης κρουστικά σήματα) ως σπηλαίωση, καθιστούν αναγκαία την περαιτέρω ανάλυση των σημάτων.

Γι’ αυτόν τον λόγο, εφαρμόστηκε η μέθοδος Φασματικής Κύρτωσης με στόχο την κατασκευή ζωνοπερατών φίλτρων (bandpass filters), τα οποία δύνανται να απομονώσουν τα χαρακτηριστικά του φαινομένου από το συνολικό μετρούμενο σήμα. Επιπλέον, οι φιλτραρισμένες χρονοσειρές αποδιαμορφώνονται με χρήση του μετασχηματισμού Hilbert, με στόχο την επιβεβαίωση της ύπαρξης πιθανής περιοδικότητας στα χαρακτηριστικά των φιλτραρισμένων σημάτων. Τα αποτελέσματα αποδεικνύουν την αποτελεσματικότητα της μεθοδολογίας, η οποία επιτυγχάνει να απομονώσει τους κρουστικούς παλμούς στις φιλτραρισμένες χρονοσειρές, και οι οποίοι διαμορφώνονται από την αλληλεπίδραση της στρεφόμενης πτερωτής με το σταθερό κέλυφος της αντλίας. Η προτεινόμενη προσέγγιση αναδεικνύει τη συσχέτιση μεταξύ της κρουστικής συμπεριφοράς του επεξεργασμένου σήματος και του μηχανισμού ενδόρρηξης των φυσαλίδων ατμού, καθώς και μεταξύ της διαμόρφωσης από τη συχνότητα περάσματος των πτερυγίων, καθώς το φαινόμενο λαμβάνει χώρα εντός της στρεφόμενης πτερωτής. Το τελευταίο συμπέρασμα συνδέει τα χαρακτηριστικά που χρησιμοποιούνται για τη διάγνωση του φαινομένου με το φυσικό μηχανισμό της βλάβης και διαμορφώνει ένα γενικό και αξιόπιστο εργαλείο διάγνωσης της ανάπτυξης σπηλαίωσης εντός των υδροδυναμικών μηχανών.

Εισαγωγή

Ε.1 Τοποθέτηση του προβλήματος

Το φαινόμενο της ατμοποίησης υγρού ρευστού σε ισοθερμοκρασιακές συνθήκες, όπου η στατική πίεση της ροής, p, μειώνεται σε τιμή μικρότερη της πίεσης ατμών, p_{sat}, ονομάζεται σπηλαίωση. Στις υδροδυναμικές μηχανές, η σπηλαίωση εμφανίζεται εντός του ρότορα, όπου η ροή επιταχύνεται σημαντικά λόγω της επιπλέον περιστροφής, αλλά και λόγω της περίπλοκης εσωτερικής του γεωμετρίας που περιλαμβάνει έντονες καμπυλότητες, πτερύγια και μικρά διάκενα. Μια τέτοια ανεπιθύμητη πτώση της στατικής πίεσης μπορεί να είναι αποτέλεσμα λανθασμένης σχεδίασης της υδροδυναμικής εγκατάστασης ή επιλογής της ίδιας της μηχανής. Μπορεί όμως να οφείλεται και σε λειτουργία της υδροδυναμικής μηχανής μακριά από το κανονικό σημείο λειτουργίας, κατά την οποία προκαλούνται τοπικές ανακυκλοφορίες και υδραυλικές απώλειες, με πρόσθετη πτώση της στατικής πίεσης.

Καθώς η διφασική αυτή ροή μεταβαίνει σε περιοχές υψηλότερων πιέσεων εντός της μηχανής, οι φυσαλίδες ατμού επαναϋγροποιούνται απότομα, προκαλώντας στιγμιαία μεγάλη αύξηση της πίεσης τοπικά, που έχει κρουστική μορφή, δημιουργεί θόρυβο και μπορεί να προκαλέσει διάβρωση και φθορά των εσωτερικών μεταλλικών επιφανειών. Ωστόσο, ο συνολικός, μηχανικός και υδραυλικός θόρυβος της μηχανής τις περισσότερες φορές καλύπτει τον θόρυβο της σπηλαίωσης, γεγονός που δυσκολεύει την έγκαιρη διάγνωσή της. Η λειτουργία της μηχανής κάτω από εκτεταμένη σπηλαίωση μπορεί να μειώσει σημαντικά την ενεργειακή απόδοσή της, αλλά και να καταστρέψει σύντομα τις εσωτερικές στερεές επιφάνειες, υποβαθμίζοντας όλα τα λειτουργικά χαρακτηριστικά της (Brennen, 2005, 2014; Παπαντώνης, 2016). Επιπλέον, η απώλεια μάζας από τις στρεφόμενες επιφάνειες (Σχ. Ε.1) οδηγεί σε επιπλέον κραδασμούς λόγω αζυγοσταθμίας, οι οποίοι επιβαρύνουν σημαντικά τις εδράσεις της μηχανής.

Συνεπώς, η αδυναμία έγκαιρης διάγνωσης του φαινομένου οδηγεί σε παρατεταμένη λειτουργία της μηχανής με χαμηλότερη απόδοση, καθώς επίσης σε καταστροφή των υδραυλικών (πτερύγια, πλήμνη και στεφάνη του ρότορα) αλλά και μηχανικών (εδράσεις και άξονας) μερών της. Όλα τα παραπάνω αιτιολογούν το ενδιαφέρον ερευνητών και μηχανικών για την έγκαιρη και αποτελεσματική διάγνωση της σπηλαίωσης, όταν αυτή εμφανίζεται εντός των υδροδυναμικών μηχανών.

Σχήμα Ε.1 Τυπική φθορά σε επιφάνειες πτερυγίων φυγοκεντρικών αντλιών λόγω εμφάνισης σπηλαίωσης (Brennen, 2014; Kamiel, 2015).

Ε.2 Σχηματισμοί σπηλαίωσης εντός υδροδυναμικών μηχανών

Οι μελέτες που ασχολούνται με τη σπηλαίωση εντός υδροδυναμικών μηχανών προσεγγίζουν το φαινόμενο από τη μακροσκοπική του σκοπιά, δηλαδή από τη στιγμή που οι φυσαλίδες ατμού συγκεντρώνονται ή μεγεθύνονται σε τέτοιο βαθμό που μπορούν να παρατηρηθούν οπτικά. Πέντε γενικοί τύποι σπηλαίωσης έχουν παρατηρηθεί με χρήση οπτικών πειραμάτων, εντός των υδροδυναμικών μηχανών i) σπηλαίωση φυσαλίδων (bubble or travelling bubble cavitation, Σχ. Ε.2a), ii) σπηλαίωση λόγω δημιουργίας δινών (vortex cavitation, Σχ. Ε.2b,c & Ε.3), iii) προσκολλημένη σπηλαίωση ή στρώμα σπηλαίωσης (attached or sheet cavitation, Σχ. Ε.2d), iv) σπηλαίωση νέφους, v) σπηλαίωση αναρροής (backflow cavitation, Σχ. Ε.3), και v) στρεφόμενη σπηλαίωση. Οι διάφοροι τύποι σπηλαίωσης περιγράφονται συνοπτικά σε αυτή την ενότητα.

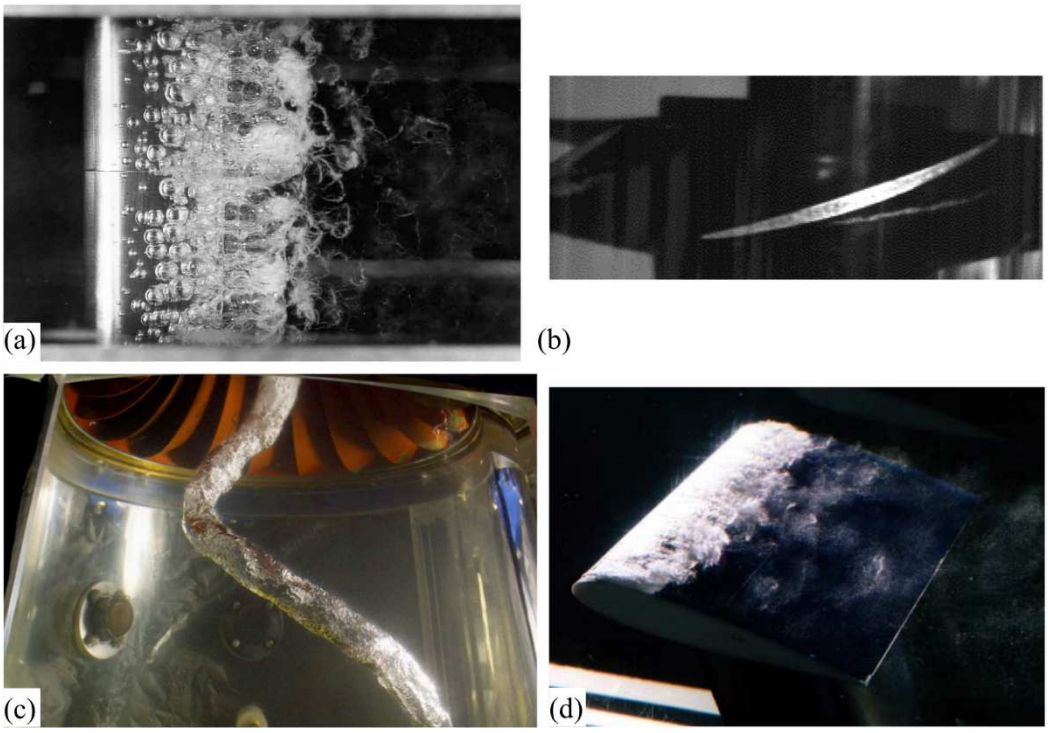

Σχήμα Ε.2 a) Σπηλαίωση φυσαλίδων στην επιφάνεια μιας NACA 4412 (Kermeen, 1956), **b)** σπηλαίωση δινών στο ακροπτερύγιο αξονικής αντλίας (Zhang D., 2015b), **c)** στήλη σπηλαίωσης στον αγωγό απαγωγής, κατάντι ενός δρομέα υδροστροβίλου Francis (Iliescu, 2008), **d)** προσκολλημένες κοιλότητες σπηλαίωσης σε υδροτομή (University of Tokyo, Applied Fluid Engineering Laboratory).

Η σπηλαίωση νέφους (Σχ. Ε.2a), αποτελείται από μεμονωμένες φυσαλίδες ατμού, οι οποίες σχηματίζονται στις περιοχές χαμηλής στατικής πίεσης και ενδορρηγνύονται περνώντας σε περιοχές υψηλής πίεσης. Αυτός ο τύπος σπηλαίωσης μπορεί να εμφανιστεί εντός υδροστροβίλων αντίδρασης και, πιο συγκεκριμένα, στην εσωτερική επιφάνεια του πτερυγίου, στην περιοχή της ακμής εισόδου, όταν λειτουργούν σε περιοχές χαμηλού ύψους (Ψ).

Η σπηλαίωση λόγω δημιουργίας δινών εμφανίζεται αρκετά συχνά και σε διαφορετικά σημεία της μηχανής, με πιο χαρακτηριστικές: i) την εμφάνιση στο ακροπτερύγιο μηχανών με ανοικτού ή ημι-ανοικτού τύπου πτερωτές/δρομείς (Σχ. Ε.2b), ii) την εμφάνιση στήλης σπηλαίωσης στον αγωγό απαγωγής, κατάντι δρομέων υδροστροβίλων αντίδρασης (Σχ. Ε.2c), iii) την εμφάνιση δινών στην περιοχή ανάμεσα στα πτερύγια δρομέων υδροστροβίλων αντίδρασης, που λειτουργούν σε πολύ χαμηλά φορτία, και iv) τη δημιουργία δινών Karman,

που σχηματίζονται κατάντι των πτερυγίων (σταθερά, οδηγητικά, δρομέα) εντός των υδροστροβίλων αντίδρασης.

Οι προσκολλημένες κοιλότητες σπηλαίωσης (Σχ. Ε2.d), παρουσιάζουν περισσότερο ενιαία και λιγότερο δυναμική από άποψη έκτασης δομή, σε σχέση με τους άλλους τύπους σπηλαίωσης. Ο συγκεκριμένος τύπος σπηλαίωσης εμφανίζεται και αλληλεπιδρά με την αποκόλληση της ροής σε περιπτώσεις όπου παρουσιάζονται αυξημένες γωνίες πρόσπτωσης.

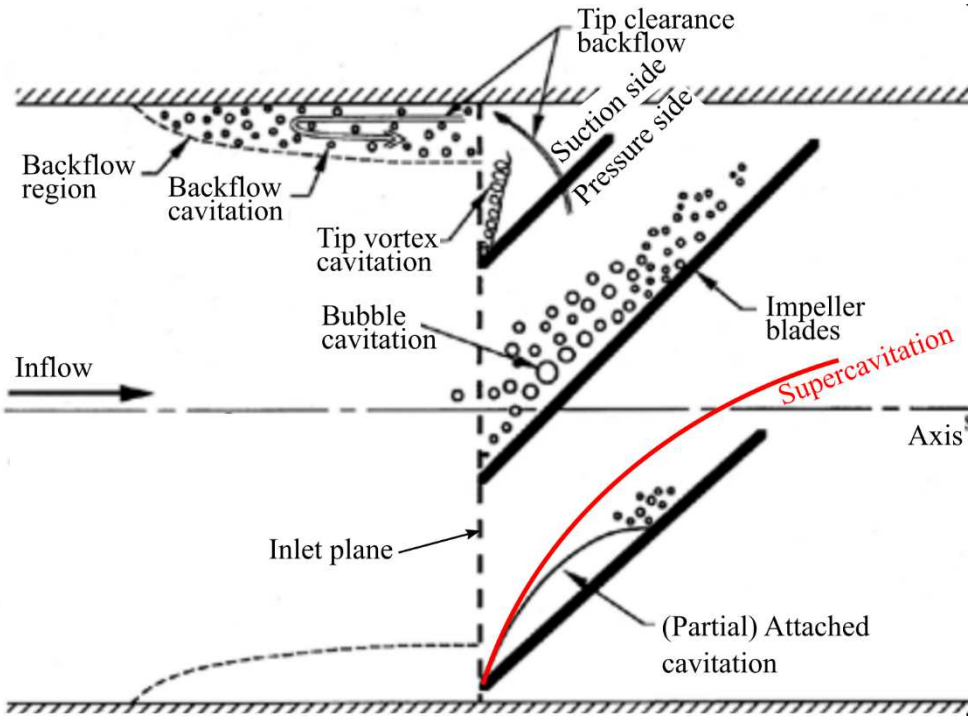

Σχήμα Ε.3 Τύποι σπηλαίωσης εντός φυγοκεντρικής αντλίας (Brennen, 2011).

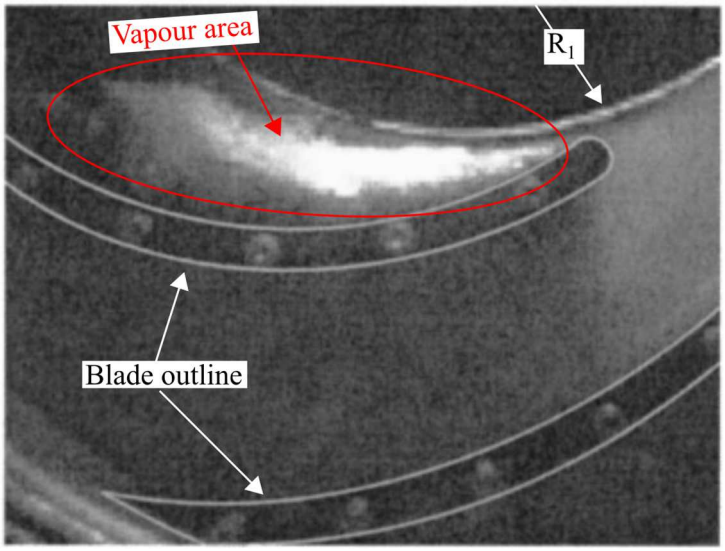

Σχήμα Ε.4 Στρεφόμενη σπηλαίωση σε φυγοκεντρική αντλία (Friedrichs, 2002).

Η σπηλαίωση αναρροής (Σχ. Ε.3) εμφανίζεται σε φυγοκεντρικές αντλίες ανοικτού ή ημι-ανοικτού τύπου, όπου η ροή τείνει να επιστρέψει προς την πλευρά υποπίεσης των πτερυγίων και προς την είσοδο της μηχανής, μέσω του διακένου στην περιοχή των ακροπτερυγίων. Η δημιουργία σπηλαίωσης στο διάκενο συνοδεύεται από τη μεταφορά της μέσω αυτών των ανακυκλοφοριών στις προαναφερθείσες περιοχές χαμηλής πίεσης (πλευρά υποπίεσης,

είσοδος), όπου ενδυναμώνεται η ήδη ανεπτυγμένη διφασική περιοχή. Τέλος η στρεφόμενη σπηλαίωση (Σχ. Ε.4) συνδεέται με το φαινόμενο της στρεφόμενης αποκόλλησης, όταν το τελευταίο συνδυάζεται με χαμηλά πεδία στατικών πιέσεων.

Ε.3 Στόχοι της ερευνητικής εργασίας

Στόχος της παρούσας εργασίας είναι η μελέτη του φαινομένου της σπηλαίωσης σε υδροδυναμικές μηχανές και η ανάπτυξη εργαλείων που θα επιτρέπουν την έγκαιρη και επιτυχημένη διάγνωσή της, καθώς και η διατύπωση ενός γενικού κριτηρίου το οποίο θα χρησιμοποιείται για τη διάγνωση του φαινομένου, πριν την πτώση του ύψους της μηχανής. Πιο συγκεκριμένα, κατασκευάζονται και χρησιμοποιούνται δύο πειραματικές διατάξεις φυγοκεντρικών αντλιών, οι οποίες επιτρέπουν την οπτική παρατήρηση του φαινομένου. Η μία διάταξη βρίσκεται στο Πανεπιστήμιο του Lancaster (UK), όπου δοκιμάζονται τρεις ημι-ανοικτού τύπου πτερωτές, και η άλλη διάταξη βρίσκεται στο Εργαστήριο των Υδροδυναμικών Μηχανών του ΕΜΠ, όπου δοκιμάζεται μια κλειστού τύπου πτερωτή. Οι μετρήσεις περιλαμβάνουν τη παραγωγή των χαρακτηριστικών καμπυλών λειτουργίας της κάθε μηχανής σε συνθήκες χωρίς και με σπηλαίωση. Μαζί με την παραγωγή των καμπυλών, διενεργούνται μετρήσεις κραδασμού και θορύβου και αναπτύσονται μέθοδοι επεξεργασίας των σημάτων, οι οποίες χρησιμοποιούνται για την έγκαιρη και αποτελεσματική διάγνωση του φαινομένου. Παράλληλα, για δύο από τις μηχανές αναπτύσεται υπολογιστικό μοντέλο προσομοίωσης της ροής, με στόχο την πληρέστερη κατανόηση των εσωτερικών χαρακτηριστικών της ροής, που ελέγχουν τον μηχανισμό της σπηλαίωσης. Το μοντέλο επικυρώνεται με βάση τα μετρούμενα αποτελέσματα των χαρακτηριστικών καμπυλών λειτουργίας καθώς επίσης και το μέγεθος και τη θέση της διφασικής περιοχής, σε διάφορα σημεία λειτουργίας.

1. Βιβλιογραφική Επισκόπηση

Η βιβλιογραφική επισκόπηση χωρίζεται σε δύο μέρη. Το πρώτο μέρος (ενότητα 1.1) έχει ως στόχο την ταξινόμηση των διαφορων τύπων βλάβης που μπορούν να εμφανίσουν οι υδροδυναμικές μηχανές. Αυτές διαφοροποιούνται βάσει των χαρακτηριστικών που παρουσιάζουν τα μετρούμενα σήματα κραδασμού ή θορύβου στα πεδία του χρόνου και της συχνότητας. Σε ορισμένες περιπτώσεις, για την ορθότερη αποτύπωση αυτών των χαρακτηρισικών προτείνεται και παρουσιάζεται η περαιτέρω επεξεργασία του σήματος με τεχνικές αποδιαμόρφωσης. Το δεύτερο μέρος (ενότητα 1.2) παρουσιάζει τις πειραματικές και υπολογιστικές εργασίες που έχουν ως στόχο τη διάγνωση της σπηλαίωσης που αναπτύσσεται σε υδροδυναμικές μηχανές. Όσον αφορά τις πρώτες, τα αποτελέσματα που παρουσιάζονται προκύπτουν από επεξεργασία, παρόμοια με αυτή που περιγράφηκε στις μετρήσεις του πρώτου μέρους (ενότητα 1.1).

1.2 Βλάβες και διεγέρσεις σε υδροδυναμικές μηχανές

1.2.1 Υδροδυναμικές διεγέρσεις

Στην ενότητα αυτή παρουσιάζονται τέσσερα είδη υδροδυναμικών μεταβατικών φαινομένων που εμφανίζονται κατά τη λειτουργία των υδροδυναμικών μηχανών, και αφορούν: i) την αλληλεπίδραση του ρότορα με το στάτορα, ii) τη δημιουργία στήλης σπηλαίωσης κατάντι του δρομέα υδροστροβίλων αντίδρασης, iii) τη δημιουργία δινών Karman, και iv) τη δημιουργια περιστροφικής αποκόλλησης.

Εκείνη η διέγερση που είναι συνεχώς παρούσα κατά τη λειτουργία υδροδυναμικών μηχανών είναι εκείνη που δημιουργείται από την αλληλεπίδραση του ρότορα και του στάτορα της μηχανής και δημιουργεί τη BPF (Blade Passing Frequency) (Gülich, 2008). Στην περίπτωση των υδροστροβίλων αντίδρασης, η ύπαρξη σταθερών και οδηγητικών πτερυγίων δημιουργεί τις αντίστοιχες διεγέρσεις (SVPS: Stay Vane Passing Frequency, GVPF: Guide Vane Passing Frequency) (Wu, 2013). Η διέγερση της αλληλεπίδρασης ρότορα-στάτορα διεγείρει την ακέραια αρμονική της περιστροφής της υδροδυναμικής μηχανής (RF), που αντιστοιχεί στον αντίστοιχο αριθμό πτερυγίων, ενώ δημιουργεί κύμα ημιτονοειδούς μορφής (Σχ. 1.1). Στο Σχ. 1.1 η BPF συνυπάρχει με τη χαμηλόσυχνη RF (Rotational Frequency) που τις περισσότερες φορές διεγείρεται από την ατελή ζυγοστάθμιση της μηχανής.

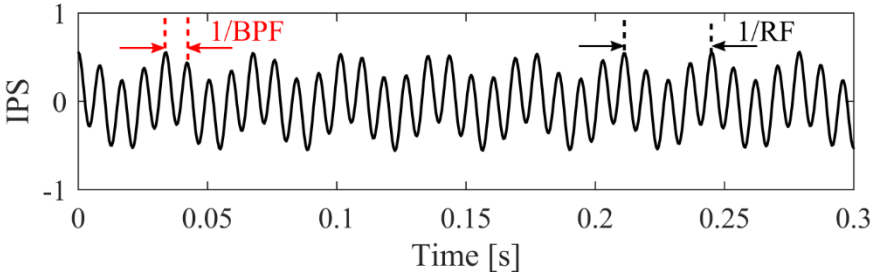

Σχήμα 1.1 Θεωρητική μορφή σήματος από φυγοκεντρική αντλία στο χρόνο (Taylor, 2005).

Η στήλη σπηλαίωσης αποτελεί την περισσότερο μελετημένη υδροδυναμική διέγερση στους υδροστροβίλους αντίδρασης καθώς οι χαμηλής συχνότητας ταλαντώσεις που προκαλεί μπορούν να επηρρεάσουν τη μηχανική αντοχή ολόκληρης της μονάδας (Jacob, 1996; Pennacchi, 2012a,b; Wu, 2013; Escaler, 2015; Papantonis, 2016; Valero, 2019). Η στήλη σπηλαίωσης δημιουργείται από την ύπαρξη συστροφής στην έξοδο του δρομέα, στα σημεία όπου η παροχή είναι διαφορετική αυτή που αντιστοιχεί στο βέλτιστο σημείο λειτουργίας (BEP: Best Efficiency Point), Φ_{BEP}. Πιο συγκεκριμένα, για $\Phi<\Phi_{BEP}$ η ροή εξέρχεται του δρομέα με συστροφή ίδιας διεύθυνσης με αυτή της περιστροφής (Ω) και δημιουργεί την ελικοειδή στήλη σπηλαίωσης (Σχ. 1.2a). Η συχνότητα της ελικοειδούς στήλης σπηλαίωσης είναι υποαρμονική της RF. Για $\Phi>\Phi_{BEP}$ η ροή εξέρχεται με συστροφή αντίθετη της περιστροφής ωστόσο η συχνότητά της είναι ίση με την RF. Στην περίπτωση αυτή, η δίνη έχει σχήμα που περισσότερο μοιάζει με κανονική μορφή δίνης (Σχ. 1.2b). Ένα παράδειγμα διάγνωσης του φαινομένου με χρήση φάσματος σε χαμηλές συχνότητες (<4· RF) δίνεται στο Σχ. 1.2c,d.

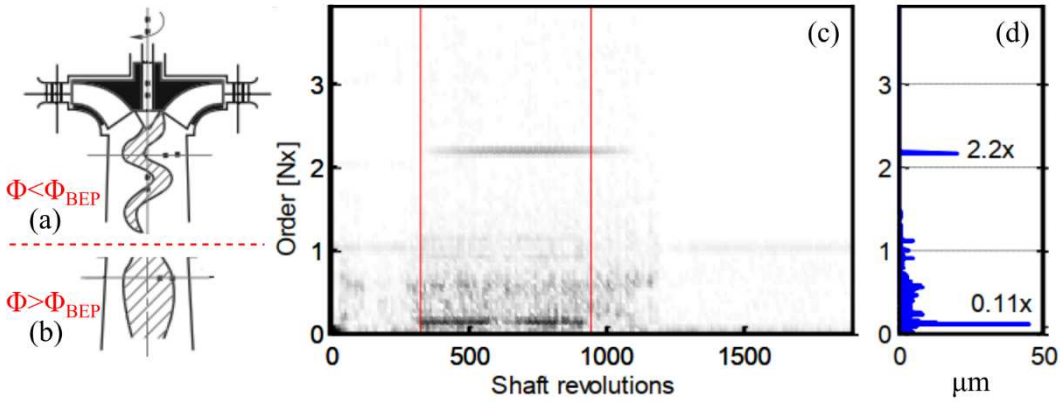

Σχήμα 1.2 a,b) Μορφή στήλης σπηλαίωσης για **a)** $\Phi<\Phi_{BEP}$, **b)** $\Phi>\Phi_{BEP}$ (Wu, 2013), **c)** φασματογράφημα, και **d**) και φάσμα συχνοτήτων ταλαντώσεων σε υδροστρόβιλο Kaplan για $\Phi<\Phi_{BEP}$ (Pennacchi, 2012a).

Οι δίνες Karman δημιουργούνται από την αποκόλληση της ροής στην ακμή φυγής των πτερυγίων, ιδίως των υδροστροβίλων αντίδρασης (Dörfler, 2012; Wu, 2013). Το αποτύπωμα της βλάβης αυτής απαντάται δύσκολα σε μετρήσεις κραδασμών ή θορύβου λόγω της μικρής του έντασης σε σχέση με το συνολικότερο θόρυβο της μηχανής. Σε μία από τις λίγες εργασίες (Escaler, 2006), μετρώνται ταλαντώσεις στην έδραση ενός μοντέλου Francis (Σχ. 1.3a), σε σημεία λειτουργίας χωρίς (μπλέ) και με (μωβ) σπηλαίωση. Η σπηλαίωση στη δεύτερη περίπτωση περιλαμβάνει σπηλαίωση στην έξοδο των πτερυγίων μαζί με σπηλαίωση που συνοδεύεται με δίνες Karman. Στο Σχ. 1.3 παρουσιάζονται τα αποτελέσματα της αποδιαμόρφωσης του σήματος και φαίνεται ότι στην περίπτωση της σπηλαίωσης διεγείρονται η RF, η BPF και η GVPF.

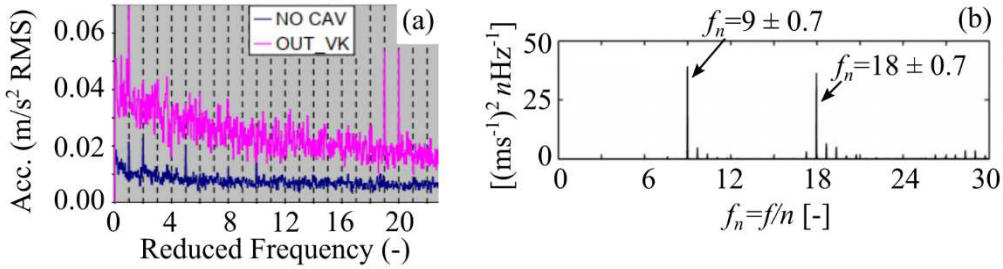

Σχήμα 1.3 a) Πεδίο συχνοτήτων του αποδιαμορφωμένου σήματος κραδασμού σε συνθήκες με και χωρίς σπηλαίωση (Escaler, 2006), **b)** Πεδίο συχνοτήτων μέτρησης κραδασμού σε συνθήκες περιστροφικής αποκόλλησης (Botero, 2014).

Τέλος η περιστροφική αποκόλληση, επίσης δεν έχει μελετηθεί αρκετά λόγω ότι δημιουργείται σε πολύ μικρές παροχές, όπου παρατηρούνται οι μέγιστες διαφορές μεταξύ της γωνίας της ροής (β_{w1}) και της γωνίας του πτερυγίου (β_1). Ενδιαφέρον παρουσιάζουν τα αποτελέσματα που αφορούν αντλίες που λειτουργούν σε ανάστροφη λειτουργία και η γωνία πρόσπτωσης είναι πιθανό να είναι αυξημένη. Σε μία τέτοια περίπτωση (Botero, 2014) το φαινόμενο διαγνώστηκε με μεθόδους αποδιαμόρφωσης στο πεδίο των συχνοτήτων μετά την συσχέτηση του με της πλευρικές συχνότητες ±0.7· RF (Σχ. 1.3b).

1.2.2 Βλάβες του Η/Μ εξοπλισμού

Οι βλάβες του Ηλεκτρομηχανολογικού (Η/Μ) εξοπλισμού χωρίζονται σε τρεις γενικές κατηγορίες, σε αυτές που αφορούν: i) συχνότητες υποαρμονικές και αρμονικές της RF, ii) φθορές στον κινητήρα, iii) φθορές στα έδρανα κυλίσεως (ρουλεμάν).

Στην πρώτη κατηγορία ανήκουν: i) η αζυγοσταθμία, ii) η κακή ευθυγράμμιση, iii) οι λυγισμένοι άξονες, και iv) η μηχανική χαλαρότητα. Όλες οι βλάβες προσδίδουν στο σήμα της ταλάντωσης στο χρόνο ημιτονοειδή μορφή, ενώ οι συχνότητες που διεγείρουν στο φάσμα, παρουσιάζονται για όλες τις περιπτώσεις στο Σχ. 1.4 (Taylor, 2005).

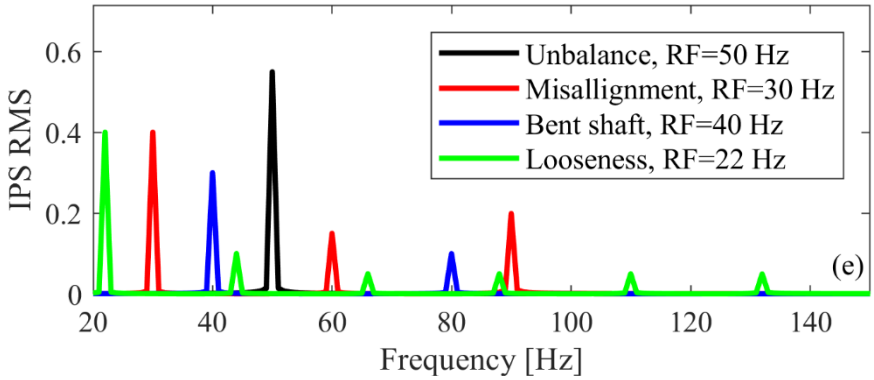

Σχήμα 1.4 Πεδίο συχνοτήτων μετρήσεων μηχανικών κραδασμών, για διαφορετικούς τύπους βλάβης (Taylor, 2005).

Στη δεύτερη κατηγορία ανήκουν οι βλάβες στην ηλεκτρική μηχανή, και πιο συγκεκριμένα αυτές που αφορούν σε επαγωγικούς κινητήρες, με τους οποίους ασχολείται η παρούσα εργασία. Για βλάβη που αφορά το στάτορα της μηχανής, αυτή παρουσιάζει παρόμοιο μηχανισμό με εκείνης της BPF (ενότητα 1.2.1), ωστόσο σε αυτή την περίπτωση διεγείρει τη δεύτερη αρμονική της συχνότητας του δικτύου (GF: Grid Frequency). Ένα τυπικό φάσμα συχνότητας που καταδεικνύει βλάβη στο στάτορα επαγωγικού κινητήρα δίνεται στο Σχ. 1.5.

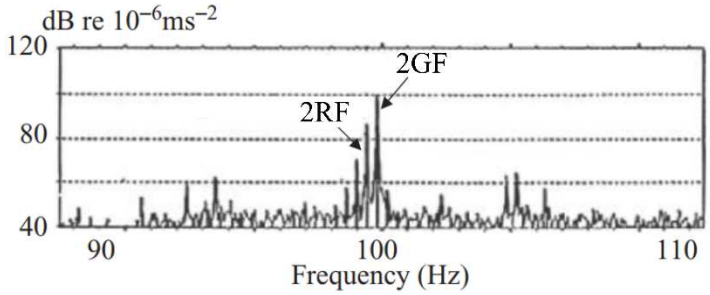

Σχήμα 1.5 Βλάβη στο στάτορα επαγωγικού κινητήρα, στο πεδίο συχνοτήτων (Randall, 2007).

Από την άλλη μεριά, η διάγνωση φθοράς στο ρότορα της μηχανής γίνεται με την αξιοποίηση των πλευρικών συχνοτήτων, οι οποίες δημιουργούνται σε απόσταση SBF_R (Side Band

Frequency Rotor) από την RF. Η τελευταία αποτελεί το γινόμενο του αριθμού των πόλων, n_p, με τη συχνότητα ολίσθησης (SF: Slip Frequency). Με αντίστοιχο τρόπο μπορεί να διαγνωστεί η χαλαρότητα, η οποία δημιουργεί πλευρικές συχνότητες με εύρος τη δεύτερη αρμονική στης GF, γύρω από τη συχνότητα περάσματος των ράβδων (ABPF: Aramture Bar Passing Frequency).

Τα ρουλεμάν αποτελούν το σημείο της μηχανής στο οποίο παραλαμβάνονται τα φορτία της μηχανής και οι φθορές που μπορεί να παρουσιάσουν αφορούν: i) τον εξωτερικό δακτύλιο, ii) τον εσωτερικό δακτύλιο, iii) τα στοιχεία κύλισης, και iv) τον κλωβό. Κάθε μία από τις βλάβες διεγείρει ξεχωριστές συχνότητες, BPFO, BPFI, BSF, FTF, οι οποίες μπορούν να υπολογιστούν βάσει των γεωμετρικών και λειτουργικών χαρακτηριστικών του κάθε ρουλεμάν. Ωστόσο, η παρουσία των τριών πρώτων βλαβών έχει ως αποτέλεσμα χτυπήματα, τα οποία διεγείρουν διάφορες ιδιοσυχνότητες της μηχανής, που σε συνδυασμό με την τυχαιότητα που εισάγει η ολίσθηση των στοιχείων κύλισης καθιστούν αδύνατη, στις περισσότερες φορές, τη διάγνωση του με χρήση του πεδίου συχνοτήτων. Γι' αυτό το λόγο, προτείνεται η χρήση μεθόδων αποδιαμόρφωσης και η μελέτη του σήματος που προκύπτει από τη χρήση φίλτρου εύρους ζώνης (band pass filter) καθώς και της αντίστοιχης περιβάλλουσας στο πεδίο του χρόνου και των συχνοτήτων. Στο σχήμα 1.6 δίνονται τα χαρακτηριστικά του σήματος για κάθε μία βλάβη.

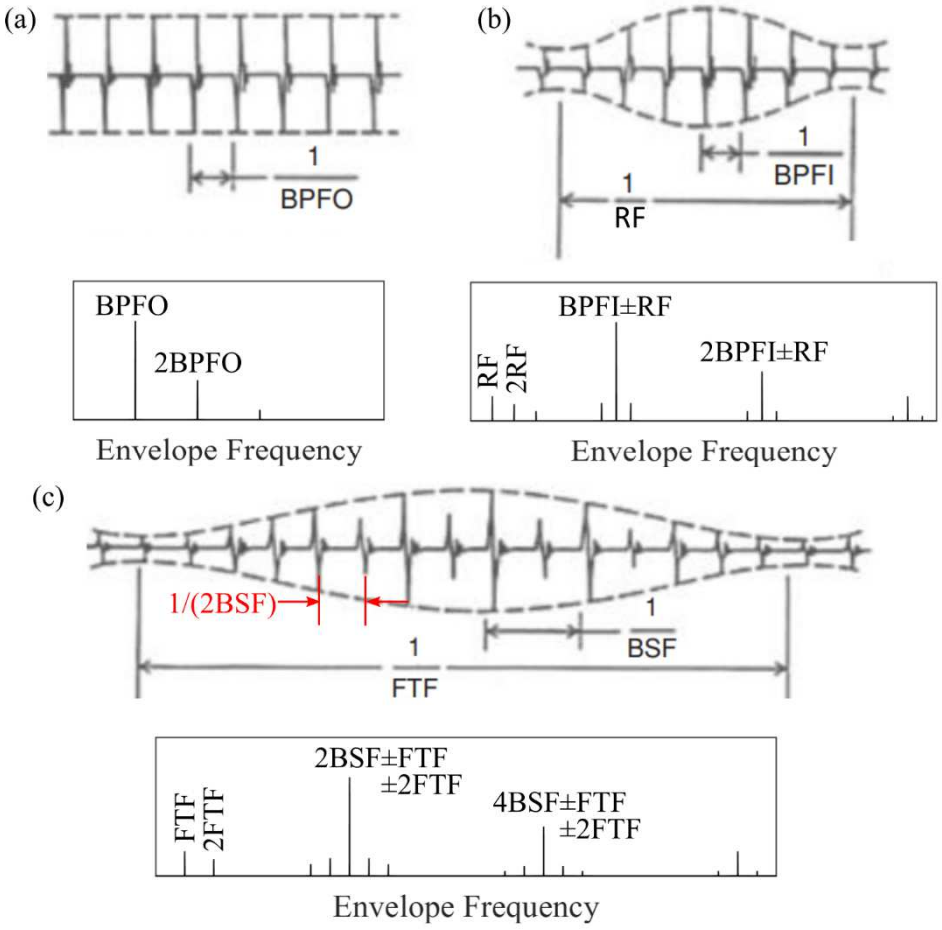

Σχήμα 1.6 Χαρακτηριστική μορφή του σήματος στο χρόνο (Randall, 2007) και στο πεδίο συχνοτήτων της περιβάλλουσας για φθορά **a)** εξωτερικού δακτυλίου, **b)** εσωτερικού δακτυλίου, και **c)** στοιχείων κύλισης.

Τέλος, η φθορά που σχετίζεται με τον κλωβό του ρουλεμάν, δεν δημιουργεί χτυπήματα, και η διάγνωσή της γίνεται βάση της παρουσίας της διακριτής της συχνότητας (FTF) και των πρώτω αρμονικών της στο πεδίο των συχνοτήτων.

1.3 Διάγνωση σπηλαίωσης σε υδροδυναμικές μηχανές

Την παρουσίαση των διάφορων τύπων στις υδροδυναμικές μηχανές ακολουθεί η επισκόπηση των πειραματικών μεθόδων διάγνωσης και των υπολογιστικών εργαλείων που χρησιμοποιούνται για τη μελέτη της εντός υδροδυναμικών μηχανών.

1.3.1 Πειραματικές μετρήσεις

Ο παραδοσιακός τρόπος διάγνωσης του φαινομένου γίνεται με την παρακολούθηση της ενέργειας που εναλλάσεται μεταξύ της μηχανής και του ρευστού (H_{tot}, Ψ). Σύμφωνα με πειραματικές μετρήσεις, η ανάπτυξη του φαινομένου, υπο συνθήκες σταθερής παροχής, οδηγεί σε πτώση του ύψους, η οποία γίνεται απότομα, στην ακραία περίπτωση όπου το φαινόμενο έχει επεκταθεί σε βαθμό που δεν επιτρέπει στη μηχανή να εναλλάσει την ενέργεια με το εργαζόμενο μέσο. Η ανάπτυξη του φαινομένου προσδιορίζεται από το καθαρό θετικό ύψος αναρρόφησης (NPSH: Net Positive Suction Head available) ή την αδιάστατη μορφή του σ, τα οποία εκφράζουν την εγκατάσταση της μηχανής και μειώνονται με την πτώση της στατικής πίεσης στην εγκατάσταση. Τυπικά παραδείγματα NPSH-H_{tot} καμπυλών υπό συνθήκες σταθερή παροχής (Q) δίνονται στο Σχ. 1.7 (καμπύλες με μαύρο χρώμα). Σε κάθε χαρακτηριστική εμφανίζονται διάφορα σημεία λειτουργίας τα οποια χαρακτηρίζουν την ανάπτυξη του φαινομένου κατά: i) την οπτική του εμφάνιση (VI: Visual Inception) $NPSH_{VI}$, ii) την έναρξη της πτώσης του H_{tot}, $NPSH_o$, iii) την 3% πτώση του H_{tot}, $NPSH_3$, και iv) την τελική πτώση του H_{tot}, $NPSH_{FC}$. Η σχέση αυτων των σημείων με την παροχή παράγει τις χαρακτηριστικές Q-NPSH, που χαρακτηρίζουν τη μηχανή και που επίσης παρουσιάζονται στο Σχ. 1.7. Από αυτές, ως ένδειξη για την ανάπτυξη του φαινομένου εντός της μηχανής συνήθως επιλέγεται η $NPSH_3$. Επομένως, ο παραδοσιακός τρόπος αναγνώρισης του φαινομένου αφορά την παρακολούθηση του H_{tot}, του οποίου η πτώση με 3% δηλώνει την ανάπτυξη της σπηλαίωσης.

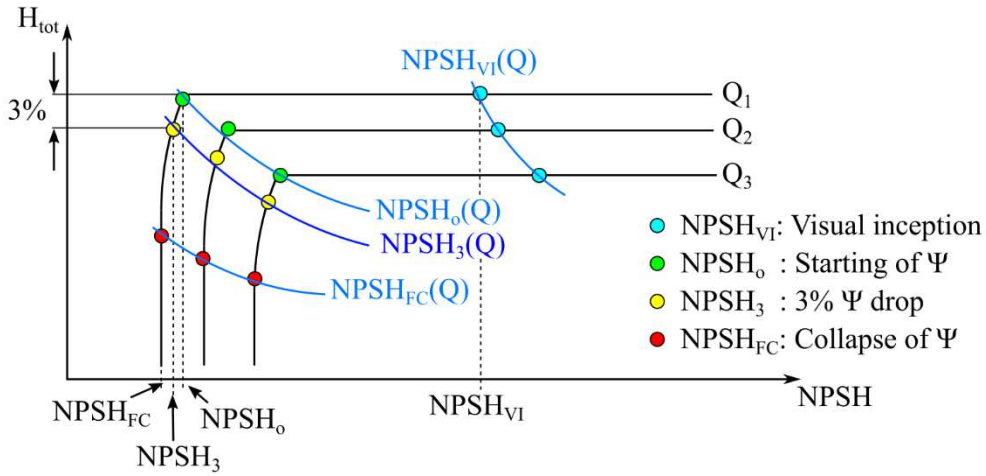

Σχήμα 1.7 Χαρακτηριστική μορφή καμπυλών NPSH-H_{tot}.

Το βασικό μειονέκτημα της παρακολούθησης του H_{tot} σχετίζεται με το γεγονός ότι δε μπορεί να διαγνώσει το φαινόμενο, παρά μόνο όταν αυτό προκαλέσεις την πτώση του ύψους. Ωστόσο, η ανάπτυξη της διφασικής περιοχής έχει ξεκινήσει από πολύ νωρίτερα ($NPSH_{VI}$) και για όσο διάστημα η μηχανή λειτουργεί μεταξύ $NPSH_{VI}$ και $NPSH_3$, ο μηχανισμός φθοράς της (ενδόρρηξη φυσαλίδων) αλλοιώνει τα χαρακτηριστικά των στερεών επιφανειών.

Για να γίνει δυνατή η έγκαιρη διάγνωση του φαινομένου προτείνονται μετρήσεις θορύβου και ταλάντωσης, οι οποίες σε πρώτη φάση, εξετάζονται στο πεδίο χρόνου και συχνοτήτων, όμοια με την πλειονότητα των βλαβών που περιγράφηκαν στην ενότητα 1.2. Ο μηχανισμός φθοράς των φυσσαλίδων δημιουργεί χτυπήματα στη μηχανή τα οποία συνήθως καλύπτονται από το συνολικό θόρυβο της τελευταίας. Γι' αυτό το λόγο είναι λίγες οι εργασίες στις οποίες

το φαινόμενο εντοπίζεται στο σήμα της μέτρησης χωρίς κάποια επεξεργασία (Al Hashmi, 2009; Duplaa, 2010; Schmidt, 2014). Στις περισσότερες περιπτώσεις, τα σήματα εξετάζονται στο πεδίο των συχνοτήτων (Σχ. 1.8), όπου αναδεικνύεται η διέγερση μεγάλων ευρών συχνοτήτων (Escaler, 2003, 2004; Cernetič, 2008; Chudina, 2009a; Ganeriwala, 2011; Zhang N., 2015a; Abdulaziz, 2017).

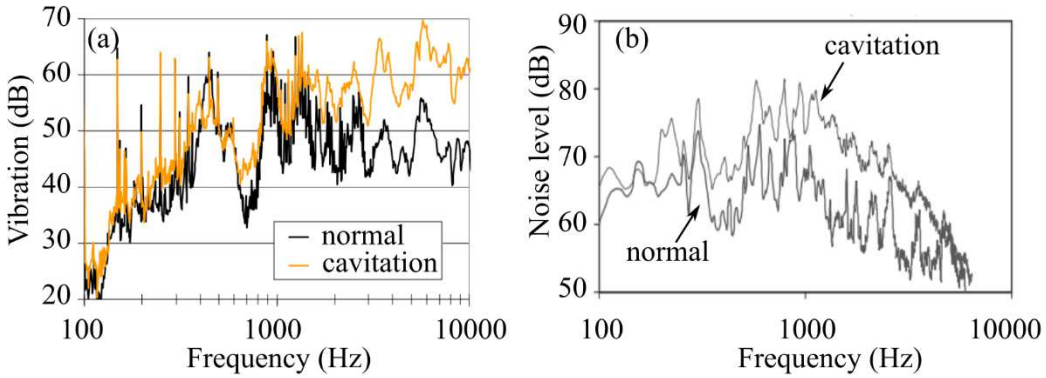

Σχήμα 1.8 Πεδίο συχνοτήτων **a)** ταλάντωσης σε αντλία με μεταλλική πτερωτή κλειστού τύπου (Cernetič, 2008) και **b)** θορύβου σε αντλία με πλαστική πτερωτή ημι-ανοικτού τύπου (Chudina, 2009a) σε συνθήκες με και χωρίς σπηλαίωση.

Αυτή η συμπεριφορά σχετίζεται με τη κρουστικότητα του φαινομένου και παρουσιάζει σημαντικές αναλογίες με τη διέγερση των ιδιοσυχνοτήτων στα ρουλεμάν. Για να ποσοτικοποιηθεί η αύξηση αυτή, οι διάφοροι ερευνητές προτείνουν τη μελέτη της ισχύος σε διακριτές συχνότητες ή σε εύρη συχνοτήτων με χρήση AE_{RMS} και powerbands (Pearsall, 1966; Varga, 1969; McNulty, 1982; Gopalakrishnan, 1985; Gülich, 1989; Bourdon, 1994; Neill, 1997; Escaler, 2003; Chudina, 2003b; Alfayez, 2004; Chudina & Prezelj, 2009; Schmidt, 2014; Zhang N., 2015a; Dong, 2019). Τα αποτελέσματα της βιβλιογραφίας αποδεικνύουν ότι τα παραπάνω εργαλεία αναγνωρίζουν την ανάπτυξη του φαινομένου, εφόσον η ένταση τους αυξάνει και μεγιστοποιείται για $\sigma<\sigma_{VI}$. Ωστόσο η μορφή των καμπυλών που παράγονται σε σχέση με το σ, αλλάζει στις διάφορες μηχανές, συνθήκες λειτουργίας και εύρη (ή διακριτές) συχνοτήτων που χρησιμοποιούνται για τον υπολογισμό των AE_{RMS} και powerbands. Ένα δεύτερο σημείο διαφοροποίησης που αναδεικνύει η μελέτη της βιβλιογραφίας αφορά τη μεγιστοποίηση της έντασης των AE_{RMS} και powerbands σε άλλα σ. Αυτές οι διαφοροποίησεις δυσκολεύουν τη δημιουργία ενός γενικού κριτηρίου διάγνωσης της σπηλαίωσης, που θα μπορεί να χρησιμοποιηθεί σε πάνω από μία μηχανές.

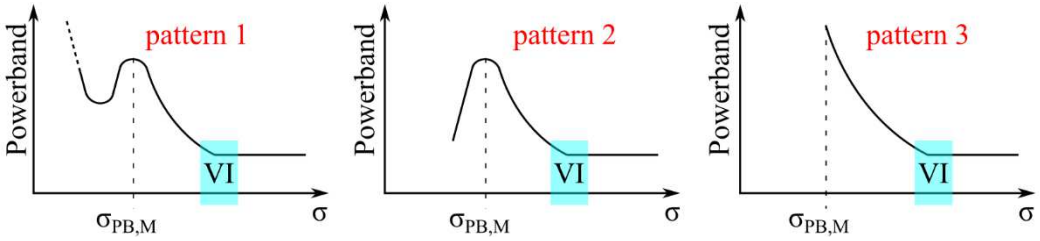

Σχήμα 1.9 Χαρακτηριστικές μορφές καμπυλών AE_{RMS} και powerbands σε σχέση με το σ.

Μία επιπλέον μέθοδος που συναντάται στη διεθνή βιβλιογραφία αφορά τη διάγνωση της σπηλαίωσης σε υδροστροβίλους, μετά την αποδιαμόρφωση του σήματος της ταλάντωσης και του θορύβου (Bourdon, 1994; Escaler, 2002, 2004). Η μέθοδος παρουσιάζει ενδιαφέροντα αποτελέσματα καθώς αναδεικνύει τη διαμόρφωση του σήματος που παράγει η σπηλαίωση από κυρίαρχες διεγέρσεις της μηχανής όπως, την αλληλεπίδραση ρότορα με στάτορα ή τη συχνότητα της στήλης σπηλαίωσης. Τυπικά αποτελέσματα αυτής της μεθόδου παρουσιάζονται στο Σχ. 1.10, όταν ο εξεταζόμενος υδροστρόβιλος αλλάζει σημεία λειτουργίας, από μερικά φορτία (30 MW) έως το ονομαστικό (65 MW).

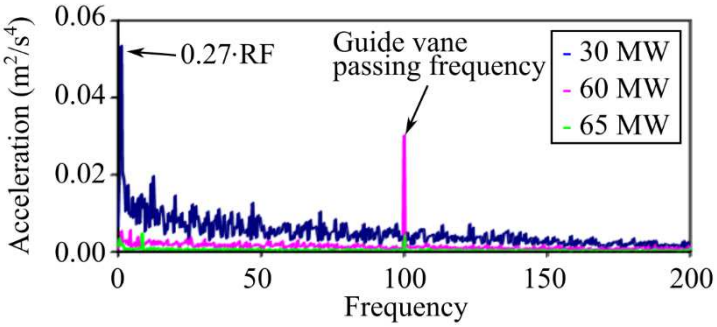

Σχήμα 1.10 Πεδίο συχνοτήτων περιβάλλουσας μηχανικών κραδασμών σε τρία διαφορετικά σημεία λειτουργίας πρωτότυπου υδροστροβίλου Francis (Escaler, 2002).

1.3.2 Υπολογιστικές προσεγγίσεις

Από μεριάς υπολογιστικών εργασιών, αυτές συνδυάζουν τη προσέγγιση RANS (Reynolds-averaged Navier-Stokes) με φυσικά μοντέλα που περιγράφουν τη διαδικασία ατμοποίησης και συμπύκνωσης (Coutier-Delgosha, 2007). Το τελευταίο επιτυγχάνεται μέσω της επίλυσης μιας επιπλέον εξίσωσης μεταφοράς, που περιλαμβάνει τους όρους αύξησης και μείωσης της υγρής φάσης. Η μοντελοποίηση των τελευταίων όρων γίνεται συνήθως με τη θεώρηση ομοιογενούς μίγματος ατμού και ρευστού (Zwart, 2004), ενώ σε ορισμένες περιπτώσεις το μίγμα περιλαμβάνει και τα μη συμπυκνώσιμα αέρια (Kunz, 2000; Singhal, 2002).

Η εφαρμογή των παραπάνω μοντέλων σε εσωτερικές διφασικές ροές υδροδυναμικών μηχανών γίνεται κυρίως για λόγους κατανόησης της εμφάνισης του φαινομένου σε διάφορες συνθήκες λειτουργίας, ενώ στη μεγάλη πλειοψηφία των εργασιών, τα αριθμητικά αποτελέσματα συνοδεύονται από πειράματα οπτικοποίησης τα οποίο πιστοποιούν τα παραγόμενα αποτελέσματα (Σχ. 1.11). Σε γενικές γραμμές, από τη μελέτη της βιβλιογραφίας συμπεραίνεται ότι αυτού του είδους η μοντελοποίηση προβλέπει με επιτυχία όχι μόνο τη μορφή των χαρακτηριστικών καμπυλών λειτουργίας (σ-Ψ) και την πτώση του ύψους αλλά και τη θέση και την έκταση της διφασικής περιοχής (Σχ. 1.11).

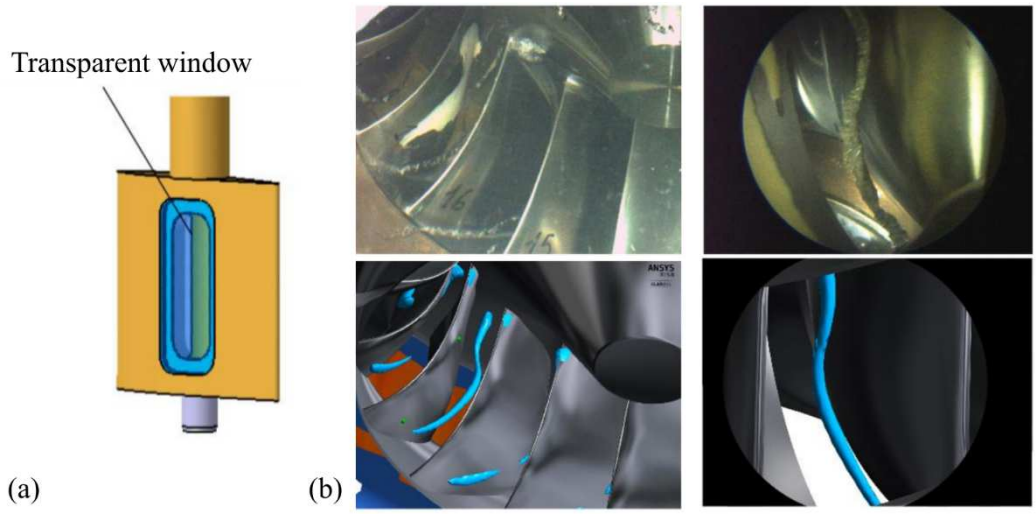

Σχήμα 1.11 a) Κατασκευή ειδικού παραθύρου στο οδηγητικό πτερύγιο υδροστροβίλου Francis για την **b)** οπτική παρατήρηση των σπηλαιωμένων δινών στην περιοχή ανάμεσα στα πτερύγια του δρομέα και τη σύγκριση με τα αριθμητικά αποτελέσματα (Yamamoto, 2016).

2. Πειραματικές Μέθοδοι και Διατάξεις

2.1 Φυγοκεντρικές αντλίες

Όπως περιγράφηκε στην ενότητα Ε.3, στην παρούσα εργασία δοκιμάζονται τέσσερις πτερωτές σε δύο φυγοκεντρικές αντλίες. Οι μετρήσεις της σπηλαίωσης (NPSH-H_{tot}, σ-Ψ) έπονται εκείνων που γίνονται σε κανονικές συνθήκες και στόχο έχουν την κατασκευή των χαρακτηριστικών καμπυλών λειτουργίας των μηχανών. Τρεις χαρακτηριστικές καμπύλες λειτουργίας κατασκευάζονται, η καμπύλη: i) του ύψους (Q-H_{tot}), ii) της ισχύος (Q-P_{mech}), και iii) του βαθμού απόδοσης (Q-η). Για την κατασκευή τους χρησιμοποιούνται οι Εξ. 2.1-2.4:

$$H_{tot} = \left(\frac{p_a}{\rho g} - \frac{p_e}{\rho g} \right) + \left(\frac{c_a^{\,2}}{2g} - \frac{c_e^{\,2}}{2g} \right) + \Delta z \tag{2.1}$$

$$\eta = \frac{\text{hydraulic power}}{\text{mechanical power}} = \frac{\rho g H_{tot} Q}{P_{mech}} \tag{2.2}$$

$$P_{mech} = M_m \Omega \tag{2.3}$$

$$P_{mech} = P_{el} \eta_{mot} \tag{2.4}$$

όπου p_a είναι η στατική πίεση στην αναρρόφηση, p_e η στατική πίεση στην κατάθλιψη, c_a η ταχύτητα στον αγωγό αναρρόφησης, c_e η ταχύτητα στον αγωγό κατάθλιψης, Δz η κάθετη απόσταση μεταξύ του επιπέδου αναρρόφησης και κατάθλιψης, ρ η πυκνότητα, g η επιτάχυνση της βαρύτητας, Q η παροχή, P_{mech} η μηχανική ισχύς, M_m η μηχανική ροπή, Ω η ταχύτητα περιστροφής, P_{el} η ηλεκτρική ισχύς και η_{mot} ο βαθμός απόδοσης του κινητήρα.

Η αδιαστατοποίηση των χαρακτηριστικών καμπυλών λειτουργίας γίνεται μέσω των Εξ. 2.5-2.7. Σε αυτές τις εξισώσεις, η v_{n2} είναι η ορθή συνιστώσα της απόλυτης ταχύτητας, η u_2 είναι εφαπτομενική ταχύτητα, d_2 η διάμετρος στην έξοδο της πτερωτής, z_s ο αιρθμός των πτερυγίων, e_2 το πάχος πτερυγίου στη d_2 και το $b_{I,2}$ το πλάτος του πτερυγίου στη d_2.

$$\Phi = \frac{v_{n2}}{u_2} = \frac{2Q}{\Omega\, d_2 \left(\pi d_2 - z_s e_2 \right) b_{I,2}} \tag{2.5}$$

$$\Psi = \frac{2gH_{tot}}{u_2^{\,2}} = \frac{8gH_{tot}}{\left(\Omega d_2 \right)^2} \tag{2.6}$$

$$N = \frac{P_{mech}}{\rho \Omega^3 d_2^{\,5}} \tag{2.7}$$

Αντίστοιχα οι χαρακτηριστικές καμπύλες λειτουργίας για τη σπηλαίωση (NPSH-H_{tot}) υπολογίζονται από την Εξ. 2.8, η οποία αδιαστατοποιείται από την Εξ. 2.9, όπου το H_{sat} εκφράζει την πίεση ατμοποίησης για συγκεκριμένη θερμοκρασία σε μέτρα στήλης ύδατος.

$$NPSH = \frac{p_e}{\rho g} + \frac{8Q^2}{g\pi^2 d_{p,e}{}^4} - H_{sat} \tag{2.8}$$

$$\sigma = \frac{NPSH}{H_{tot}} \tag{2.9}$$

2.2 Πειραματικές μέθοδοι

Για την παραγωγή των χαρακτηριστικών καμπυλών λειτουργίας σε κανονικές συνθήκες λειτουργίας, ακολουθείται η διαδικασία που περιγράφεται με τη βοήθεια του Σχ. 2.1. Πιο συγκεκριμένα, ρυθμίζονται οι στροφές της αντλίας (1), και ανοίγει πλήρως η βάνα της αναρρόφησης (3) (Σχ. 2.1α). Οι παραπάνω παράμετροι δε αλλάζουν κατά τη διάρκεια του πειράματος. Για την αλλαγή του σημείου λειτουργίας της εγκατάστασης (σημείο τομής της μπλέ και της μαύρης καμπύλης στο Σχ. 2.1b) ρυθμίζεται η βάνας της κατάθλιψης (4). Όσο η τελευταία ανοίγει τόσο ο συντελεστής απωλειών μικραίνει, η παροχή μεγαλώνει και δίνεται η δυνατότητα της παραγωγής των χαρακτηριστικών από της εξισώσεις της ενότητας 2.1.

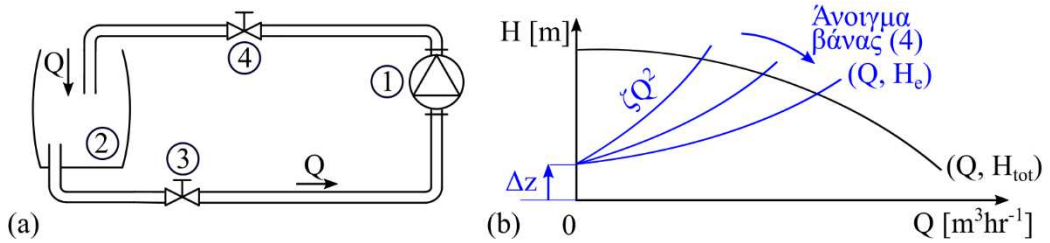

Σχήμα 2.1 a) Απεικόνιση πειραματικής διάταξης που χρησιμοποιείται για την παραγωγή των χαρακτηριστικών καμπυλών λειτουργίας μιας φυγοκεντρικής αντλίας, **b)** Απεικόνισης της μεθόδου χάραξης (Papantonis, 2016).

Για την παραγωγή των χαρακτηριστικών καμπυλών σπηλαίωσης υπό σταθερή *Q*, χρησιμοποιείται η μέθοδος αύξησης των απωλειών στον κλάδο αναρρόφησης, με το σταδιακό «κλείσιμο» της βάνας (3) (Σχ. 2.1a). Ωστόσο, επειδή το «κλείσιμο» της βάνας (3) μειώνει την παροχή, χρησιμοποιείται η βάνα στον αγωγό κατάθλιψης (4) για τη επανα-ρύθμισή της στην επιθυμητή τιμή. Τα αποτελέσματα της διαδικασίας για την παραγωγή μίας NPSH-H_{tot}, υπο σταθερή Q δίνονται στο Σχ. 2.2. Το βασικό συμπέρασμα που εξάγεται από την αποτύπωση των μετρήσεων, είναι το γεγονός ότι μειώνοντας το NPSH (OP1→…→OP10), η διαφορά των στατικών πιέσεων παραμένει σταθερή, μέχρι ενός σημείου που παρατηρείται έντονη μείωση της, η οποία και χαρακτηρίζει την πτώση του ύψους με την ανάπτυξη της σπηλαίωσης.

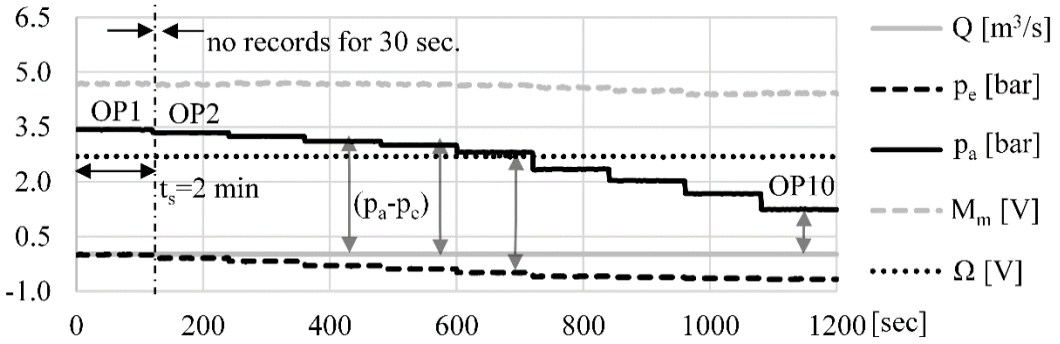

Σχήμα 2.2 Τυπικά αποτελέσματα μετρήσεων για την παραγωγή μιας καμπύλης NPSH-H_{tot}.

2.3 Μετρήσεις θορύβου και μηχανικών ταλαντώσεων

Οι μετρήσεις θορύβου και ταλάντωσης γίνονται με στόχο τη σύγκριση των σημάτων που μετρήθηκαν κάτω από διάφορες συνθήκες λειτουργίας, από τη μέγιστη έως την ελάχιστη τιμή των σ και NPSH. Η πρόθεση της παρούσας εργασίας αφορά την αναγνώριση εκείνων των χαρακτηριστικών στο μετρούμενο σήμα, που θα καθιστά δυνατή τη διάγνωση του φαινομένου και θα το διαφοροποιεί από τις βλάβες που παρουσιάστηκαν στην ενότητα 1.2. Η αναγνώριση των χαρακτηριστικών του φαινομένου γίνεται μέσω της κατάλληλης επεξεργασίας του μετρούμενου σήματος. Πιο συγκεκριμένα:

i. Το μετρημένα σήματα συγκρίνονται για τα διάφορα σημεία λειτουργίας και ανάπτυξης της σπηλαίωσης (NPSH, σ).
ii. Αναλύεται η κατανομή των μετρήσεων και η επιρροή της σπηλαίωσης στον τύπο και τα βασικά της χαρακτηριστικά.
iii. Υπολογίζονται οι τέσσερις στατιστικές ροπές (μέση τιμή, τυπική απόκλιση, στρέβλωση και κύρτωση) και αποτυπώνεται η μεταβολή τους σε σχέση με το σ.
iv. Αποτυπώνεται η μεταβατική συμπεριφορά των παραμέτρων αυτών σε σχέση με το σ.
v. Μελετάται η επιρροή της εμφάνισης του φαινομένου στο πεδίο συχνοτήτων των σημάτων, ενώ η ανάλυση διαχωρίζεται μεταξύ χαμηλών και υψηλών συχνοτήτων.
vi. Εφαρμόζεται η μέθοδος της Φασματικής Κύρτωσης (SK) με στόχο την αποδιαμόρφωση των σημάτων κραδασμού και τη μελέτη του φιλτραρισμένου σήματος αλλά και του πεδίου συχνοτήτων της περιβάλλουσας.

2.4 Πειραματικές διατάξεις

Οι τέσσερις πτερωτές που χρησιμοποιούνται στην παρούσα μελέτη παρουσιάζονται στο Σχ. 2.3. Οι τρεις πρώτες (Σχ. 2.3a-c) είναι ημι-ανοικτού τύπου και δοκιμάζονται στην πειραματική εγκατάσταση του Πανεπιστημίου Lancaster (LU, UK), ενώ η τέταρτη (Σχ. 2.3d) είναι κλειστού τύπου και δοκιμάζεται στο Εργαστήριο των Υδροδυναμικών Μηχανών του ΕΜΠ.

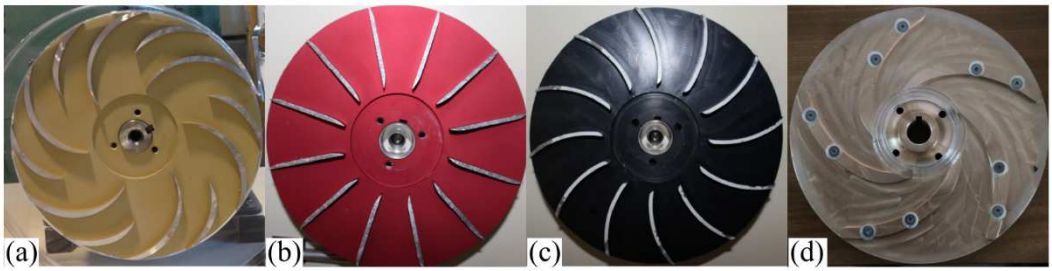

Σχήμα 2.3 Πτερωτή: **a)** No.1, **b)** No.2, **c)** No.3, **d)** No.4.

Η εργαστηριακή αντλία που είναι εγκατεστημένη στο LU (Σχ. 2.4a) έχει κέλυφος κατασκευάσμενο από διαφανές υλικό, το οποίο σε συνδυασμό με τη χρήση ημι-ανοικτού τύπου πτερωτών επιτρέπει την οπτική παρακολούθηση του φαινομένου εντός των πτερωτών. Αντίθετα, η διάταξη στο ΕΜΠ (Σχ. 2.5a) αφορά μια τυπική αντλία του εμπορίου και για την οπτικοποίηση του φαινομένου απαιτείται το άνοιγμα κατάλληλου αδιάφανου παραθύρου στο κέλυφος (Σχ. 2.5a) και η κατασκευή της στεφάνης της πτερωτής επίσης από αδιάφανο υλικό (Σχ. 2.4d). Οι θέσεις τοποθέτησης των αισθητήρων ταλάντωσης και θορύβου στις δύο διατάξεις παρουσιάζονται επίσης στα Σχ. 2.4a και 2.4b, μαζί με τα αντίστοιχα τροφοδοτικά και φίλτρα που χρησιμοποιούνται.

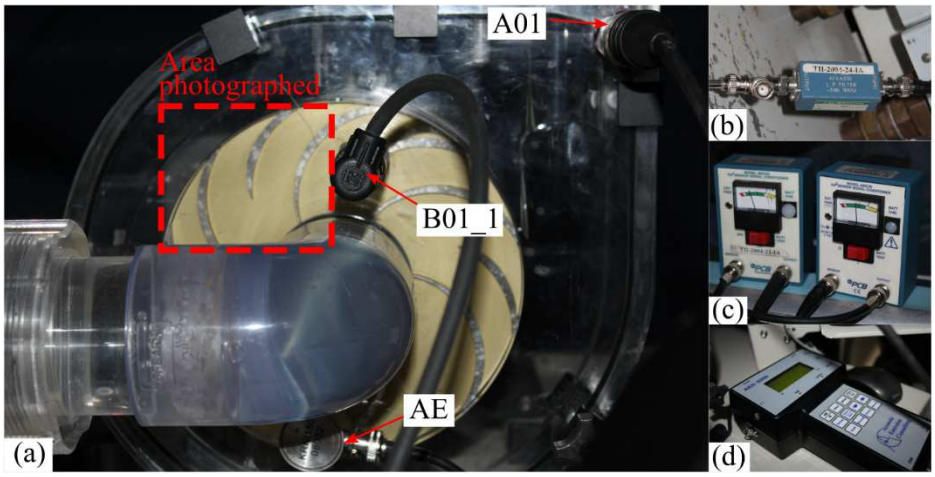

Σχήμα 2.4 a) Αντλία στο LU και θέση τοποθέτησης των αισθητήρων θορύβου και κραδασμού, **b)** αναλογικό φίλτρο, **c)** τροφοδοτικό επιταχυνσιομέτρων, **d)** σύστημα μετρήσεων ΑΕ.

Η πτερωτή No. 1 (Σχ. 2.3a) αποτελείται από δώδεκα οπισθοκλινή πτερύγια, εκ των οποίων τα έξι είναι διαχωριστικά (splitter blades). Η πτερωτή No. 2 (Σχ. 2.3b) αποτελείται από δώδεκα ακτινικά πτερύγια, ενώ η πτερωτή No. 3 (Σχ. 2.3c) αποτελείται από δώδεκα εμπροσθοκλινή πτερύγια. Τέλος, η εμπορική πτερωτή του ΕΜΠ (Σχ. 2.3d) αποτελείται από πέντε οπισθοκλινή πτερύγια. Τα επιμέρους γεωμετρικά στοιχεία των πτερωτών δίνονται στους Πίνακες 2.1, 2.2.

Πίνακας 2.1 Γεωμετρικά χαρακτηριστικά πτερωτών του LU.

	Impeller No. 1		**Impeller No. 2**		**Impeller No. 3**	
$b_{V,2}$ **[m]**	0.013		0.013		0.013	
	Inlet (1)	**Outlet (2)**	**Inlet (1)**	**Outlet (2)**	**Inlet (1)**	**Outlet (2)**
d **[m]**	0.0655	0.165	0.0655	0.165	0.0655	0.165
e **[mm]**	1.1	10.1	2.8	5.9	1	2.2
b_I **[mm]**	7.5	3	7.6	3.1	7.75	3.25
β **[deg]**	65	25	85	90	80	125

Πίνακας 2.2 Γεωμετρικά χαρακτηριστικά πτερωτών του ΕΜΠ.

	$b_{V,2}$ **[m]**	***d*** **[m]**	***e*** **[mm]**	b_I **[mm]**	β **[deg]**
Impeller	0.008	-	-	-	-
Inlet (1)	-	0.0516	3.5	7.3	25
Outlet (2)	-	0.177	6.7	5	40

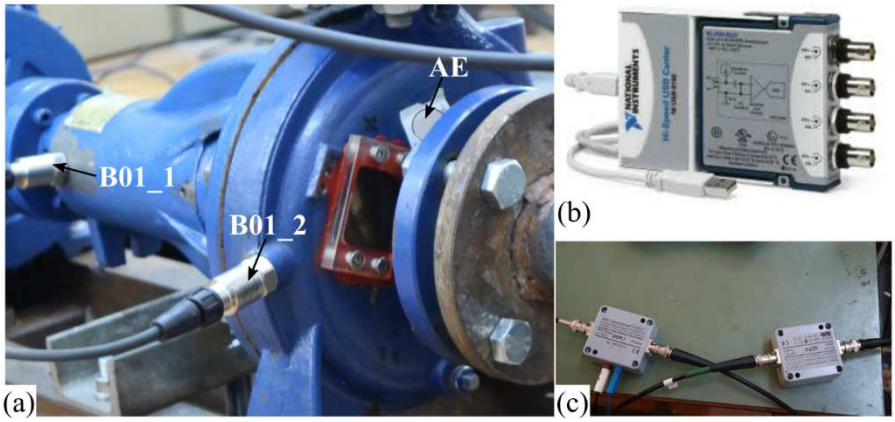

Σχήμα 2.5 a) Αντλία εγκατεστημένη στο ΕΜΠ, θέσεις τοποθέτησης αισθητήρων θορύβου και κραδασμού, **b)** DAQ, **c)** σύστημα μετρήσεων θορύβου.

3. Πειραματικές Μετρήσεις Φυγοκεντρικών Αντλιών

3.1 Εισαγωγή

Στο παρόν κεφάλαιο παρουσιάζονται τα πειραματικά αποτελέσματα των χαρακτηριστικών καμπυλών λειτουργίας των τεσσάρων πτερωτών, σε συνθήκες με και χωρίς σπηλαίωση. Επιπλέον παρουσιάζονται τα αποτελέσματα οπτικής παρακολούθησης του φαινομένου σε διαφορετικά σημεία λειτουργίας της μηχανής.

3.2 Μετρήσεις χωρίς σπηλαίωση

Στο σχήμα 3.1 παρουσιάζονται οι αδιάστατες χαρακτηριστικές καμπύλες για όλες τις πτερωτές, ενώ ταυτόχρονα δίνεται ο βαθμός απόδοσης (η_{BEP}) στο σημείο κανονικής λειτουργίας μαζί με την αδιάστατη παροχή (Φ_{BEP}), το ύψος (Ψ_{BEP}) και την ισχύ (N_{BEP}). Η μορφή των καμπυλών ύψους επηρεάζεται από τη γεωμετρία των πτερυγίων, καθώς ο λόγος dH_{tot}/dQ αυξάνει για τις οπισθοκλινείς πτερωτές (No. 1 & 4), ενώ μειώνεται για εκείνες με ακτινικά (πτερωτή No. 2) και εμπροσθοκλινή πτερύγια (πτερωτή No. 3).

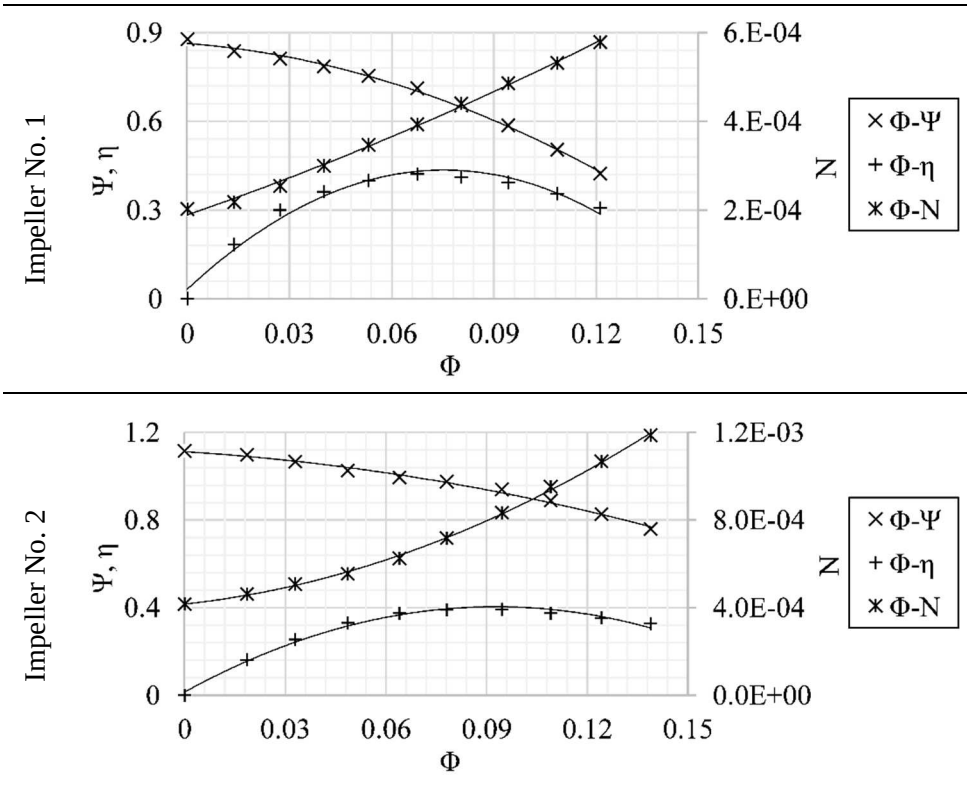

η_{BEP}	0.42
Φ_{BEP}	0.067
Ψ_{BEP}	0.711
N_{BEP}	$3.9 \cdot 10^{-4}$
n_q	844
η_{BEP}	0.39
Φ_{BEP}	0.095
Ψ_{BEP}	0.939
N_{BEP}	$8.3 \cdot 10^{-4}$
n_q	836

Impeller No. 3	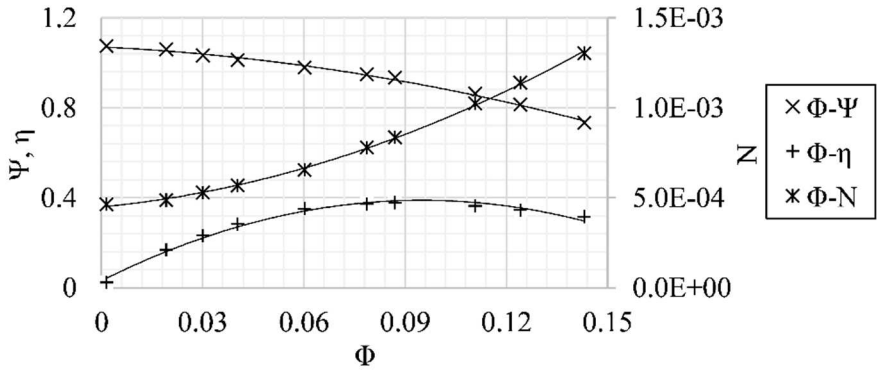	**η_{BEP}** 0.38 **Φ_{BEP}** 0.087 **Ψ_{BEP}** 0.934 **N_{BEP}** $8.3 \cdot 10^{-4}$ **n_q** 816
Impeller No. 4	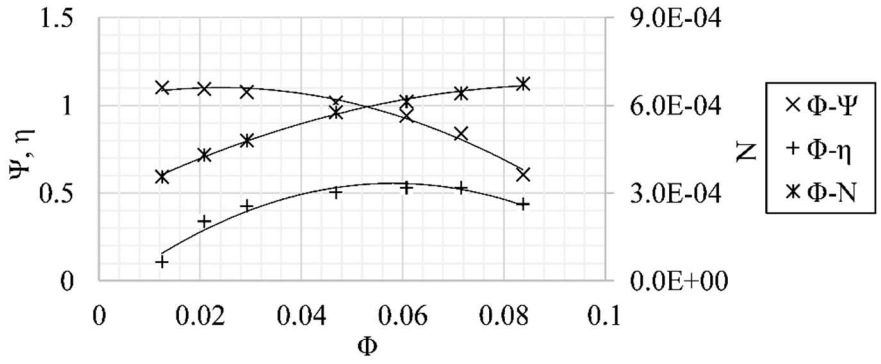	**η_{BEP}** 0.53 **Φ_{BEP}** 0.061 **Ψ_{BEP}** 0.94 **N_{BEP}** $6.1 \cdot 10^{-4}$ **n_q** 847

Σχήμα 3.1 Αδιάστατες χαρακτηριστικές καμπύλες λειτουργίας σε συνθήκες χωρίς σπηλαίωση.

3.3 Μετρήσεις με σπηλαίωση

Οι αδιάστατες χαρακτηριστικές καμπύλες σπηλαίωσης (σ-Ψ) των τεσσάρων πτερωτών παρουσιάζονται στο Σχ. 3.2. Κάθε πτερωτή δοκιμάζεται για τέσσερις διαφορετικές παροχές. Με μπλε τονίζονται τα σημεία που ξεκινάει η οπτική παρατήρηση του φαινομένου, ενώ με κόκκινο τα σημεία έντονης πτώσης του ύψους. Οι κατασκευαστικές ιδιαιτερότητες στην αντλία του ΕΜΠ, δεν επιτρέπουν την οπτικοποίηση της έναρξης του φαινομένου. Σε αυτή την εγκατάσταση, η σπηλαίωση γίνεται οπτικά αντιληπτή όταν επεκταθεί έως το μέσο του πτερυγίου. Το σημείο αυτό τονίζεται με κίτρινο χρώμα στις καμπύλες του Σχ. 3.2d.

Σε όλες τις περιπτώσεις το πείραμα ξεκινά στις μέγιστες τιμές του σ χωρίς την παρουσία ατμού στις οπτικοποιημένες περιοχές. Για τις ημι-ανοικτού τύπου πτερωτές (No. 1-3), οι πρώτοι σχηματισμοί περιοχών ατμού, παρουσιάζονται στις φωτογραφίες της πρώτης στήλης του Σχ. 3.3 και προηγούνται κατά πολύ της πτώσης του ύψους. Στην περίπτωση της πτερωτής No. 4, οι κατασκευαστικοί περιορισμοί, οδηγούν στην εμφάνιση του φαινομένου στην περιοχή όπου ξεκινά η πτώση του ύψους (κίτρινη περιοχή Σχ. 3.2).

Ενδιαφέρον προκαλεί η μεταβολή της τιμής του σ_{VI} σε σχέση με την παροχή και των γεωμετρικών χαρακτηριστικών της πτερωτής. Πιο συγκεκριμένα, για όλες τις πτερωτές, η αύξηση της παροχής οδηγεί επιτάχυνση του πεδίου ροής και τελικά σε αύξηση της τιμής του σ_{VI}. Δηλαδή, καθιστά την πτερωτή περισσότερο ευαίσθητη στην εμφάνιση και ανάπτυξη του φαινομένου.

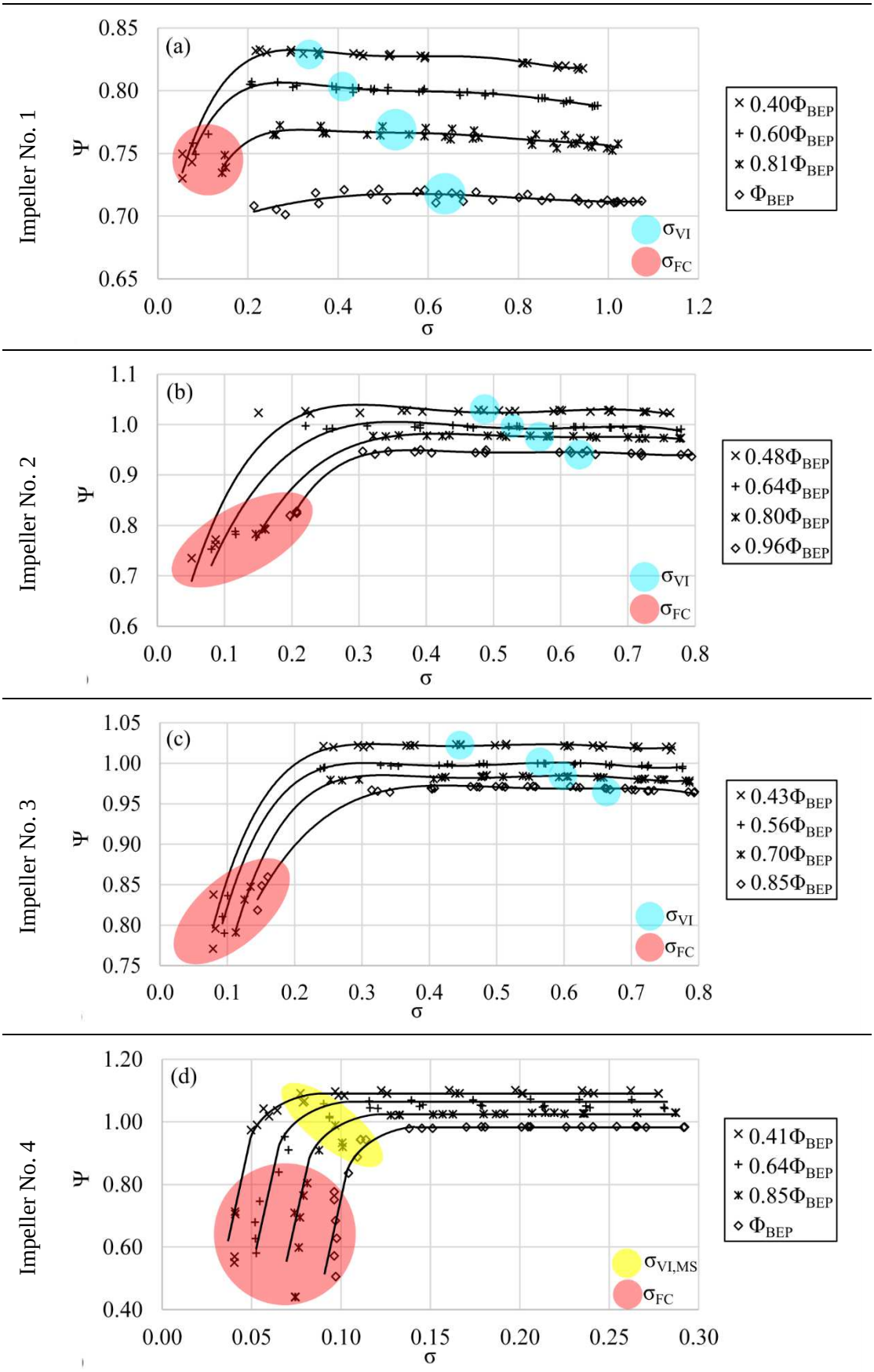

Σχήμα 3.2 Χαρακτηριστικές καμπύλες σπηλαίωσης (σ-Ψ) για κάθε πτερωτή σε τέσσερις διαφορετικές παροχές.

Πιο ευαίσθητες στην εμφάνιση και ανάπτυξη της σπηλαίωσης, αποδεικνύεται πως είναι οι πτερωτές No. 2 και 3 οι οποίες έχουν ακτινικά και εμπροσθοκλινή πτερύγια με μεγάλες γωνίες εισόδου (β_1). Επιπλέον ο αριθμός των πτερυγίων αυτών των δύο πτερωτών είναι διπλάσιος των πτερωτών 1 και 4. Ο λόγος για την αύξηση του σ_{VI} είναι πως για μεγάλες γωνίες εισόδου, η γωνία πρόσπτωσης αυξάνει και δημιουργούνται έντονες ανακυκλοφορίες στην πλευρά υποπίεσης των πτερυγίων, οι οποίες μειώνουν την τοπική τιμή της στατικής πίεσης. Αυτό το γεγονός, σε συνδυασμό με την επιτάχυνση της ροής, που προκαλείται από τον αυξημένο αριθμό πτερυγίων, εξηγεί τη μεγαλύτερη ευαισθησία των πτερωτών 2 και 3 στη σπηλαίωση.

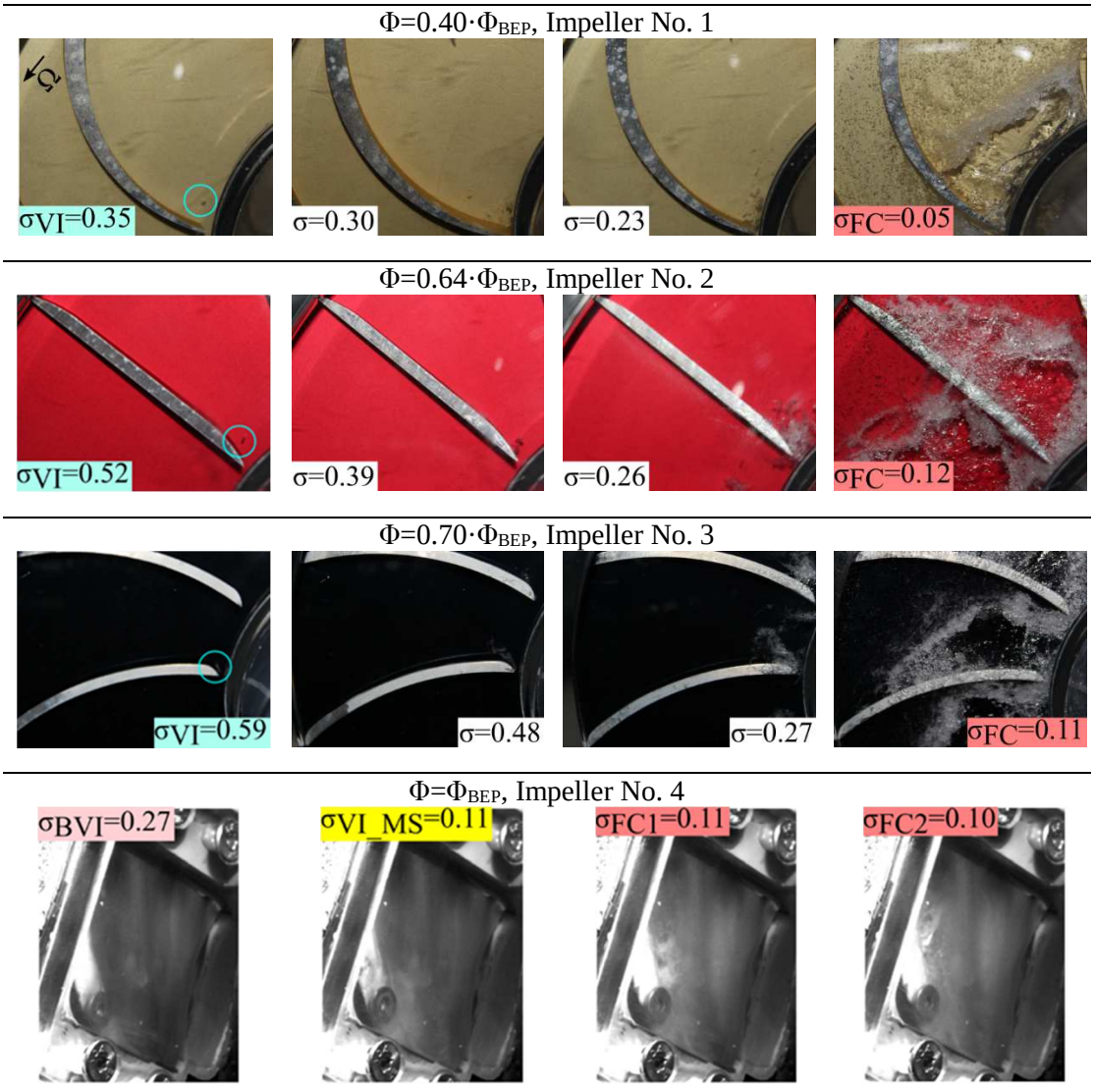

Σχήμα 3.3 Οπτικοποίηση τη ροής σε διάφορα σημεία λειτουργίας των τεσσάρων πτερωτών.

Η επιπλέον μείωση του σ αυξάνει την ανεπτυγμένη διφασική περιοχή, η οποία μεγιστοποιείται για $\sigma=\sigma_{FC}$, όπου το συνολικό ύψος που οι πτερωτές προσδίδουν στο εργαζόμενο μέσο πέφτει κατακόρυφα (κόκκινες περιοχές στο Σχ. 3.2). Σε εκείνα τα σημεία (τελευταία στήλη Σχ. 3.3) η σπηλαίωση εκτείνεται σε μεγάλο μήκος του πτερυγίου στην ακτινική διεύθυνση, ενώ το ίδιο συμβαίνει στο χώρο μεταξύ γειτονικών πτερυγίων. Η κατάληψη αυτής της περιοχής από φυσσαλίδες ατμού οδηγεί στην πτώση του ύψους (Σχ. 3.2) και του βαθμού απόδοσης της αντλίας. Η συμπεριφορά της τιμής της σ_{FC} ακολουθεί παρόμοια συμπεριφορά με αυτή που περιγράφηκε για τη σ_{VI}, σε σχέση με την παροχή και τη γεωμετρία των μηχανών.

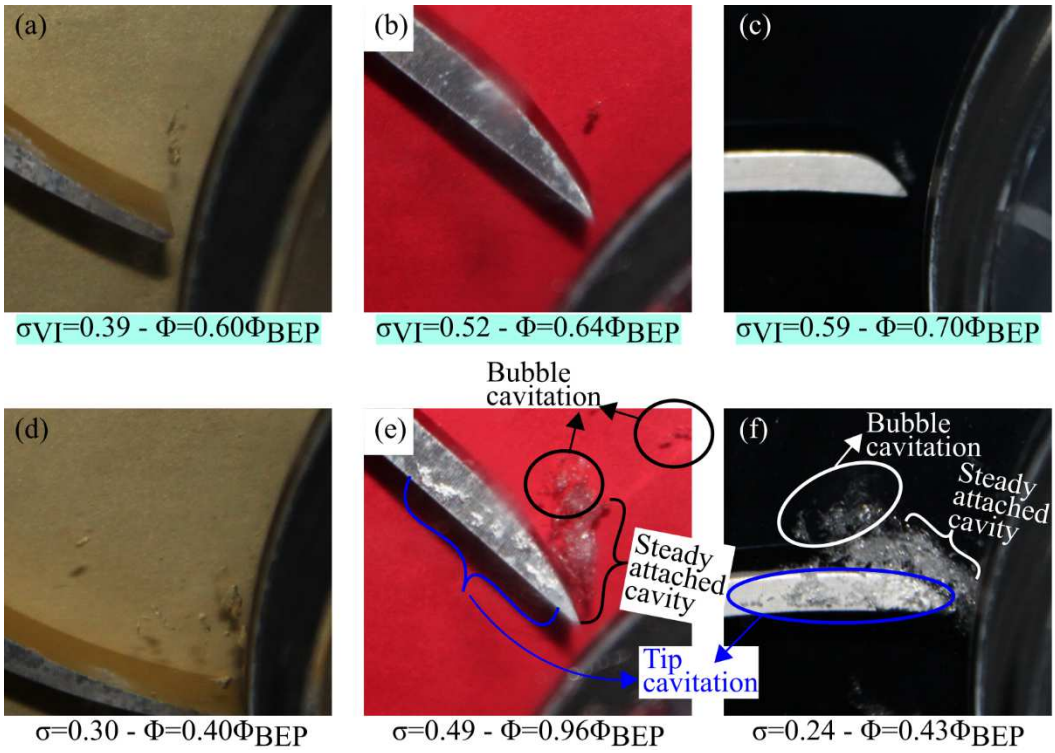

Σχήμα 3.4 Συσχέτιση των μακροσκοπικά οπτικοποιημένων χαρακτηριστικών της σπηλαίωσης με τους διάφορους τύπους εμφάνισης του φαινομένου, στα πρώιμα στάδια ανάπτυξής του.

Στα πρώτα στάδια ανάπτυξης του φαινομένου (Σχ. 3.4a-c), οι φυσσαλίδες έχουν ιδιαιτέρως δυναμική συμπεριφορά, καθώς εμφανίζονται και ενδορρηγνύονται άμεσα λόγω την κλίσης πίεσης στις πτερωτές. Η περαιτέρω πτώση του σ (Σχ. 3.4d-f), διαφοροποιεί την παραπάνω συμπεριφορά, για τις πτερωτές No. 2 και 3, λόγω των υψηλών γωνιών της πτερύγωσης του στην ακμή πρόσπτωσης. Πιο συγκεκριμένα, σε αυτές τις πτερωτές (Σχ. 3.4e,f), η αυξημένη γωνία πρόσπτωσης δημιουργεί μια προσκολλημένη κοιλότητα σπηλαίωσης (attached cavitation) της οποίας η έκταση παρουσιάζει μακροσκοπικά μόνιμα χαρακτηριστικά και δε διαφοροποιείται σημαντικά στο χρόνο. Ωστόσο, στα όρια αυτών των περιοχών δημιουργούνται φυσσαλίδες ατμού οι οποίες παρουσιάζουν δυναμική συμπεριφορά όπως στα σημεία κοντά στο σ_{VI}. Επιπλέον, στις ενδιάμεσες συνθήκες σπηλαίωσης των Σχ. 3.4e,f, φυσσαλίδες ατμού εμφανίζονται και στο διάκενο μεταξύ του ακροπτερυγίου και του κελύφους της αντλίας.

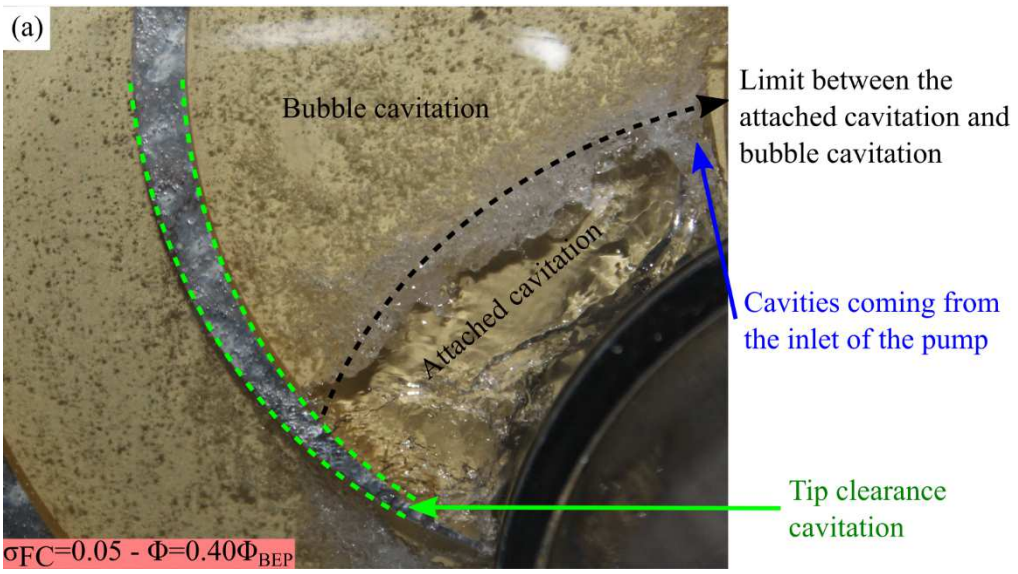

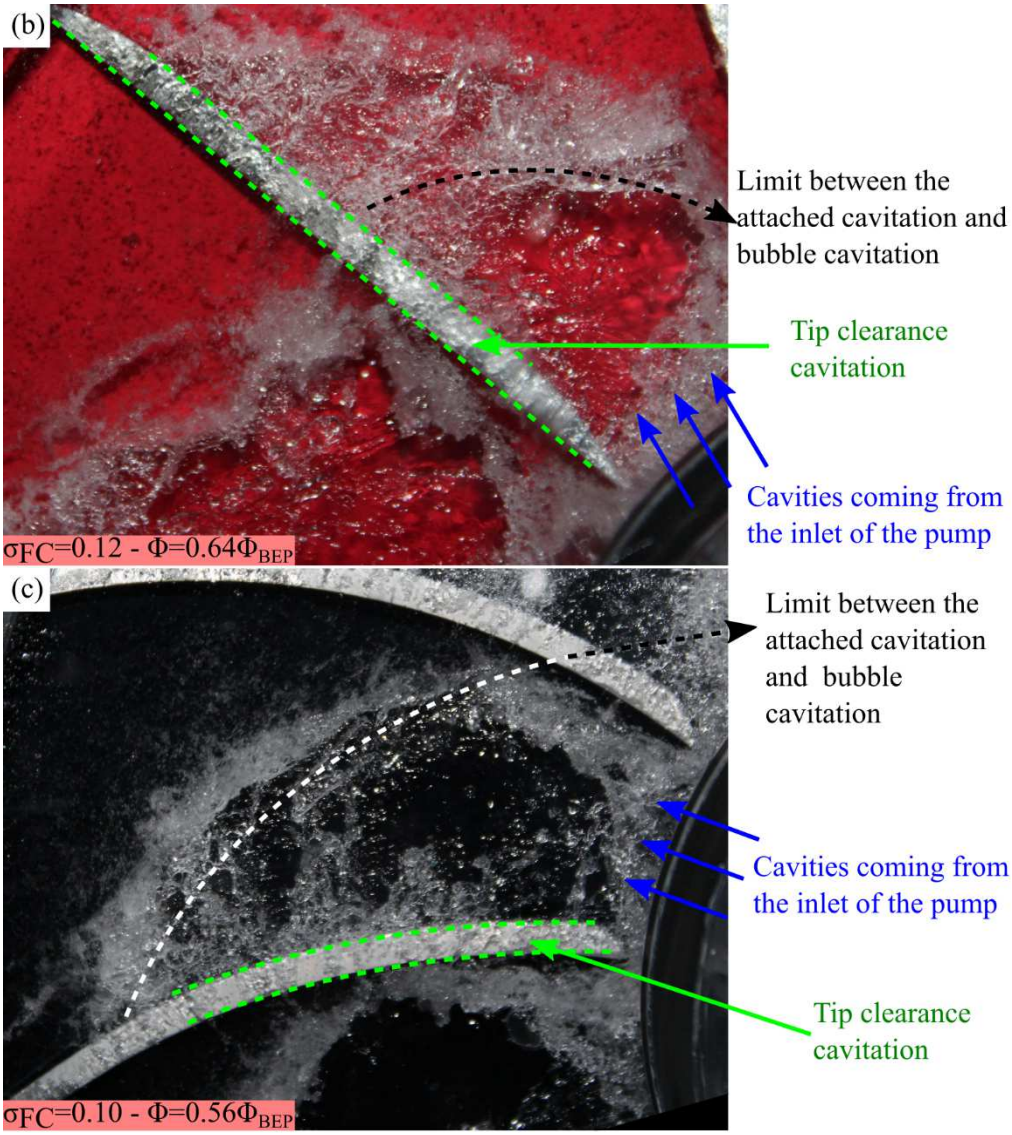

Σχήμα 3.5 Συσχέτιση των μακροσκοπικά οπτικοποιημένων χαρακτηριστικών της σπηλαίωσης με τους διάφορους τύπους εμφάνισης του φαινομένου, στο σ_{FC}.

Τέλος, στο σημείο πτώσης του ύψους για όλες τις πτερωτές, η διφασική περιοχή εκτείνεται σε σημαντικό μέρος της ροής και σύμφωνα με το Σχ. 3.5, η περιοχή αποτελείται από:

i. Μια μεγάλη περιοχή προσκολλημένης σπηλαίωσης στο κέντρο της διφασικής περιοχής.
ii. Δυναμικές φυσσαλίδες ατμού στα όρια της προσκολλημένης σπηλαίωσης.
iii. Σπηλαίωση στο διάκενο μεταξύ ακροπτερυγίου και κελύφους της αντλίας.
iv. Φυσσαλίδες ατμού που δημιουργούνται πριν την πτερωτή.

4. Υπολογιστικό Μοντέλο

4.1 Εισαγωγή

Δύο πτερωτές χρησιμοποιούνται για την υπολογιστική προσομοίωση, στην παρούσα εργασία, i) η ημι-ανοικτού τύπου πτερωτή No. 2 με τα ακτινικά πτερύγια (Σχ. 2.3b), και ii) η κλειστού τύπου πτερωτή No. 4 με τα οπισθοκλινή πτερύγια (Σχ. 2.3d). Για την υπολογιστική προσομοίωση της ροής εντός των παραπάνω αντλιών χρησιμοποιείται ο εμπορικός κώδικας FLUENT (FLUENT, 2009). Το υπολογιστικό χωρίο και στις δύο περιπτώσεις περιλαμβάνει τη συνολική γεωμετρία της μηχανής (κέλυφος και πτερωτή), ενώ για την προσομοίωση μόνιμης κατάστασης εφαρμόζεται η τεχνική των πολλαπλών πλαισίων αναφοράς (MRF: Multiple Reference Frame). Επιπλέον, χρησιμοποιείται το μοντέλο τύρβης k-ω SST (Menter, 1994), ενώ για τη μοντελοποίηση της διφασικής περιοχής εφαρμόζεται το μοντέλο των Zwart et al. (2004).

4.2 Υπολογιστικά χωρία και υπολογιστικά πλέγματα

Τα υπολογιστικά χωρία για τις δύο πτερωτές δίνονται στα Σχ. 4.1a (No. 2) και 4.1b (No. 4). Για την περίπτωση της πτερωτής No. 2, περιλαμβάνεται μεγάλο τμήμα του αγωγού εισόδου, ώστε το μοντέλο να ενσωματώνει τη στροφή 90^o στην είσοδο της μηχανής. Το συνολικό χωρίο χωρίζεται σε τέσσερα τμήματα, i) το τμήμα αγωγού εισόδου (I), ii) το τμήμα εισόδου στην πτερωτή (II), iii) το τμήμα της πτερωτής (IV), και iv) το τμήμα του κελύφους και του αγωγού εξόδου. Μεταξύ των παραπάνω τμημάτων ορίζονται τρεις διεπιφάνειες, οι οποίες παρουσιάζονται στο Σχ. 4.2a. Τα τμήματα (II), (III) επιλύονται στο στρεφόμενου συστήματος συντεταγμένων επιβάλλοντας n=1800 rpm, ενώ τα τμήματα (I) και (IV) επιλύονται στο σταθερό σύστημα συντεταγμένων.

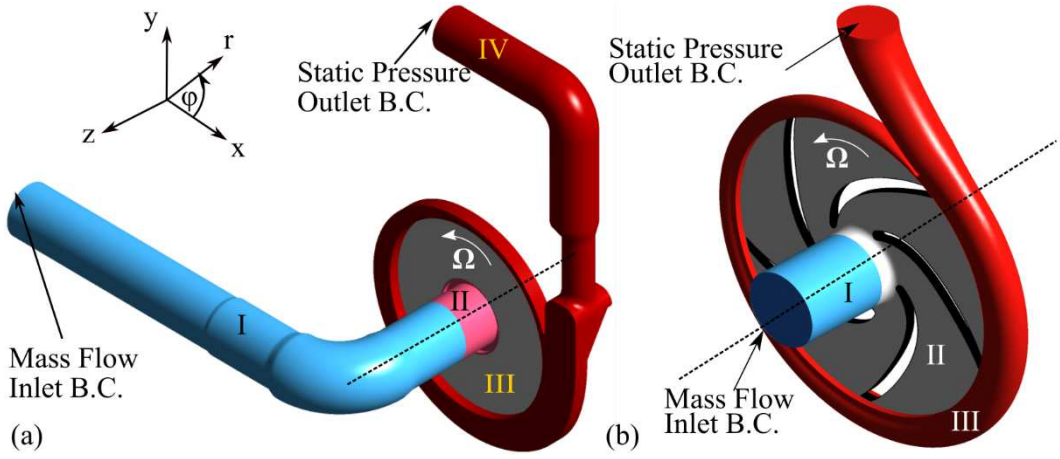

Σχήμα 4.1 Υπολογιστικό χωρίο για **a)** την πτερωτή No. 2, και **b)** πτερωτή No. 4.

Το παρών χωρίο για την πτερωτή No. 2, δεν συμπεριλαμβάνει το αξονικό διάκενο που βρίσκεται πίσω από την πλήμνη της πτερωτής, ενώ έχει αυξηθεί η διάμετρος της πτερωτής

ώστε να απομακρύνουμε την ακμή εκφυγής των πτερυγίων από τη διεπιφάνεια μεταξύ της πτερωτής και του κελύφους. Για τους αγωγούς και την πτερωτή (III), η οποία περιλαμβάνει και το διάκενο μεταξύ κινούμενου πτερυγίου και ακίνητου κελύφους (tip clearance) κατασκευάζεται δομημένο πλέγμα από εξάεδρα κελιά ενώ για τα υπόλοιπα μέρη κατασκευάζεται μη δομημένο πλέγμα από τετράεδρα κελιά τα οποία συναρμολογούνται στο λογισμικό tmerge17.0 της ANSYS (Σχ. 4.2a).

Για την πτερωτή No. 4, το συνολικό χωρίο χωρίζεται σε τρία τμήματα, i) το τμήμα αγωγού εισόδου (I), ii) το τμήμα της πτερωτής (II), και iii) το τμήμα του κελύφους (III). Μεταξύ των παραπάνω τμημάτων ορίζονται δύο διεπιφάνειες, οι οποίες παρουσιάζονται στο Σχ. 4.2b. Το τμήμα (II) επιλύεται στο στρεφόμενο σύστημα συντεταγμένων επιβάλλοντας n=2900 rpm, ενώ τα τμήματα (I) και (III) επιλύονται στο σταθερό σύστημα συντεταγμένων.

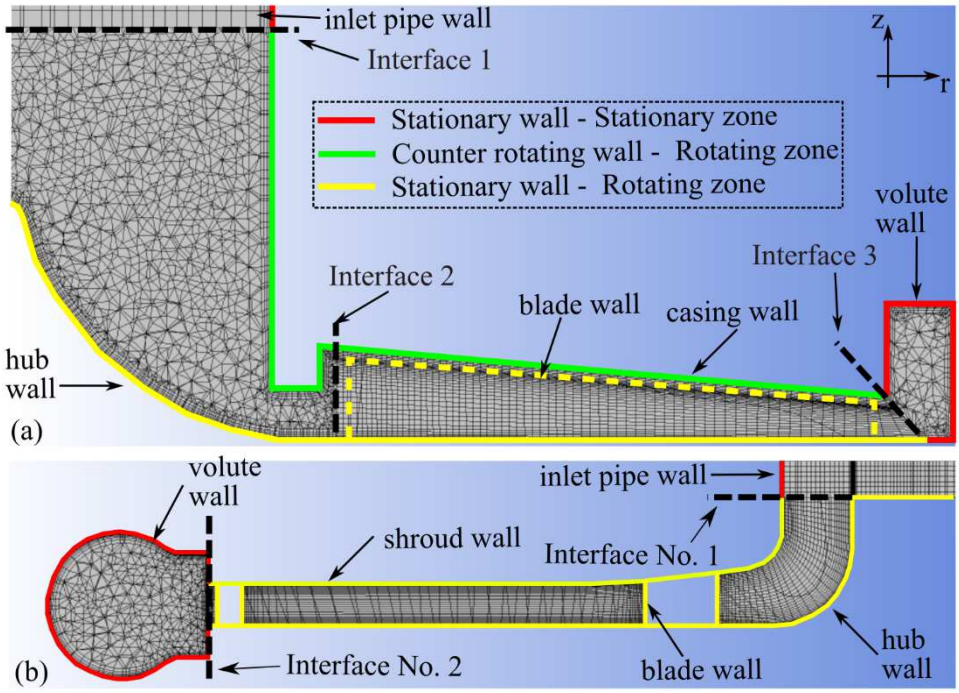

Σχήμα 4.2 Χωρική διακριτοποίηση, διεπιφάνειες και οριακές συνθήκες στα τοιχώματα **a)** της πτερωτής No. 2, και **b)** της πτερωτής No. 4.

Το χωρίο για την πτερωτή No. 4 (Σχ. 4.1b), δεν συμπεριλαμβάνει τα αξονικά διάκενα πίσω από τις επιφάνειες της πλήμνης και της στεφάνης, ενώ απλοποιείται η γεωμετρία του κοχλία στο κέντρο της πλήμνης. Για τα τμήματα (I & II) κατασκευάζεται δομημένο πλέγμα από εξάεδρα κελιά ενώ για τα υπόλοιπα μέρη κατασκευάζεται μη δομημένο πλέγμα από τετράεδρα κελιά τα οποία συναρμολογούνται στο λογισμικό tmerge17.0 της ANSYS (Σχ. 4.2b).

Η μελέτη ανεξαρτησίας της λύσης από την πυκνότητα της χωρικής διακριτοποίησης οδηγεί στη χρήση πλέγματος 3.6 και 3.2 εκατομμυρίων κελιών για τις πτερωτές No. 2, 4, αντίστοιχα.

4.3 Οριακές συνθήκες

Στα τοιχώματα των δύο χωρίων ορίζεται συνθήκη μη ολίσθησης, ενώ ανάλογα το τμήμα οι τοίχοι ορίζονται είτε ως στάσιμοι (κόκκινο και κίτρινο χρώμα στα Σχ. 4.2) είτε ως περιστρεφόμενοι αντίθετα με την οριζόμενη περιστροφή του συστήματος συντεταγμένων του τμήματος (πράσινο χρώμα στα Σχ. 4.2). Επομένως, στην περίπτωση της κλειστής πτερωτής No. 4, όλοι οι τοίχοι ορίζονται ως στάσιμοι σε τμήματα με κινούμενα και ακίνητα συστήματα συντεταγμένων. Η διαφοροποίηση που παρατηρείται στην πτερωτή No. 2, αφορά στους

τοίχους εκείνους (πράσινο χρώμα, Σχ. 4.2a) που ενώ βρίσκονται στα τμήματα (II & III), δεν κινούνται καθώς αποτελούν μέρος του κελύφους της μηχανής. Σε αυτές τις περιπτώσεις ορίζονται τοίχοι που είναι περιστρεφόμενοι αντίθετα με την οριζόμενη περιστροφή του συστήματος συντεταγμένων του τμήματος.

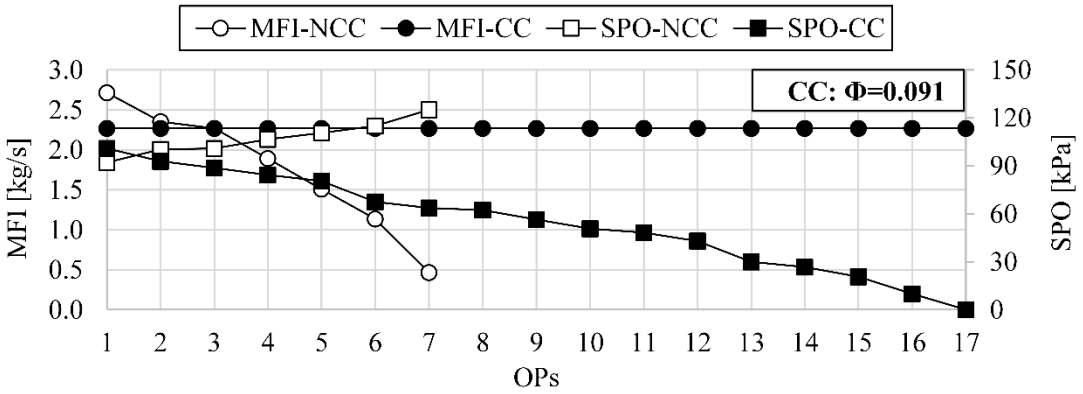

Σχήμα 4.3 Μεταβολή οριακών συνθηκών σε προσομοιώσεις με και χωρίς σπηλαίωση.

Και για τις δύο πτερωτές, στην είσοδο ορίζεται η παροχή μάζας και στην έξοδο η στατική πίεση, ενώ οι τιμές τους δίνονται από τις αντίστοιχες μετρούμενες κατά τη διάρκεια των πειραμάτων. Γι' αυτό το λόγο, στην περίπτωση των προσομοιώσεων σε κανονικές συνθήκες λειτουργίας, η μείωση της οριακής συνθήκης της παροχής στην είσοδο της μηχανής συνοδεύεται από αύξηση της στατικής πίεσης (Σχ. 4.3, λευκά σημεία). Επιπλέον, στις προσομοιώσεις που αφορούν τη λειτουργία της μηχανής με σπηλαίωση, η παροχή μένει σταθερή και το επίπεδο της στατικής πίεσης μειώνεται από την οριακή συνθήκη εξόδου (Σχ. 4.3, μαύρα σημεία).

Τέλος, για τις προσομοιώσεις σε συνθήκες σπηλαίωσης, ορίζεται λόγος όγκου ατμού, α_v=0 στην επιφάνεια εισόδου, ενώ η πίεση ατμοποίησης ορίζεται ως p=2.8 kPa και p=2.3 kPa, που αντιστοιχεί σε T=23 °C και T=20 °C για τις πτερωτές No. 2 και 4, αντιστοίχως. Αυτές είναι οι θερμοκρασίες στις οποίες διενεργούνται τα τεστ στις δύο διατάξεις.

4.4 Πιστοποίηση υπολογιστικού μοντέλου

Τα αποτελέσματα του μοντέλου, αξιολογούνται με βάση τις πειραματικές μετρήσεις και τα αποτελέσματα της οπτικοποίησης στην πτερωτή No. 2. Πιο συγκεκριμένα, σε πρώτη φάση συγκρίνονται οι χαρακτηριστικές καμπύλες λειτουργίας σε συνθήκες χωρίς σπηλαίωση (Φ-Ψ, Φ-N & Φ-η, Σχ. 4.4) και με σπηλαίωση (σ-Ψ, Σχ 4.5). Η σύγκριση αυτή, πιστοποιεί την ικανότητα του μοντέλου να προβλέψει τη μορφή των χαρακτηριστικών καμπυλών λειτουργίας, σε συνθήκες με και χωρίς σπηλαίωση. Η χαρακτηριστική Φ-Ψ (Σχ. 4.4) μειώνεται με την αύξηση της παροχής, η Φ-N (Σχ. 4.4) αυξάνεται, ενώ η μείωση του σ οδηγεί στη χαρακτηριστική πτώση του ύψους στο Σχ. 4.5.

Η τελευταία παρατήρηση αντικατοπτρίζει την αδυναμία της πτερωτή να προσδώσει ενέργεια στο εργαζόμενο μέσο, όταν η μηχανή λειτουργεί σε χαμηλά επίπεδα στατικής πίεσης. Όμοια με τις πειραματικές μετρήσεις, το σημείο πτώσης του ύψους επηρρεάζεται από την παροχή καθώς λαμβάνει χώρα σε μεγαλύτερες τιμές του σ. Οι διαφορές μεταξύ πειραματικών και υπολογιστικών αποτελεσμάτων αφορούν δύο σημεία, i) την τιμή του Ψ πριν την πτώση του ύψους, και ii) την τιμή του σ για την οποία πέφτει το ύψος. Η πρώτη ακολουθεί γενικά την τάση του μοντέλου να βελτιώνει την προσέγγιση στο ύψος όσο μετακινούμαστε προς το σημείο κανονικής λειτουργίας (Σχ. 4.5). Η δεύτερη αφορά περισσότερο τη μη μοντελοποίηση της συνεισφοράς της σπηλαίωσης που δημιουργείται στη βάνα αναρρόφησης της εγκατάστασης η οποία επιβαρρύνει την συνολικότερη ανάπτυξη της σπηλαίωσης. Επιπλέον λόγοι για τις

διαφορές στα Σχ. 4.5 είναι το γεγονός ότι η αλληλεπίδραση ρότορα-στάτορα αγνοείται κατά την παρούσα μοντελοποίηση και οι διάφορες γεωμετρικές απλοποιήσεις κατά την κατασκευή του υπολογιστικού χωρίου.

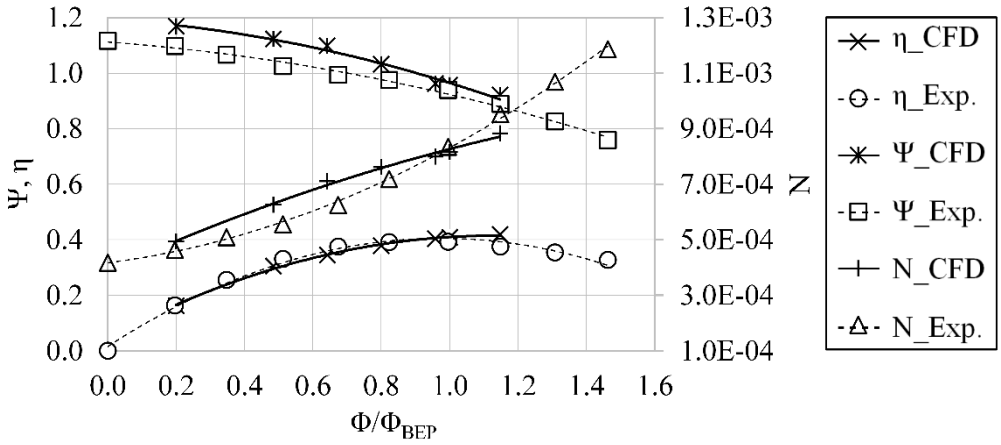

Σχήμα 4.4 Αριθμητικές και υπολογιστικές καμπύλες λειτουργίας σε μονοφασικές συνθήκες ροής για την πτερωτή No. 2.

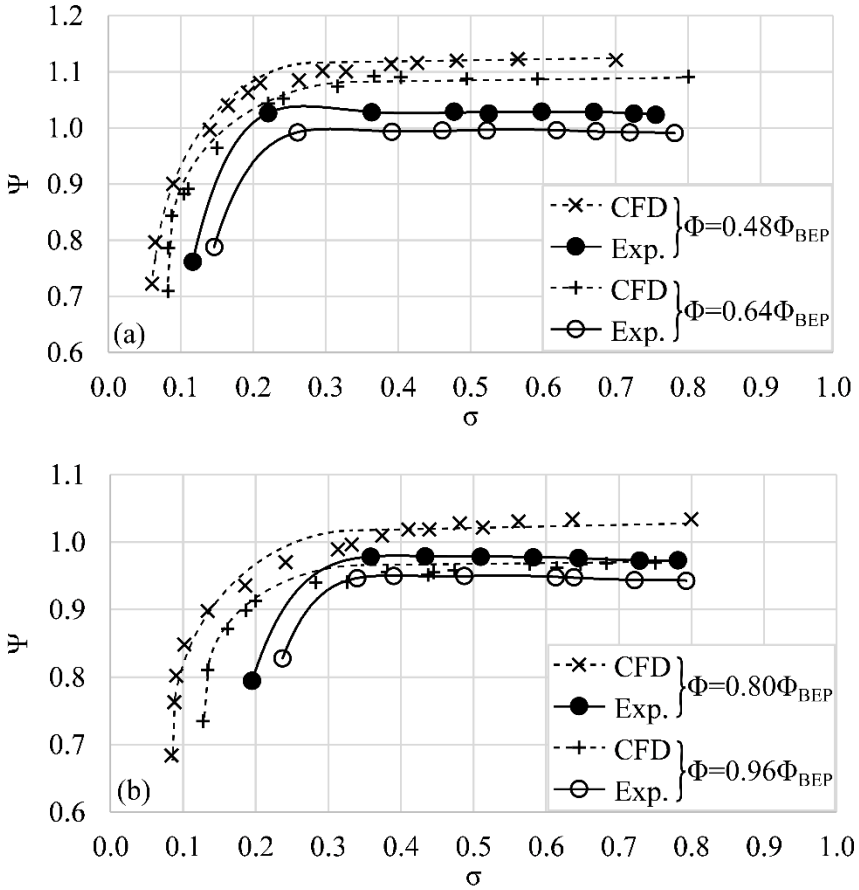

Σχήμα 4.5 Σύγκριση αριθμητικά υπολογισμένων χαρακτηριστικών καμπυλών σπηλαίωσης με τις αντίστοιχες πειραματικές, για την πτερωτή No. 2.

Σε δεύτερο χρόνο συγκρίνονται τα οπτικά αποτελέσματα της ανάπτυξης της σπηλαίωσης με τα υπολογιστικά στο Σχ. 4.6. Η υπολογισμένη από το μοντέλο διφασική περιοχή απεικονίζεται με χρήση ισοεπιφάνειας για λόγο όγκου ατμού, α_v=0.5, ενώ η ατμοποιημένη περιοχή των οπτικών πειραματικών αποτελεσμάτων αποτυπώνεται με τη διακεκομένη γραμμή (Σχ. 4.6).

Σύμφωνα με τα αποτελέσματα του Σχ. 4.6, το μοντέλο στα πρώτα στάδια ανάπτυξης του φαινομένου (Σχ. 4.6b) υποεκτιμά την ανάπτυξη της διφασικής περιοχής, ωστόσο η πρόβλεψη του βελτιώνεται αισθητά στα ενδιάμεσα στάδια του φαινομένου (Σχ. 4.6a). Η συμπεριφορά αυτή αιτιολογείται από το γεγονός ότι στα πρώτα στάδια εμφάνισης του φαινομένου οι φυσσαλίδες δεν έχουν ιδιαίτερα μόνιμη συμπεριφορά, ενώ στα ενδιάμεσα στάδια αποκτούν ένα πυρήνα προσκολλημένης κοιλότητας σπηλαίωσης τον οποίο μπορεί και τον προβλέπει αισθητά καλύτερα.

Τέλος, όταν η σύγκριση επικεντρώνεται στα σημεία πτώσης του ύψους (Σχ. 4.6c), με μια πρώτη ματιά η σύγκριση μοιάζει ικανοποιητική ωστόσο γίνεται για αισθητά διαφορετικά σ, με το υπολογιστικό να είναι σχεδόν το μισό του πειραματικού, σε αντίθεση με τα Σχ. 4.6a,b όπου τα σ είναι σχεδόν ίδια. Η τελευταία επιλογή γίνεται ώστε να έχουμε την ίδια τιμή Ψ στη σύγκριση των σημείων λειτουργίας. Το γεγονός ότι το σ πρέπει να μειωθεί στο μισό για να πάρουμε την ικανοποιητική σύγκριση του Σχ. 4.6c οφείλεται στο γεγονός ότι σε εκείνο το σημείο η διφασική περιοχή κατά την εκτέλεση του πειράματος επηρρεάζεται από τη σπηλαίωση που δημιουργείται πριν τη μηχανή, από τη θέση της βάνας. Αυτό το κομμάτι της διφασικής περιοχής οδηγεί στην πρόωρη πτώση του ύψους στις πειραματικές μετρήσεις και εξηγει τις διαφορές με τα υπολογιστικά αποτελέσματα.

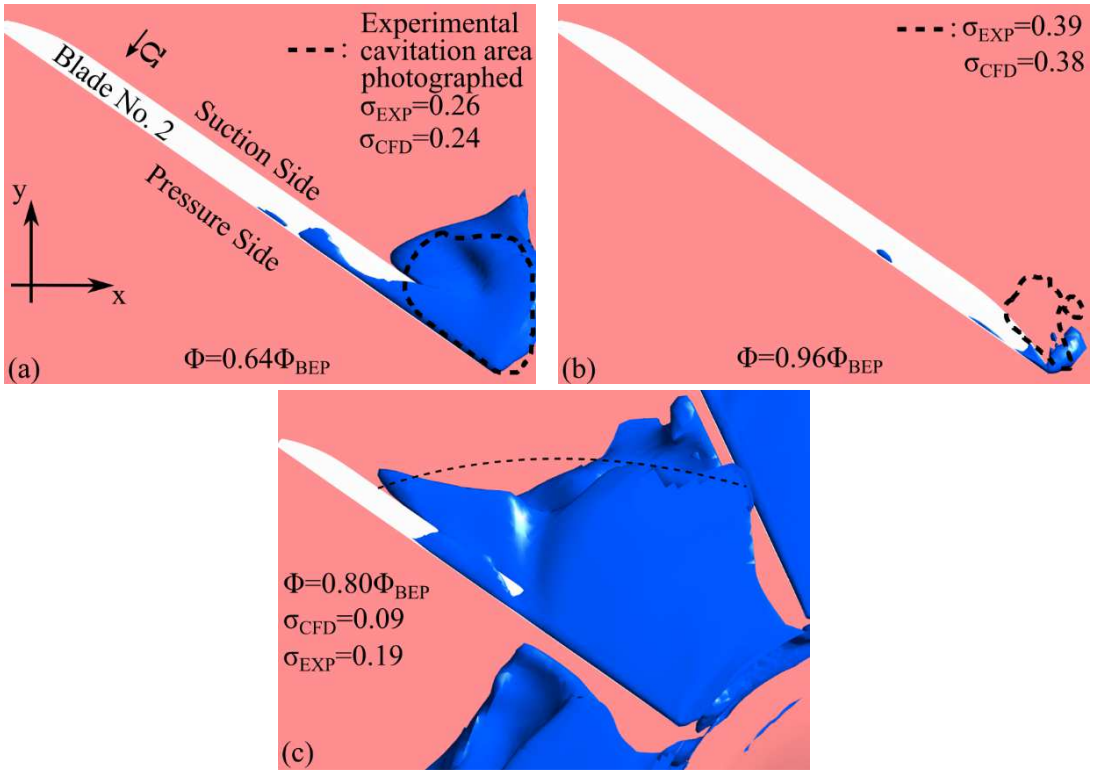

Σχήμα 4.6 Σύγκριση αριθμητικά υπολογισμένης περιοχής ατμού με τις αντίστοιχες οπτικές, για την πτερωτή No. 2.

4.5 Μοντελοποίηση επιπλέον περιπτώσεων διακένου ακροπτερυγίου

Στην παρούσα μελέτη, εξετάζεται η επίδραση του πάχους (t_{tc}) του διακένου μεταξύ των ακροπτερυγίων της πτερωτής και του κελύφους, στη λειτουργία και απόδοση της μηχανής καθώς και στην ανάπτυξη της σπηλαίωσης. Πιο συγκεκριμένα, κατασκευάζονται άλλα δυο υπολογιστικά χωρία, το ένα με μικρότερο πάχος (t_{tc}=0.5 mm, Σχ. 4.7a) από την αρχική γεωμετρία (t_{tc}=0.9 mm) και ένα με μεγαλύτερο (t_{tc}=1.5 mm, Σχ. 4.7b). Η κατασκευή του

χωρίου, του πλέγματος και η εφαρμογή των οριακών συνθηκών ακολουθεί την ίδια διαδικασία, με αυτή που περιγράφηκε για την πτερωτή No. 2.

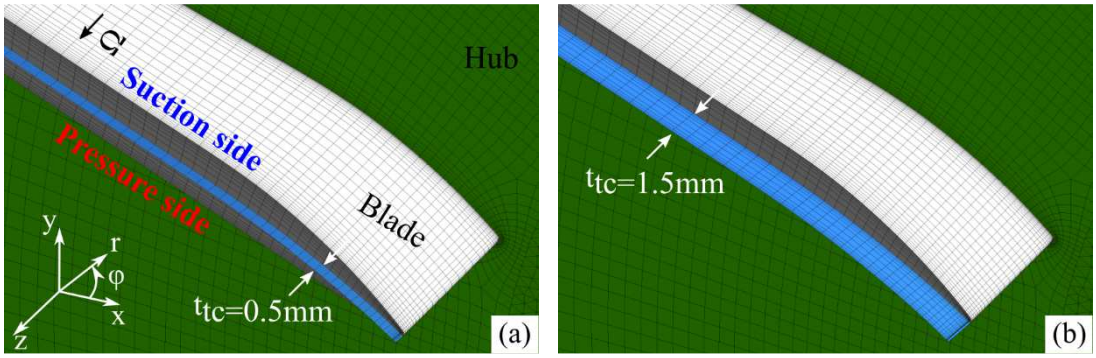

Σχήμα 4.7 Γεωμετρία και πλέγμα για τις δύο επιπλέον περιπτώσεις διακένου.

5. Αριθμητικά Αποτελέσματα

Στο Κεφάλαιο 5 παρουσιάζονται τα αποτελέσματα του υπολογιστικού μοντέλου για τις πτερωτές No. 2 και 4 αλλά και για τις επιπλέον περιπτώσεις όπου μελετάται η επίδραση του πάχους στο διάκενο μεταξύ του ακροπτερυγίου και του κελύφους της αντλίας. Το πρώτο μέρος του κεφαλαίου (ενότητα 5.2) αφορά τις προσομοιώσεις σε μονοφασικές συνθήκες λειτουργίας των αντλιών, ενώ το δεύτερο μέρος (ενότητα 5.3) περιλαμβάνει τα αποτελέσματα της σπηλαίωσης.

5.2 Λειτουργία αντλιών χωρίς σπηλαίωση

5.2.1 Πτερωτή No. 2

Στο Σχ. 5.1 παρουσιάζονται οι ισοϋψείς στατικής πίεσης για την πτερωτή No. 2 σε μια μερική παροχή (Φ=0.2·Φ_{BEP}) και σε μια παροχή που βρίσκεται κοντά στο κανονικό σημείο λειτουργίας (Φ=0.96·Φ_{BEP}). Η μη αξονοσυμμετρική συμπεριφορά της ροής παρατηρείται και σε όλα τα σημεία λειτουργίας και είναι περισσότερο έντονη για την περιοχή, όπου $R_1 \leq r \leq R_m$. Ο λόγος αυτής της συμπεριφοράς είναι η στροφή που υπάρχει πριν την είσοδο της μηχανής καθώς και η εσωτερική διαμόρφωση του κελύφους.

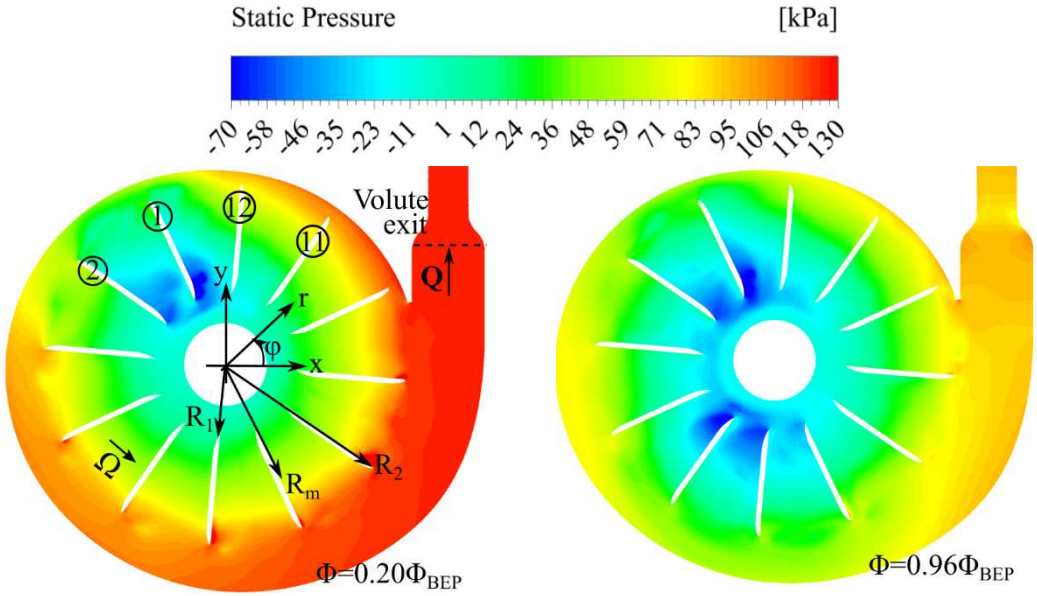

Σχήμα 5.1 Ισοϋψείς στατικής πίεσης σε διαφορετικές παροχές στο x-y επίπεδο για z=1 mm.

Σε γενικές γραμμές, σύμφωνα με το Σχ. 5.1, η στατική πίεση αυξάνει, όπως αναμένεται, στην ακτινική διεύθυνση, ενώ η αύξηση κορυφώνεται στην έξοδο του κελύφους κοντά στην αρχή του αγωγού κατάθλιψης. Τρεις μηχανισμοί επηρρεάζουν το σχηματισμό των περιοχών

χαμηλής στατικής πίεσης εντός της πτερωτής και παίζουν κομβικό ρόλο και στην ανάπτυξη της σπηλαίωσης. Ο πρώτος αφορά την παροχή˙ όταν η αντλία λειτουργεί σε υψηλές παροχές, η ροή επιταχύνεται μειώνοντας το επίπεδο στατικής πίεσης στη μηχανή. Η επιρροή αυτή γίνεται φανερή στο Σχ. 5.1, όπου οι τιμές και η έκταση τις περιοχής που χαρακτηρίζονται από αρνητικές πιέσεις, αυξάνεται με την παροχή.

Ο δεύτερος μηχανισμός συνδέεται με την ανάπτυξη ανακυλοφοριών στην πλευρά υποπίεσης των πτερυγίων της αντλίας σε υψηλές τιμές της γωνίας πρόσπτωσης. Η πτερωτή No. 2, ασχέτως παροχής παρουσιάζει υψηλές γωνίες πρόσπτωσης λόγω της ακτινικής μορφής των πτερυγίων της, όπως απεικονίζεται στα διανύσματα της σχετικής ταχύτητας στα Σχ. 5.2a,b. Τα αποτελέσματα αυτά, αναδεικνύουν την ανεπαρκή σχεδίαση του πτερυγίου της πτερωτής No. 2, ειδικά στο σημείο πρόσπτωσης της ροής και δικαιολογεί και το χαμηλό βαθμό απόδοσης που μετράτε και υπολογίζεται στα Σχ. 3.1 και 4.4, αντίστοιχα.

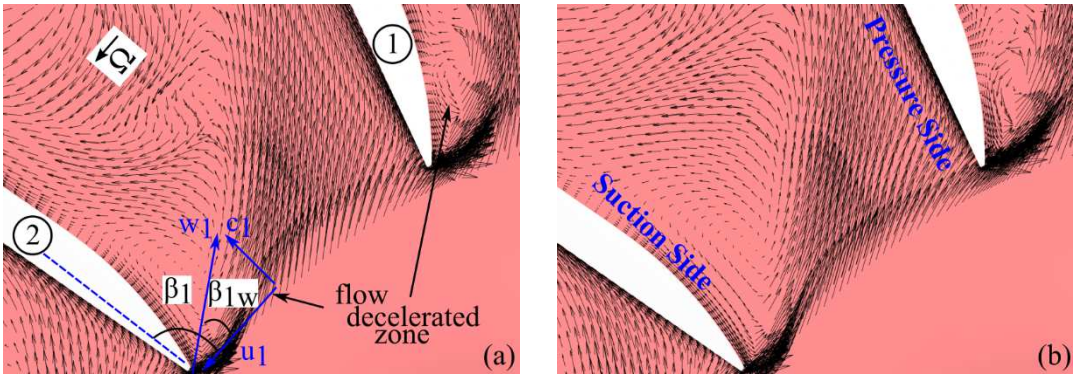

Σχήμα 5.2 Διανύσματα σχετική ταχύτητας στο επίπεδο x-y για z=1 mm για **a)** $\Phi=0.46\cdot\Phi_{BEP}$, και για **b)** $\Phi=0.96\cdot\Phi_{BEP}$.

Ένας τρίτος μηχανισμός που επηρρεάζει το βαθμό απόδοσης της μηχανής αλλά και τις περιοχές χαμηλής πίεσης και κατ' επέκταση τη δημιουργία σπηλαίωσης στη μηχανή, είναι το διάκενο μεταξύ του ακροπτερυγίου και του κελύφους. Για να διευκολυνθεί η ανάλυση της ροής σε αυτό το σημείο, η μελέτη επικεντρώνεται σε δύο αντιπροσωπευτικές περιοχές, μία κοντά στην ακμή πρόσπτωσης των πτερυγίων (LE) και μια κοντά στο μέσο του πτερυγίου (MS). Τα διανύσματα της εφαπτομενικής συνιστώσας της σχετικής ταχύτητας αποτυπώνονται σε δύο επιφάνειες, την A_1 που βρίσκεται κατά μήκος και στη μέση του διακένου, και την A_2 που βρίσκεται στο επίπεδο z-r στη γωνιακής θέση φ, που συμπίπτει με το δεύτερο πτερύγιο. Είναι σημαντικό να σημειωθεί, ότι η ανάλυση της πτερωτής 2 επικεντρώνεται στην περιοχή του πτερυγίου 2, καθώς σε εκείνο το σημείο κάνουν την οπτική τους εμφάνιση πειραματικά οι πρώτες φυσσαλίδες ατμού και είναι το σημείο που επιλέγεται για την απεικόνιση των οπτικών αποτελεσμάτων.

Τα αποτελέσματα της εφαπτομενικής συνιστώσας της σχετικής ταχύτητας στις δύο περιοχές (LE, MS) και στα δύο επίπεδα (A_1, A_2) παρουσιάζονται για τη $\Phi=0.96\cdot\Phi_{BEP}$ στο Σχ. 5.3. Σε αυτό το σημείο γίνεται εμφανές ότι ασχέτως περιοχής (LE, MS), στο επίπεδο A_1 (Σχ. 5.3a,c) η ροή ανακυκλοφορεί ($Q_{tc,bfr}$) προς τη μεριά υποπίεσης του πτερυγίου. Επιπλέον και μόνο για την περίπτωση της LE περιοχης (Σχ. 5.3a) μέρος της ροής κατευθύνεται προς την είσοδο της αντλίας. Προς την είσοδο της μηχανής ανακυκλοφορεί και ένα μέρος της ροής που παρουσιάζεται από τα διανύσματα του Σχ. 5.3b ($Q_{tc,bfr}$) , ενώ ένα δεύτερο μέρος κατευθυνέται ακτινικά προς την έξοδο της πτερωτής ($Q_{tc,TE}$). Όσο απομακρυνόμαστε από την είσοδο (Σχ. 5.3d), το κομμάτι της ροής που κατευθύνεται ακτινικά προς την έξοδο της πτερωτής ($Q_{tc,TE}$) υπερισχύει.

Οι παραπάνω ανακυκλοφορίες προκαλούνται από τη διαφορά πίεσης μεταξύ των πλευρών πίεσης και υποπίεσης της πτερύγωσης. Επιπλέον η συζήτηση των αποτελεσμάτων του Σχ. 5.3, αναδεικνύει ότι οι σχηματισμοί της ροής στο διάκενο συμφωνούν με εκείνους που διαμορφώνουν την ανάρροια σπηλαίωση και παρουσιάζονται στην ενότητα E2. Αυτό το συμπέρασμα είναι σημαντικό και η επιρροή της ανάρροιας σπηλαίωσης στη λειτουργία της

αντλίας εξετάζεται στην ενότητα 5.3.1 για την ίδια γεωμετρία. Επιπλέον, στις ενότητες 5.2.1.1 και 5.3.1.1 παρουσιάζεται η επίδραση του πάχους του διακένου στη συμπεριφορά των παραπάνω ανακυκλοφοριών και στην ανάπτυξη της σπηλαίωσης, αντίστοιχα.

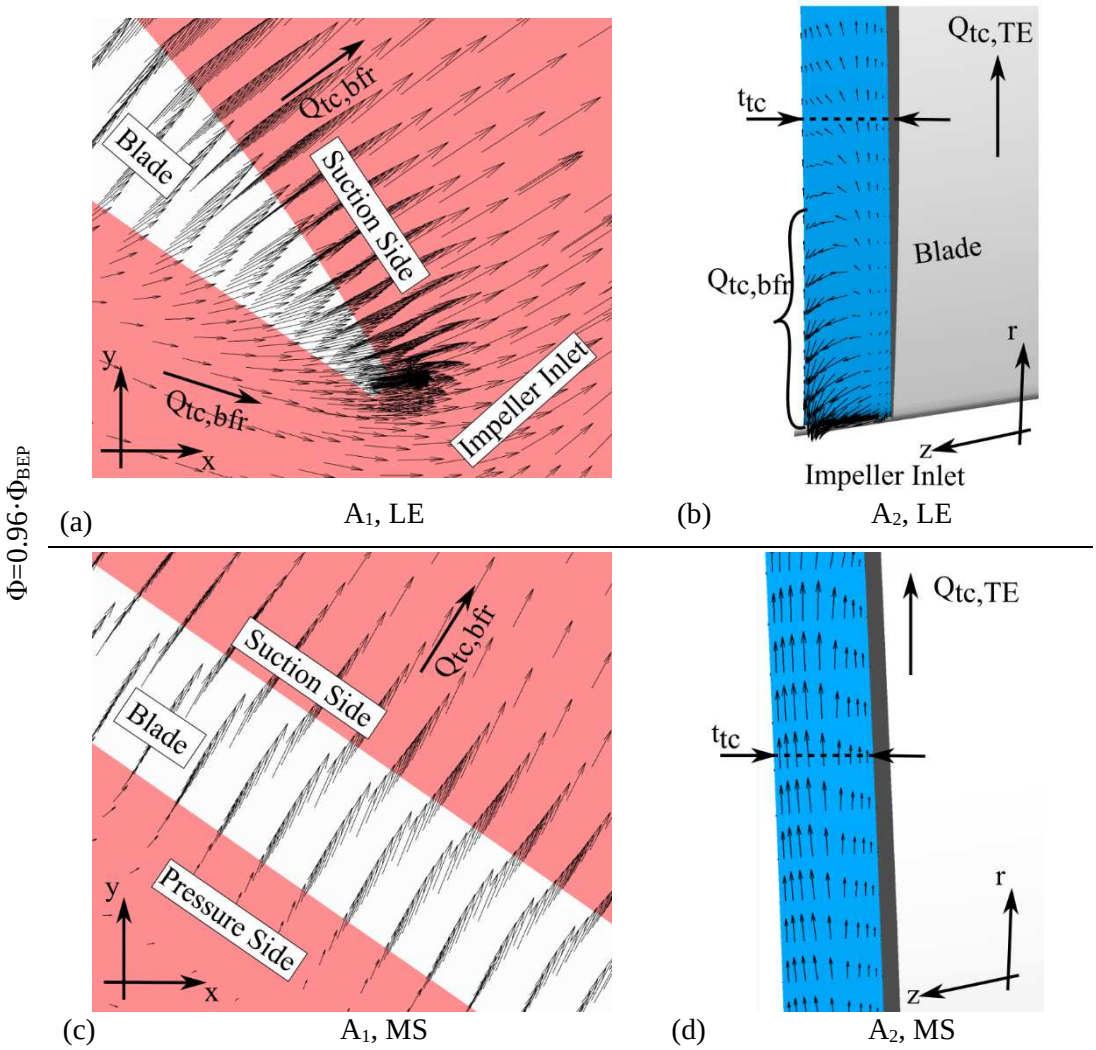

Σχήμα 5.3 Διανύσματα σχετική ταχύτητας στην περιοχή του διακένου του ακροπτερυγίου, στις περιοχές LE, MS και στα επίπεδα A_1, A_2 για $\Phi=0.96\cdot\Phi_{BEP}$.

5.2.1.1 Επιρροή του πάχους του διακένου στο ακροπτερύγιο

Η μείωση του πάχους του διακένου αυξάνει το παρεχόμενο προς το ρευστό ύψος (Σχ. 5.4a), καθώς και την ισχύ που καταναλώνει η μηχανή (Σχ. 5.4b). Η ταυτόχρονη επιρροή στην ισχύ και στο ύψος εξηγεί και τις μικρές διαφοροποιήσεις στο βαθμό απόδοσης (Σχ. 5.4a).

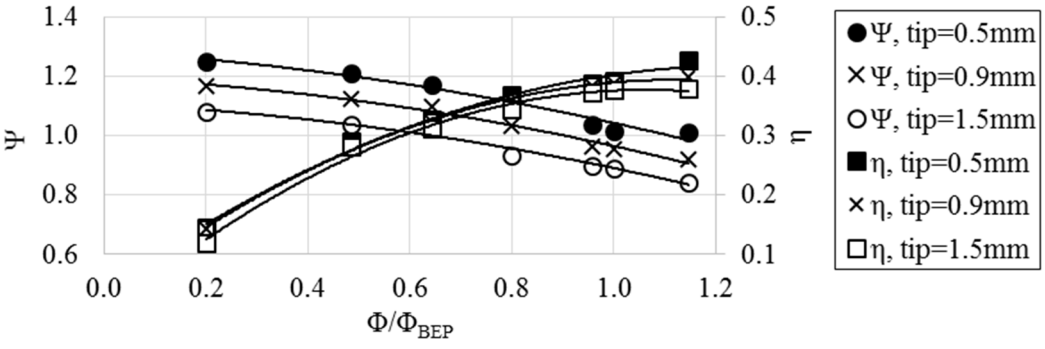

(a)

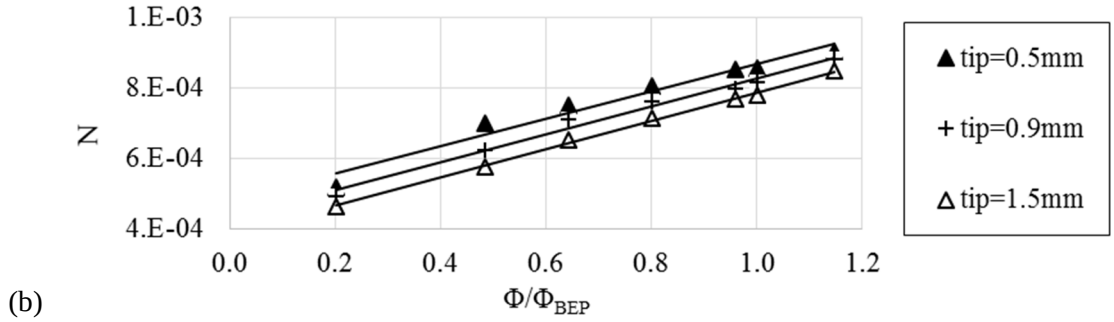

(b)

Σχήμα 5.4 Επιρροή του πάχους του διακένου στις Φ-Ψ, Φ-Ν και Φ-η.

Η επιρροή του πάχους του διακένου στις ροές ανακυκλοφορίας παρουσιάζεται στο Σχ. 5.5. Σε γενικές γραμμές οι ανακυκλοφορίες παραμένουν, ωστόσο παρατηρείται μείωση στο μέτρο των διανυσμάτων για την περίπτωση του μικρότερου παχους. Επιπλέον στην εξέταση της περιοχής A_2, LE, η περιοχή που καταλαμβάνει η ανακυκλοφορία μειώνεται αισθητά στην περίπτωση του μικρού διακένου.

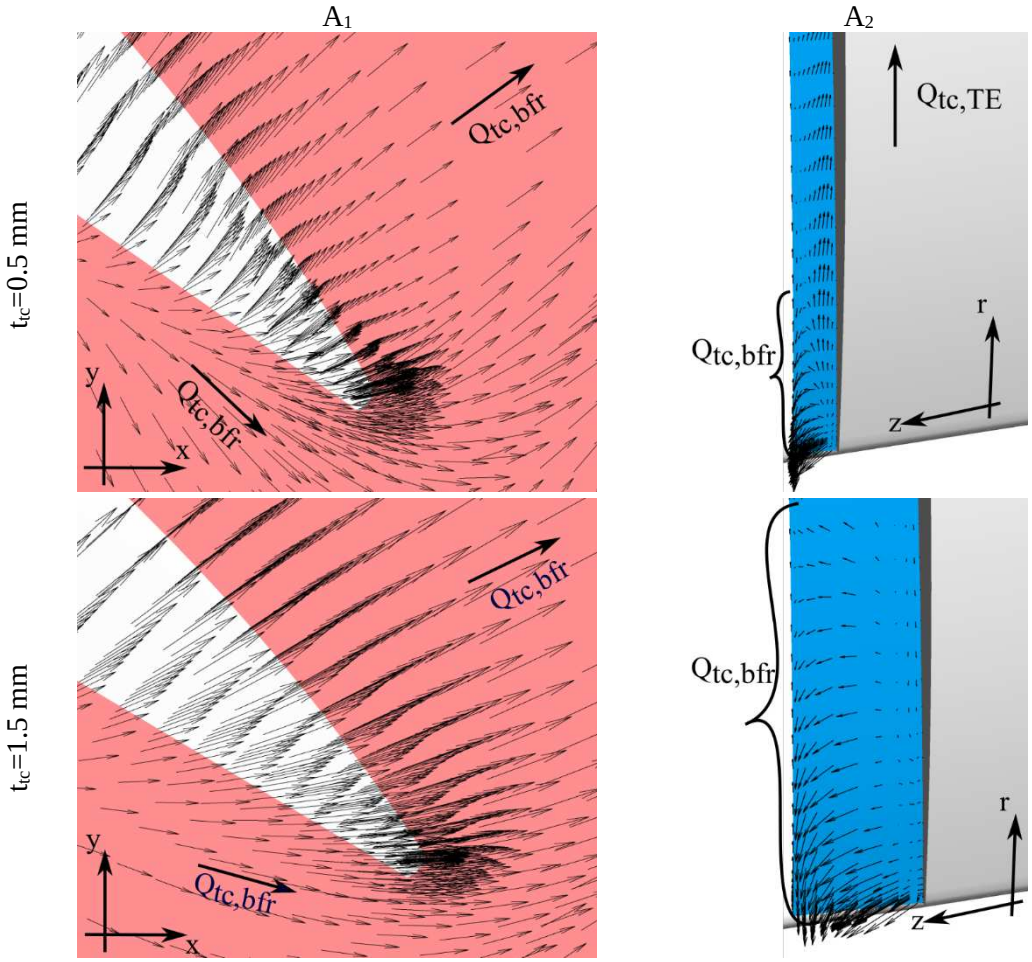

Σχήμα 5.5 Εφαπτομενική συνιστώσα της σχετικής ταχύτητας στην περιοχή της ακμής πρόσπτωσης, για δύο διαφορετικά πάχη διακένου.

5.2.2 Πτερωτή No. 4

Ικανοποιητική είναι σύγκριση των αποτελεσμάτων του μοντέλου σε σχέση με του πειράματος ως προς την παραγωγή των χαρακτηριστικών καμπυλών λειτουργίας και για την

πτερωτή No. 4 (Σχ. 5.6). Εντονότερες διαφορές εδώ παρατηρούνται στον υπολογισμό της ισχύος, οι οποίες συνδέονται με τη μοντελοποίηση των μηχανικών απωλειών στρεφόμενου δίσκου και έδρασης.

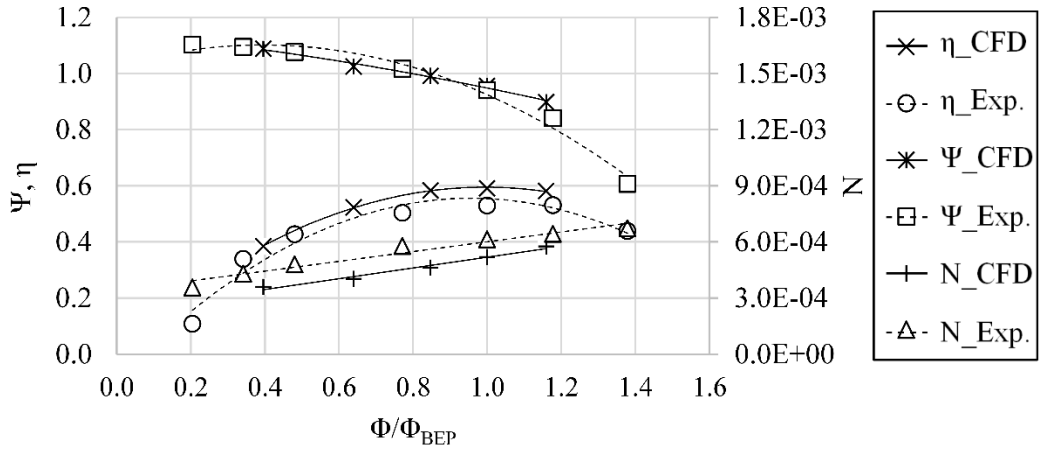

Σχήμα 5.6 Αριθμητικές και υπολογιστικές καμπύλες Φ-Ψ, Φ-N και Φ-η για την πτερωτή No. 4.

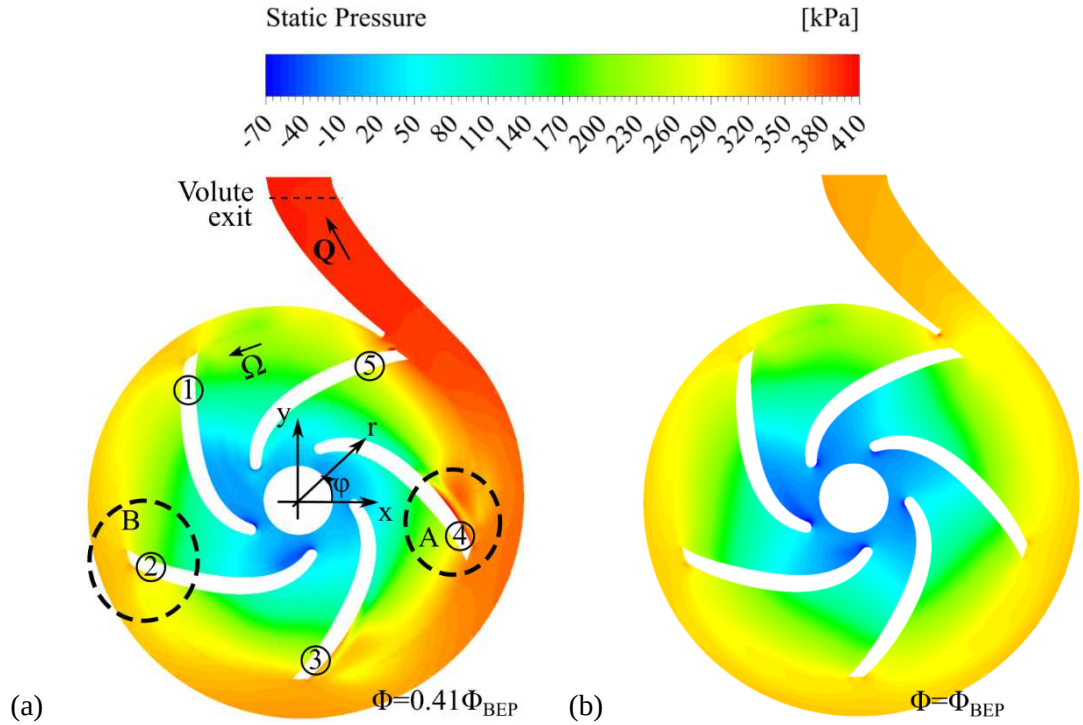

Σχήμα 5.7 Ισοϋψείς στατικής πίεσης στο μέσο x-y επίπεδο των πτερυγίων.

Η ροή στην πτερωτή No. 4 είναι περισσότερο συμμετρική (Σχ. 5.7), κυρίως γιατί το χωρίο εισόδου, όπως και η πειραματική διάταξη, δεν περιλαμβάνει κάποια στροφή κοντά στην είσοδο σε αντίθεση με το χωρίο της πτερωτής No. 2. Οι μικρές ανομοιομορφίες εντός της πτερωτής, που τονίζονται στα σημεία A, B του Σχ. 5.7a, δημιουργούνται κυρίως από το κέλυφος της αντλίας.

Η πτερωτή No. 2, στο κανονικό σημείο λειτουργίας, παρουσιάζει ελάχιστη γωνία πρόσπτωσης όπως φαίνεται και στα διανύσματα της σχετικής ταχύτητας στο Σχ. 5.8a, γεγονός που ομαλοποιεί της συνθήκες ροής στην είσοδο της πτερωτής. Αντιθέτως, όταν το φορτίο μικραίνει, όπως στο Σχ. 5.8b, η γωνία μεταξύ της ροής και του πτερυγίου αυξάνει και δημιουργούνται έντονες αποκολλήσεις στην ακμή πρόσπτωσης του πτερυγίου.

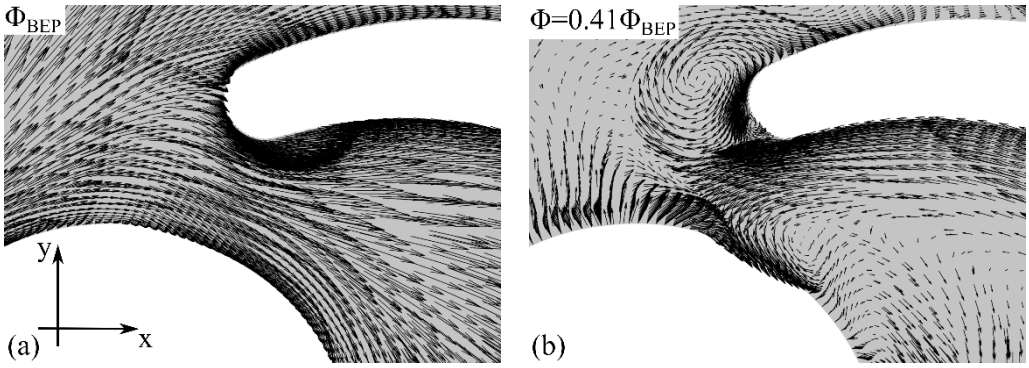

Σχήμα 5.8 Διανύσματα σχετικής ταχύτητας στο μέσο x-y επίπεδο των πτερυγίων, στην περιοχή της ακμής πρόσπτωσης.

5.3 Λειτουργία αντλιών με σπηλαίωση

5.3.1 Πτερωτή No. 2

Η εφαπτομενική συνιστώσα της σχετικής ταχύτητας μαζί με τις ισοϋψείς της στατικής πίεσης, παρουσιάζεται στην περιοχή της ακμής πρόσπτωσης (LE) στα επίπεδα A_1 και A_2, στο Σχ. 5.9. Τα αποτελέσματα του Σχ. 5.9, όπως και του Σχ. 4.6 (ενότητα 4.4) αποδεικνύουν την ανάπτυξη της διφασικής περιοχής (σκούρο μπλε περιοχής ισοϋψων στατικής πίεσης), στην περιοχή του διακένου. Η ταυτόχρονη ανακυκλοφορία που φαίνεται στα διανύσματα της ταχύτητας (Σχ. 5.9) και η οποία διέρχεται από την περιοχή του διακένου, οδηγεί τη διφασική περιοχή στην πλευρά υποπίεσης των πτερυγίων και στην είσοδο της μηχανής όπου ενισχύει την ήδη ανεπτυγμένη σπηλαίωση. Ωστόσο, το φαινόμενο αποδυναμώνεται στα σημεία πτώσης του ύψους της αντλίας (σ_{FC}) καθώς η διαφορά πίεσης που το δημιουργεί μειώνεται σημαντικά σε εκείνα τα σημεία λειτουργίας (Σχ. 5.9c,f).

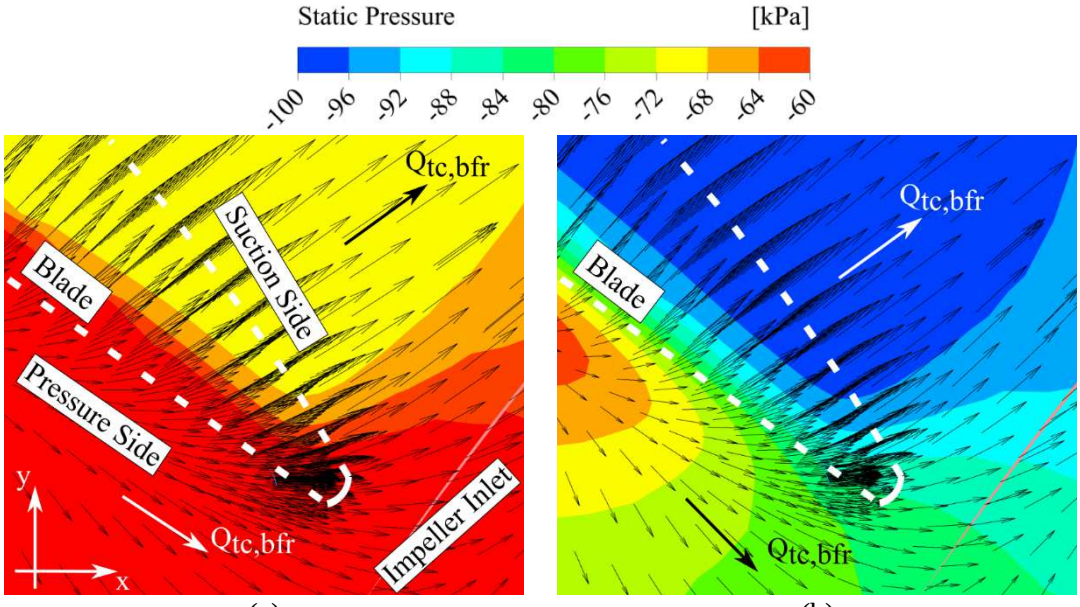

(a) (b)

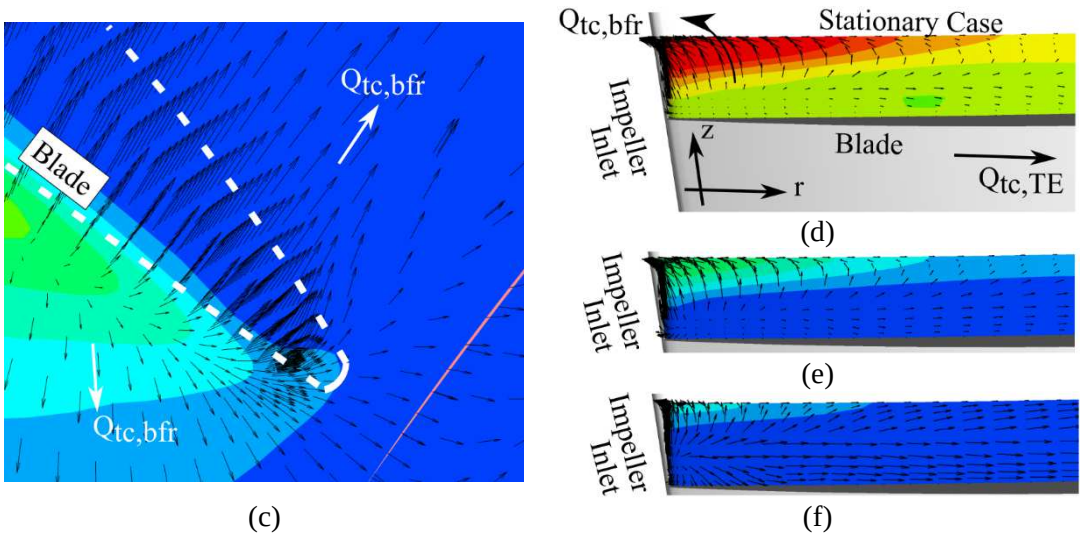

Σχήμα 5.9 Ισοϋψείς στατικής πίεσης και διανύσματα της εφαπτομενικής συνιστώσας της σχετικής ταχύτητας για $\Phi=0.96\cdot\Phi_{BEP}$ at **a)** A_1, $\sigma=0.62$, **b)** A_1, $\sigma=0.34$, **c)** A_1, $\sigma_{FC}=0.16$, **d)** A_2, $\sigma=0.62$, **e)** A_2, $\sigma=0.34$, **f)** A_2, $\sigma_{FC}=0.16$.

5.3.1.1 Επιρροή του πάχους του διακένου στο ακροπτερύγιο

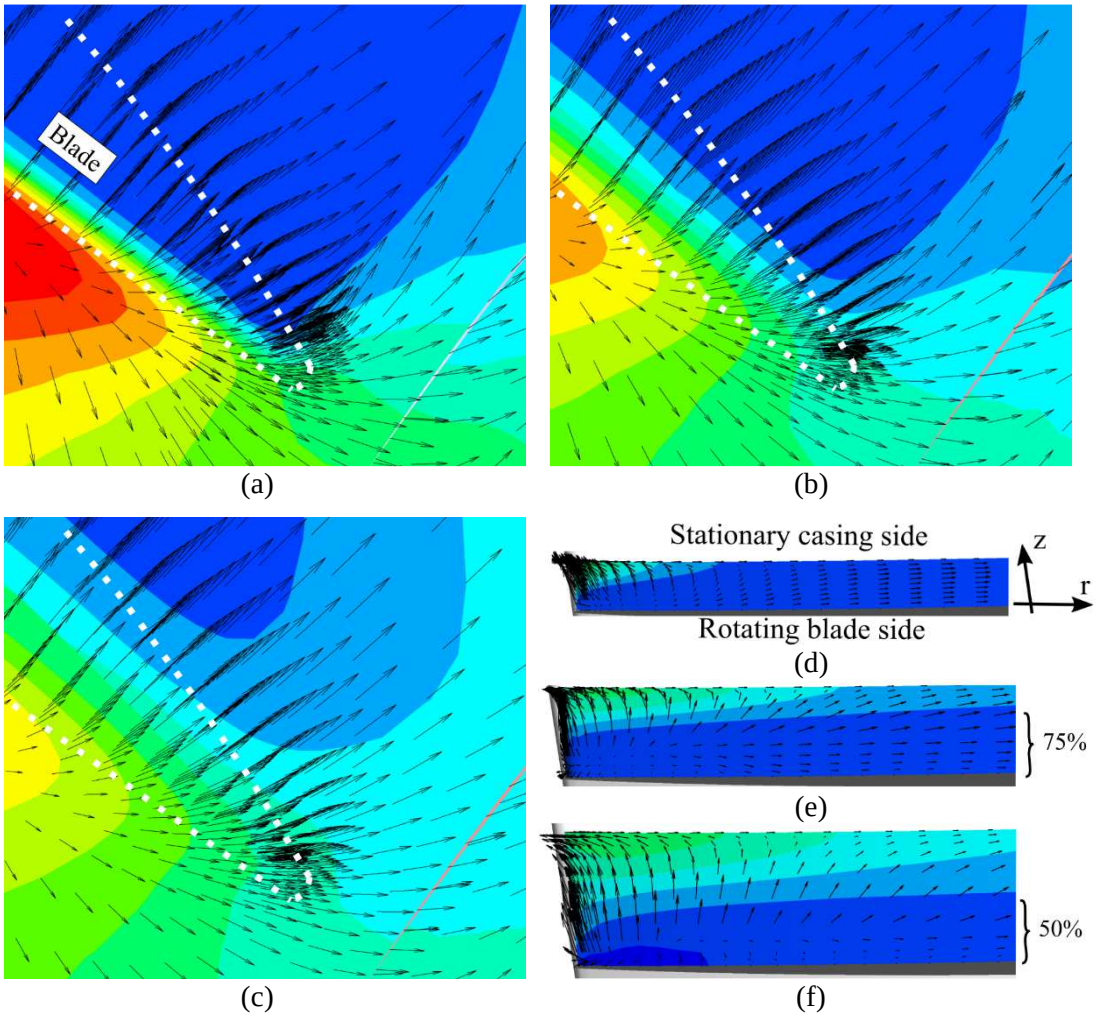

Σχήμα 5.10 Ισοϋψείς στατικής πίεσης και διανύσματα της εφαπτομενικής συνιστώσας της σχετικής ταχύτητας για $\Phi=0.80\cdot\Phi_{BEP}$ at **a)** A_1, $t_{tc}=0.5$ mm, **b)** A_1, $t_{tc}=0.9$ mm, **c)** A_1, $t_{tc}=1.5$ mm, **d)** A_2, $t_{tc}=0.5$ mm, **e)** A_2, $t_{tc}=0.9$ mm, **f)** A_2, $t_{tc}=1.5$ mm.

Όπως φαίνεται στο Σχ. 5.10, η χρήση διακένου μεγαλύτερου πάχους στης μηχανής οδηγεί σε αυξημένες ανακυκλοφορίες οι οποίες ενδυναμώνουν την ανάπτυξη της διφασικής περιοχής στις περιοχές υποπίεσης του πτερυγίου και εισόδου της μηχανής, επιβεβαιώνοντας τα αποτελέσματα που συζητούνται στις ενότητες 5.2.1.1 και 5.3.1.

5.3.2 Πτερωτή No. 4

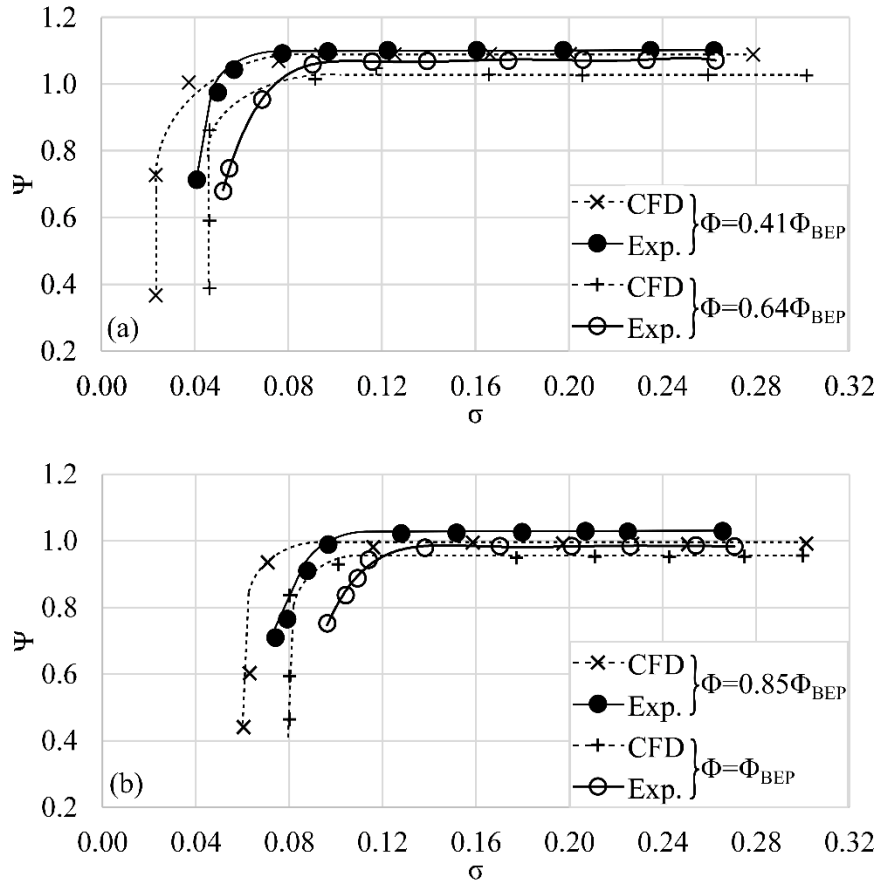

Σχήμα 5.11 Σύγκριση αριθμητικά υπολογισμένων χαρακτηριστικών καμπυλών σπηλαίωσης με τις αντίστοιχες πειραματικές, για την πτερωτή No. 3.

Η εφαρμογή του μοντέλου στην πτερωτή No. 4, επιβεβαιώνει την ικανότητα του να προβλέψει τη συμπεριφορά της καμπύλης σ-Ψ και σε πτερωτές κλειστού τύπου (Σχ. 5.11). Οι διαφορές στο ύψος και στην τιμή του σ_{FC} αιτιολογούνται από τις επιλογές που γίνονται κατά τη διάρκεια της μοντελοποίησης και έχουν συζητηθει για την περίπτωση της πτερωτής No. 2.

Το μοντέλο υπολογίζει την έναρξη της ανάπτυξης της σπηλαίωσης στην πλευρά υποπίεσης των πτερυγίων κοντά στην ακμή προσβολής (Σχ. 5.12a,b). Επιπλέον, η διφασική περιοχή αυξάνεται καθώς η τιμή του σ μειώνεται (Σχ. 5.12c,d), ενώ η μετάβαση σε σημεία λειτουργίας κοντά στο κανονικό (Σχ. 5.12), μειώνει της ασυμμετρίες στης διφασικής περιοχής στα πτερύγια της πτερωτής No. 4.

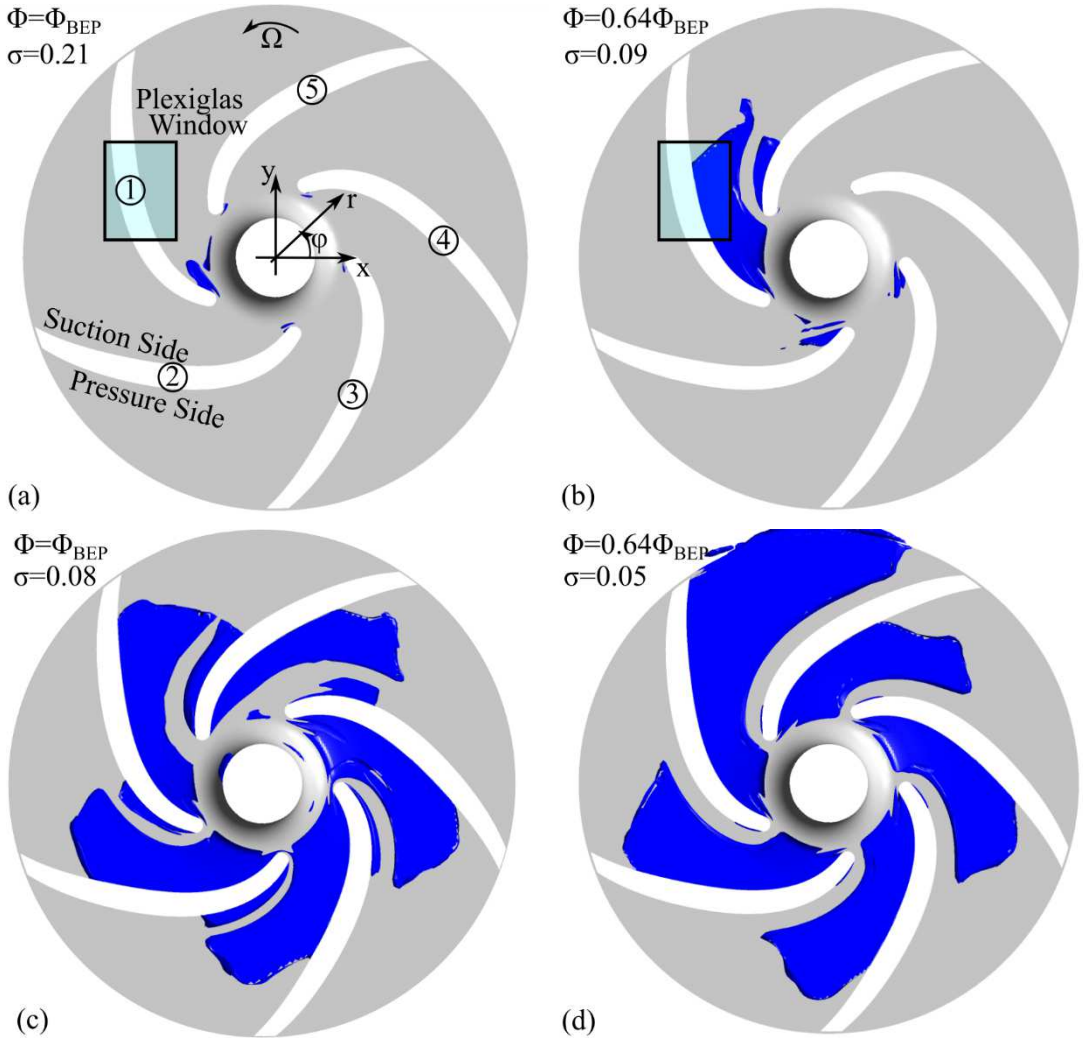

Σχήμα 5.12 Αριθμητικά αποτελέσματα της υπολογισμένης περιοχής ατμού για την πτερωτή No. 4.

6. Μετρήσεις Ταλάντωσης και Θορύβου

6.1 Εισαγωγή

Η παραγωγή των χαρακτηριστικών καμπύλων λειτουργίας για τις τέσσερις πτερωτές συνοδεύεται από τις μετρήσεις κραδασμού και θορύβου. Στο πρώτο μέρος του κεφαλαίου 6, τα σήματα αναλύονται στο χρόνο μαζί με τις στατιστικές τους ιδιότητες, οι οποίες παρουσιάζονται συναρτήσει του αδιάστατου αριθμού σπηλαίωσης Thoma, *σ*. Το δεύτερο μέρος περιλαμβάνει τη μελέτη του πεδίου συχνοτήτων και τη διερεύνηση της δυνατότητας των AE_{RMS} και των powerbands ταλάντωσης να διαγνώσουν το φαινόμενο.

6.2 Αποτελέσματα μετρήσεων στο πεδίο του χρόνου

Αρχικά, για να διευκολυνθεί και να ομαδοποιηθεί η παρουσίαση των αποτελεσμάτων σε όλο το κεφάλαιο 6, επιλέγονται κάποια χαρακτηριστικά σημεία λειτουργίας από το σύνολο των μετρήσεων, τα οποία παρουσιάζονται στον Πίνακα 6.1, για κάθε μια πτερωτή. Τα σημεία λειτουργίας που επιλέγονται αφορούν ένα σημείο χωρίς σπηλαίωση (σ_{BVI}), ένα σημείο στην περιοχή έναρξης του φαινομένου (σ_{VI}) και ένα σημείο στην περιοχή πτώσης του ύψους (σ_{FC}).

Πίνακας 6.1 Χαρακτηριστικά των σημείων λειτουργίας για κάθε πτερωτή.

	Φ [-]	**Φ/Φ$_{BEP}$**	**σ$_{BVI}$ [-]**	**σ$_{VI}$ [-]**	**σ$_{FC}$ [-]**
Impeller No.1	0.027	0.4	0.43	0.35	0.05
Impeller No.2	0.061	0.64	0.62	0.52	0.12
Impeller No.3	0.061	0.7	0.65	0.59	0.11
Impeller No.4	0.061	1	0.27	0.114	0.096

Από την απεικόνιση των μετρήσεων στο χρόνο (Σχ. 6.1 & 6.2) συμπεραίνεται ότι η ενδόρρηξη των φυσσαλίδων ατμού δεν επηρρεάζει ιδιαίτερα τις μετρούμενες χρονοσειρές στα αρχικά στάδια (σ_{VI}) της σπηλαίωσης (Σχ. 6.1b & 6.2b), καθώς το μετρούμενο σήμα δε διαφέρει ιδιαίτερα από εκείνο του σ_{BVI} (Σχ. 6.1a & 6.2a). Αντιθέτως, κατά τη διάρκεια των μετρήσεων σε σημεία με έντονη ανάπτυξη της σπηλαίωσης (σ_{FC}), κρουστικά χτυπήματα κάνουν την εμφάνιση τους στο πεδίο του χρόνου (Σχ. 6.1c & 6.2c). Τα χτυπήματα αυτά δεν εμφανίζουν ιδιαίτερα συστηματική περιοδικότητα, εκτός ορισμένων περιπτώσεων που ακολουθούν το πέρασμα των πτερυγίων (1/BPF=BPP).

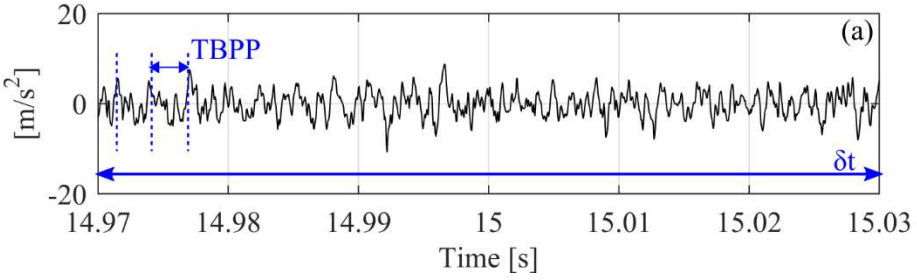

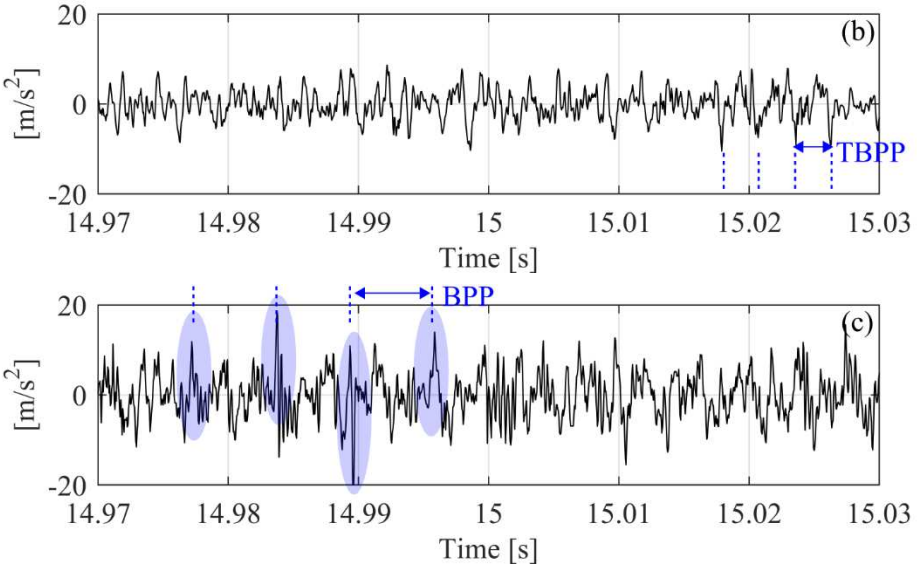

Σχήμα 6.1 Χρονοσειρές ταλάντωσης για την πτερωτή No. 1 για τον αισθητήρα A01, σε $\Phi=0.4\cdot\Phi_{BEP}$ at: **a)** σ_{BVI}, **b)** σ_{VI}, **c)** σ_{FC}.

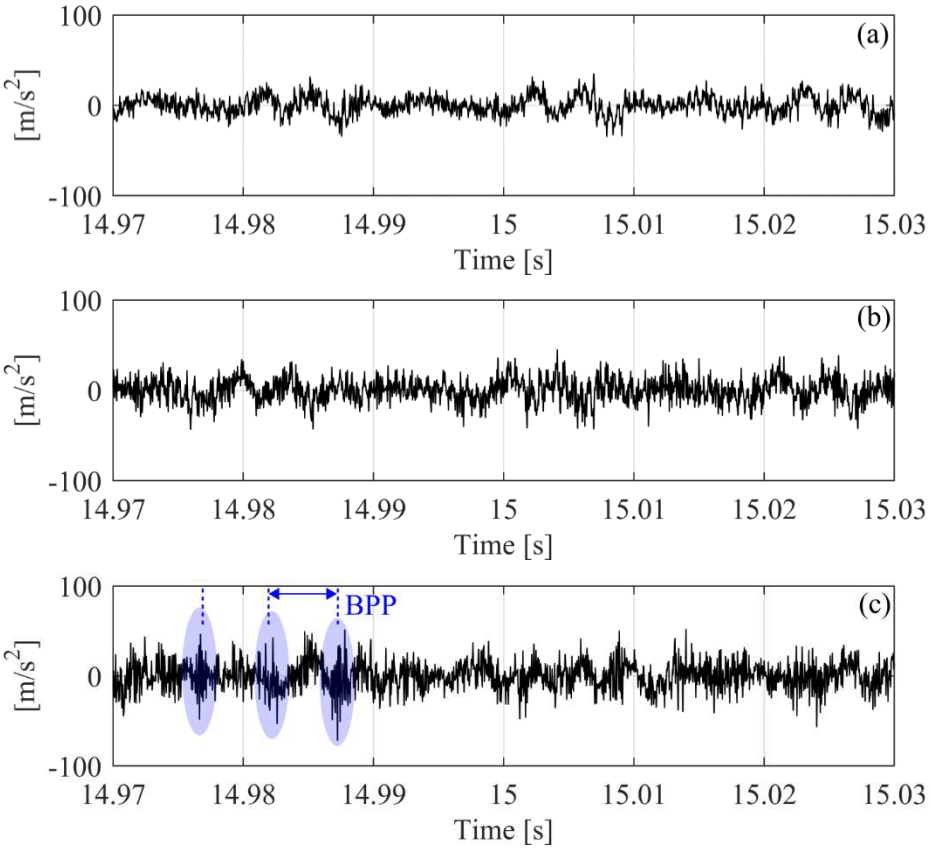

Σχήμα 6.2 Χρονοσειρές ταλάντωσης για την πτερωτή No. 4 για τον αισθητήρα B01_1, σε $\Phi=\Phi_{BEP}$ at: **a)** σ_{BVI}, **b)** σ_{VI}, **c)** σ_{FC}.

Στόχος της παρούσας εργασίας είναι η η αποκάλυψη εκείνων των χαρακτηριστικών στο σήμα που καλύπτονται από το γενικότερο θόρυβο της στα πρώτα στάδια ανάπτυξης της σπηλαίωσης. Τα αποτελέσματα που παρουσιάζονται στα Σχ. 6.1 και 6.2 για τις πτερωτές No. 1 και 4 είναι αντιπροσωπευτικά όλων των πτερωτών που δοκιμάζονται.

Η ανάλυση των ιστογραμμάτων κανονικοποιημένης συχνότητας εμφάνισης (Σχ. 6.3a) των τιμών των μετρήσεων ταλάντωσης και θορύβου καθώς και ο έλεγχος προσαρμογής της κατανομής συχνότητας των μετρήσεων στη κανονική κατανομή (Σχ. 6.3b) οδηγεί στο συμπέρασμα ότι η εμφάνιση των χτυπημάτων λόγω της σπηλαίωσης, δημιουργεί τιμές πλάτους ταλάντωσης και θορύβου αρκετά έξω από τα όρια της κανονικής κατανομής. Η σπηλαίωση δηλαδή αλλοιώνει τα χαρακτηριστικά της κατανομής, στα ακραία όρια των τιμών της τελευταίας (Σχ. 6.3b).

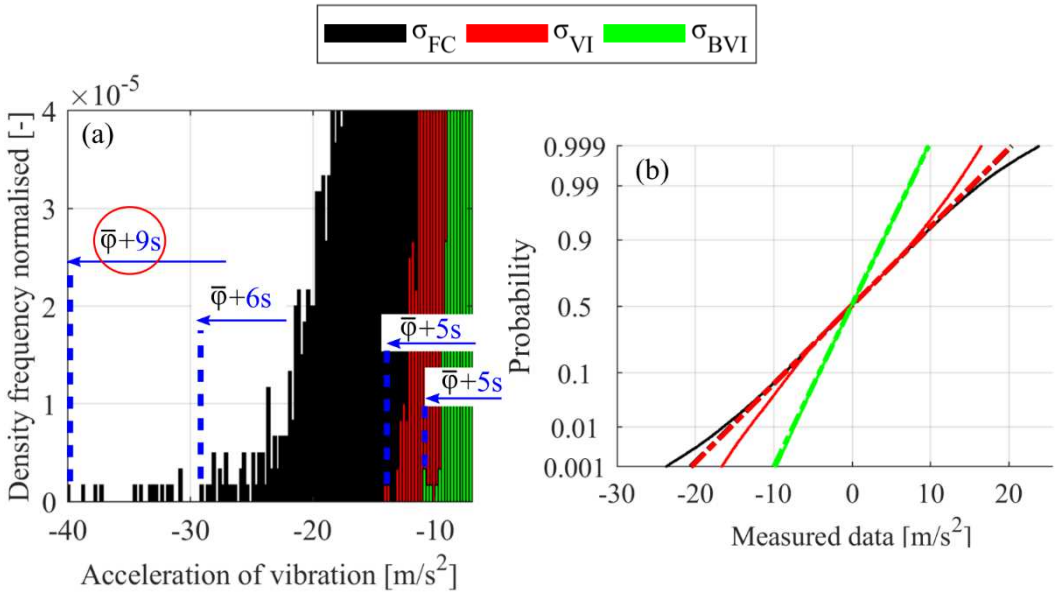

Σχήμα 6.3 a) Όρια ιστογράμματος συχνοτήτων για την πτερωτή No. 1, αισθητήρας A01 και **b)** έλεγχος προσαρμογής της κατανομής συχνότητας σε κανονική κατανομή για τις μετρήσεις της πτερωτής No. 2, αισθητήρα B01_1, στα διάφορα σημεία λειτουργίας (σ_{BVI}, σ_{VI}, σ_{FC}).

Το επόμενο βήμα αφορά την περαιτέρω διερεύνηση των στατιστικών ροπών (μέση τιμή, τυπική απόκλιση, στρέβλωση και κύρτωση) με την ανάλυση της συμπεριφορά τους σε σχέση με την ανάπτυξη του φαινομένου αλλά και τη συσχέτιση τους με αυτή τη συμπεριφορά της κατανομής.

Στο Σχ. 6.4, παρουσιάζονται τα αποτελέσματα των τεσσάρων στατιστικών ροπών σε σχέση με την ανάπτυξη του φαινομένου για την πτερωτή No. 1 και No. 4. Εδώ η ανάλυση περιλαμβάνει το σύνολο των μετρούμενων σημείων λειτουργίας (τέσσερις παροχές με όλα τα σ). Από εδώ και στο εξής η εμφάνιση σημείων πάνω στα γραφήματα με μπλε και κίτρινο χρώμα απεικονίζει το σημείο σ_{VI} για τις ημι-ανοικτού και την κλειστού τύπου πτερωτές, αντίστοιχα. Από τα αποτελέσματα του Σχ. 6.4a,b, φαίνεται ότι η τιμές της μέσης τιμής και της στρέβλωσης δεν επηρρεάζονται από την εμφάνιση της σπηλαίωσης, αντίθετα με τα αποτελέσματα της τυπικής απόκλισης, *s*, και της κύρτωσης που αυξάνονται με την πτώση του σ.

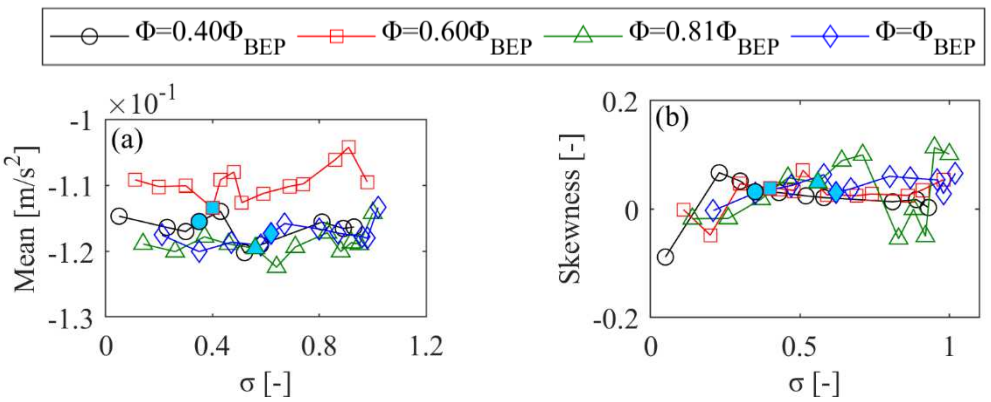

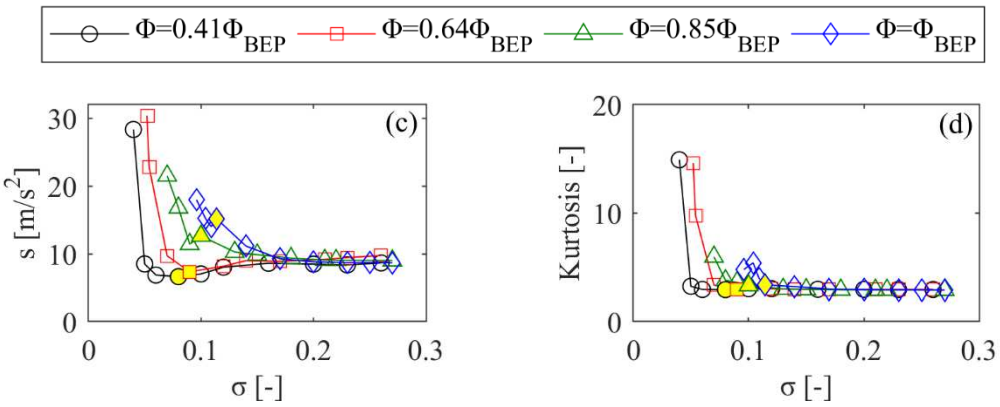

Σχήμα 6.4 Μεταβολή της **a)** μέσης τιμής, **b)** της στρέβλωσης, **c)** της τυπικής απόκλισης και **d)** της κύρτωσης για το σύνολο των μετρήσεων των πτερωτών No. 1, αισθητήρα A01 **(a,b)** και No. 4, αισθητήρα B01_2 **(c,d)** ως προς την ανάπτυξη του φαινομένου.

Ωστόσο, παρότι τα αποτελέσματα για την τυπική απόκλιση και την κύρτωση παρουσιάζουν ενδιαφέρουσα τάση, αυτή δεν είναι συστηματική για όλες τις παροχές και διαφέρει αρκετά στον εκάστοτε αισθητήρα που δοκιμάζεται.

Το επόμενο βήμα αφορά τη μελέτη των δυναμικών χαρακτηριστικών των στατιστικών ροπών σε σχέση με την εμφάνιση της σπηλαίωσης και για τη συσχέτιση με τα αποτελέσματα των Σχ. 6.3. Για να πραγματοποιηθεί η δυναμική ανάλυση, τα σήματα ομαδοποιούνται σε ομάδες των 1000 δειγμάτων και η τιμή τους παρουσιάζεται σε σχέση με τον αριθμό του δείγματος για διάφορα σημεία ανάπτυξης της σπηλαίωσης.

Από το σύνολο των ροπών μόνο τα αποτελέσματα της κύρτωσης διαφοροποιούνται σημαντικά με την εμφάνιση του φαινομένου (Σχ. 6.5). Πιο συγκεκριμένα, στο Σχ. 6.5 αποδεικνύεται ότι η έναρξη της σπηλαίωσης, αλλάζει την τιμή της κύρτωσης και τη διαφοροποιεί σημαντικά από αυτή που θα έπρεπε να είναι, αν η κατανομή ήταν κανονική. Τα αποτελέσματα επιβεβαιώνονται από όλα τα σημεία λειτουργίας, και στις τέσσερις πτερωτές για όλους τους αισθητήρες.

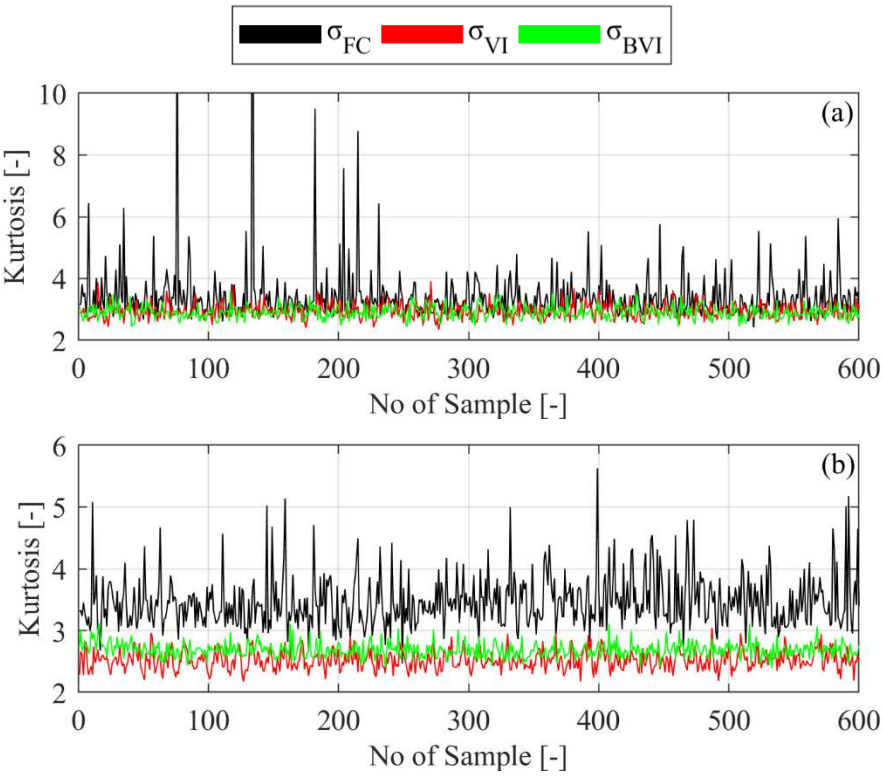

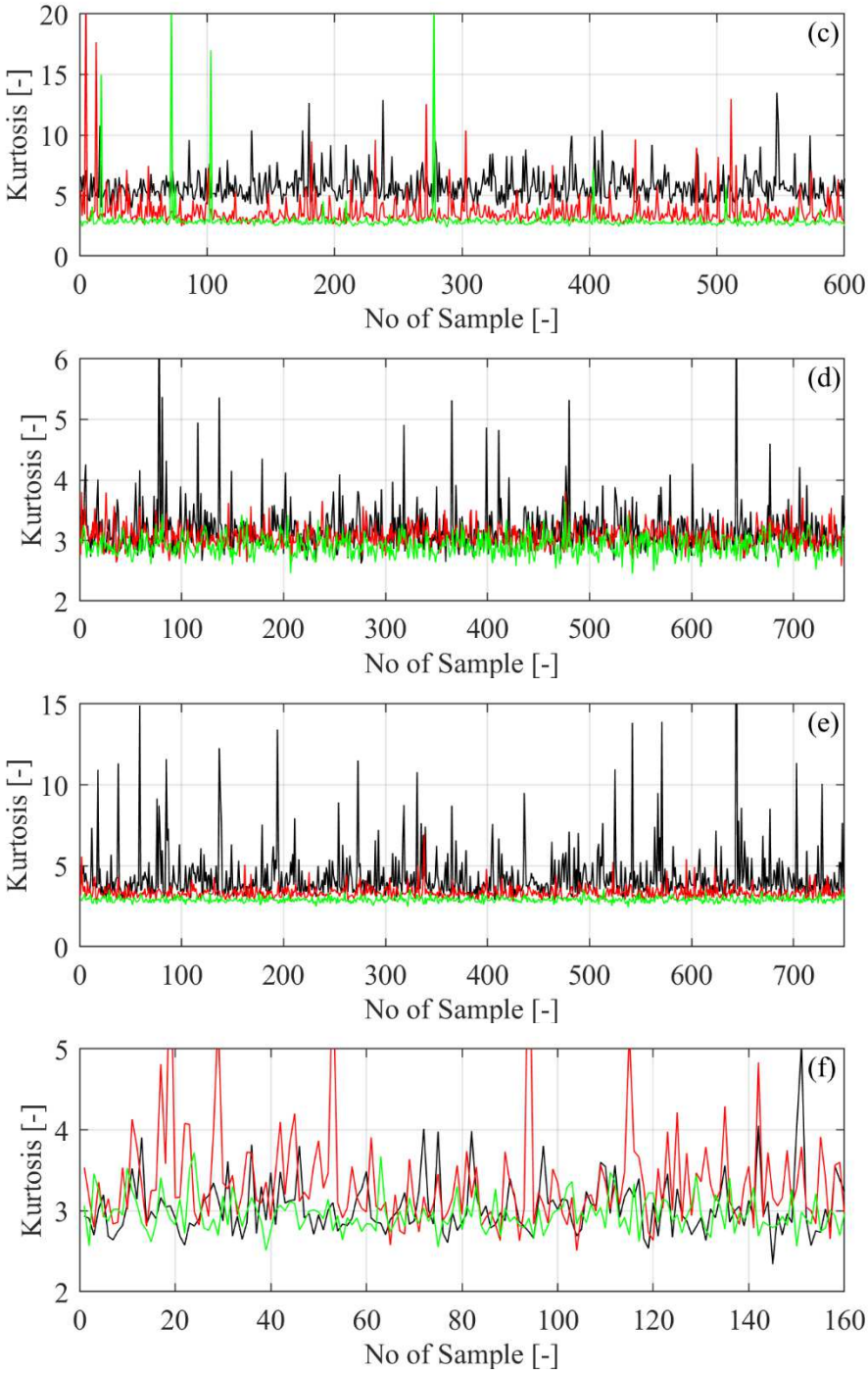

Σχήμα 6.5 Τιμή της κύρτωσης των ομαδοποιημένων τιμών για **a)** την πτερωτή No. 1, αισθητήρα A01, $\Phi=0.40\cdot\Phi_{BEP}$, **b)** την πτερωτή No.2, αισθητήρα B01_1, $\Phi=0.64\cdot\Phi_{BEP}$, **c)** την πτερωτή No.3, αισθητήρα A01, $\Phi=0.70\cdot\Phi_{BEP}$, **d)** την πτερωτή No.4, αισθητήρα B01_1, $\Phi=\Phi_{BEP}$, **e)** την πτερωτή No.4, αισθητήρα B01_2, $\Phi=\Phi_{BEP}$, **f)** την πτερωτή No.4, αισθητήρα AE, $\Phi=\Phi_{BEP}$.

6.3 Μελέτη του πεδίου συχνοτήτων

Η μελέτη των σημάτων στο πεδίο των συχνοτήτων παρουσιάζει πολύ ενδιαφέροντα χαρακτηριστικά. Πιο συγκεκριμένα, η ανάπτυξη της σπηλαίωσης διεγείρει ένα σημαντικό εύρος του πεδίου συχνοτήτων (Σχ. 6.6) που καλύπτει κυρίως της υψηλές συχνότητες της μέτρησης. Ωστόσο, η ένταση και η θέση των διεγερμένων περιοχών επηρρεάζεται σημαντικά από τα ιδιαίτερα χαρακτηριστικά κάθε πειραματικής διάταξης και μηχανής, αλλά ακόμα και από το σημείο λειτουργίας της κάθε μηχανής. Είναι επίσης σημαντικό να σημειωθεί ότι αντίστοιχες διεγέρσεις παρατηρούνται κατά καιρούς στη βιβλιογραφία (McFadden, 1984b; Prashad, 1985; Randall, 2007; Saidi, 2014) και σχετίζονται με ιδιοσυχνότητες που διεγείρονται από φθορές κρουστικής μορφής στα έδρανα κυλίσεως (ρουλεμάν).

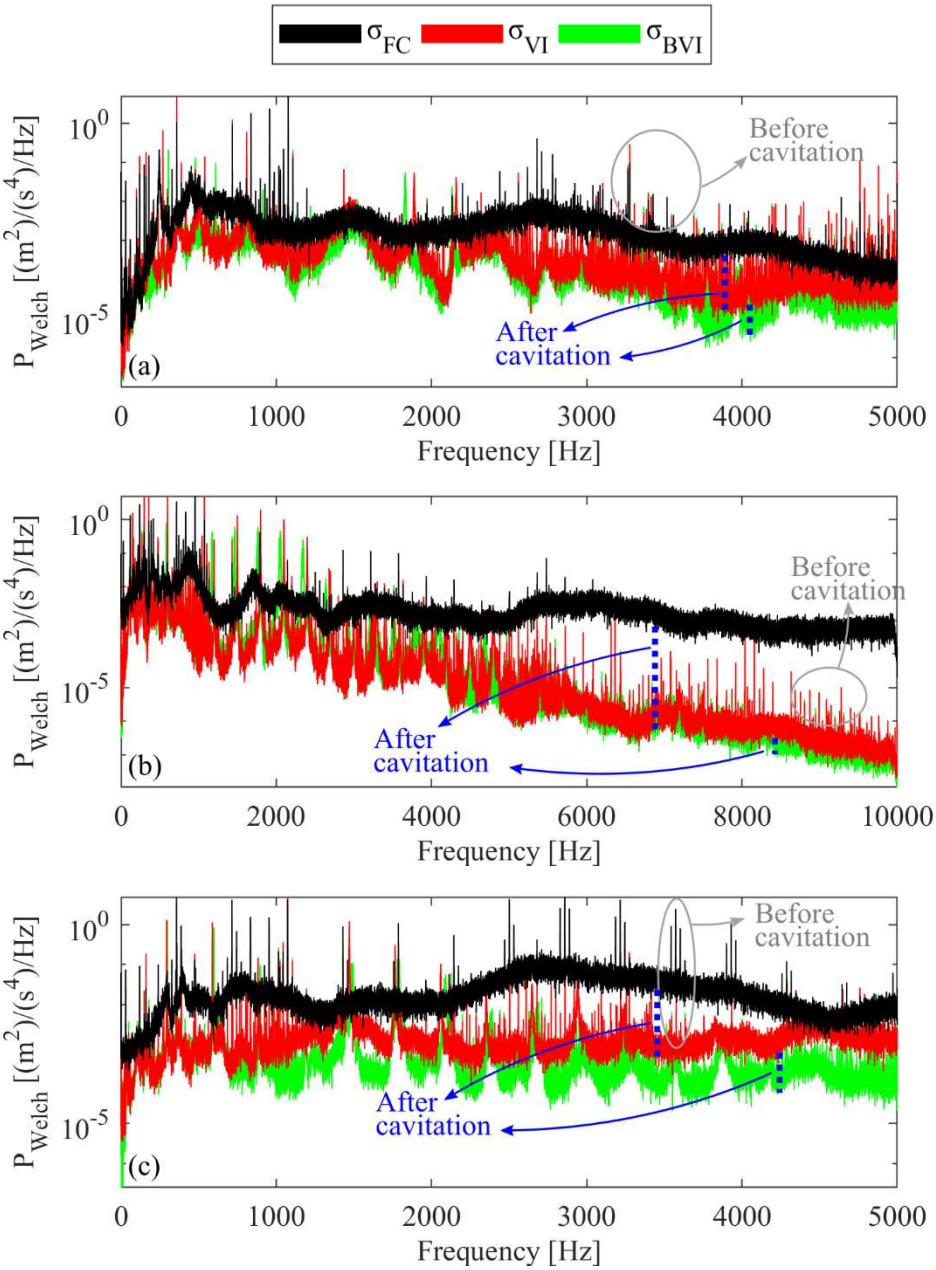

Σχήμα 6.6 Φάσματα συχνοτήτων, λογαριθμημένα στον άξονα y, σε διαφορετικά σημεία ανάπτυξης της σπηλαίωσης για: **a)** την πτερωτή No. 1, αισθητήρα A01, $\Phi=0.40\cdot\Phi_{BEP}$, **b)** την πτερωτή No. 2, αισθητήρα B01_1, $\Phi=0.64\cdot\Phi_{BEP}$, **c)** την πτερωτή No. 3, αισθητήρα A01, $\Phi=0.70\cdot\Phi_{BEP}$.

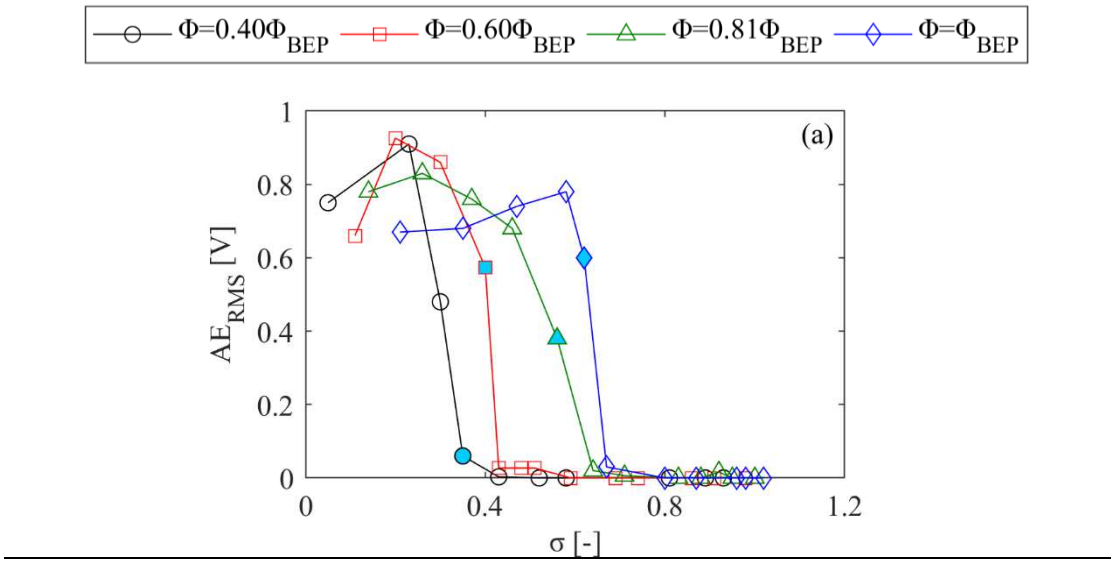
Φ=0.40Φ_BEP
Φ=0.60Φ_BEP
Φ=0.81Φ_BEP
Φ=Φ_BEP
(a)
AE_RMS [V]
σ [-]
0
0.2
0.4
0.6
0.8
1
0.4
0.8
1.2

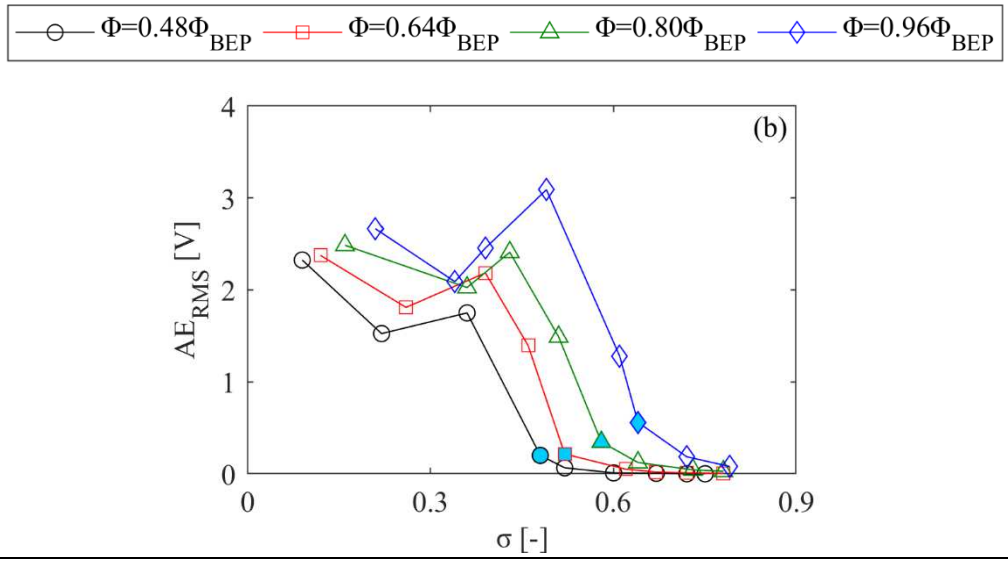
Φ=0.48Φ_BEP
Φ=0.64Φ_BEP
Φ=0.80Φ_BEP
Φ=0.96Φ_BEP
(b)
AE_RMS [V]
σ [-]
0
1
2
3
4
0.3
0.6
0.9

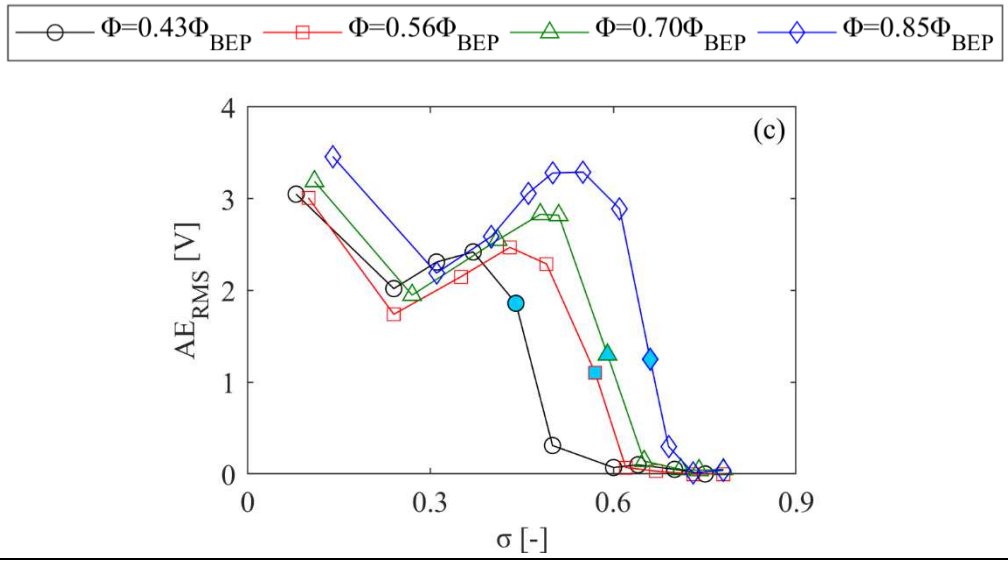
Φ=0.43Φ_BEP
Φ=0.56Φ_BEP
Φ=0.70Φ_BEP
Φ=0.85Φ_BEP
(c)
AE_RMS [V]
σ [-]
0
1
2
3
4
0.3
0.6
0.9

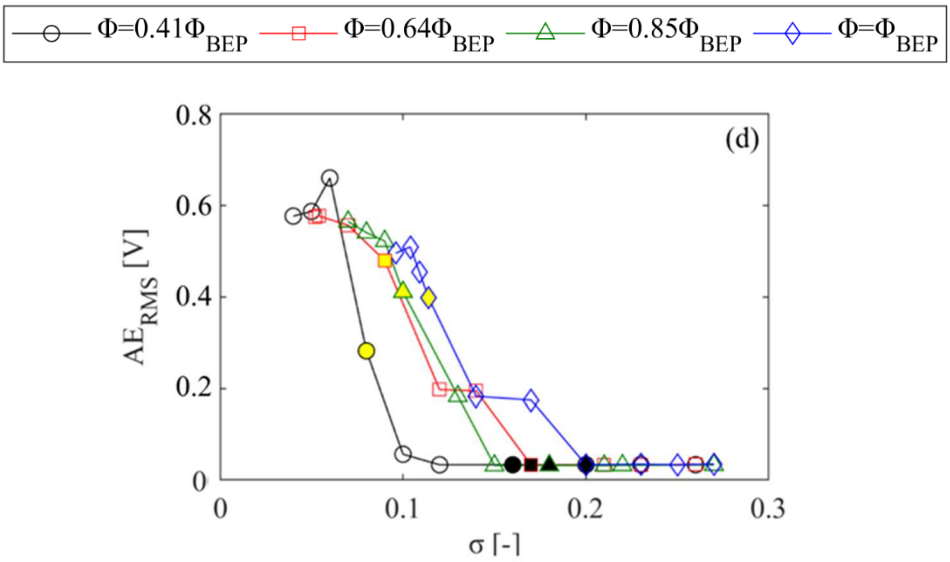

Σχήμα 6.7 AE_{RMS} σε όλες τις παροχές της **a)** πτερωτής No. 1 [100 – 150] kHz, **b)** πτερωτής No. 2 [100 – 150] kHz, **c)** πτερωτής No. 3 [100 – 150] kHz, **d)** πτερωτής No. 4 [2.5 – 80] kHz.

Ένας τρόπος να ποσοτικοποιηθεί η αύξηση του πλάτους στις διεγερμένες περιοχές του πεδίου συχνοτήτων του Σχ. 6.6 είναι με τη χρήση των AE_{RMS} για τις μετρήσεις θορύβου και των powerband για τις μετρήσεις ταλάντωσης που αθροίζουν την ισχύ στα υψηλά εύρη συχνοτήτων για κάθε αισθητήρα. Τα αποτελέσματα για όλους τους αισθητήρες, σε όλες τις παροχές για όλες τις πτερωτές που μετρήθηκαν παρουσιάζονται αναλυτικά στα Σχ. 6.7-6.11. Στις λεζάντες των σχημάτων δίνονται τα εύρη που χρησιμοποιούνται στην κάθε περίπτωση. Τα μπλε σημεία στα Σχ. 6.7-6.10, απεικονίζουν τα πειραματικά σημεία του (σ_{VI}) στην περίπτωση των ημι-ανοικτών τύπου πτερωτών, ενώ για την πτερωτή No. 4, τα κίτρινα και μαύρα σημεία αντιστοιχούν στα πειραματικά και υπολογιστικά σ_{VI} σημεία λειτουργίας, αντίστοιχα.

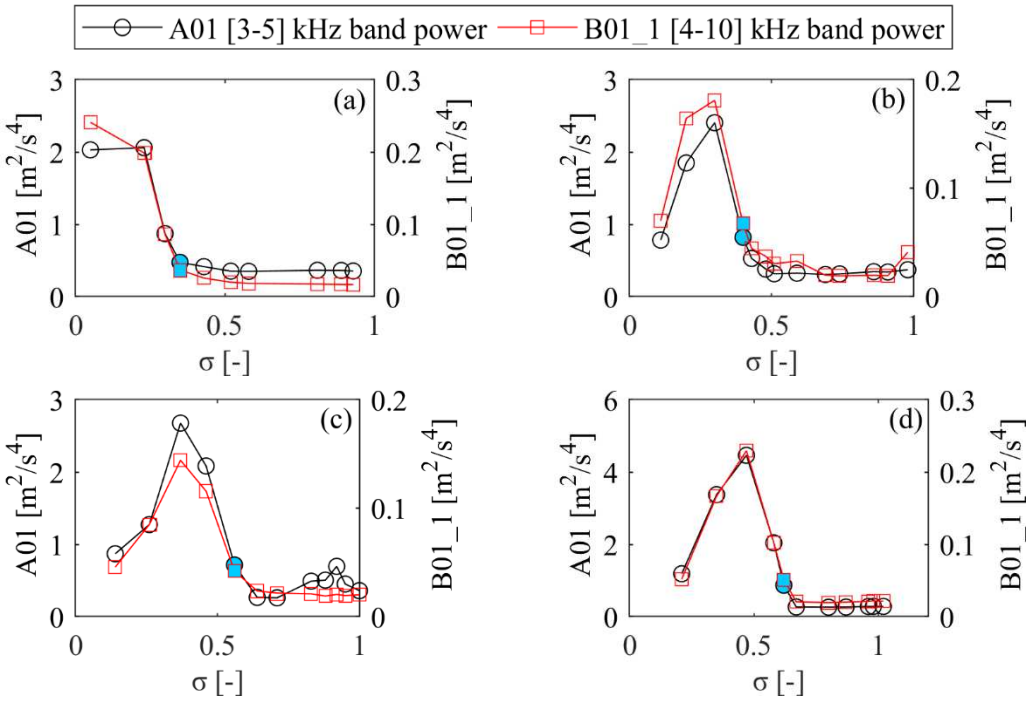

Σχήμα 6.8 Υψίσυχνο εύρος ταλάντωσης για την πτερωτή No. 1, για **a)** $\Phi=0.40\cdot\Phi_{BEP}$, **b)** $\Phi=0.60\cdot\Phi_{BEP}$, **c)** $\Phi=0.81\cdot\Phi_{BEP}$, **d)** $\Phi=\Phi_{BEP}$.

Ένα πρώτο γενικό συμπέρασμα από τα αποτελέσματα των Σχ. 6.7a-c, είναι το γεγονός ότι οι μετρήσεις θορύβου (AE_{RMS}) δύνανται να διαγνώσουν έγκαιρα τη σπηλαίωση στην περίπτωση των αντλιών που χρησιμοποιούν ανοικτού τύπου πτερωτές, αφού η τιμή τους αυξάνει κατά την παρατήρηση των πρώτων σχηματισμών φυσσαλίδων ατμού. Τα αποτελέσματα των powerbands ταλάντωσης για τις ίδιες πτερωτές (Σχ. 6.8-6.10) παρουσιάζουν παρόμοια συμπεριφορά με τα AE_{RMS}, ωστόσο η χρήση αισθητά χαμηλότερων ευρών στην περίπτωση της ταλάντωσης καθυστερεί για λίγο τη διάγνωση, ορισμένες φορές.

Ωστόσο, στην περίπτωση της κλειστής πτερωτής No. 4 (Σχ. 6.7d & 6.11), η χρήση των προτεινώμενων AE_{RMS} και powerband ταλάντωσης μεθόδων δε λειτουργεί, ιδιαίτερα στις μικρές παροχές, καθώς η αύξηση τους καθυστερεί αρκετά και συμπίπτει με την πτώση του ύψους. Ο λόγος γι' αυτές τις διαφοροποιήσεις σε ορισμένα από τα αποτελέσματα της κλειστής πτερωτής No. 4 είναι η ύπαρξη της στεφάνης η οποία δρα σαν ένα επιπλέον εμπόδιο μεταξύ του φαινομένου και του αισθητήρα, ενώ ρόλο σίγουρα παίζει και χρήση των εδράσεων κύλισης στην αντλία. Θα πρέπει να θυμίσουμε σε αυτό το σημείο, ότι οι πτερωτές No. 1-3, εγκαθίστανται σε αντλία χωρίς εδράσεις, της οποία οι φορτίσεις παραλαμβάνονται από τα ρουλεμάν του κινητήρα.

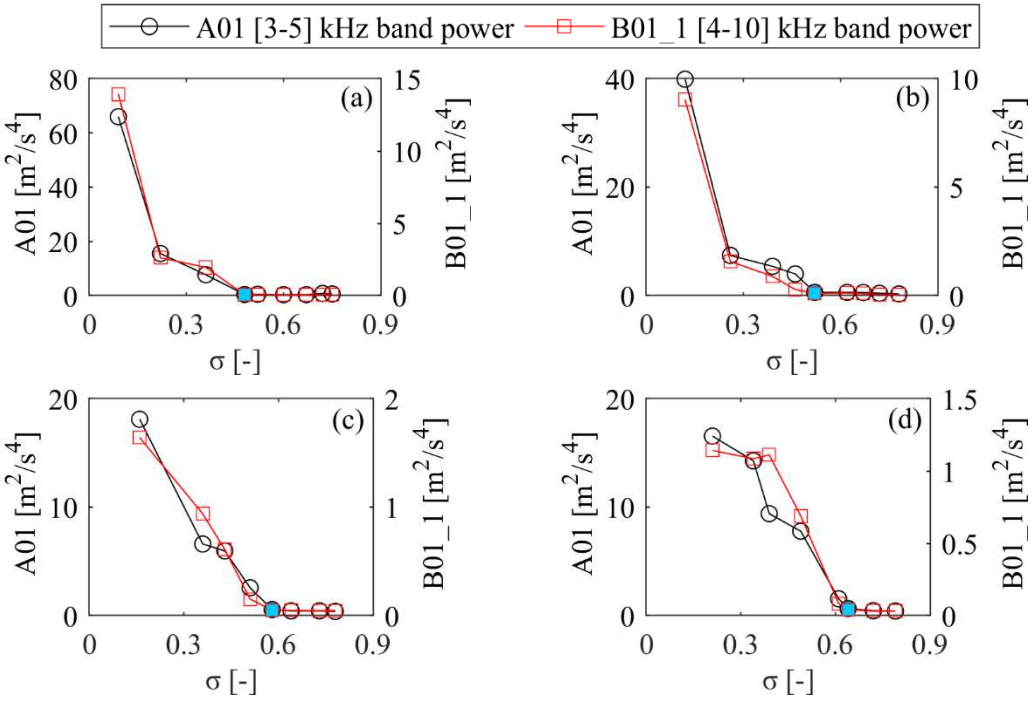

Σχήμα 6.9 Υψίσυχνο εύρος ταλάντωσης για την πτερωτή No. 2, για **a)** $\Phi=0.48\cdot\Phi_{BEP}$, **b)** $\Phi=0.64\cdot\Phi_{BEP}$, **c)** $\Phi=0.80\cdot\Phi_{BEP}$, **d)** $\Phi=0.96\cdot\Phi_{BEP}$.

Οι παραπάνω διαπιστώσεις αναδεικνύουν την αδυναμία της χρήσης των μεθόδων AE_{RMS} και powerband ταλάντωσης να διαγνώσουν έγκαιρα τη σπηλαίωση στην κλειστού τύπου πτερωτή. Ένας επιπλέον προβληματισμός αφορά την μορφή των AE_{RMS} και powerband ταλάντωσης, η οποία αλλάζει στις διάφορες εγκαταστάσεις, καθώς και στα διαφορετικά εύρη συχνοτήτων και δε συνθέτει μια συστηματική μορφή, ικανή να χρησιμοποιηθεί για τη γενικότερη διάγνωση του φαινομένου. Τα παραπάνω σε συνδυασμό με τις παρατηρήσεις πάνω στα αποτελέσματα του Σχ. 6.6 και την πιθανότητα η διεγέρση του πεδίου συχνοτήτων, που αθροίζουν τα AE_{RMS} και powerband ταλάντωσης, να μην οφείλονται στη σπηλαίωση αλλά σε βλάβη στα ρουλεμάν, οδηγούν στο συμπέρασμα ότι χρειάζεται επιπλέον δουλειά στο πεδίο της επεξεργασίας των σημάτων με στόχο τη διατύπωση ενός γενικευμένου κριτηρίου διάγνωσης της σπηλαίωσης.

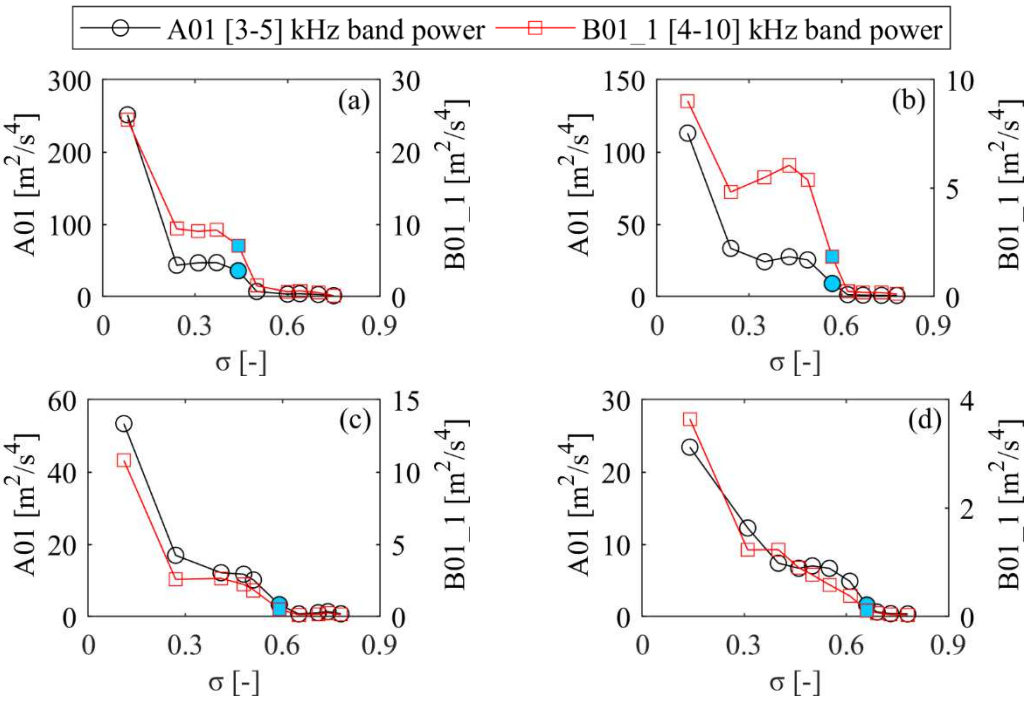

Σχήμα 6.10 Υψίσυχνο εύρος ταλάντωσης για την πτερωτή No. 3, για **a)** $\Phi=0.43\cdot\Phi_{BEP}$, **b)** $\Phi=0.56\cdot\Phi_{BEP}$, **c)** $\Phi=0.70\cdot\Phi_{BEP}$, **d)** $\Phi=0.85\cdot\Phi_{BEP}$.

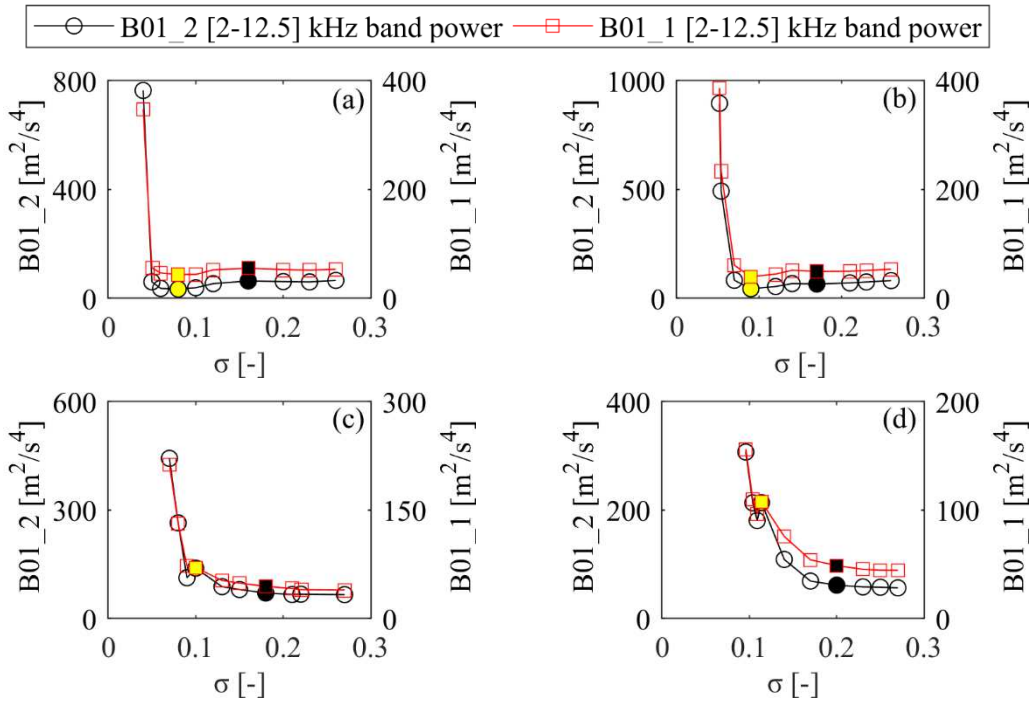

Σχήμα 6.11 Υψίσυχνο εύρος ταλάντωσης για την πτερωτή No. 4, για **a)** $\Phi=0.41\cdot\Phi_{BEP}$, **b)** $\Phi=0.64\cdot\Phi_{BEP}$, **c)** $\Phi=0.85\cdot\Phi_{BEP}$, **d)** $\Phi=\Phi_{BEP}$.

7. Φασματική Κύρτωση

7.1 Εισαγωγή

Στο παρών Κεφάλαιο προτείνεται η εφαρμογή της Φασματικής Κύρτωσης (SK: Spectral Kurtosis), για τον υπολογισμό των χαρακτηριστικών του φίλτρου εύρους ζώνης, δηλαδή της κεντρικής συχνότητας f_c και του εύρους f_r, που θα εφαρμοστεί στο μετρούμενο σήμα. Ο στόχος είναι η ανάλυση των χαρακτηριστικών του φιλτραρισμένου σήματος μηχανικών ταλαντώσεων αλλά και της περιβάλλουσας του στο πεδίο των συχνοτήτων, σε σχέση με την ανάπτυξη του φαινόμενου. Η έρευνα επικεντρώνεται στα σημεία λειτουργίας, πριν την πτώση του ύψους, στα πρώτα στάδια ανάπτυξης του φαινομένου και πιο συγκεκριμένα; στα σημεία σ_{BVI} (πριν την έναρξη της σπηλαίωσης), σ_{IN} (αρχή του φαινομένου), σ_{INT} (μέτρια ανάπτυξη του φαινομένου). Στην ενότητας 7.2 παρουσιάζονται ενδεικτικά αποτελέσματα του Fast Kurtogram, ενώ στην ενότητα 7.3 τα αποτελέσματα του φιλτραρισμένου σήματος στο χρόνο καθώς και το πεδίο συχνοτήτων της περβάλλουσας.

7.2 Αποτελέσματα του Fast Kurtogram

Η μέθοδος της φασματικής κύρτωσης εφαρμόζεται μέσω του Fast Kurtogram (FK) σε κάθε μέτρηση κραδασμού για όλα τα σημεία λειτουργίας, όλων των πτερωτών του Σχ. 3.2 (ενότητα 4.3). Τα αποτελέσματα του FK αφορούν τη μέγιστη τιμή της φασματικής κύρτωσης (MSK: Maximum Spectral Kurtosis), το εύρος του φίλτρου, f_r, που εκφράζεται με βάση το DL (Decomposition Level) και την κεντρική συχνότητα του φίλτρου, f_c. Τα πρώτα δύο παρουσιάζονται για μία παροχή κάθε πτερωτής στο Σχ. 7.1.

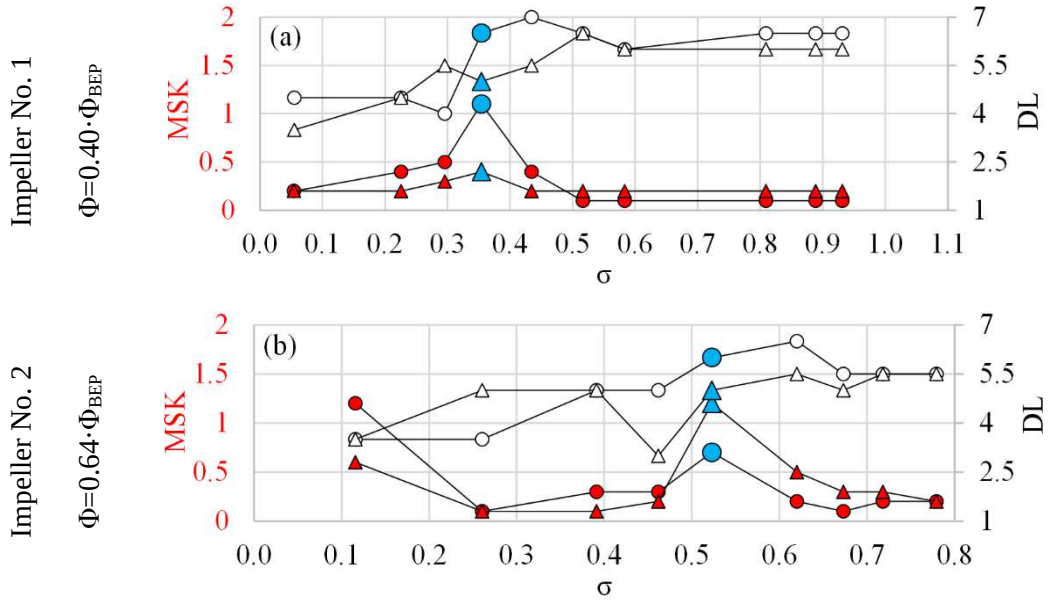

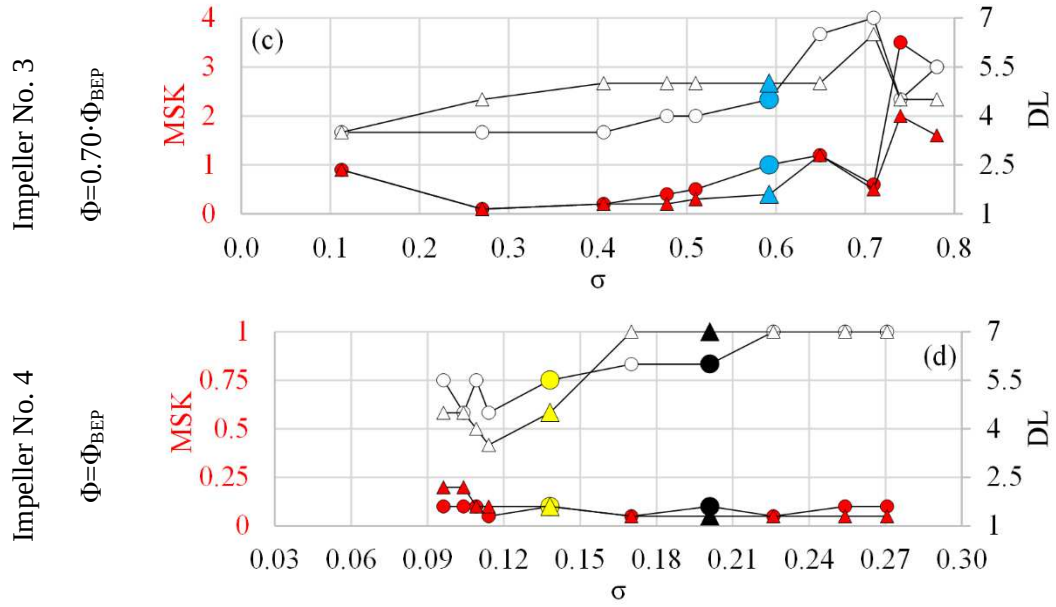

Σχήμα 7.1 Η τιμή της MSK (κόκκινο χρώμα) και η αντίστοιχη τιμή του DL (λευκά σημεία) σε σχέση με τον αδιάστατο αριθμό Thoma, σ.

Τα μπλε, κίτρινα και μαύρα σημεία δηλώνουν τα πειραματικώς και αριθμητικώς υπολογισμένα σ_{VI}, όπως και στο Κεφάλαιο 6. Στα Σχ. 7.1 με κύκλο σημειώνεται ο αισθητήρας B01_1, ενώ με τρίγωνο στα Σχ. 7.1a-c δίνεται ο αισθητήρας A01 και στο Σχ. 7.1d ο αισθητήρας B01_2.

Από τα αποτελέσματα του Σχ. 7.1 εξάγονται τρεις πολύ ενδιαφέρουσες παρατηρήσεις. Η πρώτη αφορά, το γεγονός ότι ασχέτως εγκατάστασης, αισθητήρα και πτερωτής, η ανάπτυξη του φαινομένου οδηγεί στη διέγερση μεγαλύτερου εύρους συχνοτήτων καθώς η τιμή MSK γίνεται σε μέγιστη σε μικρότερες τιμές του DL. Επίσης, η παρακολούθηση της απόλυτης MSK τιμής αυξάνει σε κάποιες περιπτώσεις με την έναρξη και την ανάπτυξη του φαινομένου (Σχ. 7.1a,b,d), ωστόσο αυτή η τάση δεν επιβεβαίωνεται σε όλα τα αποτελέσματα ((Σχ. 7.1c) και δεν την καθιστά δείκτη ανάπτυξης του φαινομένου. Τέλος, η τιμή του f_c δε δίνεται καθώς δεν ακολουθεί κάποια συγκεκριμένη τάση, ως προς το σ, γεγονός που επιβεβαιώνει τα συμπεράσματα του Σχ. 6.6 αλλά και της βιβλιογραφίας (Yiakopoulos, 2005; Randal 2007), σχετικά με την τυχαιότητα των συχνοτήτων που διεγείρονται από κρουστικά φαινόμενα.

Στο Σχ. 7.2 δίνονται ενδεικτικά αποτελέσματα του FK για τις πτερωτές No. 1 και 2.

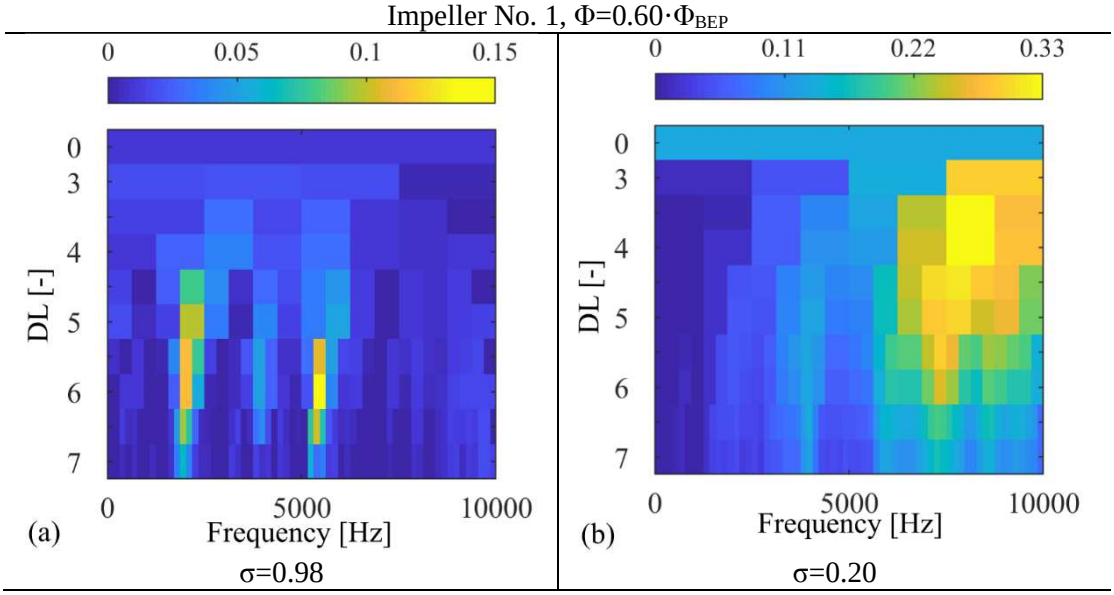

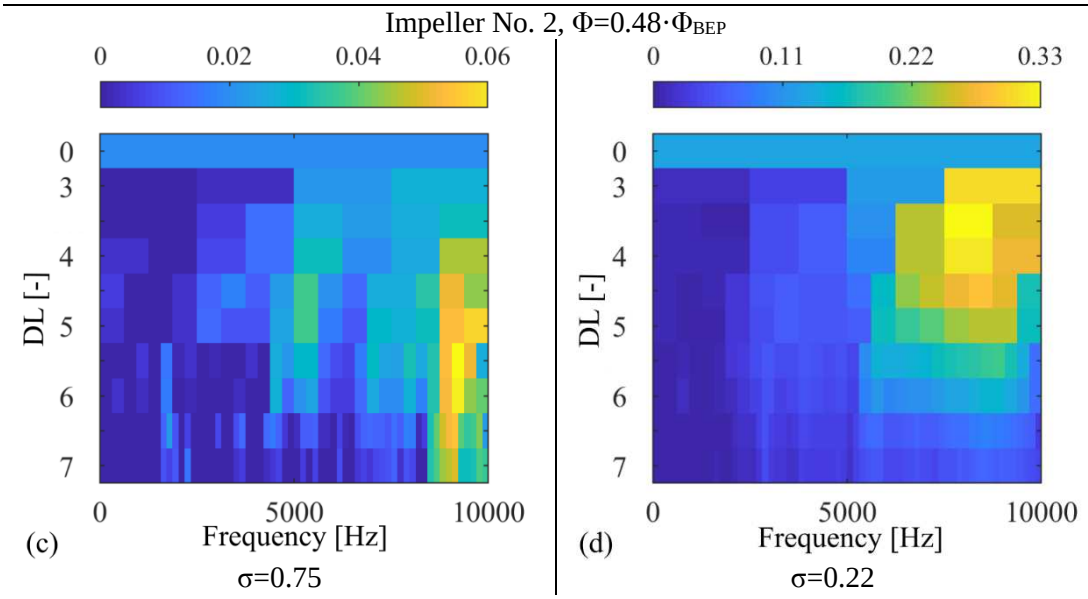

Σχήμα 7. 2 Σύγκριση αποτελεσμάτων FKs μεταξύ συνθηκών χωρίς (αριστερά) και με (δεξιά) σπηλαίωση για τον αισθητήρα B01_1.

7.3 Φίλτρανση και πεδίο συχνοτήτων της περιβάλλουσας

Στην παρούσα ενότητα παρουσιάζονται τα αποτελέσματα της εφαρμογής των φίλτρων που κατασκευάστηκαν μέσω του FK στο σήμα στο χρόνο (Σχ. 7.3) καθώς και στο πεδίο συχνοτήτων της περιβάλλουσας (Σχ. 7.4). Τα αποτελέσματα που παρουσιάζονται αφορούν σημεία λειτουργίας πριν την πτώση του ύψους των αντλιών. Σύμφωνα με τα αποτελέσματα του Σχ. 7.3, σε σημεία λειτουργίας χωρίς σπηλαίωση (Σχ. 7.3a) δεν παρατηρούνται ιδιαίτερα χαρακτηριστικά στο φιλτραρισμένο σήμα. Ωστόσο, με την έναρξη του φαινομένου, τα πρώτα χτυπήματα εμφανίζονται σε όλες τις πτερωτές, μέρος των οποίων (κόκκινη περιοχή) δεν ακολουθεί κάποια συγκεκριμένη περιοδικότητα και κάποιο μέρος που ακολουθεί τη BPP (μπλε διακεκομμένες γραμμές), όμοια με τα Σχ. 6.1, 6.2 (ενότητα 6.2).

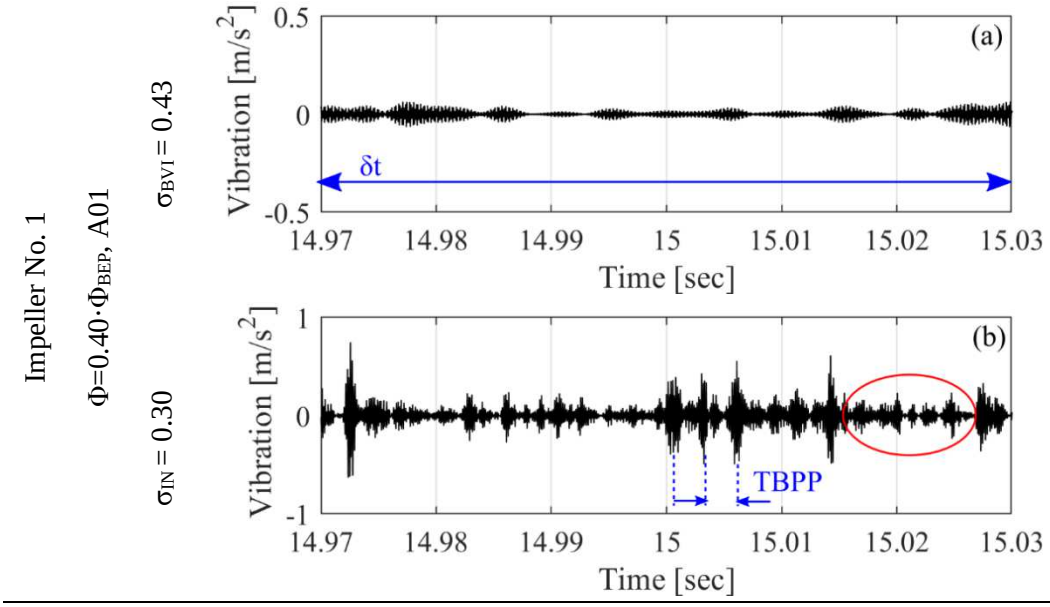

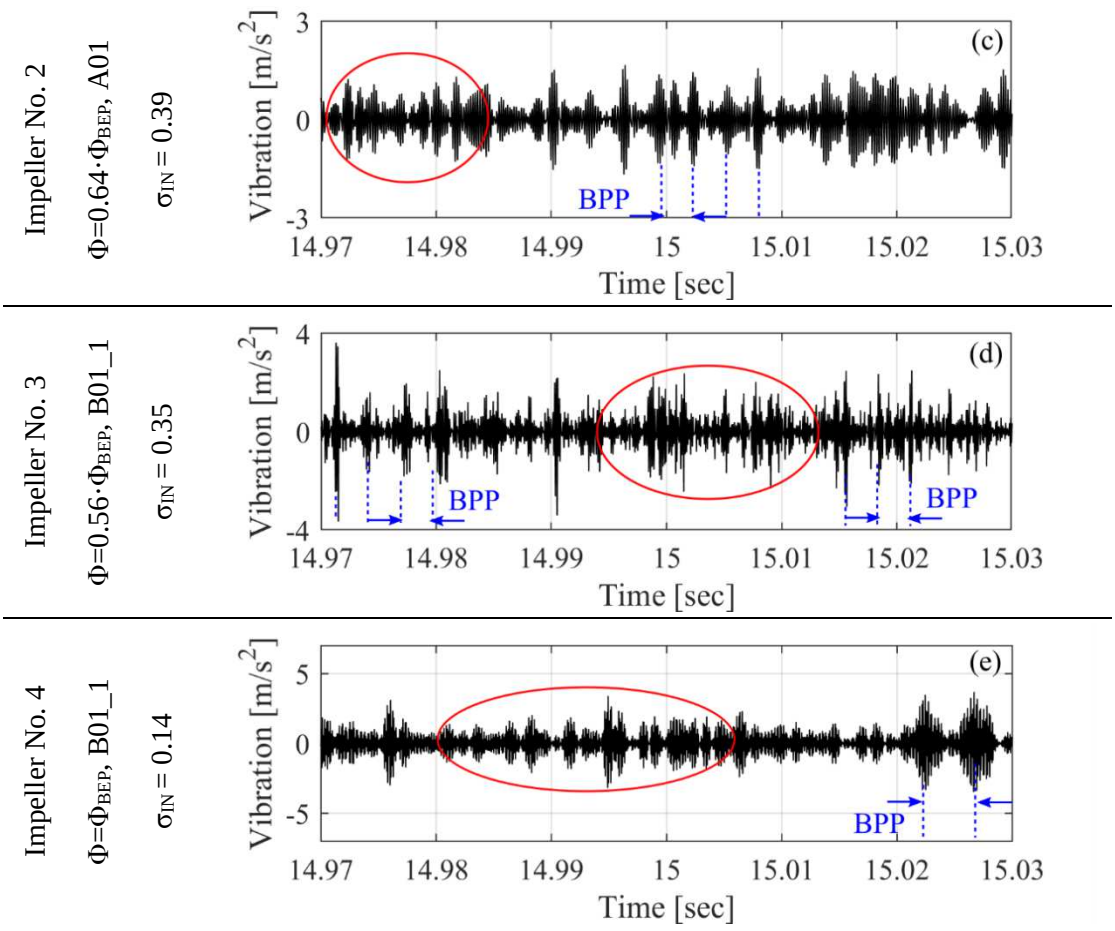

Σχήμα 7. 3 Φιλτραρισμένες χρονοσειρές σημάτων ταλάντωσης για σημεία κοντά στην έναρξη του φαινομένου.

Η σημαντική διαφορά σε σχέση με τα αποτελέσματα της ενότητας 6.1, είναι πως με τη χρήση του φίλτρου αναδεικνύουμε αυτή τη συμπεριφορά και στα αρχικά στάδια του φαινομένου.

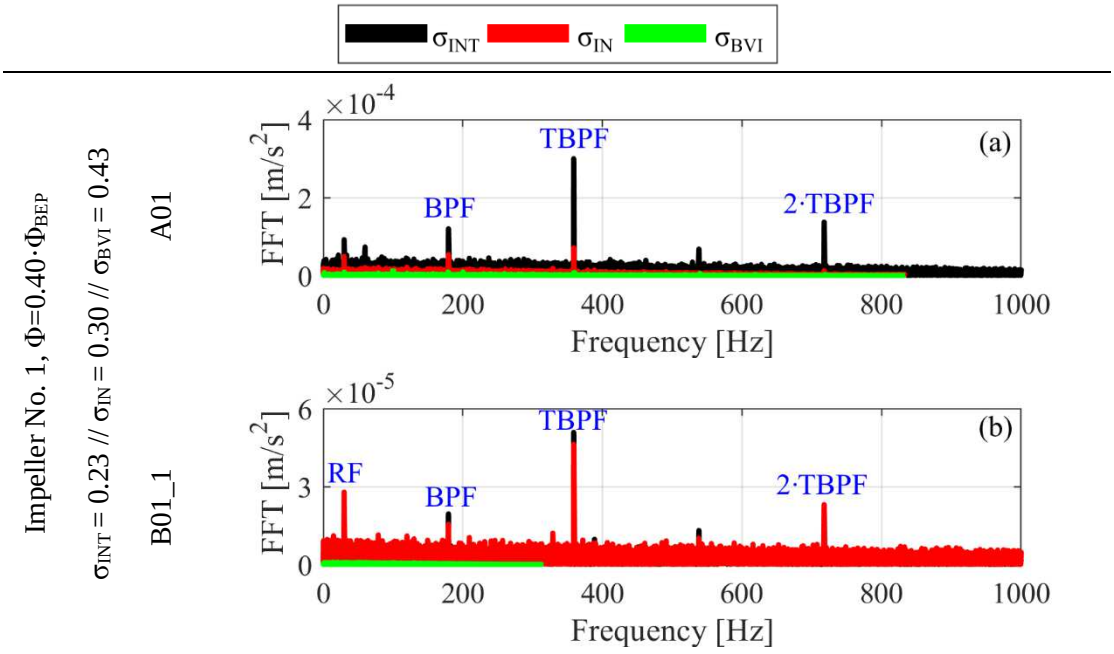

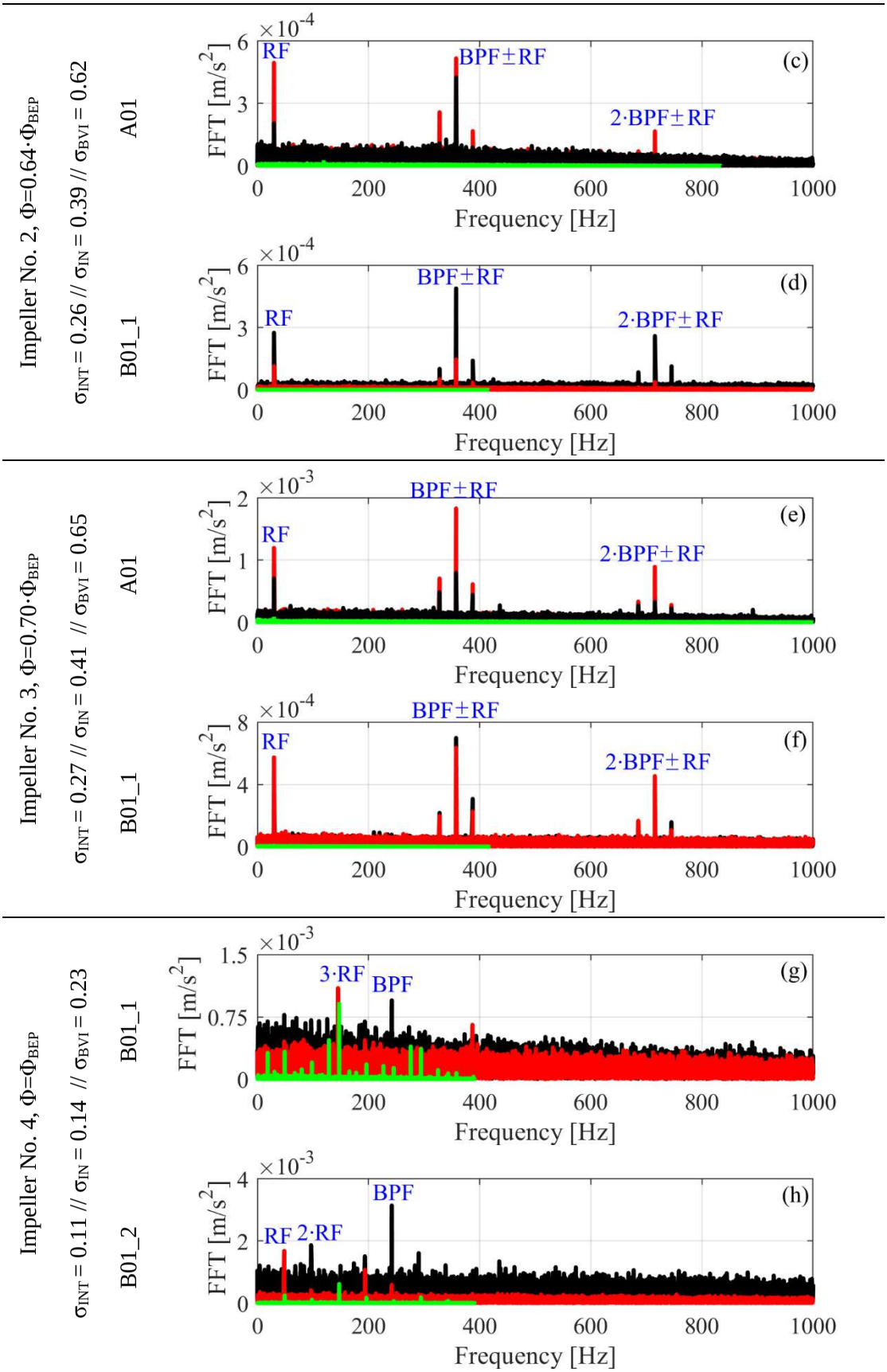

Σχήμα 7. 4 Πεδία συχνοτήτων περιβάλλουσας μετρήσεων ταλάντωσης για σημεία κοντά στην έναρξη του φαινομένου.

Επιπλέον η μελέτη του πεδίου συχνοτήτων της περιβάλλουσας (Σχ. 7.4) ενισχύει τις παρατηρήσεις που γίναν στο Σχ. 7.3 και σε σχέση με τη BPP περιοδικότητα του φαινομένου. Η χρήση λοιπόν της μεθόδου της Φασματικής Κύρτωσης και του εργαλείου Fast Kurtogram αναδεικνύει την κρουστική συμπεριφορά του φιλτραρισμένου σήματος, η οποία διαμορφώνεται από την αλληλεπίδραση του ρότορα και του στάτορα εντός της μηχανής.

Αυτή η συμπεριφορά επιβεβαιώνεται σε όλες τις μετρήσεις που γίνονται με αισθητήρες τοποθετημένους στο κέλυφος της μηχανής, σχετικά κοντά στην είσοδο της αντλίας όπου το φαινόμενο αναπτύσσεται. Επίσης αυτές οι παρατηρήσεις αναδεικνύουν την καθαρή αναλογία που υπάρχει μεταξύ των κρουστικών χτυπημάτων και της ενδόρρηξης των φυσσαλίδων ατμού (μηχανισμός βλάβης της σπηλαίωσης) και μεταξύ της διαμόρφωσης των κρουστικών σημάτων από τη BPF με το γεγονός ότι το φαινόμενο δημιουργείται και εξελίσεται εντός της περιστρεφόμενης πτερωτής. Αυτή η αναλογία είναι σημαντική γιατί συσχετίζει τα κριτήρια της διάγνωσης με το μηχανισμό βλάβης της σπηλαίωσης καθώς επίσης διότι απεμπλέκει τη διάγνωση από τα ιδιαίτερα χαρακτηριστικά κάθε πειραματικής διάταξης.

8. Συμπεράσματα

8.1 Σύνοψη των αποτελεσμάτων

Από τα αποτελέσματα της παρούσας διατριβής προκύπτουν τα ακόλουθα κύρια συμπεράσματα:

i. Η πτώση του επιπέδου στατικής πίεσης με χρήση της βάνας εισόδου στις δύο εγκαταστάσεις που μελετώνται, δημιουργεί τις συνθήκες εμφάνισης φυσσαλίδων ατμού-σπηλαίωσης. Η έκταση του φαινομένου και η δυναμική του συμπεριφορά εξαρτάται από τα γεωμετρικά και λειτουργικά χαρακτηριστικά της μηχανής.
ii. Η εμφάνιση του φαινομένου γίνεται πολύ πριν την πτώση του ύψους των αντλιών, ενώ η τελευταία λαμβάνει χώρα όταν η διφασική περιοχή έχει αναπτυχθεί μεταξύ των πτερυγώσεων.
iii. Στις ανοικτού τύπου πτερωτές, οι οπτικές παρατηρήσεις και τα υπολογιστικά αποτελέσματα επιβεβαιώνουν την ταυτόχρονη παρουσία διαφόρων τύπων σπηλαίωσης εντός της πτερωτής και πιο συγκεκριμένα:
    - Σπηλαίωση σε σχήμα σύννεφου.
    - Προσκολλημένες κοιλότητες σπηλαίωσης.
    - Ανάρροια σπηλαίωση.
iv. Το υπολογιστικό μοντέλο αναγνωρίζει εγκαίρως τη δημιουργία του φαινομένου εντός των πτερωτών που μοντελοποιούνται, ενώ προβλέπει με αποδεκτή συμφωνία τη θέση και την έκταση του. Επιπλέον αναδεικνύει τα εσωτερικά ροϊκά χαρακτηριστικά στο διάκενο του ακροπτερυγίου, τα οποία επιβεβαιώνουν την ανάπτυξη ανάρροιας σπηλαίωσης, στην περίπτωση της ανοικτού τύπου πτερωτής. Η τελευταία επηρρεάζει τη λειτουργία της αντλίας σε σπηλαίωση κυρίως στα σημεία πριν την πτώση του ύψους, καθώς μετά η ένταση των ανακυκλοφοριών μειώνεται αισθητά.
v. Από τις δοκιμές διαφορετικών τιμών πάχους στο διάκενο της ανοικτού τύπου πτερωτής συμπεραίνεται ότι η μείωση του πάχους οδηγεί σε αυξημένη ενέργεια προς το ρευστό, αυξημένη κατανάλωση ισχύος, ενώ ταυτόχρονα μειώνει την ένταση των ανακυκλοφοριών που τροφοδοτούν την ανάρροια σπηλαίωση.
vi. Η μελέτη των σημάτων θορύβου και ταλάντωσης αναδεικνύει τη δημιουργία κρουστικών χτυπημάτων στα σημεία πτώσης του ύψους. Σε μεγαλύτερα σ, αυτή η συμπεριφορά επικαλύπτεται από το συνολικότερο θόρυβο της μηχανής. Η ύπαρξη κρουστικών χτυπημάτων, δημιουργεί ακραίες τιμές πλάτους ταλάντωσης και AE, οι οποίες αλλοιώνουν την κατανομή των μετρήσεων. Επιπλέον, η παρούσα έρευνα επιβεβαιώνει την επιρροή στην τιμή της κύρτωσης, η οποία χρησιμοποιείται σε δεύτερη φάση για την φίλτρανση του μετρούμενου σήματος.
vii. Στο πεδίο συχνοτήτων, παρατηρούνται διεγερμένες περιοχές μεγάλου εύρους λόγω της ανάπτυξης του φαινομένου. Η ποσοτικοποίηση τους γίνεται με χρήση εργαλείων AE_{RMS} και powerband ταλάντωσης, τα οποία δεν επιτυγχάνουν να διαγνώσουν το φαινόμενο έγκαιρα σε όλες τις πτερωτές.
viii. Η χρήση της μεθόδου Φασματικής Κύρτωσης δημιουργεί φίλτρα τα οποία επιτυγχάνουν να εντοπίσουν τις διεγερμένες περιοχές σε όλες τις περιπτώσεις μηχανών που δοκιμάζονται στην παρούσα διατριβή. Επιπλέον επιτυγχάνει έγκαιρα να αναδείξει την καλυπτόμενη κρουστικότητα αλλά και την διαμόρφωσή της από την

αλληλεπίδραση ρότορα-στάτορα. Αυτά τα χαρακτηριστικά του φιλτραρισμένου σήματος αλλά και του πεδίου συχνοτήτων της περιβάλλουσας συνιστούν την προτεινόμενη μεθοδολογία διάγνωσης της σπηλαίωσης της παρούσας διατριβής.

8.2 Πρωτότυπα Στοιχεία και Συνεισφορά της Διατρίβης

Η συνεισφορά και τα πρωτότυπα στοιχεία της παρούσας διατριβής συνοψίζονται παρακάτω:

i. Η κατασκευή ειδικής εγκατάστασης στο ΕΥΜ του ΕΜΠ, η οποία επιτρέπει τη δοκιμή διαφορετικών πτερωτών σε ακτινική φυγοκεντρική αντλία σε συνθήκες ανάπτυξης του φαινομένου της σπηλαίωσης, με ταυτόχρονη οπτικοποίηση του φαινομένου.
ii. Η διενέργεια δοκιμών σε συνθήκες σπηλαίωσης, σε διαφορετικής γεωμετρίας πτερωτές στην εγκατάσταση του Πανεπιστημίου του Λάνκαστερ, οι οποίες συνοδεύονται από οπτικές παρατηρήσεις του φαινομένου.
iii. Η πιστοποίηση του διφασικού μοντέλου, το οποίο χρησιμοποιείται για τις προσομοιώσεις της ροής εντός των αντλιών σε μεγάλο εύρος συνθηκών λειτουργίας, με και χωρίς σπηλαίωση. Η πιστοποίηση περιλαμβάνει τη σύγκριση των αριθμητικά υπολογισμένων χαρακτηριστικών καμπυλών λειτουργίας με τις πειραματικές, καθώς και τη σύγκριση της αριθμητικά υπολογισμένη θέσης και έκτασης της διφασικής περιοχής με την οπτικά παρατηρούμενη από κατά τη διάρκεια των μετρήσεων.
iv. Την αξιολόγηση των εργαλείων AE_{RMS} και vibration powerband, με την ανάδειξη των πλεονεκτημάτων αλλά κυρίως των αδυναμιών που τα συνοδεύουν και εμποδίζουν τη διατύπωση ενός γενικού κριτηρίου διάγνωσης σπηλαίωσης.
v. Την επιλογή για την εφαρμογή της μεθόδου της Φασματικής Κύρτωσης, η οποία αιτιολογείται από τη μη-στάσιμη συμπεριφορά της τέταρτης στατιστικής ροπής (κύρτωσης) και η οποία χρησιμοποιείται επιτυχώς για το διαχωρισμό της σπηλαίωσης από τον υπόλοιπο θόρυβο της αντλίας και της αντλητικής διάταξης και καθιστά εφικτή τη διατύπωση ενός γενικού κριτηρίου διάγνωσης του φαινομένου, όταν αυτό αναπτύσσεται εντός των υδροδυναμικών μηχανών.
vi. Η συσχέτιση του κριτηρίου διάγνωση με το φυσικό μηχανισμό της βλάβης, δηλαδή των χτυπημάτων στο φιλτραρισμένο σήμα με την ενδόρρηξη των φυσαλίδων ατμού, και της διαμόρφωσης τους από το ροϊκό πεδίο που αναπτύσσεται από την αλληλεπίδραση ρότορα-στάτορα της μηχανής καθώς οι φυσαλίδες ενδορρηγνύονται εντός της περιστρεφόμενης πτερωτής.

8.3 Προτάσεις για Μελλοντική Έρευνα

Οι προτάσεις για μελλοντική έρευνα που προκύπτουν από τα συμπεράσματα της παρούσας διατριβής συνοψίζονται παρακάτω:

i. Η χρήση υπολογιστικών εργαλείων για τη μοντελοποίηση της διφασικής ροής, τα οποία επιτρέπουν την προσομοίωση της μεταβατικής συμπεριφοράς του φαινομένου, εντός της υδροδυναμικής μηχανής, ενώ θα θεωρούν μείγμα τριών ρευστών, νερού, ατμού και αέρα. Χρήση τεχνικών τα οποία επιτρέπουν την μοντελοποίηση της αλληλεπίδρασης μεταξύ του ρότορα και του στάτορα (π.χ. sliding mesh approach).

ii. Έλεγχος της επιρροής του μοντέλου που επιλέγεται για τη μοντελοποίηση της τύρβης, στην ανάπτυξη της διφασικής περιοχής. Επιλογή μοντέλου που περιγράφει την ατμοποίηση και τη συμπύκνωση της υγρής φάσης, χωρίς τη χρήση εμπειρικών συντελεστών.
iii. Διενέργεια δοκιμών σπηλαίωσης σε φυγοκεντρικές αντλίες με τη χρήση κλειστής δεξαμενής αναρρόφησης και αντλίας κενού, με στόχο την αποφυγή των επιπτώσεων που έχει στις μετρήσεις η χρήση της βάνας αναρρόφησης.
iv. Βελτίωση του εργαλείου Fast Kurtogram, με στόχο την κατασκευή φίλτρων, τα οποία θα επιτυγχάνουν την περισσότερο ευκρινή αποτύπωση των χτυπημάτων στο φιλτραρισμένο σήμα, καθώς και τη διαμόρφωση τους από το ροϊκό πεδίο.
v. Χρήση της προτεινόμενης μεθοδολογίας διάγνωσης (Φασματικής Κύρτωσης) σε διαφορετικού τύπου υδροδυναμικές μηχανές (αξονικές αντλίες και υδροστρόβιλοι) με στόχο την επιβεβαίωση των συμπερασμάτων που προκύπτουν από την παρούσα εργασία.
vi. Χρήση της προτεινόμενης μεθοδολογίας διάγνωσης (Φασματικής Κύρτωσης), σε συνδυασμό με διενέργεια μετρήσεων σε διάφορα σημεία στο κέλυφος της μηχανής, με στόχο την αναγνώριση της ακριβής θέσης ανάπτυξης της σπηλαίωσης.
vii. Μετρήσεις με στόχο τη συσχέτιση της εξέλιξης της φθοράς της μηχανής, με τα αποτελέσματα των μεθόδων που χρησιμοποιούνται για της διάγνωση της σπηλαίωσης.